Modelling the Oro Moraine Multi-Aquifer System: Role of Geology, Numerical Model, Parameter Estimation and Uncertainty.

by Joseph Beckers

A thesis
presented to the University of Waterloo
in fulfilment of the
thesis requirement for the degree of
Doctor of Philosophy
in
Earth Sciences

Waterloo, Ontario, Canada, 1998

© Joseph Beckers 1998

National Library
of Canada

Acquisitions and
Bibliographic Services

395 Wellington Street
Ottawa ON K1A 0N4
Canada

Bibliothèque nationale
du Canada

Acquisitions et
services bibliographiques

395, rue Wellington
Ottawa ON K1A 0N4
Canada

Your file Votre référence

Our file Notre référence

The author has granted a non-exclusive licence allowing the National Library of Canada to reproduce, loan, distribute or sell copies of this thesis in microform, paper or electronic formats.

The author retains ownership of the copyright in this thesis. Neither the thesis nor substantial extracts from it may be printed or otherwise reproduced without the author's permission.

L'auteur a accordé une licence non exclusive permettant à la Bibliothèque nationale du Canada de reproduire, prêter, distribuer ou vendre des copies de cette thèse sous la forme de microfiche/film, de reproduction sur papier ou sur format électronique.

L'auteur conserve la propriété du droit d'auteur qui protège cette thèse. Ni la thèse ni des extraits substantiels de celle-ci ne doivent être imprimés ou autrement reproduits sans son autorisation.

0-612-38218-4

Canada

The University of Waterloo requires the signatures of all persons using or photocopying this thesis. Please sign below, and give address and date.

Abstract

A steady-state groundwater model of the Oro Moraine aquifer system, near Barrie (Ontario), is developed. The model is used to identify controls on baseflow to the Minesing Swamp, a 7000 hectares wetland of international significance. Lithologic descriptions contained in the extensive database of well records are used to develop a hydrostratigraphic model of the predominantly glacial aquifer system and to distribute hydraulic conductivity using kriging. A pseudo-unsaturated model is developed and coupled with a recharge spreading layer to simulate the complex recharge mechanism for the aquifer system and to provide a simulation of both surface and subsurface fluxes to streams. A hypothetical flow problem illustrates that the model is able accurately predict recharge fluxes for heterogeneous aquifers. The Oro Moraine model is calibrated to water level data and stream gauge measurements using an inverse algorithm that is developed based on existing theory. The model is able to predict observed runoff and baseflow quantities to streams that are represented by Dirichlet boundaries. The adjoint method is used to identify recharge areas for streams and wetlands. It is found that the nearby Snow Valley upland is most important for groundwater discharge to the Minesing Swamp and that the Oro Moraine is the most critical recharge area for baseflow to the Matheson and Willow Creeks that flow into the swamp. Hypothetical urbanization impact calculations suggest that low to medium density residential development in the uplands will result in a modest decrease in baseflow to the swamp. This baseflow in turn only make up a relatively small fraction of the total inflow to the swamp. However, groundwater provides a relatively steady inflow of water over larger portions of the wetland which may be important for nutrient cycling and for maintaining soil moisture conditions. Subtle changes in baseflow may therefore have a large unforeseen impact on the ecology of the swamp. The urbanization impact calculations further indicate that a loss of recharge in the uplands may dramatically impact baseflow to the headwaters of local streams. The model thus provides valuable insight into crucial characteristics of the aquifer system. An application of stochastic methods to quantify model uncertainty is hampered by the complexity of the aquifer system.

Acknowledgements

I would like to thank my supervisor Dr. Emil Frind for his encouragement throughout this research. Thanks also to the members of my advisory committee and examining board, Dr. K. W. F. Howard, Dr. P. F. Karrow, Dr. S. D. Murphy, Dr. E. A. Sudicky and Dr. J. F. Sykes, for helpful suggestions and for critically reading this thesis. I am also grateful to John Molson, Paul Martin, Uli Mayer, Rob McLaren and other (former) colleagues at the University of Waterloo for their assistance, discussions and suggestions.

In-kind support provided by the Nottawasaga Valley Conservation Authority is gratefully acknowledged. Special thanks to Peter Barnett of the Ontario Geological Survey for shedding some light on the complex geologic history of the study area. Thanks also to several consulting firms in the Barrie area that provided access to their reports regarding previous hydrogeological investigations.

Thanks to Uli for the many challenging bike rides to clear my brain of the dust accumulated during too many hours spent behind a computer screen. Thanks also to Kelly and Sebastien for opening my mind to the merits of running in blazing winter storms. I am still not fully convinced though.

Finally, I would like to thank my wife Lavinia for critically reading the original draft of this thesis and for her patience in waiting for that long overdue honeymoon.

The development of the original modeling methodology [*Martin and Frind*, 1998] was funded by an NSERC operating grant to Dr. E. O. Frind, while the present work was supported by an NSERC Strategic Project Grant focused on the development of methodologies for the protection of groundwater resources in complex glacial aquifer systems in Canada. I further received funding through two Ontario Graduate Scholarships and two Davis Memorial Scholarships in Ecology.

Contents

Abstract iv

Acknowledgements vi

1 Introduction 1

2 Parameterization 9

2.1 Introduction 9

2.2 Theory and Methodology 14

2.2.1 Kriging of Hydrostratigraphic Contacts 14

2.2.2 Kriging of Hydraulic Conductivity Fields 18

2.2.3 Random Field Generation 21

2.2.4 Semivariogram Parameters 23

2.3 Summary 25

3 Numerical Model 28

3.1 Introduction 28

3.2 Theory 31

3.3 Hypothetical Example 37

3.4 Summary 46

4 Adjoint Method 48

4.1 Introduction 48

4.2 Theory 49

4.3 Hypothetical Example 54

4.4 Summary 57

5 Inverse Model 60

5.1 Introduction 60

5.2 Theory and Methodology 65

5.2.1 Calibration Performance Measures 65

5.2.2 Calibration Parameters 67

5.2.3 Minimization Algorithm 71

5.2.4 Combined Use of Head and Flow Data 74

5.2.5 Covariance of Parameter Estimates 76

5.3 Summary 77

6 Uncertainty Analysis 81

6.1 Introduction 81

6.2 Sources of Uncertainty 85

6.3 Theory 86

6.4 Summary 87

7 Oro Moraine Hydrostratigraphy 89

7.1 Introduction 89

7.2 Study Area 89

7.2.1 Physiography 89

7.2.2 Boundaries 91

7.2.3 Geology 93

7.3 Hydrostratigraphic Interpretation 95
    7.3.1 Water Well Records 95
    7.3.2 Conceptual Model 97
7.4 Interpolation Strategy and Parameters 99
7.5 Elevation of Hydrostratigraphic Contacts 105
7.6 Thickness of Hydrostratigraphic Units 105
7.7 Discussion 105

8 Oro Moraine Model 127
8.1 Introduction 127
8.2 Finite Element Mesh 127
8.3 Boundary Conditions 130
8.4 Groundwater Abstraction 133
8.5 Calibration Data 134
    8.5.1 Water Level Data 135
    8.5.2 Stream Gauge Measurements 142
    8.5.3 Calibration Weights 146
8.6 Model Calibration 146
    8.6.1 Kriging Procedure 147
    8.6.2 Initial Conductivity Distribution 149
    8.6.3 Parameters for the Recharge Boundary 155
    8.6.4 Optimization of Average Conductivities 156
    8.6.5 Local Conductivity Optimization 165
    8.6.6 Final Calibration Statistics 167
    8.6.7 Calibrated Conductivity Fields 179
8.7 Water Mass Balance 186
8.8 Uncertainty in Water Mass Balance 188
8.9 Discussion 194

9 Impact of Urbanization **199**

9.1 Introduction 199

9.2 Minesing Swamp Water Mass Balance 201

9.3 Recharge Areas 203

9.4 Urbanization Impact 208

9.5 Discussion 211

10 Summary and Conclusions **213**

Bibliography **222**

A Cross-sections **235**

List of Tables

2.1 Equations of variogram models with range a and sill b. The nugget effect is ignored. The power model applies to non-stationary datasets; for this model b is a measure of the slope and a is the power. . . . 26

5.1 Calibration options implemented in WATFLOW. 80

7.1 Legend of materials used in cross-sectional interpretation. 96

7.2 Parameters for the spatial interpolation of the aquifer/aquitard contacts. 103

7.3 Comparison of (I) ordinary and (II) universal kriging using the correlation (r^2), bias (equation 7.1) and error (equation 7.2) measures. 104

8.1 Pumping wells included in the numerical model. Information was obtained from (1) Barrie PUC 1995-1996 listings and (2) MOEE database. 134

8.2 Parameters for the spatial interpolation of the water level data. . . 136

8.3 Statistics for (I) back-kriging scattergrams and (II) trend surface analysis for temporal variations in water level data. 136

8.4 Flow rates (m^3/s) for the 4 stations used in this study. 146

8.5 Hydraulic conductivities (m/s) for lithologic categories. Literature values are from *Freeze and Cherry*, [1979]. Field data are from pumping and slug tests in the Waterloo Moraine as listed in *Martin and Frind*, [1998]. The two K distributions (I) and (II) are discussed in the text. 151

8.6 Model semivariogram parameters and anisotropy for the distribution Initial (II). The Alliston aquifer complex is comprised of AQFR3, AQTD4 and AQFR4 155

8.7 Head and flow calibration measures for several zonation scenarios considered in the text. 157

8.8 Initial and calibrated average log hydraulic conductivity values (m/s) for the 4 zonation scenarios. 159

8.9 Head and flow calibration measures discussed in the text. 161

8.10 Calibrated average log hydraulic conductivity values (m/s), with associated uncertainty expressed as one standard deviation, for the 4 objective functions. 162

8.11 Calibrated RSL log hydraulic conductivity values (m/s), with associated uncertainty expressed as one standard deviation for zonation 3, objective 2. 164

8.12 Calibration statistics for streamflow data. 168

8.13 Calibration statistics for kriged and point water levels expressed as standard deviation σ, the average error avg(ϵ) and the average absolute value of error avg$|\epsilon|$. 177

8.14 Simulated water mass balance as absolute values and as percentages of the groundwater (gw) or surface water (sw) budget, water surplus (ws), and total streamflow (tf). The water surplus is 8.53 m^3/s. . . 187

8.15 Variance in water mass balance due to uncertainty in (I) average conductivity of hydrostratigraphic units and (II) intra-formational heterogeneity. 189

9.1 Urbanization impact for target area 1 in Oro Moraine. Shown are baseflow quantities (m^3/s) and percent changes with respect to unperturbed base case. 210

9.2 Urbanization impact for target area 2 in Snow Valley Upland. Shown are baseflow quantities (m^3/s) and percent changes with respect to unperturbed base case. 211

9.3 Urbanization impact for target area 3 in Innisfill Uplands. Shown are baseflow quantities (m^3/s) and percent changes with respect to unperturbed base case. 211

List of Figures

1.1 Outline of the study area together with major geographic features. The black square in the insert indicates the location of the study area in central Ontario. 3

2.1 Multi-aquifer modeling strategy after *Martin and Frind* [1998]. . . . 12

2.2 Relationship between the hydrostratigraphic interpretation and database management. 15

2.3 Relationship between kriged, unconditional and conditional random fields through kriging error ϵ, after *RamaRao et al.* [1995]. 22

2.4 Example of an exponential semivariogram. 25

3.1 Seepage face algorithm for ponding on a low K zone (dashed rectangle) with or without the use of an RSL. Neumann boundary conditions are indicated by vertical arrows; Solid squares indicate seepage (Dirichlet) nodes. 37

3.2 Finite element meshes used in WATFLOW and SWMS 2D simulations together with parameters of the flow problem. 38

3.3 Piezometric head distribution ($\Delta h = 2$ m) and fluxes at upper model boundary for the case of a fully unconfined upper aquifer. 40

3.4 Pseudo-unsaturated relationship (solid line) together with van Genuchten relationships for aquifer (dotted line) and aquitard (dashed line) materials. 41

3.5 Piezometric head distribution ($\Delta h = 2$ m) and fluxes at upper model boundary for the case of a partially confined upper aquifer. 43

3.6 Piezometric head distribution ($\Delta h = 2$ m) and fluxes at upper model boundary for the case of a partially confined upper aquifer with the use of an RSL. 45

4.1 Normalized sensitivity of baseflow to river boundary to perturbations in recharge. 55

4.2 Range of validity for derivatives with respect to recharge. Solid line shows linear predictions from adjoint method. Squares designate actual changes resulting from direct parameter perturbations. . . . 56

4.3 Normalized sensitivity of baseflow to river boundary to perturbations in K_{xx} (top panel) and K_{zz} (bottom panel). 58

5.1 Cross-sectional schematic illustrating the pilot point zone of influence as indicated by its kriging weight contours (dotted lines, $\Delta w = 0.1$). 69

7.1 Topography of the study area. 90

7.2 a) Regional groundwater levels. b) Location of boreholes with static water level observations used to generate map a). 92

7.3 Wells and cross-sections used in the hydrostratigraphic interpretation. 98

7.4 Cross-section 33. Refer to Table (7.1) for a legend of the geologic materials. 100

7.5 Experimental and model variograms for TAQ1-BAQ2. 101

7.6 Experimental and model variograms for TAQ3-BAQ4. 102

7.7 Kriged and adjusted elevation of TAQ1. Triangles indicate the boreholes where this contact is observed. 106

7.8 Kriged and adjusted elevation of BAQ1. Triangles indicate the boreholes where this contact is observed. 107

7.9 Kriged and adjusted elevation of TAQ2. Triangles indicate the boreholes where this contact is observed. 108

7.10 Kriged and adjusted elevation of BAQ2. Triangles indicate the boreholes where this contact is observed. 109

7.11 Kriged and adjusted elevation of TAQ3. Triangles indicate the boreholes where this contact is observed. 110

7.12 Kriged and adjusted elevation of BAQ3. Triangles indicate the location where this contact is observed. 111

7.13 Kriged elevation of TAQ4. Triangles indicate the boreholes where this contact is observed. 112

7.14 Kriged elevation of the bedrock surface (BEDR). Triangles indicate the boreholes where bedrock is observed. 113

7.15 Thickness of Aquitard 1 (AQTD1). White areas indicate regions where this unit pinches out. 114

7.16 Thickness of Aquifer 1 (AQFR1). White areas indicate regions where this unit pinches out. 115

7.17 Thickness of Aquitard 2 (AQTD2). White areas indicate regions where this unit pinches out. 116

7.18 Thickness of Aquifer 2 (AQFR2). White areas indicate regions where this unit pinches out. 117

7.19 Thickness of Aquitard 3 (AQTD3). White areas indicate regions where this unit pinches out. 118

7.20 Thickness of Aquifer 3 (AQFR3). White areas indicate regions where this unit pinches out. 119

7.21 Thickness of Aquitard 4 (AQTD4). White areas indicate regions where this unit pinches out. 120

7.22 Thickness of Aquifer 4 (AQFR4). White areas indicate regions where this unit pinches out. 121

7.23 Thickness of the overburden. 123

7.24 Outcrop of the hydrostratigraphic units at the land surface. 125

8.1 2D finite element mesh. Dirichlet boundaries are shown in grey. Triangles indicate stream gauge stations. 128

8.2 3D finite element mesh illustrating the complexity in the geometry of the hydrostratigraphic units and the related vertical discretization of the domain. 129

8.3 Meteorologic stations used in calculating the water surplus distribution. Point data values shown are average annual precipitation rates (mm/yr) listed for these stations adjusted with an evapotranspiration rate of 500 mm/yr. 131

8.4 Water surplus distribution (mm/yr) and soil infiltration capacity after *NVCA*, [1988]. 132

8.5 Semivariograms for water level data. 137

8.6 Interpolated water levels for AQFR1. Triangles indicate data locations. White areas designate regions where the aquifer is unsaturated over its whole thickness or where this unit pinches out. 138

8.7 Interpolated water levels for AQFR2. Triangles indicate data locations. White areas designate regions where the aquifer pinches out. 139

8.8 Interpolated water levels for AQFR3. Triangles indicate data locations. 140

8.9 Interpolated water levels for AQFR4. Black triangles indicate data derived from overburden wells; white triangles correspond to bedrock wells. 141

8.10 Total flow (solid line) and baseflow (dashed line) for the Edenvale station during the period 1995-1996. 143

8.11 Seasonal and long term variations in total flow and baseflow for the Willow Creek (top panels) and Nottawasaga River (bottom panels) stations. 145

8.12 Role of borehole descriptions and hydrostratigraphic interpretation in kriging of log conductivity. Cross-section 33 and distribution Initial (I) were used (Table 8.5). 148

8.13 Effect of mesh discretization on spatial interpolation of log conductivity. 150

8.14 Experimental and model semivariograms for AQTD1-AQFR2 and distribution initial (II). 153

8.15 Experimental and model semivariograms for AQTD3-AQFR4 and distribution initial (II). 154

8.16 Sensitivity of head and flow calibration measures to RSL conductivity, uniform water surplus R (lines in middle panel), and residual saturation S_r. Base case parameters are $K_{RSL} = 10^{-2.7} m/s$, the variable water surplus (Figure 8.4) indicated by the triangles in the middle panel, and $S_r = 0.1$. 156

8.17 Convergence behaviour of the minimization algorithm. 163

8.18 Convergence behaviour for the pilot point calibration (KRIGMODE=2). The dashed line separates the first and second phase of the calibration as discussed in the text. 166

8.19 Vertically averaged simulated water levels for AQFR1. Triangles indicate data locations. White areas designate regions where the aquifer is predicted to be unsaturated over its whole thickness or where this unit pinches out. 169

8.20 Residuals for AQFR1. White values correspond to over-predicted heads, black values designate under-predicted heads. 170

8.21 Vertically averaged simulated water levels for AQFR2. Triangles indicate data locations. White areas designate regions where the aquifer is predicted to be unsaturated over its whole thickness or where this unit pinches out. 171

8.22 Residuals for AQFR2. White values correspond to over-predicted heads, black values designate under-predicted heads. 172

8.23 Vertically averaged simulated water levels for AQFR3. Triangles indicate data locations. 173

8.24 Residuals for AQFR3. White values correspond to over-predicted heads, black values designate under-predicted heads. 174

8.25 Vertically averaged simulated water levels for AQFR4. Black triangles indicate data derived from overburden wells; white triangles correspond to bedrock wells. 175

8.26 Residuals for AQFR4. White values correspond to over-predicted heads, black values designate under-predicted heads. 176

8.27 Scatter-plot of observed and simulated hydraulic heads. Black squares indicate overburden wells; white squares correspond to bedrock wells. 178

8.28 Average vertical conductivity distribution for AQTD1. Black triangles indicate borehole locations, white triangles designate pilot points. 180

8.29 Average horizontal conductivity distribution for AQFR1. Black triangles indicate borehole locations, white triangles designate pilot points. 181

8.30 Average vertical conductivity distribution for AQTD2. Black triangles indicate borehole locations, white triangles designate pilot points. 182

8.31 Average horizontal conductivity distribution for AQFR2. Black triangles indicate borehole locations, white triangles designate pilot points. 183

8.32 Average vertical conductivity distribution for AQTD3. Black triangles indicate borehole locations, white triangles designate pilot points. 184

8.33 Average horizontal conductivity distribution for the Alliston aquifer complex. Black triangles indicate borehole locations, white trangles designate pilot points. 185

8.34 Baseflow histograms for a) Bear Creek, b) Minesing Swamp, c) Matheson Creek and d) Willow Creek determined from a Monte Carlo analysis regarding the intra-formational heterogeneity for AQTD3. The square and line designate the mean value and 95 % confidence bounds calculated with the first order second moment method. . . . 190

8.35 Baseflow histograms for a) Bear Creek, b) Minesing Swamp, c) Matheson Creek and d) Willow Creek determined from a Monte Carlo analysis regarding the intra-formational heterogeneity for AQFR2. The square and line designate the mean value and 95 % confidence bounds calculated with the first order second moment method. . . . 191

8.36 Calibration measure histograms corresponding to the Monte Carlo runs for AQTD3 and AQFR2. The vertical dashed lines designate the final calibrated values for J_h and J_f. 192

9.1 Simplified water mass balance for Minesing Swamp. Values shown are in m^3/s. 203

9.2 Hydraulic head distribution at the water table. 205

9.3 Recharge areas for baseflow to Minesing Swamp. 206

9.4 Recharge areas for baseflow to Matheson Creek and Willow Creek upstream from Minesing Swamp. 207

9.5 Target areas for urbanization impact calculations. 209

Chapter 1

Introduction

Groundwater is an important natural resource which is increasingly impacted by human activities. As a result, this resource is threatened by contamination and over-usage. There is now general awareness that a need exists for a strategy to protect the groundwater resource. This need has certainly arisen for the Regional Municipality of Waterloo (Ontario) which depends on groundwater for most of its water supply. Water is extracted from the Waterloo Moraine, an extensive glacial aquifer complex extending over a 400 km^2 area. The Region is presently conducting a comprehensive program to inventory the groundwater resource, to define its susceptibility to contamination, and to create a basis for optimal management and protection strategies. The Waterloo Center for Groundwater Research (now CRESTech) has been assisting the Region through the development of a modeling methodology that addresses these objectives. This methodology is presented in *Martin* [1994] and *Martin and Frind* [1998].

A crucial aspect of the the Waterloo Moraine study was the delineation of capture zones for the Region's municipal wells. Groundwater flow paths in heterogeneous systems are largely controlled by the often complex inter-connectedness of the high conductivity units [e.g., *Fogg*, 1986]. In a glacial aquifer system, aquitard windows provide preferential pathways for the movement of water across these confining units. In order to realistically incorporate the hydrostratigraphy in the numerical model, *Martin* [1994] chose a three-dimensional (3D) approach.

Besides the inherent complexity of the glacial aquifer system, one of the main challenges of the Waterloo Moraine study was the limited availability of direct hydrogeologic information. The extensive borehole log database was therefore used to interpret and interpolate the glacial lithology into a consistent multi-aquifer model, and to define continuous 3D hydraulic conductivity fields within each of the hydrostratigraphic units, making use of kriging. The 3D free-surface finite element code WATFLOW [*Molson et al.*, 1992] was used to calibrate the model and to determine the hydraulic potentials and flow vectors. Capture zones for the municipal well fields of the Region were then delineated using particle-tracking.

The Oro Moraine is located near Barrie, Ontario (Figure 1.1). Similar to the Waterloo Moraine, the dominant physiographic features have been formed by extensive glacial activity. The Oro or Bass Lake Moraine, the Innisfill Uplands and the region to the west of Barrie (Snow Valley) are part of the Simcoe Uplands. These uplands are separated by steep-sided stream valleys and bordered to the west by the Minesing Basin which is part of the Simcoe Lowlands. Land use is mainly agricultural. Notable exceptions are some forested areas in the uplands, the aforementioned wetlands and the city of Barrie. A hydrogeologic investigation of this area is particularly important because the pervious sands of the Oro Moraine are thought to be the main recharge area for subsurface drainage towards the Minesing Swamp, a 7000 hectares reserve which has been categorized as "a world class resource of international significance", owing to its diverse habitats and its numerous rare plant species [*NVCA*, 1995]. Many new subdivisions are rapidly being built around the Barrie area. The groundwater system will to some degree be affected by this urbanization. Any change in the groundwater system might also affect the swamp. It is thus urgent to determine the role of groundwater in the water balance of the Minesing Swamp and to identify sensitive recharge areas for this wetland.

The present study was therefore initiated with a detailed investigation of the Oro Moraine multi-aquifer system as the main objective. The geology of the aquifer system will be interpreted using the methodology of *Martin* [1994]. The inferred hydrostratigraphy will be used as a basis for the numerical model. The numerical model is needed to identify controls on baseflow to the Minesing Swamp and to manage the impact of the urbanization.

The water mass balance of the swamp is characterized by both surface and subsurface contributions. Thus, the second objective is to develop a modeling approach with which the relative importance of these contributions can be determined. A limitation of Martin's work was the manual trial-and-error calibration of the complex Waterloo Moraine model. Automated calibration is needed instead to obtain

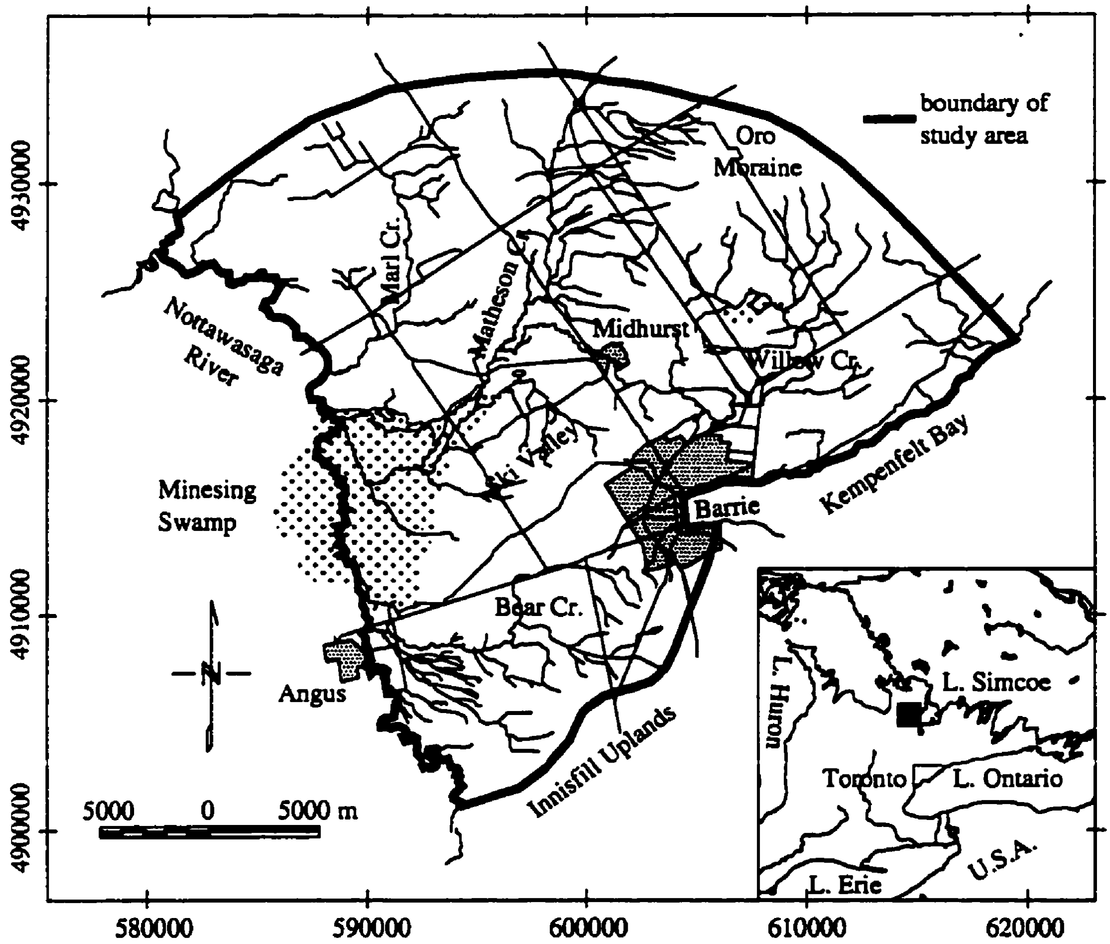
boundary of study area
Oro Moraine
Marl Cr.
Matheson Cr.
Midhurst
Willow Cr.
Nottawasaga River
Ski Valley
Minesing Swamp
Barrie
Kempenfelt Bay
Bear Cr.
Angus
Innisfil Uplands
N
5000 0 5000 m
L. Huron
L. Simcoe
Toronto
L. Ontario
U.S.A.
L. Erie
4930000
4920000
4910000
4900000
580000
590000
600000
610000
620000

Figure 1.1: Outline of the study area together with major geographic features. The black square in the insert indicates the location of the study area in central Ontario.

optimal conductivity estimates and to determine the best match to both water level and streamflow measurements. This study therefore also focuses on the implementation of an inverse algorithm in the numerical model and the testing of this algorithm in the context of the Oro Moraine problem setting. Lastly, uncertainty in the model output needs to be quantified to determine the significance of the urbanization impact calculations. An important constraint on the numerical aspects of this study will be to keep the modeling framework consistent with the methodology developed by Martin in order to incorporate the concepts of automated calibration and uncertainty analysis in the capture zone delineation for the Waterloo Region.

Many studies have demonstrated the critical role of the spatial variability in hydraulic conductivity on groundwater flow and dispersion [e.g., *Gelhar and Axness*, 1983; *Dagan*, 1982a, 1984; *Sudicky*, 1986; *Mackay et al.*, 1986; *Freyberg*, 1986]. Thus, the potential for a groundwater flow model to simulate the response of an actual system is directly affected by the reliability of the inferred hydraulic conductivity distribution. Model predictions are subject to uncertainty because this distribution is largely unknown.

Uncertainty in the hydraulic conductivity distribution is affected by its parameterization in the numerical model. Martin's approach combines a zonation with a geostatistical method, resulting in multiple conductivity fields. Besides being able to represent the sharp conductivity contrasts that may exist at aquifer/aquitard contacts, this approach also reduces uncertainty in the interpolated values of hydraulic conductivity: In the aquifer system as a whole, values may vary by more than 10 orders of magnitude. This variability is significantly less within a single hydrostratigraphic unit (hereafter also referred to as zone), and the interpolation uncertainty is reduced accordingly. However, another consequence is that uncertainty in the zonation needs to be taken into account. A third level of uncertainty results from the indirect nature of the conductivity information. Although, the lithologic descriptions may provide information on the relative magnitude of hydraulic conductivities, they are not very well suited to constrain absolute values of this property.

Stochastic analyses regarding the effect of spatially variable or uncertain model parameters have received considerable attention in the literature. Popular techniques include discrete sampling methods such as Monte Carlo [*Warren and Price*, 1961; *Freeze*, 1975; *Clifton and Neuman*, 1982; *Gomez-Hernandez and Gorelick*, 1989] or Latin Hypercube [e.g., *Iman and Conover*, 1980] and direct methods either based on first order and second moment analysis [*Benjamin and Cornell*, 1970; *Sagar*, 1978; *Dettinger and Wilson*, 1981] or on a small perturbation expansion [*Gelhar*, 1976; *Tang and Pinder*, 1977; *Bakr et al.*, 1978; *Dagan*, 1982b].

In the discrete sampling approach, the flow equation is solved in a deterministic manner for a large number of realizations of a random field. No assumptions have to be made regarding the stochastic process. However, these methods are computationally intensive. Direct methods on the other hand, derive their computational efficiency from a first order approximation of the stochastic process. As a result their application is suitable only for a limited range of parameter variability [e.g., *Gutjahr and Gelhar*, 1981; *Dagan*, 1979, 1982b]. Because the perturbation expansion approach and the first-order and second-moment method approximate the stochastic process to the same order they yield the same information on this process [*Dettinger and Wilson*, 1981]. The first-order and second-moment analysis is used here because it is not restricted to certain stationarity assumptions. The limitations associated with this method will be investigated using results obtained from Monte Carlo simulations.

Dagan [1982b] illustrated through the use of Bayes' Theorem the important role of data in reducing uncertainty in model input parameters. Conditioning of a random field ensures that it is consistent with a set of observations. Different realizations of a conditioned random field will have identical values at the data locations. The data that are used in spatially distributing hydraulic conductivity are the lithology-derived conductivity values. These data need to be taken into account when assessing model uncertainty.

Model uncertainty can be further reduced using data regarding the groundwater flow system itself. The effect of this information is incorporated during the model calibration. Several studies have shown the importance of water level data in the assessment of model uncertainty [e.g., *Clifton and Neuman*, 1982, *Townley and Wilson*, 1983; *Hoeksema and Kitanidis*, 1985b]. The trial-and-error calibration of the Waterloo Moraine model as performed by *Martin* [1994] is inappropriate in this context. Instead, a systematic procedure is needed to adequately address the effect of the calibration data on model uncertainty.

Following the introduction of stochastic analyses in the hydrogeological sciences, it was soon realized that the uncertainty associated with parameter estimates needs to be incorporated in the model calibration [e.g., *Gavelas et al.*, 1976; *Yeh and Soon*, 1976; *Cooley*, 1977; *Wilson et al.*, 1978; *Shah et al.*, 1978]. Since then a major effort has been directed towards the statistical solution of the inverse problem [*Neuman and Yakowitz*, 1979; *Neuman*, 1980; *Cooley*, 1982; *Kitanidis and Vomvoris*, 1983; *Hoeksema and Kitanidis*, 1984; *de Marsily* [1984]; *Townley and Wilson*, 1985; *Sun and Yeh*, 1985; *Carrera and Neuman*, 1986a, 1986b; *LaVenue and Pickens*, 1992; *RamaRao et al.*, 1995]. The main aspects that distinguish these estimation algorithms are the parameterization of the hydraulic conductivity field, the adoption of a measure of the goodness of the calibration, and the solution strategy used to minimize this measure [*McLaughlin and Townley*, 1996]. The parameterization has a strong influence on the well-posedness of the inverse problem and is therefore the most crucial aspect of a calibration algorithm.

Two calibration strategies are needed in the context of the adopted conductivity parameterization: a zonation approach, where piecewise constant properties are assumed [e.g., *Neuman and Yakowitz*, 1979], and the pilot point method, developed by *de Marsily* [1984], in which conductivities are optimized at selected locations (the pilot points) and their effect on the conductivity distribution is determined using kriging. A bias may exist in the initial conductivity distribution because the lithologic descriptions provide indirect information regarding this parameter. Geologic factors such as fracturing of the till aquitards and/or differential levels of consolidation as a result of the glacial load are also not taken into account by these data. The average conductivity of the hydrostratigraphic units will therefore be optimized in a strictly zonation-based approach. A combined pilot point/kriging parameterization is subsequently used to locally improve the conductivity distribution within each of these units. Based on a literature review, this appears to be the first application of such a joint parameterization in an automated calibration.

Uncertainty in model predictions may also result from the conceptualization of the processes that govern the behaviour of the actual system in the numerical code. Watershed-scale investigations are typically undertaken using free-surface (water table) models, where recharge to the groundwater system is determined as a fixed fraction of the total precipitation. However, when the surficial geology is heterogeneous, the actual amount of water that enters the subsurface is subject to considerable uncertainty. Compact unfractured tills will only transmit a minor part of the water surplus. Runoff will direct the excess water from these impermeable regions either to more pervious areas where infiltration is more easy, or to water courses. Under such conditions it may be desirable to include the surface water component of the hydrologic cycle in the numerical model. Information on the complete land-based part of the hydrologic cycle is also useful to determine a water mass balance for the Minesing Swamp and to put the urbanization impact calculations into perspective.

Coupling of the surface and subsurface flow systems implies that the vadose zone must be taken into account. On a regional scale, a physically rigorous incorporation of the unsaturated zone is not possible, not only because the required detailed information regarding the unsaturated zone parameters is unavailable, but also due to mesh discretization requirements. An alternative may be to use a pseudo-unsaturated model with a fairly coarse mesh discretization appropriate for regional-scale modeling. Pseudo-unsaturated models include the unsaturated zone through an ad-hoc scaling of the hydraulic conductivities above the water table [*Bathe and Khosgoftaar*, 1979; *Desai and Li*, 1982]. This model can be coupled with a high conductivity recharge spreading layer [*Therrien and Sudicky*, 1996] that is draped over the top of the model domain. Water is transmitted laterally in this layer, approximating the process of rainfall runoff.

Although the proposed numerical model is not suitable for a transient analysis of the complex short-term interaction of the surface and subsurface flow systems during discrete rainfall events, it has the capability of providing a steady-state water mass balance for these systems. This will be shown in the framework of the Oro Moraine study. A hypothetical cross-sectional example of a multi-aquifer system will further be used to illustrate the advantages and limitations of the modeling approach.

The emphasis of the present study thus is on adapting existing modeling techniques to the specific challenges posed by the Oro Moraine problem setting, rather than on the development of novel numerical methods. In Chapter (2), the hydraulic conductivity parameterization is discussed. Chapter (3) concerns the modified flow model. Simulations of the hypothetical flow problem are also detailed. The effect of different numerical representations of this flow problem on inferred recharge areas for a stream will be illustrated making use of the adjoint method, which is covered in Chapter (4). The adjoint method is a means of calculating sensitivity coefficients which will also be used in the model calibration (Chapter 5) and the uncertainty analysis (Chapter 6). Although the various modeling techniques have a solid basis in the literature, a major challenge still lies in their successful application to the complex Oro Moraine problem. A hydrostratigraphic model of the study area is developed in Chapter (7). Next, the numerical groundwater model is developed and calibrated. The simulated water mass balance and its uncertainty will also be discussed in Chapter (8). Chapter (9) concerns the water mass balance of the Minesing Swamp, the identification of recharge areas for the groundwater component of this mass balance and the analysis of several hypothetical urban development scenarios. In the last chapter, a summary is given regarding the Oro Moraine study and the performance of the numerical tools that have been developed as part of it.

Chapter 2

Parameterization

2.1 Introduction

Physical properties in the subsurface vary in space due to the complex processes that lead to the formation of geologic deposits. The spatial distribution of, for example, hydraulic conductivity affects groundwater flow. In a numerical model, different parameterizations of this property may lead to different simulation outcomes. This parameterization therefore is a crucial part of the modeling effort and needs to be such that the true variability in conductivity is adequately represented for the purpose of the study. A discussion of existing techniques to spatially distribute hydraulic conductivity is given below. This discussion should be seen within the context of the available information. Data consist of descriptions of lithofacies encountered during the drilling of water wells. Direct measurements of hydraulic conductivity from pumping or slug tests are unavailable in sufficient quantities and have not been used directly. However, direct measurements from the Waterloo Moraine [*Martin and Frind*, 1998] have been used in determining appropriate conductivity values for some of the lithofacies.

Inferring hydraulic properties from indirect observations such as lithologic descriptions is less reliable than making use of direct measurements. This raises questions regarding the reliability of the conductivity distribution that will be obtained in this manner. This issue will be addressed in the context of the model calibration (Chapter 5). Direct measurements of hydraulic conductivity, such as transmissivity values obtained from pumping tests, are typically limited to the high conductivity units that are targets as sources of drinking water. In his landmark paper, *Fogg* [1986] has shown that the inter-connectedness of these high conductivity zones, particularly in the vertical sense, is crucial in the behaviour of a groundwater system. The geometry and hydraulic properties of the aquitards will therefore to a large extent dictate the response of a multi-aquifer system. The lithologic descriptions that are used here provide crucial information on these low conductivity units.

Koltermann and Gorelick [1996] give an extensive review of different approaches used to mimic heterogeneity in sedimentary deposits. They distinguish a broad three-way classification into structure-imitating, process-imitating and descriptive methods. The authors further discriminate two main classes of process imitating methods: aquifer model calibration methods and geologic process models. The former of these two classes is part of any development of a groundwater model and will be discussed extensively in Chapter (5). Although on a regional scale, geologic process models may be useful in predicting heterogeneity generated in e.g. fluvial or near-shore environments, such models are inappropriate for the complex glacial deposits considered here. Descriptive and structure imitating methods are more appropriate in this context.

In discussing descriptive methods, *Koltermann and Gorelick* [1996] state that these methods "produce deterministic images of the subsurface by combining site-specific and regional data with conceptual depositional models and geologic insight". *Martin* [1994] took this approach to develop a model of the Waterloo Moraine hydrostratigraphy. Because of the complexity of the Moraine he found that it was necessary to have a strong "expert" component in the development of this model. Automated structure-imitating procedures such as indicator kriging that can generate spatial distributions of high and low conductivity zones based on well information [e.g., *Johnson and Dreis*, 1989] will not perform well in such environments. The expert component consists of a cross-sectional interpretation of borehole geologic logs with the objective of resolving the complicated aquifer geometry and inter-connectedness. The procedure developed by Martin will also be used here and is described in detail in Chapter (7).

Given the conclusions drawn by *Fogg* [1986], the development of a detailed hydrostratigraphic image of the subsurface that defines the spatial connections between individual aquifers is very important. Such an approach has several other appealing consequences. Sharp hydraulic conductivity contrasts that may exist between the aquifers and the confining units can be adequately represented. Hydraulic conductivity values in a glacial aquifer system can easily vary by 10 orders of magnitude or more. As a consequence, large uncertainties arise when interpolating point observations of hydraulic conductivity. However, within a single hydrostratigraphic unit the total variability in hydraulic conductivity may be considerably lower and the interpolation uncertainty is reduced accordingly.

The division of the subsurface into discrete aquifers and aquitards constitutes a megascopic level of characterization, where inter-formational relationships are defined. The individual hydrostratigraphic units are often made up of several types of geologic materials, each with their characteristic depositional environment. As a result, the hydrostratigraphic units exhibit fluctuations and/or trends in the flow properties. Although intra-formational, this heterogeneity is also at the megascopic level. Depositional characteristics within a single geologic unit (e.g., stratification) result in spatial variability in these properties at the macroscopic scale. Finally, microscopic heterogeneity is related to pore-to-pore variability in these properties.

Most groundwater models rely on the assumption that Darcy's law is valid and therefore use a spatial discretization at or above the macroscopic level for which this law is defined. In the case of a regional-scale groundwater model, the horizontal discretization is typically on the order of hundreds of meters. At this scale, macroscopic and microscopic variability must be lumped into effective uniform parameters for each of the finite elements that constitute this discretization. For hydraulic conductivity this lumping will lead to anisotropic properties within each element. Megascopic variability in flow properties must be explicitly defined throughout the model domain if the accurate identification of groundwater flow paths is of concern. This variability is less important for water mass balance calculations.

From the above scale considerations it is clear that conductivity variations within each aquifer and aquitard still need to be considered. The lithologic descriptions contained in the borehole logs are used to generate the input for this distribution. Thus, in the classification of *Koltermann and Gorelick* [1996], the parameterization approach that is taken is two-fold: a descriptive method is used to develop a hydrostratigraphic image of the subsurface, whereas a structure-imitating method is used to define heterogeneity in the aquifers and aquitards. As a result, two sets of point observations need to be spatially distributed: the interpreted elevations of the hydrostratigraphic contacts and lithology-derived hydraulic conductivity values (Figure 2.1).

Classical methods for spatially distributing point data include minimum cur-

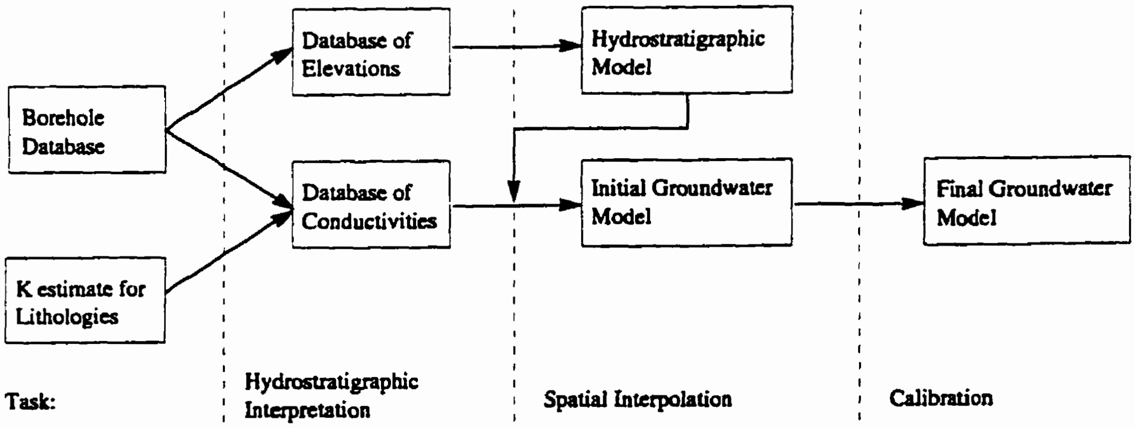
Borehole Database
K estimate for Lithologies
Database of Elevations
Database of Conductivities
Hydrostratigraphic Model
Initial Groundwater Model
Final Groundwater Model
Task:
Hydrostratigraphic Interpretation
Spatial Interpolation
Calibration

Figure 2.1: Multi-aquifer modeling strategy after *Martin and Frind* [1998].

vature procedures, moving average routines, least-squares polynomials and (cubic) splines. The use of these techniques is not recommended because they assume independence of the data values [e.g., *Davis*, 1986]. The spatial dependence that naturally exists in geologic data is better represented by spatial statistical techniques, which make use of the autocorrelation exhibited by these so-called regionalized variables. These methods reproduce observed spatial patterns without a need to address the mechanism by which geologic deposits form [*Koltermann and Gorelick*, 1996]. Because of this appealing feature, spatial statistical methods are well suited for describing the intra-formational conductivity distribution in complex glacial deposits.

Following the early work of *Matheron* [1973], and its subsequent application to aquifer characterization [*Delhomme*, 1978, 1979], kriging in particular has become very popular in hydrogeology. Kriging enables the user to calculate uncertainty in the estimated parameters. These properties are important for stochastic analyses as well as model calibration as will become clear in the corresponding chapters. *Martin* [1994] used kriging to define the conductivity distribution and his approach will be used here, although in modified form.

The total spatial variability in regionalized variables can be considered the sum of two parts: one part is taken into account by the kriged values, but the other part cannot be taken into account due to the uncertainty that exists between sample points [*Delhomme*, 1979]. The resulting smoothness of the kriged field may have significant effects on groundwater flow. For example, as the kriged elevation of a hydrostratigraphic contact reduces to a smooth surface away from the borehole locations, the presence of aquitard windows is likely underestimated. These windows are important preferential conduits for vertical flow between the aquifers. Several studies have focused on circumventing this limitation by incorporating subjective information in the kriging procedure within the framework of Bayesian statistics [e.g., *Omre and Halvorson*, 1989]. This approach was successfully applied to the simulation of geologic contacts on a local scale by *Nobre and Sykes* [1992]. However, due to the complex inter-relationship between the different geologic units in a regional-scale glacial aquifer system, any guess regarding the location of these contacts is prone to error and Bayesian kriging has not been considered here.

A further drawback of kriging is that it only yields a single realization of the interpolated field with (large) uncertainties in the interpolated values. This limitation and the lack of spatial variability can be addressed by random field generation. *Koltermann and Gorelick* [1996] give a review of several techniques that generate Gaussian random fields. Discussions on differences between these methods revolve mainly around computational cost. Here, the method of *Robin et al.* [1993] will be used for stochastic analyses. This algorithm is readily available as the code FGEN92 which can generate cross-correlated random fields in three or fewer dimensions.

Although Gaussian-based spectral techniques better represent observed fluctuations in hydraulic conductivity than kriging does, they fail to reproduce patterns of spatial connectivity specific to extreme values, as was pointed out by *Journel and Alabert* [1987]. This spatial connectivity of either high or low conductivity zones may lead to preferential pathways or barriers for groundwater flow and transport. The importance of this spatial connectivity in simulating groundwater flow patterns was illustrated in a recent comparison of several inverse methods [*Zimmerman et al.*, 1998]. This paper showed the failure of most (Gaussian-based) techniques in reproducing patterns of spatial connectedness.

Non-Gaussian based algorithms such as indicator-based methods, simulated annealing, boolean methods and Markov chains may better represent such features through the consideration of higher order statistics, training images and/or "soft" data [*Koltermann and Gorelick*, 1996]. The main limitation of these methods lies in the amount of information that needs to be fed to them and, given the type and quality of the data available in this study, these methods will not be considered here.

Below, the use of kriging in the spatial interpolation of the hydrostratigraphic contacts is discussed and relevant equations are given. The same is done in the context of interpolating hydraulic conductivity. Random field generation based on the geostatistical parameters that also underlie the kriging technique is covered. Lastly, procedures and equations used in establishing the experimental and model semivariograms that are needed to determine these geostatistical parameters are discussed.

2.2 Theory and Methodology

2.2.1 Kriging of Hydrostratigraphic Contacts

The borehole information that will be used in this study consists of a list of lithofacies and the depths at which these are encountered. Based on a conceptual model of the multi-aquifer system, lithologies with similar hydraulic properties are grouped together in hydrostratigraphic units. A database is set up for each hydrostratigraphic contact that separates these units. This database consists of a set of point observations on the elevation $z(x, y)$ of this contact at the boreholes (Figure 2.2). Spatial interpolation of the point data is necessary to provide information on the elevation of the aquifer-aquitard contact throughout the study area.

Kriging is a statistically optimal method for linearly interpolating a given distribution of point observations of some random function d. Like many statistical methods, kriging relies heavily on the assumption that the underlying dataset is normally distributed. The statistical characterization of the dataset is therefore exhausted by its first two moments. Kriging equations can be found throughout the literature [e.g., *Journel and Huijbregts*, 1978; *Davis*, 1986; *Deutsch and Journel*, 1992]. However, because of their importance for this study, these equations will also be given here. The interpolated value d_{kr} at a location $\mathbf{x}_p$ is determined as a linearly weighted average of the N available observations $d(\mathbf{x}_i)$:

$$d_{kr}(\mathbf{x}_p) = \sum_{i=1}^{N} w_i d(\mathbf{x}_i) \tag{2.1}$$

where the w_i are the unknown kriging weights. The interpolated value, which may be considered to be a single realization of the random function d, needs to be

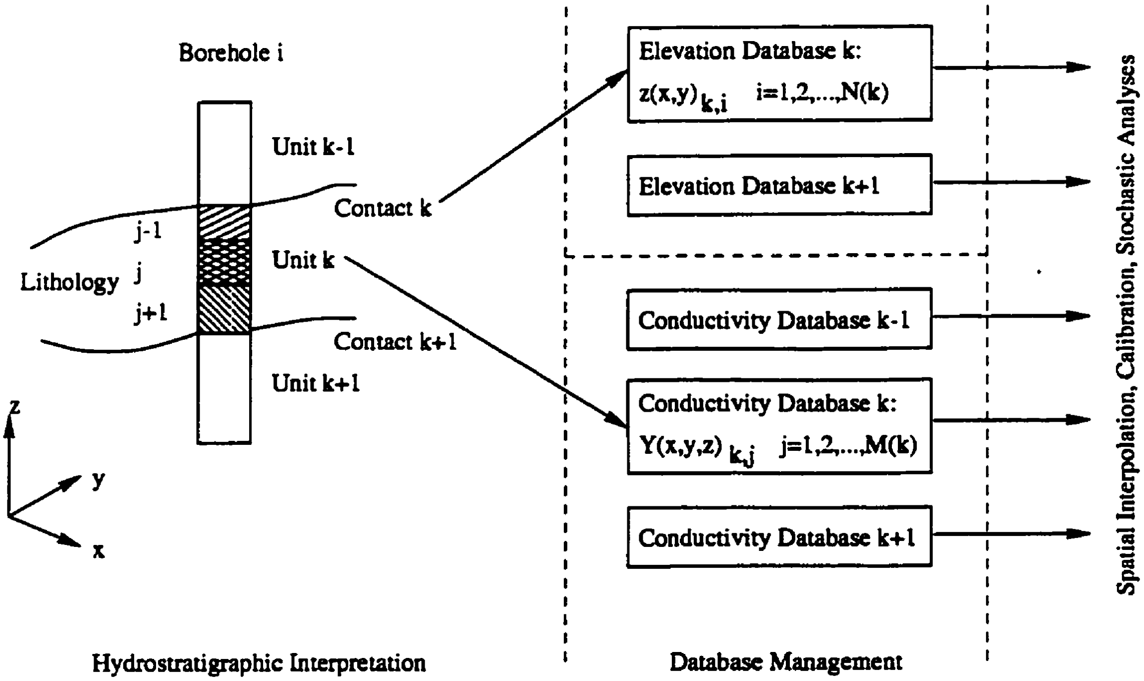
Borehole i
Unit k-1
Contact k
j-1
Lithology j
j+1
Unit k
Contact k+1
Unit k+1
z
y
x
Elevation Database k:
z(x,y)k,i i=1,2,...,N(k)
Elevation Database k+1
Conductivity Database k-1
Conductivity Database k:
Y(x,y,z)k,j j=1,2,...,M(k)
Conductivity Database k+1
Spatial Interpolation, Calibration, Stochastic Analyses
Hydrostratigraphic Interpretation
Database Management

Figure 2.2: Relationship between the hydrostratigraphic interpretation and database management.

unbiased (no systematic over- or under-estimation) and have a minimum estimation variance. Mathematically, these two conditions can be expressed as:

$$\begin{aligned} E[d_{kr}(\mathbf{x}_p) - d_0(\mathbf{x}_p)] &= 0 \\ E[(d_{kr}(\mathbf{x}_p) - d_0(\mathbf{x}_p))^2] &= min \end{aligned} \tag{2.2}$$

where E is the expectation and d_0 is the true value of the realization. It follows directly from the first of these requirements that kriging is an exact interpolator, i.e. the original data values will be preserved. In deriving the kriging equations it is further necessary to assume that d is stationary by increments which implies that:

$$\begin{aligned} E[d(\mathbf{x} + \mathbf{s}) - d(\mathbf{x})] &= 0 \\ E[(d(\mathbf{x} + \mathbf{s}) - d(\mathbf{x}))^2] &= 2\gamma(\mathbf{s}) \end{aligned} \tag{2.3}$$

in which $\gamma(\mathbf{s})$ is the semivariance which only depends on $\mathbf{s}$. Thus for any separation vector $\mathbf{s}$, the increment $d(\mathbf{x}+\mathbf{s}) - d(\mathbf{x})$ has zero expectation and a variance independent of the location $\mathbf{x}$. A random variable that conforms to these requirements is referred to as "intrinsic". Note that this requirement is weaker than that of second-order (wide-sense or weak) stationarity for which the first two moments of d itself need to be invariant with respect to a shift in location. With the additional constraint that the sum of the interpolation weights needs to equal unity, the kriging equations are set up to determine these weights. Several types of kriging equations have been derived for different restrictions regarding the data mean.

If d is first-order stationary, simple kriging or ordinary kriging may be utilized. The difference between simple and ordinary kriging is that the former requires knowledge of the data mean whereas the latter merely requires that this mean is invariant. For a set of three point observations (or control points), the ordinary kriging equations are given in matrix form as:

$$\begin{bmatrix} \gamma(\mathbf{s}_{11}) & \gamma(\mathbf{s}_{12}) & \gamma(\mathbf{s}_{13}) & 1 \\ \gamma(\mathbf{s}_{12}) & \gamma(\mathbf{s}_{22}) & \gamma(\mathbf{s}_{23}) & 1 \\ \gamma(\mathbf{s}_{13}) & \gamma(\mathbf{s}_{23}) & \gamma(\mathbf{s}_{33}) & 1 \\ 1 & 1 & 1 & 0 \end{bmatrix} \begin{bmatrix} w_1 \\ w_2 \\ w_3 \\ \mu \end{bmatrix} = \begin{bmatrix} \gamma(\mathbf{s}_{1p}) \\ \gamma(\mathbf{s}_{2p}) \\ \gamma(\mathbf{s}_{3p}) \\ 1 \end{bmatrix} \tag{2.4}$$

where $\gamma(\mathbf{s}_{ij})$ is the semivariance between points i and j and μ is a so-called Lagrange multiplier which ensures that the objectives (2.3) are met. The kriging weights thus depend on the location of the point data and the interpolation point p, as well as the covariance of the dataset as defined by the semivariogram. It can be seen that assumption (2.3) has to be made in order to be able to assess the semivariances in (2.6). If this assumption is not made the semivariances are a-priori unknown and the matrix equation cannot be solved.

In theory, all available control points should be used in evaluating (2.4). However, for large datasets this matrix problem may become exceedingly large and as the more distant data points will have a negligible weight in the estimation procedure, only a subset of the available data points is used in practice. Once the kriging weights have been determined, the interpolated value is given by (2.1) and the estimation variance $\sigma^2_{kr}(\mathbf{x}_p)$ is determined as:

$$\sigma^2_{kr}(\mathbf{x}_p) = \sum_{i=1}^{N} w_i \gamma(\mathbf{s}_{ip}) + \mu \tag{2.5}$$

where for this particular case $N = 3$. The estimation variance can, for example, be used as input to a groundwater model in order to address issues regarding the effect of parameter uncertainty on model predictions.

Geologic deposits and other phenomena that cannot be considered to be completely random, naturally exhibit background trends. If this is the case, d is no longer first-order stationary. Two possible approaches for removing background trends will be considered here. The first is to define the global shape of the trend (also referred to as drift) over the entire domain using a low-order polynomial regression, e.g. in two dimensions:

$$\hat{d}(x, y) = c_0 + c_1 x + c_2 y + c_3 x^2 + c_4 xy + c_5 y^2 + \ldots \tag{2.6}$$

where x and y refer to easting and northing respectively, and where the unknown coefficients c_i have to be estimated. After subtracting the trend, the residual dataset can again be interpolated using simple or ordinary kriging. If the drift is complex the low-order polynomial approximation (2.6) will not be valid for the entire domain and the interpolation will be biased if the data residuals (data values minus drift) are no longer normally distributed. If this is the case it is better to use universal kriging. Contrary to ordinary kriging, a low order polynomial with undetermined coefficients similar to (2.6) is embedded in the estimation procedure in order to remove the drift. For a first order polynomial (2.4) is replaced by:

$$\begin{bmatrix} \gamma(s_{11}) & \gamma(s_{12}) & \gamma(s_{13}) & 1 & x_1 & y_1 \\ \gamma(s_{12}) & \gamma(s_{22}) & \gamma(s_{23}) & 1 & x_2 & y_2 \\ \gamma(s_{13}) & \gamma(s_{23}) & \gamma(s_{33}) & 1 & x_3 & y_3 \\ 1 & 1 & 1 & 0 & 0 & 0 \\ x_1 & x_2 & x_3 & 0 & 0 & 0 \\ y_1 & y_2 & y_3 & 0 & 0 & 0 \end{bmatrix} \begin{bmatrix} w_1 \\ w_2 \\ w_3 \\ \mu \\ c_1 \\ c_2 \end{bmatrix} = \begin{bmatrix} \gamma(s_{1p}) \\ \gamma(s_{2p}) \\ \gamma(s_{3p}) \\ 1 \\ x_p \\ y_p \end{bmatrix} \tag{2.7}$$

in which the x_i and y_i are the coordinates of the control points and the interpolation point. It can be seen that the coefficients c_i and thus the drift are estimated locally, depending only the control points that are used in (2.7). In this way a more complex drift can be accounted for than by using the global regression (2.6). Both universal kriging and ordinary kriging combined with the calculation of a global trend will be considered in the interpolation of the hydrostratigraphic contacts.

2.2.2 Kriging of Hydraulic Conductivity Fields

An initial estimate of the hydraulic conductivity (K) distribution in each of the aquifers and aquitards is obtained from the same lithologic descriptions that are used to determine an image of the hydrostratigraphy. A single value of hydraulic conductivity is assigned to each of the lithofacies. These conductivity values are then interpolated using kriging (Figure 2.1).

As kriging is a Gaussian-based procedure, it requires that the data are normally distributed. It is typically held that the probability density function for hydraulic conductivity is log-normal so that Gaussian concepts can be used under a log-transformation $Y = log(K)$. Earliest evidence for the normal distribution of log hydraulic conductivity was derived from petroleum reservoir core samples [e.g., *Law*, 1944]. More recently, detailed local-scale hydrogeologic investigations have also found evidence for this log-normal behaviour [e.g., *Sudicky*, 1986, and later *Woodbury and Sudicky*, 1991]. The normal behaviour of log conductivity will also be assumed at the megascopic scale which is reasonably confirmed by available information [*Hoeksema and Kitanidis*, 1985a].

The interpolation strategy taken in the present study is modified from that used by *Martin* [1994]. For each hydrostratigraphic unit, Martin obtained a single estimate of the horizontal ($K_{xx} = K_{yy}$) and vertical (K_{zz}) hydraulic conductivity the boreholes by taking arithmetic and harmonic averages of the K values for the lithologies that were grouped together in that unit (in Figure 2.2 this averaging would be done for the three lithologies that make up unit k at the borehole). The log conductivity values obtained in this manner were then interpolated in a two-dimensional fashion to obtain laterally heterogeneous but vertically uniform hydraulic conductivity fields for the hydrostratigraphic units (examples are shown in *Martin and Frind*, 1998, Figures 12-14). It was found that the vertical averaging results in strong lateral differences and locally extreme values of anisotropy (K_{xx}/K_{zz}). A single lithologic description at a certain borehole will lead to isotropic effective properties (or alternatively any assumed small-scale anisotropy). If on the other hand many different lithologies are encountered at a certain borehole, the anisotropy ratio may become exceedingly high (values in excess of 10^6 were not uncommon). Macroscopic anisotropy thus depends critically on the number and accuracy of the lithologic descriptions and the strong lateral variability that was observed does not seem physically realistic.

Another consequence of the vertical averaging is that heterogeneities tend to be smoothed out. However, as was pointed out by *Gelhar et al.* [1977], the dimensionality of the hydraulic conductivity parameterization needs to be in accordance with that of the numerical model, i.e. vertically averaged properties are appropriate for two-dimensional models but a three-dimensional characterization should be used here.

The present approach is to interpolate the hydraulic conductivity values corresponding to the individual lithologic descriptions in a three-dimensional fashion without any vertical averaging over the extent of the hydrostratigraphic units. The conductivity value corresponding to a certain lithofacies is stored directly in the database of the corresponding hydrostratigraphic unit (Figure 2.2). Each hydrostratigraphic unit is therefore characterized by a 3D database of Y values. In the absence of a drift, the ordinary kriging equation (2.4) can be used to interpolate the point observations of log conductivity.

The spatial distribution of hydraulic conductivity is related to the geologic materials that are present in the subsurface. The distance over which Y values are correlated depends on the geometry of these deposits. More than often, several scales of heterogeneity will exist. The total variability in log hydraulic conductivity will be considered to consist of a small-scale and a large-scale component: $Y = Y_s + Y_l$.

The small-scale variability is caused by depositional features such as stratification. In the Borden aquifer, clay lenses in an otherwise sandy medium play an important role in the spatial distribution of hydraulic conductivity. The geometry of these depositional features typically results in anisotropy of the correlation structure. *Sudicky* [1986] found an isotropic horizontal correlation length $\lambda_x = \lambda_y = 2.8$ m and a vertical correlation length λ_z of 0.12 m. As discussed earlier, the small-scale variability leads to effective anisotropic flow properties for the finite elements of a regional-scale flow model. At the micro-scale, the orientation of clay minerals may also result in anisotropy. *Freeze and Cherry* [1979] state that "core samples of clays and shales seldom show vertical anisotropy greater than 10:1, and it is usually less than 3:1".

Large-scale conductivity variations depends on the geometry of sediment bodies such as eskers or glacial outwash fans [e.g., *Stanford and Ashley*, 1998]. *Delhomme* [1979] lists correlation lengths for log transmissivity from large-scale investigations ranging from less than 1 km for aluvial aquifers to over 10 km for limestone and chalk aquifers. These values where confirmed in a more elaborate statistical analysis by *Hoeksema and Kitanidis* [1985a] who also found correlation lengths of 6-16 km for two glacial aquifer systems in North America.

In discussing upscaling, *McLaughlin and Townley* [1996] suggest that the effective conductivity tensor may be calculated using, for example, the expressions derived by *Gelhar and Axness* [1983] for porous media flow. For the particular 3D case of a layered medium ($\lambda_x = \lambda_y > \lambda_z$) and mean flow parallel and perpendicular to the stratification, the following expressions for the principal components of the hydraulic conductivity tensor are given:

$$K_{ii} = K_g exp\left\{\sigma_s{}^2(1/2 - g_{ii})\right\} \qquad i \in (x, y, z) \tag{2.8}$$

where K_g is the geometric mean of hydraulic conductivity determined by the interpolated large-scale values Y_l, $\sigma_s{}^2$ is the small-scale variance, and where the components g_{ii} depend on the small-scale statistical anisotropy $\rho = \lambda_x/\lambda_z$ as:

$$\begin{aligned} g_{xx} = g_{yy} &= \frac{1}{2}\frac{1}{\rho^2 - 1}\left[\frac{\rho^2}{(\rho^2-1)^{1/2}} tan^{-1}\left\{(\rho^2-1)^{1/2}\right\} - 1\right] \\ g_{zz} &= \frac{\rho^2}{\rho^2-1}\left[1 - \frac{1}{(\rho^2-1)^{1/2}} tan^{-1}\left\{(\rho^2-1)^{1/2}\right\}\right] \end{aligned} \tag{2.9}$$

Thus the large-scale log conductivity Y_l is needed to determine the spatial distribution of K_g. This is achieved by grouping the lithologic descriptions contained in the borehole logs over intervals that correspond to the average vertical extent of the finite elements: lithologies that are observed over larger intervals are "cut up" into shorter sections whereas thin lithologies are grouped together, resulting in a single geometrically averaged conductivity. A semivariogram analysis is then used to determine the geostatistical properties of Y_l that are needed in the spatial interpolation.

The parameters $\sigma_s{}^2$ and ρ are needed to incorporate the effect of the (small-scale) variability below the discretization scale on the effective conductivity tensor (2.8). The small-scale variance is determined from the semivariogram for Y_l: as anisotropy is largely a function of the number of stratigraphic layers that are encountered, it depends on the thickness of the finite elements. For each element, $\sigma_s{}^2$ is determined by the semivariance at the vertical lag distance corresponding to this thickness. Upscaling is thus achieved to the scale of the finite elements, rather than the scale of the stratigraphic units as done by *Martin* [1994]. Although the value of ρ is unknown, its exact magnitude is not very important when the statistical anisotropy exceeds 10 (as in the case of the Borden aquifer). For this perfectly stratified case, the upscaling equations reduce to arithmetic and harmonic averages.

The upscaling parameters are quite uncertain as a result of data limitations. Anisotropy is thus poorly resolved. However, a sensitivity analysis of *Gillham and Farvolden* [1974] on a generic two-aquifer system suggests that the anisotropy ratio for such systems is not too critical, with K_{xx} being the important parameter in the aquifers and K_{zz} governing flow through the aquitards. This low sensitivity of a multi-aquifer system to anisotropy is caused by the predominantly horizontal flow in the aquifers and vertical flow in the aquitards when conductivity contrasts between these units exceed 100.

2.2.3 Random Field Generation

The kriged log conductivity values are smoothed single realizations of the actual random functions and, away from the data points, (large) uncertainties may exist in the interpolated parameters. Random fields can be used to account for this uncertainty and lack of spatial variability. As will be explained below, these two issues are strongly related. Random hydraulic conductivity fields have been used extensively to investigate the effect of spatial variability and uncertainty in this parameter [e.g., *Clifton and Neuman*, 1982; *Gomez-Hernandez and Gorelick*, 1989].

The spectral-based Gaussian random field generator of *Robin* [1991] requires the specification of a constant data mean and a covariance structure defined by the parameters of an exponential model semivariogram. As a result, the random fields that are being generated are wide-sense stationary, consistent with the specified parameters, but otherwise unconstrained, and are therefore referred to as being unconditioned. At any particular location, the mean and variance of a large number of realizations (ensemble) is equal to the data mean and variance.

In some cases it is desirable to also constrain the random fields with observations. In a hydrogeologic context, this conditioning of random fields on actual data values was first introduced by *Delhomme* [1978]. His paper gives a procedure for

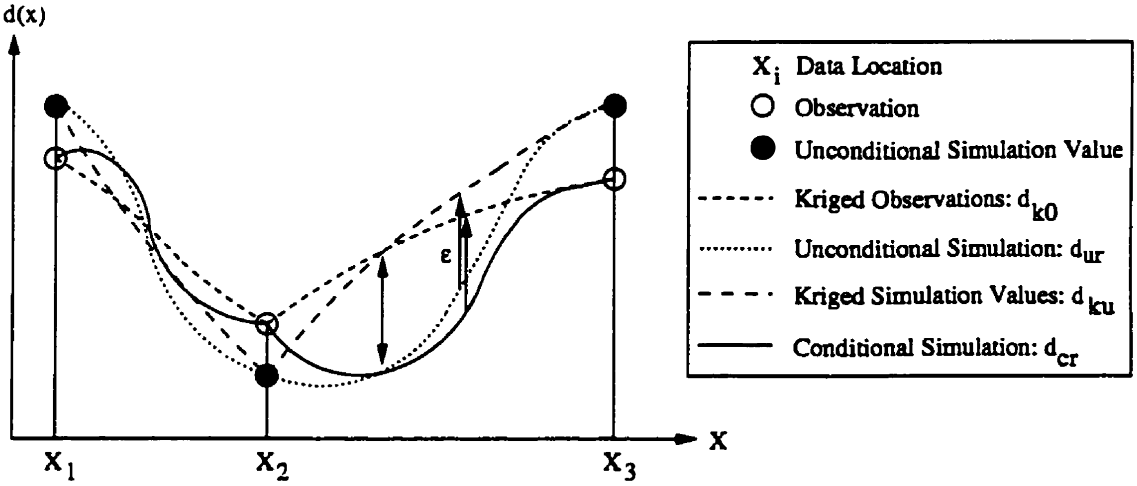
d(x)
x
x_1
x_2
x_3
ε
X_i Data Location
○ Observation
● Unconditional Simulation Value
Kriged Observations: d_{k0}
Unconditional Simulation: d_{ur}
Kriged Simulation Values: d_{ku}
Conditional Simulation: d_{cr}

Figure 2.3: Relationship between kriged, unconditional and conditional random fields through kriging error ϵ, after *RamaRao et al.* [1995].

this conditioning, which for completeness is briefly re-iterated here: the first step consists of generating a large number of unconditional realizations of a random field. Next, each of these realizations has to be made consistent with the data values. This is achieved by determining the values of the unconditioned field d_{ur} at the data locations. These values are then interpolated using kriging to given an estimate d_{ku} at any location $\mathbf{x}$. The actual data values d_0 are also kriged to give estimates d_{k0} at these locations. The value d_{cr} for the conditioned realization then is given by:

$$d_{cr}(\mathbf{x}) = d_{k0}(\mathbf{x}) + [d_{ur}(\mathbf{x}) - d_{ku}(\mathbf{x})] \tag{2.10}$$

The conditional realizations are consistent with the actual observed values d_0 due to the fact that kriging is an exact interpolator. Furthermore, these realizations are still consistent with the specified covariance because the kriging error is independent of the kriged values [*Delfiner*, 1975]. This error, which is replaced by the difference $d_{ur}(\mathbf{x}) - d_{ku}(\mathbf{x})$ in (2.10), is added to the kriged values. The resulting fluctuations in the conditional realizations reflect the uncertainty that exists in the kriging estimate [*Delhomme*, 1979].

Figure (2.3) illustrates the relationship between kriged, unconditional and conditional fields. If a large number of conditional realizations is generated, their mean and variance will be equal to the kriging estimate and variance. Because the kriging variance is less or equal to the data variance, it can be seen that conditioning leads to a reduction in the variability between individual realizations as this variability is to some degree constrained by the observations. This was shown mathematically through the use of Bayes' Theorem by *Dagan* [1982b]. The variance reduction is largest near the data points and decreases away from these points depending on the correlation length(s) of the heterogeneity. Many studies have considered the effect of this conditioning on uncertainty in groundwater flow [*Delhomme*, 1978, 1979; *Clifton and Neuman*, 1982; *Townley and Wilson*, 1983; *Hoeksema and Kitanidis*, 1985b]. Chapter (6) will discuss techniques for uncertainty analyses in groundwater flow.

The conditioning algorithm has been implemented as a post-processing routine to FGEN92. Furthermore, it has been made possible to determine random field values on the nodes or elemental centroids of an irregularly shaped mesh: Using FGEN92, the random field is generated on a fine spaced regular grid. This field is subsequently interpolated to the coarser finite element mesh using either the nearest grid value or an inverse distance weighting scheme.

2.2.4 Semivariogram Parameters

Algorithms based on the theory of regionalized variables require the specification of geostatistical parameters. The first step in determining these parameters is to calculate an experimental semivariogram (sometimes simply called variogram) from the available observations. In order to do this it is necessary to assume ergodicity of the processes that created the geologic deposits for which measurements of the random function d are made. Under this assumption, inferences on the increment $d(\mathbf{x}+\mathbf{s})-d(\mathbf{x})$ in (2.3) can be replaced by spatial moments of the single realization of $d(\mathbf{x})$ that is present in the subsurface. The semivariance $\gamma(s)$ in (2.3) is then defined as [*Matheron*, 1973]:

$$\gamma(\mathbf{s}) = \frac{1}{2N(\mathbf{s})} \sum_{i=1}^{N(\mathbf{s})} (d(\mathbf{x}_i + \mathbf{s}) - d(\mathbf{x}_i))^2 \tag{2.11}$$

where N(s) is the number of data points that are separated by a vector s. For multi-dimensional datasets, experimental variograms are created for each of the principal directions of anisotropy of the correlation structure and $\mathbf{s}$ is reduced to its modulus $|s|$. These principal directions can be found iteratively by calculating variograms for different directions of the separation vector to find those angles for which the correlation length of the heterogeneity shows extremes. A single variogram suffices if the heterogeneity is isotropic and the separation vector can be replaced by its modulus. If the data points are irregularly spaced, they need to be re-grouped by classes of distance and direction so that the mean squared differences in (2.11) can be calculated.

Under conditions of second-order stationarity, the semivariance and the covariance $\sigma^2(\mathbf{s})$ are related as:

$$\gamma(\mathbf{s}) = \sigma^2(0) - \sigma^2(\mathbf{s}) \tag{2.12}$$

where $\sigma^2(0)$ is the covariance at zero lag equal to the variance of the random function d. The autocorrelation of d is defined as $\sigma^2(\mathbf{s})/\sigma^2(0)$. Where the covariance provides a measure of the similarity of neighboring points, the semivariogram measures its dissimilarity. Both functions are therefore efficient tools for assessing the spatial correlation structure of regionalized variables. From (2.12) it follows that theoretically $\gamma(\mathbf{s}) = 0$ for zero lag distance. However, in practice semivariograms often show a non-zero cut-off at the origin. This so-called nugget effect either occurs due to observation error or is a measure of spatial variability below the measurement scale of a certain parameter.

Other features of a semivariogram are the range and the sill. The sill is the asymptotic value of the semivariance for large separation distances (Figure 2.4). The range is that lag distance at which the semivariance levels off to the sill. The range thus is a measure of the correlation length of the heterogeneity. The integral-scale [e.g., *Dagan*, 1982b] is closely related to the range but is not used as much.

de Marsily [1984] detailed a number of features that may be observed in experimental variograms which indicate "problems" with the data. A completely flat experimental variogram where the semivariance does not depend on lag distance is indicative of a random dataset with no spatial correlation. If the semivariogram does not level off, the dataset is most likely not stationary. Nested structures, where heterogeneity exists at more than one scale are indicated by a leveling off of the semivariogram at multiple lag distances and increasing values of the semivariance. Indeed, one of the major limitations of semivariogram-based methods is

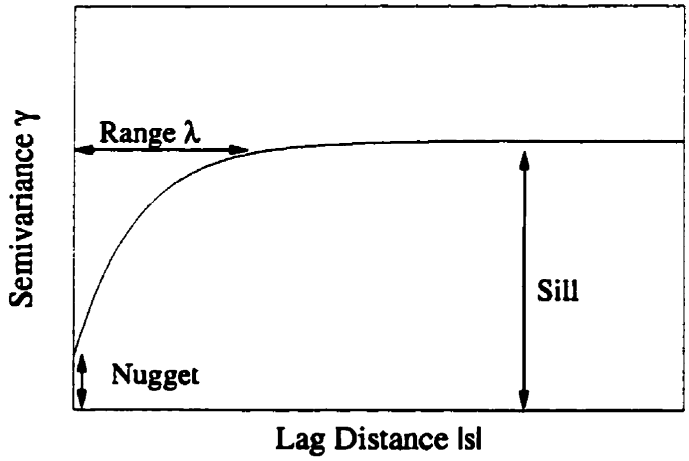

Figure 2.4: Example of an exponential semivariogram.

that a single dominant correlation scale is assumed. Nested structures will only show up if the different scales of heterogeneity are fairly similar. Heterogeneity at a scale much larger than the measurement network will not be apparent in the semivariogram; while heterogeneity at much smaller scales results in a semivariogram nugget. Fluctuations in the sill have been observed by *Johnson and Dreis* [1989] and correspond to very periodic structures. Such structures may also lead to a hole effect, where after reaching a maximum the semivariogram levels off at a lower asymptotic semivariance.

Range, sill and nugget are parameters of the model variogram that is fitted to the experimental variogram. Several types of model variograms have been proposed to fit the observed behaviour of experimental variograms. Some widely used models are given in Table (2.1). The model variograms are used to calculate the semivariances in the kriging equations (2.4) or (2.7). The model variogram parameters are also used in the random field generator FGEN92.

2.3 Summary

The proposed hydraulic conductivity parameterization combines zonation with a geostatistical approach. This parameterization better represents the spatial vari-

Model	λ	$\gamma(s)$
Spherical	a	$\begin{cases} b[\frac{3}{2}\frac{\lvert s\rvert}{a} - \frac{1}{2}(\frac{\lvert s\rvert}{a})^3] & s \leq a \\ b & s > a \end{cases}$
Exponential	$3a$	$b[1 - exp(-\lvert s\rvert/a)]$
Gaussian	$a\sqrt{3}$	$b[1 - exp(-\lvert s\rvert^2/a^2)]$
Power	∞	$b\lvert s\rvert^a$

Table 2.1: Equations of variogram models with range a and sill b. The nugget effect is ignored. The power model applies to non-stationary datasets; for this model b is a measure of the slope and a is the power.

ability in conductivity than can be achieved by using either of these options alone. The parameterization of a multi-aquifer system by a single hydraulic conductivity field would lead to a misrepresentation of the average conductivity of the individual hydrostratigraphic units. The sharp hydraulic conductivity contrasts that may exist at the aquifer/aquitard contacts can also not be simulated in this fashion. The zonation alone cannot mimic the spatial distribution of hydraulic conductivity within the individual hydrostratigraphic units. This variability is important for the development of groundwater flow paths. Furthermore, by allowing distinct geostatistical properties for each hydrostratigraphic unit, the interpolation uncertainty in hydraulic conductivity is significantly reduced, which is important in the context of an uncertainty analysis.

As a result of the chosen parameterization, two sets of point data need to be spatially distributed: the elevation of the aquifer/aquitard contacts that make up the zonation and the lithology-derived hydraulic conductivity estimates. The selected interpolation options are kriging and Gaussian random field generation. Both methods are based on the theory of regionalized variables. The main assumption in the treatment of regionalized variables is that their statistical characterization is exhausted by the covariance. This assumption may be restrictive in representing the true variability of the random fields in complex glacial aquifer systems. An investigation into the potential effects of this limitation is not warranted by the available data. However, it should be emphasized that this assumption affects every aspect of the modeling process, as the variogram parameters determine the spatial distribution of hydraulic conductivity. This distribution and its uncertainty is important in the deterministic modeling of groundwater flow, the model calibration and in stochastic analyses.

The combined zonation/kriging parameterization strategy was first developed in the context of the Waterloo Moraine study. Several improvements to this strategy have been made in the present study: The dimensionality of the hydraulic conductivity interpolation has been made consistent with that of the groundwater model. An alternative means of determining effective elemental conductivities has been proposed based on existing upscaling theory. Lastly, an existing Gaussian random field generator was augmented to allow for conditioning on a set of observations. This last contribution is part of the development of a stochastic framework for the multi-aquifer modeling.

Chapter 3

Numerical Model

3.1 Introduction

There is an increasing interest in modeling tools that integrate the surface and subsurface components of the hydrologic cycle throughout a natural watershed. Such tools are needed for the management of water resources to assure sustainability, for the protection of water quality and natural habitats, and for the prediction of the effects of the looming climate change.

Groundwater-surface water interactions take place at many different time scales. Short-term interaction occurs during discrete recharge events where subsurface processes such as interflow affect stormflow hydrographs. Seasonal rainfall variations result in fluctuations in the position of the water table and baseflow to streams. Here, the focus is on the long-term water mass balance for surface and subsurface flow and the accurate representation of infiltration to the groundwater system. This infiltration depends on a variety of physical processes as well as the surficial geology.

When modeling groundwater systems, one generally has the choice between fully saturated models, which take the water table as the top boundary, and variably saturated models that also incorporate the unsaturated zone. The former class of models requires either the specification of the location of the water table or of the recharge flux at the upper boundary. The exact location of the phreatic surface is often hard to determine. Small errors in the water table position may lead to large errors in groundwater fluxes. In contrast, the recharge flux can mostly be determined with a fair degree of accuracy. This boundary condition is therefore generally preferred and a number of state-of the art free-surface (water table) models have recently been developed [*Yeh et al.*, 1994; *Knupp*, 1996; *Diersch*, 1997]. These models are then calibrated with the average location of the water table as a target [e.g., *Frind et al.*, 1985].

Heterogeneity near the land surface will lead to a spatially variable infiltration and may also result in perched water table conditions. Under such conditions, the water table aquifer models are no longer capable of representing the recharge mechanism correctly. An incorrect representation of this recharge mechanism will have an adverse effect on, for example, the delineation of well head protection areas or predicted quantities of baseflow to streams. The actual amount of water that enters the groundwater system is uncertain as it may be limited either by the water surplus or by the near-surface geology. In a water table aquifer model this uncertainty has to be reflected by a spatially variable recharge rate. In a coupled surface-subsurface model infiltration is determined by the unknown near-surface soil properties. These parameters reflect the actual cause of the uncertainty. The water surplus on the other hand is entirely determined by precipitation and evapotranspiration, quantities that can be estimated fairly accurately.

Free-surface models can be efficiently applied to watershed-type problems, but because these models ignore the dynamics of flow in the unsaturated zone they cannot easily be integrated with surface water models that represent the dynamics of overland flow. *Chiew et al.* [1992], who coupled a rainfall-runoff model with a saturated groundwater model to better estimate infiltration to the subsurface, summarize problems encountered in such an approach.

Variably saturated models [e.g., *Huyakorn et al.*, 1986, *Celia et al.*, 1990, *Therrien and Sudicky*, 1996] can provide a valid link to surface water models. However, because these models generally operate at discretization scales of tens of centimeters in order to represent the controlling physical processes in the unsaturated zone, they are not practical to apply at a watershed scale. At the other extreme, surface water models used for watershed management involve discretization scales of kilometers to tens of kilometers. These models represent the surface water component adequately but overly simplify the dynamics of the groundwater system. Substantial gaps therefore exist, which must be bridged before the various model types can be integrated in a practical way. A prototype watershed model (HTS) that incorporates all of the controlling surface water and groundwater processes has recently been developed [*VanderKwaak*, 1999]. However, this model has only been applied to a system on the order of a few hundred meters in spatial extent using a discretization scale similar to that of a variably saturated model.

An alternative type of approach that will be explored here is the use of a pseudo-unsaturated model. This type of model takes the ground surface as the upper boundary and therefore includes all hydrogeologically significant layers of an aquifer system. Flow in the unsaturated zone is not modeled in a scientifically rigorous fashion using, for example, the equations of *van Genuchten* [1980] and *Mualem* [1976], but instead by means of an empirical scaling of the hydraulic conductivities above the water table [*Bathe and Khosgoftaar*, 1979; *Desai and Li*, 1982]. When combined with a coarse mesh discretization suitable for watershed-scale modeling, this approach has the potential of bridging the scale-gap with surface water models. Furthermore, the need to obtain detailed unsaturated zone parameters is circumvented. However, the limitations of a simplified unsaturated zone representation have to be investigated.

Rainfall runoff to streams and other surface water bodies will be simulated through the use of a recharge spreading layer. Such a high conductivity layer has previously been used to redistribute recharge atop fractured media [*Therrien and Sudicky*, 1996] or low conductivity surficial layers [*Martin and Frind*, 1998]. Stream dynamics will presently be ignored. Instead, major water courses will be represented by Dirichlet boundaries. The proposed modeling approach is not valid for simulating the complex transient interaction between surface and subsurface flow systems during discrete recharge events. The objective of this approach merely is to determine the relative importance of groundwater discharge and rainfall runoff to surface water bodies and to better simulate infiltration to the subsurface. These issues are important in modeling the Oro Moraine system and in simulating the water mass balance balance for the Minesing Swamp. Furthermore, experience gained with the pseudo-unsaturated approach may be useful for future studies of surface-subsurface systems using more accurate models such as HTS. Such a study is currently being considered for the Grand River basin in southern Ontario.

The simplified unsaturated zone representation has been implemented as an alternative module in the free-surface code WATFLOW [*Molson et al.*, 1992]. Equations and solution strategy for the free-surface and the pseudo-unsaturated modules of WATFLOW are given below. Pseudo-unsaturated model simulations for the hypothetical aquifer system will be compared to those obtained with free-surface and variably saturated representations of this flow problem.

3.2 Theory

Governing Equations and Solution Strategy

The finite element model WATFLOW is based on the general 3D form of the governing equation for transient saturated groundwater flow in heterogeneous anisotropic porous media [*Bear*, 1972]:

$$-\frac{\partial}{\partial x_i}[q_i] + Q = S_s\frac{\partial h}{\partial t} \tag{3.1}$$

where the Darcy flux q_i is defined as:

$$q_i = -K_{ij}\frac{\partial h}{\partial x_j} \tag{3.2}$$

and where h is the hydraulic head, x_i represents the spatial coordinates, K_{ij} is the hydraulic conductivity tensor, t is time, Q represents sources or sinks, and S_s is the specific storage of the porous medium. In the present study, only steady-state groundwater flow will be considered for which the time derivative on the right-hand side of (3.1) reduces to zero. Substitution of (3.2) into the resulting equation yields:

$$\frac{\partial}{\partial x_i}\left[K_{ij}\frac{\partial h}{\partial x_j}\right] + Q = 0 \tag{3.3}$$

The solution of this equation is subject to the standard Dirichlet and Neumann boundary conditions:

$$\begin{aligned} h &= \hat{h} \qquad on\ \ \Gamma_1 \\ q_i \cdot n_i &= \hat{q} \qquad on\ \ \Gamma_2 \end{aligned} \tag{3.4}$$

For the Dirichlet boundary condition, $\hat{h}$ is the specified head value along boundary segment Γ_1; for the Neumann boundary condition, $\mathbf{n}$ is a unit vector normal to boundary segment Γ_2, and $\hat{q}$ is the specified Darcy flux normal to that segment.

If the hydraulic connection between water courses and aquifers is significantly affected by stream bottom deposits it is better to use a Cauchy boundary condition such as incorporated in MODFLOW [*McDonald and Harbaugh*, 1988]. When stream-aquifer interaction is of concern, water courses should either be modeled through the St. Venant equations [e.g., *Ackerer et al.*, 1990] or by including them as analytical elements [e.g., *Mitchell-Bruker and Haitjema*, 1996]. The latter study also describes an algorithm to avoid the loss of non-existing stream flow to the aquifer system. However, these issues are beyond the focus of the present study, and streams will simply be included as Dirichlet boundaries.

The WATFLOW code uses triangular prismatic finite elements which facilitate a flexible grid refinement in the horizontal plane (e.g. around well fields) and allow the grid to be deformed to the natural shape of the water table boundary and the irregular stratigraphic contacts. Well-screens are represented as 1D line elements [*Sudicky et al.*, 1995]. The governing equations are discretized using the standard Galerkin finite element method [*Huyakorn and Pinder*, 1983], Gauss quadrature numerical integration, or the Orthogonal Subdomain Collocation (OSC) method developed by *Cordes* [1994]. The Gauss quadrature integration yields nodal influence coefficients for deformed prisms. The OSC method has the advantage that the fluid mass balance expressed by (3.1) is enforced on an elemental rather than a global basis. Cordes has shown that the Galerkin method may yield physically non-realistic oscillatory solutions near pumping wells where head gradients are steep. Under such conditions the OSC method gives much better results because the nodal connections expressed by this numerical scheme are more correct from a physical point of view. However, in this particular study, differences between the three numerical techniques have been found to be small.

To account for the first-type boundary conditions, the matrix equations are partitioned according to nodes at which h is known and those at which it is unknown:

$$\begin{aligned} [A_{ff}]\{h_f\} + [A_{fc}]\{h_c\} &= \{F_f\} \\ [A_{cf}]\{h_f\} + [A_{cc}]\{h_c\} &= \{F_c\} \end{aligned} \tag{3.5}$$

where A and F stand for the coefficient (conductance) matrix and the forcing vector containing flux terms, and where subscripts f and c designate free and constrained nodes. Only the first of these two equations is needed for the head solution. It is solved using an efficient pre-conditioned conjugate gradient solver with a block-line relaxation procedure to manage high horizontal to vertical aspect ratios for the elements [*Braess and König*, 1995].

Once the solution is obtained, the second equation in (3.5) is used to calculate the fluxes F_c to the Dirichlet nodes. In WATFLOW, these fluxes can be calculated for particular boundaries (i.e., certain streams). Contributions from the subsurface (domain) and the RSL can also be separated. This is important in the model calibration, where observations regarding both baseflow and runoff are used. A performance measure based on the type 1 flux term is further used to identify critical recharge areas for the Minesing Swamp through the adjoint method.

Free-Surface Module

The code as developed by *Molson et al.* [1992] includes a procedure to iteratively locate the water table based on the condition of zero pressure head, and satisfying the water balance corresponding to the specified recharge. As pointed out by *Knupp* [1996], the specified flux condition (3.4) for the upper boundary is in fact an approximation of the true free-surface boundary condition (also referred to as kinematic boundary condition). However, when steady-state flow is considered the two conditions are identical.

Using a user-specified lower limit for the allowed finite element thickness, the minimum number of layers that needs to be moved is calculated and the mesh deformation is applied uniformly over this stack. The location of stratigraphic boundaries that may be included in the model is maintained where possible. Horizontal and vertical conductivities are updated using arithmetical and harmonic averaging and making use of the location of the deformed elements with respect to the original (non-deformed) mesh. The convergence criterion for the Picard iteration is based on the hydraulic head updates in the domain:

$$||h_{i,k} - h_{i,k-1}|| < \Delta h_{max} \qquad i = 1, 2, ..., NN \tag{3.6}$$

where $h_{i,k}$ is the piezometric head at node i and iteration k, NN is the number of nodes in the domain, and Δh_{max} is a user-specified convergence criterion.

Pseudo-Unsaturated Module

An alternative non-linear solution procedure was implemented in WATFLOW. Rather than using the water table position as a parameter for the non-linear update of the solution, the saturation of the elements above the water table is computed through an ad-hoc exponential relationship between the pressure head $p = h - z$ and the saturation of the porous medium S:

$$\begin{aligned} S(p) &= S_r + (1 - S_r)e^{\epsilon p} \qquad && p < 0 \\ &= 1 && p \geq 0 \end{aligned} \tag{3.7}$$

where S_r is the residual saturation of the porous medium, and ϵ is a parameter determining the extent of the zone between residual and full saturation. Partial saturation of the elements results in a lower hydraulic conductivity, impeding groundwater flow. This is accomplished by setting the relative permeability of an element equal to its saturation.

In a numerical model, elemental saturations are usually calculated based on the average of the pressure heads at the adjoining nodes. However, when the vertical mesh discretization is coarse this may lead to improper saturations for those elements that straddle the water table. Changes in the solution, whereby the water table is located above or below the element centroid, may result in fluctuations between residual and full saturation. This in turn has a negative impact on the convergence behaviour of the numerical solution. It is then better to calculate an average saturation $\bar{S}$ based on a vertical integration of the relationship (3.7). As p in the element changes linearly with elevation, this vertical integration can be replaced by an integration over the pressure range found in the element:

$$\bar{S} = \frac{1}{(p_t - p_b)} \int_{p_b}^{p_t} S(p)dp \tag{3.8}$$

which can be evaluated directly. Average pressure heads are calculated for the top (p_t) and bottom (p_b) faces of each element from the values at the adjoining nodes. Due to the integration (3.8), the position of the water table is taken into account in a similar fashion as in the approach used by *Diersch* [1997].

Although not illustrated here, it was shown that for flow regimes with no recharge applied to the upper boundary, the free-surface and pseudo-unsaturated modules yield identical solutions when flow in the unsaturated zone is strongly inhibited. This is achieved with a low value for S_r and a high value for ϵ. However, this approach no longer works for the more interesting case when recharge is applied. The unsaturated zone parameters then need to be chosen such that the relative permeability and simulated head gradients above the water table are representative of the state of the actual system.

Similar to the moving mesh algorithm, the flow equation is solved with hydraulic head as the state variable, thus requiring only minor additions to the existing WATFLOW code. Convergence criteria are imposed for hydraulic head (equation 3.6) and for the saturation updates:

$$\|\bar{S}_{i,k} - \bar{S}_{i,k-1}\| < \Delta S_{max} \qquad i = 1, 2, ..., NE \tag{3.9}$$

where NE is the number of elements and ΔS_{max} is a user specified convergence criterion.

Within the context of the present study, the pseudo-unsaturated approach has several other appealing consequences that were not mentioned earlier: as there is no need for deforming the mesh the elemental conductivities do not have to be updated in each Picard iteration. This avoids a smearing of this distribution as a result of the averaging process. A fixed mesh is also desirable for stochastic analyses and in the model calibration.

Recharge Spreading Layer

The recharge spreading layer as incorporated in WATFLOW is a thin 3D layer of elements. *Martin* [1994] coupled this layer with the free-surface module to avoid ponding of water atop low-conductivity units. The layer was given a sufficiently high conductivity to facilitate the lateral movement of water on the top of the domain. As the surface water component was taken into account in determining the recharge rate, the RSL was expected to simulate the process of interflow. Here, the applied flux at the upper boundary is given by the water surplus, which is solely determined by precipitation and evapotranspiration. The RSL is coupled with the pseudo-unsaturated module at the land surface and is used to simulate runoff. Contributions to this runoff arrive from both overland flow and subsurface stormflow in the shallow soil layer (interflow). Although in this case the RSL might be better referred to as a "water surplus spreading layer", the name "recharge spreading layer" will be retained.

Several approximations are made when using the RSL to simulate overland flow. The first simplification is to ignore the inertial terms that are included in the St. Venant motion equations that more accurately describe overland flow [e.g., *Abbot*, 1979]. This approach is valid for flow on relatively flat surfaces [*Giammarco et al.*, 1996]. The surface conveyance depends on the water ponding height [e.g., *VanderKwaak*, 1999]. This non-linear effect is ignored in using the RSL. At steady state this approximation is probably not too severe. The effect of the ponding height on the surface conveyance is projected onto the unknown conductivity of the RSL. VanderKwaak further used a micro-topography dependent exchange term to couple the surface and subsurface flow systems. Here, fluid pressures are simply equated at the surface nodes of the finite element mesh.

Seepage Face Algorithm

If in a certain Picard iteration the water table wants to rise above ground surface, the recharge boundary needs to be converted to a seepage face. In the numerical model this is accomplished by switching the Neumann boundary condition to a Dirichlet condition at the corresponding nodes. In subsequent Picard iterations the vertical Darcy flux $q_{zz} = -K_{zz}dh/dz$ at the seepage nodes is compared to the recharge rate R. If this flux is downward and exceeds R, the water table is expected to drop and the seepage face constraint is switched back to a Neumann condition. If instead $q_{zz} < R$ the water table will rise and the seepage condition remains enforced. The algorithm as outlined applies to the free-surface module of WATFLOW without the use of an RSL and is a simplified version of the water table speed calculation of *Knupp* [1996] for transient flow simulations. For pseudo-unsaturated simulations, the vertical hydraulic conductivity component K_{zz} is replaced by $\hat{S}K_{zz}$. If a recharge spreading layer is used, the magnitudes of the vertical Darcy flux from the RSL and in the domain directly below a seepage node are compared. However,

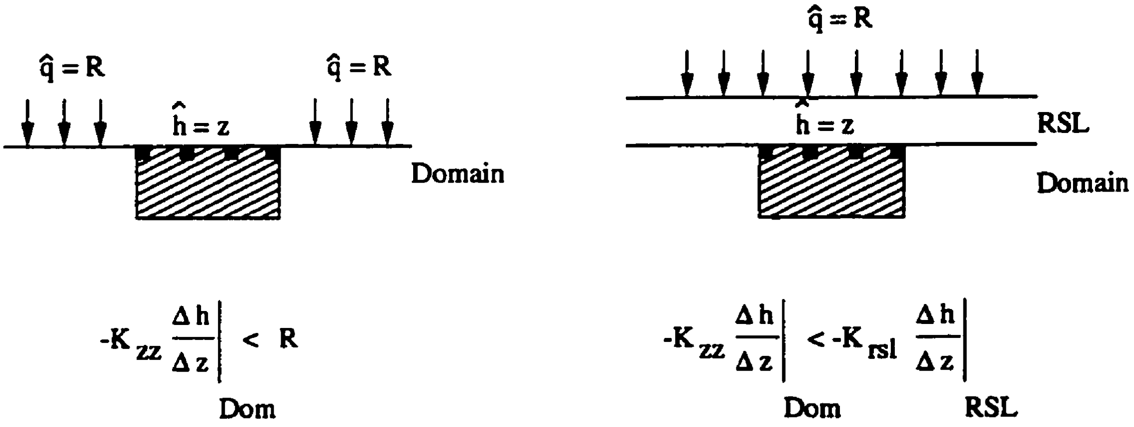
$\hat{q} = R$
$\hat{q} = R$
$\hat{h} = z$
Domain
$\hat{q} = R$
$\hat{h} = z$
RSL
Domain
$-K_{zz} \frac{\Delta h}{\Delta z}\Big|_{Dom} < R$
Dom
$-K_{zz} \frac{\Delta h}{\Delta z}\Big|_{Dom} < -K_{rsl} \frac{\Delta h}{\Delta z}\Big|_{RSL}$
Dom
RSL

Figure 3.1: Seepage face algorithm for ponding on a low K zone (dashed rectangle) with or without the use of an RSL. Neumann boundary conditions are indicated by vertical arrows; Solid squares indicate seepage (Dirichlet) nodes.

when using the RSL ponding on the land surface is mostly avoided and seepage face conditions only need to be accounted for in the traditional sense to allow for water exiting the system ($q_{zz} < 0$). Figure (3.1) illustrates the implementation of the seepage face algorithm for ponding on a low K zone with or without the use of an RSL.

3.3 Hypothetical Example

A cross-sectional flow problem was designed to reproduce the main characteristics of the study area. The domain consist of two aquifers separated by an impermeable aquitard with two windows that provide a vertical hydraulic connection (Figure 3.2). Two scenarios will be considered: in the first case, the upper aquifer is completely unconfined whereas in the second case this aquifer will be overlain by a confining unit in the upland. This upper aquifer is characteristic of the Oro Moraine, which consists of thick deposits of glacial outwash material that are partially overlain by a till unit. The regional water table in these uplands is located 30-50 m below the land surface placing the till unit in the unsaturated zone. The conductivity of the lower aquifer is an order of magnitude higher than that of the upper aquifer. As a result, groundwater flow at depth will be important. The higher conductivity was chosen because in reality multiple aquifers exist at depth.

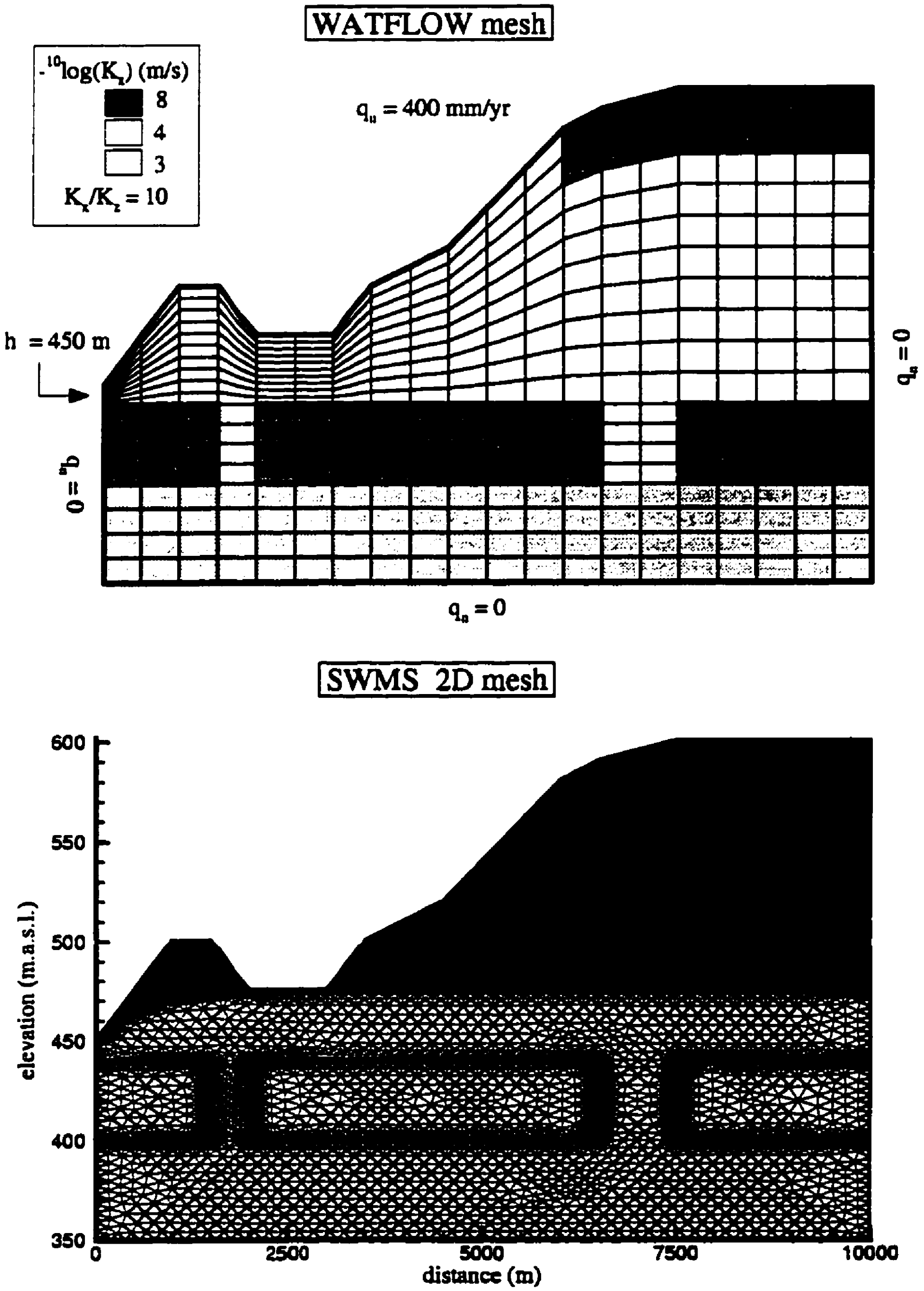
WATFLOW mesh
-¹⁰log(Kₓ) (m/s)
8
4
3
Kₓ/K_z = 10
q_n = 400 mm/yr
h = 450 m
q_n = 0
q_n = 0
q_n = 0
SWMS 2D mesh
600
550
500
450
400
350
elevation (m.a.s.l.)
0
2500
5000
7500
10000
distance (m)

Figure 3.2: Finite element meshes used in WATFLOW and SWMS 2D simulations together with parameters of the flow problem.

A recharge rate of 400 mm/yr ($1.27 \cdot 10^{-8}$ m/s), typical of the water surplus in the Moraine, is applied. The left side of the upper aquifer is constrained at $\hat{h} = 450$ m to simulate the presence of a stream. All other boundaries are impermeable. Except for the last example, no RSL will be used.

The WATFLOW simulations are carried out in 3D by extending the cross-section in the y-direction. The size of the prismatic elements is 500 m in the horizontal direction and a maximum of 16 m vertically. The unsaturated zone is not discretized more finely to retain computational efficiency. WATFLOW simulations will be compared with the two-dimensional variably saturated model SWMS 2D [*Simúnek et al.*, 1992].

SWMS 2D is a Galerkin based model that simulates water and solute movement in variably saturated media in either the horizontal or the vertical plane. The flow equation is linearized using a Picard iteration with convergence criteria similar to those implemented in WATFLOW. The program uses (modified) van Genuchten parameters for the unsaturated zone. The SWMS 2D triangular mesh was refined in this zone. Because hydraulic conductivities are input as nodal properties, the mesh was also refined around the stratigraphic contacts in order to allow comparison with the WATFLOW runs. Although the SWMS 2D code includes an option to directly calculate a steady-state solution, this does not appear to work for the 1994 version that was used here. The simulations were therefore carried out in transient mode until steady-state was achieved.

Figure (3.3) shows a three-way comparison between WATFLOW's free-surface and pseudo-unsaturated modules and SWMS 2D for the case of an unconfined upper aquifer. The parameters of the van Genuchten relationships are typical for a sandy material: $\Theta_s = 0.3$, $\Theta_r = 0.03$, $\alpha = 1$ and $n = 6$ (using the notation given in *Simúnek et al.*, 1992). The SWMS 2D simulation shows that at steady state a unit gradient develops in the unsaturated zone, consistent with what is expected theoretically. This results in a relative permeability in the unsaturated zone of $1.27 \cdot 10^{-3}$ (equal to the recharge rate divided by the vertical conductivity) and a corresponding saturation of 0.21 (Figure 3.4).

In order for the WATFLOW pseudo-unsaturated simulation to predict a unit gradient the residual saturation S_r in equation (3.7) was set to $1.27 \cdot 10^{-3}$. Experimentally it was found that the value of ϵ controls the convergence behaviour of the Picard iteration. Its value needs to be made small enough to ensure that the zone between residual and full saturation is slightly larger than the vertical mesh

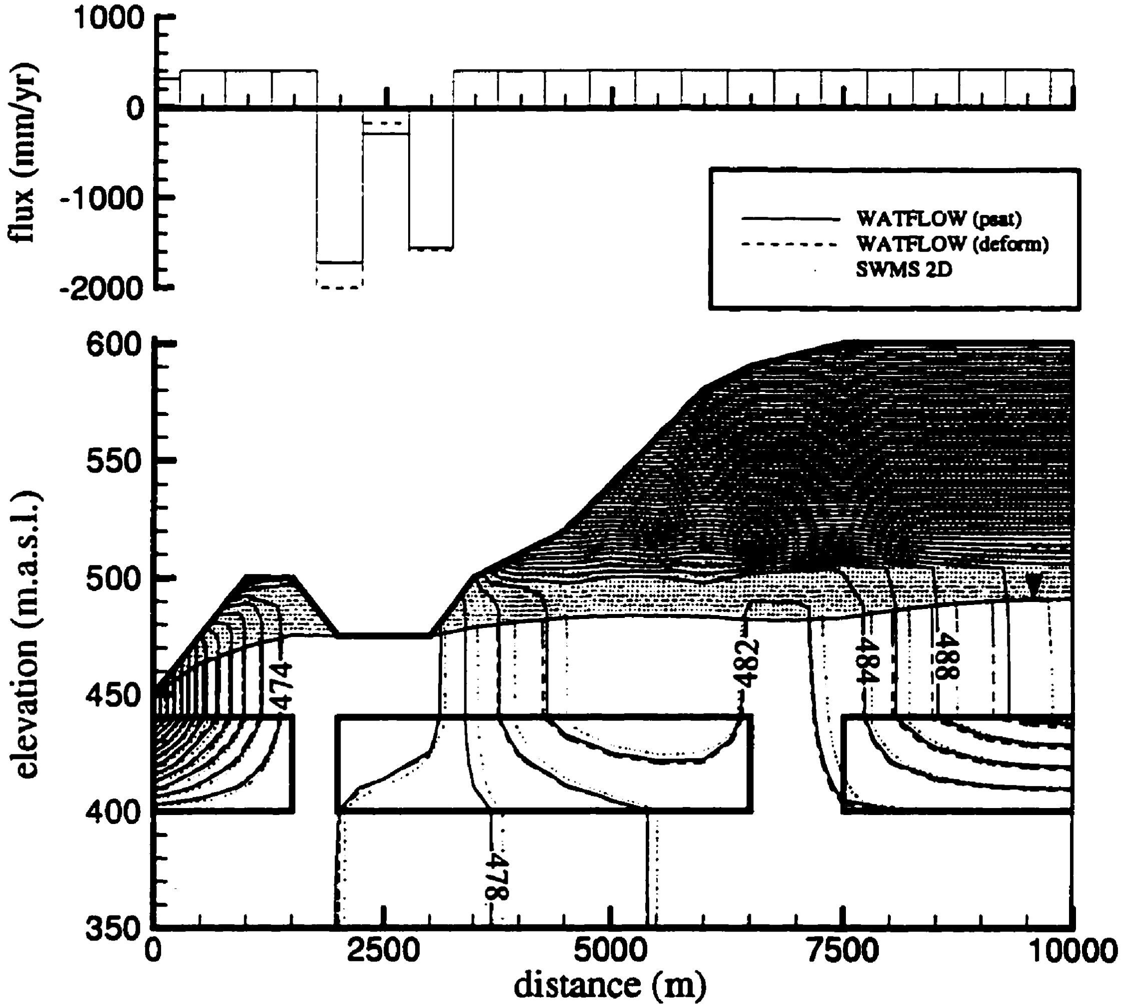

Figure 3.3: Piezometric head distribution ($\Delta h = 2$ m) and fluxes at upper model boundary for the case of a fully unconfined upper aquifer.

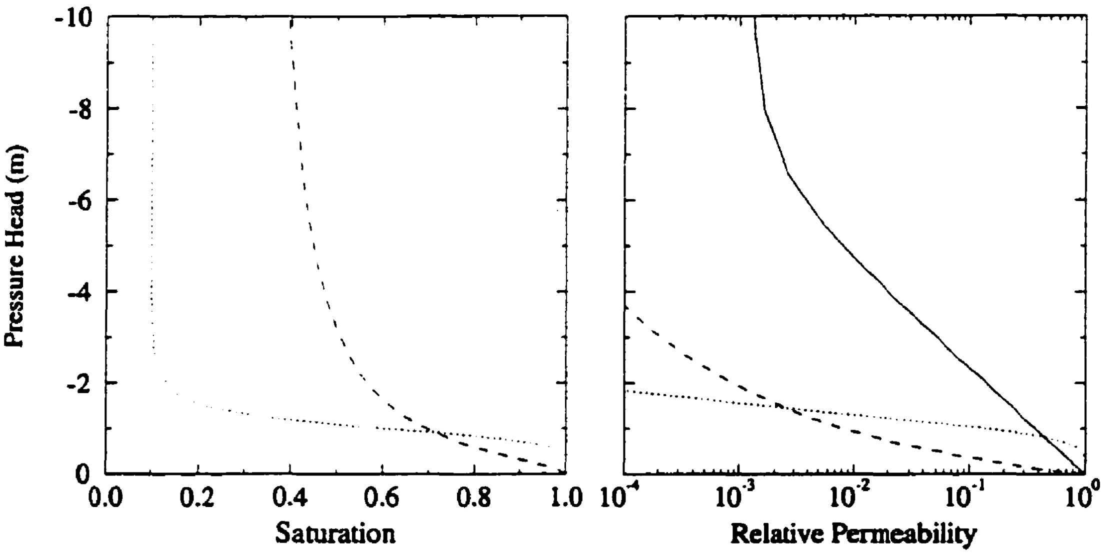

Figure 3.4: Pseudo-unsaturated relationship (solid line) together with van Genuchten relationships for aquifer (dotted line) and aquitard (dashed line) materials.

discretization. Here a value of 1.0 is used. If ϵ is set too large the solution may not converge as the Picard iteration is unable to resolve parameter changes that occur below the discretization scale. This problem mainly arises when heterogeneity exists near the water table, as is the case in the Oro Moraine model. Discrepancies between the WATFLOW pseudo-unsaturated and the SWMS 2D simulations arise near the water table and are a direct result of the mesh discretization. Dissimilarities in the bending of equipotential lines (and flow paths) are caused by the exaggerated zone between residual and full saturation for the WATFLOW simulation (Figure 3.3). A finer WATFLOW mesh would result in a closer agreement between the two solutions as larger values of ϵ are permitted.

Because flow in the unsaturated zone is essentially vertical, it is reasonable to expect that fluxes at the water table are similar for the free-surface and pseudo-unsaturated simulations. This implies that these simulations should resolve a nearly identical water table position, which is indeed the case. The seepage zone in the valley area is resolved in all solutions and exit fluxes (shown only for the WATFLOW runs) at this zone are in close agreement, suggesting that flow patterns must be similar. Differences increase away from the seepage zone with the pseudo-unsaturated module yielding a solution that is closest to the SWMS 2D simulation.

The most interesting comparison between the three simulations is from a computational perspective. Both WATFLOW simulations with 8379 nodes (21 nodes are used in the y direction) can be solved directly for steady-state with CPU run times on the order of 10^2 seconds on an IBM-RS6000. However, the SWMS 2D simulation with 22103 nodes requires a CPU time in excess of 10^6 seconds on the same machine. This difference is only partially caused by the mesh discretization. The main problem is the use of the van Genuchten parameters. Figure (3.4) shows that near the steady-state relative permeability value of $1.27 \cdot 10^{-3}$, small variations in pressure head may result in order-of-magnitude changes in this property. Small time steps are therefore needed to obtain a stable solution. SWMS 2D has an adaptive algorithm that increases the time step when the number of Picard iteration drops below a certain minimum (in this case 3). However, the maximum time step that was reached is on the order of 10^5 seconds, at which point the number of Picard iterations remained constant at 3-5. The time needed for the system to reach steady state is about 10^{10} seconds due to the slow response of the aquitard. Thus an excessively large number of time steps is needed to reach equilibrium.

This example illustrates that if one wants to include the unsaturated zone in a watershed scale study (e.g., in a combined surface-subsurface model), the use of physically realistic unsaturated zone relationships such as those by van Genuchten may lead to extremely large execution times, depending on the time scale of the problem. Thus if the long-term behaviour of the groundwater system is of concern, it may be better to use an approximate relationship which allows larger time steps or even a direct steady state solution. However, if the surface water component is of interest, time step limitations are not a constraint and physically correct unsaturated zone parameters can (and from a accuracy perspective probably *should*) be used.

Figure (3.5) compares WATFLOW's pseudo-unsaturated module with SWMS 2D for the case of a partially confined upper aquifer. SWMS 2D parameters for the aquitard are $\Theta_s = 0.5$, $\Theta_r = 0.15$, $\alpha = 2$ and n = 1.67. Discrepancies between the solutions again arise from the mesh discretization but now also from the pseudo-unsaturated relationship. SWMS 2D predicts the upper aquifer in the region beneath the confining unit to be at residual saturation, resulting in a relative permeability below 10^{-4} (Figure 3.4). However, in order to retain a stable steady

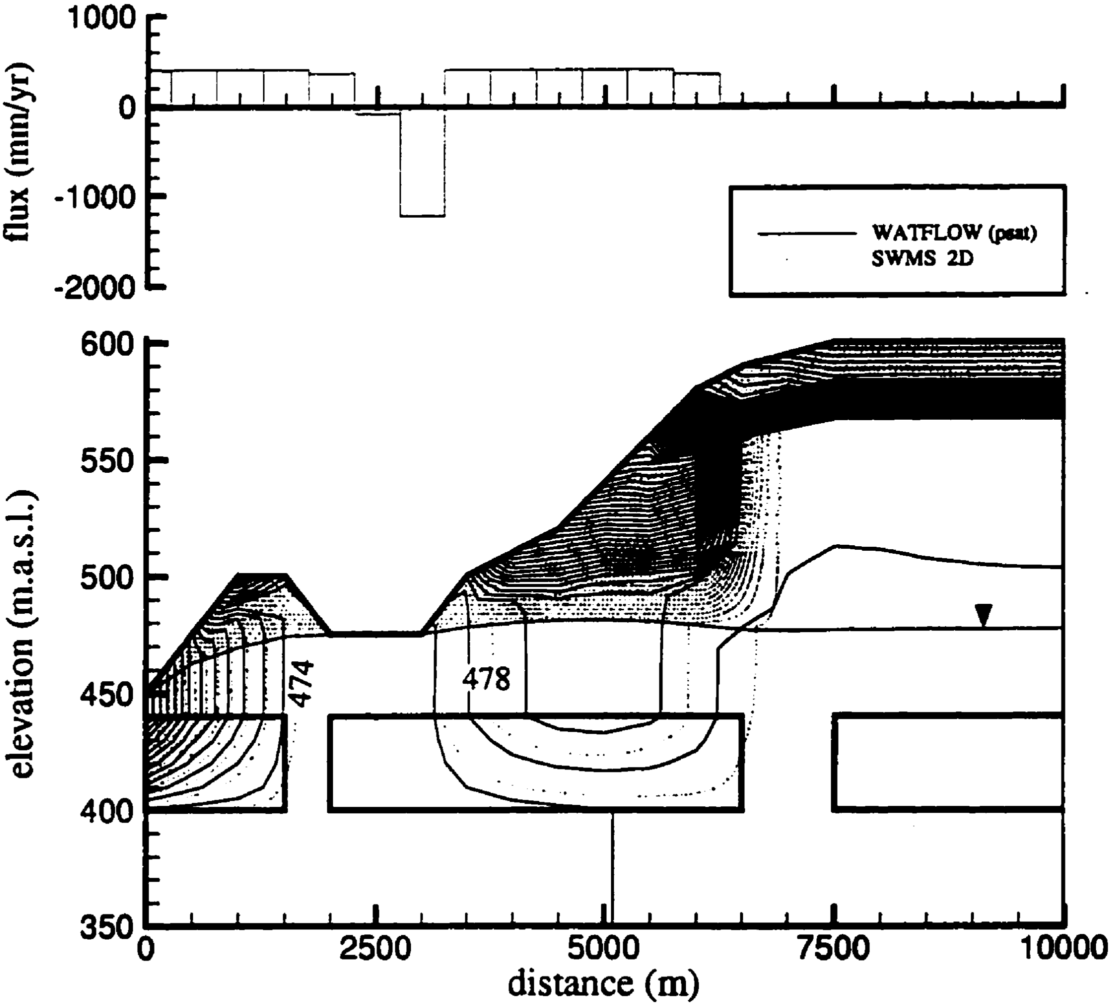

Figure 3.5: Piezometric head distribution ($\Delta h = 2$ m) and fluxes at upper model boundary for the case of a partially confined upper aquifer.

state solution with WATFLOW, it was found necessary to maintain a lower limit for S_r at $1.27 \cdot 10^{-3}$. This affects the head distribution below the confining unit. However, the agreement between the two solutions below the water table is still quite good.

Water ponds on top of the confining unit. In WATFLOW this results in an enforcement of the seepage face criterion as outlined in Section (3.2). In SWMS 2D this was simulated by imposing Dirichlet boundary conditions over the extent of the confining unit. The porous medium at the top of the confining unit is fully saturated whereas at the bottom it is only partially saturated. As a result, head gradients increase downward in this unit, where SWMS 2D predicts a more gradual steepening than the WATFLOW simulation as a result of the finer discretization. The local infiltration rate calculated by WATFLOW is about 22 mm/yr ($7 \cdot 10^{-10}$ m/s), slightly lower than the vertical conductivity. For a unit cross-section, the total recharge to the groundwater system is $0.59 \cdot 10^{-4} m^3/s$ as compared to $1.04 \cdot 10^{-4} m^3/s$ for the case with no confining unit. This reduced recharge mainly affects fluxes to the seepage zone. Groundwater flow to the river boundary is only slightly reduced.

Although not shown, the free-surface simulation for the above problem is identical to that for the scenario without a confining unit, as the aquitard is located above the water table and thus outside the solution domain. Thus, if the presence of this unit is ignored, the free-surface solution will misrepresent the recharge distribution. This in turn has a negative impact on the identification of critical recharge areas (e.g. for baseflow to the river) and on predicted baseflow quantities. A more realistic free-surface simulation can be obtained by lowering recharge over the area covered by the confining unit but this still does not take flow in the unsaturated zone into account. This zone is incorporated (although approximately) in the pseudo-unsaturated model. For the example given here, this model provides an appealing alternative to the free-surface and variably saturated models, better representing the recharge mechanism than the former, while maintaining computational efficiency compared to the latter.

The previous example does not fully address the response of a real system in that water that cannot infiltrate through the confining unit is instantaneously removed from the system and not transferred overland as it occurs naturally through rainfall runoff. This process is simulated by using the RSL. Its hydraulic conductivity was set to 10^{-4} m/s. As the inclusion of the RSL avoids ponding over the low K unit, the seepage face criterion is only enforced in the "traditional" sense, i.e. in

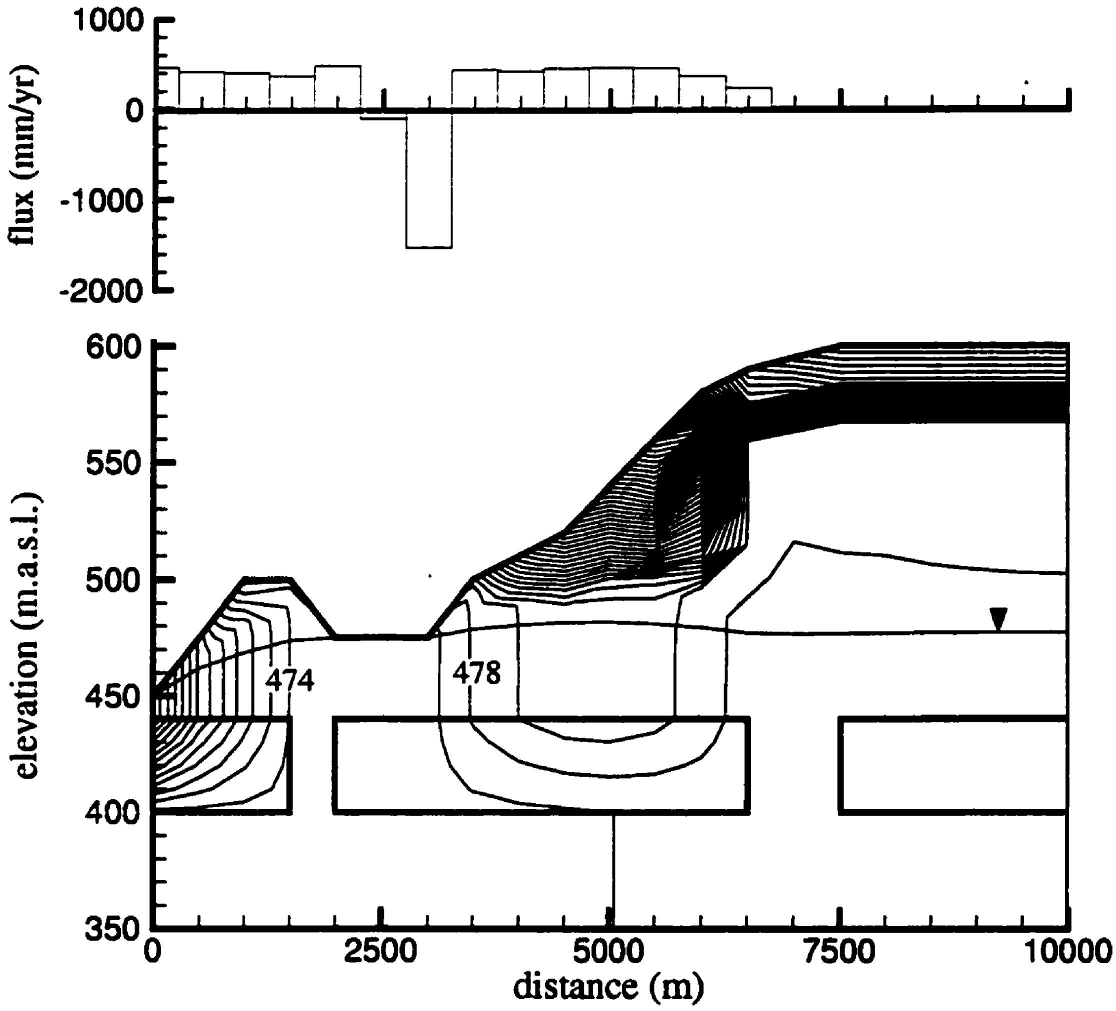

Figure 3.6: Piezometric head distribution ($\Delta h = 2$ m) and fluxes at upper model boundary for the case of a partially confined upper aquifer with the use of an RSL.

those locations where the water table wants to rise above ground surface and water leaves the system. It can be seen that recharge increases slightly on the flanks of the upland where the upper aquifer outcrops. Overall, recharge to the groundwater system increases to $0.64 \cdot 10^{-4} m^3/s$, resulting in an increased discharge at the seepage zone. The hydraulic head distribution on the other hand is hardly affected. Most of the excess recharge over the confining unit is transported to the seepage zone through the RSL. This water therefore never enters the groundwater system. The distribution of recharge between the domain and the RSL can to some degree be controlled by varying the conductivity of this layer. In the calibration of the Oro Moraine model this behavior will be used to provide a steady-state water mass balance for the groundwater and surface water systems, which is validated against constraints from stream gauge measurements.

3.4 Summary

A pseudo-unsaturated zone representation was implemented in the existing finite element code WATFLOW. Although pseudo-unsaturated models have been used in the past, their application in the published literature has been limited to the well known flow-through-a-dam and pit flooding problems in which no recharge is applied to the upper model boundary. Here, this representation is used to model flow in the unsaturated zone in an approximate fashion. Its application is intended for watershed-scale problems where heterogeneity exists near the land surface. This heterogeneity affects groundwater flow patterns in the unsaturated zone and thus the distribution of fluxes to the water table. A hypothetical example of a multi-aquifer system was used to show that under such conditions a pseudo-unsaturated zone representation better predicts the recharge mechanism than can be achieved with a free-surface model which ignores the vadose zone. This in turn affects groundwater flow paths below the water table.

The pseudo-unsaturated zone representation was also compared to a true variably saturated model. Such a model provides the most rigorous treatment of the physical processes above the water table. Discrepancies between the two models mainly arise from the coarser mesh used in the pseudo-unsaturated simulations. This results in an exaggerated transition zone between residual and full saturation, affecting the head distribution and flow paths. Differences in predicted flow regimes below the water table, which are the focus of interest, are only minor. The higher accuracy of the variably saturated model requires excessively long computer simulation times. These are caused by the need for small time steps to obtain a stable solution, and the long time span it takes for a large-scale system to reach steady state. The pseudo-unsaturated zone parameters are chosen such that a steady-state solution can be obtained directly. For watershed problems, the pseudo-unsaturated representation may thus provide a viable modeling alternative, better representing the recharge mechanism than free-surface models, while maintaining computational efficiency as compared to variably saturated models.

The pseudo-unsaturated model was coupled to a recharge spreading layer. This layer is used to simulate the process of rainfall runoff by redistributing recharge atop the model domain. Excess recharge over low conductivity units is transferred laterally, either to more pervious regions where water can infiltrate more easily, or to surface water bodies. Although rainfall runoff is only modeled in an approximate fashion, this layer thus has the potential to provide a steady state water mass balance for the surface and subsurface flow systems. This will be illustrated in the context of the calibration of the Oro Moraine model.

Chapter 4

Adjoint Method

4.1 Introduction

The sensitivity of a mathematical model to its input parameters is an important concern in any numerical investigation. Typically this concern is addressed by varying the parameter values on a one by one basis and evaluating the change in model output in order to determine which parameters are most critical to the problem that is being studied, or to determine the potential effect of uncertainty regarding these parameters. However, such a task becomes exceedingly time consuming as the problem gets more complex. The use of mathematical expressions that compute the derivative of a selected model response with respect to a set of system parameters then is an appealing alternative. Several approaches have been taken towards this goal.

The direct parameter sampling method, used in the calibration codes PEST [*Doherty*, 1994] and UCODE [*Poeter and Hill*, 1998], and the forward sensitivity method both require that a system of equations comparable in size to the main problem itself is solved for each individual parameter that is being perturbed. The computational cost of these methods is therefore comparable to simple trial and error perturbations [*Li et al.*, 1986]. In contrast, the adjoint operator approach requires the solution of two separated problems, one related to the response measure itself and one related to the sensitivity parameters. These problems need to be solved only once for a particular response measure. From the standpoint of computational cost the adjoint method is therefore superior to the other two methods, except when the number of different responses is greater than the number of input parameters [*Cacuci*, 1981]. For this reason the adjoint method is the chosen means of calculating sensitivity coefficients for most applications in the present study. An exception is the calculation of the covariance of certain parameter estimates as part of the model calibration. The forward sensitivity method will be used for that purpose (Chapter 5).

The adjoint method has been applied to a wide range of physical and engineering problems. Following its use in reservoir problems [e.g., *Chavent et al.*, 1975], the adjoint method has also become popular in hydrogeology. *Neuman* [1980] and *Townley and Wilson* [1985] used this method as part of a parameter estimation procedure for steady-state groundwater flow, where derivatives of a functional relating observed and predicted heads with respect to hydraulic conductivities were used in the solution of the inverse problem. The same derivatives can also be used to identify those locations in an aquifer system where parameter adjustments will yield the largest reduction in difference between observed and predicted heads [*LaVenue and Pickens*, 1992; *RamaRao et al.*, 1995]. The adjoint method has further been used in a stochastic framework for groundwater uncertainty analysis using a first and second moment approach [e.g., *Sykes and Thomson*, 1988; *LaVenue et al.*, 1989].

The derivation of the adjoint equations has been widely published in the literature. *Sykes et al.* [1985] give a detailed description of the use of adjoint operators for a steady-state 2D confined flow model. The equations that are given below are an extension of those in their paper to three dimensions, where the pseudo-unsaturated module of WATFLOW is used as a basis. A new performance measure will be introduced to identify critical recharge areas for the Minesing Swamp. This performance measure is based on model calculated fluxes to one or several Dirichlet boundaries. The hypothetical example from the previous chapter will be used to illustrate the effect that different numerical implementations of a flow problem may have on inferred recharge areas for baseflow to the river outflow boundary.

4.2 Theory

The adjoint method is a means of evaluating the effect of parameter perturbations on a performance measure of the system that is being modeled. Mathematically, a sensitivity measure is computed through the derivative of this response function or performance measure J with respect to a set of system parameters $\{\alpha\}$. The response function depends on both the system parameters as well as the system state, in this case hydraulic head, i.e. $J = J(\{\alpha\}, h)$. The system parameters include the horizontal and vertical hydraulic conductivities $K_{xx} = K_{yy}$ and K_{zz}, any sources or sinks Q, and specified heads $\hat{h}$ and boundary fluxes $\hat{q}$. The system parameters thus form a vector $\{\alpha\}^T = \{K_{xx}, K_{zz}, Q, \hat{h}, \hat{q}\}$. The response function can be written as:

$$J = \int_V f(\{\alpha\}, h)dV \tag{4.1}$$

where $f(\{\alpha\}, h)$ is a function that is integrated over the volume of the spatial domain V which can take different forms depending on the performance measure of interest. If the hydraulic head in a certain part of the model domain is of interest, this function can be written as:

$$f(\{\alpha\}, h) = g(\mathbf{x})h(\mathbf{x}) \tag{4.2}$$

where $g(\mathbf{x})$ is a weighting function indicating the region of interest. If instead, the magnitude of the Darcy velocity at a point $\mathbf{x}'$ is of interest the response function will look like:

$$f(\{\alpha\}, h) = \left[q_1^2 + q_2^2 + q_3^2\right]^{1/2} \cdot \delta(\mathbf{x} - \mathbf{x}') \tag{4.3}$$

The above performance measures were used by *Sykes et al.* [1985] to investigate regional flow parameters of the Leadville Formation in Utah. In the present study, baseflow to the Minesing Swamp is of interest. This wetland will be included in the mathematical model as a Dirichlet boundary condition. Although the velocity measure (4.3) could be used as a means of assessing discharge to the Minesing Swamp, it is the component of groundwater flow normal to this boundary that is really needed. This component may be difficult to determine. Furthermore, elemental velocities as determined in a Galerkin finite element code have a limited accuracy. An alternative performance measure, which uses the Dirichlet boundary flux expressed by the lower half of equation (3.5), is therefore introduced here. For a particular boundary, the response function takes the form:

$$f(\{\alpha\},h)=\sum_{i=1}^{NB}\sum_{j=1}^{NCi}A_{ij}h_j \tag{4.4}$$

where the first sum is over the NB mesh nodes that make up this boundary, the second sum is over all nodes NC connected to a certain Dirichlet node i, and A is the coefficient matrix with the conductance terms. As already mentioned in the previous chapter, the type 1 flux can be split into contributions from the domain and the recharge spreading layer, making it possible to calculate separate performance measures for these fluxes. Other response functions that will be used in this study are head and boundary flux calibration measures based on equations (4.2) and (4.4). These will be introduced in Chapter (5).

From (4.1), it follows that the marginal sensitivity of the performance measure J to changes in any specific input parameter α_k is given by:

$$\frac{dJ}{d\alpha_k}=\int_V\left[\frac{\partial J(\alpha,h)}{\partial\alpha_k}+\frac{\partial J(\alpha,h)}{\partial h}\Psi\right]dV \tag{4.5}$$

where $\Psi = dh/d\alpha_k$ is the sensitivity of the heads to the parameter α_k which is referred to as the state sensitivity. The first term of (4.5) represents the so-called direct effect or the explicit dependence of J on α_k. The second term in this equation constitutes the indirect effects due to the dependence of J on α_k through the heads. The state sensitivity can be evaluated using the deterministic equation (3.3) in combination with discrete sampling techniques such as the Monte Carlo method. However, to first order, these sensitivities can also be calculated directly. Differentiation of (3.3) with respect to α_k yields:

$$\frac{\partial}{\partial x_i}\left[\bar{S}\frac{\partial K_{ij}}{\partial\alpha_k}\frac{\partial h}{\partial x_j}+\bar{S}K_{ij}\frac{\partial\Psi}{\partial x_j}\right]+\frac{\partial Q}{\partial\alpha_k}=0 \tag{4.6}$$

where $\bar{S}$ has been introduced as the pseudo-unsaturated module of WATFLOW will be considered. The above equation is subject to the boundary conditions:

$$\begin{aligned}\Psi&=\frac{\partial\hat{h}}{\partial\alpha_k} && on\quad\Gamma_1\\ \frac{dq_i}{d\alpha_k}n_i=\left[\frac{\partial q_i}{\partial\alpha_k}+\frac{\partial q_i}{\partial h}\Psi\right]n_i&=\frac{\partial\hat{q}}{\partial\alpha_k} && on\quad\Gamma_2\end{aligned} \tag{4.7}$$

Equation (4.6) needs to be solved for each point in the domain for which the response measure needs to be evaluated. Thus the computational cost of this direct solution becomes exceedingly high if the number of points increases. The adjoint operator approach can alleviate the necessity for the direct evaluation of (4.6). Following the steps taken by *Sykes et al.* [1985], this equation is multiplied by an arbitrarily differentiable function Ψ^* and integrated over the volume of the domain. The above expression is modified making use of the adjoint operator relationship:

$$\int_V \Psi^* L(\Psi) dV = \int_V \Psi L^*(\Psi^*) dV \tag{4.8}$$

in which L signifies an arbitrary mathematical operator. Green's first identity is applied to include the boundary conditions, the symmetry of the hydraulic conductivity tensor $K_{ji} = K_{ij}$ is used, and the resulting expressions are incorporated into the marginal sensitivity equation (4.5), to yield:

$$\begin{aligned} \frac{dJ}{d\alpha_k} &= \int_V \left[\frac{\partial J(\alpha,p)}{\partial \alpha_k} + \Psi \left[\frac{\partial J(\alpha,h)}{\partial h} + \frac{\partial}{\partial x_j} \left(\bar{S} K_{ij} \frac{\partial \Psi^*}{\partial x_i} \right) \right] + \Psi^* \frac{\partial Q}{\partial \alpha_k} \right. \\ &- \left. \frac{\partial \Psi^*}{\partial x_i} \bar{S} \frac{\partial K_{ij}}{\partial \alpha_k} \frac{\partial h}{\partial x_j} \right] dV + \int_\Gamma \left[\Psi \bar{S} K_{ji} \frac{\partial \Psi^*}{\partial x_i} n_j + \Psi^* \frac{\partial \hat{q}}{\partial \alpha_k} \right] d\Gamma \end{aligned} \tag{4.9}$$

As the left-hand side of (4.6) equates to zero, no net terms have in effect been added to the marginal sensitivity. In the above expression, the state sensitivities Ψ are still unknown. The arbitrary function Ψ^* is therefore chosen such that the expressions containing these state sensitivities are eliminated:

$$\frac{\partial}{\partial x_j} \left[\bar{S} K_{ij} \frac{\partial \Psi^*}{\partial x_i} \right] + \frac{\partial J(\alpha,h)}{\partial h} = 0 \tag{4.10}$$

The above equation is known as the adjoint problem and is subject to the following boundary conditions:

$$\begin{aligned} \Psi^* &= 0 \qquad \textit{on} \ \Gamma_1 \\ \bar{S} K_{ji} \frac{\partial \Psi^*}{\partial x_i} n_j &= 0 \qquad \textit{on} \ \Gamma_2 \end{aligned} \tag{4.11}$$

The arbitrary function Ψ^* is referred to as the adjoint state or importance function. It represents the change in the value of the performance measure due to the influx of a unit volume of water at any point **x** in the domain and is therefore equivalent to a Green's response function [*Sykes et al.*, 1985]. Because of the definition of the adjoint problem, the the performance marginal sensitivity is reduced to:

$$\begin{aligned}\Sigma_k = \frac{dJ}{d\alpha_k} &= \int_V \left[\frac{\partial J(\alpha,p)}{\partial \alpha_k} + \Psi^* \frac{\partial Q}{\partial \alpha_k} - \frac{\partial \Psi^*}{\partial x_i} \bar{S} \frac{\partial K_{ij}}{\partial \alpha_k} \frac{\partial h}{\partial x_j}\right] dV \\ &+ \int_{\Gamma_1} \left[\frac{\partial \hat{h}}{\partial \alpha_k} \bar{S} K_{ji} \frac{\partial \Psi^*}{\partial x_i} n_j\right] d\Gamma_1 + \int_{\Gamma_2} \Psi^* \frac{\partial \hat{q}}{\partial \alpha_k} d\Gamma_2 \qquad (4.12)\end{aligned}$$

in which now all terms are known. The heads are found as part of the solution of the primary problem; the adjoint states are the solution of the adjoint problem. The first term in (4.12) represents the direct sensitivity effect. From examination of equations (4.2)-(4.4) it can be seen that this direct effect is non-zero only for those finite elements at which a velocity or boundary flux response is evaluated as these measures depend on the elemental hydraulic conductivity values. The head performance measure depend only indirectly on the system input parameters through the solution of the flow equation. The second and remaining terms of (4.12) represent the marginal sensitivity to any sources or sinks, hydraulic conductivity, prescribed boundary heads and prescribed boundary fluxes including recharge at the top boundary.

The marginal sensitivity Σ_k represents the change in the value of the performance measure for a unit change in α_k. As this sensitivity depends on the solution of the primary problem as well as on the system parameters themselves, the marginal sensitivities are local derivatives related to the assumed parameter values. Thus if these parameters are changed, the adjoint problem needs to be resolved. The numerical implementation of the adjoint equations in the context of a Galerkin finite element discretization is given by *Sykes et al.* [1985] and will not be repeated here. From a computational perspective it should be noted that the global stiffness matrix in (4.10) is equal to that of the flow problem and therefore does not need to be re-assembled. The primary and adjoint problems only differ in their right-hand side load term. Although this implies that both problems can be solved by a single call to the solver, this option has not been used as the computational burden of the linear adjoint problem is minor compared to the solution of the non-linear flow problem.

Sometimes it is more convenient to express the marginal sensitivities in a non-dimensional form:

$$\frac{dJ_k/J}{d\alpha_k/\alpha_k} = \frac{d(ln\ J)}{d(ln\ \alpha_k)} \tag{4.13}$$

These normalized sensitivities express the percent change in the performance measure as a result of a unit change in α_k. For uncertainty analyses or parameter estimation the conductivities are typically transformed to the logarithmic domain so that Gaussian concepts can be used. The sensitivity of a response measure to $Y =^{10} log(K)$ is calculated as:

$$\frac{dJ}{dY} = ln(10)K\frac{dJ}{dK} \tag{4.14}$$

4.3 Hypothetical Example

The hypothetical multi-aquifer system from the previous chapter is revisited to illustrate the effect that different numerical implementations of this flow problem may have on the identification of critical recharge areas for the river boundary. Baseflow to this boundary is used as a performance measure. The scenario of a partially confined upper aquifer is considered.

Martin and Frind [1998] used reverse-in-time particle tracking to delineate capture zones for well fields of the Waterloo Region. The present study is concerned with the identification of critical recharge areas for the Minesing Swamp, which can also be determined using this method. However, an alternative procedure is provided by calculating the derivative of the baseflow F_c to this boundary with respect to local perturbations in the recharge rate R: dF_c/dR.

Figure (4.1) shows the percent change in baseflow that results from a 1 % local change in recharge. High sensitivity values thus indicate important recharge areas. When WATFLOW's free-surface module is used (deform) without regard for the presence of the confining unit, the whole upland area is seen as important for baseflow to the river. When the pseudo-unsaturated module is used (psat), the

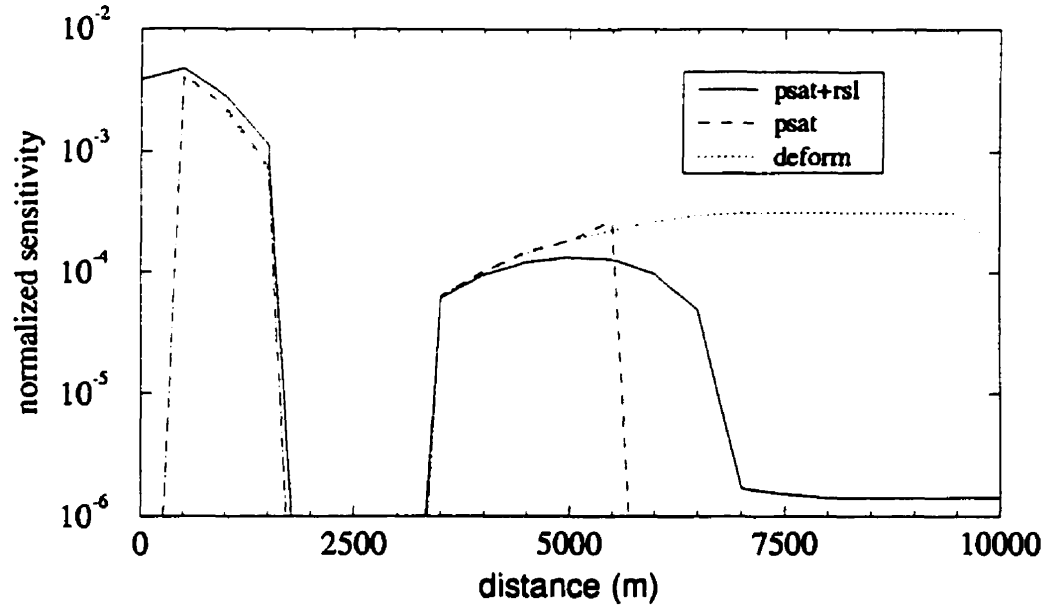

Figure 4.1: Normalized sensitivity of baseflow to river boundary to perturbations in recharge.

effect of the confining unit is taken into account. Because a Dirichlet boundary condition is assigned to the corresponding nodes at the land surface there is no sensitivity to local recharge. Any recharge over the seepage zone also does not affect baseflow to the river. When the recharge spreading layer is introduced (psat+rsl), sensitivity coefficients at the nodes of the confining unit become non-zero as excess recharge is transferred laterally and partially enters the subsurface on the flank of the upland. However, because this effect is subtle (Figure 3.6), sensitivity values are still quite modest, except at the edge of the aquitard. Thus when the unsaturated zone is included, only the exposed side of the upper aquifer is seen as important for groundwater discharge to the river. All solutions further indicate that local recharge near the river is most critical to this baseflow.

Urban development often results in large local changes in infiltration. Impervious surfaces may comprise anywhere between 10-90 % of an urban area. Stormwater collection systems will capture most of the precipitation on these surfaces. A confined aquifer responds linearly to such changes and the first order sensitivity co-

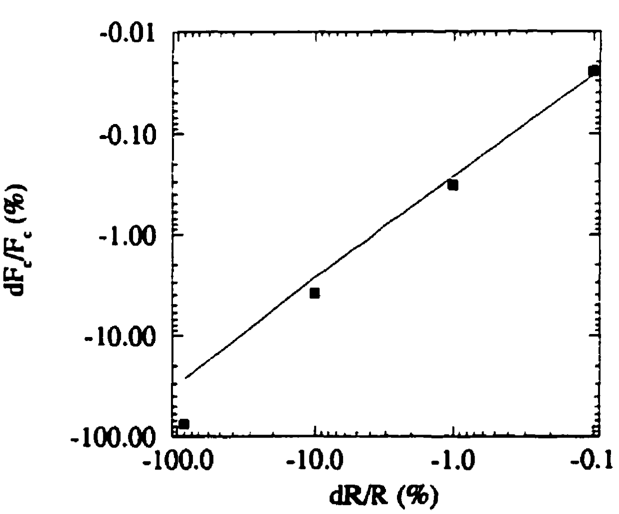

Figure 4.2: Range of validity for derivatives with respect to recharge. Solid line shows linear predictions from adjoint method. Squares designate actual changes resulting from direct parameter perturbations.

efficients will yield accurate predictions of the resulting impact on the flow system. However, in a non-linear system, these coefficients have a limited range of validity. To illustrate this, actual changes in the calculated baseflow to the river are compared to the linear predictions from the sensitivity coefficients, where recharge is reduced uniformly over the model domain. Figure (4.2) shows that for perturbations that are interesting for urbanization impact calculations (i.e., recharge reductions in excess of 10 %), the linear predictions start to deviate significantly from the actual changes. It is thus better to use direct parameter perturbations for such calculations.

Derivatives with respect to the elemental conductivities always have a limited range of validity, even if the flow problem itself is linear. This limited range of validity is important for the model calibration and uncertainty analysis.

Another accuracy aspect results from the non-linear dependence of the pseudo-saturation on the fluid pressures in the unsaturated zone. Although this dependence can be incorporated in the adjoint equations [e.g., *Sykes and Thomson*, 1988], the error introduced by ignoring it is relatively minor. Numerical experiments indicate that the error in the sensitivity coefficients is on the order of 5-25 % for small conductivity perturbations. Largest errors are found when conductivities in the finite elements close to the water table are perturbed. Conductivity variations in these elements have the largest effect on the zone between residual and full saturation in which pseudo-saturations are updated. For larger conductivity perturbations the error caused by the limited range of validity of the first order derivatives is dominant.

Sykes et al. [1985] illustrated the use of derivatives with respect to conductivity in identifying groundwater flow paths. Figure (4.3) shows these derivatives for the example under consideration. Flow paths between the river and its recharge areas are indicated by positive sensitivities as an increase in conductivity will facilitate groundwater flow along them. Positive conductivity changes away from the flow paths have the opposite effect, diverting groundwater away from the river and leading to reduced baseflow. The largest sensitivity to K_{xx} is found close to the river. Normalized values approach unity for those elements adjoining this boundary as a result of the so-called direct effect. High sensitivity values are further found in the saturated part of the aquifers where horizontal flow dominates. Negative values are found directly to the right of the seepage zone. A local increase in horizontal conductivity will increase discharge to this zone, reducing baseflow to the river. The sensitivity to vertical conductivities is highest in the aquitard windows, in those parts of the confining units where head gradients are steep and in the unsaturated zone of the upper aquifer where vertical flow dominates. Baseflow to the river in general is insensitive to those aquitard regions where head gradients are subtle and groundwater flow is sluggish. This observation also holds true for the section of the upper aquifer under the confining unit. The sensitivity analysis thus is useful for understanding the behaviour of the flow system. Derivatives with respect to hydraulic conductivity will also be used in the inverse model and uncertainty analysis.

4.4 Summary

The adjoint method was introduced as a tool for sensitivity analyses. This method has been widely used in groundwater investigations. The derivation of the adjoint equations for the pseudo-unsaturated zone representation are a trivial extension of

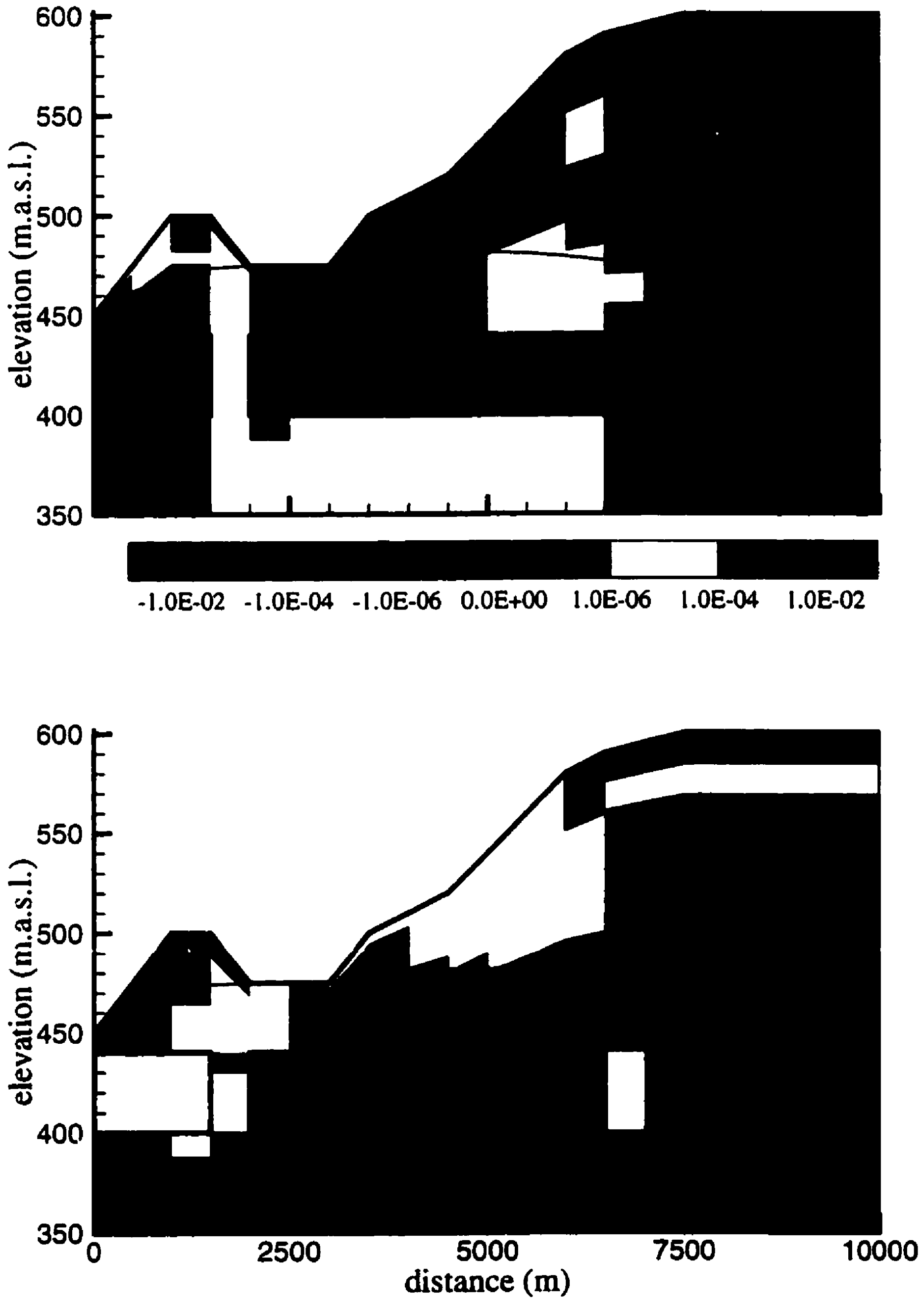

Figure 4.3: Normalized sensitivity of baseflow to river boundary to perturbations in K_{xx} (top panel) and K_{zz} (bottom panel).

existing theory for steady-state confined systems. The main contribution made in this chapter therefore is the introduction of a new performance measure based on model-calculated fluxes to Dirichlet boundaries. This performance measure can be used to identify critical recharge areas for surface waters which are included in the numerical model as specified head boundaries. A performance measure expressing the difference between observed and simulated fluxes will further be used as part of the model calibration.

The hypothetical example introduced in the previous chapter was used to illustrate the effect that different numerical implementations of a flow problem may have on inferred recharge areas for a stream. An inappropriate model will misrepresent the recharge mechanism. This has an adverse impact on the proper identification of critical recharge areas. It was further shown that the derivatives with respect to recharge have a limited range of validity. For urbanization impact calculations, in which large reductions in recharge may be considered, it is better to use a direct perturbation of this parameter.

Mapping the sensitivity of a model response to elemental conductivity values is a powerful tool for identifying groundwater flow paths. Sensitivity coefficients with respect to hydraulic conductivity will also be used in the model calibration and in the uncertainty analysis. An important consideration for these applications is that the validity of the first-order coefficients breaks down for large perturbations in hydraulic conductivity as a result of the non-linear dependence of a groundwater system on this property. Another accuracy aspect is the dependence of the pseudo-saturation on fluid pressures in the unsaturated zone. This dependence was ignored in deriving the adjoint equations. However, the error introduced by this simplification is relatively minor.

Chapter 5

Inverse Model

5.1 Introduction

The inverse problem in groundwater modeling has received considerable attention in the past two decades. Although still an imperfect tool, inverse modeling does facilitate the calibration of groundwater models and has many benefits over manual trial-and-error calibration. Inverse modeling ensures that optimal parameter values are obtained. Furthermore, information is provided regarding the quality of the calibration, any data shortcomings and confidence intervals for the parameters estimates. With the advent of calibration tools such as PEST [*Doherty*, 1994], MODFLOWP [*Poeter and Hill*, 1997] and UCODE [*Poeter and Hill*, 1998], inverse modeling has come within reach of the practicing hydrogeologist.

In the scientific literature, the application of inverse models has mostly been limited to well monitored single aquifer systems where transmissivity and transient hydraulic head data are available from pumping tests [e.g., *Neuman et al.*, 1980; *Clifton and Neuman*, 1982; *Hoeksema and Kitanidis*, 1984; *Carrera and Neuman*, 1986c; *LaVenue and Pickens*, 1992; *LaVenue et al.*, 1995; *Sun et al.*, 1995]. However, many practical calibration problems are hampered by data limitations. Information on the hydraulic conductivity distribution can often only be derived from borehole geologic logs. Transient water level data may not be available. It is well known that static water levels alone are not very well suited to constrain the conductivity distribution. This is certainly true in 3D systems where head gradients may be subtle. Sparse and noisy water level data further hamper the identification of the "true" conductivity distribution. Sparse observations provide limited constraints on head gradients throughout the system. These gradients may therefore be poorly modeled even when the point water levels are on the average adequately matched. The above problems are important in the present study. The focus of this chapter will therefore be the development of a calibration strategy that can overcome the limitations imposed by the data. This development will be done within the framework of existing inverse modeling techniques.

The parameters that enter a steady-state groundwater model are soil properties, recharge, sources or sinks, and prescribed heads and boundary fluxes. All of these parameters are to some degree uncertain and should therefore be taken into account during model calibration. However, specified heads can typically be estimated with a fairly high degree of accuracy. Only zero flux Neumann boundary conditions are used here. Although the validity of chosen Dirichlet and Neumann boundaries may in some instances be a matter of concern, this issue is not considered here. The areal recharge is subject to considerable uncertainty. The percentage of the precipitation that enters the subsurface varies spatially depending on factors such as climate, topography, soil type, land use, and vegetation. These factors determine the amount of precipitation that is lost to the atmosphere (evapotranspiration) and the distribution of the remaining water surplus between the surface and subsurface systems. In the approach taken here, the recharge flux is solely determined by precipitation and evapotranspiration, quantities that are known fairly accurately. The simulated runoff and infiltration depend on the conductivity distribution of the recharge spreading layer and the uppermost part of the model domain, as well as on the pseudo-unsaturated parameters. The uncertainty that exists in the quantity of water that enters the groundwater system is thus reflected by these unknown properties. Anticipating results that will be presented later, it was found that reasonable variations in the pseudo-unsaturated parameters have a negligible effect on the model calibration. Consequently, only hydraulic conductivity is considered as a calibration parameter.

Following its introduction in reservoir engineering, inverse modeling has also become popular in the hydrogeological sciences [*Gavelas et al.*, 1976; *Yeh and Soon*, 1976; *Cooley*, 1977; *Wilson et al.*, 1978; *Shah et al.*, 1978; *Neuman and Yakowitz*, 1979; *Neuman*, 1980; *Cooley*, 1982; *Kitanidis and Vomvoris*, 1983; *Hoeksema and Kitanidis*, 1984; *de Marsily*, 1984; *Townley and Wilson*, 1985; *Sun and Yeh*, 1985; *Carrera and Neuman*, 1986a, 1986b; *LaVenue and Pickens*, 1992; *RamaRao et al.*, 1995]. In their recent review, *McLaughlin and Townley* [1996] state that the inverse method can be characterized by "(1) the way it describes spatial variability (the parameterization it adopts), (2) the forward equation it uses to relate parameters to measurements, (3) the performance measure it uses to define "good" parameter estimates, and (4) the solution technique it uses to find these estimates". The forward (flow) equation has already been covered in Chapter (3) so that only the remainder of these four points need to be addressed here.

The parameterization of the hydraulic conductivity field is a crucial aspect of the inverse problem as it has a strong influence on its well-posedness and on the physical plausibility of its solution [*McLaughlin and Townley*, 1996]. In general the number of unknowns in a flow problem greatly exceeds the quantity of information that is available. The main objective of the parameterization therefore is to reduce this number of unknowns.

Borehole logs are used here to determine an initial hydraulic conductivity distribution. Inverse methods have been developed based on a geologic parameterization [e.g., *Sun et al.*, 1995]. A similar approach will be used in Chapter (8) to optimize the conductivity values that are assigned to the individual lithologies.

The simplest approach to parameterization is to divide the subsurface into discrete zones which are believed to have piecewise constant flow properties. The geostatistical approach is also popular, where the pilot point method pioneered by *de Marsily* [1984] has been widely applied in the recent literature. Kriging is used to obtain an initial distribution of the log conductivity field. Making use of the geostatistical parameters of this field, the conductivity at a number of pilot points with fixed location is estimated from the calibration data. The conductivity field is then updated using the pilot point conductivities as additional constraints. This method is appealing in that it fits well with the adopted conductivity parameterization. Furthermore, the pilot point algorithm is flexible enough to allow for more than one conductivity field.

The lithologic descriptions at best provide an order of magnitude estimate of hydraulic conductivity. Furthermore, the values that are assigned to the individual lithologies are used to distribute hydraulic conductivity in all hydrostratigraphic units. However, a clay in a glaciofluvial environment is not necessarily characterized by the same conductivity value as a clay in a lacustrine deposit. Geologic factors such as different levels of consolidation resulting from the load imposed by glaciers are also not taken into account. The conductivity of the till aquitards may be influenced by fracturing. The lithologic descriptions thus have a limited use for constraining the conductivity distribution. It will be assumed that although these descriptions may not yield accurate absolute conductivity values, they do provide information on their relative magnitude. The average conductivity of the hydrostratigraphic units is then optimized to remove any bias that may exist as a result of the above limitations.

Because intra-formational heterogeneity is taken into account, conductivity values may also have to be adjusted locally. The calibration approach that will be taken therefore consists of two stages: first the average conductivity of the hydrostratigraphic units is optimized in an entirely zonation-based approach. Next, the conductivity distribution within these units is adjusted using a joint zonation/pilot point parameterization. In the first phase, global changes are made to the system and the recharge spreading layer conductivity will also be modified. In the second phase, the parameters of this layer will be considered optimized.

Many different criteria have been introduced to determine the goodness of the estimated parameters. *McLaughlin and Townley* [1996] show that most of these criteria can be considered special cases of the maximum a posteriori formulation of the estimation problem. In its most general form this formulation does not require that the forward (flow) equation is linear or that the probability density function of the unknown parameters is Gaussian. However, in most applications these probability densities are assumed to be normally distributed when formulating the estimation problem. Examples are the maximum likelihood algorithm of *Kitanidis and Vomvoris* [1983], the maximum a posteriori method of *Gavelas et al.* [1976] and least squares (L2) estimation procedures. Calibration measures based on an L2 norm are most widely used and will also be applied here. An example of a non-Gaussian approach is the L1 based inverse method of *Xiang et al.* [1992] which is considered more robust than the L2 norm if the data contain outliers.

The work of *Neuman and Yakowitz* [1979] and *Neuman* [1980] focused on the effect of noise in the water level data. It was shown that even the slightest amount of noise can corrupt the solution of the inverse problem to the degree that parameter estimates become unstable. These authors used a penalty criterion minimizing the difference between the prior (non-calibrated) and posterior (calibrated) transmissivity fields. This additional constraint stabilizes the solution and improves its plausibility, provided that the initial distribution is physically reasonable. However, when the prior conductivity field is derived from indirect information, such a criterion does not necessarily make sense and a different approach needs to be used to mitigate the effect of data noise.

Yeh et al. [1983] used kriging to reconstruct the head field in a 2D model domain from a set of discrete observations. By filling in the missing information on head variations throughout the domain, the range of conductivity values that can match the data is reduced and hydraulic gradients are better constrained. Furthermore, the kriged heads are less susceptible to noise than the data values themselves as the effect of random noise is to some degree eliminated in the interpolation. Outliers in the data can be detected using tools such as back-kriging [*de Marsily*, 1984] or a visual inspection of the interpolated water level maps.

The use of kriged heads as a calibration objective is only correct if the interpolation accurately represents the true head distribution. Vertical gradients in a multi-aquifer system exhibit lateral variations depending on the closeness of recharge and discharge areas and the continuity and hydraulic properties of the aquitards. Information on these vertical gradients is limited as water level observations are sparse. An interpolation of the head data across the confining units may therefore be prone to error. A 2D interpolation within the individual aquifers is more reliable. Because hydraulic head variations in a lateral sense tend to be gradual, it may be expected that a covariance model can adequately represent this variability. Back-kriging will be used to test this hypothesis. Furthermore, the performance of kriged heads and point water levels as calibration measures will be compared.

Baseflow regression data are often used in the calibration of groundwater models. As these fluxes are related to groundwater velocities such data typically put more stringent constraints on the conductivity distribution than head observations. Here it is also desirable to constrain the conductivity of the recharge spreading layer with information from surface runoff. Streams for which flow measurements are available will be entered in the numerical model as Dirichlet boundaries. The flux to these boundaries can be calculated from a partitioning of the coefficient matrix. An objective function is then specified that minimizes the least squares difference between the observed and model predicted fluxes.

In solving the inverse problem a choice needs to be made between a linear and a non-linear approach. Examples of linear solution methods are the direct approach [*Sagar et al.*, 1975; *Yeh et al.*, 1983] and the perturbation method [*Hoeksema and Kitanidis*, 1984]. Non-linear solution methods of the estimation problem are more generally applicable. These methods have been popular in part because they mimic the iterative process of manual model calibration. Most commonly used in groundwater applications are the Gauss-Newton and gradient based methods. The solution method of *Neuman* [1980] will be used here and is discussed in more detail in the next section.

5.2 Theory and Methodology

5.2.1 Calibration Performance Measures

Inverse methods minimize an objective function that describes the fit of the model to a set of observations. An often used performance measure is the weighted least squares residual between model predicted (h) and observed (h^*) hydraulic heads:

$$J_h = \sum_{i=1}^{NH} c_i \left[h_i - h_i^*\right]^2 \tag{5.1}$$

where NH is the number of point head data and the c_i are the calibration weights. An alternative performance measure will be considered which takes the L2 norm between vertically averaged hydraulic heads in each aquifer a and the 2D kriged water level data for that hydrostratigraphic unit. Mathematically this is expressed as:

$$J_h = \sum_{a=1}^{NA} \sum_{i=1}^{NNXY} c_i(a) \sum_{j=jba}^{jta} \delta_{i,j}(a) \left[h_{i,j} - h_{kr}^*(a)\right]^2 \tag{5.2}$$

where NA is the number of aquifers, $NNXY$ is the number of horizontal mesh nodes, and where the last sum is taken over those nodes ($jba \leq j \leq jta$) that are part of aquifer a and that are below the water table. The $h_{kr}^*(a)$ designate the kriged water levels. The $\delta_{i,j}$ represent the weight of the nodal head values in the vertical averaging and thus depend on the vertical discretization of the finite element mesh and the saturated thickness of the aquifer:

$$\delta_{i,j}(a) = \frac{1}{2} \frac{z_{i,min(j+1,jta)} - z_{i,max(j-1,jba)}}{z_{i,jta} - z_{i,jba}} \tag{5.3}$$

Hydraulic conductivities can also be constrained by flow measurements. In this case the performance measure is based on the least squares difference between the observed flux $F^*(s)$ for a certain stream segment (s) and the type I flux calculated using equation (4.4):

$$J_f = \sum_{s=1}^{NS} c(s) \left[\sum_{i=1}^{NB} \sum_{j=1}^{NC(i)} A_{ij} h_j - F^*(s) \right]^2 \tag{5.4}$$

where the first sum is over the NS stream segments for which measurements are available, the second sum is over the NB mesh nodes that are used for a particular stream segment in the numerical model, NC is the number of nodes connected to a certain Dirichlet node i, and A is the coefficient matrix with the conductance terms. The type 1 flux can be split into contributions from the domain and the recharge spreading layer, enabling the separation of contributions from baseflow and rainfall runoff.

In short-hand form the above objective functions can be written as:

$$J = (\mathbf{o} - \mathbf{o}^*)^T \mathbf{C} (\mathbf{o} - \mathbf{o}^*) \tag{5.5}$$

where $\mathbf{o}^*$ is a vector of observations (point or interpolated heads and/or stream flows), $\mathbf{o}$ is the corresponding vector of model predictions and $\mathbf{C}$ is a matrix containing the weight associated with each observation on the diagonal and with zero off-diagonal terms. These weights need to be inversely proportional to the measurement error or observational noise [e.g., *Cooley and Naff*, 1990]. For the more general case of correlated noise, the matrix $\mathbf{C}$ also contains off-diagonal terms. *Hill* [1998] states that the inclusion of these off-diagonals does not appear to significantly affect calibration results.

For the interpolated water levels, the inverse of the kriging variance σ^2_{kr} is used to determine the c_i. This expresses the uncertainty that exists in the spatial interpolation. For this performance measure another complexity arises in that, as the model is calibrated and the position of the water table changes, either more or less horizontal mesh nodes are included in equation (5.2). To account for the changing water table position in determining the convergence of J_h, a correction factor is introduced:

$$c_i(a) = \frac{1}{\sigma_i^2} \frac{\sum_i^{(0)} 1/\sigma_i^2}{\sum_i^{(r)} 1/\sigma_i^2} \tag{5.6}$$

The denominator of the correction term constitutes the sum of all weights c_i for some iteration step r in the calibration, the numerator is given by the same sum at the start of the calibration. For a confined aquifer system, this correction factor reduces to unity.

5.2.2 Calibration Parameters

The objective function J is minimized either by adjusting the average conductivity of a zone (PARAM=1) or by perturbing the K field locally (pilot point option, PARAM=2). In the zonation option, RSL conductivities may also be optimized. Currently, the RSL parameters are kept fixed in the pilot point option.

Zonation Option

For PARAM=1, the effect of a uniform change in hydraulic conductivity in unit k on the objective function is calculated by a direct sum of the elemental sensitivity coefficients:

$$\frac{dR}{dY_k^z} = \sum_{j=1}^{NE(k)} \frac{dR}{dY_{k,j}^*} \tag{5.7}$$

where $NE(k)$ designates the number of elements of unit k. The elemental sensitivity coefficients are calculated using the adjoint method. Horizontal and vertical conductivities may be adjusted independent of one another or not. In the first case (KZADD=0), the derivatives in equation (5.7) are calculated separately with respect to $Y_{xx} = Y_{yy}$ and Y_{zz}. If KZADD=1 the anisotropy ratio is kept fixed. The total sensitivity is then calculated by adding the derivatives with respect to Y_{xx} and Y_{zz}. Conductivities for the RSL are taken to be isotropic and horizontal and vertical sensitivity coefficients are added by default.

Pilot Point Option

A pilot point is characterized by its spatial coordinates and the log conductivity value Y^p assigned to it. Once the pilot point conductivity has been determined, it is added to the database of conductivity measurements (log K values from lithologic descriptions and any pilot point conductivities from previous iterations) of the corresponding hydrostratigraphic unit. Through kriging, the conductivity in this unit will be modified in the neighborhood around the pilot point. The modifications are thus not uniform as in the zonation approach, but increase in magnitude towards the new pilot point, depending on the kriging weights.

The pilot point selection, its addition to the appropriate database and the subsequent kriging will be referred to as the "outer iteration" of the calibration algorithm. This outer iteration is limited to the pilot point option. The "inner iteration" constitutes the estimation procedure to optimize the calibration parameters and this iteration is taken in both pilot point and zonation options.

de Marsily [1984] pioneered the concept of pilot points as parameters of calibration. He assigned their location based on some empirical concepts. *LaVenue and Pickens* [1992] made use of the adjoint method to locate the pilot points where their potential for reducing the objective function is highest. This potential is quantified by the sensitivity dJ/dY^p of the objective function J with respect to the pilot point log conductivity. The target locations are the centroids of the finite elements. This constitutes an approximation to the actual optimal locations. The severity of this approximation depends on the discretization scale of the mesh. The potential locations are ranked in descending order of the magnitude of the absolute values $|dJ/dY^p|$. The pilot points are taken from the top of this ranked list. The number of pilot points that is selected determines the number of degrees of freedom of the inner iteration.

RamaRao et al. [1995] found that the sequential addition of pilot points is superior to simultaneous optimization of more than one pilot point if the same total number of pilot points is allowed. This is explained by the gradual spatial variation of the sensitivity coefficients. Large sensitivities may be found over a certain region of the domain and if multiple pilot points are selected these tend to be clustered in this region. The perturbation that would otherwise be assigned to a single pilot point is now smeared out over the multiple points. The additional pilot points therefore do not lead to an increased reduction of the objective function. Without

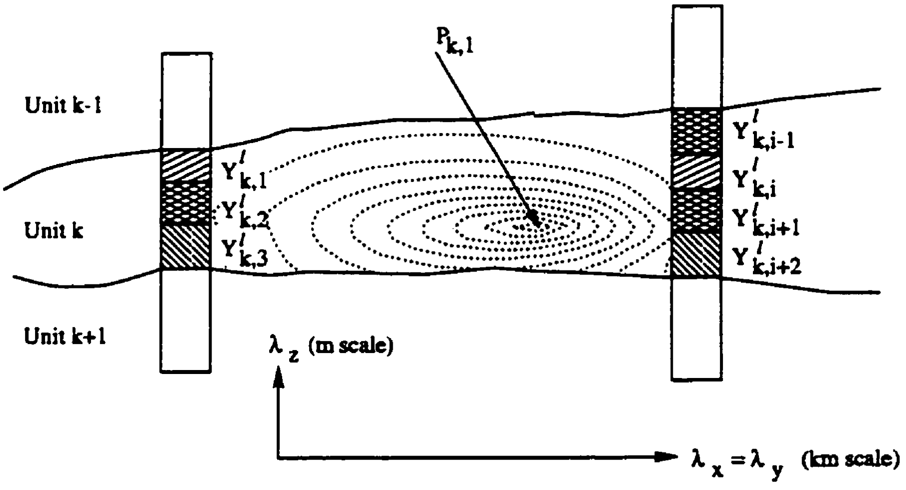

Figure 5.1: Cross-sectional schematic illustrating the pilot point zone of influence as indicated by its kriging weight contours (dotted lines, $\Delta w = 0.1$).

any further numerical experimentation, only one pilot point will be selected per outer iteration. The ratio of vertical and horizontal elemental conductivities is by default kept fixed in the pilot point option (KZADD=1).

Let $P_{k,NP(k)}$ be a pilot point added to a set of $NL(k)$ observations (hydraulic conductivities Y^l from lithologic descriptions) and the $NP(k)-1$ pilot points previously assigned to hydrostratigraphic unit k. The kriging estimate of the log conductivity Y^* at the centroid of element j for that hydrostratigraphic unit is then given by:

$$Y^*_{k,j} = \sum_{i=1}^{NL(k)} w_{j,i} Y^l_{k,i} + \sum_{i=1}^{NP(k)} w_{j,i} Y^p_{k,i} \tag{5.8}$$

where the $w_{j,i}$ are the kriging weights. When the conductivity of the new pilot point is perturbed, the kriged conductivity in all $NE(k)$ elements of unit k will also be altered, causing the objective function J to change. The kriging effect depends on the neighborhood of borehole conductivity data, any pilot points from previous iterations and the statistical anisotropy. The horizontal correlation length $\lambda_x = \lambda_y$ is typically of kilometer scale whereas λ_z is on the order of tenth of meters. The addition of the pilot point has no effect on the conductivity in the other hydrostratigraphic units. These concepts are schematically illustrated in

Figure (5.1). Using the chain rule it can be seen that:

$$\frac{dJ}{dY^p_{k,NP(k)}} = \sum_{j=1}^{NE(k)} \frac{dJ}{dY^*_{k,j}} \frac{dY^*_{k,j}}{dY^p_{k,NP(k)}} = \sum_{j=1}^{NE(k)} w_{j,NP(k)} \frac{dJ}{dY^*_{k,j}} \tag{5.9}$$

where the $dJ/dY^*_{k,i}$ again are the sensitivity coefficients calculated using the adjoint method. At the end of this procedure, the location with the highest value of $|dJ/dY^p|$ is taken as the new pilot point. For a very large grid, the calculation of dJ/dY^p requires considerable computational time because the kriging equations need to be solved for each potential pilot point location. *RamaRao et al.* [1995] considered a slightly different ad-hoc algorithm whereby the pilot point is located at the element centroid where dJ/dY^* reaches its absolute maximum value, thus ignoring the effect of kriging. After locating this point, the exact derivative (5.9) is used for optimization the pilot point conductivity. In this case kriging is only required for the single point thus considerably reducing the computational burden. The authors found that this non-optimal location of the pilot points leads to a misfit reduction that never reaches the value that is attained with the optimal location, even if the algorithm is allowed more pilot points. This is in agreement with the observations made by *Keidser and Rosbjerg* [1991] regarding the sensitivity of the algorithm to the location of the pilot points. However, as the computational burden is highly important in this 3D application, the non-optimal location will still be used.

Three options have been introduced as part of the pilot point selection. The first option is to simply locate pilot points as outlined above (KRIGMODE=1). Contrary to the situation where conductivity (transmissivity) measurements are derived from pumping tests and can formally be assigned confidence intervals, the reliability of the lithologic descriptions as a tool for assigning K values depends on a variety of factors that cannot be assessed (including the driller's patience in recording the lithologies that are encountered). The conductivity values that are obtained may be representative of the local hydrogeology but can also be in total error. If the algorithm indicates that a pilot point should be located near a borehole, one might want to remove the corresponding descriptions from the database. In the second option (KRIGMODE=2) this is achieved by deactivating all borehole conductivities that are located in a neighborhood around the new pilot point. This neighborhood is specified in terms of the correlation lengths of the K field. In this way, the effect of the non-optimal location of the pilot points is minimal and potentially bad data are removed from the database. Presently, this is done in an automated fashion. However, it would be preferable to let the user decide whether or not any borehole information should be deleted. Options for user interaction will be explored in future versions of the calibration code. If one wants to honor all borehole conductivities, the effect of the non-optimal pilot point location may become important. If a pilot point is positioned near one or more boreholes, its effect on the kriged conductivity field will be small and a limited improvement of the calibration measure will be achieved. The third option (KRIGMODE=3) constrains pilot point target locations to be some distance away from the boreholes, where this distance again is specified in terms of the correlation lengths of the K field.

The plausibility and uniqueness of the solution depend on the number of degrees of freedom of the inverse method. As shown by *Keidser and Rosbjerg* [1991], the number of pilot points is the equivalent of the number of zones in a zonation approach. Increasing the number of pilot points thus deteriorates the uniqueness of the solution of the inverse problem. However, here the pilot points will be introduced on a sequential basis until the objective function is minimized to a satisfactory degree. The trade-off between over-parameterization and under-calibration can thus be evaluated in each step of the inversion algorithm and the total number of pilot points can be limited to reflect the amount of information that is available. Compared to zonation where the number of zones and their geometry must be determined a-priori, the pilot point method offers much more flexibility. It amounts to optimizing sequentially the number of zones and their geometry.

By determining the optimal location of the new pilot point, the changes in parameter value that are required to minimize the objective function are reduced. When the parameter locations are not optimally selected, the changes in the parameter values that are required to minimize the objective function are often large. Optimal location of the pilot points thus further increases the plausibility of the solution. The strength of the pilot point method lies in its ability to produce smooth log conductivity fields which are physically plausible while giving an acceptable fit to the head data [*McLaughlin and Townley*, 1996].

5.2.3 Minimization Algorithm

The calibration parameters are optimized in the non-linear inner iteration. The optimization algorithms consists of an unconstrained Newton iterative search with a subsequent imposing of constraints. The following equation is applied to perturb the calibration parameters until convergence is achieved:

$$\mathbf{Y}^{(r+1)} = \mathbf{Y}^{(r)} + \beta^{(r)}\mathbf{u}^{(r)} \tag{5.10}$$

where $\mathbf{Y}$ is the vector of conductivities to be optimized, r is the inner iteration index, $\mathbf{u}$ is the search vector, and β is the step length for the update. The vector length is equal to the number of parameters that is being optimized. For the pilot point option (PARAM=2) the number of degrees of freedom is always one and $\mathbf{Y}$ and $\mathbf{u}$ reduce to scalars. The steps taken in the inner iteration are given in point form below:

1. Choose the initial set of parameters $\mathbf{Y}^{(r)}$, $r = 1$. For the zonation option these are the average log conductivities of the hydrostratigraphic units and the RSL log K values. In the pilot point option, the initial parameter is the kriged log conductivity at the pilot point location.

2. Compute the heads $\mathbf{h}^{(r)} = \mathbf{h}(\mathbf{Y}^{(r)})$, the objective function (5.5) and its gradient $\mathbf{g}^{(r)}$ with respect to the calibration parameters:

$$\mathbf{g}^{(r)} = \frac{J}{d\mathbf{Y}}\bigg|_{\mathbf{V}=\mathbf{Y}^{(r)}} \tag{5.11}$$

3. Compute the updating direction $\mathbf{u}^{(r)} = \mathbf{u}(\mathbf{g}^{(r)}, \mathbf{g}^{(r-1)}, ...)$. Contrary to what common sense might dictate, advancing along the direction of steepest descent $\mathbf{g}$ is not the fastest way of finding the optimum conductivity vector $\mathbf{Y}$ that minimizes the objective function. Previous investigations have considered the algorithms of Fletcher-Reeves, Broyden and Davidson-Fletcher-Powell [*Luenberger*, 1973] for improving the convergence of the inner iteration. *Carrera and Neuman* [1986b] compared the performance of these algorithms for a 2D inverse problem. They found that convergence of the non-linear iteration could be improved by switching from one method to the other when the former slows down or fails to converge. However, the performance of the Fletcher-Reeves conjugate gradient method alone also was found to be quite good and it will be used here. In this method, the updating direction is given by:

$$\mathbf{u}^{(r)} = -\mathbf{g}^{(r)} + \nu^{(r)}\mathbf{u}^{(r-1)} \tag{5.12}$$

where $\nu^{(r)} = ||\mathbf{g}^{(r)}||/||\mathbf{g}^{(r-1)}||$. A "pacer" iteration with $\nu^{(r)} = 0$ is used after each *NY* iterations, *NY* being the dimension of the search vector. By advancing along the direction vector the new values of the parameters are obtained.

4. The optimum step length for the advance is determined by minimizing $J(\mathbf{Y}^{(r+1)})$ with respect to $\beta^{(r)}$ and thus by solving [*Neuman*, 1980]:

$$\frac{\partial J(\mathbf{Y}^{(r+1)})}{\partial \beta^{(r)}} = 0 \tag{5.13}$$

Substituting a Taylor expansion of the heads vector **h**,

$$\mathbf{h}^{(r+1)} = \mathbf{h}^{(r)} + \beta^{(r)} \frac{\partial \mathbf{h}^{(r)}}{\partial \beta^{(r)}} \tag{5.14}$$

into the objective function J, invoking (5.13) and retaining only first order derivatives leads to:

$$\beta^{(r)} = -\frac{(\mathbf{b}^{(r)})^T \mathbf{C}(\mathbf{o}^{(r)} - \mathbf{o}^*)}{(\mathbf{b}^{(r)})^T \mathbf{C} \mathbf{b}^{(r)}} \tag{5.15}$$

in which an expression for the vector $\mathbf{b} = \partial \mathbf{h}/\partial \beta$ can be obtained using Newton's method:

$$\sum_{j=1}^{NN} A_{ij}^{(r)} b_j^{(r)} = -\sum_{k=1}^{NV} \frac{\partial F_i^{(r)}}{\partial Y_k^{(r)}} u_k^{(r)} \qquad i = 1, 2, ..., NN \tag{5.16}$$

where A_{ij} is the stiffness matrix of the direct problem (flow equation) and F_i the right-hand side forcing vector. The above matrix equation is solved subject to the condition that $b_i^{(r)} = 0$ at all nodes i where the head is prescribed. Specified flux nodes used in solving the flow equations now reduce to zero-flux Neumann conditions. As the left-hand side matrix in (5.16) is the same as that of the primary problem it does not have to be re-assembled. The derivative of the forcing vector with respect to the log conductivities is readily calculated where the effect of kriging (PARAM=2) or the piecewise constant conductivities (PARAM=1) should again be taken into account through the chain rule (i.e., equations 5.7 and 5.9). Appendix A of *Neuman* [1980] gives a derivation of the above equation. It has been found necessary to limit the parameter adjustments to some prescribed maximum to avoid problems such as overshoot of the update and to obtain smooth convergence of the inner iteration. This is achieved by enforcing $\beta^{(r)}|u_{max}^{(r)}| \leq \Delta Y_{max}$, where $u_{max}^{(r)}$ is the maximum entry in the direction vector and ΔY_{max} is a user-defined maximum allowed conductivity update.

5. Update the parameters $\mathbf{Y}^{(r+1)} = \mathbf{Y}^{(r)} + \beta^{(r)}\mathbf{u}^{(r)}$ and impose the constraints. These constraints consist of upper and lower limits for each of the conductivities that are being optimized. These can, for example, be derived from geostatistical parameters.

6. Check for convergence. The inner iteration is halted if a prescribed number of maximum iterations is exceeded or if the following two criteria are met: (a) $J^{(r)} \geq \mu_0 J^{(r-1)}$ where μ_0 is a number between 0 and 1 and (b) $||\mathbf{g}^{(r)}|| \leq \mu_1 ||\mathbf{g}^{(r-1)}||$ where μ_1 is a prescribed positive tolerance.

7. If convergence is not achieved, let $r = r + 1$ and return to step 2. If convergence is achieved, the optimization algorithm (inner iteration) is completed. For the zonation option this also completes the calibration procedure. For PARAM=2, the new pilot point is added to the database of the corresponding hydrostratigraphic unit and the execution of the program continues with a check for convergence of the outer iteration. Convergence criteria for this outer loop are those of the inner iteration plus the requirement that $J \leq J_{min}$ where J_{min} is a prescribed minimum for the objective function. The outer iteration can also be halted if a specified maximum number of pilot points has been exceeded.

5.2.4 Combined Use of Head and Flow Data

The calibration algorithm as implemented in WATFLOW has two options for combining head and flow data. The first alternative (COMBINE=1) is to lump all data into a single performance measure. All calculations as described in the previous sections are then performed on the cumulative objective function $J_h + J_f$. Although the calibration weights that are introduced remove dimensional differences between the different data types, it is still clear that when the amount of head data is much greater than the number of flow measurements, any inversion based on a lumped objective function will be dominated by the former dataset. As a result, the estimated conductivities will largely depend on the head data.

A simple approach that was attempted to remedy this problem is to increase the weight of the flow measurements. However, in calibrating the Oro Moraine model it was found that this leads to an unstable inversion. This is caused by differences in sensitivity of the head and flow measurements to changes in conductivity, where the large conductivity contrasts that exist in a multi-aquifer setting may also play an important role. In a complex system, the objective function surfaces [e.g., *Poeter and Hill*, 1997] associated with the two data types will typically be quite different. The gradient vectors for these measurements may then significantly differ in direction. This has an adverse impact on the stability of a joint inversion. Increasing the weight of the discharge measurements is thus not a viable option.

The second option is to use only a single type of data in the calibration. The decision regarding which type of measurement to use can either be made by the user (DATASET=1 for head data, DATASET=2 for flow data) or it is based on the relative magnitude of the objective functions (DATASET=0). For example, if at some point $J_h > J_f$ then then the head data will be used ($J = J_h$) and vice versa.

A mechanism was implemented to ensure that (in most cases) the fit to both sets of data is improved, even when using only a single set. This is achieved by calculating the gradient vector (step 2 of inner iteration) for each data type individually and retaining only those entries that have a consistent sign (COMBINE=2). For example, if head data are the current calibration objective:

$$\begin{aligned} g(i)^{(r)} &= g(i)_h^{(r)} && g(i)_h^{(r)} \cdot g(i)_f^{(r)} > 0 \\ &= 0 && g(i)_h^{(r)} \cdot g(i)_f^{(r)} \leq 0 \end{aligned} \tag{5.17}$$

where subscripts h and f designate head and flow calibration measures. In this case, only the head data would be used for the remainder of the inner iteration. The inner iteration now can also be halted if none of the entries in the search vectors for head and flow data have a consistent sign. The above restriction on the search vector is not always sufficient to ensure that the match to both data types is improved simultaneously. Problems may arise when the head data require a larger conductivity update than the flow data or vice versa. However, criterion (5.18) has mostly been found to be adequate. It results in a convergence behaviour of the inner iteration that is more guided by the flow measurements than can be achieved by simply lumping the data. If COMBINE=3, the sign check is skipped thus allowing more freedom in improving the calibration of the selected dataset. For PARAM=2, the COMBINE=2 option ensures that only those elements are considered as pilot points for which a local conductivity change will simultaneously improve head and flow data. This is achieved by comparing the sign of the derivatives of the performance measures with respect to the elemental log conductivities.

5.2.5 Covariance of Parameter Estimates

One of the advantages of an automated calibration is that the uncertainty in the estimated conductivities can be determined. Two levels of uncertainty need to be considered: (1) uncertainty in the average zonal conductivities, and (2) uncertainty in the kriged conductivity distribution. The second source of uncertainty is determined through conditional probability [e.g., *Dagan*, 1982b]. Making use of relationship (2.12), it follows that the conditional covariance $\sigma(\mathbf{x}_i, \mathbf{x}_j)$ is given by:

$$\sigma(\mathbf{x}_i, \mathbf{x}_j) = \sigma_{ij} - \sum_{k=1}^{NL+NP} w_{ik}\sigma_{kj} \tag{5.18}$$

where σ_{ij} is the unconditional covariance determined by the adopted model semivariogram, equation (2.12), and the separation vector for two points i and j and where the w_{ik} designate the kriging weights for the NL borehole conductivities and NP pilot point K values. Equation (5.18) illustrates the conditioning effect that measurements have on parameter uncertainty as already discussed in Section (2.2.3). The additional information provided by the pilot point conductivities thus further reduces uncertainty.

Uncertainty in the average (zonal) conductivities can be calculated from the second moment of the error term:

$$\mathbf{e_Y} = \hat{\mathbf{Y}} - \mathbf{Y} \tag{5.19}$$

where $\mathbf{Y}$ is a vector containing the "true" and unknown average conductivities and $\hat{\mathbf{Y}}$ is the estimate of $\mathbf{Y}$. Assumptions that are made in this analysis are (1) measurement errors in the calibration data are normally distributed, (2) the model responds approximately linear to perturbations in the estimated parameters, and

(3) the model accurately represents the actual system such that the residuals between observations and model predictions entirely result from data errors [e.g., *Poeter and Hill*, 1997]. The first two points are typical of any first order second moment analysis. The third point is of concern if the numerical model is incomplete or incorrect.

The covariance $\sigma(\mathbf{e_Y})$ of the estimation error for the average conductivities is given by [*Neuman and Yakowitz*, 1979; *Neuman*, 1980]:

$$\sigma(\mathbf{e_Y}) \approx \frac{J}{ND - NZ}(\mathbf{Z}^T\mathbf{C}\mathbf{Z})^{-1} \tag{5.20}$$

where J is the (lumped) calibration measure, ND is the total number of (head and flow) measurements, NZ is the number of adjustable parameters (zones), and where $\mathbf{Z}$ is a Jacobian (or sensitivity) matrix whose components are defined as:

$$Z_{ij} = \partial \hat{o}_i / \partial \hat{Y}_j \tag{5.21}$$

where the $\hat{o}$ are the final model predictions associated with the observations o^*. The forward sensitivity method is used to calculate $\mathbf{Z}$ as the number of zones will typically be small compared to the number of responses. For example, if only point head data are used, the number of responses is equal to NH. Using the adjoint method, the sensitivity of performance measure (4.2) would have to be evaluated for each data point individually. The forward sensitivity method then is more efficient. When flow data are used, the total sensitivity consists of a direct part related to the dependence of the conductance terms in (4.4) on the elemental conductivities and an indirect part caused by the dependence of this performance measure on the modeled heads.

5.3 Summary

An inverse modeling algorithm was developed based on existing theory. The minimization algorithm itself consists of an unconstrained Gauss-Newton iterative search with a subsequent imposing of upper and lower bounds on the estimated parameters. Hydraulic conductivity values presently are the only adjustable parameters. The parameterization of the conductivity field may either consist of a zonation or a combined zonation/pilot point approach. When the model consists of a single zone (aquifer) it is also possible to strictly use a pilot point parameterization. Kriging is used to calculate the effect of the pilot points on the conductivity distribution in their zone of influence. The algorithm thus incorporates the two most popular methods of improving the well-posedness of the inverse problem by reducing the number of degrees of freedom. The covariance of the zonal conductivity estimates is computed through a first order second moment analysis, making use of the final calibration statistics. The covariance of the kriged conductivity fields is derived from the geostatistical parameters and the conductivity data through conditional probability.

In the present study, a zonation is derived from the hydrostratigraphic interpretation of the multi-aquifer system. Adjustable parameters are either the average conductivity of the hydrostratigraphic units or point conductivity values within these units. Lithologic descriptions have a limited use for describing the spatial distribution of hydraulic conductivity. It is assumed that although these descriptions may not provide accurate absolute conductivity values, they do provide information on the relative magnitude of these values. Average conductivities are then optimized to account for any bias that may have been introduced as a result of the indirect nature of the data. The pilot points are used to achieve local conductivity updates within the hydrostratigraphic units to refine the model calibration.

The main contribution made in this chapter is the development of two least-squares performance measures to address concerns regarding the quality of the head data and to allow for the simultaneous use of both hydraulic heads and flow measurements in the calibration. The first performance measure is based on kriged heads rather than point water level observations. The second calibration measure uses the difference between observed and calculated fluxes to certain Dirichlet boundaries that are incorporated in the model to simulate the presence of streams and other surface water bodies.

Kriged water levels fill in the missing information on head variations throughout the model domain. This is expected to reduce the range of parameter values that can match the data, stabilizing the model calibration. Furthermore, hydraulic gradients will be better constrained. Baseflow regression data are often used in the calibration of groundwater models. In the present study it is also desirable to constrain the conductivity of the recharge spreading layer with information from surface runoff. An important objective of the model calibration will thus be, not only to validate the numerical model against observed groundwater discharge to streams, but also to provide a steady-state simulation of runoff to these water courses. This will be illustrated in the calibration of the Oro Moraine model.

Flag		Description
PARAM	1	Zonation parameterization. Although heterogeneity within each zone is allowed, conductivities are updated uniformly.
	2	Pilot point parameterization. Becomes joint zonation/ pilot point method if multiple zones are defined.
KRIGMODE	1	Pilot points and other conductivity data have same status.
	2	K data in neighborhood of pilot points are eliminated.
	3	Pilot points must be located some distance from K data.
KZADD	0	Estimate horizontal and vertical conductivities independently (only applicable if PARAM=1).
	1	Horizontal and vertical conductivities are adjusted uniformly.
DATASET	0	Let program decide whether to use head or flow data.
	1	Always use head data.
	2	Always use flow measurements. (DATASET flag is only activated if COMBINE $\neq$ 1).
COMBINE	1	Lump head and flow calibration measurements.
	2	Enforce sign check on gradient vector for head and flow data while calibrating to a single data type.
	3	Completely ignore other data while calibrating to a single set.

Table 5.1: Calibration options implemented in WATFLOW.

Chapter 6

Uncertainty Analysis

6.1 Introduction

One of the objectives of this study is to assess the impact of certain urbanization scenarios on the water mass balance of the Minesing Swamp. Because the reliability of such predictions is a matter of concern they should be cast in a probabilistic framework. Confidence intervals on the water mass balance are needed to determine the significance of calculations regarding the impact of urbanization.

Following the work of *Freeze* [1975], stochastic analyses have become popular in the hydrogeological sciences to address the effect of parameter variability and uncertainty in groundwater systems. Several different approaches have been developed towards this problem and these can be distinguished by (1) the assumptions made regarding the statistical characteristics of the input parameters, and (2) the method used to determine the effect of this parameter uncertainty on the response of the groundwater system. The second aspect may or may not involve assumptions regarding the statistical nature of the system response that is of interest.

Freeze [1975] considered a one-dimensional groundwater problem where the hydraulic conductivity in each of the blocks of the spatial domain was randomly generated from a log-normal distribution. It was quickly pointed out that by assuming spatial independence, the correlation structure that is observed in actual systems is ignored [*Gelhar et al.*, 1977]. As a result, parameter and model uncertainty are over-estimated. The theory of regionalized variables takes the partially deterministic and partially random nature of geologic deposits into account. The kriging and multi-dimensional spectral techniques discussed in Chapter (2) are examples of popular methods based on this theory. Unconditional and conditional random conductivity fields were introduced in the hydrogeological sciences for stochastic analyses by *Delhomme* [1979]. As discussed earlier, unconditional fields are only consistent with the correlation structure exhibited by the data whereas conditional random fields are also consistent with the data values themselves. The effect of conditioning therefore is to reduce uncertainty. In the context of the model calibration, conditioning is achieved by including the effect of the head and discharge data on uncertainty in the estimated hydraulic conductivity distribution.

The most common methods for uncertainty analysis can be grouped into two broad categories: worst case scenario analysis and non-worst case scenario analysis. The objective of the worst case analyses is to identify extrema in the model response. This is typically done by evaluating the model output at the extreme (vertex) values of its input parameters. In the Waterloo Moraine study, *Martin and Frind* [1998] performed such an analysis by opening or closing aquitard windows and evaluating the effect this has on the simulated capture zones. Such an approach is fairly cost-effective. However, only a limited number of scenarios are evaluated in this fashion and extreme cases of changes in the capture zone geometry may remain undetected. In general, a limitation of worst-case scenario analysis is that the verteces of the system response not necessarily coincide with those of the input parameters.

The non-worst case analysis methods are more general and more commonly used in hydrogeology. These methods can be sub-divided into two groups: sampling and linearization methods. The most common of the latter methods are the first-order and second-moment analysis [e.g., *Benjamin and Cornell*, 1970; *Sagar*, 1978; *Dettinger and Wilson*, 1981] and the small perturbation approach using a spectral solution [e.g., *Gelhar*, 1976; *Bakr et al.*, 1978; *Gutjahr et al.*, 1978; *Gelhar and Axness*, 1983] or not [*Tang and Pinder*, 1977; *Dagan*, 1982b]. Because these methods approximate the stochastic process to the same order they should yield the same information.

The linearization methods assume that the system response and all uncertain parameters can be represented by the sum of a deterministic and a random fluctuating part. The random fluctuations are assumed to be Gaussian in nature such that their statistical structure is fully contained in the (co)variance. Expressions for the statistical moments of the system response are then found in terms of the statistical moments of the fluctuating quantities. However, the system response is Gaussian in nature only if the (transformed) input parameters are normally distributed and if the system response is perfectly linear with respect to perturbations in these parameters. As a result, these methods are only applicable to small perturbations. The Gaussian behaviour of the input parameters can mostly be ensured by a simple transformation as in the case of hydraulic conductivity.

The spectral methods further require that the head random field be stationary [e.g., *Bakr et al.*, 1978]. For one- and two dimensional flows the analysis is thus limited to infinite domains. In three dimensions hydraulic head may be locally stationary under very general conditions [*Gutjahr and Gelhar*, 1981]. However, the first-order and second-moment method is not restricted by this stationarity requirement and it will be used here. The method results in linear predictions intervals. Linear intervals are calculated in popular codes such as MODFLOWP [*Poeter and Hill*, 1997] and UCODE [*Poeter and Hill*, 1998].

Several approaches have been taken to circumvent the limitations of linearization methods. *Townley* [1984] employs a second order correction to the standard first order second moment method. *Sitar et al.* [1987] use a first order reliability method to calculate higher order moments of the model predictions. Another alternative is the likelihood method as introduced by *Vechia and Cooley* [1987]. An appealing feature of this last method is that it simultaneously determines confidence intervals for the input parameters through a non-linear regression and prediction intervals for a certain model response. The prediction intervals thus take the non-linearity of the problem into account and are also consistent with the calibration data.

The likelihood method consists of an iterative procedure to determine the extreme values of the model input parameters that still match the calibration data with some specified level of significance. Confidence bounds for the model output are then determined making use of these extreme values. The likelihood method is therefore in essence a worst-case scenario analysis and it is subject to the same limitations. It appears to be restricted to a zonation parameterization for which the number of adjustable parameters is relatively small. This limitation makes it unsuitable for the present study.

Discrete sampling techniques such as the Monte Carlo method give the most general approach to stochastic analyses. In a Monte Carlo analysis an approximate probability density function for the system response can be attained by performing a deterministic analysis in which the input parameters are randomly chosen according to their distribution function. By solving the flow equation itself, the non-linearity of the system response is taken into account and the limitation to small parameter perturbations is circumvented. A disadvantage of a Monte Carlo analysis is the computational cost of solving the flow problem repeatedly. The computational burden can to some degree be limited by using the more efficient Latin Hypercube sampling technique [*Iman and Conover*, 1980]. Another problem is that the random realizations of the input parameters not necessarily result in a model solution that is consistent with the calibration data. *RamaRao et al.* [1995] solved this problem by calibrating each randomly generated transmissivity field to the water level data. The exceedingly high computational burden of such an analysis makes it inappropriate for the present study.

Recently, *Cooley* [1997] compared predictions intervals generated with the first order second moment method, the likelihood method, and two boot-strap methods. Boot-strap methods generate many datasets from a single sample (the actual data), and are thus conceptually similar to a Monte Carlo analysis. The first of these methods does not take the calibration data into account whereas the latter incorporates this information in a fashion that is operationally similar to the work of *RamaRao et al.* [1995]. The physical problem involved an infiltrating stream crossing a heterogeneous aquifer. Cooley's comparison is of interest to the present study because the problem was highly non-linear and because performance measures regarding both hydraulic head and stream infiltration were considered. It was found that prediction intervals determined with the likelihood method were virtually exact. For hydraulic head, only the first of the bootstrap methods resulted in inaccurate confidence intervals; the outcomes of the other three methods were very similar. Prediction intervals for the streamflow infiltration by the linearization and first bootstrap methods were similar and inaccurate whereas the second bootstrap method gave satisfactory results. However, the computational burden of this method far exceeded that of the likelihood method.

Based on computational burden and the accuracy of the prediction intervals the likelihood method should be the preferred technique for a stochastic analysis. However, due to constraints from the chosen hydraulic conductivity parameterization the first-order and second-moment method is used instead. Further limitations associated with the uncertainty analysis will be discussed in the next section. In Chapter (8) the accuracy of the first order second moment method will be investigated by a comparison with results obtained from some Monte Carlo simulations.

6.2 Sources of Uncertainty

Three levels of uncertainty exist a result of the conductivity parameterization and the nature of the information regarding this parameter: (1) uncertainty in the location of the stratigraphic contacts, (2) uncertainty in the average conductivity of the hydrostratigraphic units and (3) uncertainty in the intra-formational conductivity distribution.

Uncertainty in the location of the aquifer/aquitard contacts will not be considered directly. In the calibration of the Oro Moraine model (Chapter 8) it will become evident that the conductivity distribution strongly depends on the zonation provided by these contacts, where aquifer inter-connectedness is an important issue. Random realizations of the aquifer/aquitard contacts provide better vertical connections for groundwater flow than the kriged surfaces, significantly altering the flow system. The use of these realizations in an uncertainty analysis without a re-calibration of the model is therefore inappropriate. Furthermore, in regions were a certain hydrostratigraphic unit pinches out, the elevation of the corresponding aquifer/aquitard contacts needs to be constrained and the associated uncertainty becomes meaningless. On the other hand, the development of such zones is the most crucial aspect of uncertainty regarding the location of the hydrostratigraphic contacts. Uncertainty in the hydrostratigraphy is taken into account in a limited fashion in the calibration by considering alternative zonation scenarios for the numerical model.

As a result of the chosen parameterization and the proposed two-phase calibration, the true mathematical covariance of the log hydraulic conductivity field is "split" into two parts: one part expresses the correlation in the intra-formational heterogeneity through the kriging equations. The other part gives the correlation between the hydrostratigraphic units as determined from the model calibration. The two levels of uncertainty cannot be taken into account simultaneously because the inter-formational covariance applies to the average conductivities, whereas the intra-formational covariance applies to the elemental conductivity values. This makes a separate analysis necessary. Consequently, no true predictions intervals can be calculated for the model output. However, the variance that results from each of the sources of uncertainty can be determined. Furthermore, the relative importance of the two sources of uncertainty can be assessed.

6.3 Theory

In the first-order and second-moment method, the mean and variance of a selected system response J are obtained from a multi-dimensional Taylor series expansion of this response about the mean values of the parameters α:

$$\begin{aligned} J(\alpha) = J(\alpha_0) &+ \left.\frac{dJ}{d\alpha^T}\right|_{\alpha=\alpha_0} (\alpha - \alpha_0) + \frac{1}{2}\left.\frac{d^2J}{d\alpha^{2T}}\right|_{\alpha=\alpha_0} (\alpha - \alpha_0)^2 \\ &+ \frac{1}{6}\left.\frac{d^3J}{d\alpha^{3T}}\right|_{\alpha=\alpha_0} (\alpha - \alpha_0)^3 + \ldots \end{aligned} \tag{6.1}$$

where α_0 designates the mean values. The expected value of the system response is given by:

$$E[J(\alpha)] = J(\alpha_0) + \frac{1}{2}\left.\frac{d^2J}{d\alpha^{2T}}\right|_{\alpha=\alpha_0} \sigma(\alpha) + \ldots \tag{6.2}$$

involving only even order derivatives of the system response. If this response is perfectly linear with respect to perturbations in the system parameters, the second and all higher order derivatives in (6.2) are zero and the expected value of the system response reduces to the response at the mean parameter values. Despite the non-linear dependence of the flow equations on hydraulic conductivity in particular, the assumption of linearity is still made in most investigations and the higher order derivatives in (6.2) can only be ignored when the coefficient of variation of the system parameters is small. In the first-order and second-moment method, the assumption of linearity and/or a small perturbation is made such that the mean and variance of the system response are approximated by:

$$\begin{aligned} E[J(\alpha)] &= J(\alpha_0) \\ \sigma[J(\alpha)] &= E[(J(\alpha) - J(\alpha_0))^2] = \frac{dJ}{d\alpha^T}\sigma(\alpha)\frac{dJ}{d\alpha^T}^T \end{aligned} \tag{6.3}$$

The sensitivity coefficients that result from the linearization of the stochastic equations are efficiently calculated using the adjoint equations given in Chapter (4).

An illustration of the limited range of validity of these sensitivity coefficients is given in Figure (4.2). The covariance $\sigma(\alpha)$ of the either the average zonal or the intra-formational conductivities is calculated using the equations given in Section (5.2.5).

Prediction or confidence intervals are intervals in which the true predictive quantity is likely to occur with some specified probability [*Hill*, 1998]. A 100(1- a)x100% confidence interval for J is given by

$$J(\alpha_0) \pm z_{1-a/2} \left[\frac{dJ}{d\alpha^T} \sigma(\alpha) \frac{dJ}{d\alpha^T}^T \right]^{1/2} \tag{6.4}$$

where $z_{1-a/2}$ is the (1-a/2)x100 percentile of the N(0,1) normal distribution. The z-statistic is used if $\sigma(\alpha)$ is known. If this covariance is determined through a model regression the student t-test needs to be used instead to account for the number of degrees of freedom in the inverse problem. Most studies do not actually determine these intervals but only give the mean and variance of the model output as calculated using equations (6.3). Given the limitations of the stochastic analysis that were discussed earlier, that will also be the case here.

6.4 Summary

A brief overview of existing techniques for uncertainty analyses was given in this chapter. Two of these techniques will be used in the present study: the first-order and second-moment method and Monte Carlo sampling. The first order and second method derives its computational efficiency from a linearization of the stochastic process. As a result, confidence bounds determined with this method are only valid for a limited range of variability in the model input parameters. In the Monte Carlo method no assumption is made regarding the stochastic process as an approximate probability density function for the system response is attained by performing a deterministic analysis in which the input parameters are randomly chosen according to their distribution function. The main disadvantage of a Monte Carlo analysis is the computational cost of solving the flow problem repeatedly.

Three levels of uncertainty exist a result of the conductivity parameterization and the nature of the information regarding this parameter: (1) uncertainty in the location of the stratigraphic contacts, (2) uncertainty in the average conductivity of the hydrostratigraphic units and (3) uncertainty in the intra-formational conductivity distribution. Uncertainty in the location of the hydrostratigraphic contacts will not be evaluated directly. It will only be taken into account in a limited fashion as part of the model calibration. The remaining two levels of uncertainty are evaluated independently to determine the resulting variances in the simulated water mass balance. The first-order and second-moment method will be used for that purpose. Monte Carlo sampling will only be used to investigate accuracy aspects of the first-order second-moment analysis.

Chapter 7

Oro Moraine Hydrostratigraphy

7.1 Introduction

A hydrostratigraphic model of the study area is developed in this chapter. A general introduction to the study area is provided. The processing of the Ministry of the Environment and Energy (MOEE) database of water well records is explained and the conceptual model for the hydrostratigraphic interpretation is presented. The interpolation method used to generate a laterally continuous hydrostratigraphic model is discussed. This interpolation results in maps of the elevation of the aquifer/aquitard contacts and the thickness of the hydrostratigraphic units. Important characteristics of the hydrostratigraphic model are discussed and compared with results from previous (hydro)geologic investigations.

7.2 Study Area

7.2.1 Physiography

As groundwater flow from the Oro Moraine towards the Minesing Swamp is of interest, the study area was chosen to encompass all subwatersheds that drain towards this wetland from the surrounding uplands to the east. The dominant physiographic features have been formed by extensive glacial activity resulting in a topographic relief ranging from 160 m.a.s.l to 420 m.s.a.l. (Figure 7.1). The Oro

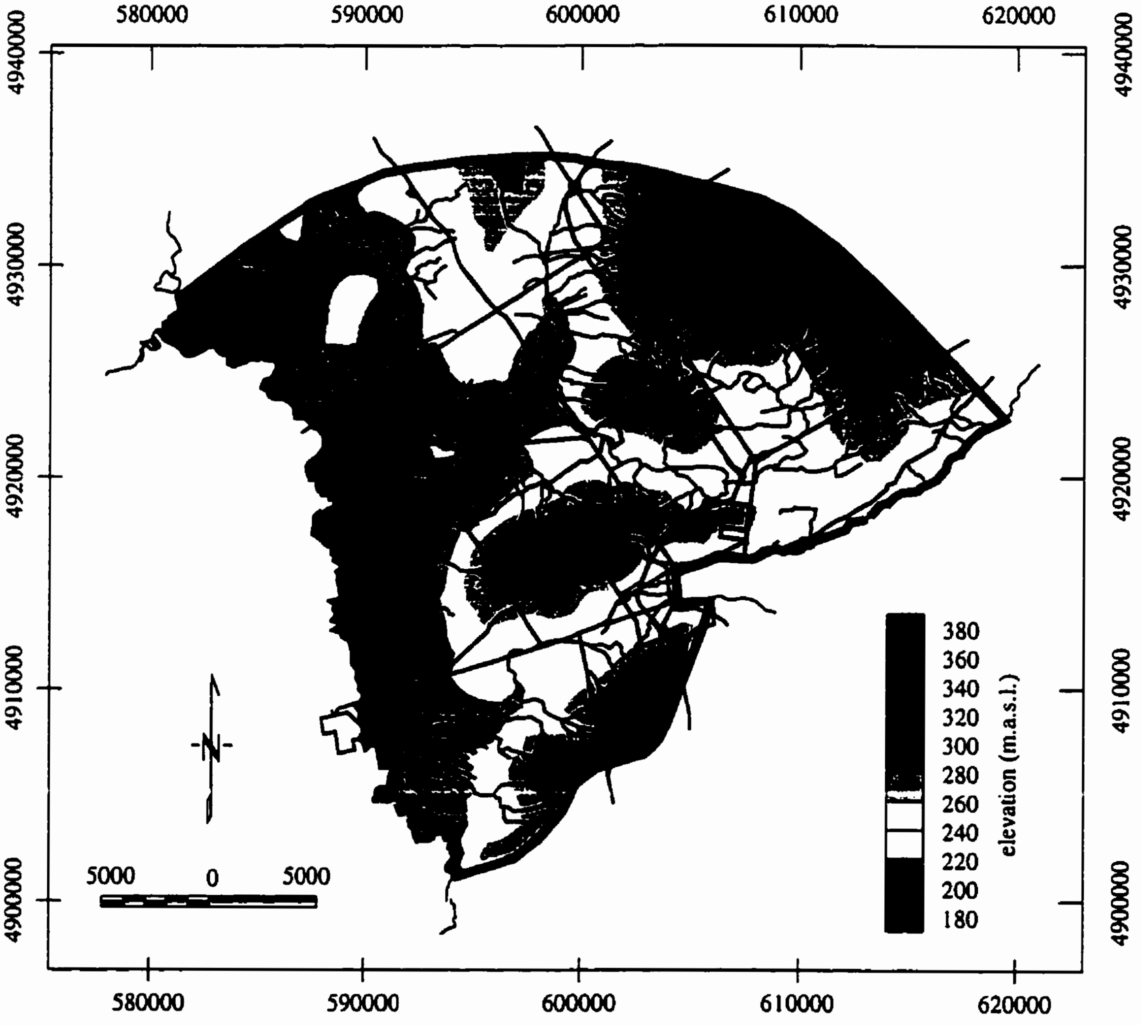
580000
590000
600000
610000
620000
4940000
4930000
4920000
4910000
4900000
N
5000
0
5000
380
360
340
320
300
280
260
240
220
200
180
elevation (m.a.s.l.)

Figure 7.1: Topography of the study area.

or Bass Lake Moraine, the Innisfill Uplands and the region to the west of Barrie (Snow Valley) are part of the Simcoe Uplands (Figure 1.1). These uplands are separated by steep-sided stream valleys and bordered to the west by the Minesing Basin which is part of the Simcoe Lowlands. The Minesing Swamp is located within this basin. Willow Creek is the largest water course inside the study area. It flows from the Oro Moraine towards the Nottawasaga River and includes two class 1-3 wetlands of Provincial significance: Little Lake north of Barrie and the Dalston Lake complex in the Willow Creek headwaters. Other streams are the Matheson, Bear and Marl Creeks. Land use is mainly agricultural. Notable exceptions are some forested areas in the uplands, the aforementioned wetlands and the city of Barrie [*NVCA*, 1995]. New subdivisions are rapidly being developed around Barrie and east of Angus.

7.2.2 Boundaries

Boundaries for a groundwater model should, where possible, coincide with natural features such as drainage divides or major streams. The location of drainage divides can be evaluated from a regional map of groundwater levels. The map shown in Figure (7.2a) was created by interpolating observed static water levels selected from the MOEE database of well records. Multiple wells within a 300 m distance range were removed from the database, where deeper boreholes were retained in order to limit the bias towards shallow wells. Figure (7.2b) shows the location of the boreholes that were used in the spatial interpolation. Ordinary kriging was used to interpolate the observed water levels after a low order trend was removed from the data. Water levels were interpolated in a 2D fashion, thus ignoring vertical hydraulic gradients.

Figure (7.2a) closely resembles a similar map by the Ministry of the Environment [*MOE*, 1977] for the deeper part of the groundwater system known as the Alliston aquifer complex. The Oro Moraine is the main recharge area for groundwater flow east of the Nottawasaga River. Groundwater diverges away from the Moraine southward towards Lake Simcoe (Kempenfelt Bay) and westward towards the Nottawasaga River and Georgian Bay. An investigation of groundwater resources for the Township of Oro-Medonte revealed that this pattern exists in all three overburden aquifers that were identified under the Moraine [*Terra-Probe*, 1995]. This indicates that at least locally good hydraulic connections exist between

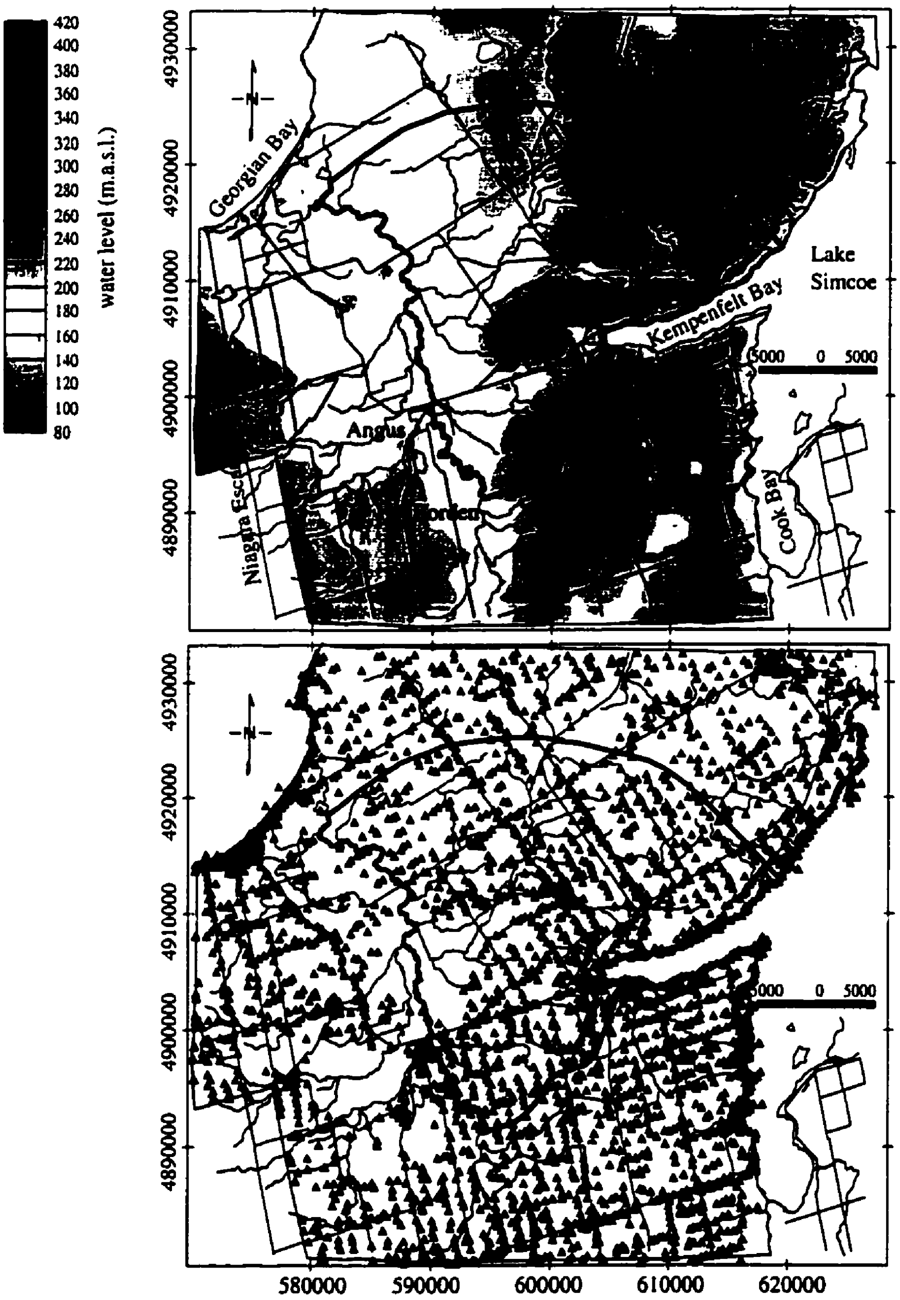
water level (m.a.s.l.)
420
400
380
360
340
320
300
280
260
240
220
200
180
160
140
120
100
80
N
Georgian Bay
Lake Simcoe
Kempenfelt Bay
Angus
Borden
Niagara Esc
Cook Bay
5000 0 5000
4930000
4920000
4910000
4900000
4890000
580000
590000
600000
610000
620000

Figure 7.2: a) Regional groundwater levels. b) Location of boreholes with static water level observations used to generate map a).

the individual aquifers, reducing the potential for strong vertical differences in the flow system.

The northern and eastern boundaries of the study area are chosen to parallel inferred groundwater flowpaths originating at the Oro Moraine. These boundaries also coincide with drainage divides for streams flowing towards the Nottawasaga River (the Willow, Matheson and Marl Creeks) and streams either draining into Lake Simcoe or Georgian Bay (Figure 7.2). Kempenfelt Bay delimits the study area to the southeast. The Innisfill Uplands form a natural drainage divide between the Nottawasaga River and Lake Simcoe. The Nottawasaga River is chosen as the western boundary of the study area. Although the hydraulic connection between the deeper two aquifers and the Nottawasaga River may be weak due to the presence of a thick confining unit (refer to Sections 7.6 and 7.7), this river is still expected to be a valid boundary for the groundwater model as it is the approximate location of a divide between the flow systems originating at the Niagara Escarpment and the Oro Moraine (Figure 7.2). As a result of these converging flow systems, the Minesing Basin is an area of groundwater discharge, where many wells drilled into the Alliston aquifer complex are artesian [*MOE*, 1977].

7.2.3 Geology

The geology of the study area consists of unconsolidated Pleistocene deposits that cover a bedrock consisting mainly of limestone of Ordovician age which in turn overlies the Precambrian granitic-gneiss of the Canadian Shield. Important recent deposits consist of muck found in swampy depressions in both highlands and lowlands. A brief overview of the geology is given here. Detailed descriptions can be found in *Deane* [1950] and *Chapman and Putnam* [1984]. Quaternary geologic maps are available for the eastern half of the study area [*Barnett*, 1992].

The topography of the bedrock surface results from erosion by pre-glacial streams and the abrasive work of advancing and retreating glaciers. The Laurentian River is believed to have been the major pre-glacial outlet for the Upper Great Lakes. *Spencer* [1890] was the first to propose this ancient stream which connected Georgian Bay with Lake Ontario near Toronto. The associated stream valley is the main feature of the local bedrock topography. However, due to a lack of boreholes that penetrate to bedrock the exact location of this stream valley remains somewhat uncertain. *Deane* [1950] proposed that it turned into Lake Simcoe along Kempenfelt

Bay and then, with a sharp turn southward, left by way of Cook Bay (Figure 7.2). *White and Karrow* [1971] suggested that Kempenfelt Bay is only a secondary intake channel and that the main valley actually runs on a more direct north-south route. In the most recent bedrock topography map to date, *Eyles et al.* [1993] also interpret the Laurentian Valley to run roughly underneath the contemporary Nottawasaga River along the western edge of the study area. It is yet unclear how the Laurentian Valley affects regional groundwater flow patterns.

The Great Lakes region was strongly affected by glaciation from the Labradorian centre of the Laurentide Ice sheet. Most deposits result from the last glaciation during the Wisconsin period, although the deeper units could be substantially older [*Barnett*, 1992]. The deposits consist of glacial, glaciofluvial and glaciolacustrine materials with various degrees of grain size and sorting and strongly varying hydrologic properties. The study area is thought to have been mostly overridden by successive ice advances. As a result, the deeper part of the overburden is dominated by ground-moraine which consists mainly of sandy till derived from the granites of the Canadian Shield [*Chapman and Putnam*, 1984]. Towards the south the clay content increases due to the inclusion of local limestone material, making the till more compact. The layers of till are primarily interbedded with glaciolacustrine sediments. Flat areas of outwash sand and gravel may also be found. During the most recent glacial stage the Simcoe Uplands are believed to have been interlobate [*Barnett*, 1992] which has resulted in extensive kame deposits consisting of strata of gravel, sand and silt that accumulated along the ice-front at the mouths of glacial streams.

Some of the steep-walled valleys in the study area are thought to be part of a larger system of tunnel valleys: valleys carved by a catastrophic release of glacial meltwater. This event is believed to have been triggered by the retreat of glaciers beyond the Niagara Escarpment providing a sudden outlet for large amounts of meltwater. The steepness of the valleys, the occurrence of erosional streamlined forms and eskers within the valleys are suggested as evidence to support this origin [*Barnett*, 1990]. Willow Creek and Kempenfelt Bay are believed to be tunnel valleys with gravel deposits resting directly on the bedrock surface. Coarse deposits at depth in the flat-lying area extending from Kempenfelt Bay towards Angus (Figure 7.1) are known as the Barrie-Borden aquifer. Several high yield municipal wells for Barrie and Angus are screened in this aquifer. Wells penetrating to the same depth interval in the surrounding uplands exhibit considerably less yield [K.

Wice (Barrie PUC) and J. Easton (Dixon Hydrogeology), personal communications; *MOE*, 1977]. In low lying areas not affected by the catastrophic meltwater release a layer of till may be found resting on the bedrock surface.

The surficial geology of the Lowlands consists of post-glacial deposits of lacustrine sands, silts and clays, carried by streams or eroded from the shoreline of ancient lake Algonquin. These materials settled on the bottom of the lake or were deposited along its beaches. Coarser deposits of sand and gravel are also found in many places associated with shorelines of Lake Algonquin.

As a result of the complex geologic history of the study area, the stratigraphy of the Simcoe Lowlands is substantially different from that of the Uplands. This hampers the laterally continuous hydrostratigraphic interpretation that will be presented in the next section.

7.3 Hydrostratigraphic Interpretation

7.3.1 Water Well Records

The MOEE database of water well records is the main source of subsurface geologic information that has been used in this study. The MOEE records contain information on the location of the well (UTM easting and northing in meters), its elevation, the static level of the water table at the time of drilling, as well as a description of the geologic formations encountered during drilling according to a standard list of 52 materials, 33 descriptive terms (e.g. hardness, grain size, sorting) and 9 colours, together with the distance from the top of the well to the bottom of these formations [*MOE*, 1981]. Following the approach of *Martin* [1994] this vast range of geologic descriptions was reduced to a limited number of lithologies that reflect the hydrostratigraphy and that can be used to correlate and spatially interpolate this information (Table 7.1). The MOEE database was augmented with 6 wells drilled by the OGS in or near the study area [*Barnett*, 1991].

An interpretation of all available well records (roughly 3000 for the study area) is not possible within a reasonable time-frame. Furthermore, because of the large discretization scale of a regional groundwater model, not all of the data need to be incorporated. An initial data selection was therefore undertaken based on the depth of the wells and the number of lithologic descriptions in the borehole logs. These criteria were incorporated in a computer program to sort the dataset, where well clusters (multiple wells within a 300 m radius) were eliminated and deeper wells and/or wells containing more information were retained. This procedure therefore discards shallow boreholes which comprise the bulk of the MOEE database and are of limited use in the hydrostratigraphic interpretation.

Symbol	Material
■	Clay Silty Clay Sandy Clay Gravelly Clay
▨	Clayey Silt Silt Sandy Silt Gravelly Silt Clayey Sand
░	Silty Sand Fine Sand Medium Sand Coarse Sand Gravel
▤	Limestone Bedrock
□	Unknown

Table 7.1: Legend of materials used in cross-sectional interpretation.

Because water supply is the main interest for drilling the wells, less attention is generally being given to accurately describing the geologic formations. The geologic information therefore tends to be of moderate to poor quality. Another complicating factor is the manner in which the vertical location of the top of the boreholes is determined: elevations are read from topographic maps with a contour interval of 25 feet and are thus subject to uncertainty on that order of magnitude. This uncertainty further depends on the steepness of the topography as well as the accuracy with which the horizontal position of the wells is determined and plotted on the maps. Given these data limitations, a further selection of reliable wells based on quality and coherency of the neighboring records was required, where logs that were poorly correlated with surrounding logs, and that did not reflect geologic variability, were discarded.

The final dataset consists of 619 wells (Figure 7.3). Although the wells are mostly confined to roadside locations, the dataset covers the study area fairly uniformly. A notable exception is the Minesing Swamp area where no wells have been drilled. The dataset covers an area that is slightly larger than the study domain itself in order to avoid boundary effects in the spatial interpolation. A total of 64 cross-sections were used in the spatial correlation of the borehole information.

The cross-sections were initially generated making use of the United Nations software package Groundwater for Windows (GWW). Later, a program was developed to generate DXF files that can be imported into AutoCAD. This procedure has the advantage that the interpolated hydrostratigraphic contacts and other features such as water levels can easily be incorporated in the cross-sections.

7.3.2 Conceptual Model

In the hydrostratigraphic interpretation, adjacent geologic units with similar hydrologic properties are grouped together. Following *Martin* [1994], 3 major categories are distinguished: (1) good aquifer materials such as sands and gravels, (2) aquitard materials such as clays, and (3) materials that have neither good aquifer nor pure aquitard characteristics (silts). These categories are shown in distinct grey-tones (Table 7.1).

The conceptual model of the overburden, based on the geologic history of the study area as well as previous hydrogeologic investigations (Section 7.7), is comprised of a system of 4 aquifers and 4 aquitards. The upper part of the limestone bedrock may be expected to be hydraulically active due to the abrasive work done by advancing and retreating glaciers. However, the hydrogeologic parameters of this bedrock aquifer will be lumped with those of the deepest overburden aquifer as information at depth is scarce.

Cross-section 33 (Figure 7.4), located to the northwest of Barrie (Figure 7.3), displays most of the features that are relevant to the conceptual model. The upper 2 overburden aquifers (A1 and A2) are semi-confined. Aquifer 1 (A1) exists only in the uplands and consists of thick deposits of glacial outwash material. It outcrops

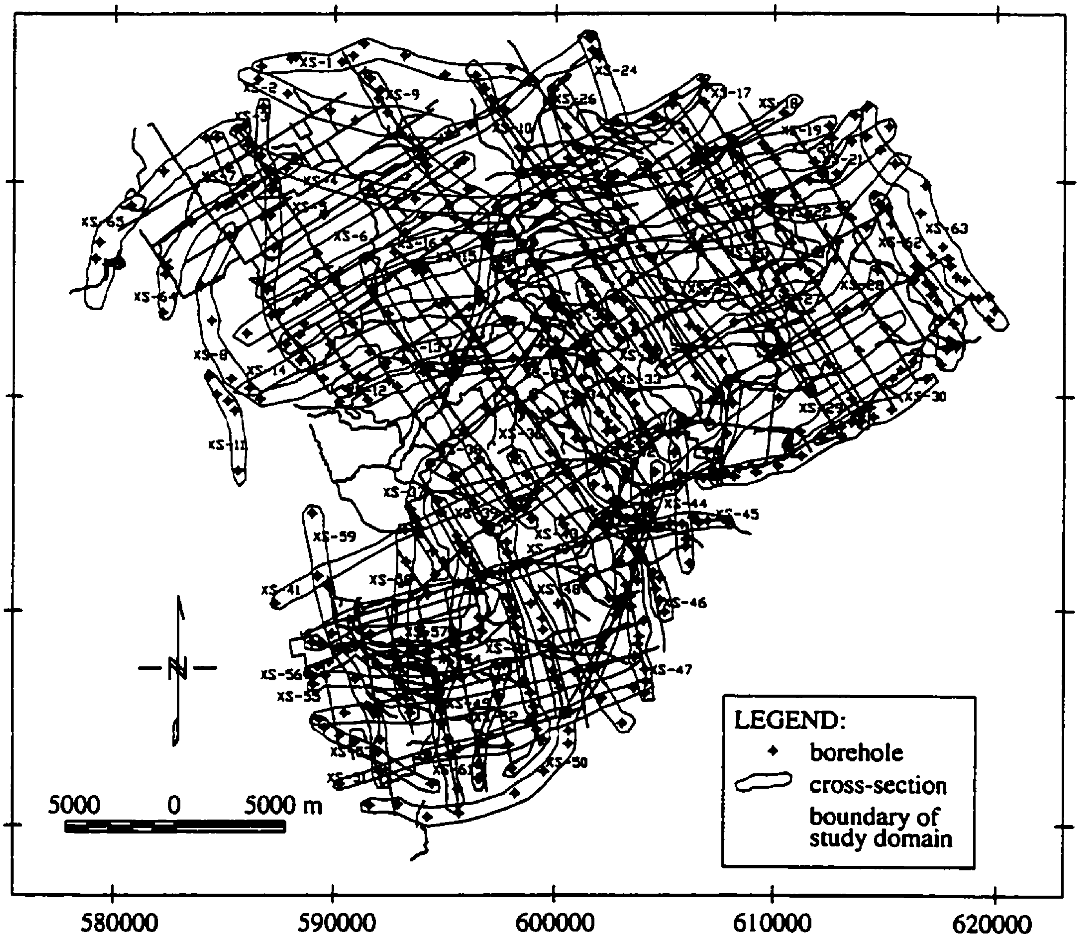
4930000
4920000
4910000
4900000
580000
590000
600000
610000
620000
N
5000 0 5000 m
LEGEND:
◆ borehole
cross-section
boundary of study domain
XS-1
XS-2
XS-9
XS-24
XS-26
XS-17
XS-18
XS-19
XS-21
XS-63
XS-62
XS-30
XS-6
XS-8
XS-14
XS-11
XS-64
XS-65
XS-12
XS-13
XS-16
XS-33
XS-44
XS-45
XS-46
XS-47
XS-50
XS-59
XS-41
XS-56
XS-55
XS-57

Figure 7.3: Wells and cross-sections used in the hydrostratigraphic interpretation.

along the steep sloped valley walls. Aquifer 2 (A2) outcrops in the valley floors. The lower two aquifers (A3 and A4) are fully confined and are part of the Alliston aquifer complex which has been suggested to extend from the Oak Ridges Moraine to Georgian Bay [*MOE*, 1977].

Figure (7.4) also illustrates the main problem associated with the laterally continuous interpretation. The delineation of the top and bottom surfaces of Aquifer 3 result in a thick unit under the Willow Creek valley. However, this aquifer locally consists mainly of fine grained materials. The overlying deposits are also of low permeability. This sequence, together with the coarse grained nature of Aquifer 4 which is only observed in wells located in the Willow Creek valley (boreholes 5711984, 5709550 and 5709326), may be the signature of a tunnel valley overlain by Lake Algonquin lacustrine deposits. The community of Midhurst receives its water from this tunnel valley aquifer [*Easton*, 1998]. Further evidence of such systems in the borehole data is scarce.

No attempt has yet been made to apply an alternative conceptual model in the geologic interpretation of the valley areas. Instead, the different stratigraphy of the Simcoe Lowlands is as much as possible taken into account using the present conceptual model. This conceptual model is appropriate for the Simcoe Uplands which make up the largest portion of the study area (Figure 7.1). This approach has lead to a good correspondence with information from Quaternary geologic maps (Section 7.7). The next chapter will highlight some limitations of the resulting hydrostratigraphic model.

7.4 Interpolation Strategy and Parameters

The output of the cross-sectional interpretation and correlation is the observed depth of the aquifer/aquitard contacts at the borehole locations. The depth of these contacts needs to be interpolated to delineate the geometry of aquifers and aquitards throughout the study area. First, any trend that may exist in the data is removed. The spatial variability of the residual data (that part of the data not explained by the trend) is expressed in terms of model variogram parameters and ordinary kriging is used to interpolate these residuals. The trend is then added back to the interpolated values.

Table (7.2) lists the number of borehole observations constraining each of the

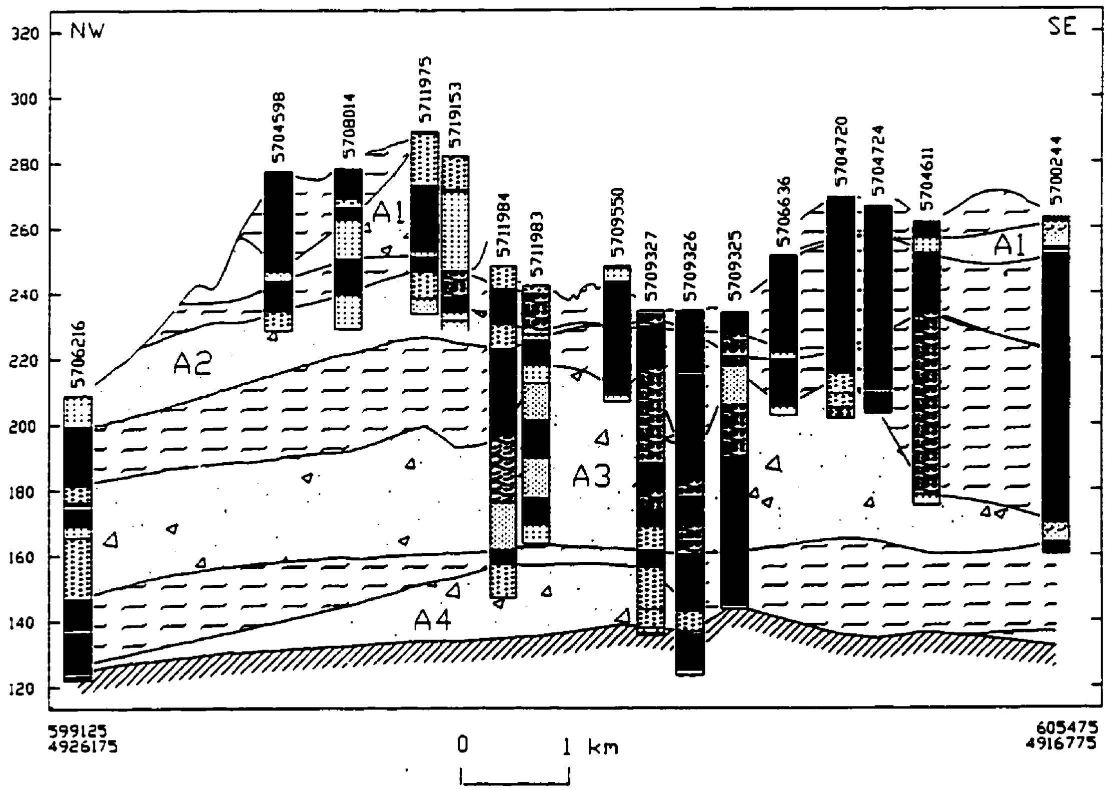
NW
SE
Elevation (m.a.s.l.)
320
300
280
260
240
220
200
180
160
140
120
5706216
5704598
5708014
5711975
5719153
5711984
5711983
5709550
5709327
5709326
5709325
5706636
5704720
5704724
5704611
5700244
A1
A1
A2
A3
A4
599125
4926175
0
1 km
605475
4916775

Figure 7.4: Cross-section 33. Refer to Table (7.1) for a legend of the geologic materials.

aquifer/aquitard contacts, the order of the background trend, and the goodness of fit (r^2) of the trend surface to the observed elevations (TAQ1 designates top of Aquifer 1, BAQ1 is bottom of Aquifer 1 etc., BEDR indicates bedrock). The order of the trend surface polynomial (equation 2.6) was increased until the addition of new terms was no longer considered significant based on a student t-test [e.g., *Davis*, 1986]. The experimental and model variograms for the data residuals are shown in Figures (7.5) and (7.6). The dominant variability in the elevation of the aquifer/aquitard contacts is correlated over several kilometers (range in Table 7.2). TAQ1 exhibits the greatest degree of variability (sill). Unlike the deeper stratigraphic units, it was not overridden by progressive glacial advances. Nugget values are zero for all variograms. Fluctuations in the sill of several of the semivariograms suggest the presence of periodic features in the aquifer/aquitard contacts that are not resolved by the covariance model (refer to Section 2.2.4).

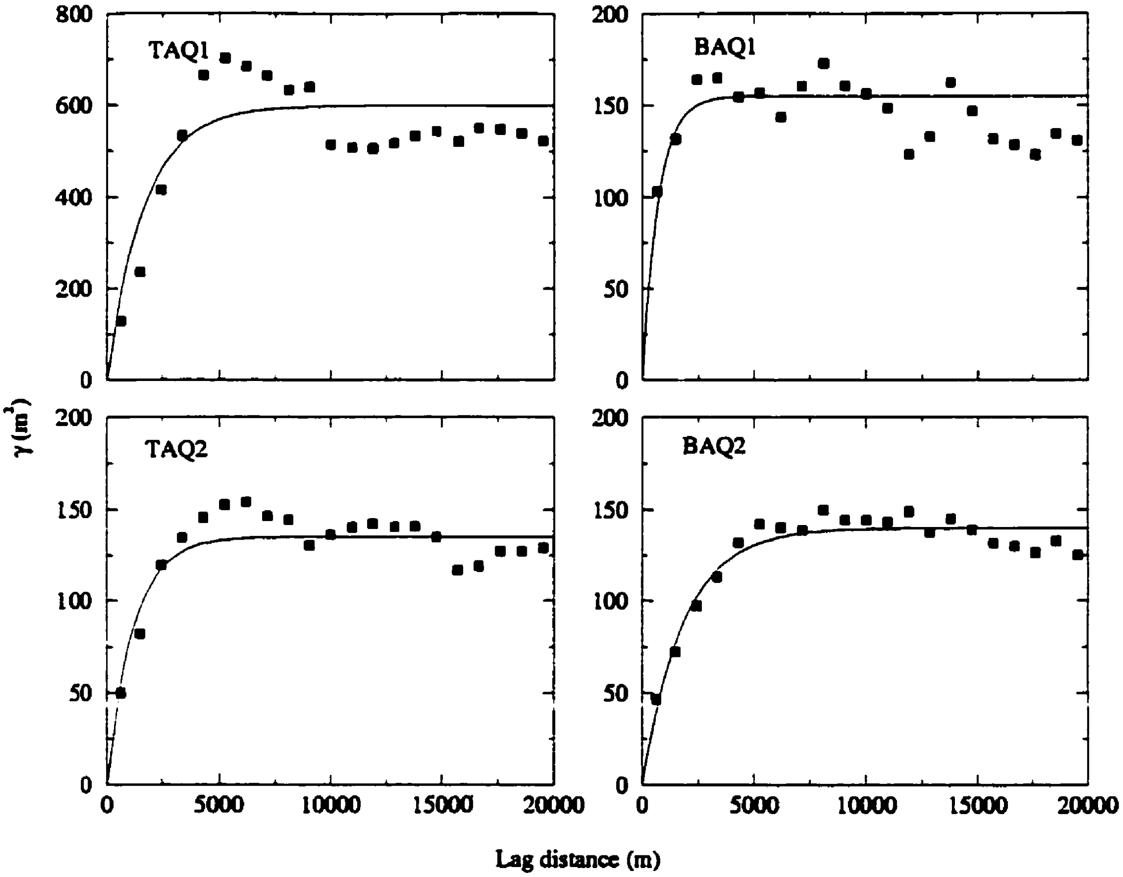

Figure 7.5: Experimental and model variograms for TAQ1-BAQ2.

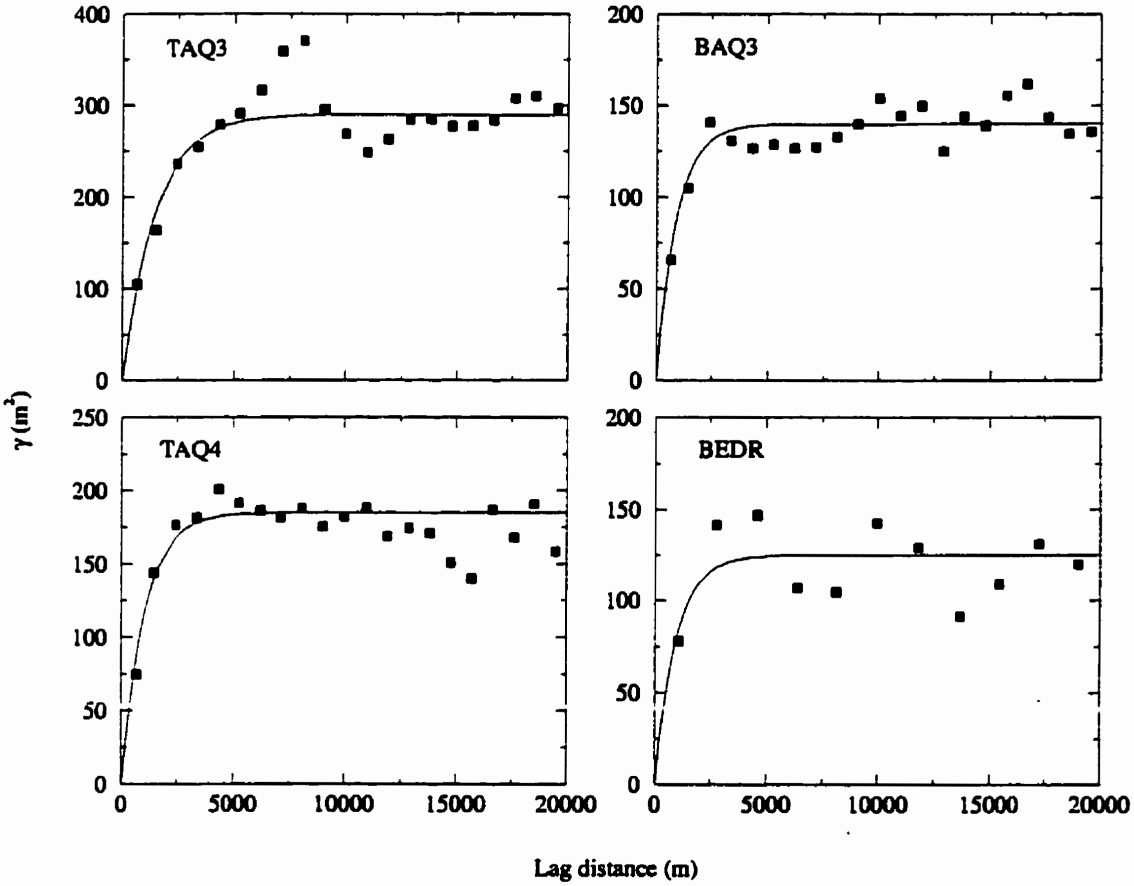

Figure 7.6: Experimental and model variograms for TAQ3-BAQ4.

Boreholes		Trend		Variogram	
		Order	r^2	sill (m^2)	range (m)
TAQ1	289	2	0.60	550	4500
BAQ1	220	3	0.85	145	2100
TAQ2	497	4	0.83	135	3575
BAQ2	429	2	0.76	140	5550
TAQ3	369	3	0.61	290	4300
BAQ3	182	2	0.74	140	2700
TAQ4	116	2	0.61	175	3025
BEDR	60	2	0.72	115	2850

Table 7.2: Parameters for the spatial interpolation of the aquifer/aquitard contacts.

It is typically held that, when compared to ordinary kriging, universal kriging provides superior interpolation results if the data exhibit a complex trend. Under such conditions, the approach used here may yield biased estimates of the interpolated values. To investigate this concern, ordinary and universal kriging were compared based on back-kriging scattergram statistics. Data points were removed from the database on a one-by-one basis and the remaining observations were used to interpolate back to the location of the eliminated point. Comparisons are based on the correlation value (r^2) of the scatter points, the bias between the observed and kriged elevations as well as the coherency between the kriging errors and the estimation variance. According to *de Marsily* [1984], no bias exists in the interpolated values if:

$$\frac{1}{N}\sum_{i=1}^{N}(z_i - z_i^*) \approx 0 \qquad (7.1)$$

where the z_i are the observed elevations and the z_i^* are the kriged elevations. The kriging errors are coherent with the estimation variance σ_z^2 if:

$$\frac{1}{N}\sum_{i=1}^{N}\left(\frac{z_i - z_i^*}{\sigma_z}\right)^2 \approx 1 \qquad (7.2)$$

Back-kriging scattergrams were generated using 30 control points. For brevity, variogram parameters for universal kriging are not given. The interpolated values for both ordinary and universal kriging exhibit a bias that is small compared to the uncertainty in the borehole elevations (Table 7.3, also refer to Section 7.3.1). The degree of bias for the two interpolation methods is comparable. However, correlation values and kriging error indicate that ordinary kriging (I) provides interpolation estimates that are superior to those obtained from universal kriging (II). For the latter method, a non-uniform azimuthal distribution of control points may lead to the extrapolation of an estimated drift to areas for which it is inappropriate. This occurs when interpolating across the Minesing Swamp.

		I			II	
	r^2	bias (m)	error	r^2	bias (m)	error
TAQ1	0.91	0.12	1.68	0.89	0.16	3.91
BAQ1	0.91	0.17	1.86	0.80	−0.17	3.23
TAQ2	0.92	0.10	2.71	0.91	0.10	5.11
BAQ2	0.89	−0.12	3.69	0.79	−0.01	6.65
TAQ3	0.77	0.08	3.08	0.62	−0.38	6.97
BAQ3	0.84	−0.16	1.97	0.65	0.18	7.31
TAQ4	0.68	−0.46	2.15	0.52	−0.25	6.43
BEDR	0.72	0.19	2.04	0.67	−0.15	7.79

Table 7.3: Comparison of (I) ordinary and (II) universal kriging using the correlation (r^2), bias (equation 7.1) and error (equation 7.2) measures.

The differences between ordinary and universal kriging result from a few outliers. Because ordinary kriging, in combination with the calculation of a *global* trend, yields more stable results it is preferred. Kriging errors are considerably larger than the estimation uncertainty (Table 7.3). This is possibly due to the simplified representation of the true variability in the aquifer/aquitard contacts by a covariance model. Attempts to define anisotropic and/or spatially variable variograms were unsuccessful and are not warranted, given the limited amount of data that is available.

7.5 Elevation of Hydrostratigraphic Contacts

Ordinary kriging with 30 control points was used to interpolate the aquifer/aquitard contacts. In some locations the interpolated contacts may cross. Rules are therefore needed to to correct their elevation in order to avoid negative thicknesses for the hydrostratigraphic units. The following rules are applied: (1) if the elevation exceeds that of the topography it is corrected to ground surface, (2) if a contact reaches below the bedrock surface it is adjusted to its elevation, (3) if two aquifer/aquitard contacts cross both are corrected to their mean elevation. The kriged and adjusted aquifer/aquitard contacts are shown in Figures (7.7)-(7.14). Although the uppermost two stratigraphic units only exist in the uplands, the adjusted elevation of TAQ1 and BAQ1 is shown throughout the study area.

7.6 Thickness of Hydrostratigraphic Units

The thickness of each of the hydrostratigraphic units was calculated by taking the difference in elevation of the two contacts delineating that unit (Figures 7.15-7.22). The contouring is cut off at an arbitrary minimum thickness of 1 m. White areas therefore indicate regions where a hydrostratigraphic unit pinches out. Thick aquifer units are potential areas of high yield for water wells. Thick aquitard units inhibit the vertical movement of groundwater between aquifers.

7.7 Discussion

The conceptual model presented in Section (7.3.2) is consistent with interpretations of the aquifer system made in previous investigations. Three aquifers were identified in a hydrogeologic assessment for the Township of Oro-Medonte [*Terra-Probe*, 1995]. This township is located east of a line between Little Lake and the Matheson Creek headwaters. The upper boundaries of these aquifers were put at 260-290 m.a.s.l, 220-245 m.a.s.l. and below 200 m.a.s.l. respectively, elevation ranges are in agreement with those of aquifers 2-4 in the Oro Moraine area (Section 7.5). It is further mentioned that "there seems to be an even higher aquifer (> 300 m.a.s.l.) in the upper reaches of the moraine". This uppermost aquifer and the underlying

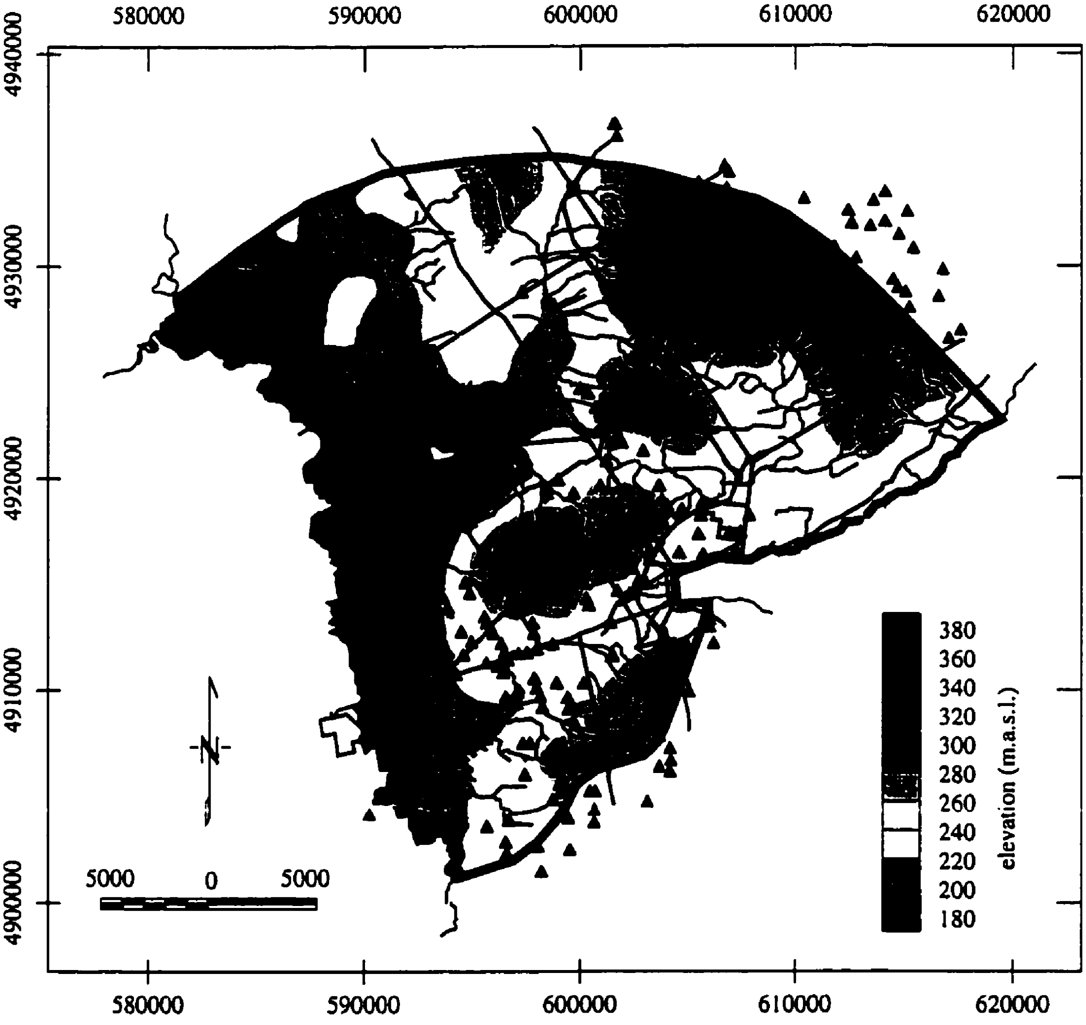
580000
590000
600000
610000
620000
4940000
4930000
4920000
4910000
4900000
N
5000
0
5000
380
360
340
320
300
280
260
240
220
200
180
elevation (m.a.s.l.)

Figure 7.7: Kriged and adjusted elevation of TAQ1. Triangles indicate the boreholes where this contact is observed.

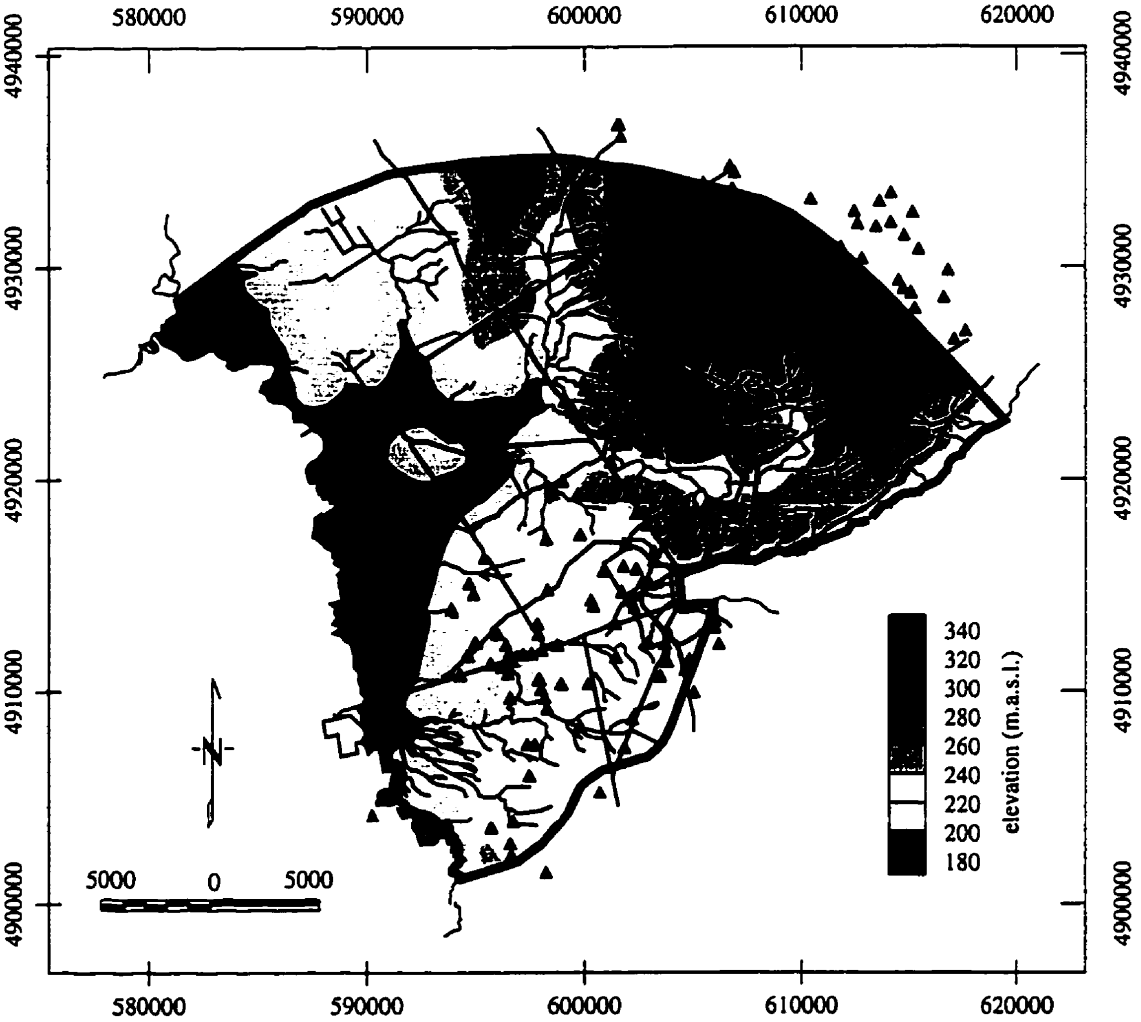
580000
590000
600000
610000
620000
4940000
4930000
4920000
4910000
4900000
N
5000
0
5000
340
320
300
280
260
240
220
200
180
elevation (m.a.s.l.)

Figure 7.8: Kriged and adjusted elevation of BAQ1. Triangles indicate the boreholes where this contact is observed.

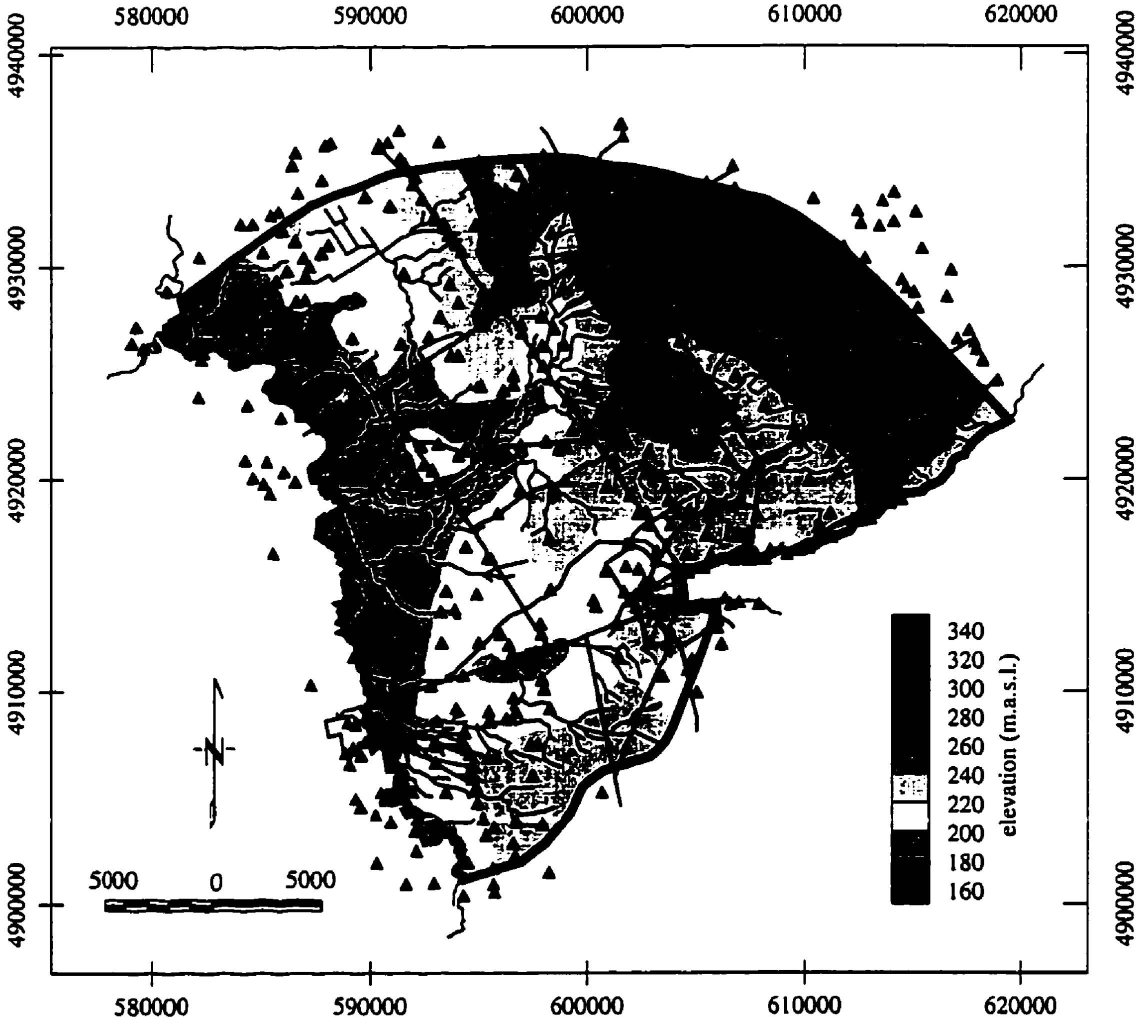
580000
590000
600000
610000
620000
4940000
4930000
4920000
4910000
4900000
N
5000
0
5000
340
320
300
280
260
240
220
200
180
160
elevation (m.a.s.l.)

Figure 7.9: Kriged and adjusted elevation of TAQ2. Triangles indicate the boreholes where this contact is observed.

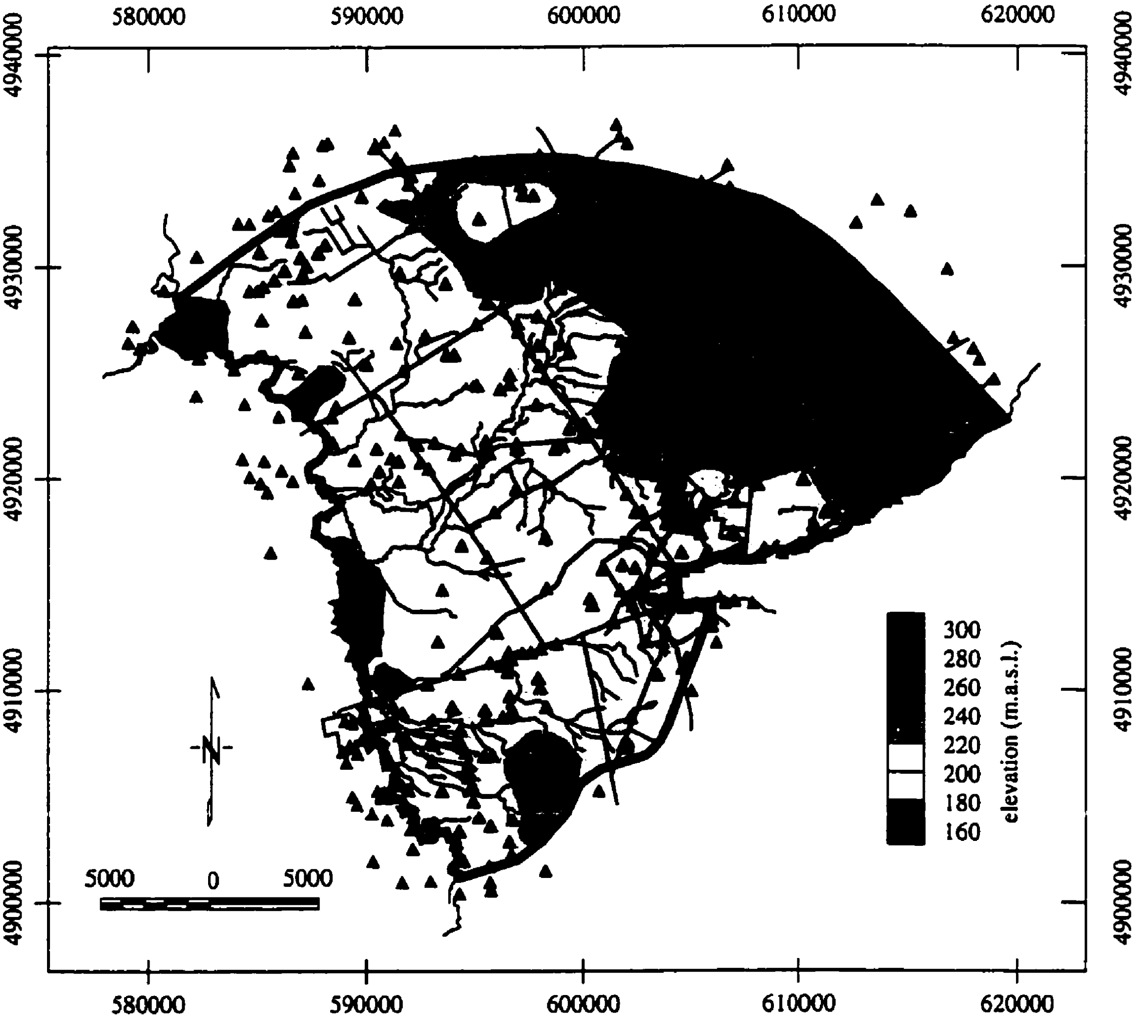
580000
590000
600000
610000
620000
4940000
4930000
4920000
4910000
4900000
N
5000
0
5000
300
280
260
240
220
200
180
160
elevation (m.a.s.l.)

Figure 7.10: Kriged and adjusted elevation of BAQ2. Triangles indicate the boreholes where this contact is observed.

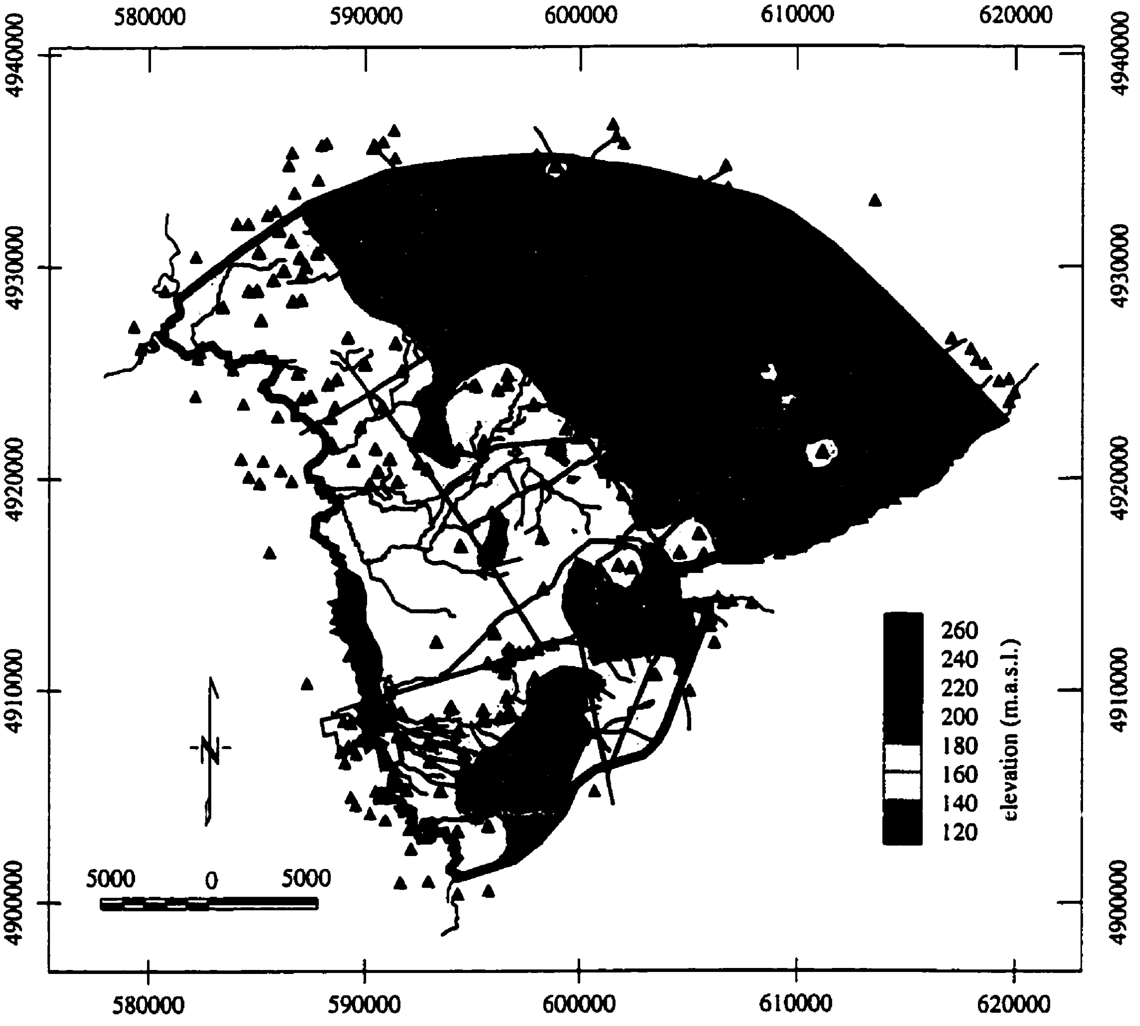
580000
590000
600000
610000
620000
4940000
4930000
4920000
4910000
4900000
N
5000
0
5000
260
240
220
200
180
160
140
120
elevation (m.a.s.l.)

Figure 7.11: Kriged and adjusted elevation of TAQ3. Triangles indicate the boreholes where this contact is observed.

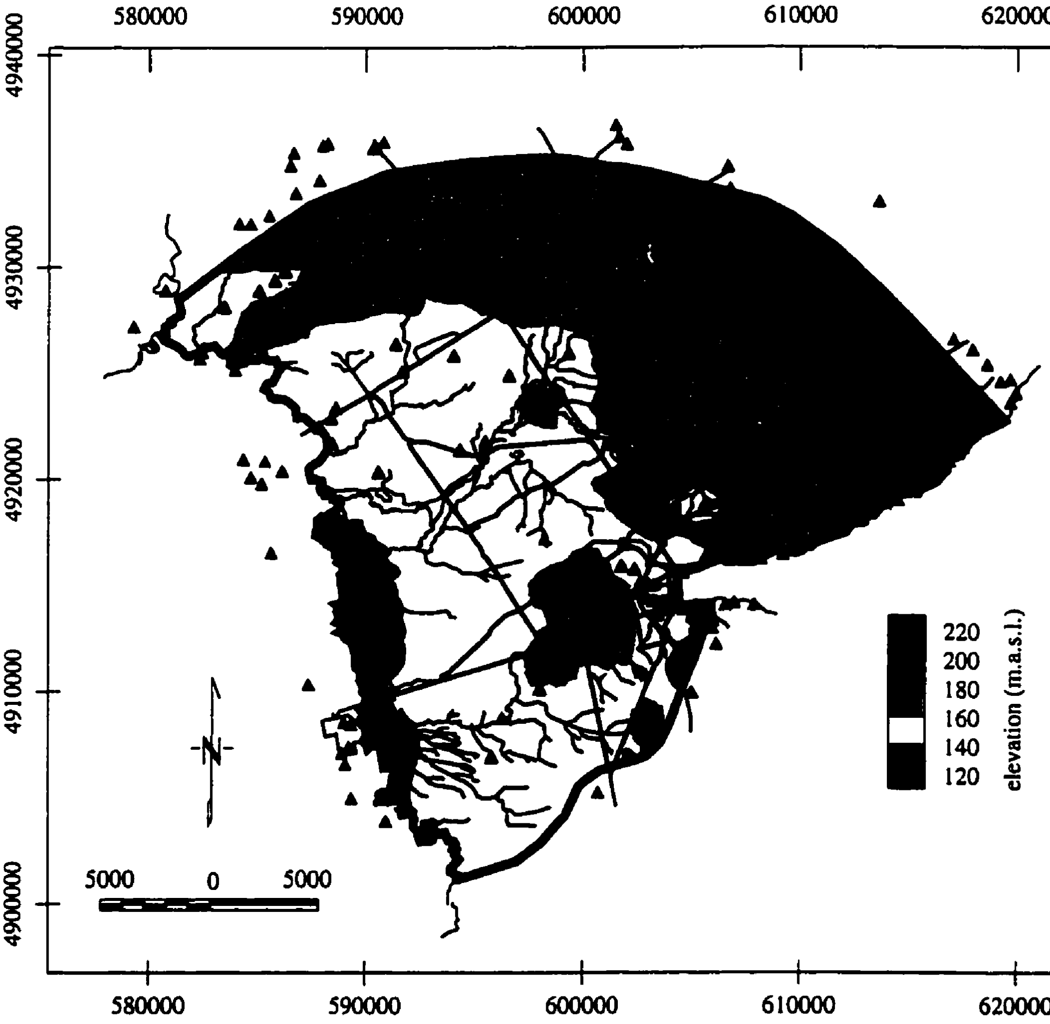
580000
590000
600000
610000
620000
4940000
4930000
4920000
4910000
4900000
N
5000
0
5000
220
200
180
160
140
120
elevation (m.a.s.l.)

Figure 7.12: Kriged and adjusted elevation of BAQ3. Triangles indicate the location where this contact is observed.

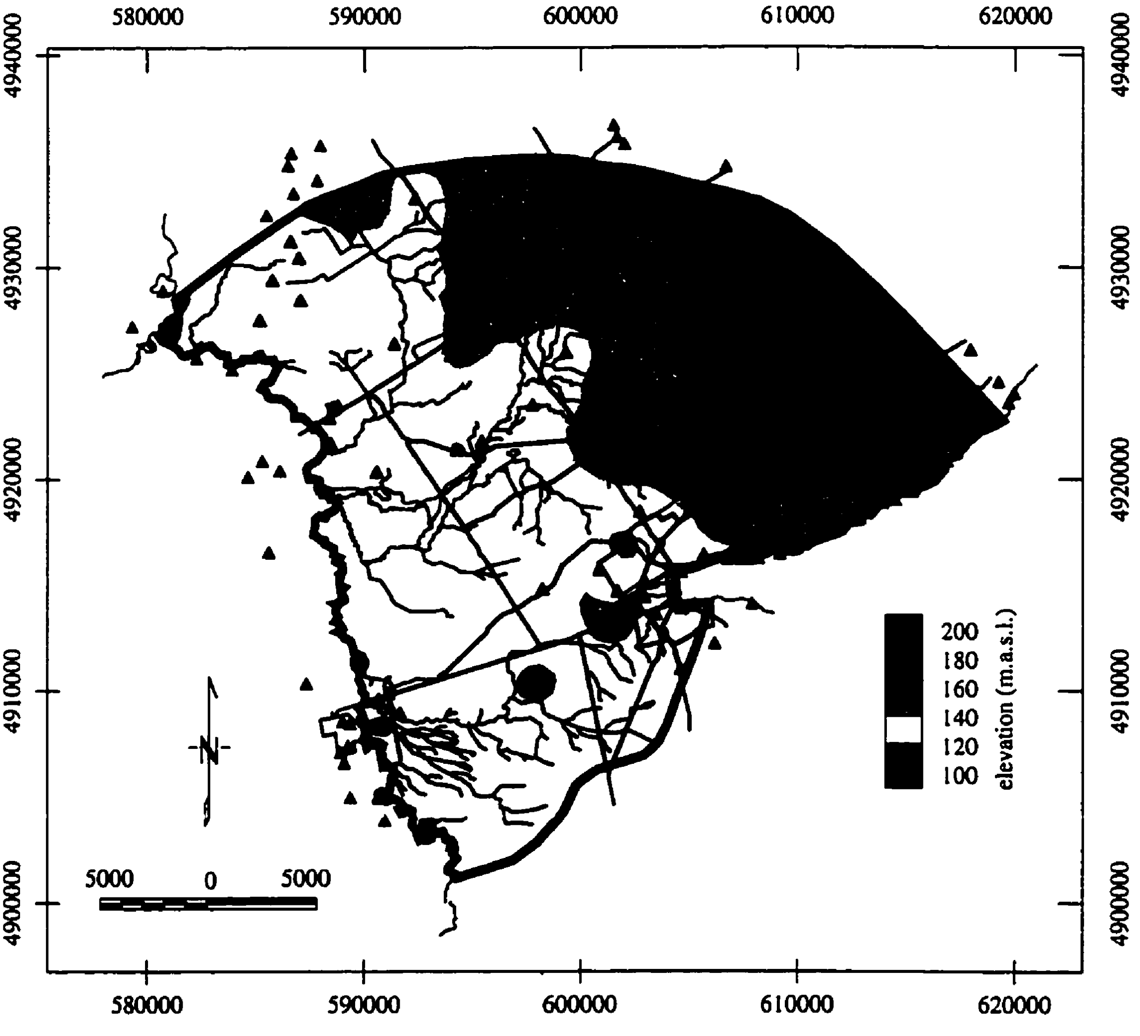
580000
590000
600000
610000
620000
4940000
4930000
4920000
4910000
4900000
N
5000
0
5000
200
180
160
140
120
100
elevation (m.a.s.l.)

Figure 7.13: Kriged elevation of TAQ4. Triangles indicate the boreholes where this contact is observed.

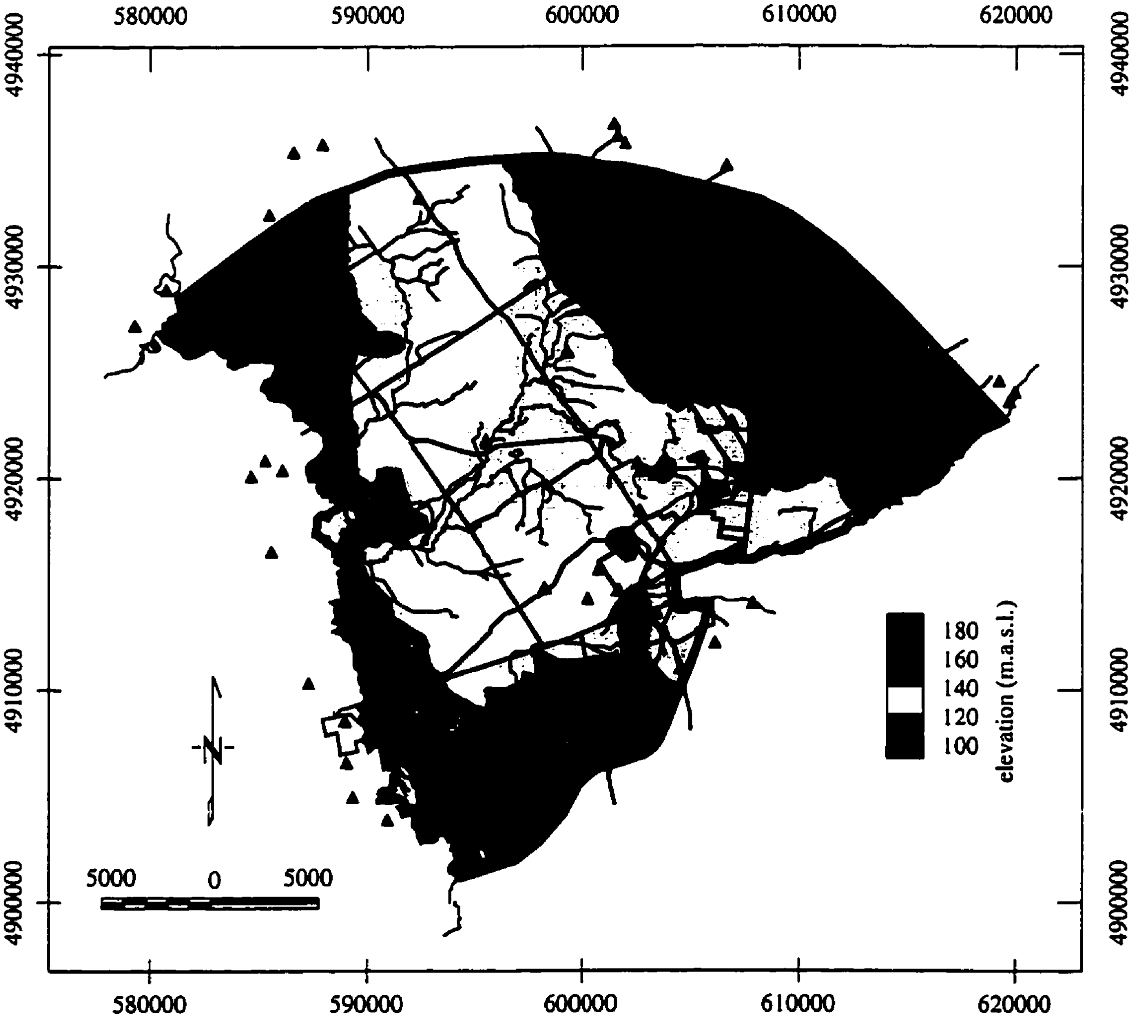
580000
590000
600000
610000
620000
4940000
4930000
4920000
4910000
4900000
N
5000
0
5000
180
160
140
120
100
elevation (m.a.s.l.)

Figure 7.14: Kriged elevation of the bedrock surface (BEDR). Triangles indicate the boreholes where bedrock is observed.

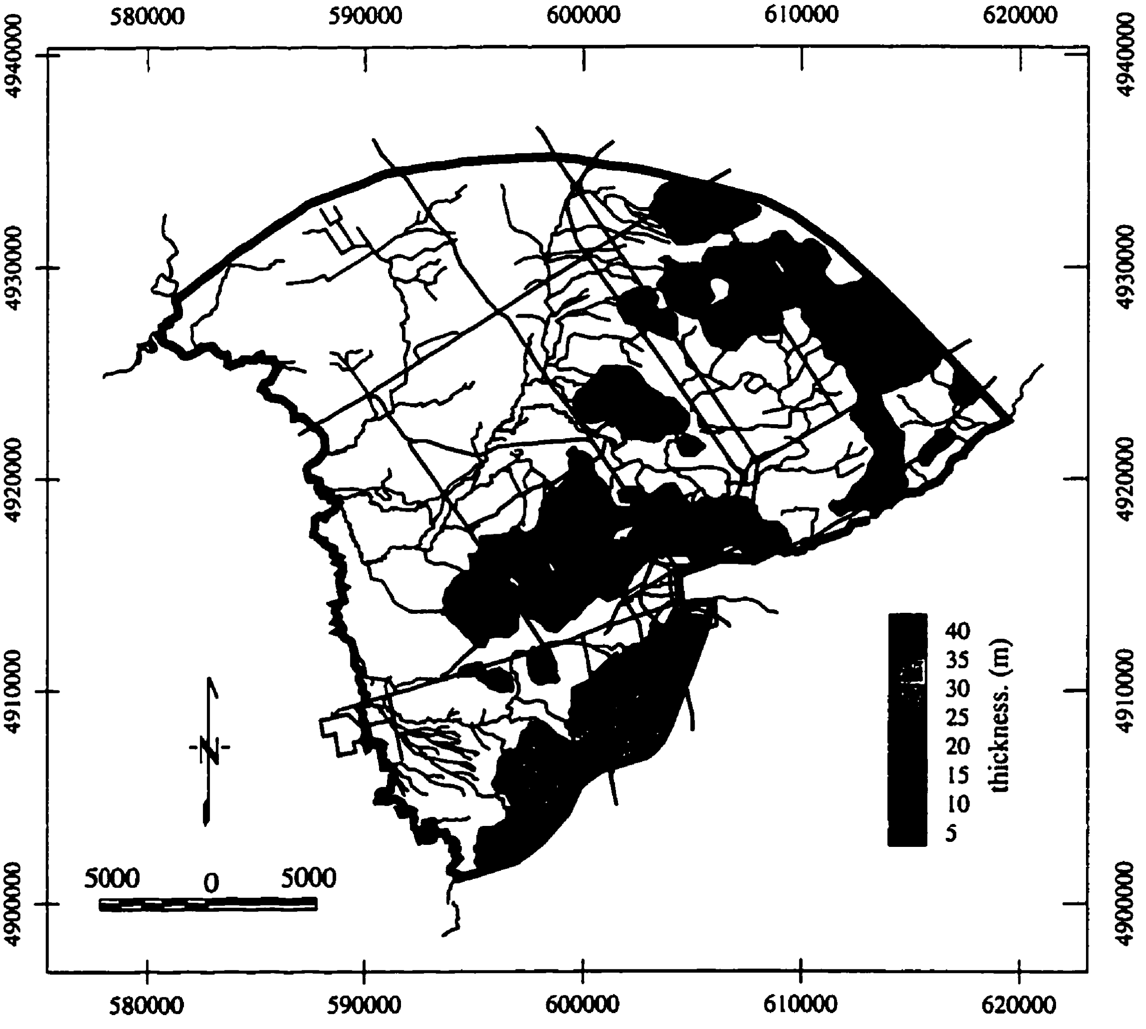
580000
590000
600000
610000
620000
4940000
4930000
4920000
4910000
4900000
N
5000
0
5000
40
35
30
25
20
15
10
5
thickness (m)

Figure 7.15: Thickness of Aquitard 1 (AQTD1). White areas indicate regions where this unit pinches out.

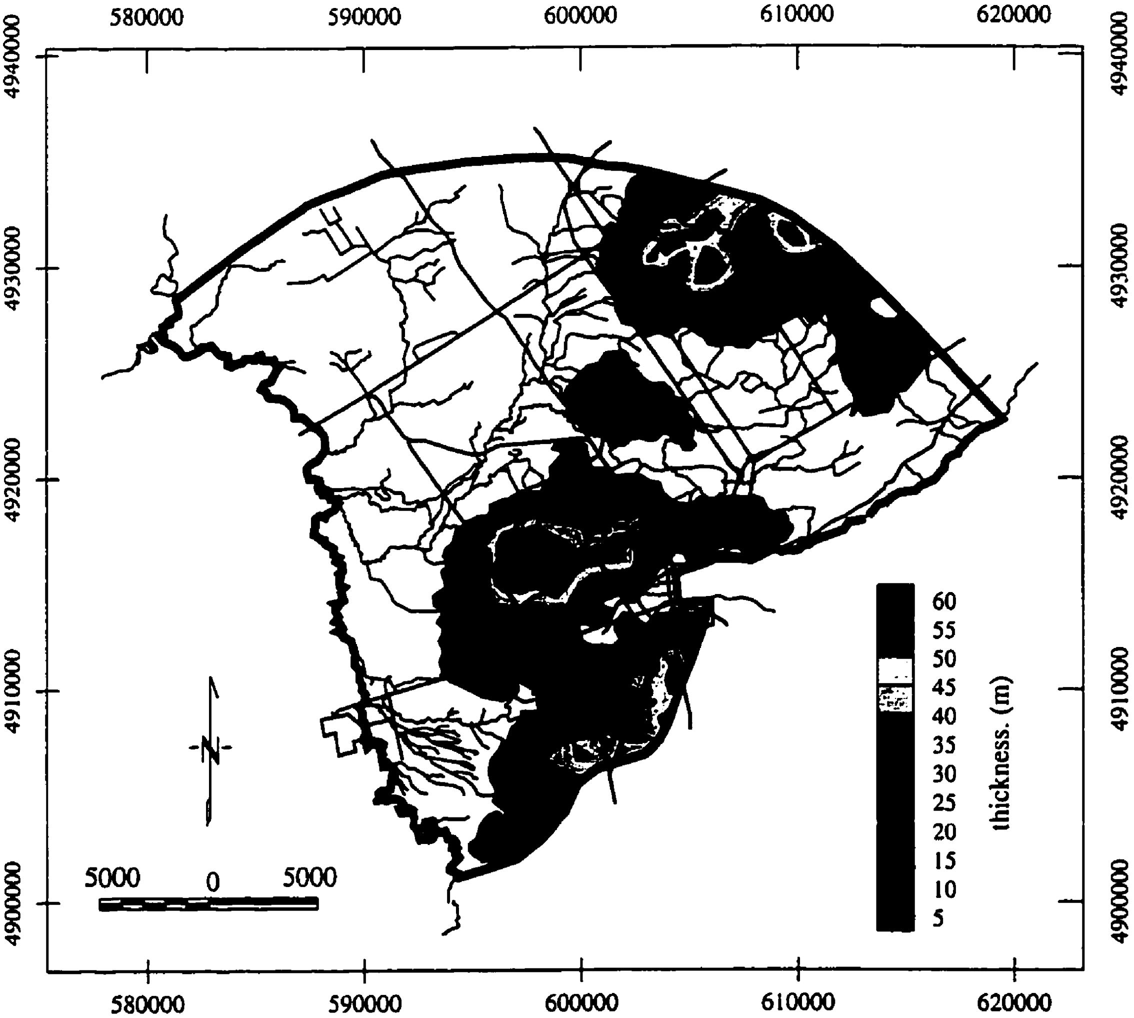
580000
590000
600000
610000
620000
4940000
4930000
4920000
4910000
4900000
N
5000
0
5000
60
55
50
45
40
35
30
25
20
15
10
5
thickness. (m)

Figure 7.16: Thickness of Aquifer 1 (AQFR1). White areas indicate regions where this unit pinches out.

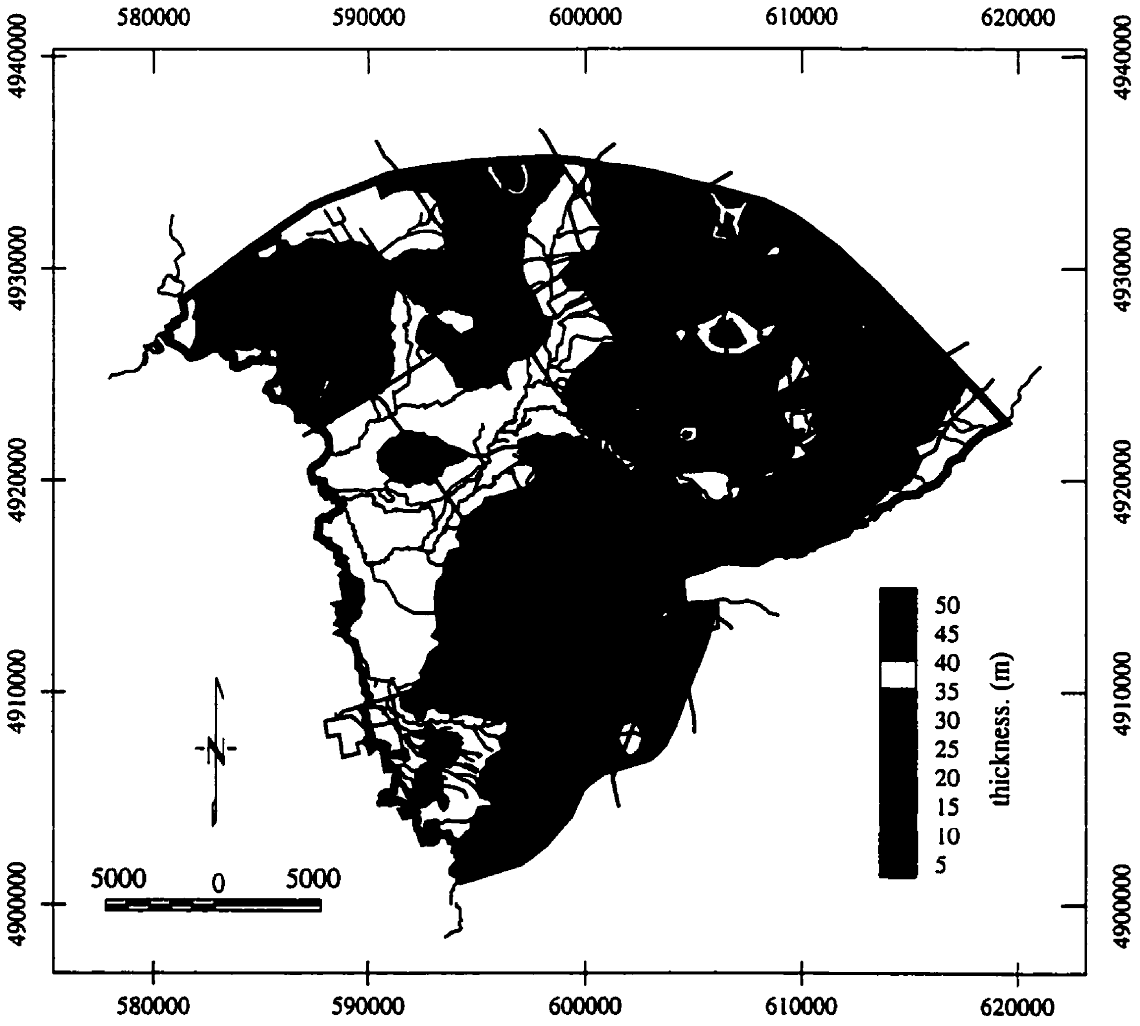
580000
590000
600000
610000
620000
4940000
4930000
4920000
4910000
4900000
N
5000 0 5000
50
45
40
35
30
25
20
15
10
5
thickness. (m)

Figure 7.17: Thickness of Aquitard 2 (AQTD2). White areas indicate regions where this unit pinches out.

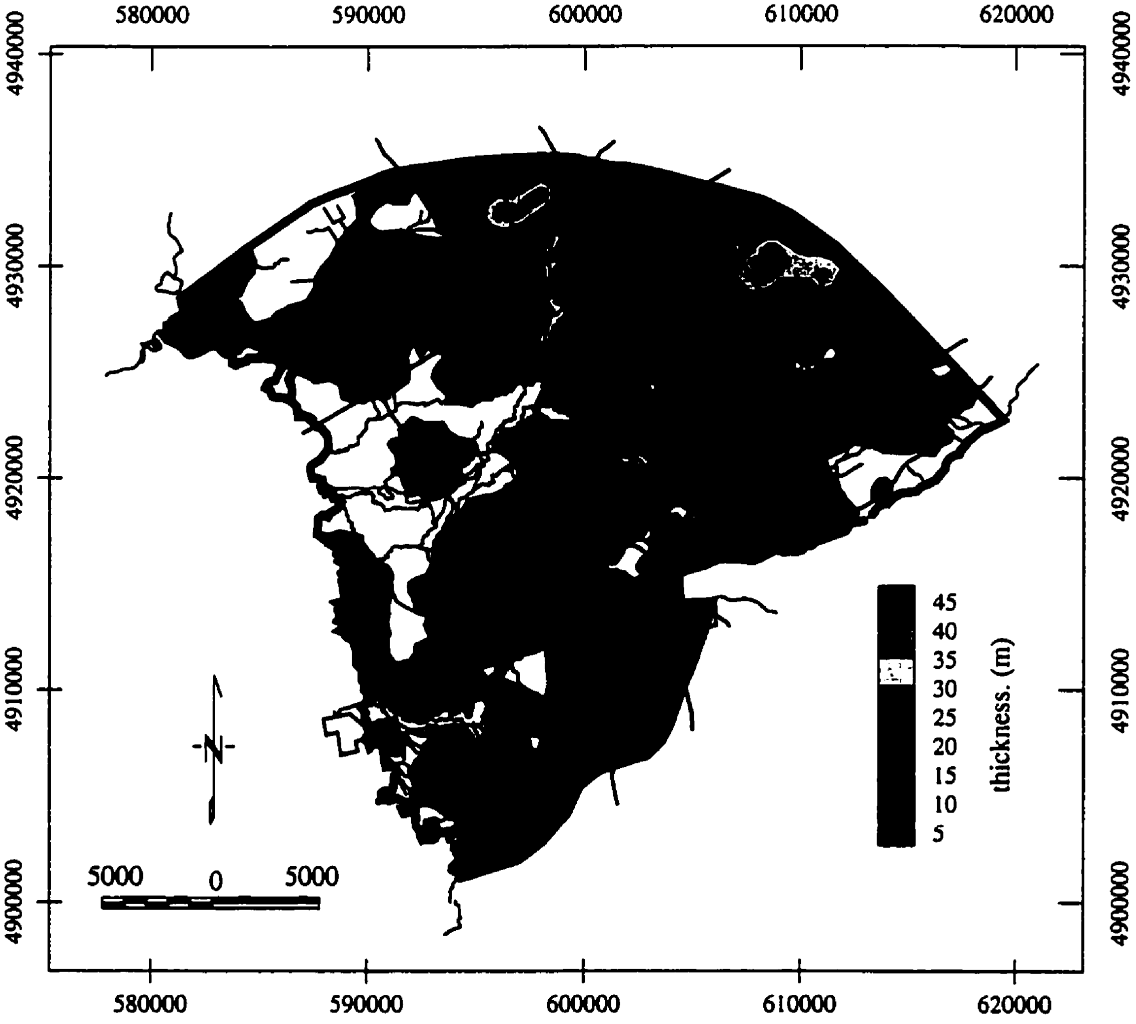
580000
590000
600000
610000
620000
4940000
4930000
4920000
4910000
4900000
N
5000 0 5000
45
40
35
30
25
20
15
10
5
thickness (m)

Figure 7.18: Thickness of Aquifer 2 (AQFR2). White areas indicate regions where this unit pinches out.

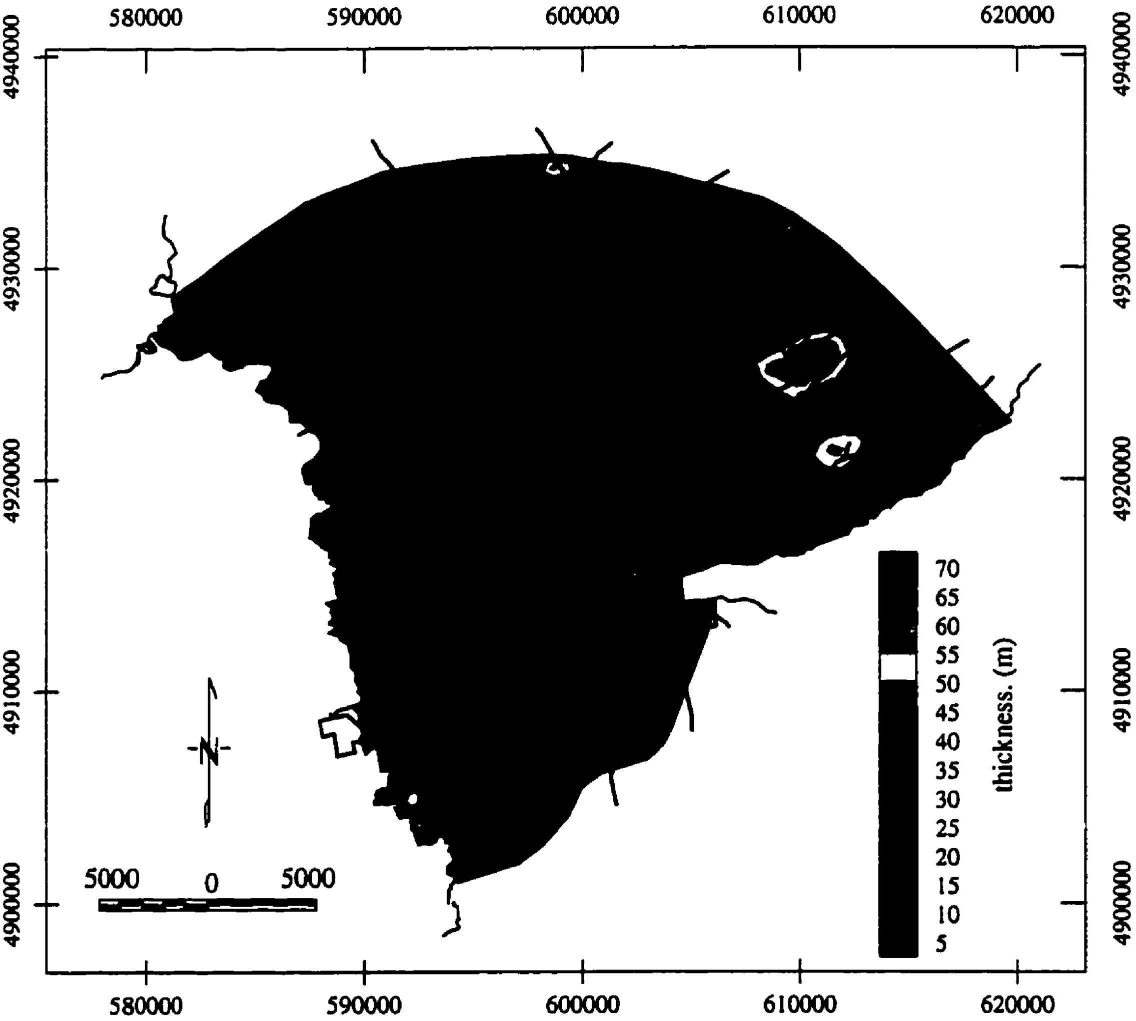
580000
590000
600000
610000
620000
4940000
4930000
4920000
4910000
4900000
N
5000
0
5000
70
65
60
55
50
45
40
35
30
25
20
15
10
5
thickness. (m)

Figure 7.19: Thickness of Aquitard 3 (AQTD3). White areas indicate regions where this unit pinches out.

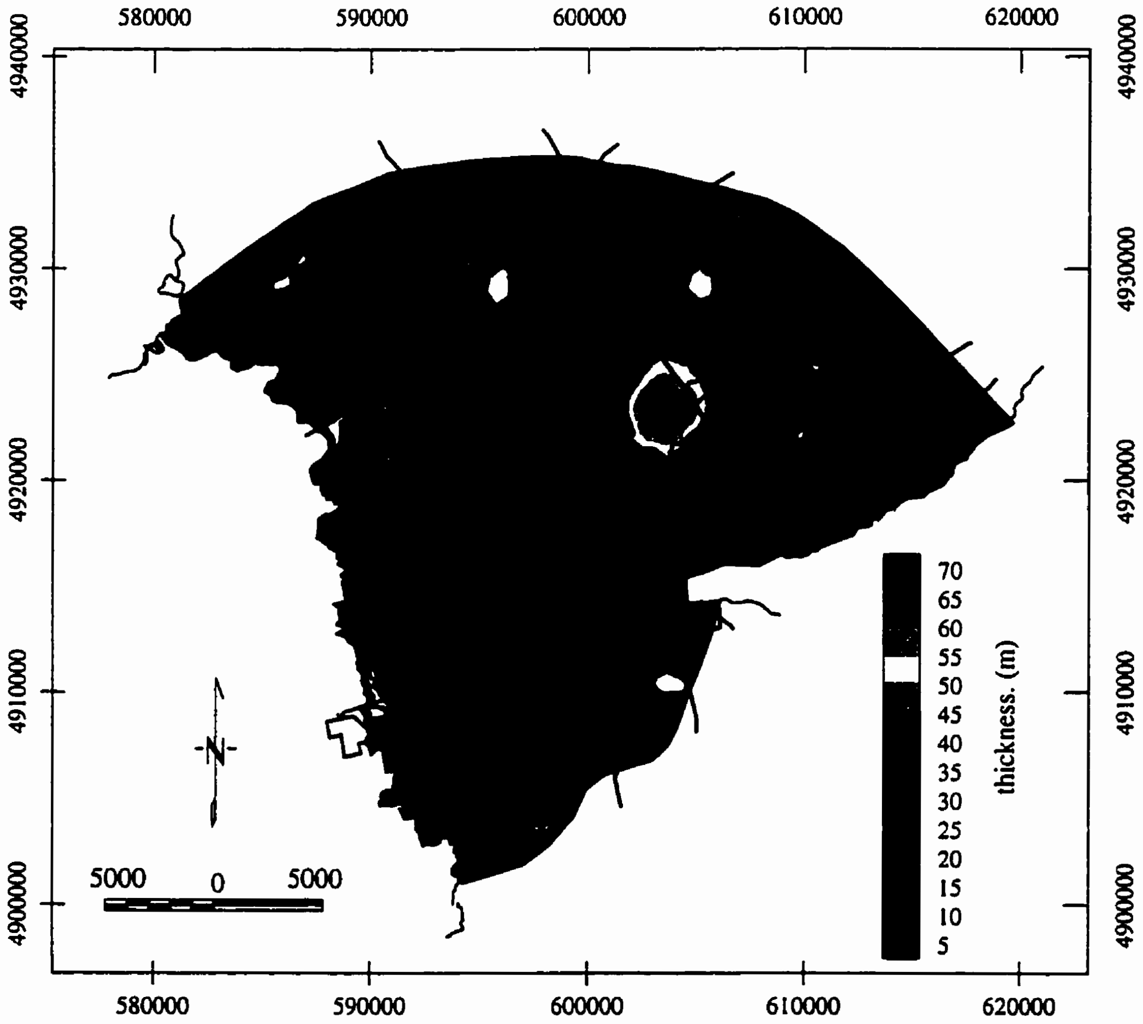
580000
590000
600000
610000
620000
4940000
4930000
4920000
4910000
4900000
N
5000
0
5000
70
65
60
55
50
45
40
35
30
25
20
15
10
5
thickness (m)

Figure 7.20: Thickness of Aquifer 3 (AQFR3). White areas indicate regions where this unit pinches out.

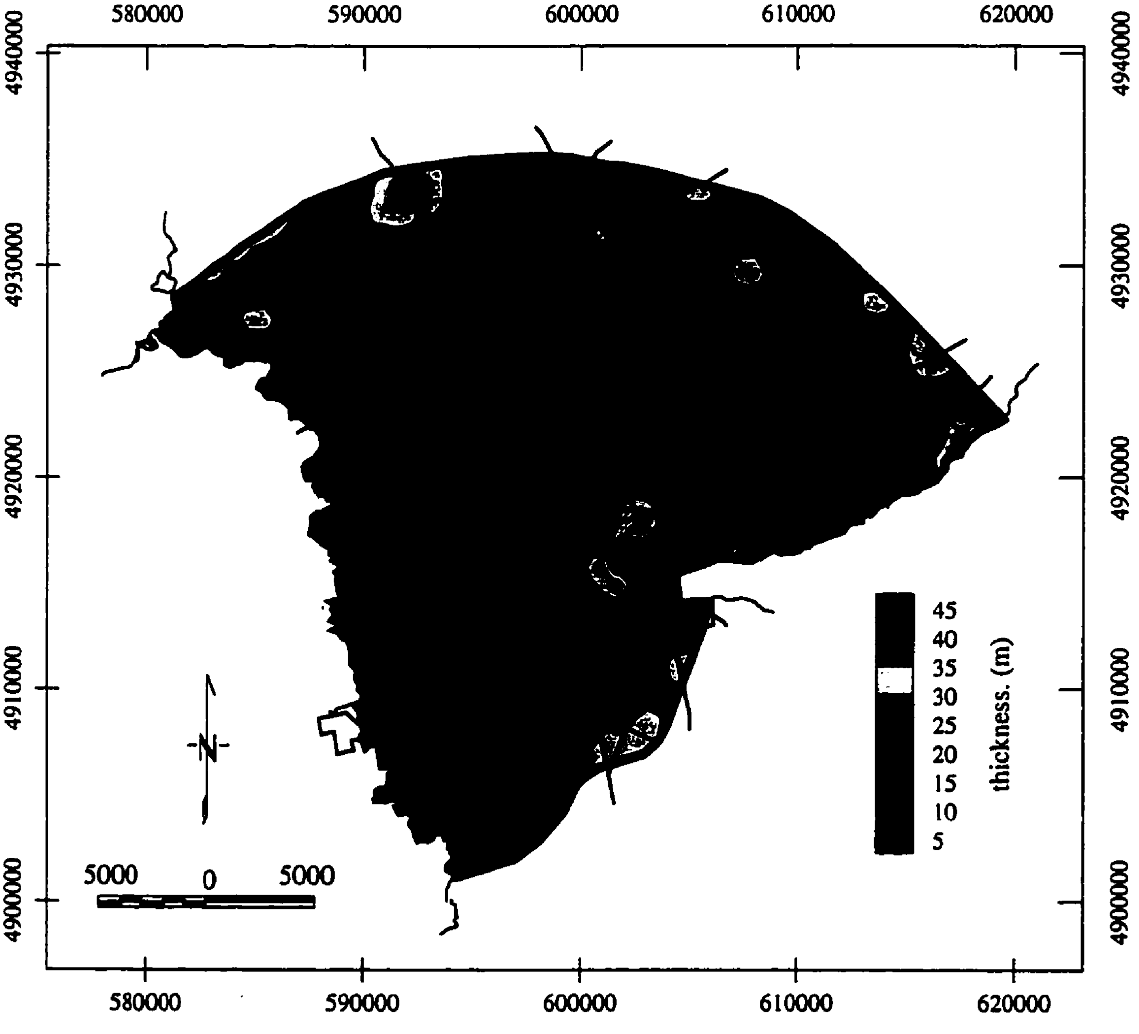
580000
590000
600000
610000
620000
4940000
4930000
4920000
4910000
4900000
N
5000 0 5000
45
40
35
30
25
20
15
10
5
thickness (m)

Figure 7.21: Thickness of Aquitard 4 (AQTD4). White areas indicate regions where this unit pinches out.

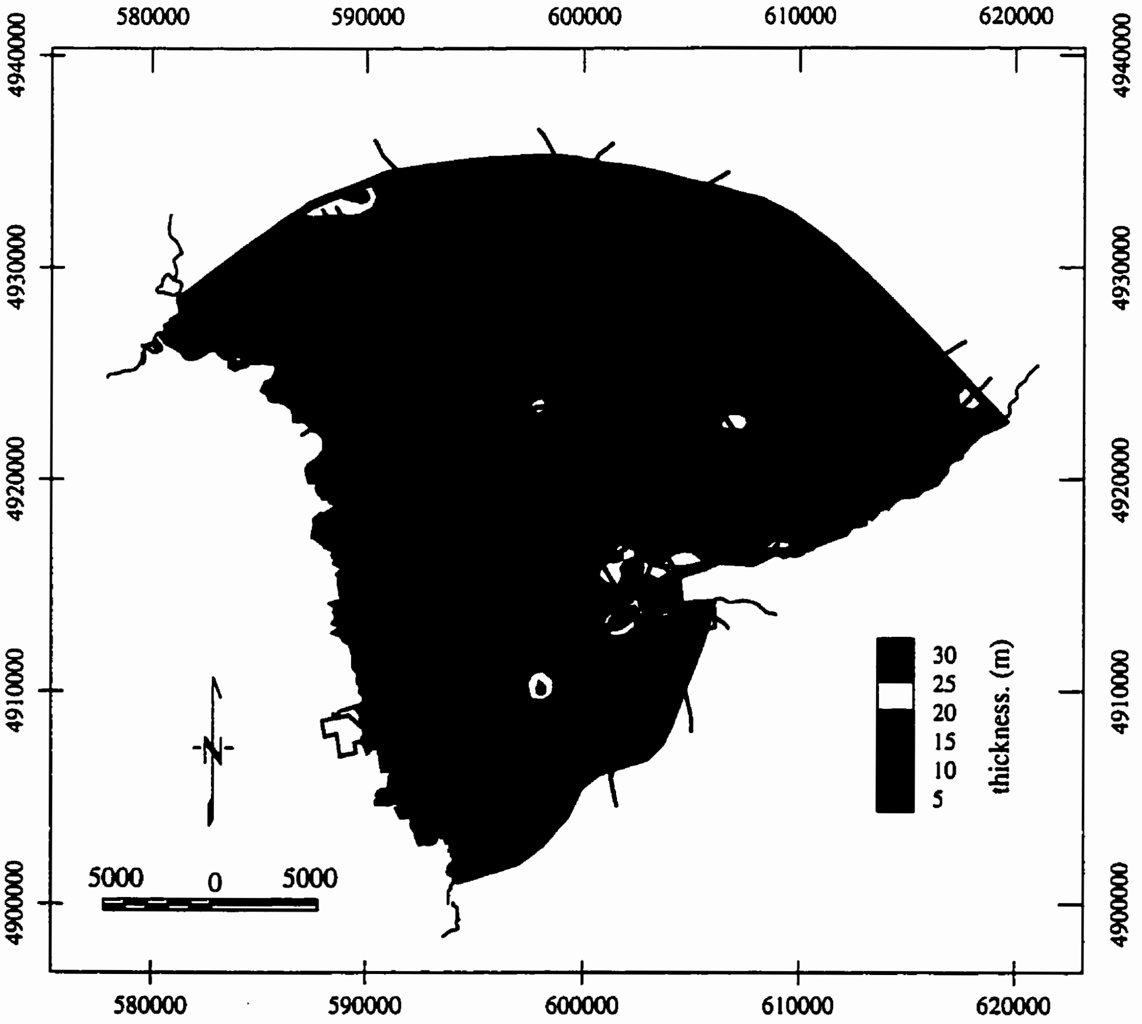
580000
590000
600000
610000
620000
4940000
4930000
4920000
4910000
4900000
N
5000
0
5000
30
25
20
15
10
5
thickness. (m)

Figure 7.22: Thickness of Aquifer 4 (AQFR4). White areas indicate regions where this unit pinches out.

aquifer 2 were delineated by *Dixon Hydrogeology* [1992] in an environmental impact assessment for existing and proposed aggregates in part of the Oro Moraine, just to the northeast of the study area. The cross-sectional interpretations shown in this assessment were used as a starting point for this study (cross-sections 20 and 21, refer to Appendix A). A system of three or four separate aquifers was also identified to the west of Barrie [S. Lee, (Dixon Hydrogeology), personal communication].

The bedrock surface shows a gradual $SW - NE$ increase in elevation from the presumable location of the Laurentian Channel in the Minesing Basin (Figure 7.14, also refer to Section 7.1) towards the Oro Moraine. The elevation range of 100-180 m.a.s.l. agrees well with earlier bedrock topography maps [*Burwasser and Ford*, 1974a, 1974b]. A first order regression of the observed bedrock elevations reveals that, on the average, this surface dips at an angle of 0.08^o (1.4 m/km). This dip is partly a result of post-glacial uplift. The aquifer/aquitard contacts generally dip in the same direction (S57W) at an angle of 0.12^o, consistent with the dominant south-southwest direction of ice movement. The overburden ranges in thickness from 40-220 m (Figure 7.23), with a pattern that closely follows that of the surface topography (Figure 7.1). Such detailed patterns are not evident in existing maps [*Burwasser and Ford*, 1974c, 1974d] as the authors merely interpolate drift thicknesses observed at discrete boreholes and do not directly take the surface topography into account. Here, this thickness is determined as the difference between the bedrock elevation and surface topography maps.

Quaternary geologic maps have been published for the study area. The information contained in these maps has not been used in the hydrostratigraphic interpretation. However, the elevation of the interpolated and adjusted aquifer/aquitard contacts was used to predict the outcrop of the hydrostratigraphic units at the ground surface (Figure 7.24). Below, the predicted outcrops are compared to the Quaternary geologic maps to validate the hydrostratigraphic model. First, a comparison is made for the eastern half of the study area, based on the recently published maps of *Barnett* [1992].

The outcrop of Aquitard 1 largely coincides with the occurrence of glacial deposits draping the uplands and valley walls [*Barnett*, 1992, map unit 8]. These deposits have been identified as lodgement till, melt-out till and flow till. This cover appears to be quite continuous. In some locations it is overlain by glaciolacustrine fine grained sediments (map unit 10) or muck deposits. The semi-confined Aquifer 1 outcrops at the valley walls and consists of ice-contact stratified sands

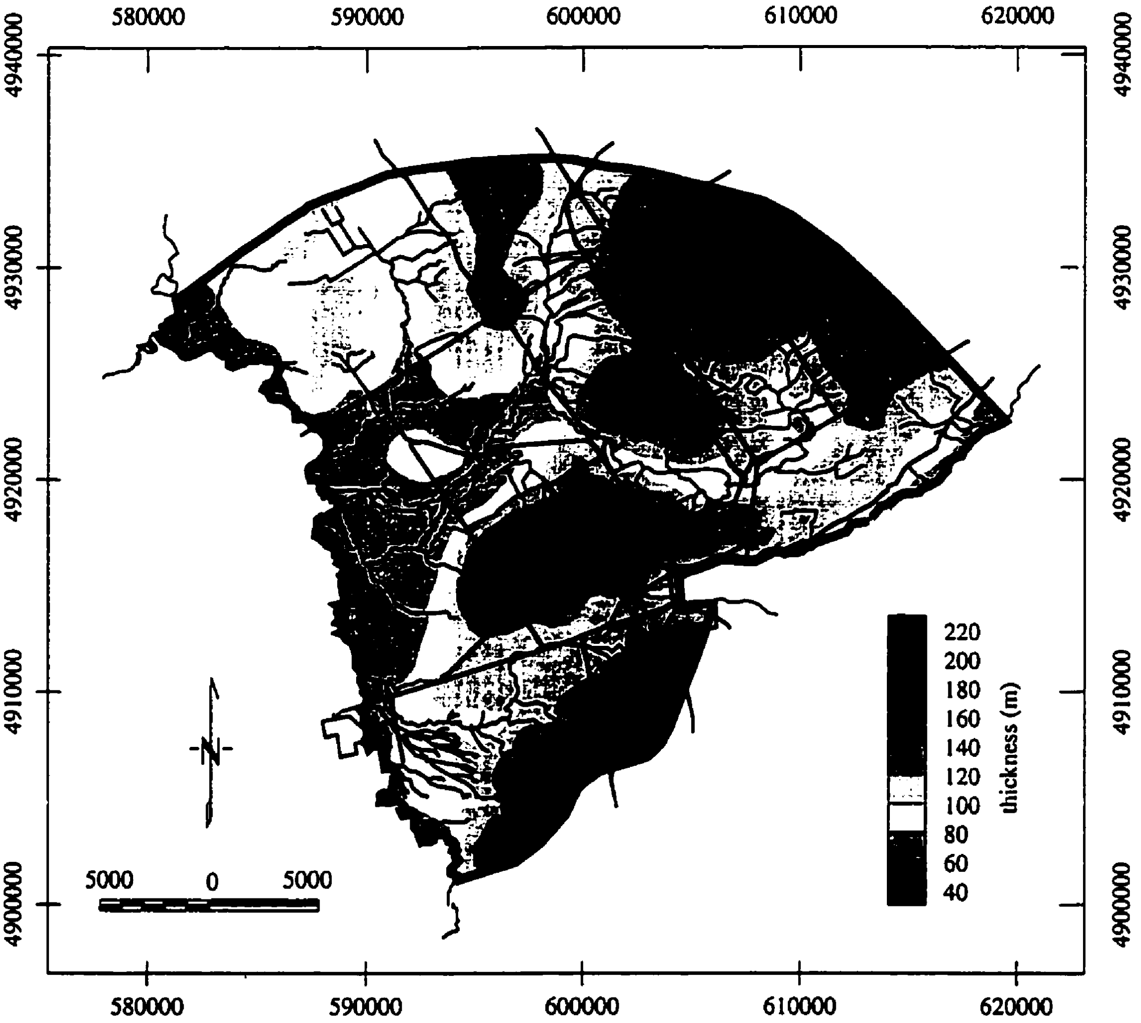
580000
590000
600000
610000
620000
4940000
4930000
4920000
4910000
4900000
5000
0
5000
N
220
200
180
160
140
120
100
80
60
40
thickness (m)

Figure 7.23: Thickness of the overburden.

and gravelley sands (map unit 9). This aquifer is a very pronounced unit that exists only in the uplands with a maximum thickness exceeding 80 m (Figure 7.16). Few outcrops of this unit have been identified in the upper reaches of the uplands by *Barnett* [1992]. This agrees with the continuous nature of Aquitard 1 as it has been inferred here. The main discrepancy is the pinch-out of Aquitard 1 in the northern-most part of the Oro Moraine which is evident in the Quaternary geologic maps but not in the interpretation given here. Except in the Innisfill Uplands, the cover provided by aquitard 1 is relatively thin (Figure 7.15).

Deposits on the Willow Creek valley floor have been identified by *Barnett* [1992] as glaciolacustrine materials of fine sand to silt (map unit 11) and glaciolacustrine beach and bar sediments (map unit 12). The former materials correspond to the outcrops of Aquitard 2 whereas the latter correspond to the occurrence of Aquifer 2. Aquitard 2 has been interpreted here to cover most of the valley floor although it locally is thin (Figure 7.17). The semi-confined Aquifer 2 has few outcrops in the Willow Creek valley but is more pronounced in areas that are associated with Lake Algonquin. The corresponding deposits can be found on the Quaternary geologic maps that are available for the western half of the study area [*Burwasser and Boyd*, 1974; *Burwasser and Cairns*, 1974]. Geologic units given below correspond to the legends for these older maps. In the Matheson Creek valley, the outcrop of Aquifer 2 is characterized by glaciolacustrine silts (map unit 10a) and sands (map unit 11b). In the elevated eastern section of the Minesing Basin, Aquifer 2 is comprised of beach gravels (map unit 12), lacustrine sands (map unit 11c) and outwash sands (map unit 7c). These outwash sands also provide the surficial cover in the flat-lying area between Barrie and Borden and locally make up Aquifer 1. Ice contact deposits (map unit 8c) are found along the steep sloped uplands bordering this area to the north and south.

In the Innisfill Uplands, the surficial cover (Aquitard 1) is provided by a sandy loam till (map unit 4). This cover is also present in parts of the Snow Valley Upland, although not as continuous as the outcrop of Aquitard 1 in Figure (7.24). The northwest corner of the study area is characterized by a sandy silt till (map unit 3) as well as glaciolacustrine clays (map unit 10b), silts (map unit 10a) and sands (maps unit 11b). These materials locally comprise Aquitard 2.

Under the uplands Aquifer 2 is confined and must consist of materials of glacial origin such as overridden glaciofluvial deposits. Similarly, Aquitard 2 is likely comprised of till in these areas. However, no constraints regarding this makeup can be

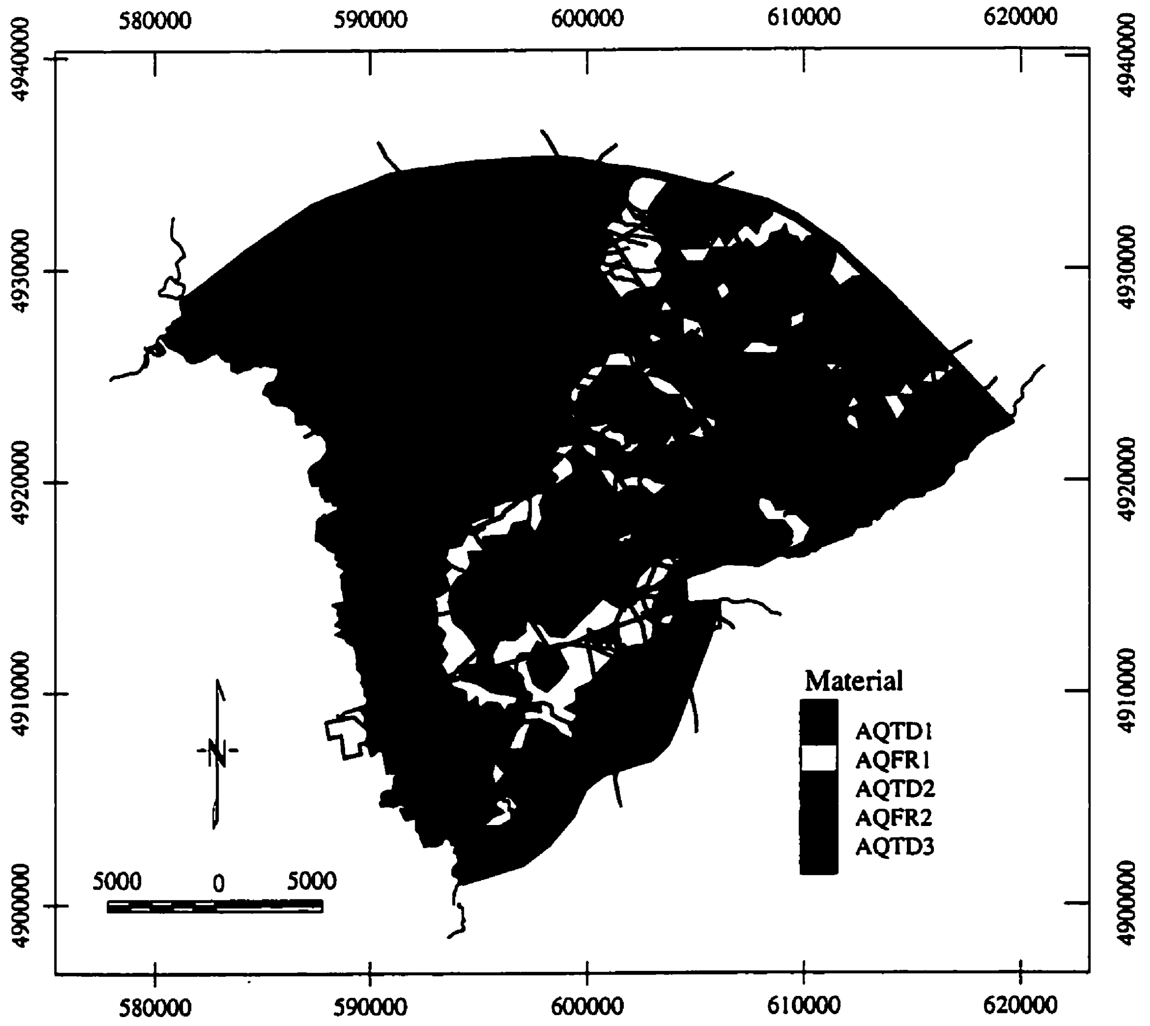
580000
590000
600000
610000
620000
4940000
4930000
4920000
4910000
4900000
N
5000
0
5000
Material
AQTD1
AQFR1
AQTD2
AQFR2
AQTD3

Figure 7.24: Outcrop of the hydrostratigraphic units at the land surface.

derived from the Quaternary geologic maps. Based on information from outside the study area, *Barnett* [1991] suggests that at greater depth there are possibly two more layers of till. These older layers of till constitute the deeper confining units. High quality information on the deeper geology is limited to the 6 stratigraphic boreholes drilled by the OGS [*Barnett*, 1992]. Due to the shallow extent of most of these boreholes, their value for testing the conceptual model of the overburden aquifer system is limited. The OGS wells can be found in cross-sections 24a (OGS 90-6 and 90-7 above and in the Coldwater River valley respectively), 49 (OGS 90-10) and 63 (OGS 90-8, 90-9 and 90-15) in Appendix (A). All 6 boreholes show the confining units to be a combination of poorly sorted diamicton (till) and laminated lacustrine clays and silts. Typical aquifer materials range from well sorted interbedded sands to poorly sorted pebbly gravel. The only borehole that extends to bedrock is OGS 90-7. It shows a stratigraphic sequence that is typical of tunnel valleys. The coarse deposits that presumably result from the catastrophic release of meltwater are underlain by a till unit that is located directly on the bedrock surface. Unfortunately, the neighboring borehole OGS 90-6 does not penetrate deep enough to compare the stratigraphic sequence down to the bedrock surface.

In general the agreement between the hydrostratigraphic model that was developed from the MOEE database and other available information appears to be quite good. The correspondence between Figure (7.24) and the Quaternary geologic maps is encouraging given the complex nature of the overburden and the fact that different sources of information have been used in generating these maps. The inferred hydrostratigraphy should therefore be a valid basis for the numerical model that is presented in the next chapter. However, future efforts should focus on directly including the high quality surficial geologic information in the hydrostratigraphic interpretation. This will improve the representation of the near-surface geology in the numerical model.

Chapter 8

Oro Moraine Model

8.1 Introduction

The Oro Moraine model is developed and calibrated in this chapter. The 3D finite element mesh with recharge and other boundary conditions is discussed. Pumping wells with abstraction rates are listed. The processing of the water level and streamflow data for the model calibration is detailed. Hydraulic conductivity is taken to be the only adjustable parameter in the calibration. An initial conductivity distribution is obtained from the lithologic descriptions contained in the MOEE database. The conductivity values that are assigned to each of the 14 lithofacies are optimized. Next, the average conductivity of each of the hydrostratigraphic units is adjusted. Local conductivity adjustments are made to refine the model calibration. Final calibration statistics are given and the simulated water mass balance and its uncertainty is detailed. This is followed by a discussion of data and model requirements to refine the Oro Moraine model in future studies.

8.2 Finite Element Mesh

A two-dimensional triangular mesh was generated within the model domain (Figure 8.1). The main branches of the Bear, Willow, Marl and Matheson Creeks (Figure 1.1) are incorporated as internal features to specify boundary conditions

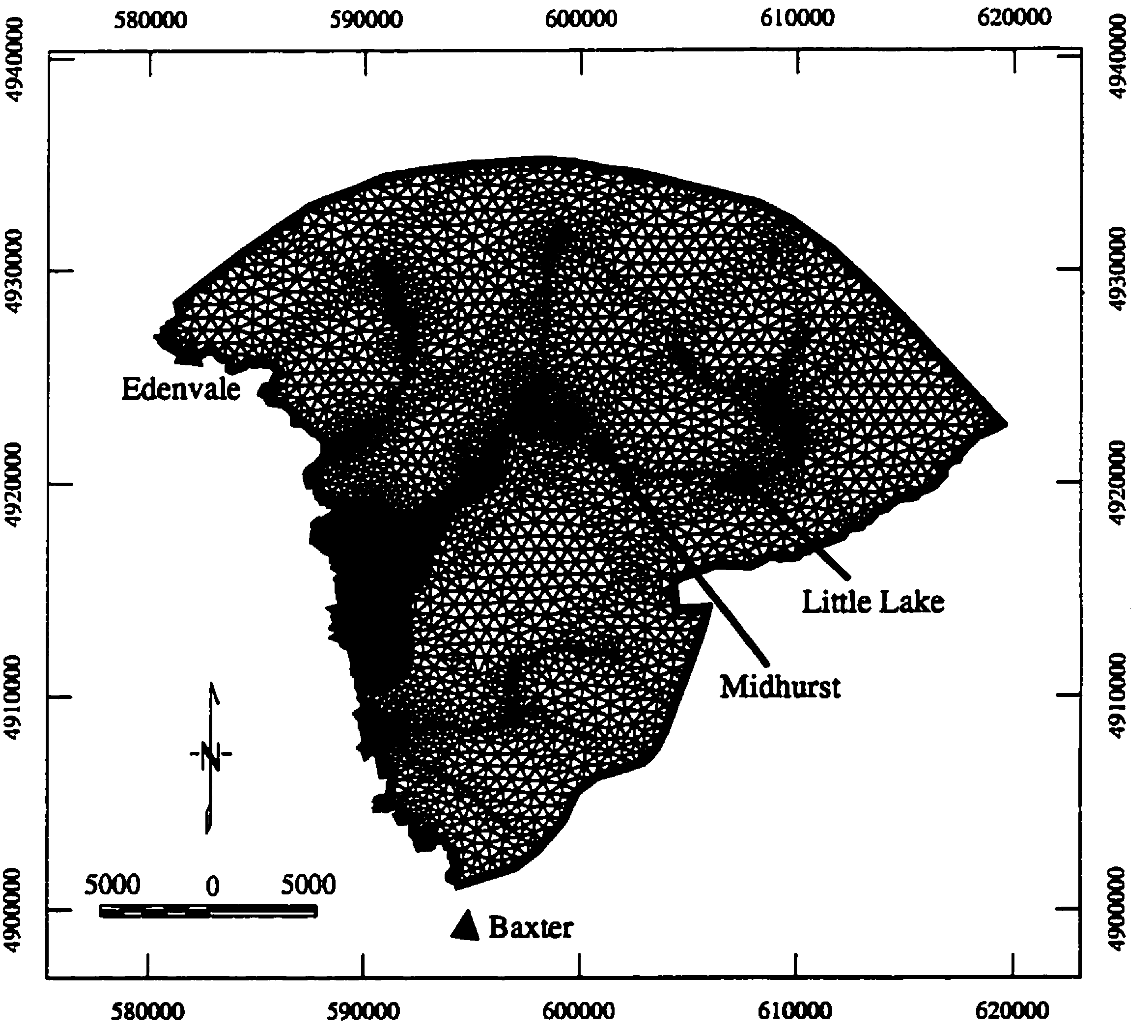
580000
590000
600000
610000
620000
4940000
4930000
4920000
4910000
4900000
Edenvale
Little Lake
Midhurst
Baxter
N
5000 0 5000

Figure 8.1: 2D finite element mesh. Dirichlet boundaries are shown in grey. Triangles indicate stream gauge stations.

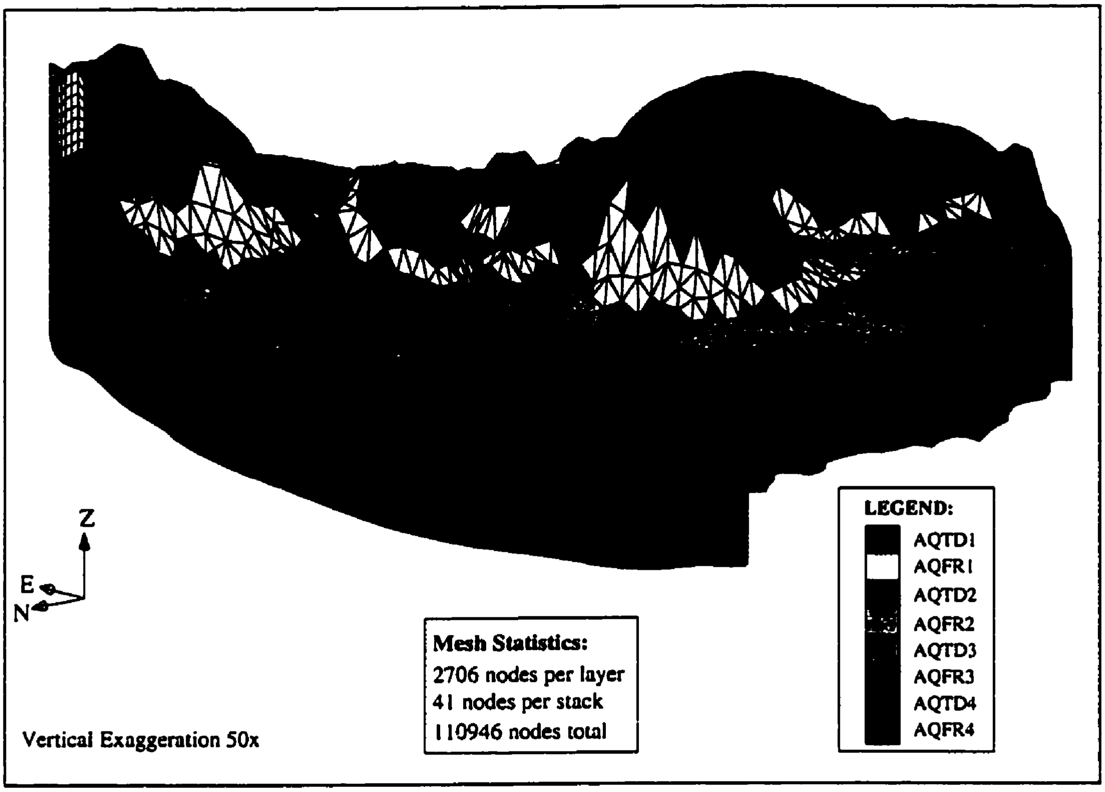
Z
E
N
Vertical Exaggeration 50x
Mesh Statistics:
2706 nodes per layer
41 nodes per stack
110946 nodes total
LEGEND:
AQTD1
AQFR1
AQTD2
AQFR2
AQTD3
AQFR3
AQTD4
AQFR4

Figure 8.2: 3D finite element mesh illustrating the complexity in the geometry of the hydrostratigraphic units and the related vertical discretization of the domain.

and calculate fluxes to these streams. The average size of the sides of the triangular elements is 500 m. This is adequate to represent the spatial variability in the aquifer/aquitard contacts as well as the lateral variability in conductivity.

The three-dimensional mesh was generated from the 2D mesh by stacking triangular-prismatic finite elements. By deforming the top and bottom faces of these elements the hydrostratigraphy was incorporated in the mesh. First, the elevation of the hydrostratigraphic contacts was interpolated to the nodes of the 2D mesh using the procedure outlined in Section (7.4). The 3D mesh was generated with the elevation of these contacts as a constraint for the vertical nodal locations. The number of element layers for each hydrostratigraphic unit was chosen based on its maximum thickness and the vertical correlation of the corresponding conductivity field.

In order to retain accuracy of the numerical solution it is necessary to enforce a minimum element thickness of 1 m. Because the finite element mesh needs to be continuous in regions where the hydrostratigraphic units pinch out, it is not always possible to ensure that the aquifer/aquitard contacts are exactly represented. This is certainly true for the upper two units which only exist in the Simcoe Uplands (Figures 7.15 and 7.16) In the Simcoe Lowlands, the elements corresponding to AQTD1 and AQFR1 become part of the underlying hydrostratigraphic units. Because of these complicating factors, the actual hydrostratigraphic unit that a certain element is grouped into needs to be determined when spatially distributing hydraulic conductivity. A zone or material number is assigned to each element by comparing the elevation of its centroid to the elevation of each of the hydrostratigraphic contacts. This number, together with the nodal indices and coordinates completely defines the 3D finite element mesh (Figure 8.2). The zone number is used to link each element to the appropriate database of hydraulic conductivities (Figure 2.1).

8.3 Boundary Conditions

The different geologic materials that outcrop at the land surface (Figure 7.24) will cause infiltration and runoff to vary spatially. Consequently, the fraction of the water surplus that enters the subsurface is uncertain at any particular location. The hypothetical flow problem of Chapter (3) was used to illustrate that a pseudo-unsaturated model coupled with a recharge spreading layer (RSL) can handle the complex recharge mechanism of heterogeneous aquifers. This modelling approach is also used for the study area.

A spatially variable water surplus is applied at the top of the RSL. Constraints were obtained from climate data for several meteorological stations located in and around the study area (Figure 8.3). A uniform evapotranspiration rate of 500 mm/yr [*Environment Canada*, 1980] was subtracted from the precipitation measurements to obtain the water surplus. Climate normals for the period 1961-1990 [*Environment Canada*, 1993] show a 2-5 % increase in precipitation with respect to the 1951-1980 time span [*Environment Canada*, 1982]. Data from both time spans were used uncorrected as this increase is modest compared to the spatial trend.

The meteorological station data were interpolated using inverse distance weight-

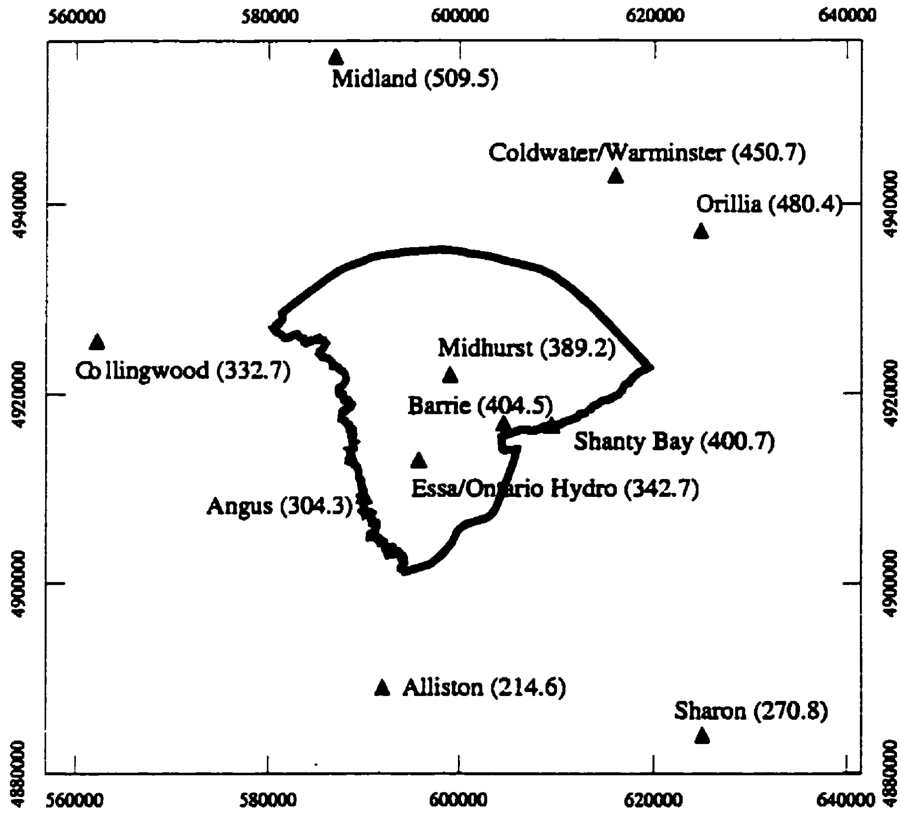
560000
580000
600000
620000
640000
4940000
4920000
4900000
4880000
Midland (509.5)
Coldwater/Warminster (450.7)
Orillia (480.4)
Collingwood (332.7)
Midhurst (389.2)
Barrie (404.5)
Shanty Bay (400.7)
Essa/Ontario Hydro (342.7)
Angus (304.3)
Alliston (214.6)
Sharon (270.8)

Figure 8.3: Meteorologic stations used in calculating the water surplus distribution. Point data values shown are average annual precipitation rates (mm/yr) listed for these stations adjusted with an evapotranspiration rate of 500 mm/yr.

ing after a second order trend ($r^2 = 0.84$) was removed. Kriging was not used due the scarcity of the data points. The resulting water surplus distribution indicates a SSW-NNE trend of increasing values from 300 mm/yr to 430 mm/yr towards the snow-belt region of Georgian Bay (Figure 8.4). The total yearly water surplus over the 696 km^2 study area is $2.69 \cdot 10^8$ m^3 (8.53 m^3/s)

Figure (8.4) also shows a qualitative zonation of the study area in terms of infiltration capacity. This zonation was the basis for a surface hydrologic model of the Nottawasaga River basin [*NVCA*, 1988]. Several infiltration categories ranging from very good (good A) to very poor (poor D) were identified based on soil classifications as well as land use. Wetland areas are indicated as "muck". The classification "Urban" for the city of Barrie was added for the purpose of this study.

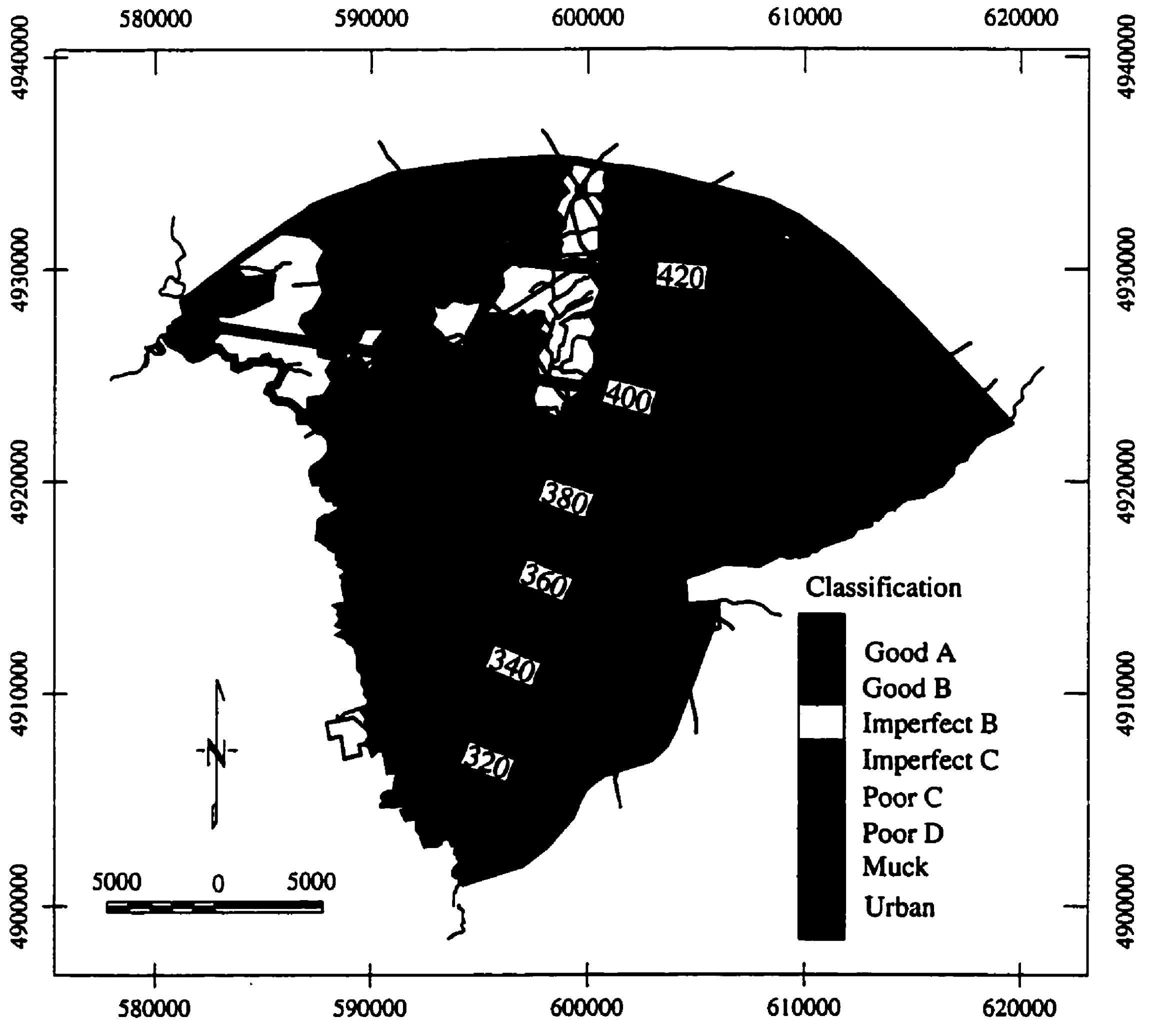
580000
590000
600000
610000
620000
4940000
4930000
4920000
4910000
4900000
420
400
380
360
340
320
N
5000 0 5000
Classification
Good A
Good B
Imperfect B
Imperfect C
Poor C
Poor D
Muck
Urban

Figure 8.4: Water surplus distribution (mm/yr) and soil infiltration capacity after *NVCA*, [1988].

Regions with a poor infiltration capacity have a high potential for rainfall runoff and vice versa. The soil zones shown in Figure (8.4) will therefore be considered in constraining a spatially variable conductivity for the recharge spreading layer.

Dirichlet boundary conditions are applied to the Nottawasaga River, the Minesing Swamp, Kempenfelt Bay and the main branches of the Willow, Marl and Matheson Creeks (Figure 8.1). Prescribed heads are enforced at the top layer of the domain (i.e. the node layer that separates it from the RSL) except for Kempenfelt Bay where the upper 30 m of the mesh is of Dirichlet type. All other lateral boundaries are assigned zero flux conditions. The selection of the boundaries for the model domain was discussed in Section (7.2.2).

8.4 Groundwater Abstraction

Pumping may have a considerable impact on the water mass balance of the groundwater system. A ranking of water wells contained in the MOEE database based on pumping *test* rates shows that almost all major activity is concentrated near Barrie. Roughly half of the cumulative rate is accounted for by municipal wells operated by the Barrie PUC. Abstraction rates for the municipal wells in the years 1995 and 1996 were obtained from the Barrie PUC (Table 8.1). The total pumping rate is approximately 0.42 m^3/s $(13 \cdot 10^6 m^3/yr)$. Based on the information provided by the query of the MOEE database, the tabulated wells were included in the numerical model with pumping rates multiplied by a factor 2 to account for private (industrial) water use. Pumping rates for municipal wells operated by the township of Oro-Medonte (roughly east of a line between Little Lake and the Matheson Creek headwaters) were also obtained but local usage is relatively minor ($< 0.001 m^3/s$ for individual wells). These wells were therefore not included in the model. Unfortunately, actual abstraction rates could not be obtained for Essa TWP (south of the road between Angus and Barrie) and Springwater TWP (remainder of the study area). However, for these townships only one well, at Midhurst (MOEE well 5718755), was found to have a significant test rate (0.04 m^3/s). This well was also included in the model with a doubled abstraction rate, giving a total usage in this area that is reasonably consistent with recent estimates [*Easton*, 1998]. Well-screens are represented in WATFLOW as 1D line elements (Chapter 3).

The cumulative effect of small private wells may be an important unknown

	Easting	Northing	Screen (m.a.s.l.)	Q ($10^{-2}m^3/s$)
Perry[1]	603340	4914940	169 – 175	2.35
John[1]	602980	4914060	122 – 142	1.97
Wood[1]	603540	4913460	189 – 208	2.89
Tiffin[1]	602420	4913980	132 – 147	2.25
Gowan[1]	604880	4913900	166 – 181	1.67
Johnson 9[1]	606960	4917400	167 – 183	3.51
Huronia[1]	606180	4912480	165 – 173	1.48
Heritage 11[1]	604600	4915640	158 – 177	2.85
Centenial 12[1]	604440	4914400	135 – 153	6.60
Johnson 13[1]	606950	4917380	167 – 183	3.26
Heritage 14[1]	604610	4915650	158 – 177	4.11
Centenial 15[1]	604400	4915000	154 – 175	6.88
Midhurst[2]	601900	4921800	147	4.00

Table 8.1: Pumping wells included in the numerical model. Information was obtained from (1) Barrie PUC 1995-1996 listings and (2) MOEE database.

factor in the water balance. The cumulative rate for all pumping tests of MOEE listed wells is 2.2 m^3/s. Although this does not include wells that have been drilled after 1985, many of the older wells listed in the MOEE database are no longer in use. Test rates are typically 2-3 times higher than the actual abstraction rates. The total applied pumping rate of 0.88 m^3/s should therefore represent the bulk of the water abstraction in the study area. This volume accounts for about 10 % of the water surplus.

8.5 Calibration Data

Calibration data for the groundwater model consist of water level data from the MOEE database and stream gauge measurements obtained for the 4 stations shown in Figure (8.1). Static water level data alone are not sufficient to reliably constrain the hydraulic conductivity distribution of a groundwater model. Streamflow data are therefore used to validate the water balance of the numerical model against the real system. The discharge data also provide information on the distribution of the water surplus between the surface and groundwater systems.

8.5.1 Water Level Data

Water level data were selected from boreholes used in the hydrostratigraphic interpretation. Because in this interpretation an emphasis was put on deeper wells, these data were augmented with nearby shallow wells in order to provide additional information on vertical gradients between the aquifers. The data were categorized by aquifer and subsequently kriged in a two-dimensional fashion using the approach outlined for the interpolation of the aquifer/aquitard contacts. This approach ignores the vertical correlation that exists in the hydraulic head distribution. However, information on vertical gradients is limited as in the uplands most wells are screened in the shallow aquifers, whereas information on the deeper aquifers is mainly available in the valley areas. Given these concerns, a 2D interpolation within each aquifer was considered more reliable than a 3D interpolation.

A low-order trend was removed from the data and semivariograms were determined for the residuals (Figure 8.5). Fluctuations in the sill of some of the experimental semivariograms suggest the presence of unresolved head variations (Section 2.2.4). Although this may be perceived as a potential problem it should be taken into account that the trend surfaces alone already account for most of the spatial variability in hydraulic head (r^2 values in Table 8.2). Kriging was applied to the residuals using 30 control points (18 points for aquifer 4) after which the calculated trend was added back to the interpolated values. Back-kriging was used as an aid for detecting outliers in the datasets. This technique proved to be helpful in areas where clusters of data inhibited a visual inspection of the water level maps. Originally, the water level map for aquifer 1 revealed a pattern closely resembling that of the elevation of BAQ1 in the Oro Moraine, indicating perched water table conditions. The corresponding 8 data points were removed from the database. These observations are no longer present in Figure (8.6) but were used in generating the regional water level map (Figure 7.2).

The back-kriging statistics (Table 8.3) suggest that the adopted interpolation approach adequately represents the spatial variability in the head data: the bias in the kriged values is small and the normalized error calculated using expression (7.2)

Boreholes		Trend		Variogram	
		Order	r^2	sill (m^2)	range (m)
AQFR1	103	3	0.72	550	4500
AQFR2	155	3	0.92	145	2100
AQFR3	134	3	0.95	135	3575
AQFR4	18	3	0.94	140	5550

Table 8.2: Parameters for the spatial interpolation of the water level data.

is reasonably close to unity, indicating that the deviations between observed and kriged values are consistent with the interpolation uncertainty. The kriged water levels should therefore accurately describe the true piezometric head distribution that exists in the aquifers.

The interpolated head data (Figures 8.6-8.9) illustrate the complex flow patterns that characterize the groundwater system. All three uplands (figure 7.1) are important recharge areas for the shallow aquifers. Flow patterns change only gradually downward, suggesting that the aquifer system is vertically well connected. At depth, groundwater flow from the Oro Moraine towards the Minesing Basin dominates as the other recharge areas become less important. The water level maps were compared to one another to ensure the correct direction of vertical gradients near inferred recharge and discharge areas, providing another control on the spatial interpolation.

	I			II	
	r^2	bias (m)	error	mean (m)	$\sigma(m)$
AQFR1	0.92	−0.36	0.68	2.50	11.3
AQFR2	0.95	−0.24	0.58	0.88	9.80
AQFR3	0.97	0.16	0.73	3.39	8.60
AQFR4	0.93	0.25	1.34		

Table 8.3: Statistics for (I) back-kriging scattergrams and (II) trend surface analysis for temporal variations in water level data.

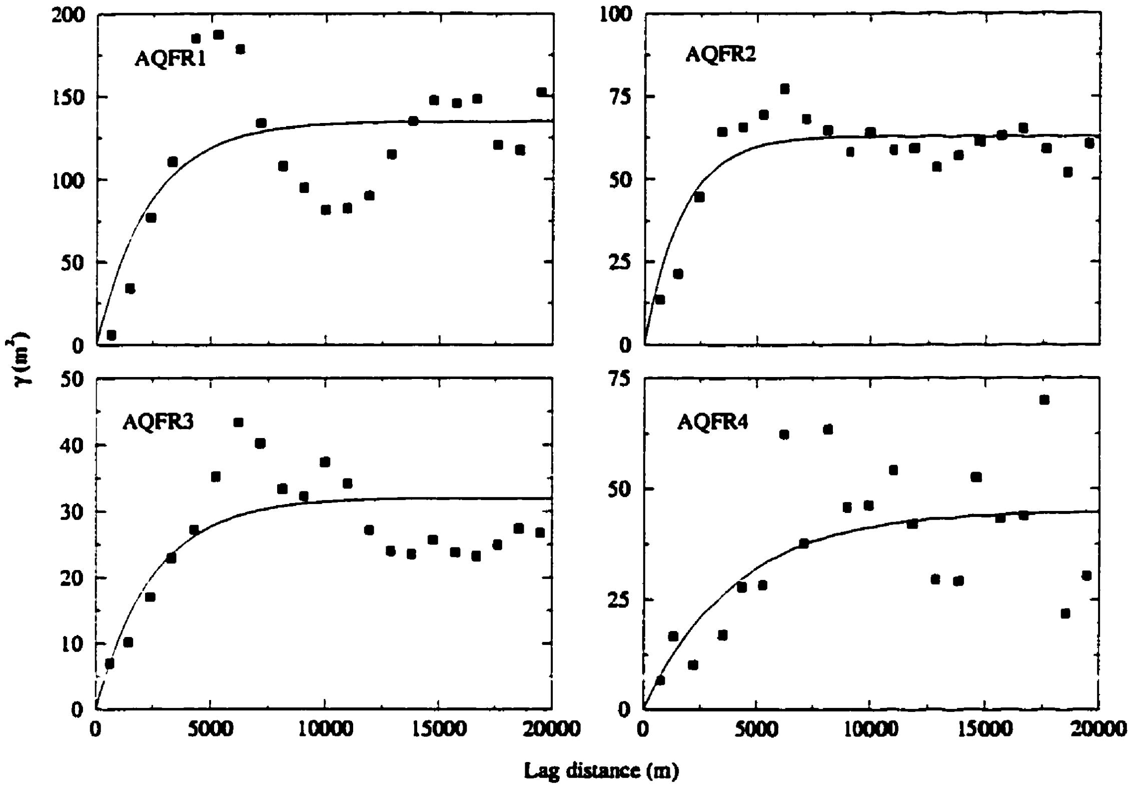

Figure 8.5: Semivariograms for water level data.

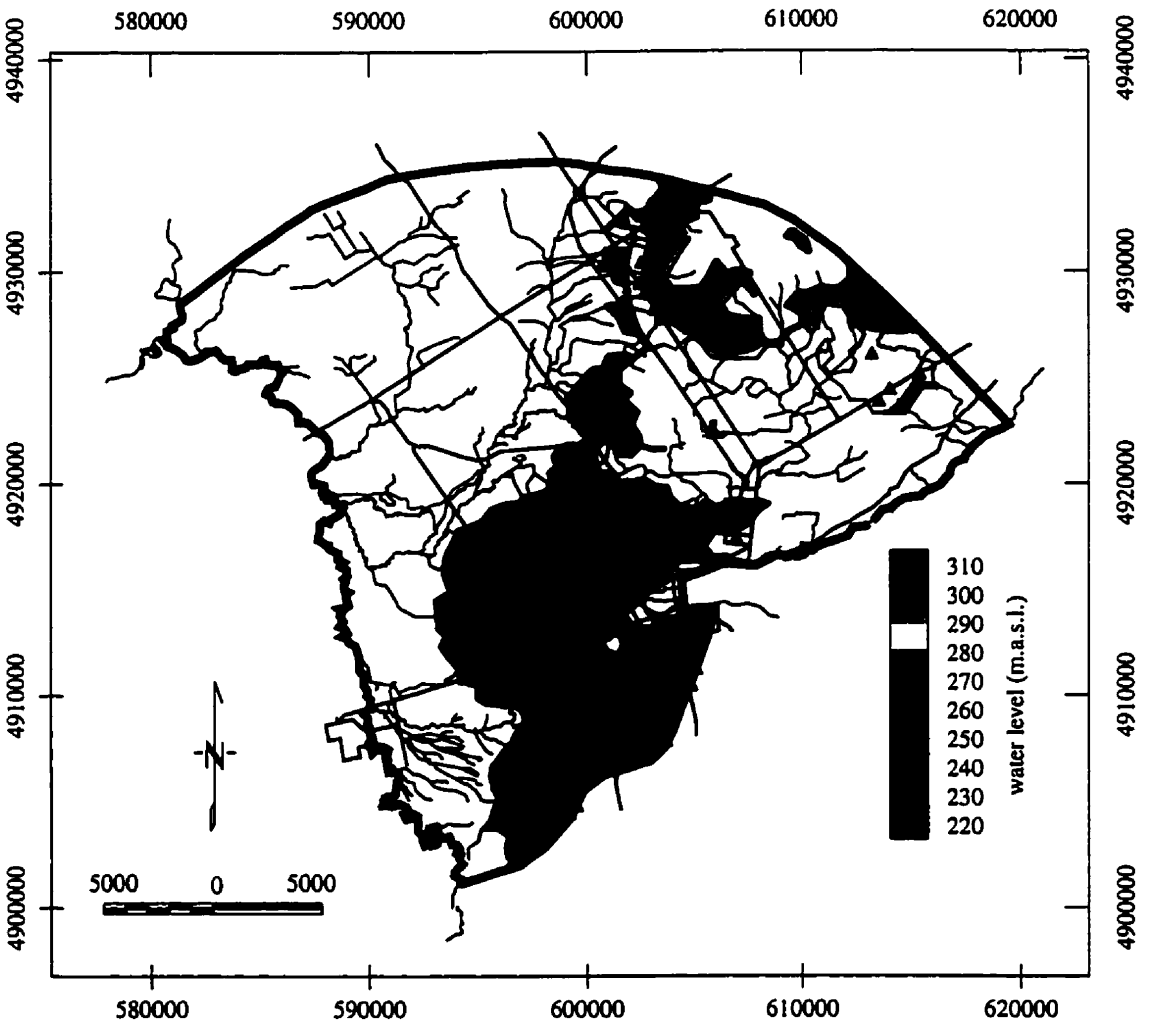
580000
590000
600000
610000
620000
4940000
4930000
4920000
4910000
4900000
N
5000
0
5000
310
300
290
280
270
260
250
240
230
220
water level (m.a.s.l.)

Figure 8.6: Interpolated water levels for AQFR1. Triangles indicate data locations. White areas designate regions where the aquifer is unsaturated over its whole thickness or where this unit pinches out.

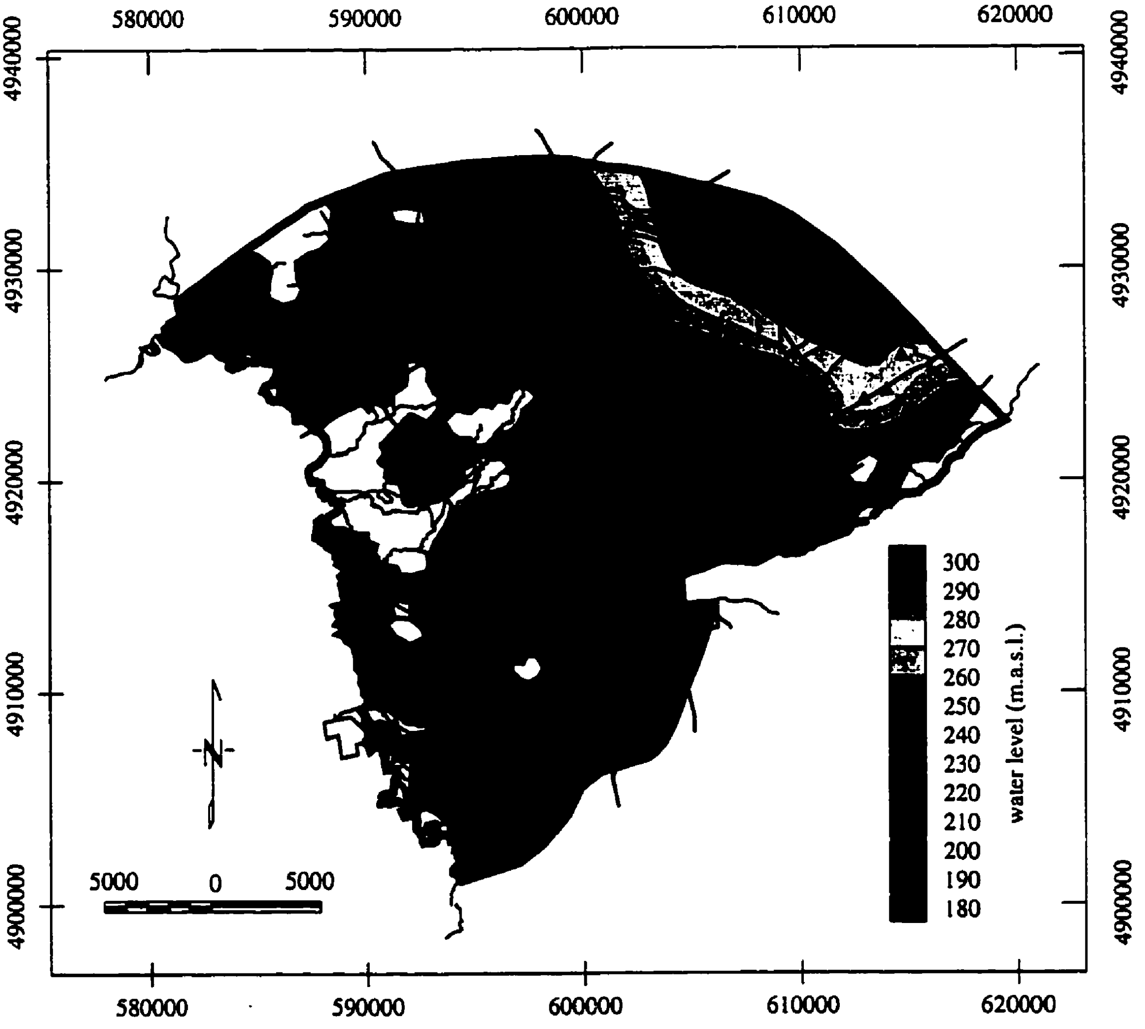
580000
590000
600000
610000
620000
4940000
4930000
4920000
4910000
4900000
N
5000
0
5000
300
290
280
270
260
250
240
230
220
210
200
190
180
water level (m.a.s.l.)

Figure 8.7: Interpolated water levels for AQFR2. Triangles indicate data locations. White areas designate regions where the aquifer pinches out.

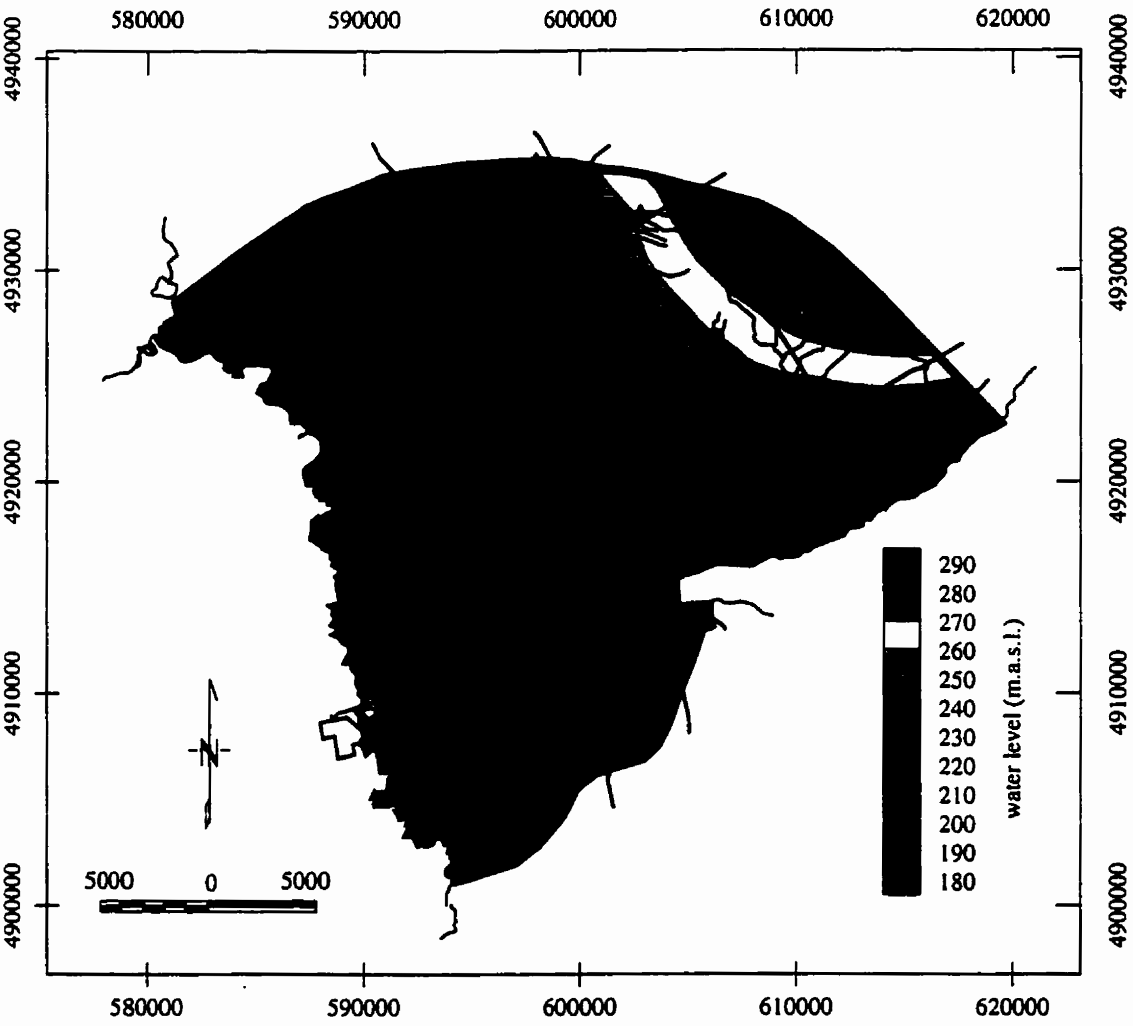
580000
590000
600000
610000
620000
4940000
4930000
4920000
4910000
4900000
N
5000
0
5000
290
280
270
260
250
240
230
220
210
200
190
180
water level (m.a.s.l.)

Figure 8.8: Interpolated water levels for AQFR3. Triangles indicate data locations.

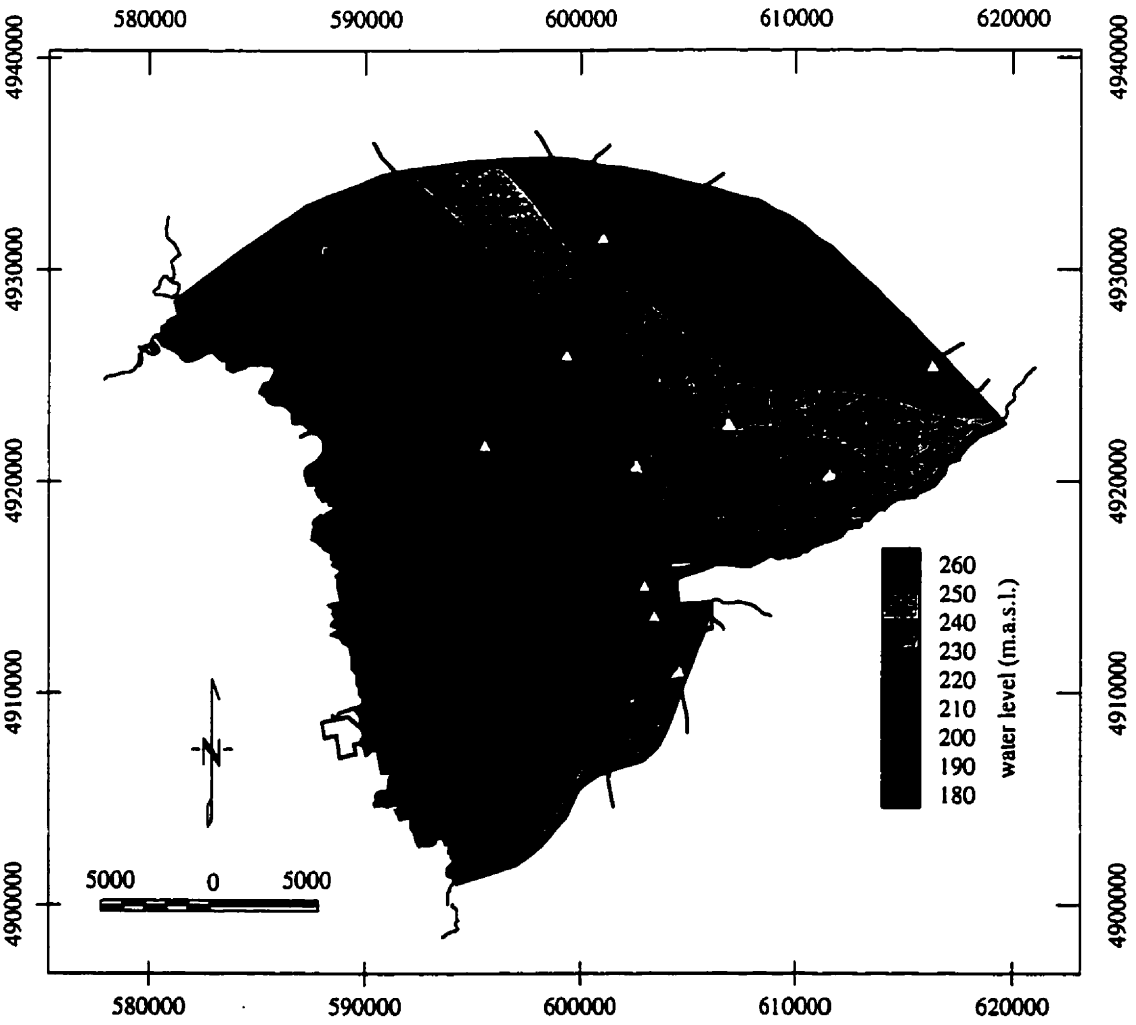
580000
590000
600000
610000
620000
4940000
4930000
4920000
4910000
4900000
N
5000
0
5000
260
250
240
230
220
210
200
190
180
water level (m.a.s.l.)

Figure 8.9: Interpolated water levels for AQFR4. Black triangles indicate data derived from overburden wells; white triangles correspond to bedrock wells.

The water level map for aquifer 4 was created using constraints from both overburden and bedrock wells. This is correct as long as the overburden and bedrock are hydraulically well connected. The water level map and back-kriging do not indicate any evidence of the contrary, although control points are scarce. Higher density brine water at depth may be of concern for the numerical modelling. A query of the MOEE database did not reveal any systematic information regarding the presence of brine in the aquifer system.

Possible temporal variations in the water level data were explored by selecting from each database observations made prior to 1960 and more recent measurements. A more detailed classification by decade was hampered by a lack of data. Sufficient data were unavailable for aquifer 4 for any temporal analysis. Trend surfaces of order 3 were determined for the two time spans. The earlier period was then subtracted from the more recent one. The mean of differences at the 2D mesh nodes (Table 8.3) suggests slightly higher water levels for the more recent period. Although in view of the large scatter, this increase may not be significant in itself, it does coincide with an apparent increase in precipitation and streamflow.

8.5.2 Stream Gauge Measurements

Daily measurements were obtained for 4 stream gauge stations (Figure 8.1). Unfortunately the Edenvale station has only been in place since 1990. Because its record is very short, the resulting data may be unreliable due to short-term climatological effects. The other stations have records ranging from 17 to 40 years providing good control on temporal variations in streamflow. Records for these stations were available on CD-ROM [*Environment Canada*, 1990]. Data for the Edenvale station were obtained directly from Environment Canada.

The total discharge of a stream fluctuates greatly during the year due to the episodic nature of precipitation events. Contributions to this discharge come from overland flow, interflow, direct precipitation and baseflow. Direct precipitation is relatively unimportant and will be ignored here. Subsurface stormflow in the shallow soil layer (interflow) may be significant on hillslopes [e.g., *Freeze and Cherry*, 1979]. Runoff due to interflow and overland flow constitutes the largest contribution to the stream hydrograph and shows the greatest temporal fluctuations. The baseflow component is more constant over time, although seasonal water table

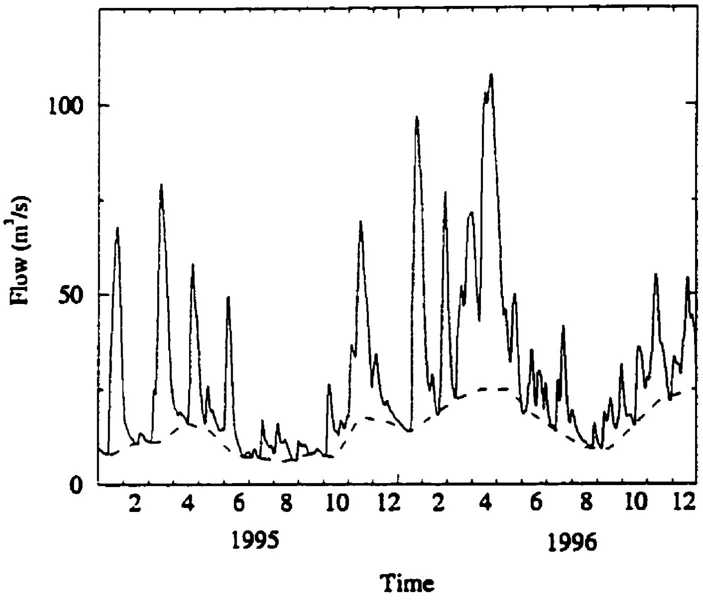

Figure 8.10: Total flow (solid line) and baseflow (dashed line) for the Edenvale station during the period 1995-1996.

fluctuations will result in some variability. Regional-scale flow systems are characterized by response times in the order of years or sometimes even decades. Baseflow contributions from these flow systems should therefore be relatively constant. The baseflow component of a stream hydrograph is typically determined by connecting the troughs in the total discharge [e.g., *Freeze and Cherry*, 1979]. Here, this was accomplished by determining the lowest measured value of total discharge for each month (Figure 8.10). This value then is considered representative for the baseflow during that period.

Seasonal and long term variations in daily flows were determined (Figure 8.11). Total flow and baseflow are highest during the snow melt period at the end of the winter (March, April) and lowest near the end of the summer (August). The baseflow value for this last period is taken to be representative of the contribution from the regional flow system. It should be noted that in using the low-flow value for a steady-state simulation of the flow system, the groundwater component of the hydrologic cycle may be somewhat underestimated. A transient simulation of the flow system is needed to investigate the origin of seasonal variations in streamflow generation. Unfortunately, the quality of the water level measurements is inadequate to constrain the corresponding temporal head variations for such an analysis.

A clear trend of increasing total flow after 1970 is visible in the yearly averaged record for the Baxter station (Figure 8.11). Although less pronounced, this trend is also apparent in the baseflow record. Any trend for the Willow Creek stations is obscured by the strong yearly variations. However, the apparent increase in discharge upstream of Baxter is consistent with evidence from the precipitation and water level records for the study area itself. As these increases are relatively modest they will be ignored. Discharge values as used in this study are summarized in Table (8.4).

The stream gauge measurements are used to define several calibration objectives. The 17.46 m^3/s increase in total discharge between the Baxter and Edenvale stations is due to contributions from the study area and the subwatersheds to the west of the Nottawasaga River. Streams originating at the Niagara Escarpment are larger (Figure 7.2) and are therefore expected to be more important. The gauging stations for these streams are unfortunately located too far away from the Nottawasaga River to be of use. The subwatershed areas were used instead as a criterion to determine the contribution of the model domain to the observed streamflow accumulation for the Nottawasaga River. These areas were estimated from a map. The southeast part of the study area not associated with the Willow Creek makes up roughly 15 % of the total domain. The remainder of the study area that drains towards the Minesing Basin comprises an estimated 35 % of all subwatersheds that contribute to the streamflow accumulation between Baxter and Edenvale. This fraction results in a accumulation of 6 m^3/s that is attributed to the Oro Moraine system. This value is reasonably consistent with with the calculated water surplus of 8.5 m^3/s (Section 8.3) and water losses to Kempenfelt Bay (15 % of the water surplus or 1.27 m^3/s) and pumping (0.88 m^3/s). The baseflow accumulation between the Baxter and Edenvale stations is 5.11 m^3/s. The contribution from the Oro Moraine system is taken to be 34 % of this value, or 1.76 m^3/s. Runoff therefore must account for 4.24 m^3/s. These last two values are used in the model calibration. The corresponding simulated values are the integrated contributions from all Dirichlet boundaries except Kempenfelt Bay (Figure 8.1).

Calibration objectives for the Willow Creek are easier to determine as no as-

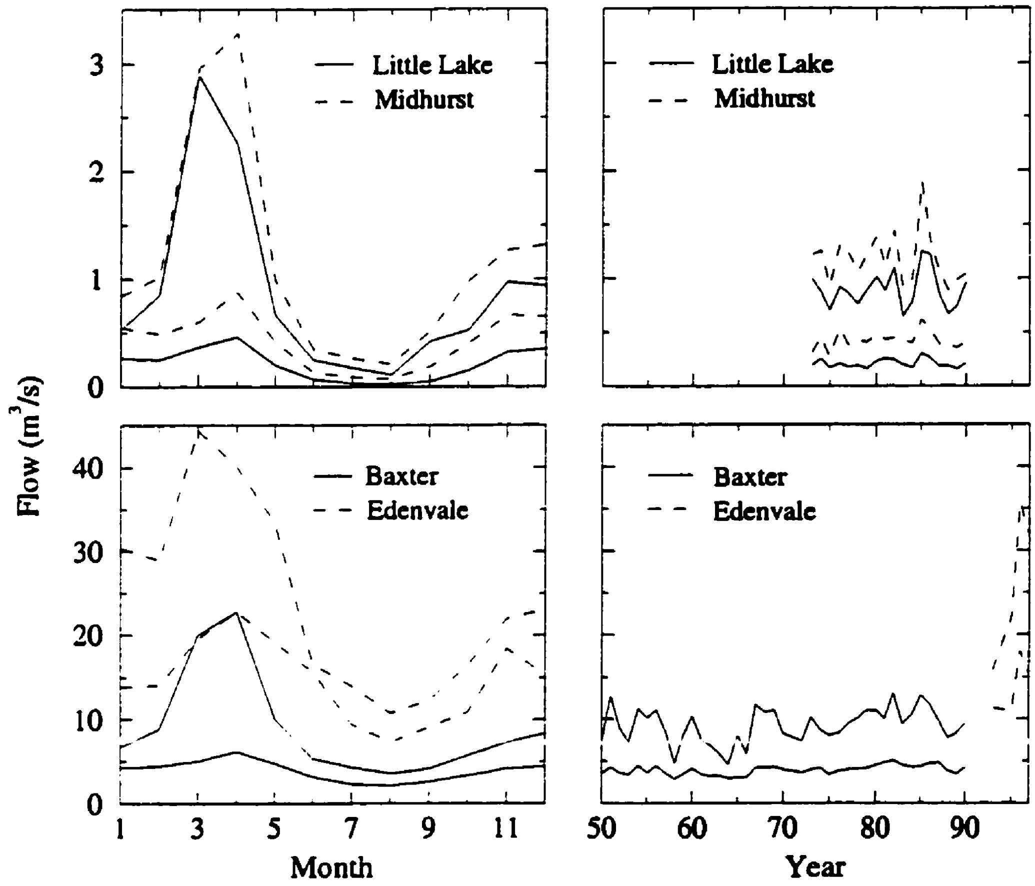

Figure 8.11: Seasonal and long term variations in total flow and baseflow for the Willow Creek (top panels) and Nottawasaga River (bottom panels) stations.

Station	record used	total flow	baseflow	runoff
Baxter (2ED003)	1947 – 1990	8.87	2.60	6.27
Edenvale (2ED027)	1993 – 1997	26.3	7.71	18.6
Little Lake (2ED009)	1973 – 1990	0.89	0.08	0.81
Midhurst (2ED010)	1973 – 1990	1.18	0.11	1.07

Table 8.4: Flow rates (m^3/s) for the 4 stations used in this study.

sumptions have to be made regarding contributions from outside the study area. The baseflow (0.08 m^3/s) and runoff (0.81 m^3/s) components for the Little Lake station are used as constraints for the headwaters of the Willow Creek. Differential values between the Little Lake and the Midhurst stations are calibration objectives for this segment of the creek. These values are 0.03 m^3/s for baseflow and 0.26 m^3/s for runoff. Baseflow in the upper reaches of the Willow Creek accounts for roughly 10 % of the total streamflow, whereas this value is about 29 % for the Nottawasaga River.

8.5.3 Calibration Weights

Calibration weights need to be assigned to the data to account for measurement error and to eliminate dimensional differences [e.g., *Hill*, 1998]. The standard deviation for the point head data is estimated to be about 5 m, taking into account the difficulties encountered in determining the elevation of the top of the boreholes (Section 7.3.1) and the smaller error made in measuring the water levels. Seasonal water level fluctuations are also potentially important. The water level data are given a weight $1/\sigma^2 = 0.04$. The procedure outlined in Chapter (5) is followed for assigning weights to the kriged heads. The error associated with the discharge measurements is taken to be 20 % and weights are determined accordingly.

8.6 Model Calibration

The numerical model must be consistent with the water level and streamflow data. This is achieved in the model calibration. The boundary conditions and groundwater abstraction rates discussed in the previous sections are considered known. The only adjustable parameters therefore are the subsurface and recharge spreading layer conductivities.

Initially, the hydraulic conductivity distribution is derived solely from the lithologic descriptions contained in the MOEE well records. Only those boreholes are used that were selected for the hydrostratigraphic interpretation. A single conductivity value is assigned to each of the 14 overburden lithofacies listed in Table (7.1). Conductivity values are then stored in the database of the hydrostratigraphic unit that the corresponding borehole lithology is grouped into (Figure 2.1). Making use of kriging, the point values of log conductivity are interpolated in a 3D fashion to the centroids of those finite elements that are part of this hydrostratigraphic unit.

8.6.1 Kriging Procedure

Because lithologic descriptions are used for determining conductivity values, the estimation of the semivariogram parameters that are needed for the kriging procedure is a matter of concern. The sparse borehole coverage is yet another problem. It was found that no reliable experimental horizontal semivariograms can be calculated. Vertical semivariograms are better constrained because the correlation along the axis of the boreholes incorporates a large number of data points. Vertical semivariograms are used to estimate the correlation length in this direction as well as the data sill and the nugget, if present. The horizontal correlation length for each conductivity field is assumed to be the average value of the range for the two aquifer/aquitard contacts delineating the corresponding hydrostratigraphic unit. The rationale for this assumption is that the depositional processes that resulted in the geometry of the aquifer/aquitard contacts are also responsible for the intraformational heterogeneity.

The point conductivities are interpolated with principal directions that are given by the average dip of the hydrostratigraphic units (Section 7.7). The point values are grouped into octants around the interpolation point to ensure an even azimuthal distribution. Four control points are used per octant.

Figure (8.12) illustrates the relationship between the hydrostratigraphic interpretation, the lithologic descriptions and the resulting conductivity distribution. The zonation provided by the aquifer/aquitard contacts ensures that each hydrostratigraphic unit has a distinct mean conductivity and that the sharp conductivity

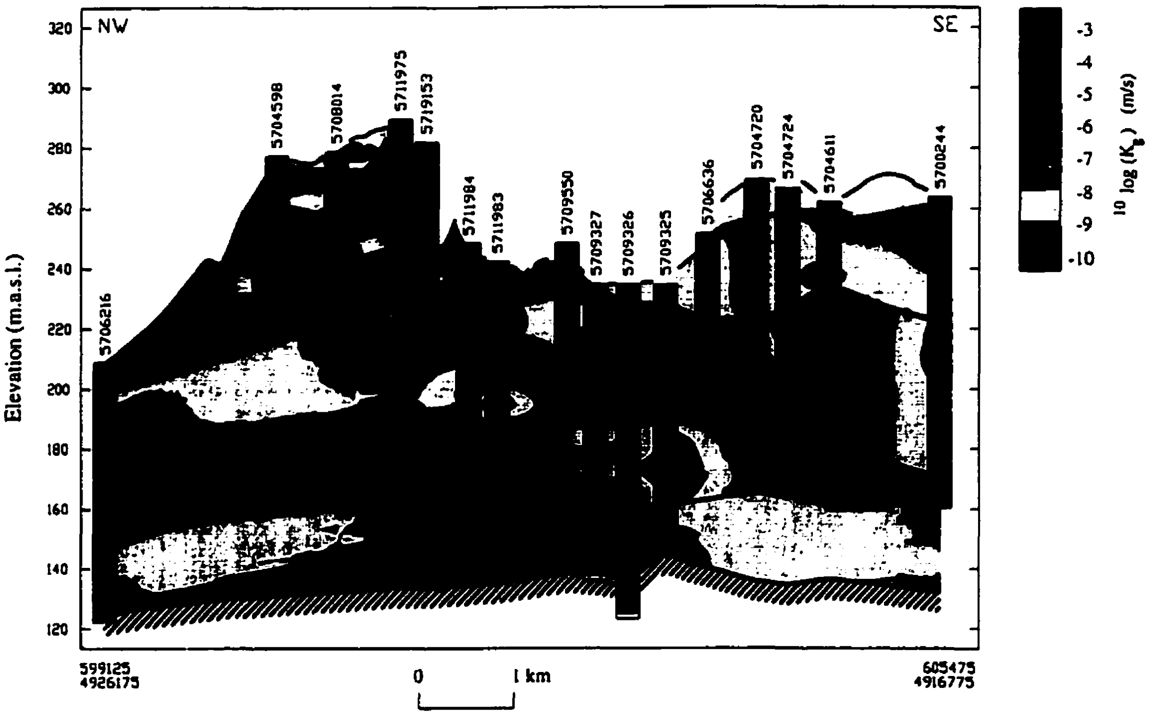

Figure 8.12: Role of borehole descriptions and hydrostratigraphic interpretation in kriging of log conductivity. Cross-section 33 and distribution Initial (I) were used (Table 8.5).

contrasts that may exist between aquifers and aquitards are accurately represented. Conductivity values vary smoothly within each hydrostratigraphic unit.

Figure (8.12) was constructed by interpolating to densely spaced points on the cross-section. In reality this interpolation is performed to the finite elements which have a finite dimension. To obtain a representative value for these REVs, the kriging is often done to several points in each finite element. An average conductivity value is then determined through a Gauss quadrature scheme. Here, it will be assumed that the mesh discretization is fine enough for kriging to the element centroid to provide an accurate K value. This assumption considerably limits the computational burden of kriging. This is important in the context of the pilot point calibration in which kriging is applied many times. Figure (8.13) illustrates the effect of the mesh discretization on the conductivity distribution. Although compared to Figure (8.12) some of the spatial variability is lost, dominant features are still reasonably reproduced. The material number assigned to each element is used to account for areas where hydrostratigraphic units pinch out. In this case the elements used for AQTD1 and AQFR1 in the uplands are grouped into AQTD2 in the Willow Creek valley. Together with the 3D nature of the spatial interpolation this results in a more realistic conductivity distribution than obtained with the 2D interpolation by finite element layer used by *Martin* [1994].

The spatial variability in conductivity below the discretization scale further results in anisotropic effective properties for each of the finite elements. These effective conductivities $K_{xx} = K_{yy}$ and K_{zz} are calculated using the procedure outlined in Section (2.2.2). The small-scale variability is determined from the vertical semivariogram as that value that corresponds to the average thickness of the finite element. Anisotropy thus depends on the vertical discretization scale. Note that *Gelhar and Axness* [1983] used the natural log in equations (2.9) whereas the more convenient 10 log scale is used here.

8.6.2 Initial Conductivity Distribution

A single geologic material may be characterized by a conductivity range that varies over several orders of magnitude. Typical values for the 14 lithofacies are given in Table (8.5). Different combinations of the K values assigned to the individual lithofacies will lead to different conductivity distributions in the subsurface. The geostatistical parameters used in the kriging are altered as well. As these parameters control the spatial interpolation, model calibration and uncertainty are also affected. For a proper convergence of an inverse problem the initial parameters should be reasonably close to their actual values. The dependence of the hydraulic conductivity distribution on the K values assigned to the lithofacies therefore is a crucial aspect of this study. Clearly, this dependence is also a weak point. This weakness is a direct result of the available information. The K values for the individual lithofacies should be optimized for the Oro Moraine problem, using constraints from the calibration data and other available information. A combined kriging/sensitivity analysis was used for this purpose.

The initial set of conductivities (I) given in Table (8.5) is loosely based on the final calibrated values determined for the Waterloo Moraine model [*Martin and Frind*, 1998]. The resulting conductivity distribution is characterized by average K_g values for the aquitards on the order of $10^{-9} - 10^{-8}$ m/s (Figure 8.12). The

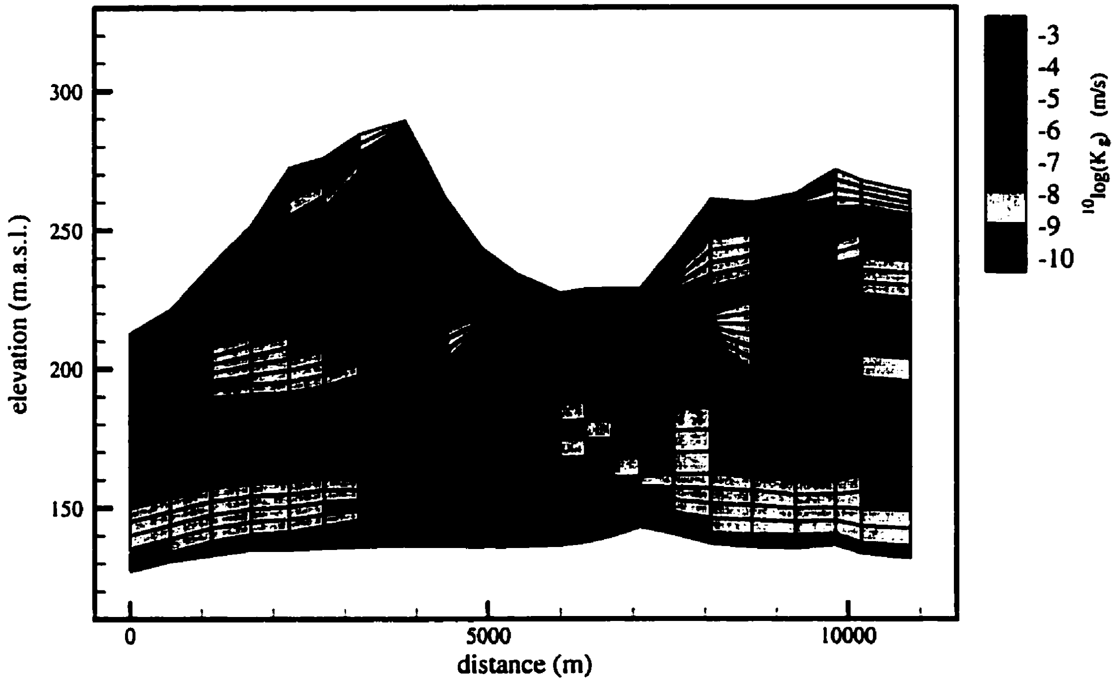

Figure 8.13: Effect of mesh discretization on spatial interpolation of log conductivity.

Material	Literature	Field Measurements	(I)	(II)
Clay	$10^{-12} - 10^{-9}$	$3 \cdot 10^{-11} - 2 \cdot 10^{-9}$	$3 \cdot 10^{-11}$	$9 \cdot 10^{-10}$
Silty Clay	$10^{-11} - 10^{-9}$	-	$3 \cdot 10^{-10}$	$3 \cdot 10^{-9}$
Sandy Clay	$10^{-10} - 10^{-7}$	-	$3 \cdot 10^{-9}$	$1 \cdot 10^{-8}$
Gravelly Clay	$10^{-9} - 10^{-7}$	$1 \cdot 10^{-10} - 1 \cdot 10^{-7}$	$3 \cdot 10^{-8}$	$8 \cdot 10^{-8}$
Clayey Silt	$10^{-9} - 10^{-7}$	$2 \cdot 10^{-8} - 3 \cdot 10^{-7}$	$1 \cdot 10^{-8}$	$2 \cdot 10^{-8}$
Silt	$10^{-9} - 10^{-5}$	$1 \cdot 10^{-10} - 1 \cdot 10^{-6}$	$1 \cdot 10^{-7}$	$5 \cdot 10^{-8}$
Sandy Silt	$10^{-8} - 10^{-6}$	$2 \cdot 10^{-9} - 4 \cdot 10^{-7}$	$1 \cdot 10^{-6}$	$1 \cdot 10^{-7}$
Gravely Silt	$10^{-7} - 10^{-5}$	$1 \cdot 10^{-7} - 1 \cdot 10^{-6}$	$3 \cdot 10^{-6}$	$1 \cdot 10^{-6}$
Clayey Sand	$10^{-7} - 10^{-5}$	-	$3 \cdot 10^{-6}$	$4 \cdot 10^{-6}$
Silty Sand	$10^{-6} - 10^{-4}$	$1 \cdot 10^{-6} - 1 \cdot 10^{-6}$	$3 \cdot 10^{-6}$	$1 \cdot 10^{-5}$
Fine Sand	$10^{-6} - 10^{-4}$	$3 \cdot 10^{-6} - 2 \cdot 10^{-4}$	$1 \cdot 10^{-5}$	$6 \cdot 10^{-5}$
Medium Sand	$10^{-6} - 10^{-2}$	$4 \cdot 10^{-6} - 4 \cdot 10^{-4}$	$1 \cdot 10^{-4}$	$2 \cdot 10^{-4}$
Coarse Sand	$10^{-4} - 10^{0}$	$4 \cdot 10^{-4} - 2 \cdot 10^{-3}$	$1 \cdot 10^{-3}$	$7 \cdot 10^{-4}$
Gravel	$10^{-4} - 10^{0}$	$4 \cdot 10^{-4} - 2 \cdot 10^{-3}$	$1 \cdot 10^{-2}$	$2 \cdot 10^{-3}$

Table 8.5: Hydraulic conductivities (m/s) for lithologic categories. Literature values are from *Freeze and Cherry*, [1979]. Field data are from pumping and slug tests in the Waterloo Moraine as listed in *Martin and Frind*, [1998]. The two K distributions (I) and (II) are discussed in the text.

vertical movement of water across these confining units is inhibited, and water levels in the lower 2 aquifers, where the pumping wells are screened, are underestimated resulting in a value for the kriged head calibration measure J_h of $0.34 \cdot 10^6$. The flow data are also poorly matched: $J_f = 0.80 \cdot 10^4$.

The K values assigned to the lithofacies can be optimized in a semi-automated fashion, making use of the sensitivity of the calibration data to the elemental conductivities and the kriging weights that are used in determining these conductivities. Using the chain rule, the sensitivity of the lumped calibration measure $J = J_h + J_f$ to the log conductivity value Y^l for lithology l is given by:

$$\frac{dJ}{dY^l} = \sum_{i=1}^{NE} \frac{dJ}{dY_i} \frac{dY_i}{dY^l} \tag{8.1}$$

where NE is the number of elements and where the conductivity Y_i is determined by a weighted sum of the NL borehole conductivities Y_j^l used in the kriging procedure:

$$Y_i = \sum_{j=1}^{NL} w_j Y_j^l \tag{8.2}$$

Combining these two equations leads to:

$$\frac{dJ}{dY^l} = \sum_{i=1}^{NE} \frac{dJ}{dY_i} \left(\sum_{j \in Y^l} w_j \right) \tag{8.3}$$

where the second sum is taken only over those control points that correspond to lithology l. The derivatives with respect to the elemental conductivities are calculated using the adjoint method where the sensitivity with respect to Y_{xx} and Y_{zz} is lumped. Anisotropy is determined by the upscaling equations and is independent of the kriging. The dependence of the horizontal and vertical conductivities on the Y^l values is therefore identical.

The Y^l values are adjusted based on the sensitivity coefficients. New semivariogram parameters are determined and kriging is re-applied using these parameters. The flow equation is solved for the new conductivity distribution, calibration statistics are determined and the sensitivities are re-calculated. This iterative procedure is repeated until no further adjustments to the Y^l values can be made without violating constraints from literature values and the order that should exist between conductivity values for the different geologic materials.

The final K values are given as distribution (II) in Table (8.5). Figures (8.14) and (8.15) give the corresponding vertical semivariograms for each of the 8 hydrostratigraphic units. Table (8.6) lists the parameters of the exponential model semivariograms. For some hydrostratigraphic units these parameters are subject to considerable uncertainty as a result of the poorly defined semivariograms.

A noticeable feature of distribution (II) in comparison with the values given by *Martin and Frind* [1998] is the smaller range of conductivities. This results in a reduced K contrast between the aquifers and aquitards, less intra-formational heterogeneity and thus also reduced kriging uncertainty. The values for the sill of the model semivariograms are fairly consistent with the 0.7-1.5 range listed by

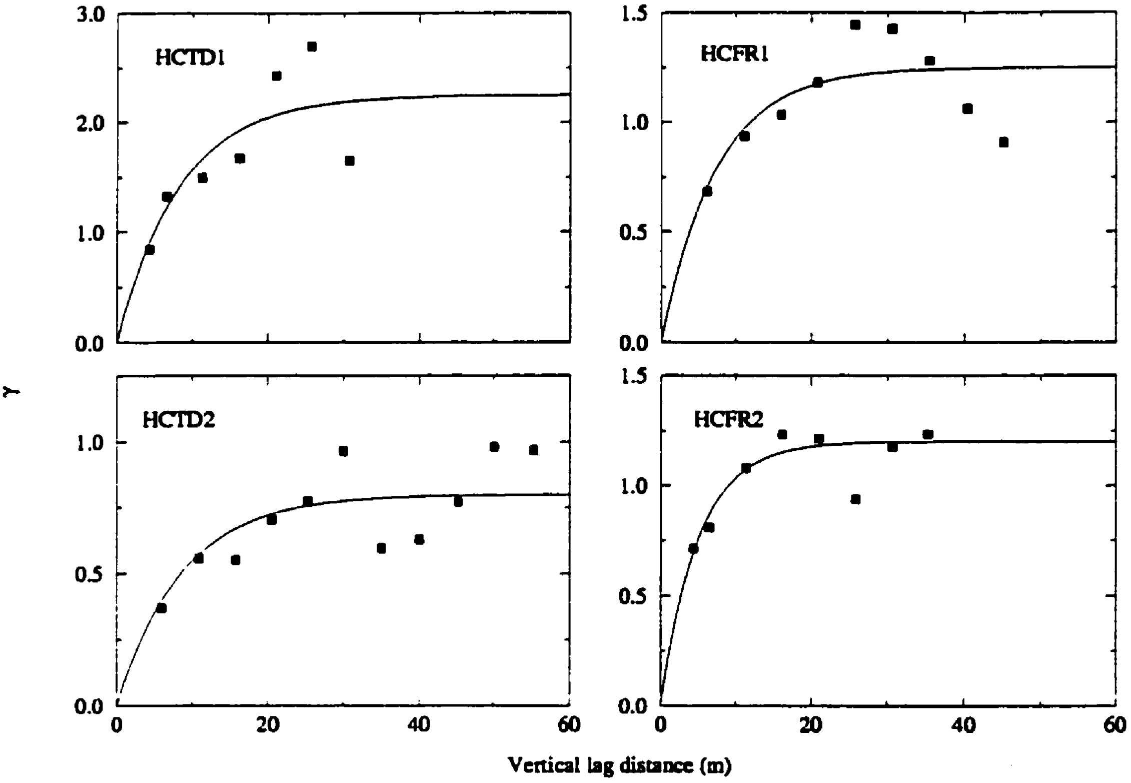

Figure 8.14: Experimental and model semivariograms for AQTD1-AQFR2 and distribution initial (II).

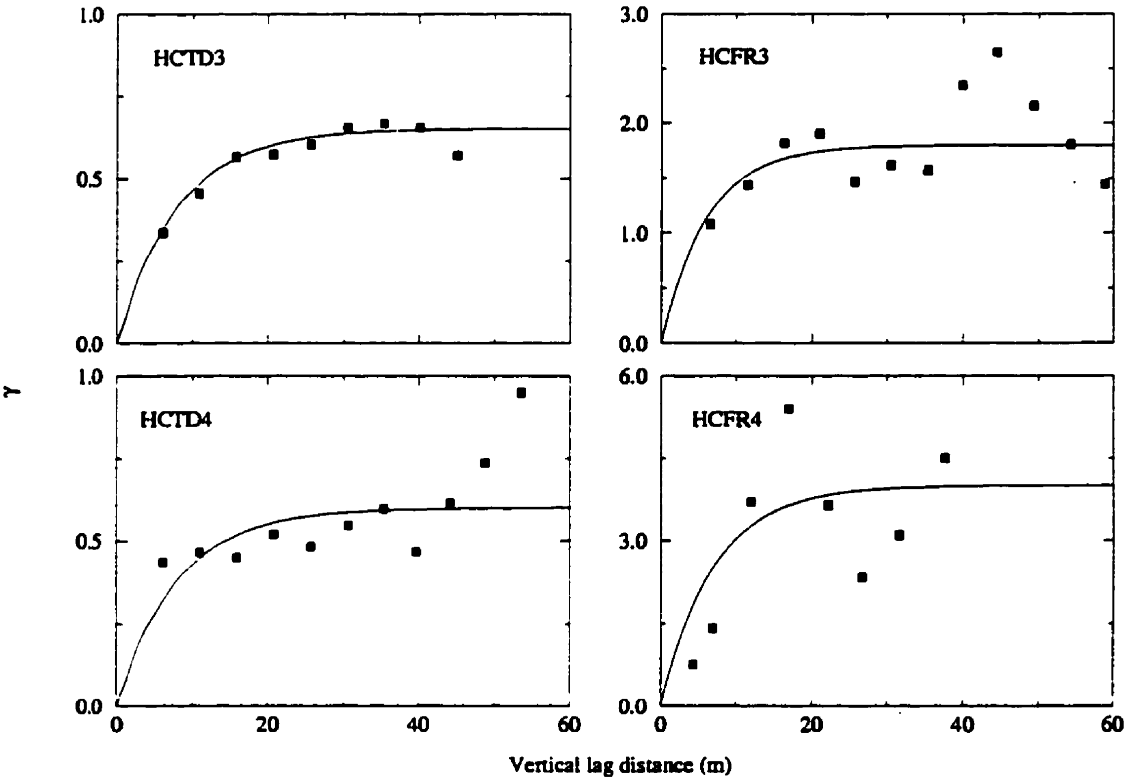

Figure 8.15: Experimental and model semivariograms for AQTD3-AQFR4 and distribution initial (II).

	range (m)		sill	anisotropy
	horizontal	vertical		
AQTD1	4500	25	2.25	$1.1 \cdot 10^1 - 5.4 \cdot 10^3$
AQFR1	3300	22	1.25	$7.1 \cdot 10^0 - 3.1 \cdot 10^2$
AQTD2	2838	26	0.80	$5.0 \cdot 10^0 - 5.1 \cdot 10^1$
AQFR2	4563	15	1.20	$9.3 \cdot 10^0 - 4.0 \cdot 10^2$
AQTD3	4900	24	0.65	$5.0 \cdot 10^0 - 3.4 \cdot 10^1$
AQFR3	3500	18	2.80	$2.5 \cdot 10^1 - 3.7 \cdot 10^4$
AQTD4	2863	24	0.60	$4.6 \cdot 10^0 - 2.8 \cdot 10^1$
AQFR4	2938	21	4.00	$4.1 \cdot 10^1 - 8.7 \cdot 10^4$
Alliston	3100	52	4.50	$1.1 \cdot 10^1 - 2.1 \cdot 10^5$

Table 8.6: Model semivariogram parameters and anisotropy for the distribution Initial (II). The Alliston aquifer complex is comprised of AQFR3, AQTD4 and AQFR4

Hoeksema and Kitanidis [1985a] for several glacial aquifer systems in North America (values are converted from the natural log scale used by the authors). The K values are also in reasonable agreement with direct conductivity measurements made in various glacial materials of the Waterloo Moraine (Table 8.5).

Distribution (II) results in increased water levels in the lower aquifers. The improved calibration measures are $J_h = 0.19 \cdot 10^6$ (-44 %) and $J_f = 0.67 \cdot 10^4$ (-16 %). This distribution is used as a start for the automated calibration. It results in an anisotropic conductivity distribution with K_{xx}/K_{zz} values varying between 5 and $8.7 \cdot 10^4$. A value of 3 was assumed to for the micro-scale anisotropy.

8.6.3 Parameters for the Recharge Boundary

As mentioned earlier, only hydraulic conductivity is considered as an adjustable parameter in the calibration. However, at the recharge boundary a number of other parameters may crucially affect the model response. The effect of variations in these parameters was determined to validate the calibration approach.

Variations in the RSL conductivity, the water surplus R and the residual saturation S_r affect the calibration measures J_h and J_f (Figure 8.16). Variations in these

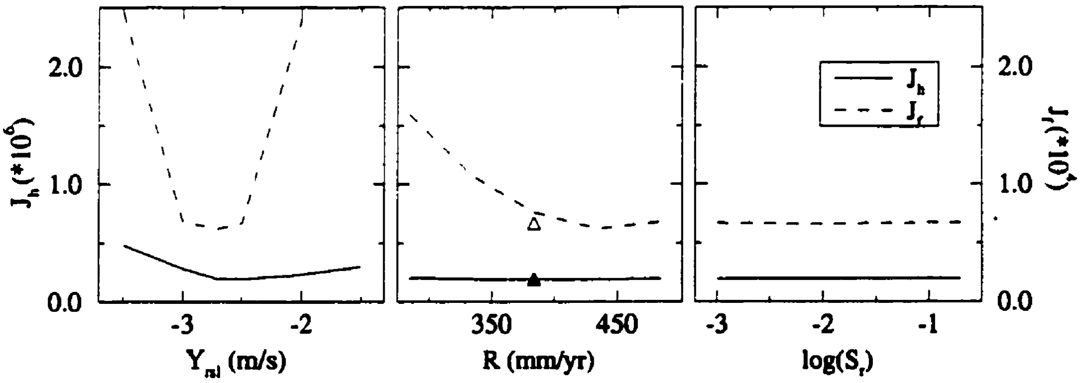

Figure 8.16: Sensitivity of head and flow calibration measures to RSL conductivity, uniform water surplus R (lines in middle panel), and residual saturation S_r. Base case parameters are $K_{RSL} = 10^{-2.7}m/s$, the variable water surplus (Figure 8.4) indicated by the triangles in the middle panel, and $S_r = 0.1$.

parameters cause only minor changes in the head calibration measure, the RSL conductivity having the largest effect. Variations in the flow calibration measure are more pronounced with an optimum value near $K_{RSL} = 10^{-2.7}m/s$. Large variations in water surplus are needed to cause similar changes in J_f. The best uniform water surplus (435 mm/yr) gives a fit to the streamflow data that is comparable to the spatially variable water surplus determined in Section (8.3). Variations in S_r do not result in any significant changes in either calibration measure. This parameter was therefore kept fixed at a relatively high value of 0.1, facilitating the convergence of the flow solution.

8.6.4 Optimization of Average Conductivities

The calibration code presented in Chapter (5) was run in PARAM=1 mode to optimize the average conductivities of each of the hydrostratigraphic units. In all except one example, horizontal and vertical conductivities are adjusted simultaneously (KZADD=1). Unless mentioned otherwise, the minimization algorithm solely uses the kriged head data (DATASET=1). However, a sign check is enforced to eliminate entries in the search vector that are not expected to simultaneously reduce the flow calibration measure (COMBINE=2).

Zonation Alternatives

Table (8.7) compares the final calibration measures for 4 different zonation options. The corresponding conductivity values (Table 8.8) are averages before upscaling (i.e. the large-scale conductivity K_g in equation 2.8). Calibration results are also compared based on the difference between the initial and final calibrated conductivities as expressed by:

$$J_Y = \frac{\sum_{i=1}^{NZ}[\hat{Y}_i - Y_i^*]^2}{NZ} \tag{8.4}$$

where NZ is the number of zones, and where $\hat{Y}$ and Y^* are the estimated and initial log conductivities respectively.

Zonation	J_h	J_f	Characteristics
1	$0.12 \cdot 10^6$	$0.59 \cdot 10^2$	Zonation from conceptual model
2	$0.11 \cdot 10^6$	$0.11 \cdot 10^3$	AQFR1 split into 3 separate zones
3	$0.56 \cdot 10^5$	$0.30 \cdot 10^2$	As 2 but lower 3 units grouped as Alliston
4	$0.42 \cdot 10^5$	$0.88 \cdot 10^1$	As 3 but alternate zonation for RSL

Table 8.7: Head and flow calibration measures for several zonation scenarios considered in the text.

Zonation 1 consists of the 8 hydrostratigraphic units that comprise the conceptual model of the aquifer system. As figure (8.16) suggests that the RSL conductivity is quite important in the calibration, this layer was given a zonation based on the outcrop of the 5 upper hydrostratigraphic units as shown in Figure (7.24). The total number of zones (unknowns) therefore is 13. The discussion given below will focus on the subsurface conductivities, as these can be offset against other (hydro)geologic evidence.

For zonation 1, a higher conductivity value is found for AQTD2 than for AQFR2 which is unrealistic (Table 8.8). Simulated heads were found to be sensitive to the horizontal conductivity of the uppermost aquifer. This parameter controls the ease with which water can flow out of the flanks of the uplands and thus the amount of water that enters the deeper aquifer system. More freedom in the calibration was achieved by allowing separate parameters for each of the uplands that make of AQFR1 (zonation 2, with 2+2 additional parameters as the RSL is also assigned more zones). This approach leads to more realistic conductivity values and a match to the head data that is almost identical to that obtained with zonation 1. The poorer fit to the flow data results from the low conductivity value assigned to AQTD1.

Both zonation 1 and 2 result in a poor fit to measured heads in the bottom aquifer near Barrie where most of the pumping activity takes place. The continuity and low conductivity of the bottom two aquitards inhibits groundwater flow to this aquifer. The geometry of AQTD3 is constrained by a fair number of observations but few boreholes penetrate below aquifer 3 (Table 7.2; Figures 7.10-7.13). The actual continuity of AQTD4 therefore is quite uncertain. Previous investigations have often identified the lower two aquifers as a single unit known as the Alliston aquifer complex [e.g., *MOE*, 1977]. Based on this knowledge, a third zonation was considered by lumping these aquifers and the intermediate confining layer into a single zone. This leads to a two-aquifer system separated by discrete pockets of aquitard, representative of a discontinues till layer. The geostatistical parameters for the resulting conductivity field are given in Table (8.6). Although the total number of adjustable parameters is now reduced to 15, it can be seen that the match to the calibration data is significantly improved. Furthermore, this is achieved with relatively modest conductivity perturbations.

An important objective of the calibration is to constrain the steady-state water mass balance for both the surface and subsurface flow systems. An alternative zonation for the RSL was therefore considered based on a surface water modelling study done as part of the Ontario/Canada flood damage reduction plan (zonation 4, Figure 8.4). This zonation results in the best match to both head and flow data. However, the corresponding conductivity perturbations are large. Furthermore, except for baseflow to the Willow Creek headwaters, zonation 3 generally provides a slightly better match to the flow measurements. This zonation is therefore preferred.

The estimated K values strongly depend on the chosen zonation. Values for the confining units vary most. It can be seen that the three zonation options that

	Initial (II)	Zonation 1	Zonation 2	Zonation 3	Zonation 4
AQTD1	−7.50	−4.52	−7.22	−4.99	−4.52
AQFR1	−4.08	−4.82			
Oro Moraine	−4.15		−3.42	−3.72	−4.39
Snow Valley	−4.12		−4.99	−5.21	−5.31
Innisfill	−3.96		−3.93	−4.75	−4.59
AQTD2	−7.89	−4.84	−5.66	−7.34	−7.61
AQFR2	−4.34	−6.24	−4.59	−4.17	−4.68
AQTD3	−8.17	−7.86	−7.51	−6.51	−5.25
AQFR3	−4.45	−4.44	−4.91		
AQTD4	−7.92	−7.18	−7.70		
AQFR4	−4.26	−4.11	−5.82		
Alliston	−5.88			−6.46	−6.69
J_Y		2.88	0.95	1.45	2.52

Table 8.8: Initial and calibrated average log hydraulic conductivity values (m/s) for the 4 zonation scenarios.

provide the best fit to the flow measurements all resolve a high conductivity for the uppermost aquitard. As a result, infiltration will be (nearly) equivalent to the water surplus. This agrees with observations made in previous groundwater investigations in the upper reaches of the Oro Moraine. It was, for example, noted that even during spring melt, surface runoff was minimal and infiltration was quick [*Dixon Hydrogeology*, 1992]. High infiltration rates are possibly found in all areas covered by the uppermost aquitard (Figure 8.4). *Gerber* [1994] made similar observations in an analysis of groundwater recharge to the central portion of the Oak Ridges Moraine, north of Toronto. He states that "many aquifers may be receiving substantial recharge through areas previously considered relatively impermeable, such as glacial diamict."

The relatively low conductivity of AQTD2 is consistent with the notion that this confining unit is comprised of relatively compact Lake Algonquin lacustrine clays in the valley areas (Section 7.7). In these locations, recharge to the groundwater system may be limited by the properties of this unit. However, in the Oro Moraine it was observed that outcrops of the clayey till that locally makes up AQTD2 are characterized by small fractures at spacings that increase downward from 1-2 cm to approximately 10 cm [*P. Barnett*, personal communication]. The conductivity of this unit may therefore be significantly higher in the uplands, providing a good hydraulic connection between the upper two aquifers. It is unknown how deep the fractures penetrate.

The relatively high K value determined for AQTD3 suggests that this till unit may be fractured as well. However, another possible explanation is that the continuity of this unit is over-estimated due to a lack of borehole information. The preferred zonation 3 further suggests that AQTD4 is much less continuous than inferred from the hydrostratigraphic interpretation.

The above discussion illustrates that the properties of the low conductivity units are important for the response of the multi-aquifer system. The adopted zonation (and therefore the hydrostratigraphic interpretation) crucially affects the estimated properties of these units and the calibration fit that is obtained. The zonation of the recharge spreading layer also is important. This layer should therefore be given more detailed consideration in future studies. The above discussion further illustrates that the calibration algorithm should be augmented with a penalty criterion based on equation (8.4), as used in the work of *Neuman* [1980]. Such a criterion will improve the plausibility of the solution of the inverse problem by limiting the difference between initial and final conductivity values.

Calibration Measures and Solution Strategy

The calibration results discussed so far were obtained using kriged heads in combination with flow measurements. Table (8.9) illustrates the effect of different (combinations of) objective functions on the model calibration for the preferred zonation 3.

Different calibration objectives lead to relatively small variations in the match to the kriged heads and point water levels but result in order of magnitude changes in J_f. When only point water levels are considered (objective 1), the discharge data are poorly simulated ($J_f = 0.22 \cdot 10^3$). This suggests that overall groundwater flow patterns are poorly predicted by the calibrated model. The kriged heads (objective 2) better constrain these flow patterns leading to a significantly improved fit to the discharge data ($J_f = 0.37 \cdot 10^2$), even though these measurements are not included in the calibration. The match to the observed flows is improved even further when

Calibration Objective	J_h		J_f
	Kriged	Point	
1. Point water levels	$0.46 \cdot 10^5$	$0.18 \cdot 10^4$	$0.22 \cdot 10^3$
2. Kriged heads	$0.39 \cdot 10^5$	$0.21 \cdot 10^4$	$0.37 \cdot 10^2$
3. Kriged heads and flow data	$0.56 \cdot 10^5$	$0.29 \cdot 10^4$	$0.30 \cdot 10^2$
4. Point water levels and flow data	$0.51 \cdot 10^5$	$0.25 \cdot 10^4$	$0.47 \cdot 10^1$

Table 8.9: Head and flow calibration measures discussed in the text.

these measurements are included in the calibration (objective 3): $J_f = 0.30 \cdot 10^2$. The kriged and point heads are not simulated as well for this case because of the additional constraints imposed on the calibration by the flow measurements. The flow data are best simulated ($J_f = 0.47 \cdot 10^1$), when combined with the point water levels (objective 4), although this difference is caused by a single measurement: baseflow to the Willow Creek headwaters.

Based on the above comparison one might argue that the point water level data should be used in the calibration as these are easiest to match and allow most freedom in simulating the observed flows. However, the few discharge measurements put limited constraints on the system. Although the observed streamflow accumulation for the Nottawasaga River provides information on the overall water mass balance, fluxes to individual tributary streams that contribute to this accumulation remain unknown. The calibration results obtained with the kriged heads alone (Table 8.9) suggest that this calibration measure may aid in simulating fluxes to those water courses for which no streamflow measurements are available. This is achieved by filling in the hydraulic head variations between the individual point water level measurements making use of the geostatistical properties derived from the data. The measurements alone put limited constraints on groundwater flow patterns. The kriged heads are therefore preferred over the point water level data.

The kriged heads also lead to smaller conductivity adjustments than obtained when using the point water level data (Table 8.10), increasing the plausibility of the solution. Furthermore, confidence bounds on the estimated parameters are significantly narrowed. The kriged heads therefore eliminate some of the uncertainty that exists as a result of the indirect nature of the conductivity information. The few discharge measurements have a negligible weight in the calculation of uncertainty.

Their main effect is to change the optimum parameter values and therefore also the flow solution and the sensitivity coefficients used in equation (5.20). This in turn results in altered confidence bounds for the parameter estimates.

Overall, the conductivity estimates are fairly stable with respect to the chosen calibration measure(s). Objective 3 combines relatively small conductivity adjustments with an acceptable fit to the observed flows. Baseflow to the Willow Creek headwaters has been found to be very sensitive to the local conductivity distribution. Improving this simulated baseflow will be addressed in the pilot point calibration.

	Objective 1	Objective 2	Objective 3	Objective 4
AQTD1	-5.49 ± 0.72	-5.37 ± 0.19	-4.99 ± 0.10	-4.68 ± 0.20
Oro Moraine	-3.96 ± 0.17	-3.62 ± 0.03	-3.72 ± 0.03	-3.90 ± 0.19
Snow Valley	-5.09 ± 0.18	-4.97 ± 0.03	-5.21 ± 0.04	-5.05 ± 0.22
Innisfill	-5.40 ± 0.16	-5.23 ± 0.04	-4.75 ± 0.04	-5.11 ± 0.16
AQTD2	-7.22 ± 0.09	-7.53 ± 0.03	-7.34 ± 0.03	-7.62 ± 0.12
AQFR2	-5.18 ± 0.30	-4.23 ± 0.09	-4.17 ± 0.03	-4.68 ± 0.10
AQTD3	-5.14 ± 0.15	-6.40 ± 0.04	-6.51 ± 0.03	-5.24 ± 0.14
Alliston	-6.37 ± 0.05	-6.62 ± 0.02	-6.46 ± 0.02	-6.64 ± 0.06
J_Y	2.21	1.37	1.45	2.42

Table 8.10: Calibrated average log hydraulic conductivity values (m/s), with associated uncertainty expressed as one standard deviation, for the 4 objective functions.

The results for the joint use of head and flow data given so far were obtained by enforcing a sign check on the entries of the search vector. As discussed in Chapter (5), this approach was introduced to allow the few flow measurements to have a stronger influence on the minimization algorithm than can be achieved by lumping the objective functions J_h and J_f. This is illustrated for the preferred zonation 3 (Figure 8.17). When using the cumulative objective function (COMBINE=1), the final value of J_h is quite similar to that obtained from using the kriged heads alone, indicating that these data dominate the inversion. The behaviour of J_f in this case is erratic and its final value of $0.45 \cdot 10^2$ is slightly higher than the match achieved when solely using the kriged heads (Table 8.9). The enforcement of the sign check (COMBINE=2) leads to conductivity updates that follow a path through the pa-

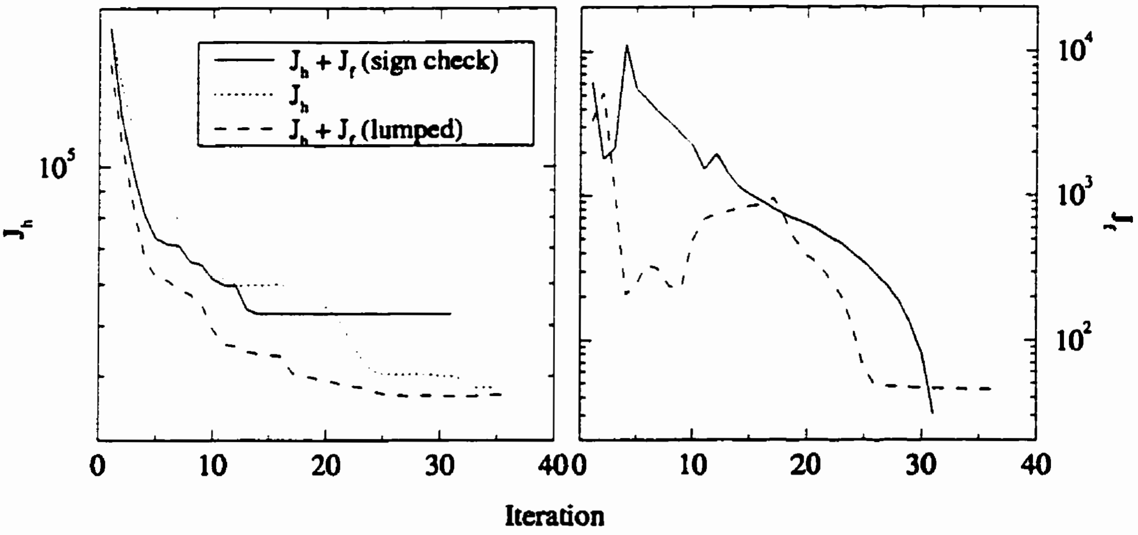

Figure 8.17: Convergence behaviour of the minimization algorithm.

rameter space that is more guided by the flow data (and thus the objective function surface for J_f), where the algorithm in this case is halted because no simultaneous improvement can be made in the match to the two datasets. This approach leads to a smoother convergence for J_f (except when large improvements in J_h can be made) and a final set of parameters that should be closer to the global minimum in the objective function surface for J_f than that of the lumped objective function. This solution strategy is preferred with regard to constraining the system water mass balance.

Recharge Spreading Layer Parameters

The RSL parameters that were determined for the preferred solution (zonation 3, objective 3 and COMBINE=2) are listed in Table (8.11). Lowest values are resolved for the four upland zones related to the AQTD1 and AQFR1. This results from the need to limit runoff from the steep slopes of these uplands to increase the potential for local infiltration. The low RSL K values associated with the three zones of AQFR1 also inhibit exit fluxes out of the flanks of the uplands. Highest conductivity values are found atop the low conductivity units in the valley areas, facilitating the runoff of excess water to the Dirichlet boundaries. This may be the signature of a lack of smaller tributary creeks in the numerical model.

AQTD1	-3.21 ± 0.05
Oro Moraine	-4.80 ± 0.97
Snow Valley	-3.55 ± 0.11
Innisfill	-3.81 ± 0.31
AQTD2	-1.92 ± 0.02
AQFR2	-2.41 ± 0.07
AQTD3	-1.84 ± 0.06

Table 8.11: Calibrated RSL log hydraulic conductivity values (m/s), with associated uncertainty expressed as one standard deviation for zonation 3, objective 2.

The full covariance matrix of the parameter estimates was calculated using equation (5.20). For the preferred solution, significant correlation was observed only between the conductivity for aquifer 2 and that for the corresponding RSL zone: r = -0.67.

Anisotropy and Intra-Formational Heterogeneity

The results presented so far were obtained by adjusting horizontal and vertical conductivities uniformly (KZADD=1). Anisotropy was determined from the geostatistical parameters of the conductivity fields and is therefore quite uncertain. To investigate whether anisotropy can be resolved more accurately using the calibration data, the inverse model was also run in KZADD=0 mode to optimize average Y_{xx} and Y_{zz} values independently. As in all previous runs, lower and upper bounds for log conductivity were set generously: -7 and -1 for the aquifers, and -12 and -4 for the aquitards. These bounds were never reached in any of the previous runs. However, in this case several parameters did attain physically non-realistic limit values and for some zones the vertical conductivity was found to be higher than the horizontal conductivity. This indicates that the data do not contain enough information to constrain all parameters independently. It is thus best to keep anisotropy fixed in the calibration.

Because lithologic descriptions are used to constrain the intra-formational heterogeneity, its reliability is a point of concern. Furthermore, the need to distribute hydraulic conductivity within the aquifers and aquitards may be questioned, arguing that it is the geometry and average properties of the hydrostratigraphic units that have the largest impact on the system behaviour. To address these concerns, the model was calibrated using uniform conductivities for the hydrostratigraphic units. As an initial guess, uniform Y_{xx} and Y_{zz} values were calculated from the kriged conductivity fields. These values were then optimized keeping anisotropy fixed (KZADD=1). The final calibration measures $J_h = 0.83 \cdot 10^5$ and $J_f = 0.62 \cdot 10^5$ indicate that compared to the preferred solution (objective 3 in Table 8.9), the groundwater system is poorly represented by the model. This illustrates (1) that heterogeneity within the aquifers and aquitards needs to be accounted for to accurately simulate the head and flow measurements and (2) that the conductivity distribution derived from the lithologic descriptions aids in better simulating the flow system.

8.6.5 Local Conductivity Optimization

After optimizing the average conductivity values some calibration data were still not adequately matched. Simulated hydraulic heads near the Barrie pumping wells are underestimated and baseflow to the Willow Creek headwaters is under-predicted. This baseflow bias corresponds to low hydraulic heads in the upper reaches of Oro Moraine. These issues are addressed in the second phase of the calibration (PARAM=2).

By trial-and-error it was determined that the best results are obtained when sequentially addressing the above calibration concerns. No means has been found to ensure that the match to head and flow data can be improved simultaneously in the pilot point option. The most important limitation in this respect results from ignoring the kriging effect in locating of the pilot points. Although a conductivity increase or decrease for the finite element corresponding to the pilot point may simultaneously improve the match to both head and flow data this does not necessarily hold true for the whole region that is affected by the addition of this pilot point.

In the first step, the match to the kriged heads is refined. During this phase, the flow measurements are completely ignored (DATASET=1, COMBINE=3). It was found that after the addition of 36 pilot points the head calibration objective could no longer be significantly improved. Baseflow to the Willow Creek headwaters was

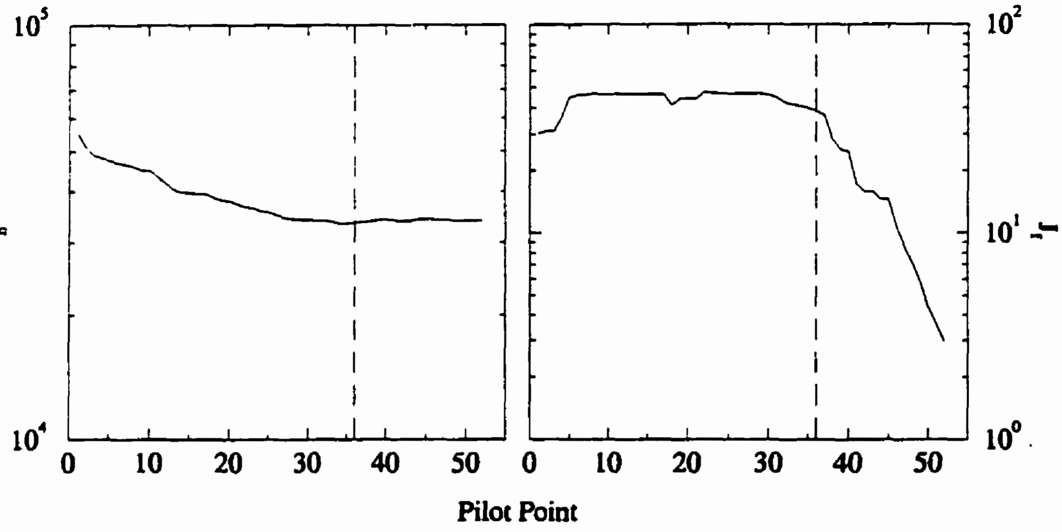

Figure 8.18: Convergence behaviour for the pilot point calibration (KRIGMODE=2). The dashed line separates the first and second phase of the calibration as discussed in the text.

the focus of the second phase of the pilot point calibration. It was found necessary to also include baseflow to the Willow Creek between Little Lake and Midhurst as a calibration objective to retain an acceptable fit to this measurement. Other streamflow data were ignored as the corresponding simulated values are only slightly affected by the addition of the new pilot points. A sign check with respect to the kriged head data was enforced in the placement of the pilot points (DATASET=2, COMBINE=2). After the addition of 15 pilot points a good fit was obtained to the two Willow Creek baseflow measurements.

Figure (8.18) shows the convergence behaviour of the calibration measures J_h and J_f for the preferred kriging option KRIGMODE=2. Although in the first phase the streamflow data are ignored, the modifications made to the conductivity fields only result in minor changes to the flow calibration measure. The match to the kriged heads is only slightly affected in the second phase of the calibration.

The performance of the different options for location the pilot points and treating the borehole derived conductivity values was compared. The option KRIGMODE=2 allows the greatest flexibility in locating the pilot points and ensures a maximum effect of these points on the conductivity distribution as neighboring lithologic descriptions are removed from the database. The final calibration measures for this option are $J_h = 0.34 \cdot 10^5$ and $J_f = 0.29 \cdot 10^1$. A total of 51 pilot points were included and the 136 lithologic descriptions that were located within one correlation length (i.e. semivariogram range) of these points were removed. A total of 6928 descriptions were used in the initial conductivity distribution. Thus overall modifications made to the conductivity fields are relatively minor. If all lithologic descriptions are honored without any constraints on the location of the pilot points (KRIGMODE=1) the final calibration statistics are $J_h = 0.35 \cdot 10^5$ and $J_f = 0.67 \cdot 10^1$ (again using 36+15 pilot points). Modifications made to the conductivity field in this case are even smaller. The kriging weight of those pilot points that are located near boreholes is limited. This kriging effect is ignored in locating the pilot point. The final head calibration measure is similar to that for the previous example. However, the flow calibration measure is significantly higher. This results from the sensitivity of baseflow to the Willow Creek headwaters to the local conductivity distribution. For KRIGMODE=3 possible pilot point locations are restricted to be one correlation length away from the lithologic descriptions. This approach leads to calibration measures $J_h = 0.36 \cdot 10^5$ and $J_f = 0.11 \cdot 10^2$. The KRIGMODE=2 results are therefore preferred.

8.6.6 Final Calibration Statistics

The final calibration results are plotted in a format slightly modified from ASTM standards [*ASTM*, 1997]. Average simulated heads for each aquifer, together with the corresponding calibration residuals (simulated minus observed heads), are shown in Figures (8.19)-(8.26). Scatterplots of observed versus simulated heads for the individual aquifers are given in Figure (8.27).

Water levels in Aquifer 1 are mostly under-predicted (Figure 8.20). The overall trend in the water level measurements for the other aquifers is well matched. The main calibration discrepancy corresponds to the highest water levels (Figure 8.27), which are found under the Oro Moraine upland. Water levels are locally under-predicted by about 20 m. This discrepancy was observed for each of the parameterization options and calibration objectives considered, suggesting a cause other than a deficiency in the conductivity distribution. Because this discrepancy persists down to aquifer 3 (Figure 8.24), perched water table conditions cannot provide an explanation. Furthermore, the potential for perched conditions was addressed in selecting the water level data (Section 8.5.1).

The persistent under-prediction of heads in the upper aquifer suggests a deficiency in the conceptual model of the aquifer system. Figure (7.24) shows a very pronounced outcrop for aquifer 1 in the Oro Moraine, extending considerably into the Matheson Creek valley. Local water levels will to a large degree be determined by the lowest elevation of the bottom of aquifer 1. Cross-sections 17, 18a and 26a show that the local interpretation of this contact is at best difficult to make (Appendix A, refer to Figure 7.3 for a location of the cross-sections). Quaternary geologic information supports this hypothesis as only localized outcrops of glacial outwash material are found on the eastern flank of the Matheson Creek valley [*Burwasser and Boyd*, 1974, refer to Section 7.7]. Future calibration efforts need to consider the effect of locally raising the interpreted elevation of BAQ1.

An inaccurate representation of the hydrostratigraphy may therefore very well be the cause of the calibration discrepancy observed in the Oro Moraine. If the western outcrop of Aquifer 1 is restricted to the higher reaches of this upland, water levels may increase by the amount needed. A secondary effect would be to limit outflow towards Matheson Creek, increasing groundwater discharge towards the Willow Creek headwaters which currently is under-predicted (Table 8.12). It was discussed earlier that the inferred northern-most extent of Aquitard 1 in the Oro Moraine does not agree with deposits shown on Quaternary geologic maps (Section 7.7). However, a removal of this cover will not likely resort in much effect as its conductivity is such that local infiltration is not inhibited.

Station	Baseflow		Runoff	(m^3/s)
	Observed	Simulated	Observed	Simulated
Nottawasaga River	1.890	2.216 (+17%)	4.610	5.203 (+13%)
Willow Cr. (LL-Midh.)	0.030	0.026 (−13%)	0.260	0.253 (− 3%)
Willow Cr. headwaters	0.080	0.060 (−25%)	0.810	0.723 (−11%)

Table 8.12: Calibration statistics for streamflow data.

Although attenuated, under-predicted water levels in the Oro Moraine and Snow Valley upland areas appear to persist down to Aquifer 2 (Figure 8.22). Over-predicted water levels in the northwest corner of the domain (AQFR3, Figure 8.24)

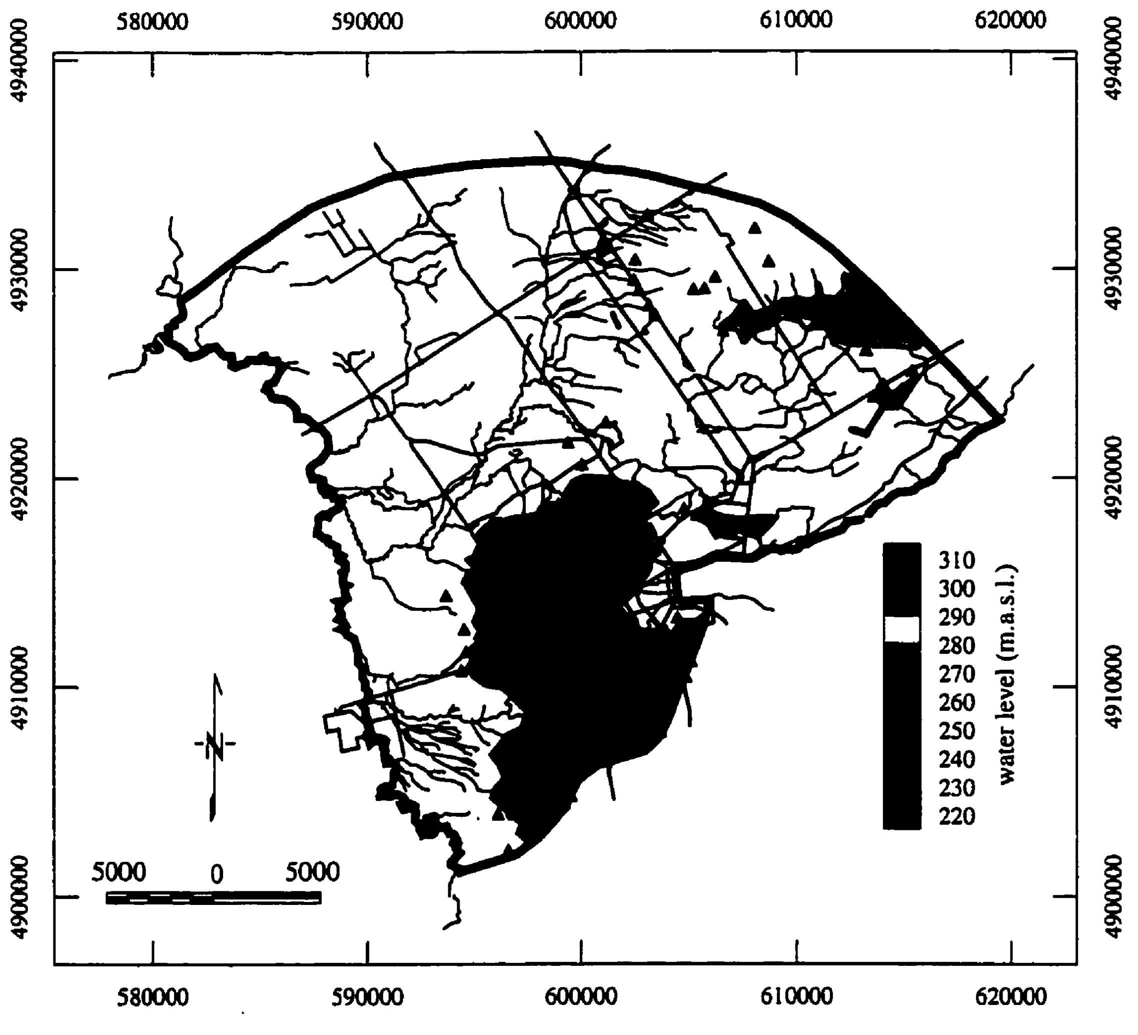
580000
590000
600000
610000
620000
4940000
4930000
4920000
4910000
4900000
5000
0
5000
N
310
300
290
280
270
260
250
240
230
220
water level (m.a.s.l.)

Figure 8.19: Vertically averaged simulated water levels for AQFR1. Triangles indicate data locations. White areas designate regions where the aquifer is predicted to be unsaturated over its whole thickness or where this unit pinches out.

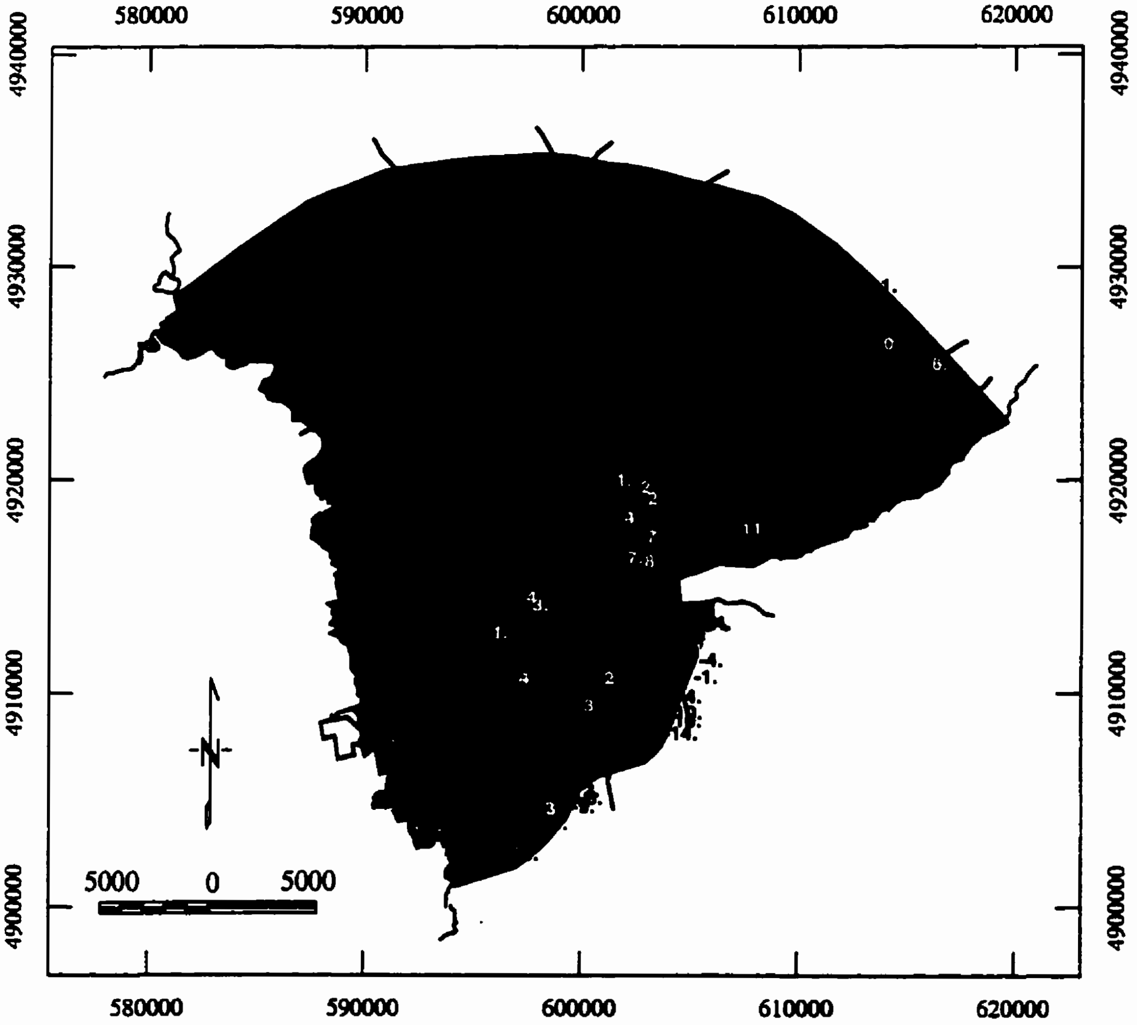
580000
590000
600000
610000
620000
4940000
4930000
4920000
4910000
4900000
N
5000
0
5000
1.
0
6.
1.
2
2
4
7
7.8
11
4
3.
1.
4
2
3
-4.
-1.
14.
3

Figure 8.20: Residuals for AQFR1. White values correspond to over-predicted heads, black values designate under-predicted heads.

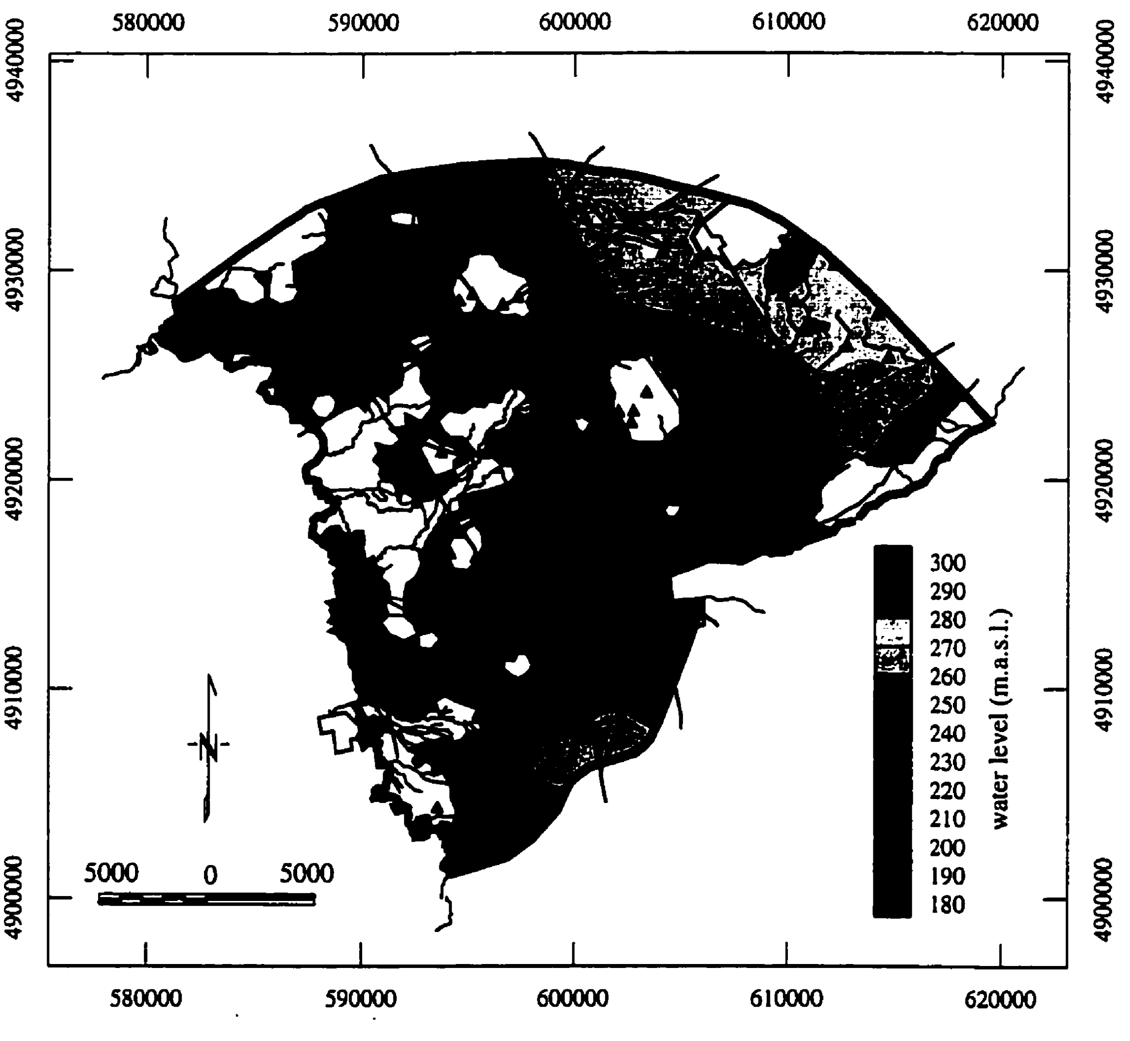
580000
590000
600000
610000
620000
4940000
4930000
4920000
4910000
4900000
N
5000 0 5000
300
290
280
270
260
250
240
230
220
210
200
190
180
water level (m.a.s.l.)

Figure 8.21: Vertically averaged simulated water levels for AQFR2. Triangles indicate data locations. White areas designate regions where the aquifer is predicted to be unsaturated over its whole thickness or where this unit pinches out.

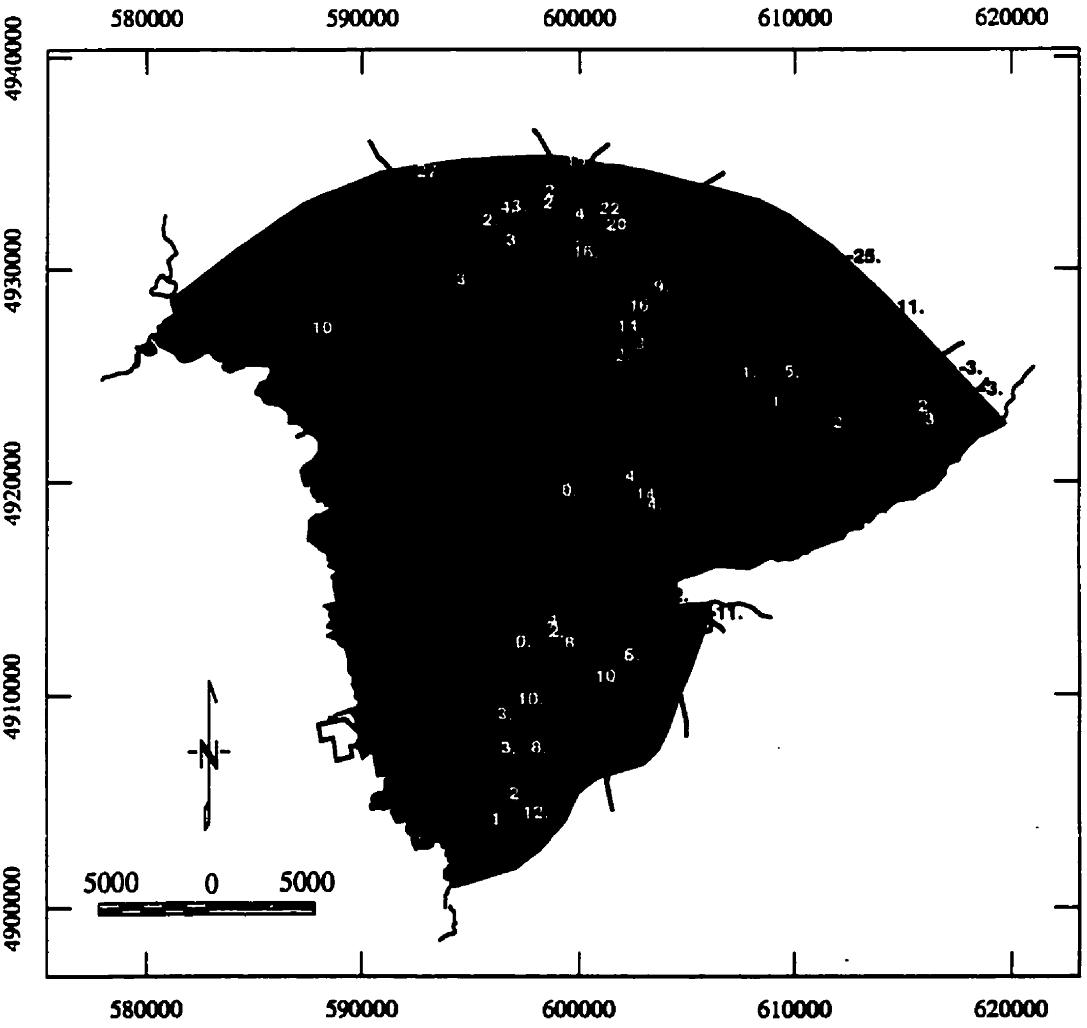
580000
590000
600000
610000
620000
4940000
4930000
4920000
4910000
4900000
-N-
5000
0
5000
-25.
11.
-3.
10

Figure 8.22: Residuals for AQFR2. White values correspond to over-predicted heads, black values designate under-predicted heads.

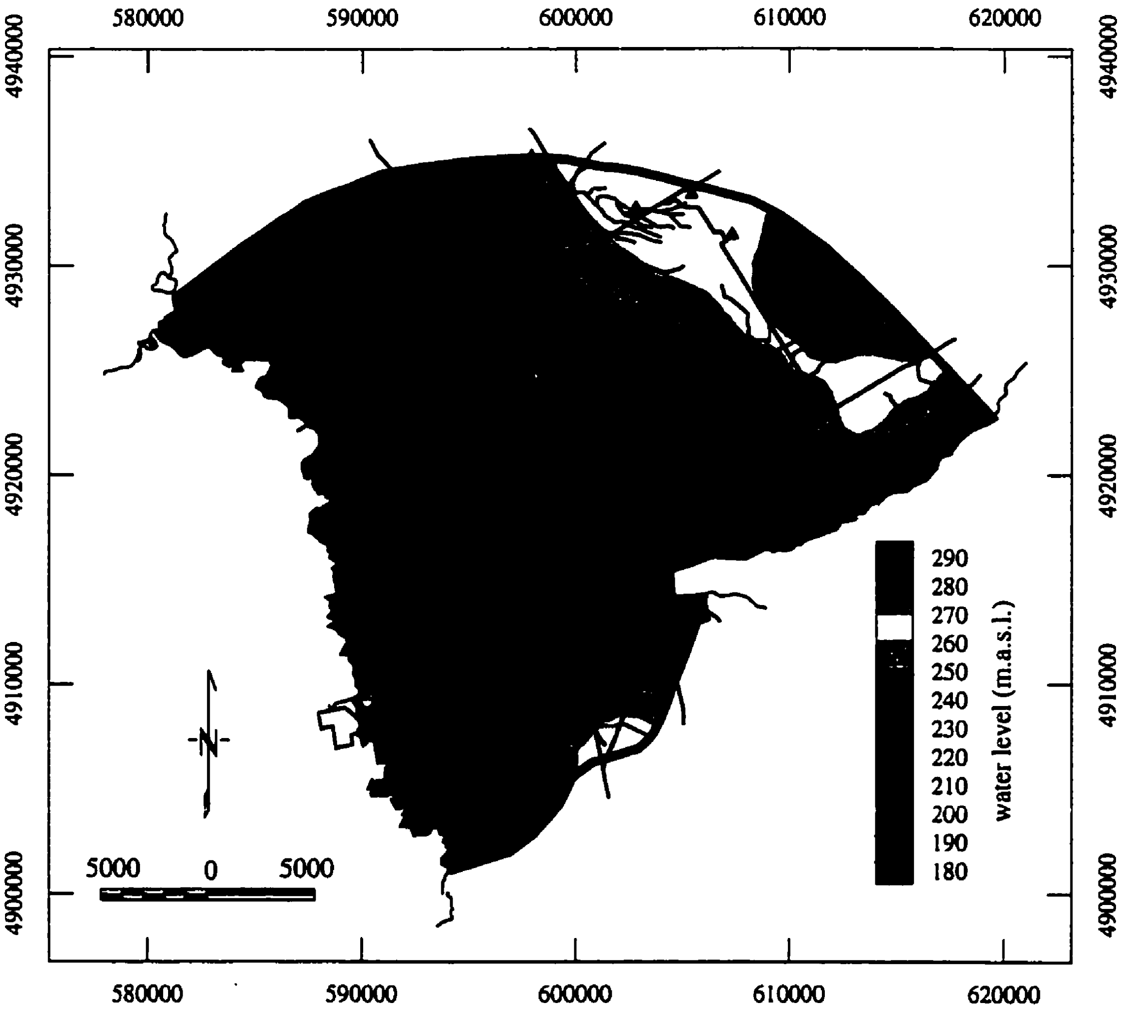
580000
590000
600000
610000
620000
4940000
4930000
4920000
4910000
4900000
5000
0
5000
N
290
280
270
260
250
240
230
220
210
200
190
180
water level (m.a.s.l.)

Figure 8.23: Vertically averaged simulated water levels for AQFR3. Triangles indicate data locations.

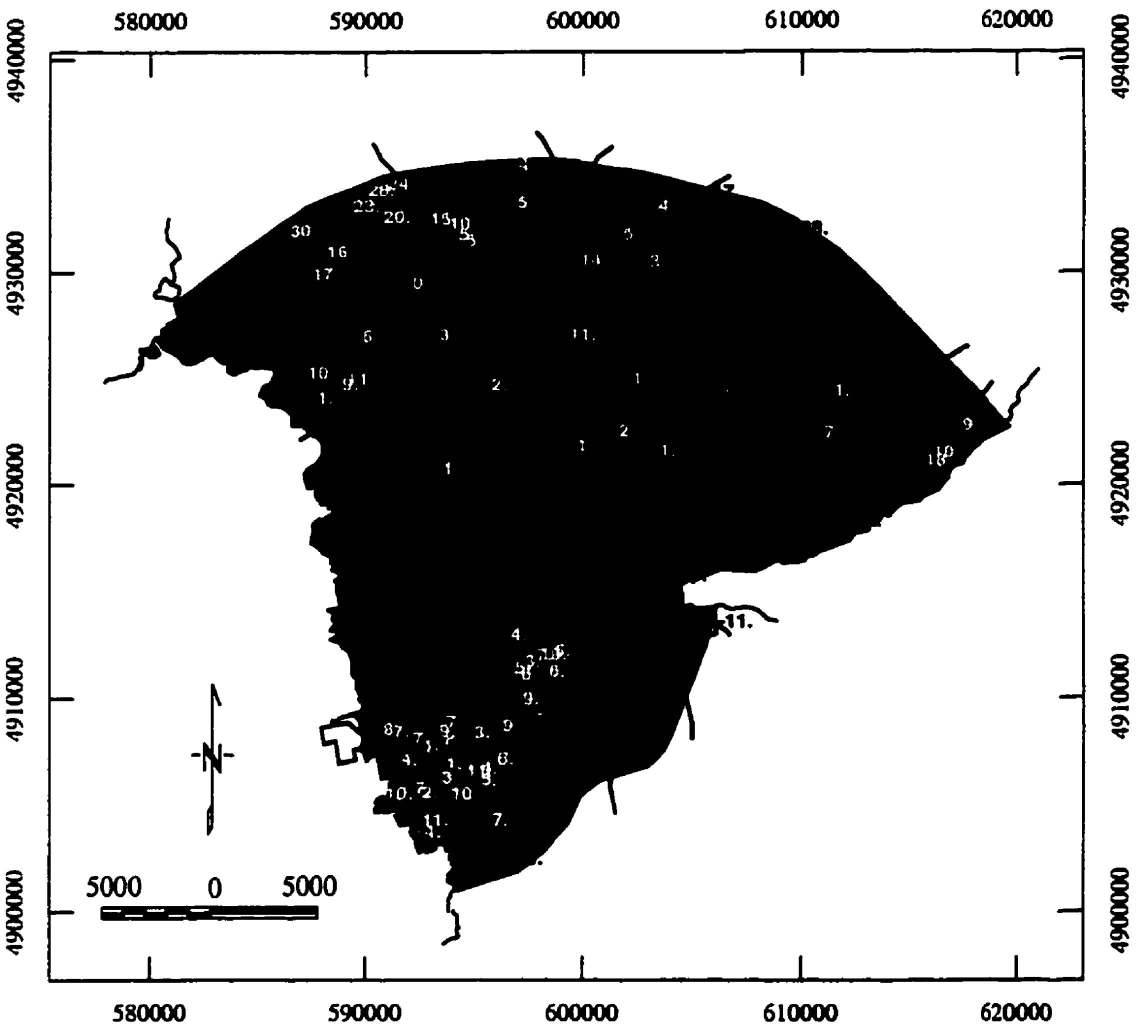
580000
590000
600000
610000
620000
4940000
4930000
4920000
4910000
4900000
N
5000 0 5000
11.

Figure 8.24: Residuals for AQFR3. White values correspond to over-predicted heads, black values designate under-predicted heads.

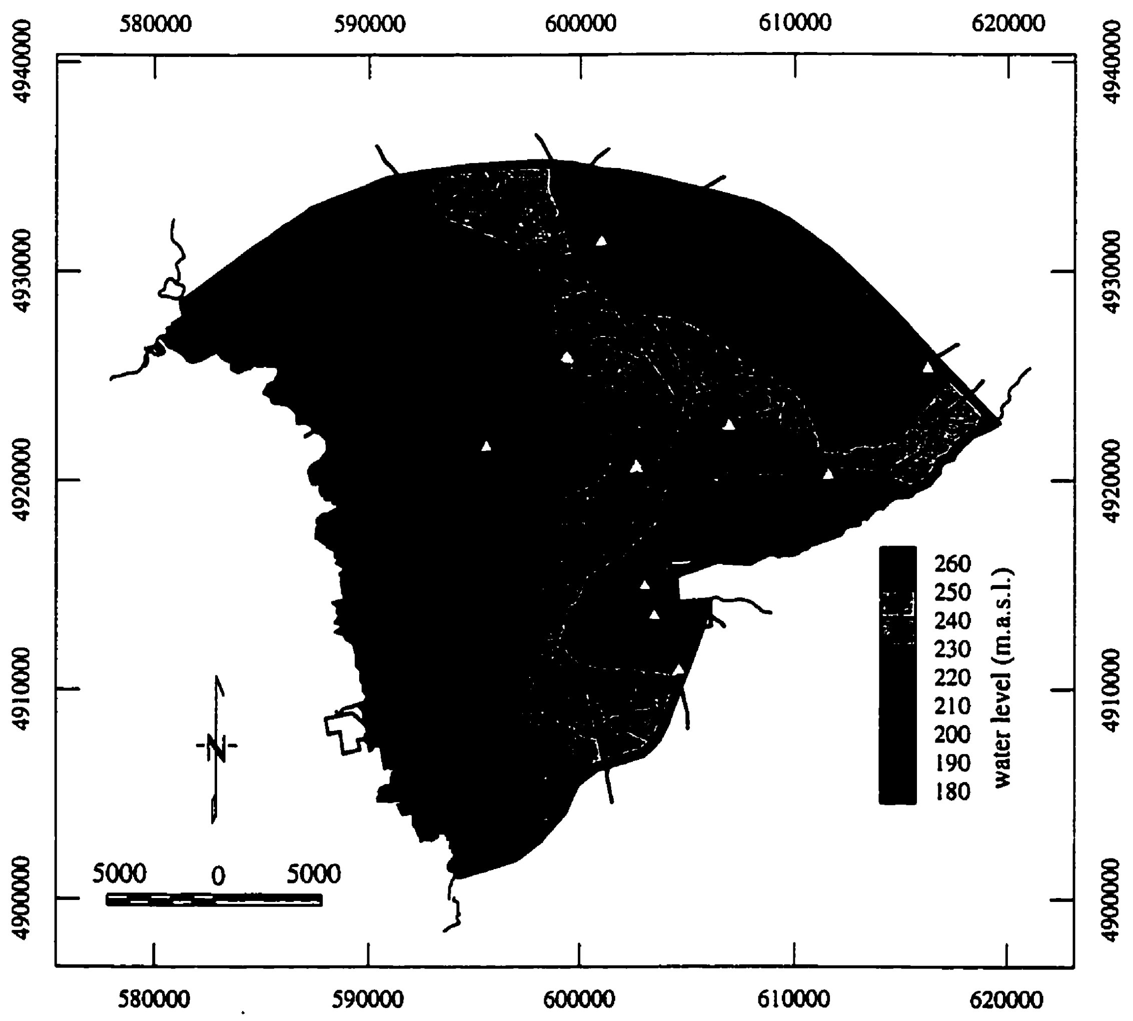
580000
590000
600000
610000
620000
4940000
4930000
4920000
4910000
4900000
N
5000
0
5000
260
250
240
230
220
210
200
190
180
water level (m.a.s.l.)

Figure 8.25: Vertically averaged simulated water levels for AQFR4. Black triangles indicate data derived from overburden wells; white triangles correspond to bedrock wells.

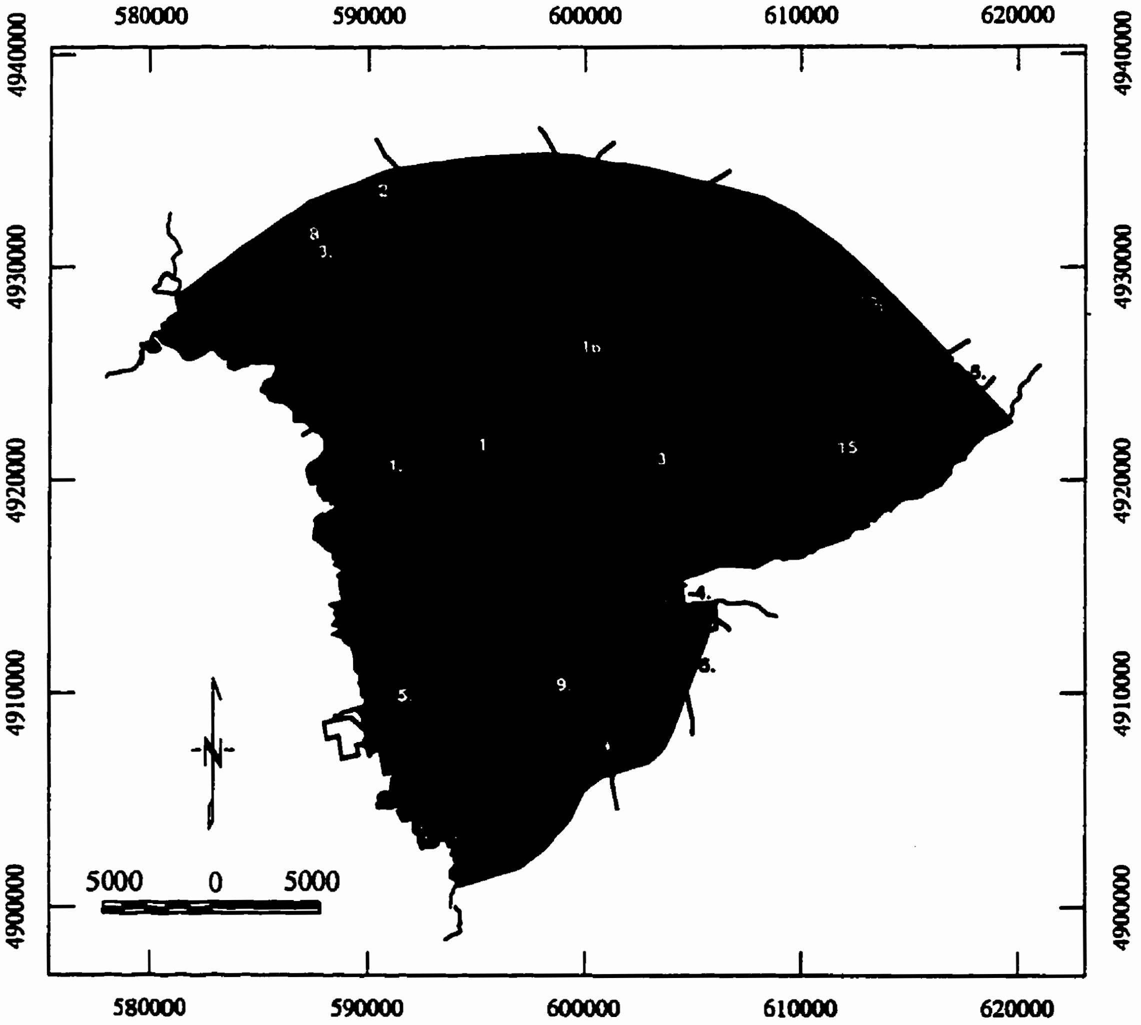
580000
590000
600000
610000
620000
4940000
4930000
4920000
4910000
4900000
2
8
3.
16
1
1.
3
15
8.
4.
6.
5.
9.
N
5000
0
5000

Figure 8.26: Residuals for AQFR4. White values correspond to over-predicted heads, black values designate under-predicted heads.

may indicate that the model boundary locally does not conform to groundwater flow paths. Actual flow paths may be directed more towards Georgian Bay than towards the Nottawasaga River. Water levels in Aquifers 2 and 3 near Barrie are somewhat under-predicted.

Overall, the head calibration is satisfactory, certainly in the deeper aquifers. The average error (bias) between the kriged water levels and the simulated heads is small (Table 8.13) considering the approximately 100 m observed head drop between the Oro Moraine and the Minesing Basin. The higher bias found for the point data in the upper two aquifers results entirely from the under-predicted water levels in the Oro Moraine (Figure 8.27). Note that calibration statistics for the kriged water levels are limited to the saturated part of the domain, thus largely ignoring the Oro Moraine upland in the case of aquifer 1.

	Kriged	Heads		Point	Heads	
	σ	avg(ϵ)	avg$\lvert\epsilon\rvert$	σ	avg(ϵ)	avg$\lvert\epsilon\rvert$
AQFR1	8.7	−2.4	6.6	10.7	−7.0	8.2
AQFR2	10.8	−3.3	8.3	10.9	−4.7	8.4
AQFR3	9.4	0.3	7.2	8.9	1.2	6.7
AQFR4	6.6	1.0	5.3	6.0	−0.1	4.8
Bedrock				7.8	−2.3	6.4

Table 8.13: Calibration statistics for kriged and point water levels expressed as standard deviation σ, the average error avg(ϵ) and the average absolute value of error avg$|\epsilon|$.

The remaining scatter between observed and simulated heads (Figure 8.27) partly results from errors in the water level data, mainly those caused by unreliable information regarding the elevation of the boreholes. It is therefore crucial that this elevation is accurately determined, either by using digital topographic information or through a field survey of a number of key boreholes. Other causes of the remaining scatter are the simplified representation of the true (hydro)geologic complexity in the numerical model and errors in the calibrated model. The discussion given in this section suggests that a re-examination of some of the geologic data and boundary conditions should be a preamble in further refining the calibration of the Oro Moraine model.

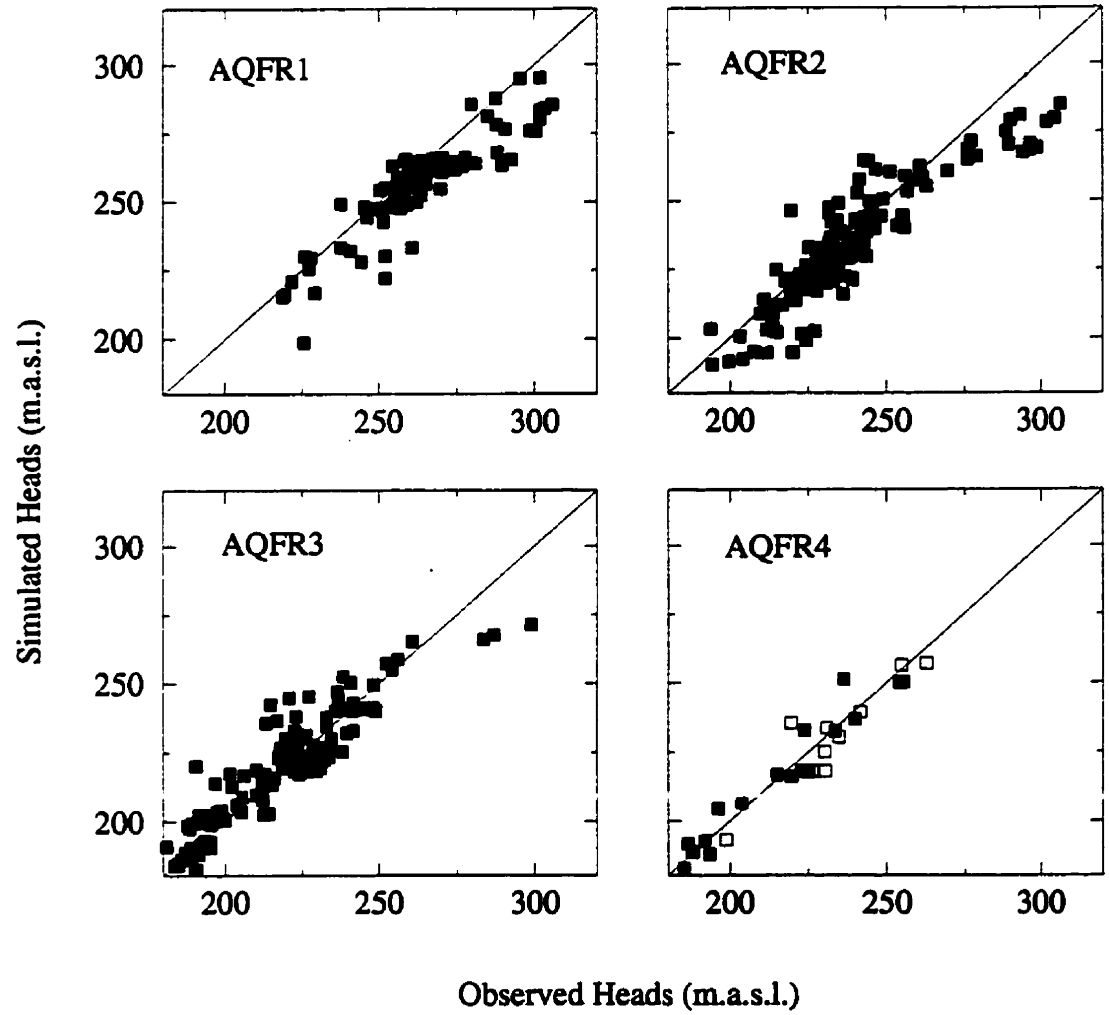

Figure 8.27: Scatter-plot of observed and simulated hydraulic heads. Black squares indicate overburden wells; white squares correspond to bedrock wells.

Except for baseflow to the Willow Creek headwaters, all streamflow data are matched within the assumed data error of 20 % (Table 8.12). The bias between the total observed and model predicted fluxes to the Nottawasaga River is 0.9 m^3/s. This bias may be caused by errors in the model calibration. However, an equally likely explanation may be found in the short data record for the Edenvale station and the assumptions made in determining the contributions from the study domain and the subwatersheds to the west of the Minesing Basin (Section 8.5.2).

8.6.7 Calibrated Conductivity Fields

The final calibrated conductivity distributions are shown in Figures (8.28-8.33). For the aquifers, the vertical arithmetic average of K_{xx} is shown. For the aquitards, the vertical harmonic average of K_{zz} was calculated. Notable are the high average conductivity of aquitard 1 and the lateral differences in conductivity between the individual uplands that comprise aquifer 1.

The addition of the pilot point results in local changes in the conductivity fields. In some locations the pilot points appear to occur in clusters. This is certainly the case for the Alliston aquifer complex in the northwest corner of the domain. The clustering is a result of the non-optimal location of the pilot points in which the effect of kriging is ignored. In KRIGMODE=2, no constraints are put on the location of pilot points relative to one another. In other areas, the pilot points are mostly located at different depths in a hydrostratigraphic unit. As a result of the anisotropic nature of the conductivity correlation structure, the vertical influence of a pilot point is limited. The placement of the pilot points is thus affected by this correlation structure which is poorly constrained at best. A drawback of the pilot point method is its dependence on the geostatistical parameters [e.g., *Keidser and Rosbjerg*, 1991]. This drawback can to some degree be mitigated by locating the pilot points optimally. The calibration of the Oro Moraine model indicates that the methodology for automatically placing the pilot points needs to be refined in future versions of the calibration code.

An option for including the kriging effect in locating the pilot points needs to be added to the inverse model. This will ensure that pilot points are located optimally and some distance away from boreholes and one another. However, due to computational requirements the kriging effect can only be accounted for in relatively small domains (Chapter 5). Alternatives will therefore be explored to allow for user

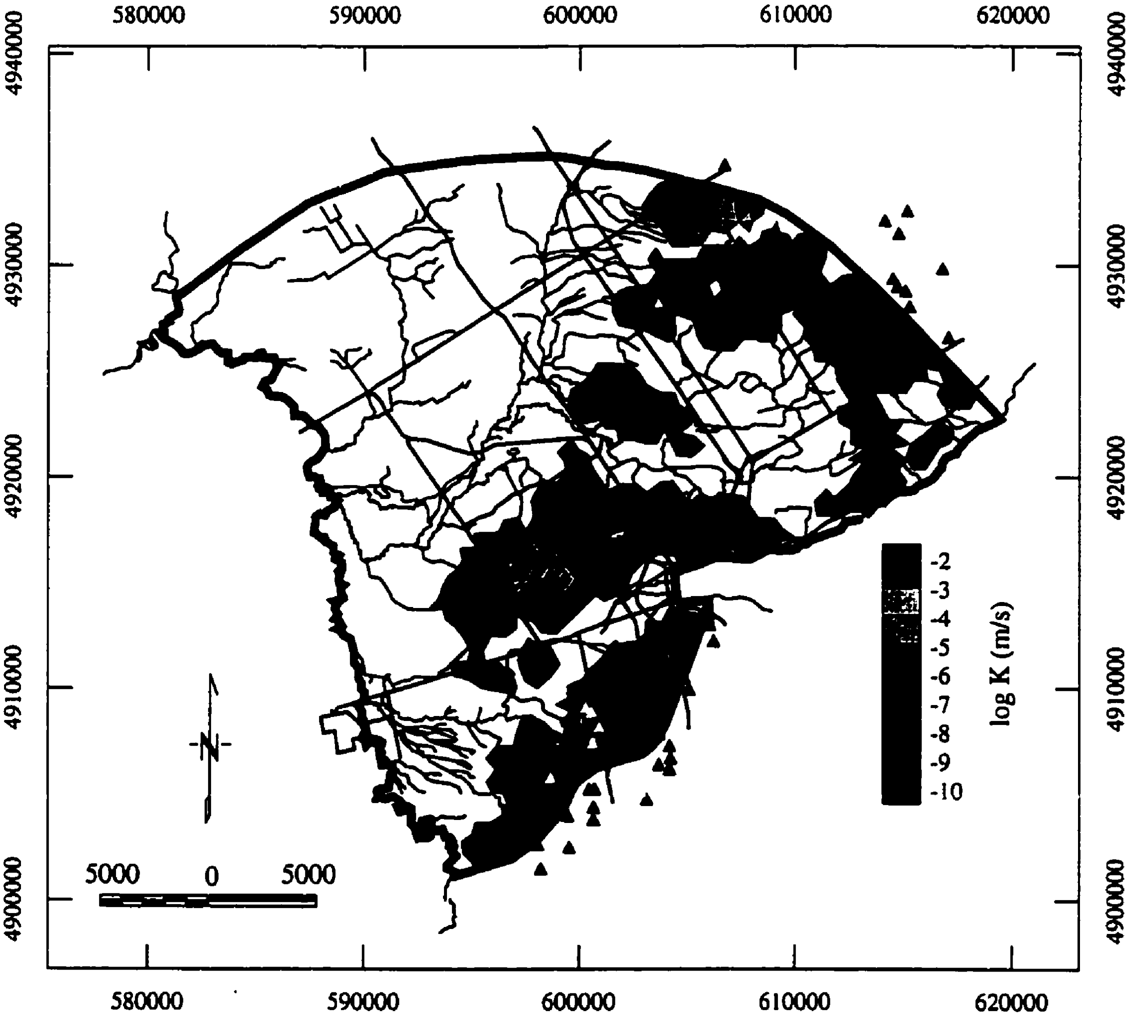
580000
590000
600000
610000
620000
4940000
4930000
4920000
4910000
4900000
-2
-3
-4
-5
-6
-7
-8
-9
-10
log K (m/s)
N
5000
0
5000

Figure 8.28: Average vertical conductivity distribution for AQTD1. Black triangles indicate borehole locations, white triangles designate pilot points.

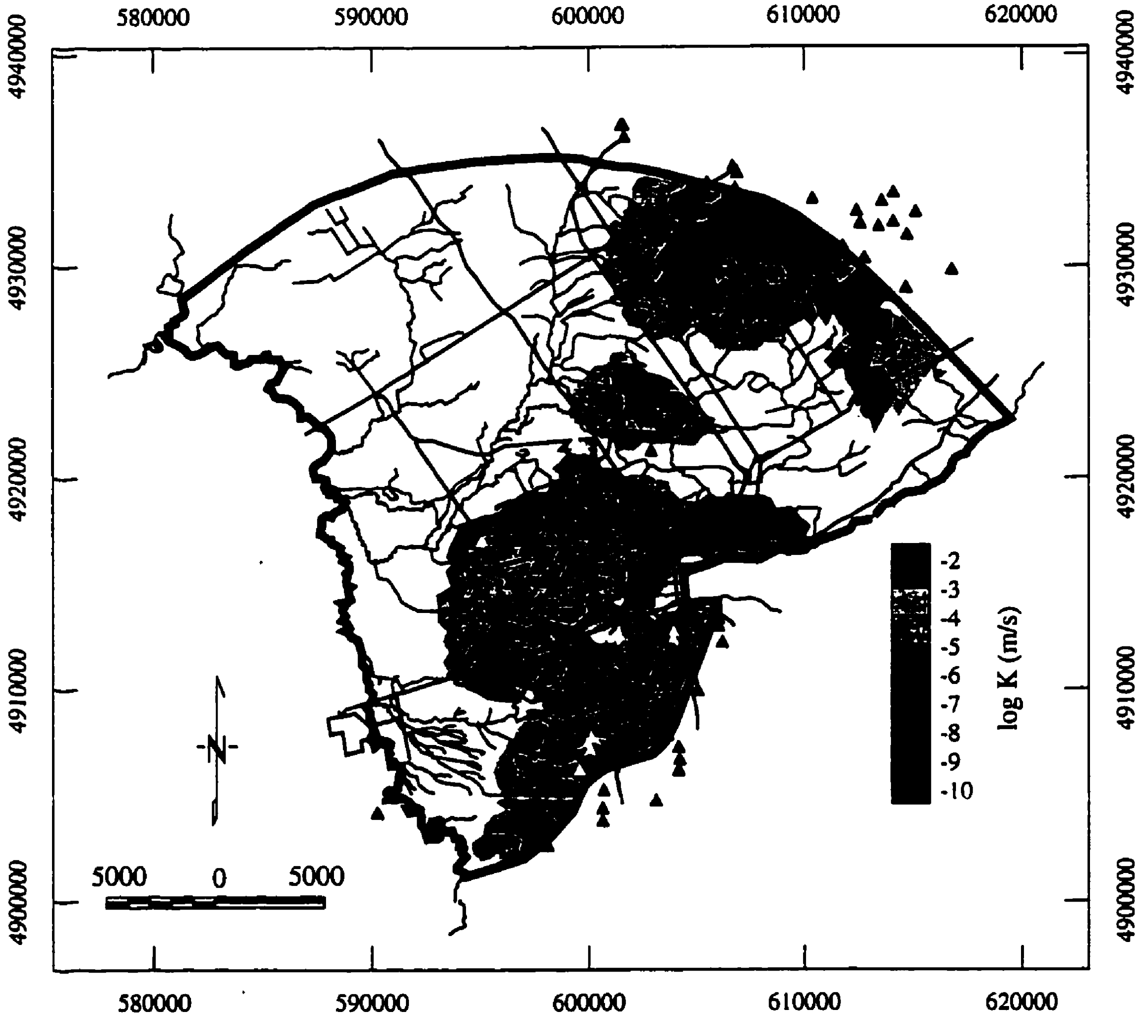
580000
590000
600000
610000
620000
4940000
4930000
4920000
4910000
4900000
N
5000 0 5000
-2
-3
-4
-5
-6
-7
-8
-9
-10
log K (m/s)

Figure 8.29: Average horizontal conductivity distribution for AQFR1. Black triangles indicate borehole locations, white triangles designate pilot points.

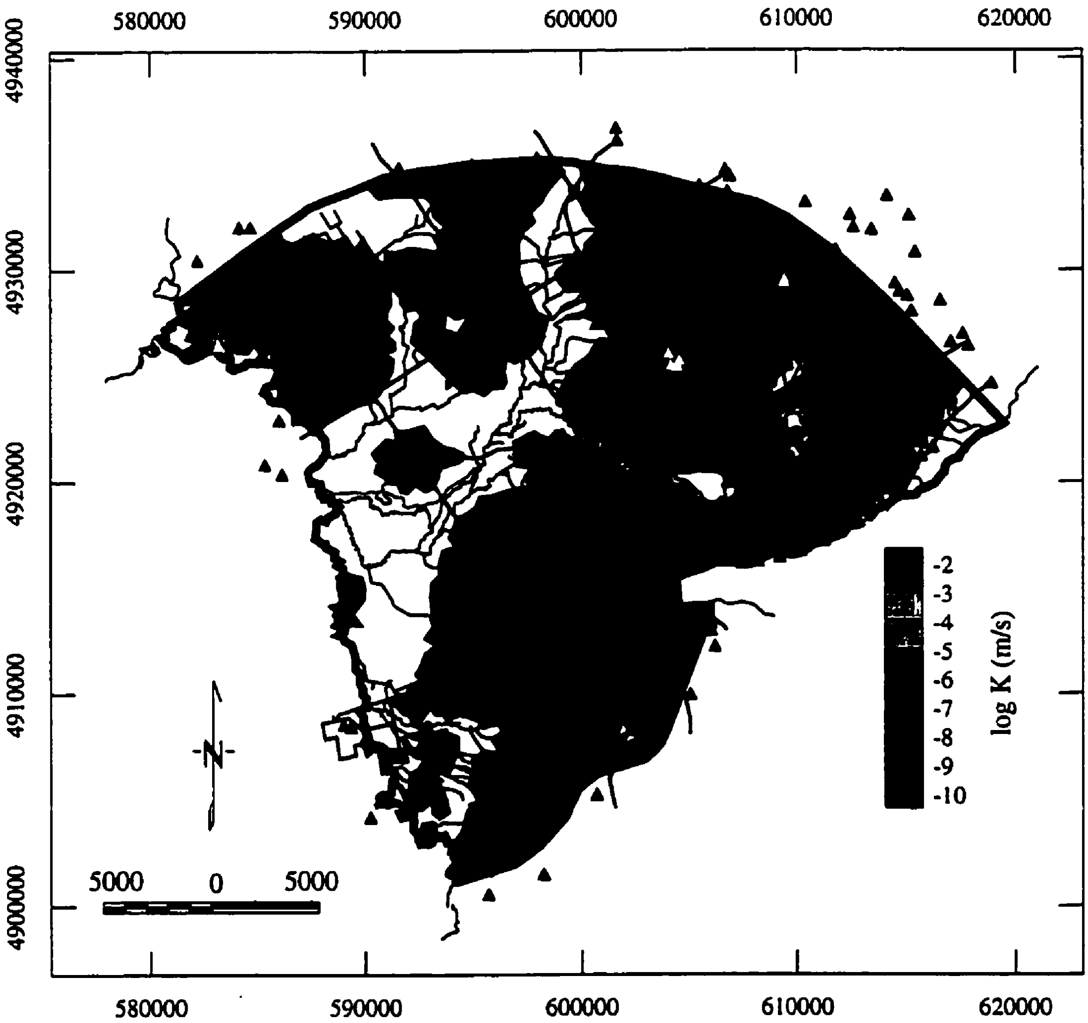
580000
590000
600000
610000
620000
4940000
4930000
4920000
4910000
4900000
N
5000
0
5000
-2
-3
-4
-5
-6
-7
-8
-9
-10
log K (m/s)

Figure 8.30: Average vertical conductivity distribution for AQTD2. Black triangles indicate borehole locations, white triangles designate pilot points.

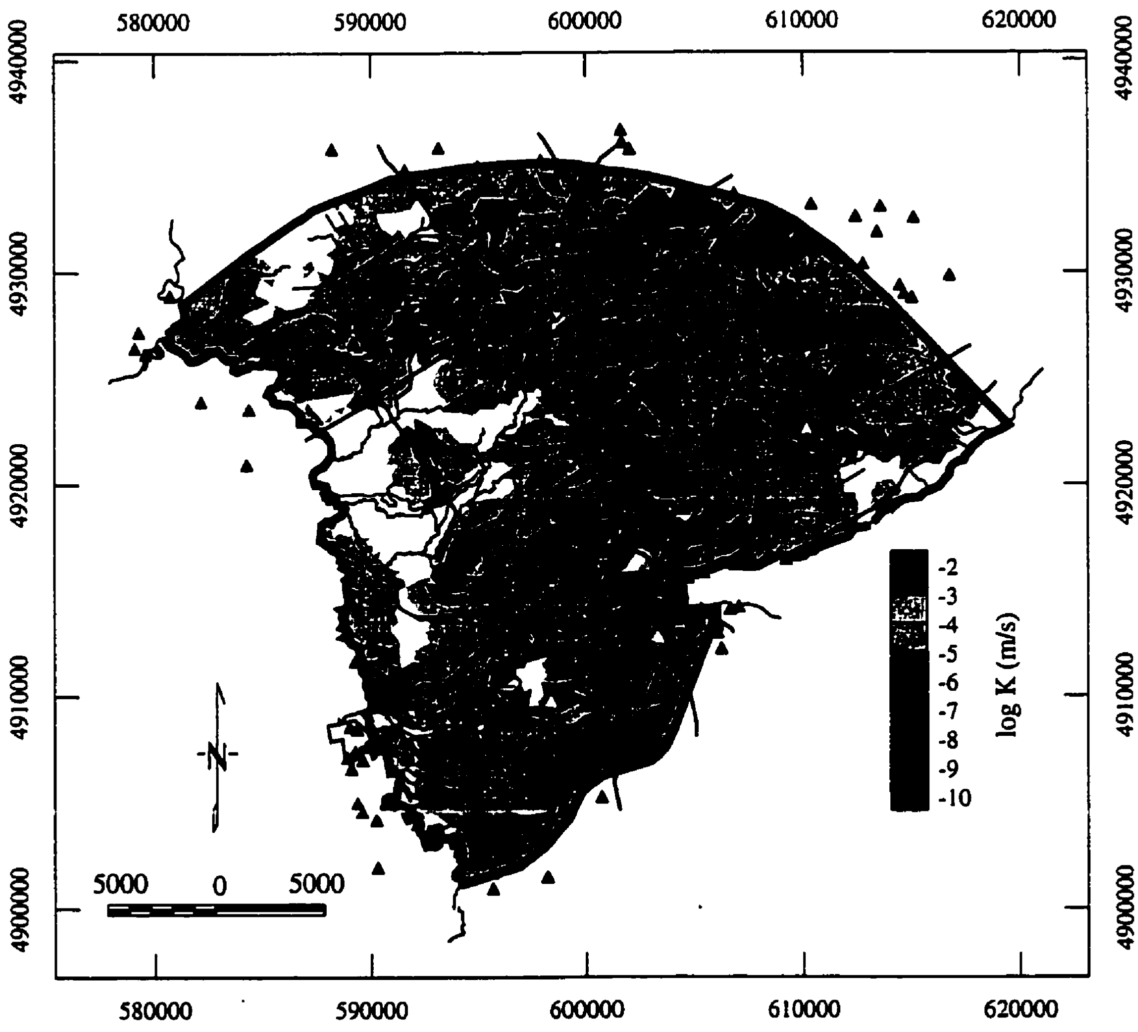
580000
590000
600000
610000
620000
4940000
4930000
4920000
4910000
4900000
-N-
5000 0 5000
-2
-3
-4
-5
-6
-7
-8
-9
-10
log K (m/s)

Figure 8.31: Average horizontal conductivity distribution for AQFR2. Black triangles indicate borehole locations, white triangles designate pilot points.

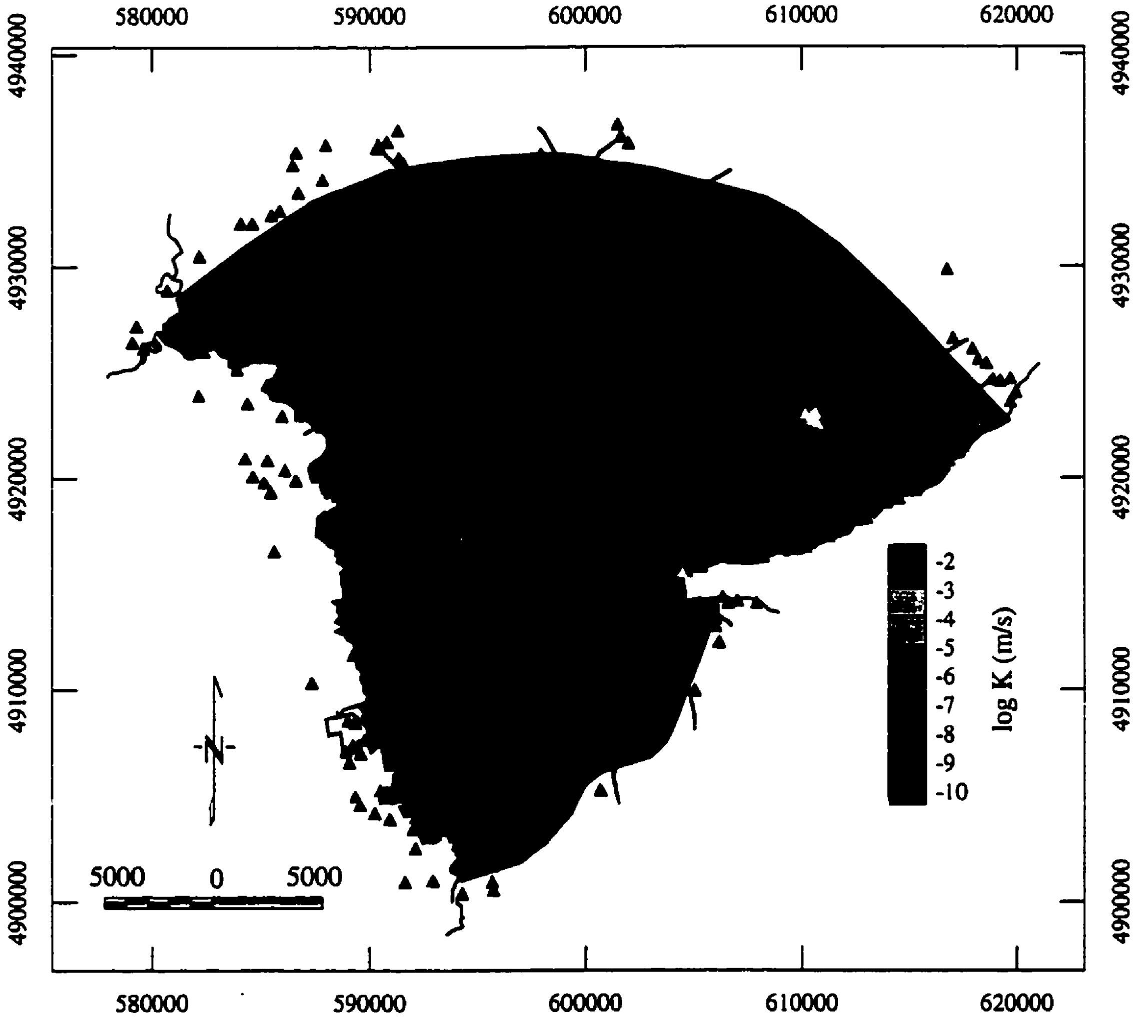
580000
590000
600000
610000
620000
4940000
4930000
4920000
4910000
4900000
-N-
5000 0 5000
-2
-3
-4
-5
-6
-7
-8
-9
-10
log K (m/s)

Figure 8.32: Average vertical conductivity distribution for AQTD3. Black triangles indicate borehole locations, white triangles designate pilot points.

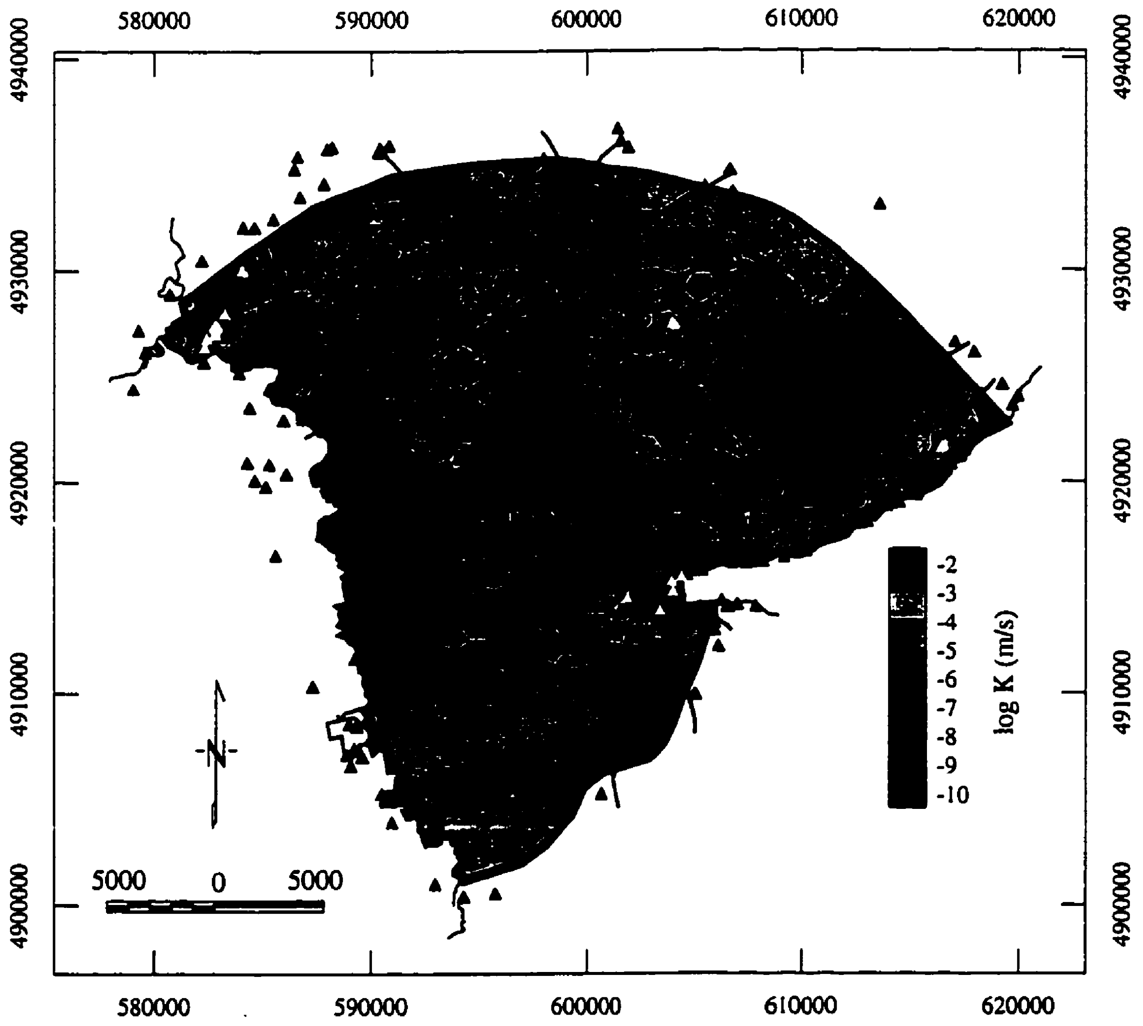
580000
590000
600000
610000
620000
4940000
4930000
4920000
4910000
4900000
-N-
5000 0 5000
-2
-3
-4
-5
-6
-7
-8
-9
-10
log K (m/s)

Figure 8.33: Average horizontal conductivity distribution for the Alliston aquifer complex. Black triangles indicate borehole locations, white trangles designate pilot points.

input if the existing (non-optimal) algorithm indicates that a pilot point should be located near one or more boreholes. Constraints further need to be imposed on the location of pilot points with respect to one another in order to avoid the clustering that was observed here. In general, a drawback of automatically locating the pilot points is that this does not incorporate any constraints from stratigraphic features that may provide preferential pathways and barriers for flow. An option for the user to manually position pilot points based on geologic information will therefore also be included in the calibration code. In this manner, systematically located pilot points can be used to delineate areas of preferential high or low conductivity caused by geologic features.

Overall the model calibration was refined with relatively small modifications to the intra-formational heterogeneity. Furthermore, except in the upper reaches of the Willow Creek the system water mass balance, was not significantly altered by the addition of the pilot points. Because this mass balance is the focus of the remainder of this study, the present calibration was considered adequate.

8.7 Water Mass Balance

The WATFLOW code calculates a detailed water mass balance for the numerical model (Table 8.14). Pumping accounts for a significant part of the water budget. Simulated fluxes to Kempenfelt Bay are about half the anticipated value of 1.27 m^3/s (Section 8.5.2). This is a result of the pumping activity in the Barrie area. Pilot points were located between these wells and Kempenfelt Bay, facilitating the capture of water derived from Lake Simcoe (Figure 8.33). Although the high conductivity values assigned to the pilot points are realistic, given the local presence of a Tunnel Valley aquifer, the municipal water wells are in reality thought to receive their water from groundwater recharge in the upland areas. The addition of the pilot points did reduce groundwater discharge to Kempenfelt Bay by only 0.12 m^3/s, not enough to account for the discrepancy that is thought to exist based on the rationale given in Section (8.5.2). Flow of groundwater from the upland areas to the pumping wells should be facilitated in the numerical model. This mechanism could be provided by the inclusion of the Barrie-Borden aquifer in the hydrostratigraphic model. Due to a lack of data constraining its geometry, this Tunnel Valley aquifer was not included in the present model. Increased flow from the Snow Valley and Innisfill Uplands towards the Barrie area would reduce fluxes to the Minesing Basin. This to some degree affects the result that will be presented in Chapter (9) regarding the water mass balance of the Minesing Swamp.

Baseflow accounts for only 8 % of the total fluxes to Bear Creek (Table 8.14). Groundwater discharge is also relatively unimportant for the upper reaches of Willow Creek (Section 8.5.2). The model predicts the baseflow component to increase sharply where the Willow Creek enters the Simcoe Lowlands, downstream of Midhurst. This agrees with the anticipated effect of topography on groundwater flow patterns [e.g., *Freeze and Witherspoon*, 1967]. In general, baseflow quantities are found to be highest in the Minesing Basin. The model predicts baseflow to be important for the "cold water" Matheson Creek, with a 31 % contribution to the total streamflow. Overall, the groundwater component accounts for 34 % of the total water budget of the study area.

	Groundwater		Surface Runoff	
	m^3/s	gw/ws/tf	m^3/s	sw/ws/tf
Pumping	0.88	31/10/ –		
Bear Creek	0.04	2/ 1/ 8	0.45	8/ 5/92
Kempenfelt Bay	0.11	4/ 1/ –	0.55	10/ 6/ –
Marl Creek	0.29	10/ 3/31	0.65	12/ 8/69
Matheson Creek	0.37	13/ 4/31	0.82	15/10/69
Minesing Swamp	0.36	13/ 4/27	0.98	17/11/73
Nottawasaga River	0.35	12/ 4/29	0.85	15/10/71
Willow Creek	0.49	17/ 6/27	1.33	24/16/73
Total	2.88	100/34/ –	5.65	100/66/ –

Table 8.14: Simulated water mass balance as absolute values and as percentages of the groundwater (gw) or surface water (sw) budget, water surplus (ws), and total streamflow (tf). The water surplus is 8.53 m^3/s.

8.8 Uncertainty in Water Mass Balance

The variances in the water mass balance corresponding to uncertainty in the average conductivity of the hydrostratigraphic units (I) and uncertainty in the intra-formational heterogeneity (II) were calculated using the first-order second-moment method (Table 8.15). The former level of uncertainty (I) is determined using the full covariance matrix (equation 5.20) corresponding to the confidence bounds given for objective 3 (Table 8.10). In this case, the sensitivity coefficients in equation (6.3) are lumped for each hydrostratigraphic unit as the average conductivities for these units are of concern. The second level of uncertainty (II) is determined using equations (5.18) and (6.3), where the elemental sensitivity coefficients are now used directly.

The intra-formational uncertainty is most important. The resulting variances are about an order of magnitude higher than those related to uncertainty in the average conductivity of the hydrostratigraphic units. Confidence bounds given in Table (8.10) suggest that this latter source of uncertainty would have been more important if the point water levels had been used in the calibration. In calculating confidence bound for the average conductivity values, the uncertainty in the interpolated head distribution was taken into account through the calibration weights (5.6) that enter equation (5.20). Nevertheless, the kriged heads reduce the uncertainty that exists as a result of the indirect nature of the conductivity information. At least from this point of view, the need for direct measurements of hydraulic conductivity is therefore reduced by this alternative calibration measure.

The confidence bounds on the average conductivities are tight (Table 8.10) and the first-order second-moment method is adequate for the uncertainty analysis as non-linearity with respect to conductivity perturbations is not expected to significantly affect the calculations. Furthermore, the confidence bounds were determined making use of the calibration statistics. The resulting model uncertainty therefore is consistent with constraints imposed by the kriged heads and flow measurements. The WATFLOW code presently has no check to ensure that the weighted calibration residuals are normally distributed (refer to Section 5.2.5). However, the small bias between kriged and simulated heads (Table 8.13) and the point water level scatterplot (Figure 8.27) suggest that this requirement is reasonably met. One standard deviation (square root of values listed in Table 8.15) comprises 1-17 % of the predicted baseflow quantities and 1-4 % of the simulated runoff values (Ta-

	Groundwater		Surface Runoff	
	I	II	I	II
Bear Creek	$2.24 \cdot 10^{-5}$	$5.66 \cdot 10^{-3}$	$2.63 \cdot 10^{-4}$	$2.38 \cdot 10^{-3}$
Kempenfelt Bay	$3.42 \cdot 10^{-4}$	$4.42 \cdot 10^{-3}$	$9.61 \cdot 10^{-5}$	$7.41 \cdot 10^{-4}$
Marl Creek	$1.48 \cdot 10^{-3}$	$2.07 \cdot 10^{-2}$	$6.03 \cdot 10^{-4}$	$7.31 \cdot 10^{-3}$
Matheson Creek	$1.86 \cdot 10^{-3}$	$1.67 \cdot 10^{-2}$	$2.99 \cdot 10^{-4}$	$8.65 \cdot 10^{-3}$
Minesing Swamp	$2.21 \cdot 10^{-4}$	$7.48 \cdot 10^{-3}$	$6.70 \cdot 10^{-5}$	$3.34 \cdot 10^{-3}$
Nottawasaga River	$1.67 \cdot 10^{-5}$	$1.20 \cdot 10^{-3}$	$3.78 \cdot 10^{-4}$	$8.99 \cdot 10^{-4}$
Willow Creek	$5.76 \cdot 10^{-4}$	$2.81 \cdot 10^{-2}$	$2.49 \cdot 10^{-3}$	$8.48 \cdot 10^{-3}$

Table 8.15: Variance in water mass balance due to uncertainty in (I) average conductivity of hydrostratigraphic units and (II) intra-formational heterogeneity.

ble 8.14), intervals that compare favorably with the assumed measurement error in the streamflow data of 20 %.

Issues related to non-linearity and constraints imposed by the calibration data still need to be investigated for the case of the intra-formational heterogeneity. This was done by a comparison with Monte Carlo simulations. Results are discussed for aquifer 2 and aquitard 3. Only 100 realizations were used in each case. This number is inadequate to determine the various moments of the model predicted fluxes. However, it is sufficient for the discussion that will be given next.

Figure (8.34) gives histograms for the simulated baseflow to three creeks and the Minesing Swamp calculated from the conditional realizations generated for aquitard 3. The mean and linear 95 % confidence bounds calculated using expression (6.4) are also given ($z_{0.025} = 1.96$). Because the variance in log conductivity for aquitard 3 is modest (Table 8.6), the predictions of the first order second moment method are in reasonable agreement with the range of baseflows seen in the histograms, except for Willow Creek. This agreement breaks down for aquifer 2 (Figure 8.35) which is more heterogeneous. The effect of model non-linearity with respect to conductivity variations becomes increasingly important. For the Bear and Matheson Creeks, the mean values of the random realizations are significantly different from the baseflow quantities found using the kriged conductivity field. The linear confidence bounds are generally smaller than the baseflow variability seen in the histograms. The disagreement between the first-order second-moment method and the Monte Carlo

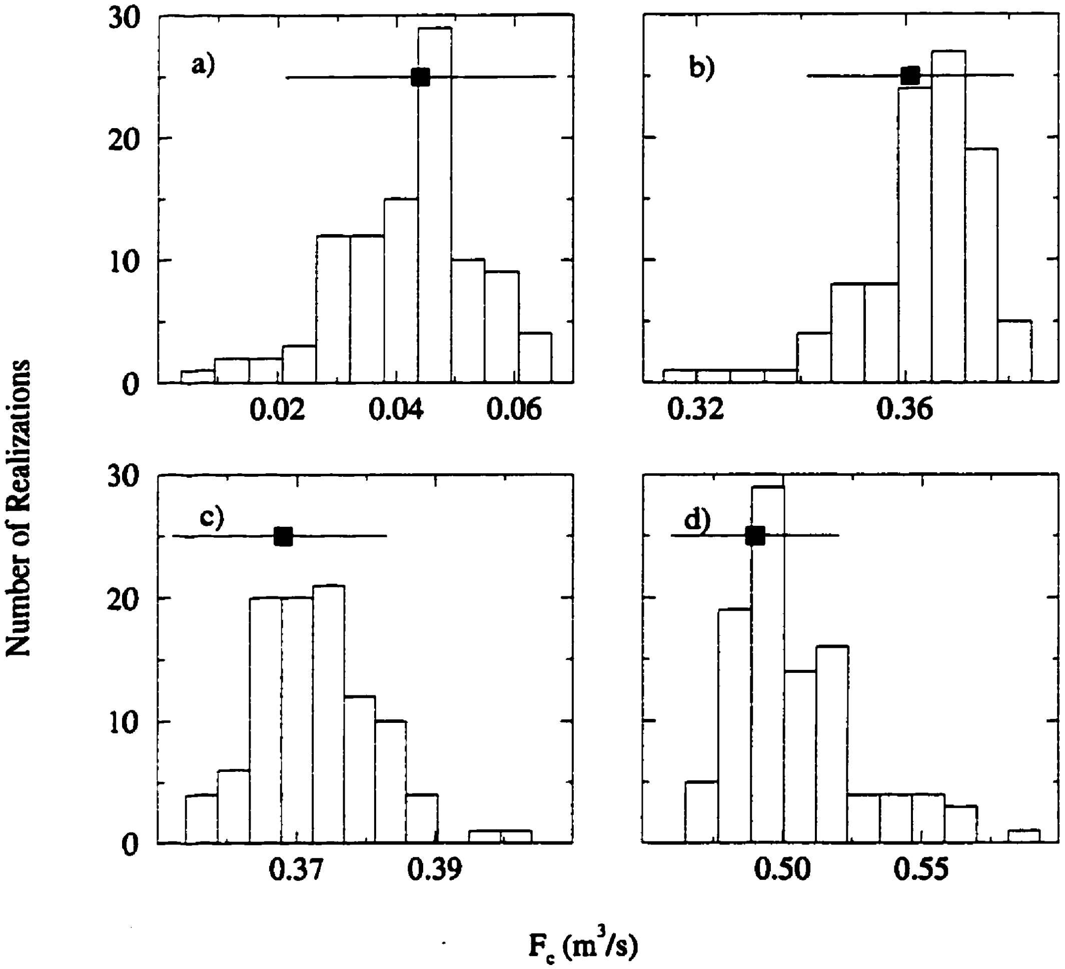

Figure 8.34: Baseflow histograms for a) Bear Creek, b) Minesing Swamp, c) Matheson Creek and d) Willow Creek determined from a Monte Carlo analysis regarding the intra-formational heterogeneity for AQTD3. The square and line designate the mean value and 95 % confidence bounds calculated with the first order second moment method.

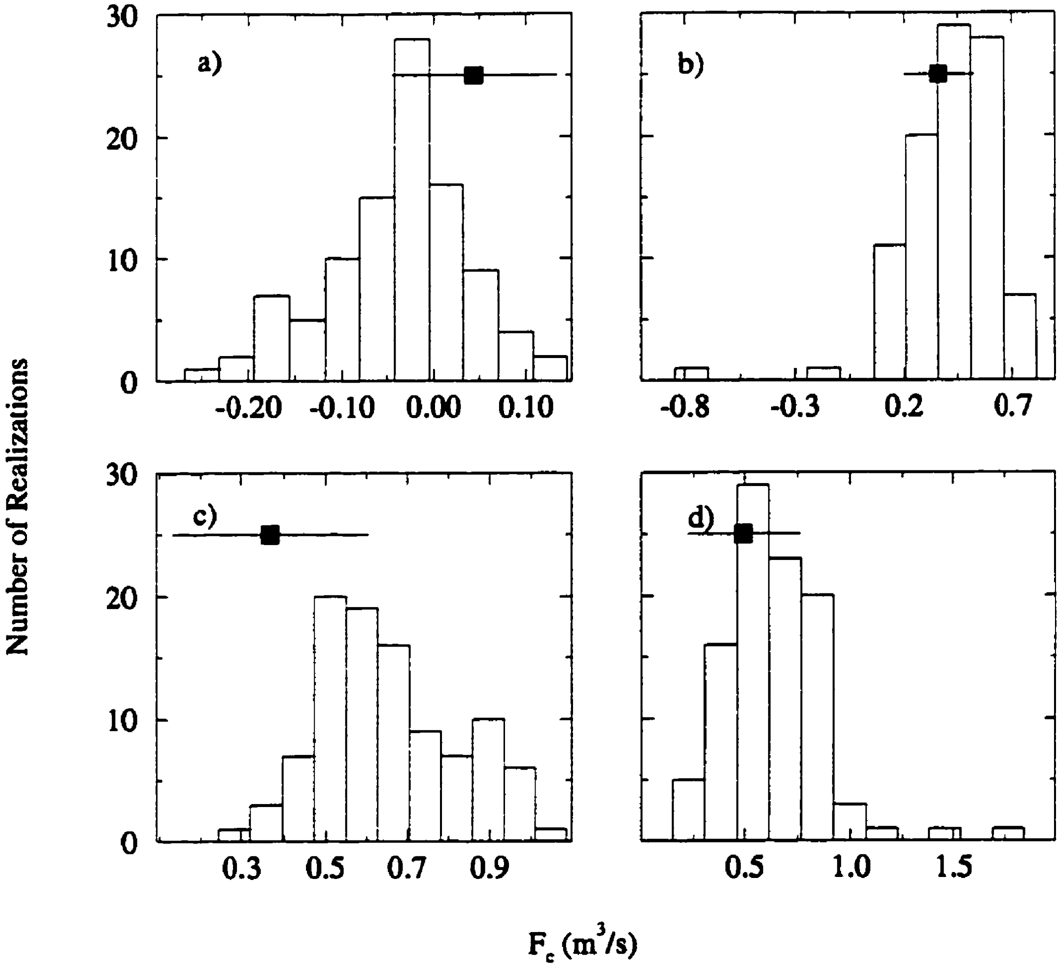

Figure 8.35: Baseflow histograms for a) Bear Creek, b) Minesing Swamp, c) Matheson Creek and d) Willow Creek determined from a Monte Carlo analysis regarding the intra-formational heterogeneity for AQFR2. The square and line designate the mean value and 95 % confidence bounds calculated with the first order second moment method.

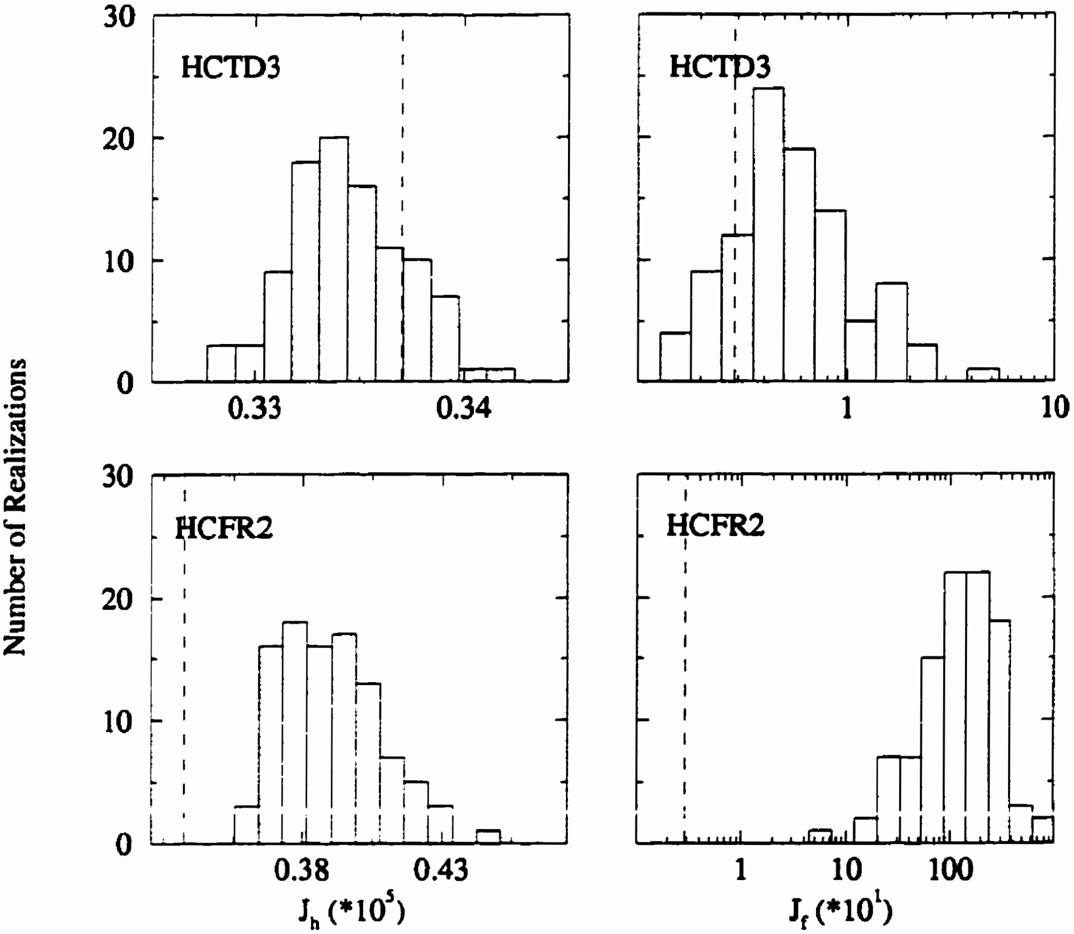

Figure 8.36: Calibration measure histograms corresponding to the Monte Carlo runs for AQTD3 and AQFR2. The vertical dashed lines designate the final calibrated values for J_h and J_f.

simulations increases when heterogeneity is even more pronounced, as in the case of the Alliston aquifer complex.

The baseflow variability seen in the histograms (Figures 8.34 and 8.35) suggest that some of the random realizations are not necessarily consistent with the calibration data. The random realizations result in large fluctuations in baseflow to the upper reaches of Willow Creek, causing order of magnitude variations in J_f (Figure 8.36). For aquitard 3, the random realizations result in calibration measures that are more or less centered around the final calibrated values. However, for aquifer 2 all realizations are characterized by calibration measures that are biased towards higher values. None of these realizations are consistent with the calibration data.

One possible means of incorporating the effect of the calibration data on model uncertainty is to filter out those realizations that result in an objective function that is significantly higher than that of the calibrated model. It is clear that for aquifer 2, none of the realizations would pass such a test and a different approach needs to be taken.

The calibration bias observed for aquifer 2 results from the greater conductivity variability in the random fields, creating pathways and barriers for flow that are not present in the kriged field. The average conductivity values determined in the first phase of the model calibration are appropriate for this kriged field but not for the random realizations. Each realization therefore needs to be calibrated to remove the bias seen in Figure (8.36). This approach was used by *RamaRao et al.* [1995]. However a large number of realizations is required to reliably determine the stochastic moments of some model output. When multiple hydrostratigraphic units are considered this problem becomes even worse as all conductivity fields need to be varied simultaneously. This requires and excessive amount of realizations. On the other hand, the solution of the flow problem alone requires about 40 minutes on a Pentium 266 machine, resulting in nearly 3 days of runtime for just 100 realizations. The first phase of the calibration was observed to take anywhere from 1 day (for the preferred parameterization and objective function) to 1 week of computer time. The pilot point calibration requires about a week of CPU time. Thus, it is clear that, even when using a more efficient sampling technique like Latin Hypercube, a discrete sampling approach to determining model uncertainty is not feasible for the Oro Moraine investigation.

The smaller confidence bounds predicted by the first-order second-moment method

(Figures 8.34 and 8.35) may be in better agreement with the calibration data. However, uncertainty is still large. A comparison of Tables (8.14) and (8.15) shows that, when expressed as one standard deviation, uncertainty in baseflow caused by the intra-formational heterogeneity comprises anywhere from 24 % to greater than 100 % of the predicted fluxes. For surface runoff these intervals are 2-11 %. The addition of pilot points inadequately addresses the effect of the calibration data on uncertainty in the conductivity fields. This problem is emphasized by the large conductivity variations and the associated non-linearity of the stochastic process. These problems hamper the first order second moment analysis. Other concerns associated with the present analysis are: (1) the representation of the true conductivity distribution by a simple covariance model and (2) the nature and quality of the conductivity information, where the geostatistical parameters are uncertain as a result of the poorly defined experimental variograms. Although hard to quantify, these problems are likely to be severe.

Neither of the two selected methods of uncertainty analysis did perform entirely satisfactorily. The likelihood method of *Vechia and Cooley* [1987] has the potential of providing a cost-effective alternative to address issues regarding non-linearity and the role of the calibration data in model uncertainty. However, the use of this method would require that the conductivity parameterization is modified to a strictly zonation-based approach (Chapter 6). Such an approach is not favored because in this complex aquifer system it is difficult to identify zones of similar hydrogeologic properties in a lateral sense, as illustrated by Figures (8.28)-(8.33). A poor zonation will lead to a poor representation of the true conductivity distribution in the numerical model and thus to poor simulation results. This problem was circumvented by using a combined zonation/geostatistical parameterization in which kriging is used to interpolate hydraulic conductivity within each hydrostratigraphic unit. This parameterization should therefore be maintained even though it does not allow for a detailed stochastic analysis.

8.9 Discussion

A numerical model of the study area was developed and calibrated in this chapter. The calibrated model was found to provide a satisfactory match to measured heads, and the baseflow and runoff component of observed streamflows. Some discrepancies remain. Predicted water levels are too low in the Oro Moraine upland area. This was attributed to the pronounced outcrop of the uppermost aquifer along the eastern slope of the Matheson Creek valley. In the northwest corner of the study area, the model boundary may not accurately follow groundwater flow paths. Groundwater fluxes to Kempenfelt Bay may be under-predicted due to the absence of the Barrie-Borden aquifer in the model, forcing the Barrie municipal wells to derive part of their water from Lake Simcoe. The Willow Creek Tunnel Valley aquifer may also be important [*Easton*, 1998]. Although the absence of this aquifer did not result in significant calibration errors it may become more important if the detailed identification of groundwater flow paths is of concern, such as for capture zone delineation. Overall, the present hydrostratigraphic model already provides a good representation of the aquifer system.

Thus, in refining the Oro Moraine model, a first step should be a re-evaluation of some of the geologic data and model boundaries. Given the lack of high quality deep borehole information constraining the geometry of the tunnel valley aquifers, geophysical data would be useful. Seismic profiling is an excellent tool for delineating the hydrostratigraphy of the (glacial) overburden as illustrated by the Oak Ridges Moraine example [e.g., *Hinton et al.*, 1997]. Thus, an indirect benefit of the inverse model is the identification of deficiencies in the conceptual model and the need for additional data.

A comparison of model zonation alternatives suggested that the lower-most aquitard is not as continuous as was inferred in the hydrostratigraphic interpretation. The conceptual model of the aquifer system was therefore revised by lumping the lower two aquifers into a single unit. The intermediate till layer is included as discrete pockets of low-conductivity material. This unit is known from previous investigations as the Alliston aquifer complex, which has been suggested to extend from the Oak Ridges Moraine to Georgian Bay. The automated inversion enables the user to objectively compare alternative conceptual model scenarios, as illustrated by the above example. Such a comparison should be a crucial part of any calibration [e.g., *Hill*, 1998]. The implementation of an inverse algorithm in the WATFLOW code has thus been one of the major advances made in this study.

Based on the experience gained in calibrating the Oro Moraine problem, several improvements are suggested for the inverse algorithm. A plausibility criterion limiting the difference between initial and final conductivities should be included. The importance of using such a criterion in stabilizing the inversion and improving its plausibility was already shown by *Neuman and Yakowitz* [1979]. It was not yet used in the present inverse algorithm, arguing that the calibrated conductivity distribution does not necessarily need to be close to the initial estimate provided by the lithologic descriptions (Chapter 5). However, in this chapter this criterion was widely used to discriminate between alternative model options. The non-optimal location of the pilot points was found to be a point of concern, in agreement with conclusions drawn in previous investigations [e.g., *RamaRao et al.*, 1995]. The kriging effect should therefore be included in automatically locating the pilot points. This will ensure that pilot points are located optimally and some distance away from boreholes and one another. However, the use of this feature is only feasible for relatively small domains. Alternatives therefore need to be explored to improve the existing (non-optimal) algorithm. One option is to allow for user input if this algorithm indicates that a pilot point should be located near any boreholes. Constraints further have to be imposed on the location of pilot points with respect to one another. A drawback of automatically locating the pilot points is that this does not incorporate any constraints from stratigraphic features that may provide preferential pathways and barriers for flow. An option to manually locate pilot points will therefore also be included in future versions of the calibration code.

The remaining scatter between observed and simulated heads partly results from errors in the water level data, mainly those caused by unreliable information regarding the elevation of the boreholes. It is therefore crucial that this elevation is more accurately determined, either by using digital topographic information or through a field survey of a number of key boreholes. The crucial role of the poorly resolved geostatistical parameters of the conductivity distribution in the model calibration was also found to be a point of concern. Presently, these geostatistical parameters are solely based on the conductivity values assigned to the lithologic descriptions. Although direct measurements from pumping and slug tests were used as constraints in determining appropriate K values for the individual lithofacies, these measurements need to be directly used in calculating the geostatistical properties of the conductivity fields. This implies that pumping tests need to be performed at strategic locations in the aquifer system. A calibration of the model against transient pumping test data will also put tighter bounds on the conductivity distribution, better constraining groundwater fluxes and reducing model uncertainty.

Model uncertainty related to the conductivity distribution was considered through a first-order second-moment analysis. A comparison with Monte Carlo simulations revealed that the role of non-linearity and the calibration data in model uncertainty was not adequately addressed. Furthermore, a simultaneous consideration of all sources of model uncertainty was not possible as a result of limitations imposed by the conductivity parameterization. The model calibration illustrates that the hydrostratigraphy plays a crucial role in the response of the multi-aquifer system. The lack of information regarding the hydrostratigraphy is therefore perhaps the most important factor governing model uncertainty. However, given the limitations discussed in Chapter (6), this uncertainty could not be investigated in a systematic fashion. For this complex system, uncertainty issues can therefore only be addressed in a limited fashion by considering certain extreme model scenarios. Such an approach was already taken by *Martin and Frind* [1998], where the effect of the absence or presence of aquitard windows on the delineation of water well capture zones was determined. A more complete uncertainty analysis does not make sense given the limitation discussed above.

The calibration results suggest that despite its limitations, the numerical modelling approach does result in an accurate simulation of steady state fluxes for both the surface and subsurface flow systems. The water surplus was determined using spatially variable precipitation data and a uniform evapotranspiration rate. No attempt was made to define a spatially variable evapotranspiration as the effect of the non-uniform water surplus on the model calibration was found to be subtle. The recharge spreading layer conductivity was important in matching the flow data. Two zonation options for this layer were considered. This zonation should be given further consideration in future studies.

Pumping was found to comprise a significant part of the groundwater budget. Water abstraction from private water wells is an important unknown factor in the water mass balance of the Oro Moraine system. More detailed information on pumping activity in the study area therefore needs to be collected.

The available streamflow measurements put limited constraints on details of the water mass balance, such as contributions from individual streams to the observed total accumulation for the Nottawasaga River. For example, model results indicate that groundwater discharge to Bear Creek is highly uncertain. Unlike the Willow Creek headwaters, this baseflow is not constrained by any observations. Discharge information for the presently non-monitored streams is needed to resolve details of the water mass balance, to validate the model predictions and to reduce uncertainty in these predictions. The de-commissioning of the Willow Creek station at Little Lake in 1996 is unfortunate in this respect. Because the "cold water" Matheson Creek is considered important as a fish habitat [*NVCA*, 1995] it would be particularly useful to monitor this stream. From a numerical perspective, the effect of the mesh discretization and the number of Dirichlet boundaries that are included in the model on predicted fluxes may need to be addressed. In the present steady-state analysis, the relative contribution of baseflow and runoff to the total observed streamflows remains somewhat uncertain. Transient simulations of the flow system are needed to determine the origin of seasonal variations in streamflow generation and to better constrain the groundwater and surface water budgets.

Chapter 9

Impact of Urbanization

9.1 Introduction

The numerical model of the Oro Moraine aquifer system was developed with the objective of providing the Nottawasaga Valley Conservation Authority with a tool that can be used to manage the impact of urban development on the state of the Minesing Swamp. This chapter provides the onset for this application and highlights the associated limitations of the model.

Urban development leads to a loss of vegetative cover (forests, agricultural land) and an increase in hardened surfaces (asphalt, gravel), altering the existing local water budget. Impervious surfaces may comprise anywhere from 10 % of low density residential areas to 90 % of high density downtown business districts. The fraction of the impervious surfaces that is directly connected to the stormwater collection system largely determines the amount of precipitation that will be captured. Traditional systems served a single purpose: to convey runoff away from a site and into the receiving body (stream or lake) as quickly as possible. More recently, these systems have undergone improvements, mainly in response to their detrimental effect on surface waters.

The capture of rainfall runoff in a stormwater collection system and its subsequent release into a water course typically leads to increased peak flow during storm events, heightened flooding risks, river bank erosion and reduced water quality. Although important, these issues cannot be addressed with the present model. Surface water models or coupled surface-subsurface models which include the stream dynamics are needed for that purpose.

Stormwater detention ponds and artificial wetlands slow down the release of runoff to the receiving body. Detention ponds may result in focused recharge to the groundwater system. A modern stormwater system is presently being implemented in a new development area on the west side of the City of Waterloo (Ontario). The direct infiltration of rooftop runoff is facilitated. Rainfall that is being captured along road sides is also allowed to infiltrate after undergoing a cleaning procedure. Such a modern stormwater system has the potential to increase recharge compared to natural conditions as evapotranspiration is decreased. This may lead to a higher water table position with possible detrimental side effects. Groundwater quantity related issues concerning the various aspects of stormwater collection systems can be addressed with the WATFLOW code by an appropriate manipulation of boundary conditions. This is the focus of an ongoing study of the Waterloo Westside development project (*T. Radcliffe*, Department of Earth Sciences). In the present study, only hypothetical examples will be given to illustrate how the model can be manipulated to simulate the impact of urban development and to illuminate some crucial characteristics of the Oro Moraine groundwater system.

Water quality is also of concern. Contaminants that enter stormwater collection systems (e.g. road salt) impact both groundwater and surface water quality. Other sources of contamination such as leaking gasoline storage tanks primarily affect the groundwater system. Whether or not groundwater contamination becomes a problem for surface water quality largely depends on the time of travel in the subsurface. The impact of urban development on groundwater quality cannot directly be addressed by the present model although it does provide a basis for contaminant transport simulations.

The capture of rainfall by a stormwater collection system more than often leads to reduced recharge to the groundwater system, affecting the baseflow to streams and wetlands. Fluxes that are lost as baseflow will instead enter these surface waters as streamflow after their release as stormwater runoff. However, the groundwater and surface water components of the hydrologic cycle play different roles in, for example, the ecology of the Minesing Swamp. Streamflow is spatially focused and subject to significant temporal variations. High flows and ice jams associated with spring melt result in temporary flooding conditions along the fringes of the Nottawasaga River [e.g., *Fleming*, 1853]. Groundwater provides a relatively steady inflow of water over larger portions of the wetland. Subtle changes in baseflow and hydraulic gradients may have a large impact on the distribution of vegetation as this distribution is partially related to soil moisture conditions. The occurrence of different plant species may also depend on the geochemical composition of the groundwater. These issues are being addressed in a detailed field study by *Bradford and Watt* [1998].

Baseflow may also be crucial to the "cold water" Matheson Creek which is considered important as a fish habitat [*NVCA*, 1995]. Groundwater provides a steady inflow of water with a relatively constant temperature. The groundwater geochemistry may be important for the occurrence of aquatic plant species which provide a food supply for fish. In general, the quantity and quality of groundwater and surface waters are important for maintaining this habitat.

A water mass balance for the Minesing Swamp is estimated. This mass balance is needed to put the urbanization impact calculations into perspective. Critical recharge areas for the Minesing Swamp and the Willow and Matheson Creeks are identified. Selected areas in each of the three uplands are then used to illustrate how the model can be used to assess the potential impact of urban development on baseflow quantities and to provide insight into the behaviour of the aquifer system.

9.2 Minesing Swamp Water Mass Balance

The model-predicted fluxes (Table 8.14) and the measured and assumed streamflow quantities (Section 8.5.2) can be used to obtain a rough estimate of the water mass balance for the Minesing Swamp. The urbanization impact calculations that will be presented later should be compared to this water mass balance.

The streamflow for the Nottawasaga River at the inflow end of the Minesing Swamp is taken to be the total measured discharge at the Baxter station (8.87 m^3/s) plus simulated fluxes (baseflow plus runoff) to Bear Creek (0.49 m^3/s) and estimated fluxes to the upstream end of the Nottawasaga River. This upstream segment comprises about 25 % of the total length of the Nottawasaga River in the study area. The model-predicted flux for this stream (1.2 m^3/s) is therefore multiplied by 0.25 and then divided by 0.35 to account for the fact that the contribution from the Oro Moraine system was assumed to represent only 35 % of the total accumulation. This leads to an influx along the Nottawasaga River of 10.2 m^3/s.

The streamflow at the outflow end of the Minesing Swamp is calculated in a similar fashion by taking the total measured flow at the Edenvale station (26.3 m^3/s) and subtracting simulated fluxes to Marl Creek (0.94 m^3/s) and estimated fluxes to the downstream end of the Nottawasaga River (again taking this segment to be 25 % of the total length of the river). This yields an outflow value of 24.5 m^3/s.

The contribution of the subwatersheds to the west of the study area to the total flow accumulation in the Nottawasaga River was assumed to be 11.5 m^3/s (Section 8.5.2). This value is corrected to account for baseflow and runoff directly to the river (65/35 times the simulated flux of 1.2 m^3/s), leaving 9.3 m^3/s to enter the Nottawasaga River as streamflow through the Mad and Pine Rivers and Coates Creek which originate at the Niagara Escarpment (Figure 7.2).

Direct precipitation on the swamp and groundwater discharge account for 1.34 m^3/s (Table 8.14). The Nottawasaga River accumulates about 1.71 m^3/s in the wetland area (the remaining 50 % of 1.2 m^3/s, divided by 0.35), leading to a total local influx in the Minesing Basin of 3.1 m^3/s.

The model predicted baseflow and runoff to the Matheson and Willow Creeks amount to 3.01 m^3/s. These fluxes enter the Minesing Swamp as streamflow. The water mass balance is summarized in Figure (9.1). The discrepancy between the estimated inflow and outflow is 1.1 m^3/s. This error results from the remaining bias in the calibrated model with respect to measured fluxes for the Nottawasaga River (Table 8.12).

The assumptions made in the above calculations show that in order to better constrain the water mass balance of the Minesing Swamp the subwatersheds to the west of the Nottawasaga River should be included in any future study. The quantity of flow from these subwatersheds and the pathways by which water enters the Minesing Basin are uncertain factors in the calculations. It is well possible that the higher contribution attributed to the western subwatersheds solely results from streamflow. However, this extra complexity has been ignored as the main objective of the calculations is to provide insight into the relative importance of fluxes from the study area.

The calculations suggest that local fluxes (direct precipitation, runoff and baseflow) to the Minesing Basin account for about 12 % of the total inflow. The contribution of streamflow from the Willow and Matheson Creeks is nearly identical.

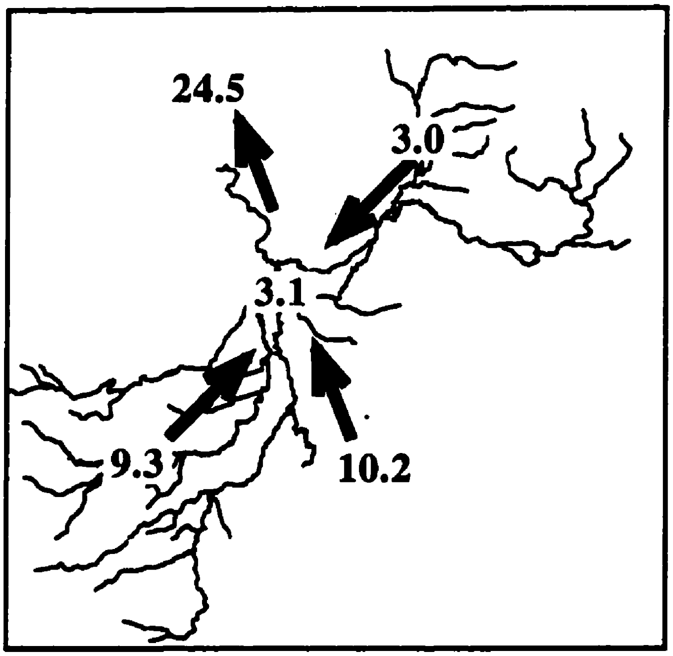

Figure 9.1: Simplified water mass balance for Minesing Swamp. Values shown are in m^3/s.

Baseflow directly to the Minesing Swamp equals 0.36 m^3/s (Table 8.14) or about 1.5 % of the total inflow. Groundwater discharge to the creeks amounts to 0.86 m^3/s, or 4 % of the total inflow. Recharge areas for these contributions to the water mass balance of the Minesing Swamp will be identified in the next section.

9.3 Recharge Areas

Figure (9.2) shows the steady-state hydraulic head distribution at the water table. The Oro Moraine is the main recharge area for the groundwater system but the Innisfill and Snow Valley Uplands are also important. Groundwater flow diverges away from these uplands in a complex topography dominated pattern. This pattern persists at depth where even in the lower aquifers the Snow Valley Upland acts as a flow divide (Figures 8.19-8.25). Water entering the groundwater system in the Oro Moraine therefore either flows towards Kempenfelt Bay or the Nottawasaga

River downstream of the Minesing Swamp. Recharge at the Innisfill Uplands will mostly discharge to the Nottawasaga River upstream of the swamp and towards Kempenfelt Bay. These observations are important for understanding the relative importance of the individual recharge areas for baseflow to the Minesing Swamp.

Similar to the hypothetical example given in Chapter (4), the importance of recharge areas for baseflow is calculated using the adjoint method. The normalized sensitivity of the baseflow F_c with respect to the local recharge rate R is determined: $dF_c/dR{\cdot}R/F_c$. This derivative reflects the percent change in baseflow resulting from a 1 % change in recharge over a unit area.

Figure (9.3) shows recharge areas for baseflow to the Minesing Swamp itself. Because direct precipitation on this wetland never enters the (deeper) groundwater system, it has no effect on the baseflow quantity. This is indicated by a negligible magnitude of the sensitivity coefficients. Similarly, precipitation near other Dirichlet boundaries will likely enter these streams as direct runoff through the recharge spreading layer. The probability for a water particle to enter the groundwater system generally increases towards the uplands. The sensitivity coefficients suggest that the Snow Valley Upland is the most important recharge area for groundwater discharge to the Minesing Swamp. The sensitivity of this baseflow to recharge from the other Uplands is orders of magnitude lower. A detailed field study by *Bradford and Watt* [1998] suggests that water entering the groundwater system in the Snow Valley Upland discharges to the Minesing Swamp through the Lake Algonquin beach bar deposits that comprise aquifer 2 along the eastern edge of the wetland (Figure 7.24). Bradford further observes subtle downward hydraulic gradients in the shallow peat layer that covers the lower-lying areas closer to the Nottawasaga River. Groundwater should therefore contribute most to the water mass balance of the eastern part of the Minesing Swamp.

Figure (9.4) illustrates recharge areas for baseflow to the Willow and Matheson Creeks. The Oro Moraine is most important for these water courses, although recharge from the Snow Valley Upland also provides a significant contribution. The Innisfill Upland provides only a minor contribution to this baseflow.

The numerical model thus predicts the Innisfill Upland to be least important for the groundwater contribution to the water balance of the Minesing Swamp. However, the discussion given earlier indicates that this conclusion is quite dependent on whether or not the Snow Valley Upland acts as a flow divide and thus on water levels in the deeper aquifers under this upland. These water levels on the

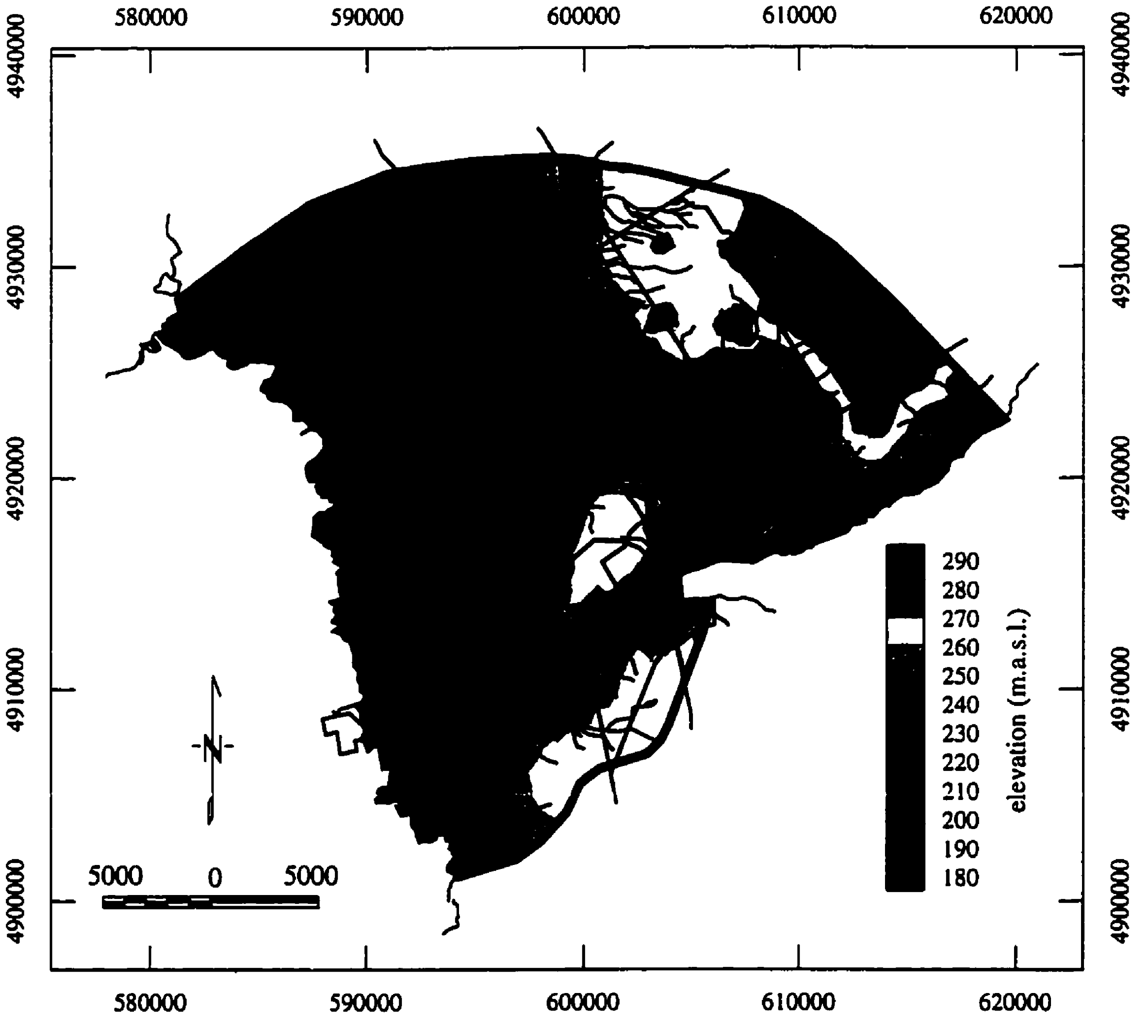
580000
590000
600000
610000
620000
4940000
4930000
4920000
4910000
4900000
N
5000
0
5000
290
280
270
260
250
240
230
220
210
200
190
180
elevation (m.a.s.l.)

Figure 9.2: Hydraulic head distribution at the water table.

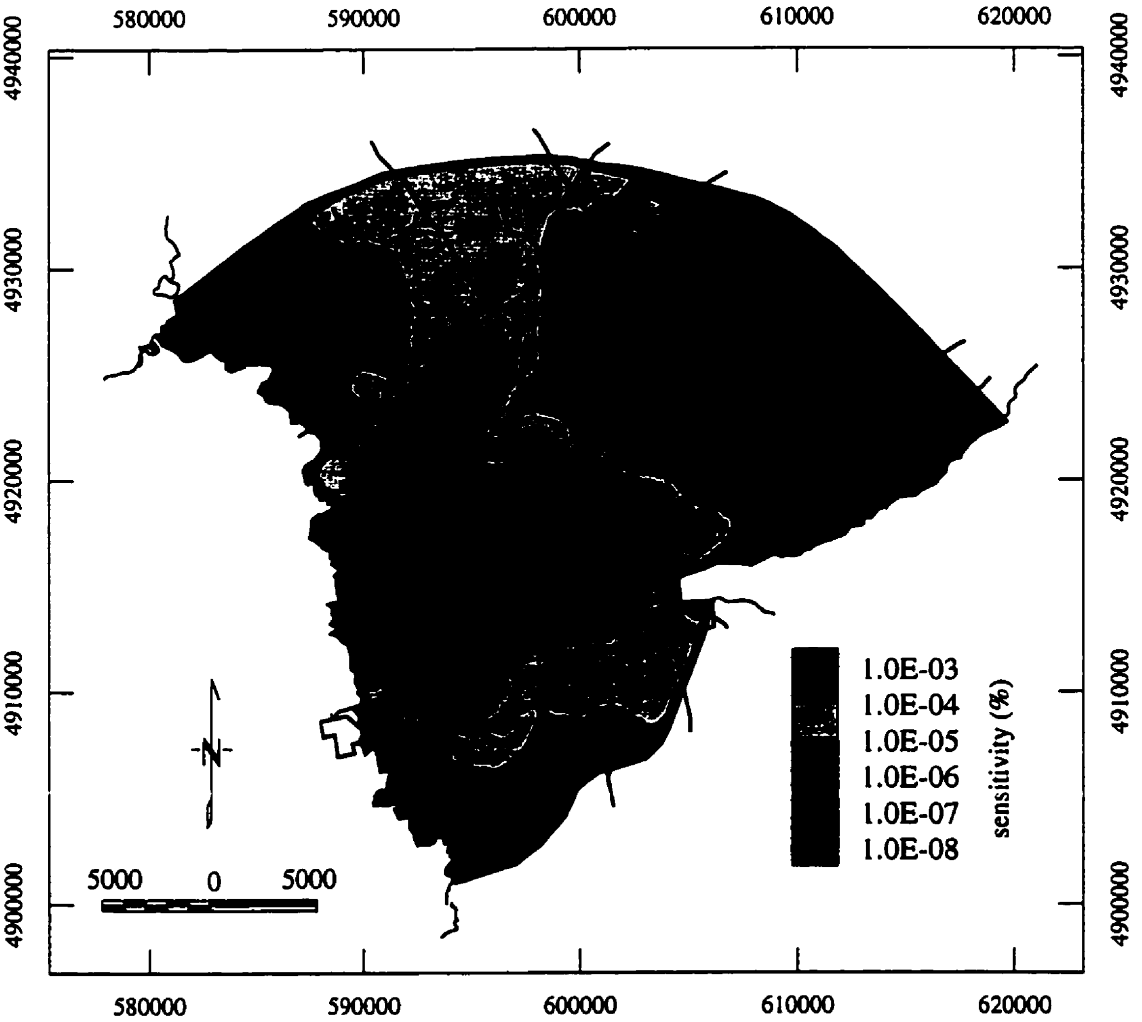
580000
590000
600000
610000
620000
4940000
4930000
4920000
4910000
4900000
N
5000
0
5000
1.0E-03
1.0E-04
1.0E-05
1.0E-06
1.0E-07
1.0E-08
sensitivity (%)

Figure 9.3: Recharge areas for baseflow to Minesing Swamp.

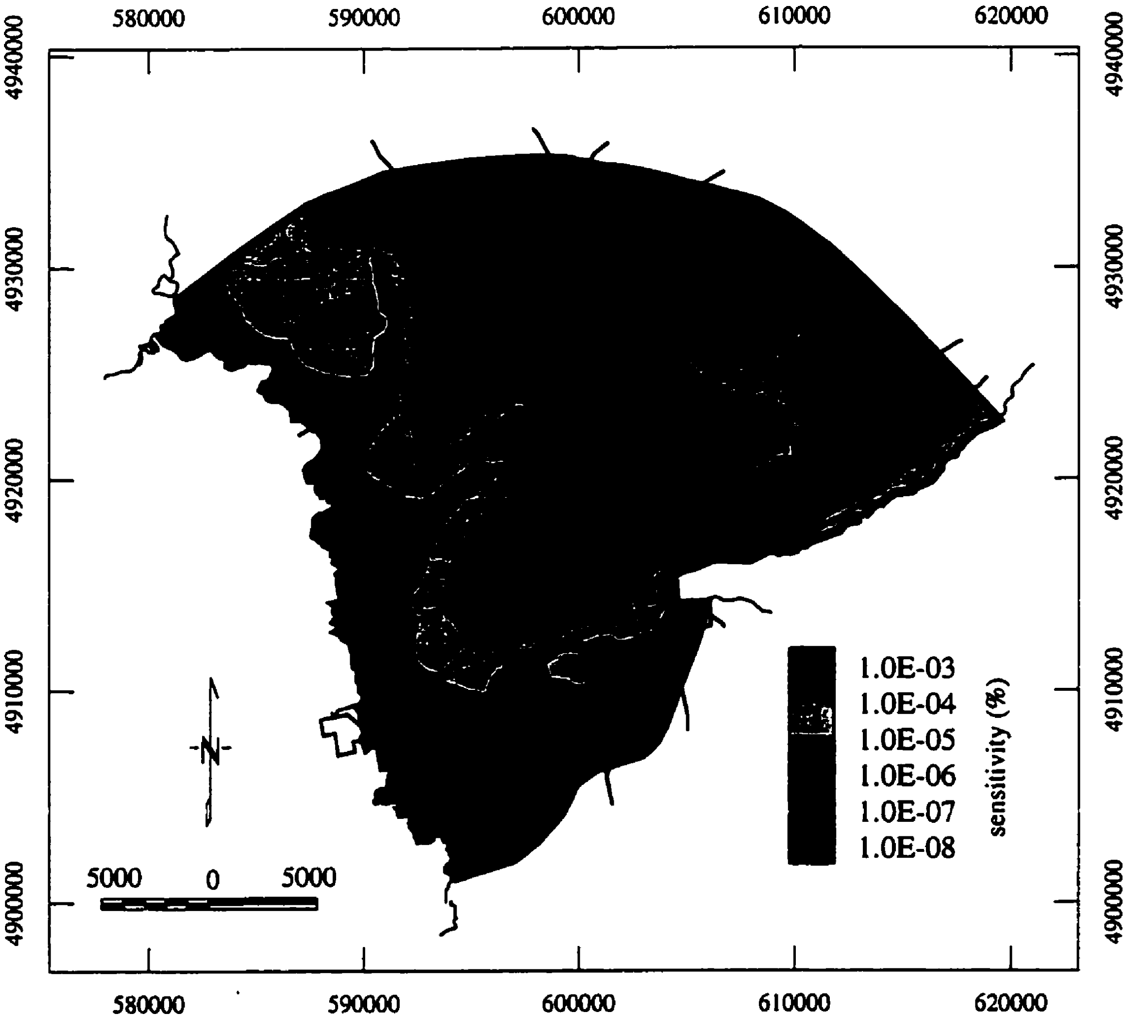
580000
590000
600000
610000
620000
4940000
4930000
4920000
4910000
4900000
N
5000 0 5000
1.0E-03
1.0E-04
1.0E-05
1.0E-06
1.0E-07
1.0E-08
sensitivity (%)

Figure 9.4: Recharge areas for baseflow to Matheson Creek and Willow Creek upstream from Minesing Swamp.

are poorly constrained by observations (Figures 8.7-8.9). A preliminary calibrated model for which water levels under the Snow Valley Upland were lower, showed the Innisfill Uplands to be more important for baseflow to the Minesing Swamp [*Beckers and Frind*, 1998]. However, a significant bias between observed and simulated hydraulic heads did remain for this earlier model. The present results are therefore more accurate.

9.4 Urbanization Impact

Hypothetical examples will be given whereby recharge over selected areas of the study domain is reduced uniformly by 10, 50 and 90 %. These values are taken to be typical of low, medium and high density urban areas, the former type of residential development being more typical for the study area. The objective of these examples is to illustrate how the model can be manipulated to simulate the impact of urban development and to illuminate some crucial characteristics of the groundwater system.

The three uplands were found to play a distinct role in groundwater flow patterns and the water mass balance of the Oro Moraine system. A target area was selected in each upland to assess the potential impact that local urban development may have on the water mass balance of the Minesing Swamp (Figure 9.5). In order to facilitate comparison of the model predictions, the target areas were made equally large, roughly comprising 7x4 km^2. All finite elements whose centroids fall within the rectangular areas are included in the analysis. Recharge is lowered over these finite elements to simulate the impact of urbanization. A certain quantity of the water surplus is thus completely removed. In reality this water would enter the water courses after being released by the stormwater collection system. Because the focus here is on the groundwater, the above approach is adequate.

Target area 1 in the Oro Moraine comprises 27 km^2 (2.8 % of whole domain). Recharge over this area is 0.37 m^3/s or 4.3 % of the total water surplus. Reduced recharge in the Oro Moraine has little effect on direct groundwater discharge to the Minesing Swamp (Table 9.1), consistent with the sensitivity analysis given in the previous section. Recharge to the Willow and Matheson Creeks is significantly affected. For the Willow Creek, contributions to the streams segments above and below Midhurst were separated to illustrate that baseflow to the headwaters is most

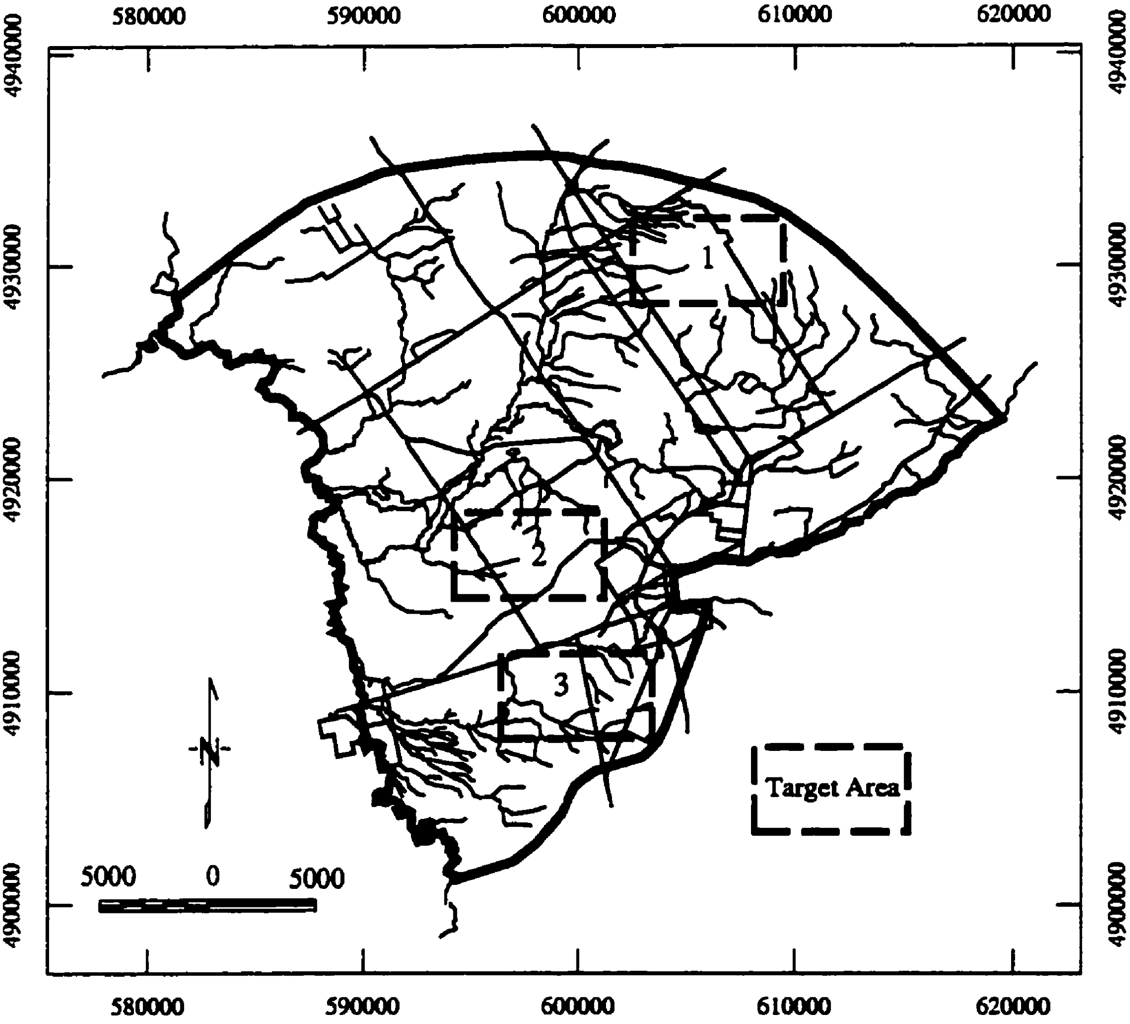

580000
590000
600000
610000
620000
4940000
4930000
4920000
4910000
4900000
1
2
3
N
5000
0
5000
Target Area

Figure 9.5: Target areas for urbanization impact calculations.

dramatically impacted by the recharge perturbations. For very large reductions, the upper reaches of Willow Creek start losing streamflow to the groundwater system. The effect of the lowered recharge on groundwater fluxes to Matheson Creek and the downstream end of Willow Creek is more subtle. Reduced fluxes to Marl Creek and the downstream end of the Nottawasaga River constitute the remaining effect of the lowered recharge.

	$\Delta R/R$						
	0%	−10%		−50%		−90%	
Bear Cr.	0.044	0.044	0%	0.044	0%	0.044	0%
Matheson Cr.	0.368	0.364	−1%	0.346	−6%	0.327	−10%
Minesing Sw.	0.361	0.361	0%	0.361	0%	0.361	0%
Willow Cr.	0.494	0.482	−2%	0.430	−13%	0.377	−24%
upstream	0.085	0.075	−12%	0.036	−57%	−0.005	−106%
downstream	0.409	0.407	−1%	0.394	−4%	0.382	−7%

Table 9.1: Urbanization impact for target area 1 in Oro Moraine. Shown are baseflow quantities (m^3/s) and percent changes with respect to unperturbed base case.

Target area 2 comprises 28 km^2 (2.9 % of whole domain). Recharge over this area is 0.30 m^3/s or 3.5 % of the total water surplus. As expected, local recharge perturbations in the Snow Valley Upland do reduce baseflow to the Minesing Swamp (Table 9.2). Groundwater discharge to Willow Creek is also lowered, again with the largest impact on the headwaters of this stream. Baseflow to Bear Creek is significantly reduced as well whereas the Matheson Creek is not affected in this case. Reduced fluxes to Kempenfelt Bay and the Nottawasaga River constitute the remaining effect of the lowered recharge. Lowered hydraulic heads near the Barrie pumping wells indicate that these wells derive part of their water from this upland.

Target area 3 comprises 28 km^2 (2.9 % of whole domain). Recharge over this area is 0.17 m^3/s or 2.0 % of the total water surplus. Infiltration losses in the Innisfill Uplands have a negligible effect on the groundwater mass balance of the Minesing Swamp (Table 9.3). However, local baseflow to Bear Creek is impacted quite dramatically. Reduced fluxes to Kempenfelt Bay and the upstream end of the Nottawasaga River constitute the remaining effect of the lowered recharge. Water

	$\Delta R/R$						
	0%	−10%		−50%		−90%	
Bear Cr.	0.044	0.044	−1%	0.039	−10%	0.035	−19%
Matheson Cr.	0.368	0.368	0%	0.368	0%	0.368	0%
Minesing Sw.	0.361	0.350	−3%	0.306	−15%	0.262	−27%
Willow Cr.	0.494	0.493	0%	0.480	−3%	0.469	−5%
upstream	0.085	0.084	−1%	0.080	−6%	0.076	−11%
downstream	0.409	0.408	0%	0.400	−2%	0.393	−4%

Table 9.2: Urbanization impact for target area 2 in Snow Valley Upland. Shown are baseflow quantities (m^3/s) and percent changes with respect to unperturbed base case.

levels near the Barrie pumping wells are also reduced.

	$\Delta R/R$						
	0%	−10%		−50%		−90%	
Bear Cr.	0.044	0.024	−44%	−0.053	−220%	−0.131	−397%
Matheson Cr.	0.368	0.368	0%	0.368	0%	0.368	0%
Minesing Sw.	0.361	0.361	−3%	0.361	−15%	0.360	−1%
Willow Cr.	0.494	0.494	0%	0.494	0%	0.494	0%
upstream	0.085	0.085	0%	0.085	0%	0.085	0%
downstream	0.409	0.409	0%	0.409	0%	0.409	0%

Table 9.3: Urbanization impact for target area 3 in Innisfill Uplands. Shown are baseflow quantities (m^3/s) and percent changes with respect to unperturbed base case.

9.5 Discussion

The hypothetical urbanization calculations suggest that low to medium density residential development will result in a modest impact on baseflow to the Minesing

Swamp. These groundwater fluxes in turn make up a relatively small fraction of the total inflow to the swamp. However, the groundwater and surface water components of the hydrologic cycle play largely different roles in the wetland ecology. Streamflow is spatially focused and subject to significant temporal variations. Groundwater provides a relatively steady inflow of water over larger portions of the wetland which may be important for nutrient cycling and for maintaining soil moisture conditions. Subtle changes in baseflow and hydraulic gradients may therefore have a large unforeseen impact on the ecology of the swamp.

The headwaters of the Willow and Bear Creek were found to be highly sensitive to local changes in infiltration. This is explained by the nature of the flow system. Part of the recharge to the uppermost aquifer leaves the groundwater system through the exposed sides of this unit along the flanks of the uplands, feeding the headwaters. The associated baseflow quantities are small and depend entirely on this shallow flow system in the upper aquifer. The headwaters are therefore easily affected by a local loss of recharge.

The Minesing Swamp, Matheson Creek and the downstream end of Willow Creek are being fed by the deeper aquifer system. These surface waters are less sensitive to local changes in infiltration because recharge is received from the other uplands as well. Furthermore, baseflow quantities in the lowlands are considerably higher and will therefore be impacted to a lesser degree by localized urban development.

The numerical model thus provides valuable insight into the behaviour of the aquifer system. The examples further illustrate how the model can be used to assess the potential impact of urban development on the groundwater system and on baseflow quantities. The benefit of using improved but more costly stormwater collection systems can be determined in a similar fashion by an appropriate manipulation of boundary conditions. In this manner, the impact of urbanization on baseflows to wetlands and streams can be managed by addressing specific development scenarios.

Chapter 10

Summary and Conclusions

The present study was initiated with a detailed investigation of the Oro Moraine multi-aquifer system as the main objective. This investigation was undertaken because the pervious sands of the Moraine are thought to be the main recharge area for subsurface drainage towards the Minesing Swamp, a 7000 hectares reserve which has been categorized as "a world class resource of international significance", owing to its diverse habitats and its numerous rare plant species. Many new subdivisions are rapidly being built in the area. Any resulting change to the groundwater system may have a detrimental impact on the Minesing Swamp. An important goal of this study therefore was to investigate the role of groundwater in the water balance of the swamp, to identify sensitive recharge areas for baseflow to this wetland, and to determine the potential impact of urbanization on this baseflow. A numerical model was established for that purpose.

The water mass balance of a wetland is characterized by both surface and subsurface contributions. Thus, another objective was to develop a modeling approach with which the relative importance of these contributions can be determined. A further important focus of this study was the implementation of an inverse algorithm in the numerical model and the testing of this algorithm in the context of the Oro Moraine study. Automated calibration is needed to obtain optimal conductivity estimates and to determine the best match to both water level and streamflow measurements. A final goal was to quantify uncertainty in the model output to determine the significance of the urbanization impact calculations. An important constraint on the numerical aspects of this study was to keep the modeling framework consistent with the methodology developed for the Waterloo Moraine study in order to incorporate concepts of automated calibration and uncertainty analysis in the delineation of capture zones for the municipal wells of the Region.

The study area was chosen to encompass all subwatersheds that drain towards the Minesing Swamp from the surrounding uplands to the east. The dominant physiographic features within the study area have been formed by extensive glacial activity. The Oro or Bass Lake Moraine, the Innisfill Uplands and the Ski Valley area are part of the Simcoe Uplands. These broad rolling till plains are separated by steep-sided stream valleys and are bordered to the west by the Minesing Basin which is part of the Simcoe Lowlands. The Minesing Swamp is located within this basin. Willow Creek is the largest water course within the study area. It flows from the Oro Moraine towards the Nottawasaga River. Other streams are the Matheson, Bear and Marl Creeks. The southeast section of the study area is bounded by Kempenfelt Bay (Lake Simcoe).

The geologic history of the study area is complex. The overburden deposits rest on a bedrock surface that is mainly comprised of limestone. In the Simcoe Uplands, the overburden is entirely comprised of materials of glacial origin. Some of the steep-sloped valleys that are part of the Simcoe Lowlands are thought to have been formed by a catastrophic release of glacial meltwater. Coarse grained high conductivity materials are found at the bottom of these so-called Tunnel Valleys. These materials are then overlain by post-glacial deposits related to ancient Lake Algonquin. The makeup of the overburden in the Simcoe Uplands and Lowlands is thus quite different.

The hydrostratigraphy of the aquifer system was interpreted making use of a total of 619 boreholes and 64 cross-sections. The conceptual model of the overburden that was used throughout this interpretation is a system of 4 aquifers and 4 aquitards, consistent with constraints from previous hydrogeologic investigations. The bedrock surface shows a gradual $SW - NE$ increase in elevation from the Minesing Basin towards the Oro Moraine. The hydrostratigraphic contacts generally dip in the same direction, as a result of the dominant south-southwest direction of ice movement. The predicted outcrop of the hydrostratigraphic units appears to be in reasonable agreement with surficial materials shown on Quaternary geologic maps. Aquitard 1 provides a surficial till cover in the uplands. Aquifer 1 also only exists in the uplands but is very pronounced with a maximum thickness exceeding 80 m. Aquitard 2 has been interpreted to cover most of the lowlands. The semi-confined Aquifer 2 outcrops in the Matheson Creek valley and the Minesing

Swamp, areas that are associated with the margins of Lake Algonquin. Geologic information from outside the study area suggests that at greater depth there are possibly 2 more layers of till. These older layers of till constitute the deeper 2 confining units. Information regarding the makeup of these deeper units is limited to 6 boreholes drilled by the Ontario Geologic Survey. An important contribution of the present study therefore is to provide valuable insight into the hydrostratigraphy. Such knowledge was previously limited to selected locations in the study area.

When the surficial geology is strongly heterogeneous, as in the case of the Oro Moraine, the recharge mechanism is complex. The physical processes above the water table are ignored in the free-surface models that are typically used in watershed-scale investigations. An alternative modeling approach was therefore used to address these concerns and to provide a steady state simulation of both surface and subsurface water fluxes. This latter aspect is important with regard to constraining the water mass balance of the Minesing Swamp. This approach consists of coupling a pseudo-unsaturated model with a so-called recharge spreading layer.

In the pseudo-unsaturated model, a simple exponential relationship is used to describe the saturation of the porous medium in the vadose zone, and the relative permeability is set equal to this pseudo-saturation. A hypothetical example of a multi-aquifer system was used to show that under heterogeneous near-surface conditions a pseudo-unsaturated model better predicts the recharge mechanism than can be achieved with a free-surface model which ignores the vadose zone. The pseudo-unsaturated model was also compared to a true variably saturated model. Discrepancies between the two models mainly arise from the coarser mesh used in the pseudo-unsaturated simulations. Differences in predicted flow regimes below the water table, which are the focus of interest, are only minor. The pseudo-unsaturated representation thus provides a viable modeling alternative, better representing the recharge mechanism than free-surface models, while maintaining computational efficiency as compared to variably saturated models.

The recharge spreading layer is used to simulate the process of rainfall runoff by redistributing recharge atop the model domain. Although such a high conductivity layer has been used in the past to simulate infiltration for fractured or heterogeneous porous media, no constraints were imposed on the fluid fluxes in this layer. However, the recharge spreading layer conductivity was found to be very important for the model simulations. In the present study, the fluxes in this layer are therefore compared to the runoff component of measured streamflows. The Oro Moraine model was calibrated using these runoff constraints as well as baseflow and water level measurements.

The calibration was performed using an inverse algorithm that was developed based on existing theory. The inverse model uses a minimization algorithm that consists of an unconstrained Gauss-Newton iterative search with a subsequent imposing of upper and lower bounds on the estimated parameters. Hydraulic conductivity values presently are the only adjustable parameters. The parameterization of the conductivity field may either consist of a zonation or a combined zonation/pilot point approach. This appears to be the first application of such a joint parameterization. Kriging is used to calculate the effect of the pilot points on the conductivity distribution in their zone of influence. The covariance of the zonal conductivity estimates is computed using a standard first-order second-moment analysis, making use of the final calibration statistics. The covariance of the kriged conductivity fields is derived from the geostatistical parameters and the conductivity data through conditional probability.

The zonation was derived from the hydrostratigraphic interpretation of the multi-aquifer system. Adjustable parameters are either the average conductivities of the hydrostratigraphic units or point conductivity values within these units. In the first phase of the calibration, average conductivities were optimized to account for any bias introduced as a result of using the lithologic descriptions to spatially distribute conductivity. The pilot points were used to achieve local conductivity updates within the hydrostratigraphic units to refine the model calibration.

Two new least-squares performance measures were introduced as part of the development of the inverse model. The first is a measure based on kriged heads rather than point water level observations. The second calibration measure uses calculated fluxes to certain Dirichlet boundaries that are incorporated in the model to simulate the presence of streams and other surface water bodies.

Kriged heads were found to better constrain the groundwater flow system and put tighter bounds on the conductivity distribution, thus reducing model uncertainty. This is achieved by filling in the missing head information between the individual point water level data. Because hydraulic head variations tend to be gradual, kriging can adequately represent this spatial variability. Furthermore, the kriged heads are less susceptible to noise than the data values themselves as the effect of random noise is to some degree eliminated in the interpolation.

The head calibration was found to be satisfactory although some local discrepancies remain. Simulated heads were found to under-predict observed water levels in the Oro Moraine area. This was attributed to the pronounced outcrop of the uppermost aquifer along the eastern slope of the Matheson Creek valley. Calibration results further suggest that the lowermost aquitard unit is less continuous than was inferred in the hydrostratigraphic interpretation. The conceptual model of the aquifer system was therefore revised by lumping the lower two aquifers into a single unit. This unit is known from previous investigations as the Alliston aquifer complex, which has been suggested to extend from the Oak Ridges Moraine to Georgian Bay.

Observed baseflow and runoff provide crucial information on the distribution of recharge between the surface and subsurface systems. Data from four stream gauge stations located along the Nottawasaga River and in the upper reaches of Willow Creek were obtained. Contributions to the streamflow accumulation in the Nottawasaga River arrive from the Minesing Swamp as well as the Bear, Marl, Matheson and Willow Creeks. The calibration results indicate that the numerical model is able to accurately simulate observed steady state runoff and baseflow. The relative contribution of baseflow and runoff to the total observed streamflows remains somewhat uncertain in the present steady-state analysis. Transient simulations of the flow system are needed to determine the origin of seasonal variations in streamflow generation and to better constrain the relative importance of surface and subsurface fluxes.

Baseflow from the Innisfill Uplands accounts for only 8 % of the total fluxes to Bear Creek. Both model simulations and stream gauge data show that groundwater also does not contribute significantly to the upper reaches of Willow Creek. The model predicts the baseflow component to increase sharply where the Willow Creek enters the Simcoe Lowlands, downstream of Midhurst. In general, baseflow quantities are found to be higher in the Minesing Basin. Groundwater is also important for the "cold water" Matheson Creek which is considered an important fish habitat.

Overall, the groundwater component accounts for 34 % of the total water budget. Recharge was calculated from spatially variable precipitation data while assuming a uniform evapotranspiration rate. No attempt was made to determine a spatially variable evapotranspiration as the effect of the non-uniform water surplus on the model calibration was found to be subtle. The water mass balance for the calibrated model indicates that pumping accounts for about 10 % of the total water budget and for about 30 % of the groundwater component. Water abstraction from private water wells is an important unknown factor in the water mass balance of the Oro Moraine system. More detailed information on pumping activity in the study area therefore needs to be collected.

Groundwater fluxes to Kempenfelt Bay are most likely under-predicted because the model allows the Barrie municipal wells to derive part of their water from lake Simcoe. Flow of groundwater from the surrounding upland areas to the these pumping wells should be facilitated. This mechanism could be provided by the inclusion of the Barrie-Borden aquifer in the conceptual model. Due to a lack of data constraining its geometry, this Tunnel Valley aquifer was not included in the present conceptual model. Increased flow towards the Barrie area would reduce fluxes to the Minesing Basin. This calibration discrepancy therefore to some degree affects the simulated water mass balance of the Minesing Swamp.

The model calibration and mass balance results illustrate that the hydrostratigraphy plays a crucial role in modeling the multi-aquifer system. These results further suggest that in refining the numerical model a first step should be a re-evaluation of some of the geologic data and a revision of the conceptual model to account for the different geologic history of the Simcoe Lowlands. However, in general the present hydrostratigraphic model already provides an adequate representation of the multi-aquifer system.

The hypothetical urbanization calculations suggest that low to medium density residential development will result in a modest impact in baseflow to the Minesing Swamp. These direct groundwater fluxes in turn make up a relatively small fraction of the total inflow to the swamp. However, the groundwater and surface water components of the hydrologic cycle play different roles in wetland ecology. Streamflow is spatially focused and subject to significant temporal variations. Groundwater provides a relatively steady inflow of water over larger portions of the wetland which may be important for nutrient cycling and for maintaining soil moisture conditions. Subtle changes in baseflow and hydraulic gradients may therefore have a large unforeseen impact on the ecology of the swamp.

The headwaters of the Willow and Bear Creek were found to be quite sensitive to local changes in infiltration. The associated baseflow quantities are small and depend entirely on this shallow flow system in the upper aquifer. The Minesing Swamp, Matheson Creek and the downstream end of Willow Creek are being fed by the deeper aquifer system. These surface waters are therefore less sensitive to local changes in recharge. The numerical model thus provides valuable insight into the behaviour of the aquifer system.

The available streamflow measurements put limited constraints on details of the water mass balance, such as contributions from individual streams to the observed total accumulation for the Nottawasaga River. This limitation affects the reliability of the water mass balance and the urbanization impact calculations. A preliminary stochastic analysis suggests that these calculations are subject to considerable uncertainty. More stream gauge measurements are therefore crucial in refining the Oro Moraine model.

Uncertainty in the conductivity distribution was taken into consideration through a first order second moment analysis. Through a comparison with Monte Carlo simulations it was shown that model non-linearity and the role of the calibration data are not yet adequately addressed in the uncertainty analysis. Monte Carlo simulations do not provide a viable alternative for a detailed stochastic analysis due to the high computational cost associated with the need to calibrate every realization of the conductivity fields. The calculation of true confidence intervals for the water mass balance was not possible as a result of the combined zonation/kriging conductivity parameterization. The likelihood method has the potential of providing a cost-effective and accurate alternative but the use of this method would require that the conductivity parameterization is modified to a strictly zonation-based approach. Such an approach is not favored because it is difficult to identify zones of similar hydrogeologic properties in a lateral sense. This problem was circumvented by using a combined zonation/geostatistical parameterization. This parameterization should therefore be maintained even though it does not allow for a detailed stochastic analysis.

Compared to the Waterloo Moraine study, several advances have been made from a numerical perspective. A pseudo-unsaturated model was developed that provides an appealing alternative to the mesh deformation that was previously used. Because the coupling with the recharge spreading layer is now achieved at the land surface, the runoff component of measured streamflows can be used to constrain the distribution of fluxes in this layer. The pseudo-unsaturated model also allows for a fixed mesh which is appealing in the context of the model calibration. The manual trial-and-error calibration that was used for the Waterloo Moraine model was replaced by an automated inversion. This ensures that optimum conductivity values are determined. This enables the user to objectively compare alternative modeling scenarios, as illustrated by the Oro Moraine example. Such a comparison is a crucial part of any model calibration. Optimal parameter estimates are also important in the context of an uncertainty analysis. Although some progress was made, this stochastic analysis was largely hampered by limitations imposed by the model parameterization. However, the sensitivity of the model calibration to the hydrostratigraphy suggests that the lack of information regarding the location of the aquifer/aquitard contacts is the most important factor governing model uncertainty. This source of uncertainty can be considered, although in a limited fashion, by determining the effect of certain extreme model scenarios, such as the opening or closing of aquitard windows. Such an approach was already taken as part of the Waterloo Moraine investigation.

Insight was provided into data and other requirements to further refine the Oro Moraine model. Information on the tunnel valley aquifer systems is needed. Delineating these aquifers is important if the detailed identification of groundwater flow paths is of concern, such as for the identification of water well capture zones. Given the lack of high quality deep borehole information constraining the geometry of the tunnel valley aquifers, geophysical data would be useful. Seismic profiling is an excellent tool for delineating the hydrostratigraphy of the (glacial) overburden.

The poorly determined borehole elevations and the resulting uncertainty in the water level measurements are important factors limiting the model reliability. It is therefore crucial that the borehole elevations are more accurately determined, either by using digital topographic information or through a field survey of a number of key boreholes. The crucial role of the poorly resolved geostatistical parameters of the conductivity distribution in the model calibration and uncertainty analysis was found to be a point of concern. Direct measurements of hydraulic conductivity from pumping or slug tests are needed to better constrain subsurface hydrogeologic properties and to more precisely determine the geostatistical parameters. Additional information on water abstraction from municipal and private pumping wells should also be collected to better constrain the system water mass balance. Additional gauging data for presently non-monitored streams are required to provide insight into details of this mass balance. Crucial dynamics of the aquifer system are revealed by its response to pumping tests as well as by seasonal variations in water levels and streamflow generation. A calibration of the model to such transient data will put tighter limits on the conductivity distribution, better constraining groundwater fluxes and reducing model uncertainty.

The Oro Moraine model may in the future be used for groundwater quantity related land use planning. Furthermore, the City of Barrie is presently considering a groundwater resources investigation for new municipal wells in the Willow Creek valley. Important issues are the optimal management of these wells, the delineation of their capture zones and an investigation into the potential for interference with baseflow to the sensitive Willow Creek headwaters. The hydrogeologic characterization of the study area and the resulting numerical model provide a valuable basis for such applications.

Bibliography

Abbot, M. B., *Computational hydraulics - elements of the theory of free surface flows*, Pitman, Boston, MA, 1979.

Ackerer, P., M. Esteves, and R. Kohane, Modelling interactions between groundwater and surface water: a case study, in Computational methods in subsurface hydrology: proceedings of the eighth international conference on computational methods in water resources, 72–82, Venice, Italy, June 11-15, 1990.

ASTM, *Annual book of ASTM standards*, Periodical by American Society for Testing and Materials, Philadelphia, 1997.

Bakr, A. A., L. W. Gelhar, A. L. Gutjahr, and J. R. MacMillan, Stochastic analysis of spatial variability in subsurface flows 1. Comparison of one- and three-dimensional flows, *Water Resour. Res.*, *14*(2), 263–271, 1978.

Barnett, P. J., Tunnel valleys: evidence of catastrophic release of subglacial meltwater, central-southern Ontario, in Abstracts with programs, 3, Northeastern section Geol. Soc. Amer., Syracuse, New York State, 1990.

Barnett, P. J., Preliminary report on the stratigraphic drilling of Quaternary sediments in the Barrie area, Simcoe County, Ontario, Ontario Geological Survey, Open File Report 5755, 1991.

Barnett, P. J., Quaternary geology of the eastern half of the Barrie and Elmvale map areas, Ontario Geological Survey, Open File Map 200, scale 1:50000, 1992.

Bathe, K. J., and M. R. Khosgoftaar, Finite element free surface seepage analysis without mesh iteration, *Int. J. Num. Anal. Meth. Geom.*, *3*, 13–22, 1979.

Bear, J., *Dynamics of fluids in porous media*, Dover Publications Inc., New York, NY, 1972.

Beckers, J., and E. O. Frind, Hydrogeologic investigation of the Oro Moraine multi-aquifer system, in Groundwater in a watershed context, Canada Center for Inland Waters, Burlington, Ontario, Dec 2-4, 1998.

Benjamin, J. R., and C. A. Cornell, *Probability, statistics and decision for Civil Engineers*, Mc.Graw-Hill, New York, NY, 1970.

Bradford, A. L., and W. E. Watt, Hydrogeological and other controls on the distribution of plant communities at Minesing Swamp, Ontario, Canada, in GSA 1998 Annual Meeting, Toronto, Oct 26-29, 1998.

Braess, D., and C. König, A fast conjugate gradient algorithm for three-dimensional groundwater flow problems, Ruhr-Universitat Bochum, Germany, 1995.

Burwasser, G. J., and S. T. Boyd, Quaternary Geology of the Orr Lake area, (western half) - Nottawasaga area (eastern half), Southern Ontario, Ontario Division of Mines, Preliminary Map P.975, Geol. Ser. scale 1:50000, 1974.

Burwasser, G. J., and B. D. Cairns, Quaternary Geology of the Barrie Lake area, (western half), Southern Ontario, Ontario Division of Mines, Preliminary Map P.978, Geol. Ser. scale 1:50000, 1974.

Burwasser, G. J., and M. J. Ford, Bedrock topography of the Barrie area, southern Ontario, Ontario Division of Mines, Preliminary Map P.979, scale 1:50000, 1974b.

Burwasser, G. J., and M. J. Ford, Bedrock topography of the Orr Lake area, southern Ontario, Ontario Division of Mines, Preliminary Map P.976, scale 1:50000, 1974a.

Burwasser, G. J., and M. J. Ford, Drift thickness of the Barrie area, southern Ontario, Ontario Division of Mines, Preliminary Map P.980, scale 1:50000, 1974c.

Burwasser, G. J., and M. J. Ford, Drift thickness of the Orr Lake area, southern Ontario, Ontario Division of Mines, Preliminary Map P.977, scale 1:50000, 1974d.

Cacuci, D. G., Sensitivity theory for non-linear systems, I, Nonlinear functional analysis approach, *J. Math. Phys.*, *22*, 2794–2802, 1981.

Carrera, J., and S. P. Neuman, Estimation of aquifer parameters under steady state conditions 1. Maximum likelihood method incorporating prior information, *Water Resour. Res.*, *22*(2), 199–210, 1986a.

Carrera, J., and S. P. Neuman, Estimation of aquifer parameters under steady state conditions 2. Uniqueness, Stability and Solution Algorithms, *Water Resour. Res.*, *22*(2), 211-227, 1986b.

Carrera, J., and S. P. Neuman, Estimation of aquifer parameters under steady state conditions 3. Application to synthetic and field data, *Water Resour. Res.*, *22*(2), 228–242, 1986c.

Celia, M. A., E. T. Bouloutas, and R. L. Zarba, A general mass-conservative numerical solution for the unsaturated flow equation, *Water Resour. Res.*, *26*(7), 1483–1496, 1990.

Chapman, L. J., and D. F. Putnam, *The physiography of southern Ontario*, Ontario Geological Survey, Special Volume 2, 1984.

Chavent, G., M. Dupuy, and P. Lemonnier, History matching by use of optimal theory, *Soc. Petrol. Eng. J.*, *15*(1), 74–86, 1975.

Chiew, F. H. S., T. A. McMahon, and I. C. O'Neill, Estimating groundwater recharge using an integrated surface and groundwater modelling approach, *Journal of Hydrology*, *131*, 151–186, 1992.

Clifton, P. M., and S. P. Neuman, Effects of kriging and inverse modeling on conditional simulation of the Avra Valley aquifer in Southern Arizona, *Water Resour. Res.*, *18*(4), 1215–1234, 1982.

Cooley, R. L., A method of estimating parameters and assessing reliability for models of steady groundwater flow, 1, Theory and numerical properties, *Water Resour. Res.*, *13*(2), 603–617, 1977.

Cooley, R. L., Incorporation of prior information into nonlinear regression groundwater models 1. Theory, *Water Resour. Res.*, *18*(4), 965–976, 1982.

Cooley, R. L., Confidence intervals for ground-water models using linearization, likelihood and bootstrap methods, *Groundwater*, *35*(5), 869–880, 1997.

Cooley, R. L., and R. L. Naff, Regression modeling of ground-water flow, in U.S. Geological Survey techniques in water-resources investigations, book 3, chapter B4, 232 p, 1990.

Cordes, C. Bahnkurven in potentialstromung. Ph.D. thesis, Fachbereich bauingenieure, Universitat Kassel, Germany, 1994.

Dagan, G., Models of groundwater flow in statistically homogeneous porous formations, *Water Resour. Res.*, *15*(1), 47-63, 1979.

Dagan, G., Stochastic modeling of groundwater flow by unconditional and conditional probabilities 2. The solute transport, *Water Resour. Res.*, *18*(4), 835–848, 1982a.

Dagan, G., Stochastic modeling of groundwater flow by unconditional and conditional probabilities 1. Conditional simulation and the direct problem, *Water Resour. Res.*, *18*(4), 813-833, 1982b.

Dagan, G., Solute transport in heterogeneous porous formations, *J. Fluid. Mech.*, *145*, 151-177, 1984.

Davis, J. C., ***Statistics and data analysis in Geology***, J Wiley and Sons, New York, NY, 1986.

de Marsily, G., Spatial variability of properties in porous media: A stochastic approach, in Fundamentals of transport phenomena in porous media, edited by J. Bear, and M. Corapcioglu, *NATO-ASI Ser. E (82)*, 721–769, 1984.

Deane, R. E., *Pleistocene geology of the Lake Simcoe District, Ontario*, Geological Survey of Canada, Memoir 256, 1950.

Delfiner, P., Linear estimation of non stationary spatial phenomena, in Advanced geostatistics in the mining industry, edited by M. Guarascio, 49–68, D Reidel, Hingham, Mass, 1975.

Delhomme, J. P., Kriging in the hydrosciences, *Adv. Water Resour.*, *1*(5), 251-266, 1978.

Delhomme, J. P., Spatial variability and uncertainty in groundwater flow parameters: A geostatistical approach, *Water Resour. Res.*, *15*(2), 269–280, 1979.

Desai, C. S., and G. C. Li, Transient free surface flow through porous media using a residual procedure, in Proc. 4th Int. Symp. on Finite Element Methods in Flow Problems, 621–632, Tokyo, July, 1982.

Dettinger, M. D., and J. L. Wilson, First order analysis of uncertainty in numerical models of groundwater flow part 1. Mathematical development, *Water Resour. Res.*, *17*(1), 149–161, 1981.

Deutsch, C. V., and A. G. Journel, *GSLIB: Geostatistical Software Library and User's guide*, Oxford University Press, New York, 1992.

Diersch, H. J. G., Treatment of free surfaces in 2D and 3D groundwater modeling, submitted to, *Mathematische Geologie*,, 1997.

Dixon Hydrogeology, Oro seventh line Aggregate pits hydrogeology study, 1992.

Doherty, PEST, Watermark Computing, Corinda, Australia, 278 pp, 1994.

Easton, J., Willow Creek tunnel valley aquifer, Simcoe County, in Groundwater in a watershed context, Canada Center for Inland Waters, Burlington, Ontario, Dec 2-4, 1998.

Environment Canada, Atmospheric Environment Service, Climate of Southern Ontario, 1980.

Environment Canada, Atmospheric Environment Service, Canadian Climate Normals, 1951-1980: temperature and precipitation - Ontario, 1982.

Environment Canada, Water Resources Branch, HYDAT CD-ROM version 3.0, surface water data to 1990, 1990.

Environment Canada, Atmospheric Environment Service, Canadian Climate Normals - Ontario, 1961-1990, 1993.

Eyles, N., J. Boyce, and A. A. Mohajer, The bedrock surface of the western Lake Ontario region: evidence of reactivated basement structures?, *Geographie Physique et Quaternaire*, *47*(3), 269–283, 1993.

Fleming, S., The valley of the Nottawasaga, *Canadian Journal*, *1*, 223–226, 1853.

Fogg, G., Groundwater flow and sand body interconnectedness in a thick multiple aquifer system, *Water Resour. Res.*, *22*(5), 679–694, 1986.

Freeze, R. A., A stochastic-conceptual analysis of one-dimensional groundwater flow in nonuniform homogeneous media, *Water Resour. Res.*, *11*(5), 725–741, 1975.

Freeze, R. A., and J. A. Cherry, *Groundwater*, Prentice-Hall, Englewood Cliffs, NJ, 1979.

Freeze, R. A., and P. A. Witherspoon, Theoretical analysis of regional groundwater flow: 2. Effect of water-table configuration and subsurface permeability variation, *Water Resour. Res.*, *3*, 623–634, 1967.

Freyberg, D. L., A natural gradient experiment on solute transport in a sand aquifer 2. Spatial moments and the advection and dispersion of nonreactive tracers, *Water Resour. Res.*, *22*(13), 2031–2046, 1986.

Frind, E. O., G. B. Matanga, and J. A. Cherry, The dual formulation of flow for contaminant transport modeling 2. The Borden aquifer, *Water Resour. Res.*, *21*(2), 170–182, 1985.

Gavelas, G. R., P. C. Shah, and J. H. Seinfeld, Reservoir history matching by Bayesian estimation, *Soc. Petrol. Eng. J.*, *16*(6), 337, 1976.

Gelhar, L. W., Effects of hydraulic conductivity variations on groundwater flows, in Second International Symposium on Stochastic Hydraulics, Int. Ass. for Hydraul. Res., Lund, Sweden, Aug 2-4, 1976.

Gelhar, L. W., and C. L. Axness, Three-dimensional stochastic analysis of macrodispersion in aquifers, *Water Resour. Res.*, *19*(1), 161–180, 1983.

Gelhar, L. W., A. A. Bakr, A. L. Gutjahr, and J. R. MacMillan, Comments on 'A stochastic conceptual analysis of one dimensional groundwater flow in nonuniform homogeneous media' by R Allen Freeze, *Water Resour. Res.*, *13*(2), 477–479, 1977.

Gerber, R., Recharge analysis for the central portion of the Oak Ridges Moraine, M.Sc. thesis, Dept. of Geology, University of Toronto, 1994.

Giammarco, P. D., E. Todini, and P. Lamberti, A conservative finite elements approach to overland flow: the control volume finite element formulation, *Journal of Hydrology*, *175*, 267–291, 1996.

Gillham, R. W., and R. N. Farvolden, Sensitivity analysis of input parameters in numerical modeling of steady state regional groundwater flow, *Water Resour. Res.*, *10*(3), 529–538, 1974.

Gomez-Hernandez, J. J., and S. M. Gorelick, Effective groundwater model parameters: influence of spatial variability of hydraulic conductivity, leakance and recharge, *Water Resour. Res.*, *25*(3), 4–5–419, 1989.

Gutjahr, A. L., and L. W. Gelhar, Stochastic models of subsurface flow: Infinite versus finite domains and stationarity, *Water Resour. Res.*, *17*(2), 337–350, 1981.

Gutjahr, A. L., L. W. Gelhar, A. A. Bakr, and J. R. MacMillan, Stochastic analysis of spatial variability in subsurface flows 2. Evaluation and Application, *Water Resour. Res.*, *14*(5), 953–960, 1978.

Hill, M. C., Methods and guidelines for effective model calibration, Technical report, USGS water-resources investigations report 98-4005, 1998.

Hinton, M. J., S. E. Pullan, J. A. Hunter, A. Pugin, H. A. J. Russel, D. S. Sharpe, L. D. Dyke, and P. J. Barnett, Regional scale integration of geophysical, geological and hydrogeological data in glacial sediments, in AGU 1997 Fall Meeting, EOS, Transactions 78(46), F318, 1997.

Hoeksema, R. J., and P. K. Kitanidis, An application of the geostatistical approach to the inverse problem in two-dimensional groundwater modeling, *Water Resour. Res.*, *20*(7), 1003–1020, 1984.

Hoeksema, R. J., and P. K. Kitanidis, Analysis of the spatial structure of properties of selected aquifers, *Water Resour. Res.*, *21*(5), 563–572, 1985a.

Hoeksema, R. J., and P. K. Kitanidis, Comparison of gaussian conditional mean and kriging estimation in the geostatistical solution of the inverse problem, *Water Resour. Res.*, *21*(6), 825–836, 1985b.

Huyakorn, P. S., and G. F. Pinder, *Computational methods in subsurface flow*, Academic Press, Orlando, Fla, 1983.

Huyakorn, P. S., E. P. Springer, V. Guvanasen, and T. D. Wadsworth, A three-dimensional finite-element model for simulating water flow in variably saturated porous media, *Water Resour. Res.*, *22*(13), 1790–1808, 1986.

Iman, R. L., and W. J. Conover, Small sample sensitivity analysis techniques for computer models with an application to risk assessment, *Commun. Statist. Theor. Meth.*, *A9*(7), 1749–1842, 1980.

Johnson, N. M., and S. J. Dreis, Hydrostratigraphic interpretation using indicator geostatistics, *Water Resour. Res.*, *25*(12), 2501–2010, 1989.

Journel, A. G., and F. Alabert, Focussing on spatial connectivity of extreme-valued attributes: stochastic indicator models of reservoir heterogeneity, *SPE Tech. Pap.*, *18324*, 1987.

Journel, A. G., and C. J. Huijbregts, *Mining geostatistics*, Academic Press, New York, 1978.

Keidser, A., and D. Rosbjerg, A comparison of four inverse approaches to groundwater flow and transport parameter identification, *Water Resour. Res.*, *27*(9), 2219–2232, 1991.

Kitanidis, P. K., and E. G. Vomvoris, A geostatistical approach to the inverse problem in groundwater modeling (steady state) and one-dimensional simulations, *Water Resour. Res.*, *19*(3), 677–690, 1983.

Knupp, P., A moving mesh algorithm for 3-D regional groundwater flow with water table and seepage face, *Adv. Water Resour.*, *19*(2), 83–95, 1996.

Koltermann, C. E., and S. M. Gorelick, Heterogeneity in sedimentary deposits: a review of structure-imitating, process-imitating and descriptive approaches, *Water Resour. Res.*, *32*(9), 2617–2658, 1996.

LaVenue, A. M., R. W. Andrews, and B. S. RamaRao, Groundwater travel time uncertainty analysis using sensitivity derivatives, *Water Resour. Res.*, *25*(7), 1551–1566, 1989.

LaVenue, A. M., and J. F. Pickens, Application of a coupled adjoint sensitivity and kriging approach to calibrate a groundwater flow model, *Water Resour. Res.*, *28*(6), 1543–1569, 1992.

LaVenue, A. M., B. S. RamaRao, G. de Marsily, and M. G. Marietta, Pilot point methodology for automated calibration of an ensemble of conditionally simulated transmissivity fields 2. Application, *Water Resour. Res.*, *25*(7), 495–515, 1995.

Law, J., A statistical approach to the interstitial heterogeneity of sand reservoirs, *Trans. AIME*, *155*, 202–222, 1944.

Li, J., A. Lu, N. Z. Sun, and W. W. W. Yeh, A comparative study of sensitivity coefficient calculation methods in groundwater flow, in Porceedings of the sixt international conference on finite elements in water respurces, Lisbon, Portugal, edited by J. Bear, and M. Corapcioglu, 346–358, 1986.

Luenberger, D., *Introduction to linear and nonlinear programming*, Addison-Wesley, Reading, Mass., 1973.

Mackay, D. M., D. L. Freyberg, P. V. Roberts, and J. A. Cherry, A natural gradient experiment on solute transport in a sand aquifer 1. Approach and overview of plume movement, *Water Resour. Res.*, *22*(13), 2017–2029, 1986.

Martin, P. J., Modeling of the North Waterloo multi-aquifer system, M.Sc. thesis, Dept. of Earth Sciences., University of Waterloo, 1994.

Martin, P. J., and E. O. Frind, Modeling a complex multi-aquifer system: The Waterloo Moraine, *Groundwater*, *36*(4), 679–690, 1998.

Matheron, G., The intrinsic random functions and their applications, *Adv. Appl. Prob.*, *5*(3), 439–468, 1973.

McDonald, M. G., and A. W. Harbaugh, A modular three-dimensional finite-difference ground-water flow model, *U.S. Geological Survey*, *Open-File Report 83-875*, 1988.

McLaughlin, D., and L. R. Townley, A reassessment of the groundwater inverse problem, *Water Resour. Res.*, *32*(5), 1131–1161, 1996.

Mitchell-Bruker, S., and H. M. Haitjema, Modeling steady state conjunctive groundwater and surface water flow with analytic elements, *Water Resour. Res.*, *32*(9), 2725–2732, 1996.

MOE, Major aquifers in Ontario: Alliston aquifer complex, Prepared by the Ministry of the Environment, Water Resources Branch, 1977.

MOE, Water wells records for Ontario, Simcoe 1946-1977, Ministry of the Environment, Water Resources Branch, 1981.

Molson, J. W., E. O. Frind, and C. D. Palmer, Thermal energy storage in an unconfined aquifer 2. Model development, validation and application, *Water Resour. Res.*, *28*(10), 2857–2867, 1992.

Mualem, Y., A new model for predicting the hydraulic conductivity of unsaturated porous media, *Water Resour. Res.*, *12*(3), 513–522, 1976.

Neuman, S. P., A statistical approach to the inverse problem of aquifer hydrology 3. Improved solution method and added perspective, *Water Resour. Res.*, *16*(2), 331–346, 1980.

Neuman, S. P., G. E. Fogg, and E. A. Jacobson, A statistical approach to the inverse problem of aquifer hydrology 2. Case Study, *Water Resour. Res.*, *16*(1), 33–58, 1980.

Neuman, S. P., and S. Yakowitz, A statistical approach to the inverse problem of aquifer hydrology 1. Theory, *Water Resour. Res.*, *15*(4), 845–860, 1979.

Nobre, M. M., and J. F. Sykes, Application of Bayesian kriging to subsurface characterization, *Can. Geotech. J.*, *29*, 589–598, 1992.

NVCA, Nottawasaga Valley Conservation Authority, Canada/Ontario flood damage reduction program: Watershed hydrology study for Nottawasaga, Pretty and Batteaux rivers, Black Ash, Silver and Sturgeon Creeks, Volume I - Technical Report, Prepared by MacLaren Plansearch, 1988.

NVCA, Nottawasaga Valley watershed management plan, Prepared by the Nottawasaga Conservation Authority, Draft, 1995.

Omre, H., and K. Halvorson, The Bayesian bridge between Simple and Universal kriging, *Math. Geol.*, *21*, 767–786, 1989.

Poeter, E. P., and M. C. Hill, Inverse models: A necessary next step in groundwater modeling, *Groundwater*, *35*(2), 250–260, 1997.

Poeter, E. P., and M. C. Hill, Ucode, a computer code for universal inverse modeling, *Computers and Geosciences*,, submitted, 1998.

RamaRao, B. S., A. M. LaVenue, G. de Marsily, and M. G. Marietta, Pilot point methodology for automated calibration of an ensemble of conditionally simulated transmissivity fields 1. Theory and computational experiments, *Water Resour. Res.*, *31*(3), 475–493, 1995.

Robin, M. J. L. Cross-correlated random field generation with the direct Fourier Transform method. Ph.D. thesis, Dept. of Earth Sciences, University of Waterloo, 1991.

Robin, M. J. L., A. L. Gutjahr, E. A. Sudicky, and J. L. Wilson, Cross-correlated random field generation with the direct Fourier Transform method, *Water Resour. Res.*, *29*(7), 2385–2397, 1993.

Sagar, B., Galerkin finite element procedure for analyzing flow through random media, *Water Resour. Res.*, *14*(6), 1035–1044, 1978.

Sagar, B., S. Yakowitz, and L. Duckstein, A direct method for the identification of parameters of dynamic nonhomogeneous aquifers, *Water Resour. Res.*, *11*(4), 563–570, 1975.

Shah, P. C., G. R. Gavelas, and J. H. Seinfeld, Error analysis in history matching: The optimum level of parameterization, *Soc. Petrol. Eng. J.*, *18*(3), 219, 1978.

Simúnek, J., T. Vogel, and T. van Genuchten, The SWMS 2D code for simulating water flow and solute transport in two-dimensional variably saturated media, Version 1.1, Technical report, U.S. Salinity Laboratory, USDA, ARS, Riverside, CA, 1992.

Sitar, N., J. D. Cawlfield, and A. Der-Kiureghian, First-order reliability approach to stochastic analysis of subsurface flow and contaminant transport, *Water Resour. Res.*, *23*(5), 794–804, 1987.

Spencer, J. W., Origin of the basins of the Great Lakes of America, *Amer. Geol.*, *7*, 86–97, 1890.

Stanford, S. D., and G. M. Ashley, Using three-dimensional geologic models to map glacial aquifer systems: an example from New Jersey, in SEPM concepts in hydrogeology and environmental geology No. 1, 69–84, 1998.

Sudicky, E. A., A natural gradient experiment on solute transport in a sand aquifer: spatial variability of hydraulic conductivity and its role in the dispersion process, *Water Resour. Res.*, *22*(13), 2069–2082, 1986.

Sudicky, E. A., A. J. A. Unger, and S. Lacombe, A noniterative technique for the direct implementation of well bore boundary conditions in three-dimensional heterogeneous formations, *Water Resour. Res.*, *31*(2), 411–415, 1995.

Sun, N. Z., M. C. Jeng, and W. W. Yeh, A proposed geologic parameterization method for parameter identification in three-dimensional groundwater modeling, *Water Resour. Res.*, *31*(1), 89–102, 1995.

Sun, N. Z., and W. W. Yeh, Identification of parameter structure in groundwater inverse problem, *Water Resour. Res.*, *21*(6), 869–883, 1985.

Sykes, J. F., and N. R. Thomson, Parameter identification and uncertainty analysis for variably saturated flow, *Adv. Water Resour.*, *11*(12), 185–191, 1988.

Sykes, J. F., J. L. Wilson, and R. W. Andrews, Sensitivity analysis for steady state groundwater flow using adjoint operators, *Water Resour. Res.*, *21*(3), 359–371, 1985.

Tang, D. H., and G. F. Pinder, Simulation of groundwater flow and mass transport, *Adv. Water Resour.*, *1*(1), 25–30, 1977.

Terra-Probe, Hydrologic assessment for preparation of the official plan, township of Oro-Medonte, County of Simcoe, File 95567, December, 1995.

Therrien, R., and E. A. Sudicky, Three-dimensional analysis of variably-saturated flow and solute transport in discretely-fractured porous media, *J. Contam. Hydrol.*, *23*, 1–44, 1996.

Townley, L. R., Second order effects of uncertain transmissivities on predictions of piezometric heads, in Finite elements in water resources, Proceedings of the 5th international conference, Burlington, Vt, USA, June, 1984.

Townley, L. R., and J. L. Wilson, Conditional second moment analysis of groundwater flow: The cumulative effects of transmissivity and head measurements, in International conference on groundwater and man (1): the investigation and assessment of groundwater resources, *Austr. Water Resour. Council Ser. 8*, Sydney, Dec 5-9, 1983.

Townley, L. R., and J. L. Wilson, Computationally efficient algorithm for parameter estimation and uncertainty propagation in numerical models of groundwater flow, *Water Resour. Res.*, *21* (12), 1851–1860, 1985.

van Genuchten, M. T., A closed-form equation for predicting the hydraulic conductivity of unsaturated soils, *Soil Sci. Soc. Am. J.*, *44*, 892–898, 1980.

VanderKwaak, J. E. Numerical simulation of flow and chemical transport in integrated surface-subsurface hydrologic systems. Ph.D. thesis, (in preparation) Dept. of Earth Sciences., University of Waterloo, 1999.

Vechia, A. V., and R. L. Cooley, Simultaneous confidence and prediction intervals for non-linear regression models with application to a groundwater flow model, *Water Resour. Res.*, *23*(7), 1237–1250, 1987.

Warren, J. E., and H. S. Price, Flow in heterogeneous porous media, *Soc. Pet. Eng. J.*, *1*, 153–169, 1961.

White, O. L., and P. F. Karrow, New evidence for Spencer's Laurentian River, in Proc. 14th Conf. Great Lakes Res., 394–400, Internat. Assoc. Great Lakes Res., 1971.

Wilson, J. L., P. Kitanidis, and M. Dettinger, State and parameter estimation in groundwater models, in Chapman conference on the application of Kalman filtering to Hydrology, Hydraulics and water resources, AGU, Pittsburgh, Pa, May, 1978.

Woodbury, A. D., and E. A. Sudicky, The geostatistical characteristics of the Borden aquifer, *Water Resour. Res.*, *27*(4), 533–546, 1991.

Xiang, Y., J. F. Sykes, and N. R. Thomson, A composite L1 parameter estimater for model fitting in groundwater flow and solute transport simulation, *Water Resour. Res.*, *29*(6), 1661–1673, 1992.

Yeh, G. T., J. R. Chen, and J. A. Bensabat, A three-dimensional finite-element model of transient free surface flow in aquifers, in X Intern. Conf. on Comp. Meth. Water Resour., 131–138, 1, July, 1994.

Yeh, W. W.-G., and Y. S. Soon, A systematic optimization procedure for the identification of inhomogeneous aquifer parameters, in Advances in groundwater hydrology, 72–82, American Water Res. Ass., Mineapolis, Minn., 1976.

Yeh, W. W.-G., Y. S. Soon, and K. S. Lee, Aquifer parameter identification with kriging and optimum parameterization, *Water Resour. Res.*, *19*(1), 225–233, 1983.

Zimmerman, D. A., G. de Marsily, C. A. Gotway, M. G. Marietta, C. L. Axness, R. L. Beauheim, R. L. Bras, J. Carrera, G. Dagan, P. B. Davies, D. P. Gallegos, A. Galli, J. Gomez-Hernandez, P. Grindrod, A. L. Gutjahr, P. K. Kitanidis, A. M. LaVenue, D. McLaughlin, S. P. Neuman, B. S. RamaRao, C. Ravenne, and Y. Rubin, A comparison of seven geostatistically based inverse approaches to estimate transmissivities for modeling advective transport by groundwater flow, *Water Resour. Res.*, *34*(6), 1373–1413, 1998.

Appendix A

Cross-sections

Cross-sections used in the hydrostratigraphic interpretation (Figure 7.3) are shown on the following pages. A legend for the geologic symbols used in the boreholes is given in Table 7.1. UTM coordinates of the start and end points of the cross-sections are shown in the bottom corners. The elevation given on the vertical axes are in meters above sea level. Intersection points with other cross-sections are indicated at the bottom axes. The MOEE identification numbers of the boreholes are plotted above the wells. Aquifers are indicated by triangles and dots and are labeled A1 through A4, aquitard units are designated by the flex symbols. The geometry of the aquifer/aquitard contacts results from kriging of the interpreted elevation of these contacts at the boreholes. Where the interpolated contacts reach above the ground surface or below the bedrock, they are constrained to follow these surfaces. If the aquifer/aquitard contacts cross they are constrained to their mean elevation and the corresponding unit pinches out.

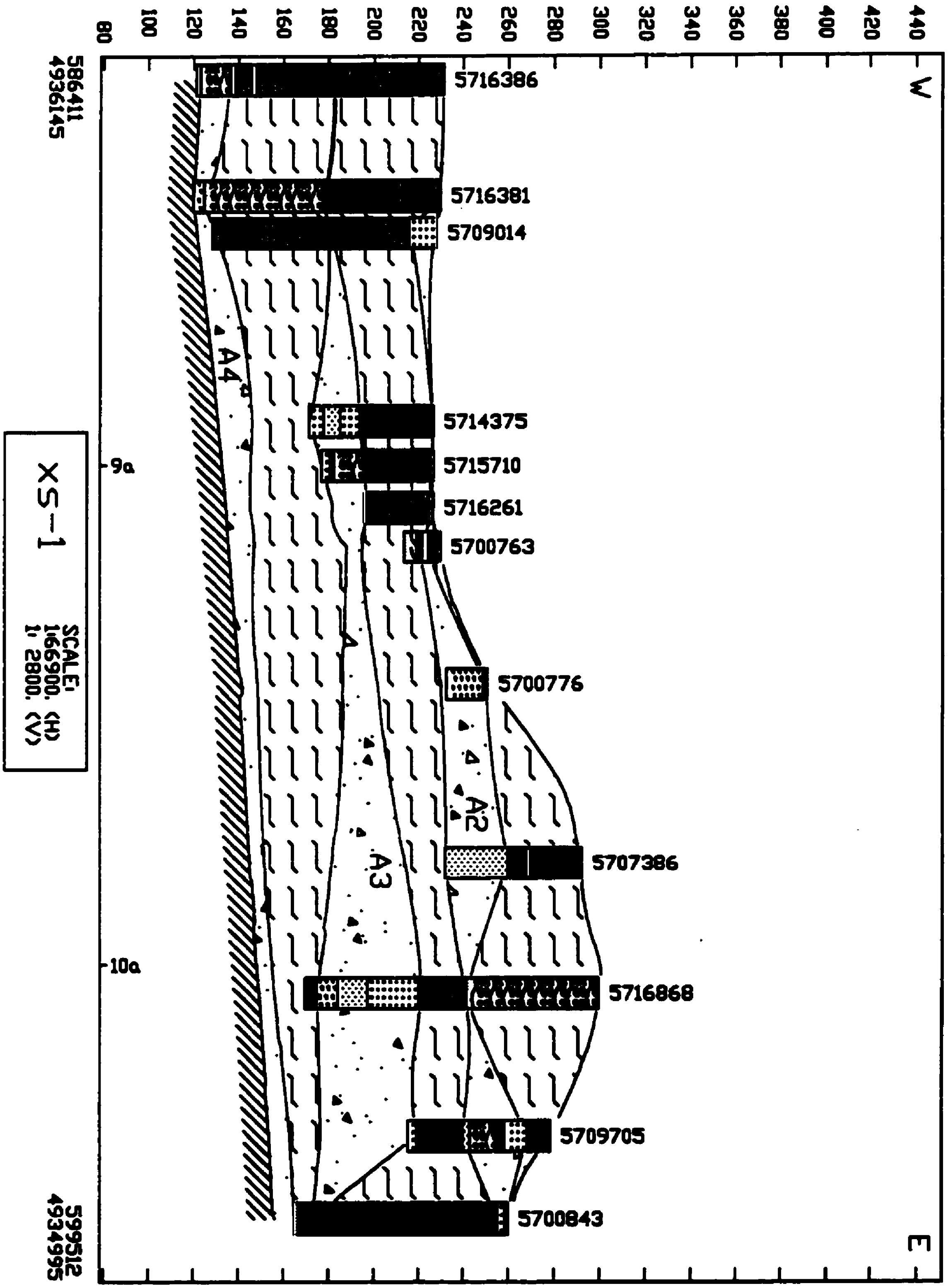
XS-1
SCALE:
1:66900. (H)
1: 2800. (V)
586411
4936145
599512
4934995
W
E
80
100
120
140
160
180
200
220
240
260
280
300
320
340
360
380
400
420
440
9a
10a
A4
A3
A2
5716386
5716381
5709014
5714375
5715710
5716261
5700763
5700776
5707386
5716868
5709705
5700843

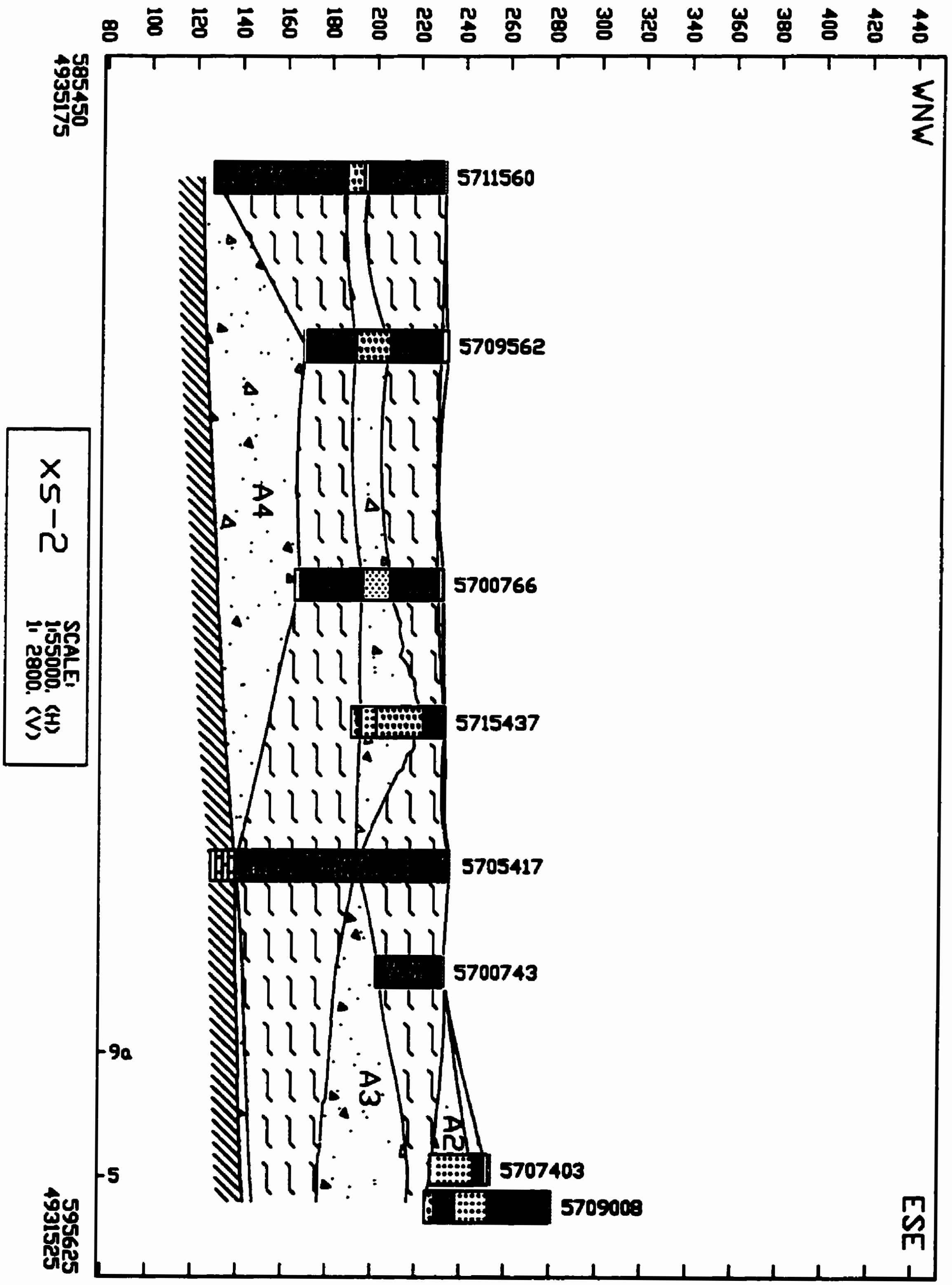
WNW
ESE
80
100
120
140
160
180
200
220
240
260
280
300
320
340
360
380
400
420
440
585450
4935175
595625
4931525
5711560
5709562
5700766
5715437
5705417
5700743
5707403
5709008
A4
A3
A2
9a
5
XS-2
SCALE:
155000. (H)
1: 2800. (V)

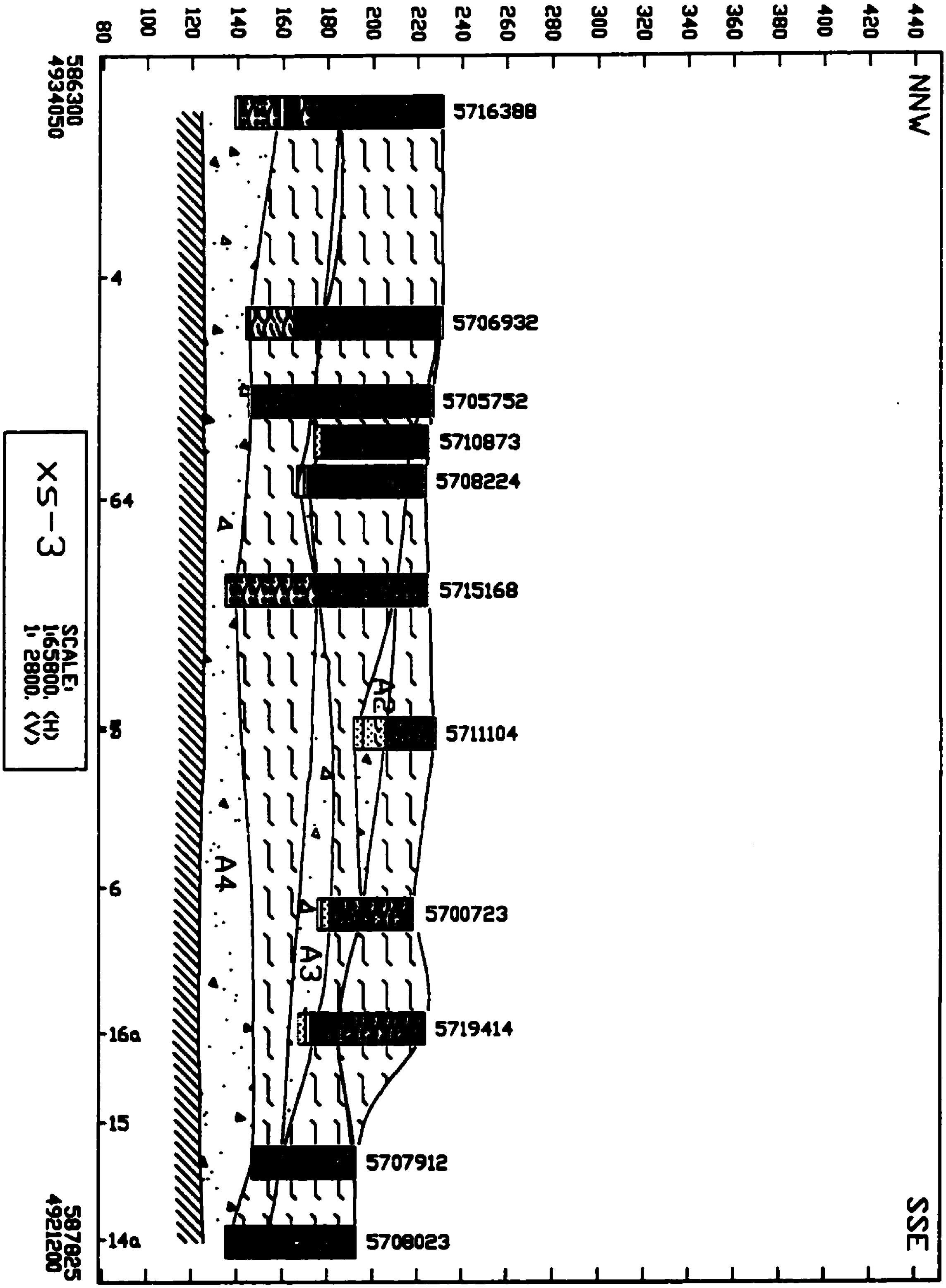
NNW
SSE
80
100
120
140
160
180
200
220
240
260
280
300
320
340
360
380
400
420
440
586300
4934050
587825
4921200
4
64
5
6
16a
15
14a
5716388
5706932
5705752
5710873
5708224
5715168
5711104
5700723
5719414
5707912
5708023
A2
A3
A4
XS-3
SCALE:
165800. (H)
1: 2800. (V)

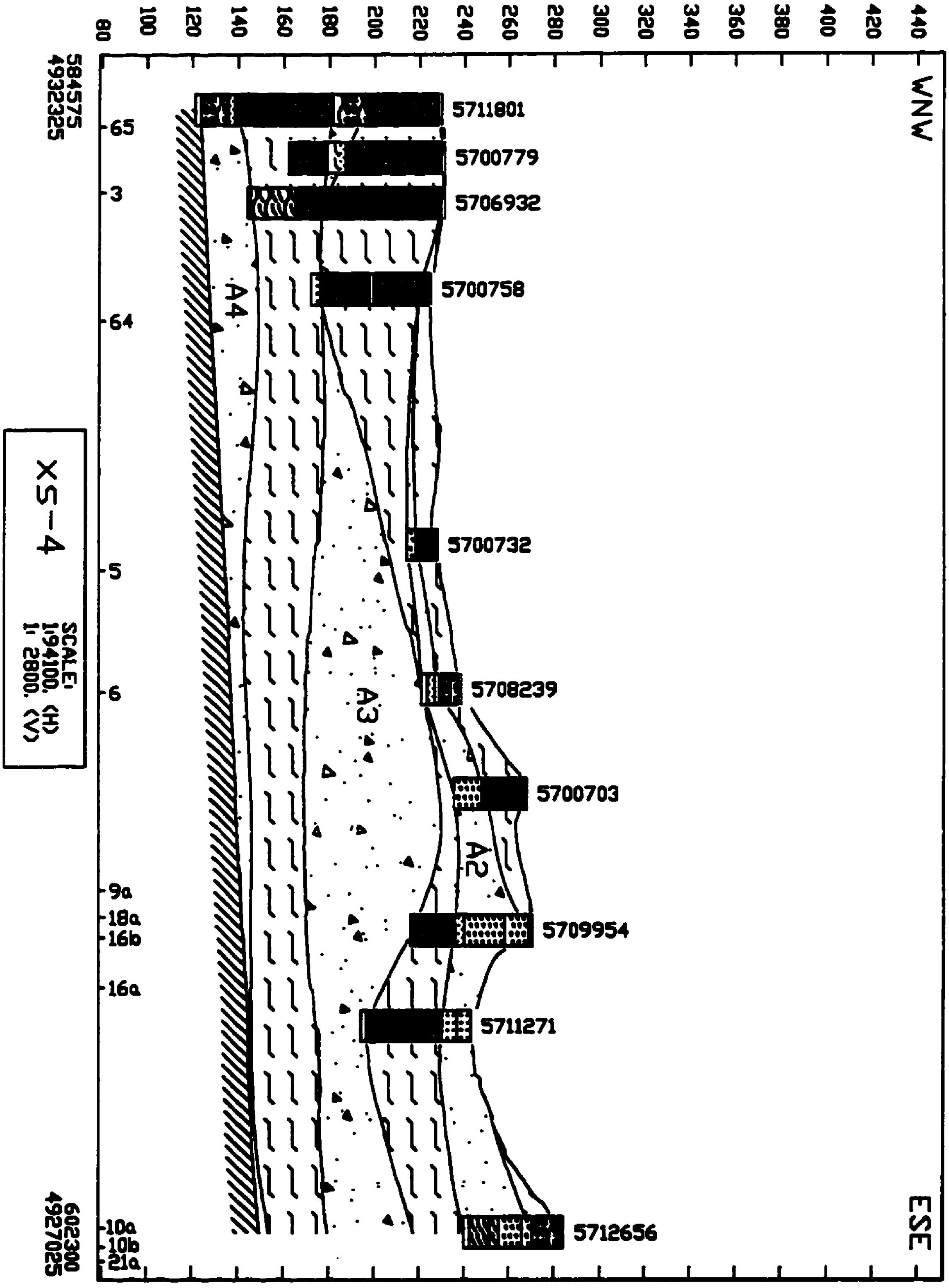
WNW
ESE
440
420
400
380
360
340
320
300
280
260
240
220
200
180
160
140
120
100
80
584575
4932325
602300
4927025
65
3
64
5
6
9a
18a
16b
16a
10a
10b
21a
5711801
5700779
5706932
5700758
5700732
5708239
5700703
5709954
5711271
5712656
A4
A3
A2
XS-4
SCALE: 1:94100. (H)
1: 2800. (V)

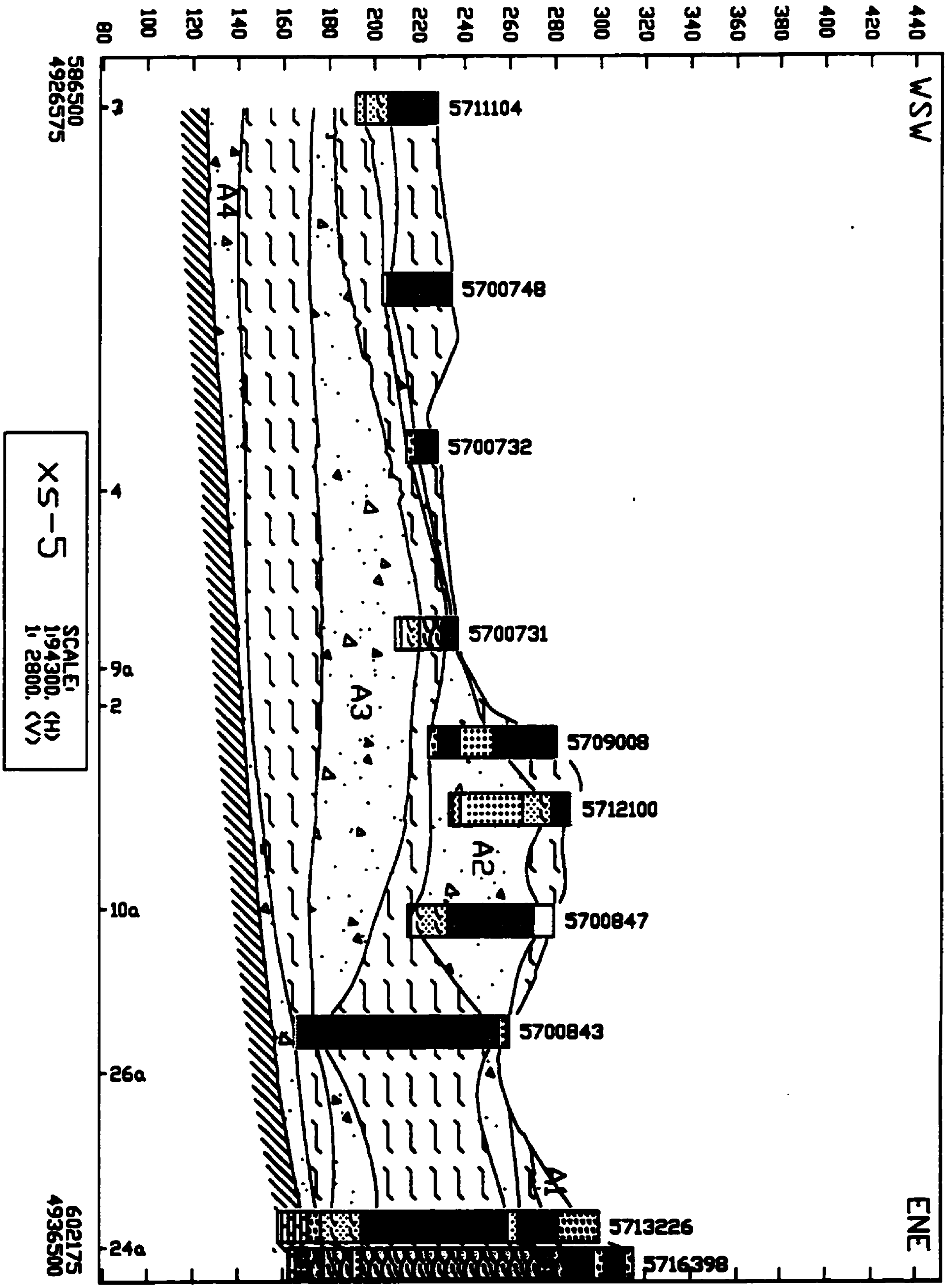
WSW
ENE
80
100
120
140
160
180
200
220
240
260
280
300
320
340
360
380
400
420
440
586500
4926575
602175
4936500
3
4
9a
2
10a
26a
24a
5711104
5700748
5700732
5700731
5709008
5712100
5700847
5700843
5713226
5716398
A1
A2
A3
A4
XS-5
SCALE:
1:94300. (H)
1: 2800. (V)

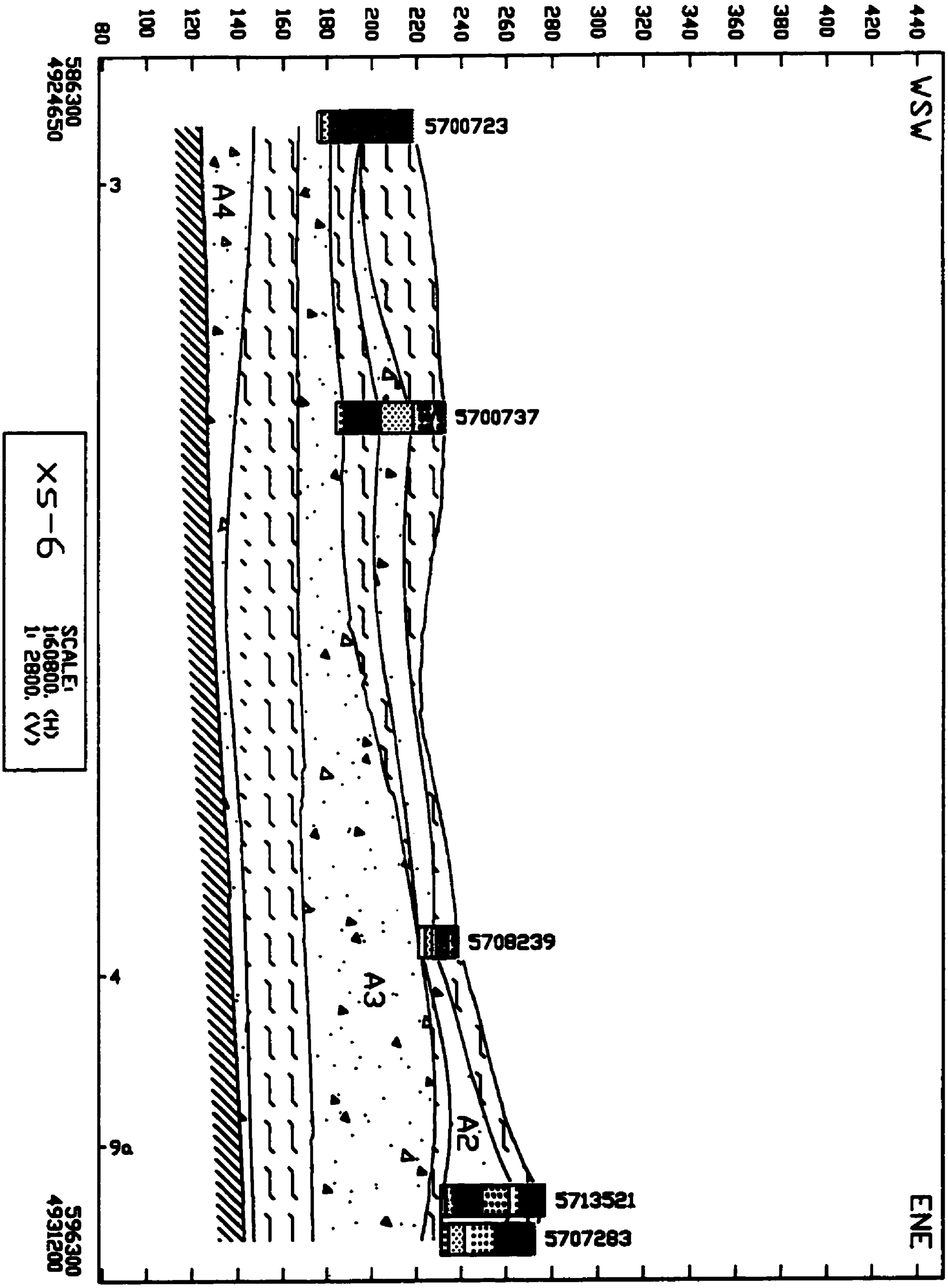
WSW
ENE
440
420
400
380
360
340
320
300
280
260
240
220
200
180
160
140
120
100
80
5700723
5700737
5708239
5713521
5707283
A4
A3
A2
3
4
9a
586300
4924650
596300
4931200
XS-6
SCALE:
1:60800. (H)
1: 2800. (V)

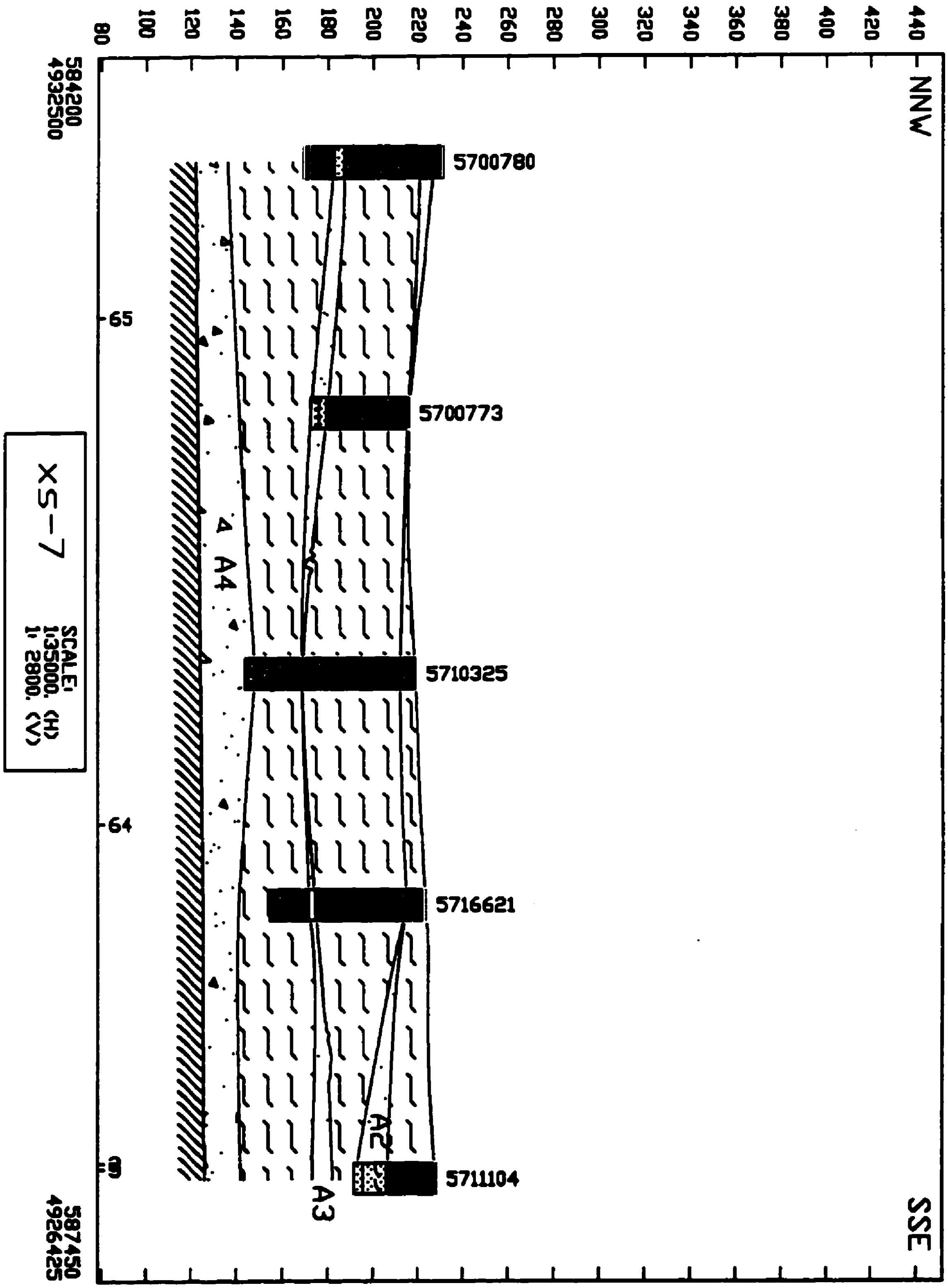
NNW
SSE
80
100
120
140
160
180
200
220
240
260
280
300
320
340
360
380
400
420
440
5700780
5700773
5710325
5716621
5711104
A4
A3
A2
65
64
63
584200
4932500
587450
4926425
XS-7
SCALE:
1:35000. (H)
1: 2800. (V)

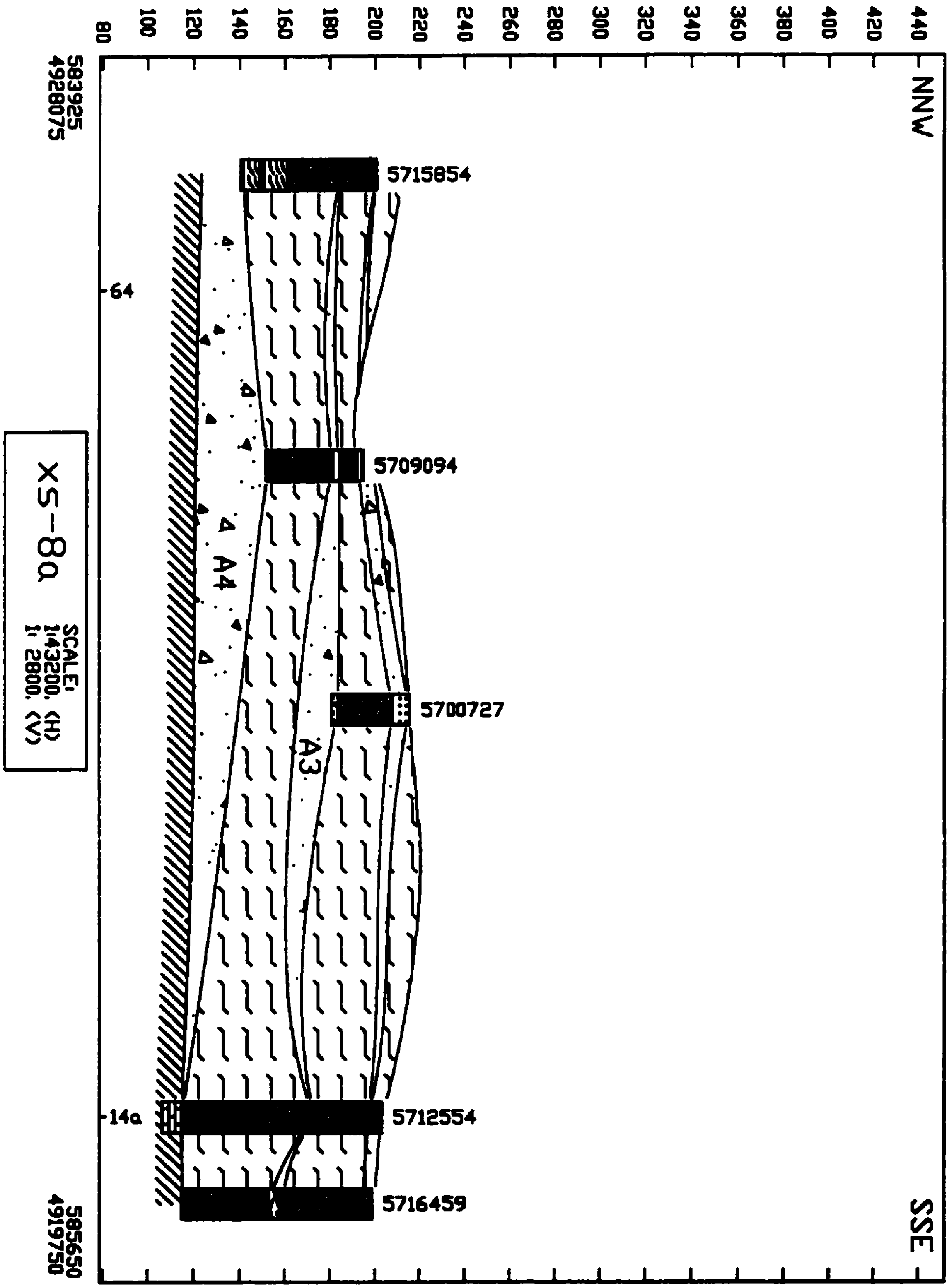
NNW
SSE
440
420
400
380
360
340
320
300
280
260
240
220
200
180
160
140
120
100
80
583925
4928075
585650
4919750
64
14a
5715854
5709094
5700727
5712554
5716459
A4
A3
XS-8a
SCALE:
1:43200. (H)
1: 2800. (V)

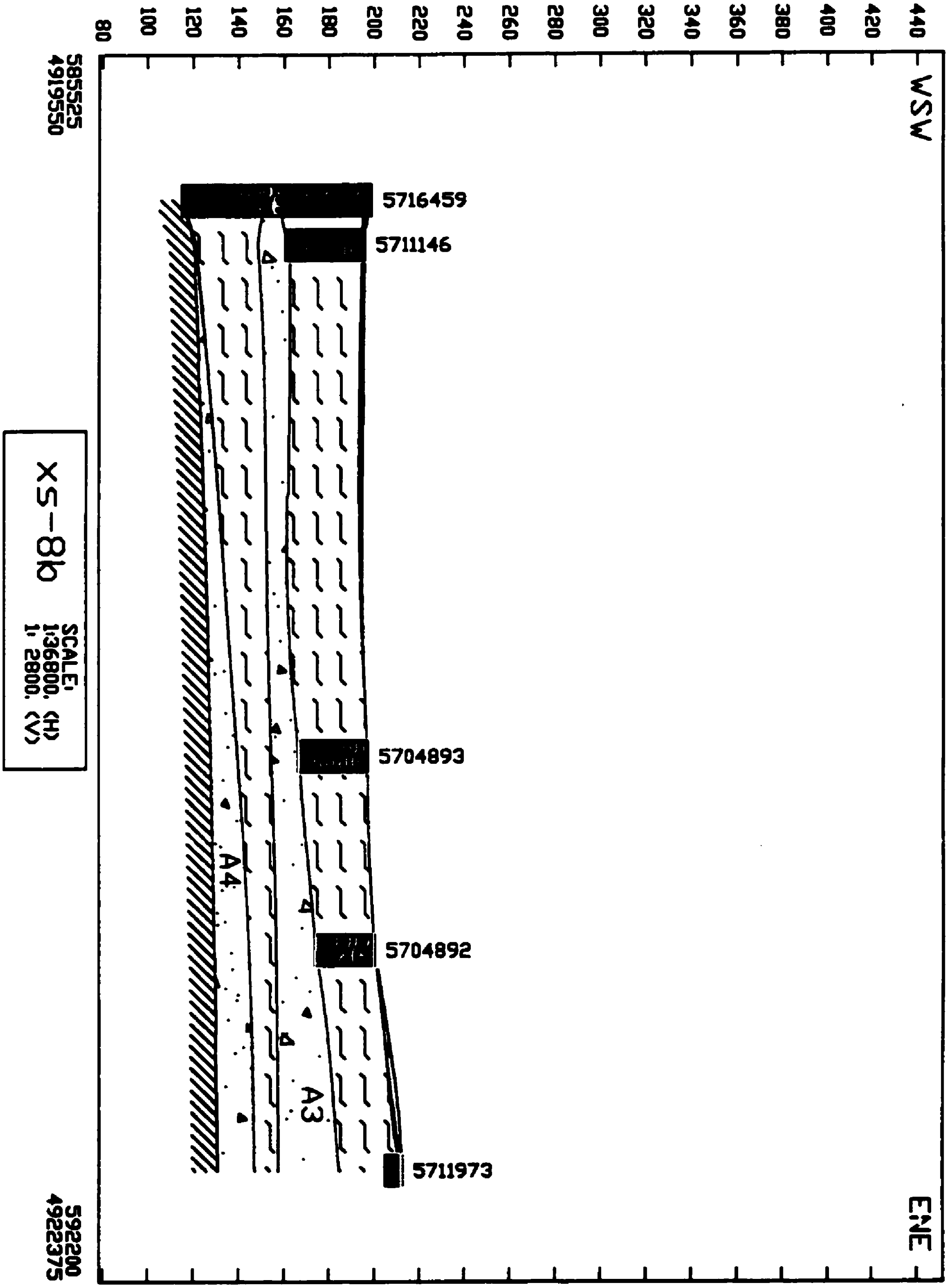
WSW
ENE
80
100
120
140
160
180
200
220
240
260
280
300
320
340
360
380
400
420
440
585525
4919550
592200
4922375
5716459
5711146
5704893
5704892
5711973
A4
A3
XS-8b
SCALE:
1:36800. (H)
1: 2800. (V)

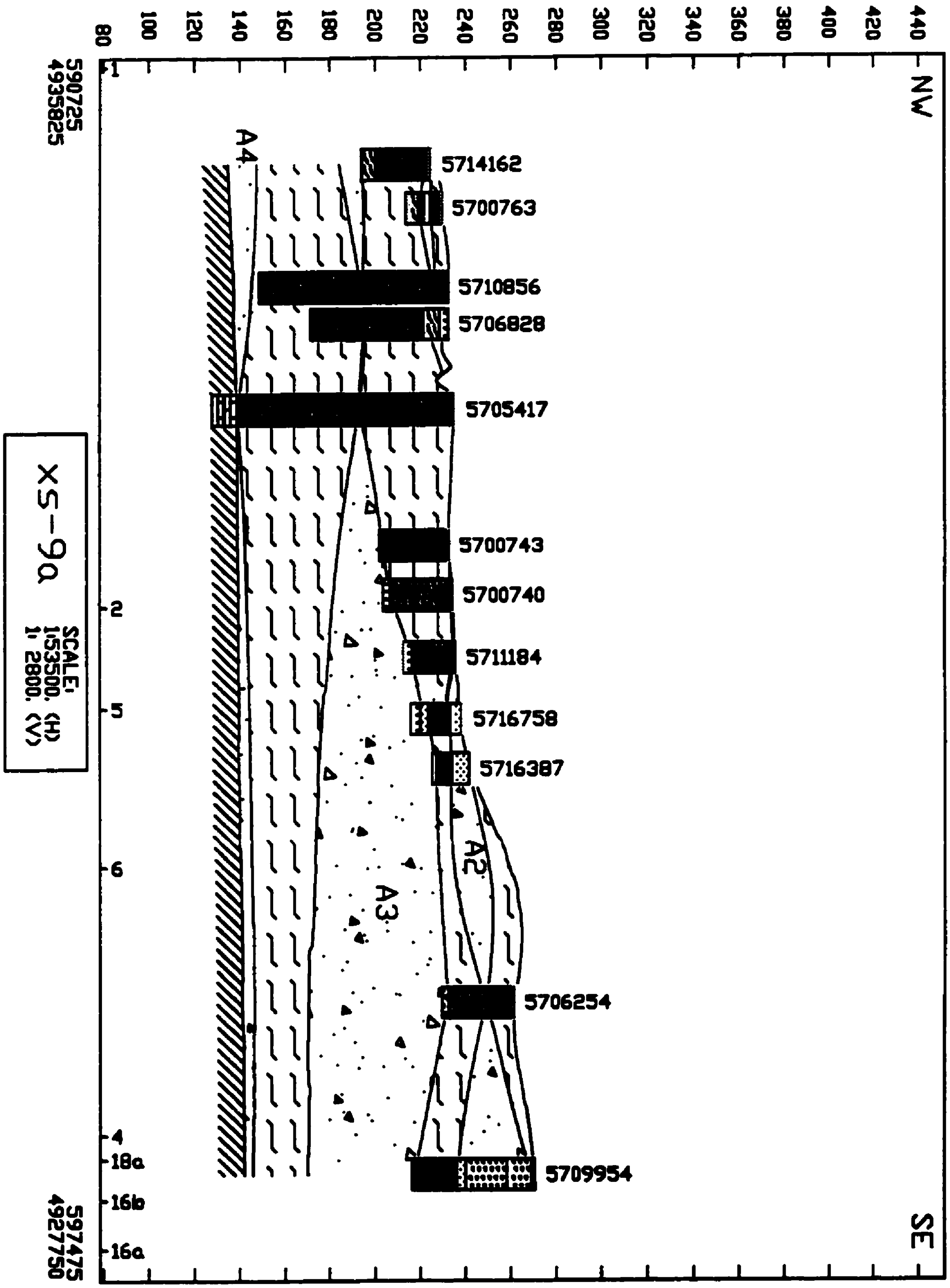
XS-9a
SCALE: 1:53500. (H)
1: 2800. (V)
590725
4935825
597475
4927750
NW
SE
80
100
120
140
160
180
200
220
240
260
280
300
320
340
360
380
400
420
440
1
2
5
6
4
18a
16b
16a
A4
A3
A2
5714162
5700763
5710856
5706828
5705417
5700743
5700740
5711184
5716758
5716387
5706254
5709954

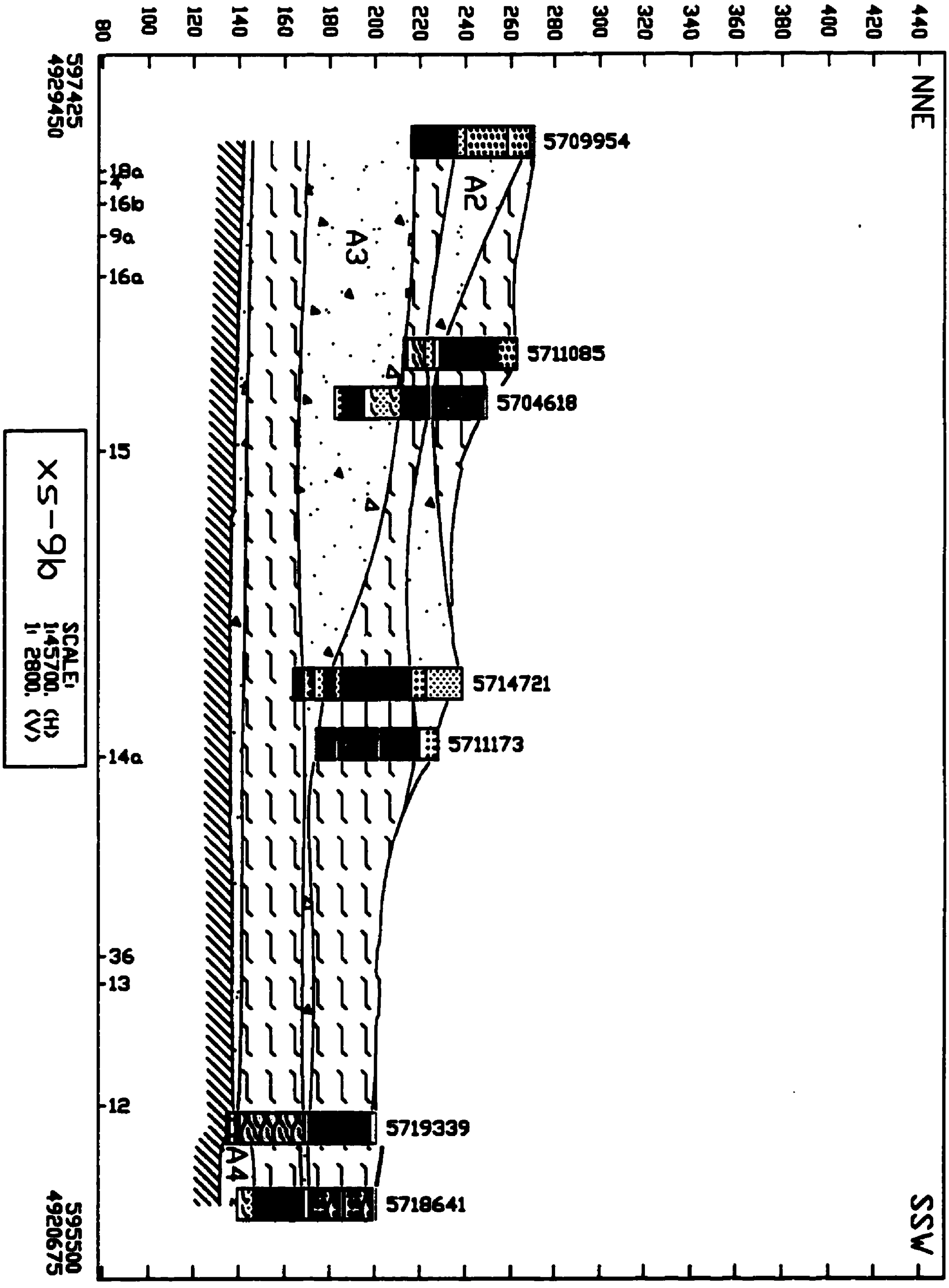
NNE
SSW
80
100
120
140
160
180
200
220
240
260
280
300
320
340
360
380
400
420
440
5709954
5711085
5704618
5714721
5711173
5719339
5718641
A2
A3
A4
597425
4929450
595500
4920675
18a
4
16b
9a
16a
15
14a
36
13
12
XS-9b
SCALE:
1:45700. (H)
1: 2800. (V)

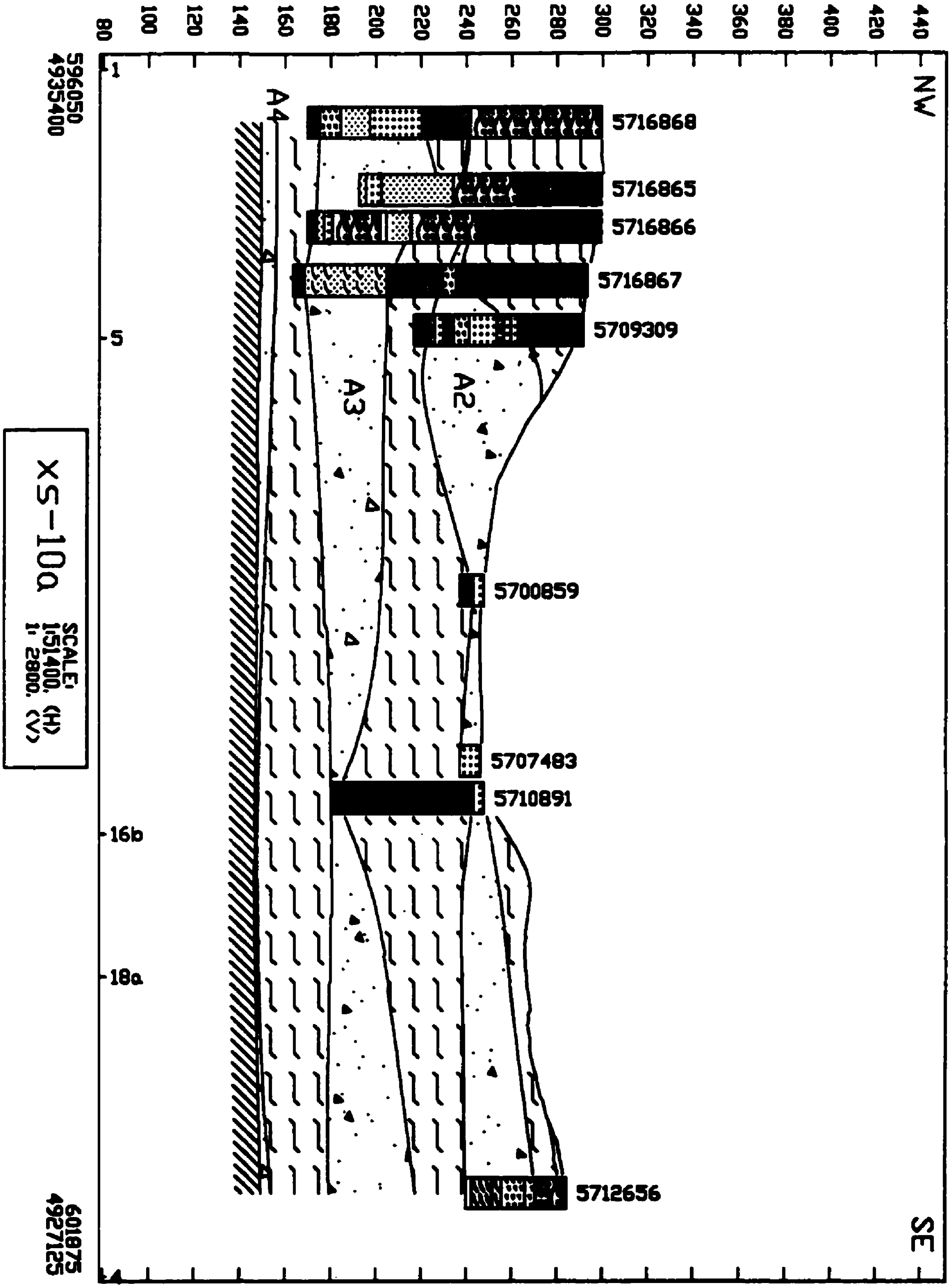
NW
SE
80
100
120
140
160
180
200
220
240
260
280
300
320
340
360
380
400
420
440
1
5
16b
18a
596050
4935400
601875
4927125
5716868
5716865
5716866
5716867
5709309
5700859
5707483
5710891
5712656
A2
A3
A4
XS-10a
SCALE: 1:51400. (H)
1: 2800. (V)

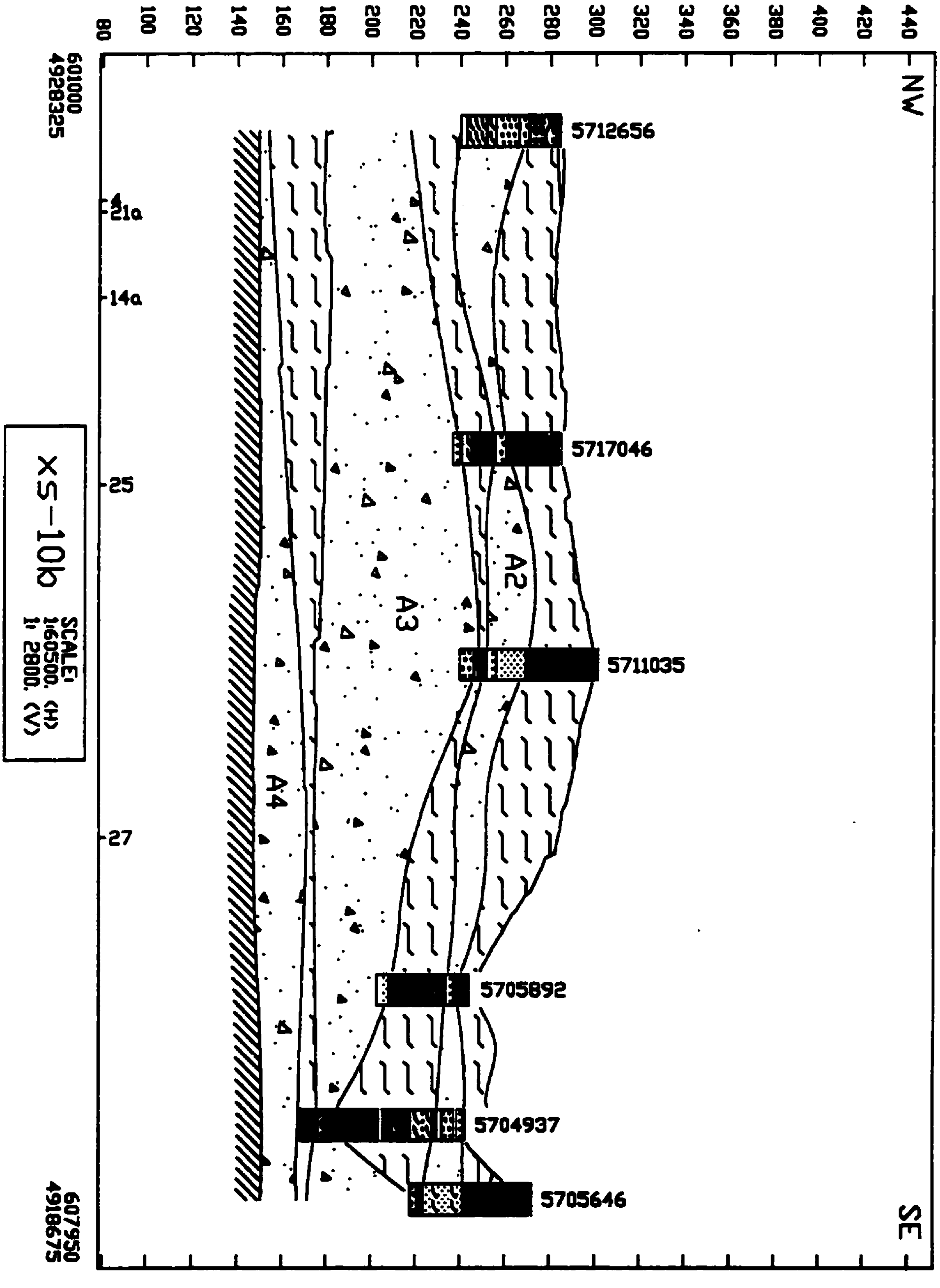
NW
SE
80
100
120
140
160
180
200
220
240
260
280
300
320
340
360
380
400
420
440
601000
4928325
607950
4918675
4
21a
14a
25
27
5712656
5717046
5711035
5705892
5704937
5705646
A2
A3
A4
XS-10b
SCALE:
1:60500. (H)
1: 2800. (V)

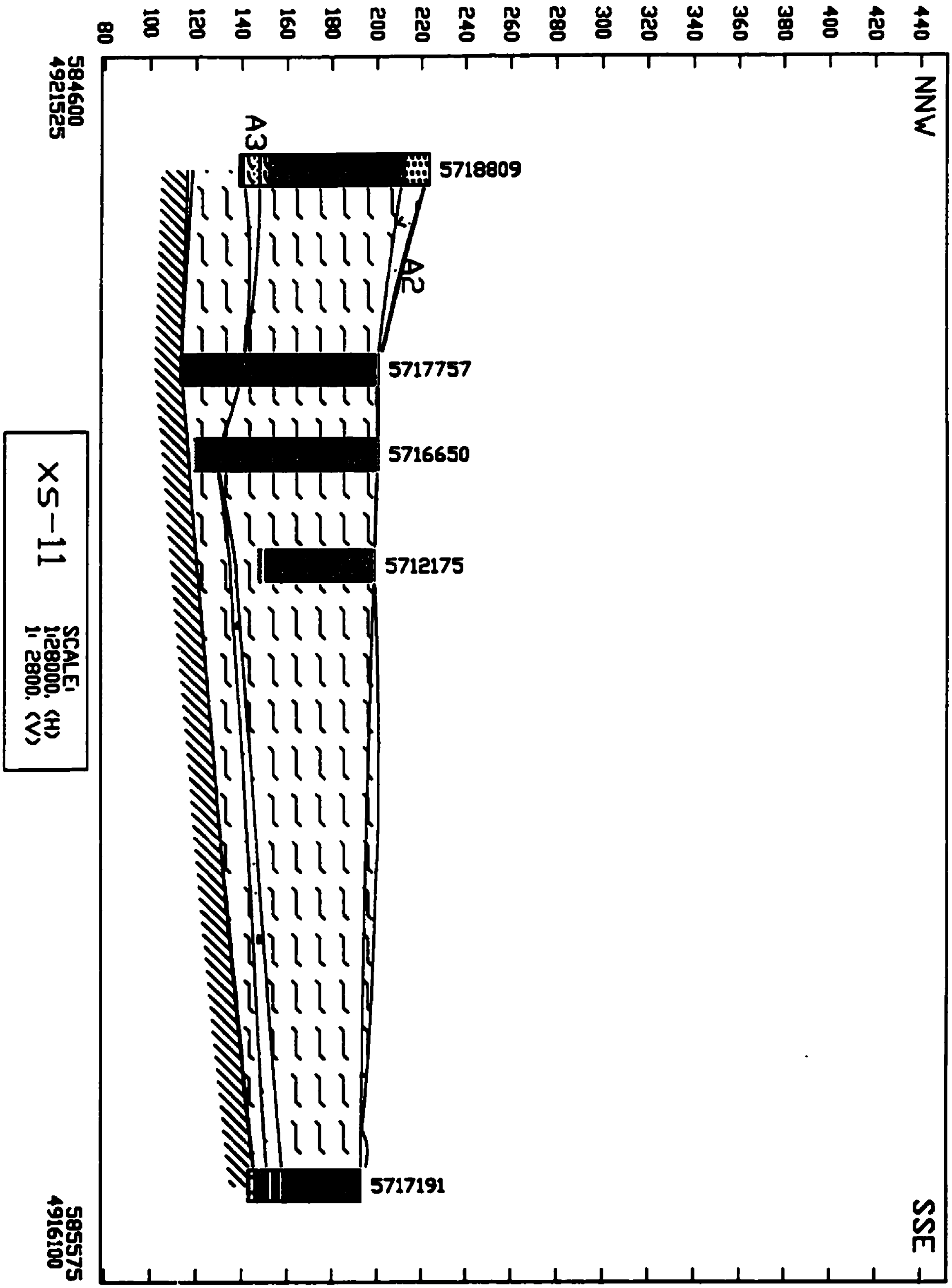
NNW
SSE
80
100
120
140
160
180
200
220
240
260
280
300
320
340
360
380
400
420
440
584600
4921525
585575
4916100
A3
A2
5718809
5717757
5716650
5712175
5717191
XS-11
SCALE:
1:28000. (H)
1: 2800. (V)

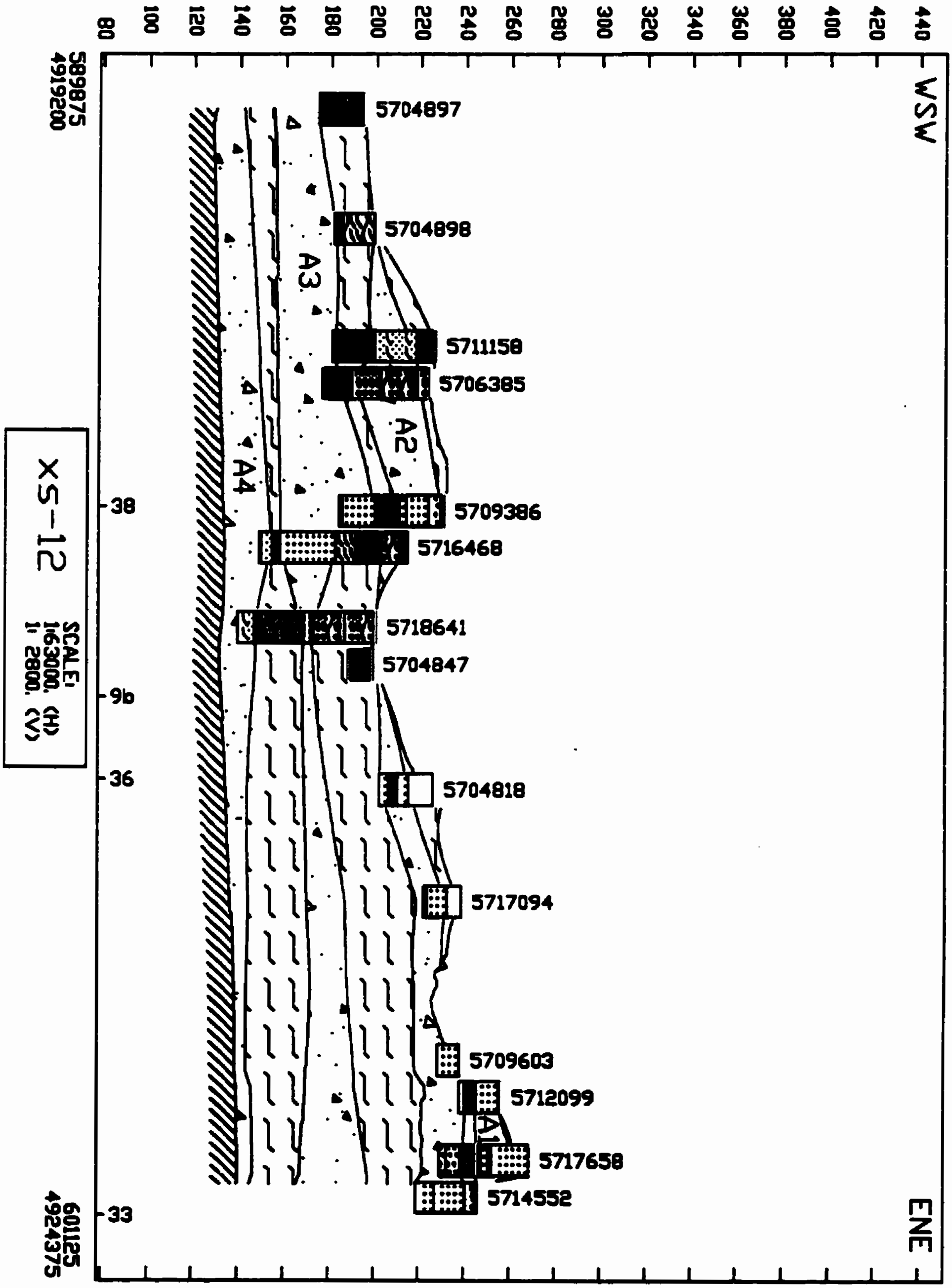
XS-12
SCALE:
1: 63000. (H)
1: 2800. (V)
WSW
ENE
589875
4919200
601125
4924375
80
100
120
140
160
180
200
220
240
260
280
300
320
340
360
380
400
420
440
38
9b
36
33
A1
A2
A3
A4
5704897
5704898
5711158
5706385
5709386
5716468
5718641
5704847
5704818
5717094
5709603
5712099
5717658
5714552

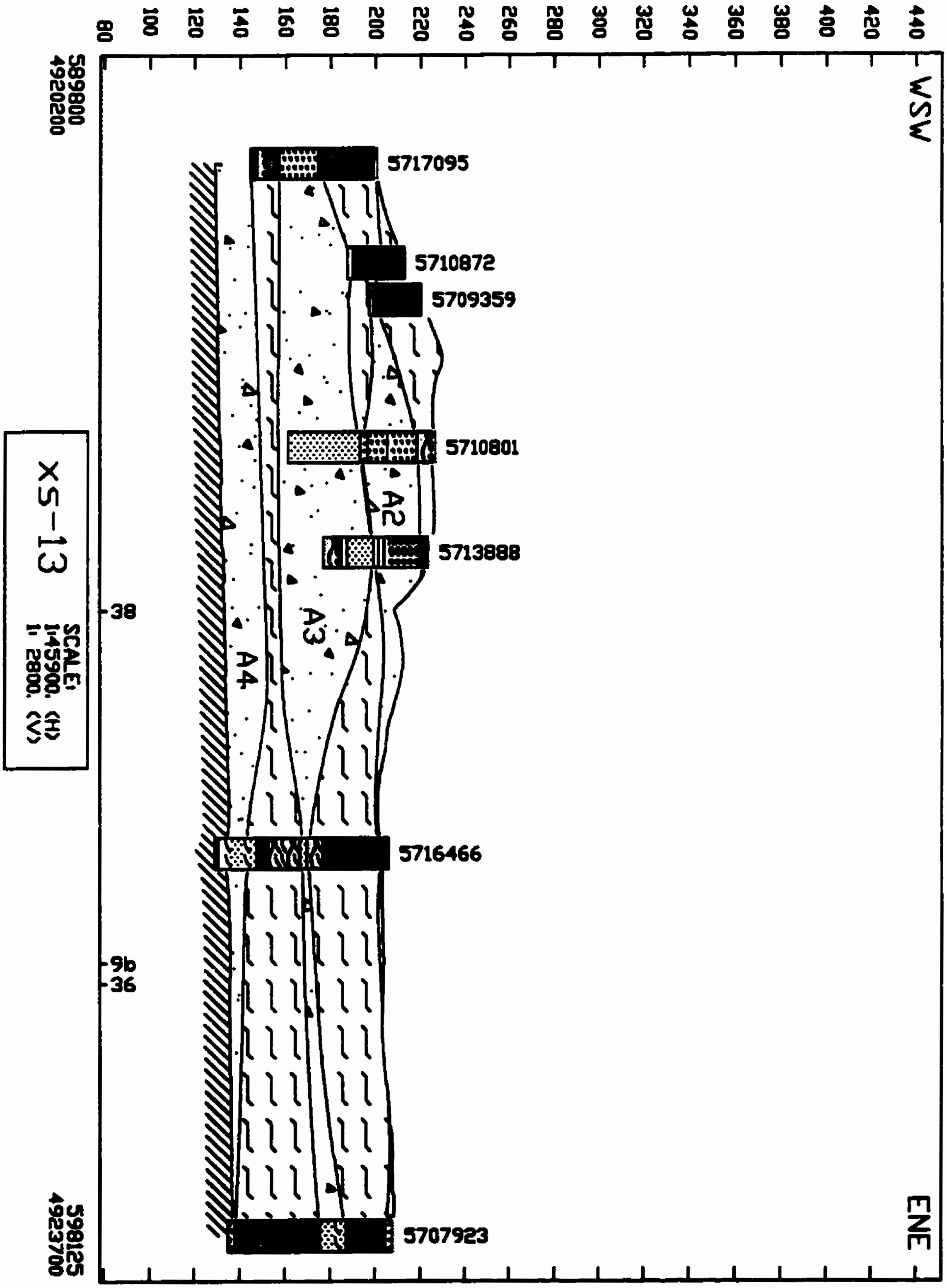
WSW
ENE
80
100
120
140
160
180
200
220
240
260
280
300
320
340
360
380
400
420
440
5717095
5710872
5709359
5710801
5713888
5716466
5707923
A2
A3
A4
38
9b
36
589800
4920200
598125
4923700
XS-13
SCALE:
1:45900. (H)
1: 2800. (V)

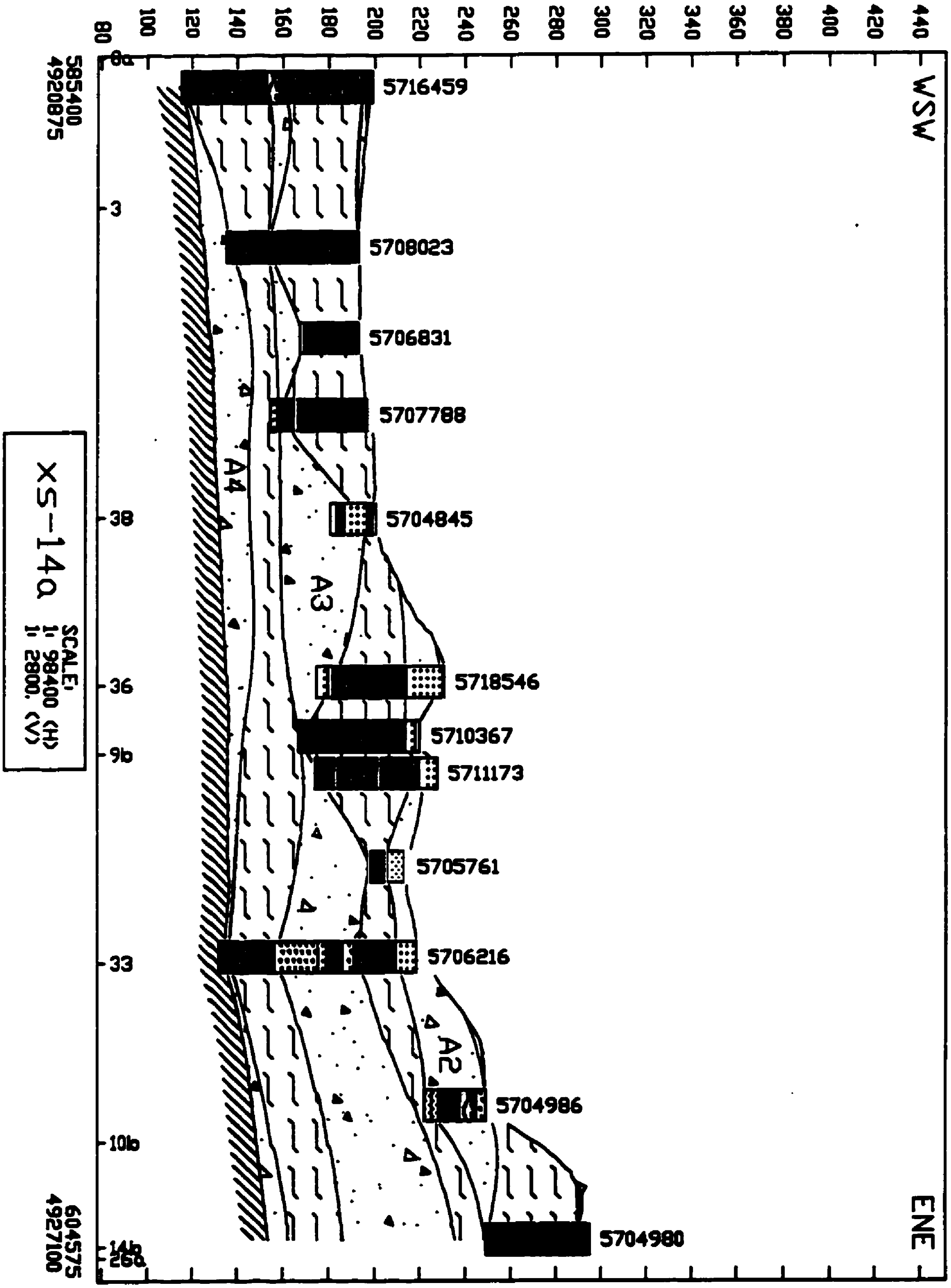
WSW
ENE
80
100
120
140
160
180
200
220
240
260
280
300
320
340
360
380
400
420
440
585400
4920875
604575
4927100
8a
3
38
36
9b
33
10b
14b
26a
5716459
5708023
5706831
5707788
5704845
5718546
5710367
5711173
5705761
5706216
5704986
5704980
A4
A3
A2
XS-14a
SCALE:
1: 98400 (H)
1: 2800. (V)

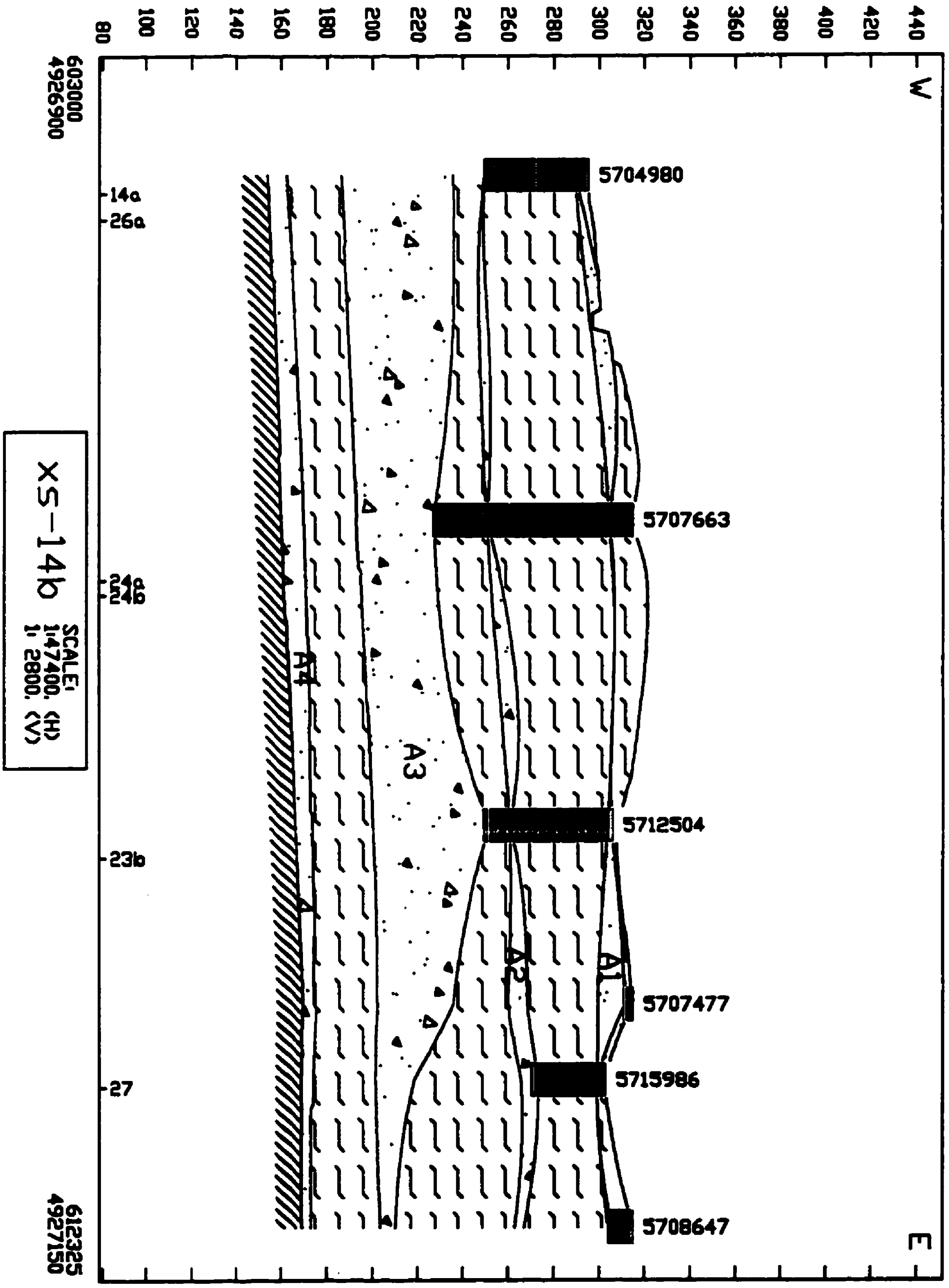
W
E
80
100
120
140
160
180
200
220
240
260
280
300
320
340
360
380
400
420
440
603000
4926900
612325
4927150
14a
26a
24a
24b
23b
27
5704980
5707663
5712504
5707477
5715986
5708647
A1
A2
A3
A4
XS-14b
SCALE: 1:47400. (H)
1: 2800. (V)

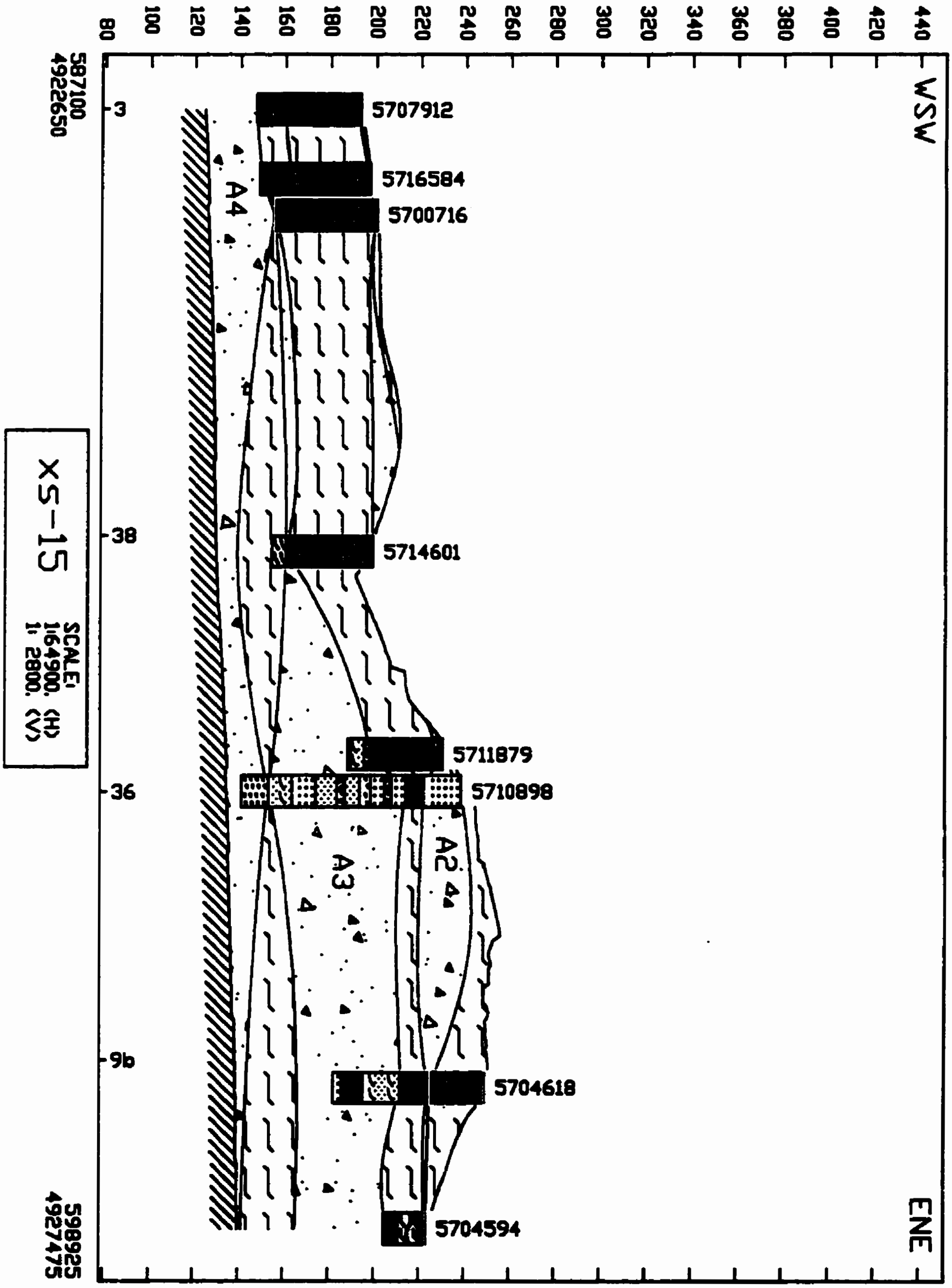
WSW
ENE
80
100
120
140
160
180
200
220
240
260
280
300
320
340
360
380
400
420
440
587100
4922650
598925
4927475
3
38
36
9b
5707912
5716584
5700716
5714601
5711879
5710898
5704618
5704594
A4
A3
A2
XS-15
SCALE:
1:64900. (H)
1: 2800. (V)

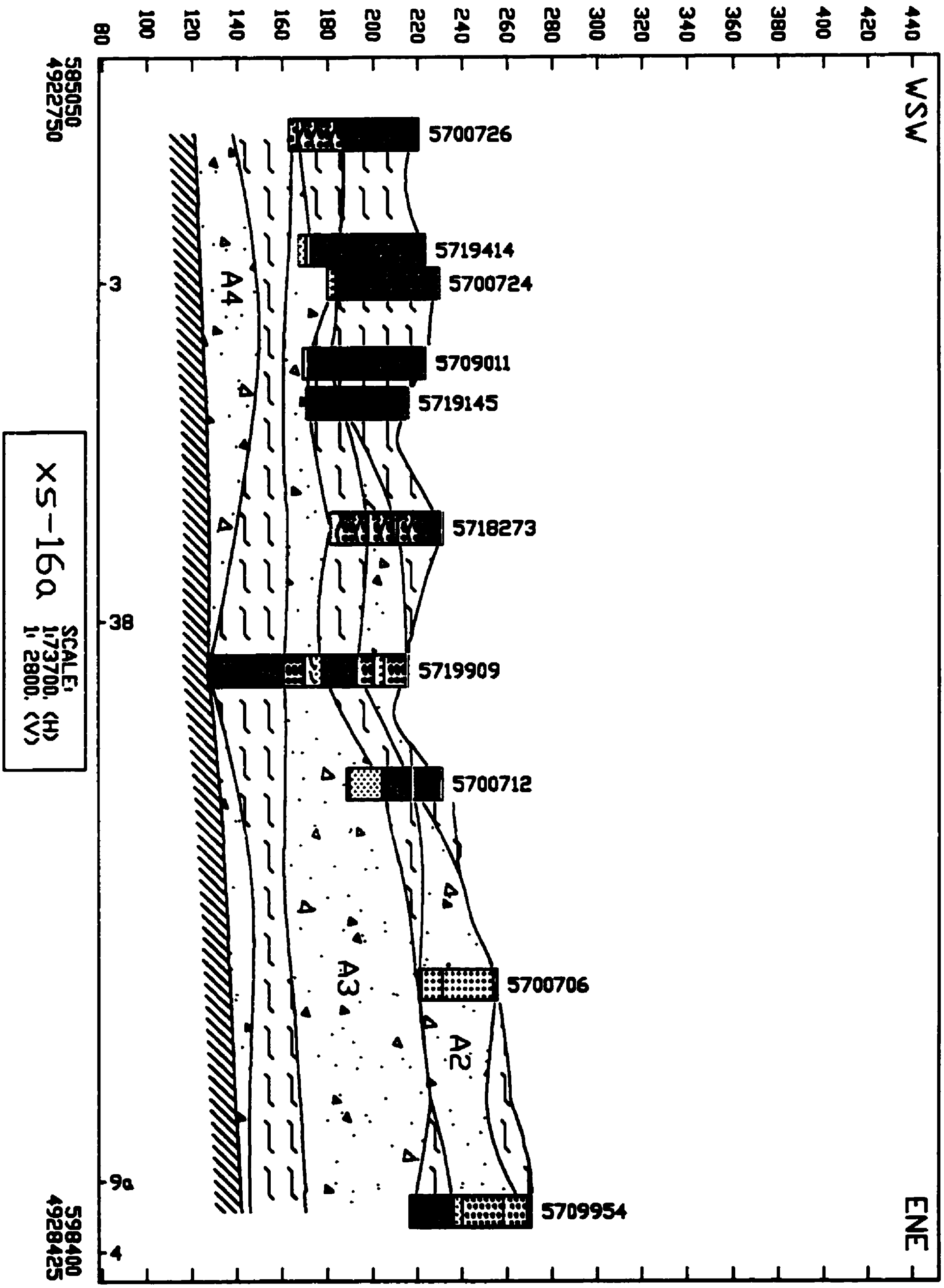
WSW
ENE
80
100
120
140
160
180
200
220
240
260
280
300
320
340
360
380
400
420
440
585050
4922750
598400
4928425
3
38
9a
4
5700726
5719414
5700724
5709011
5719145
5718273
5719909
5700712
5700706
5709954
A4
A3
A2
XS-16a
SCALE:
1:73700. (H)
1: 2800. (V)

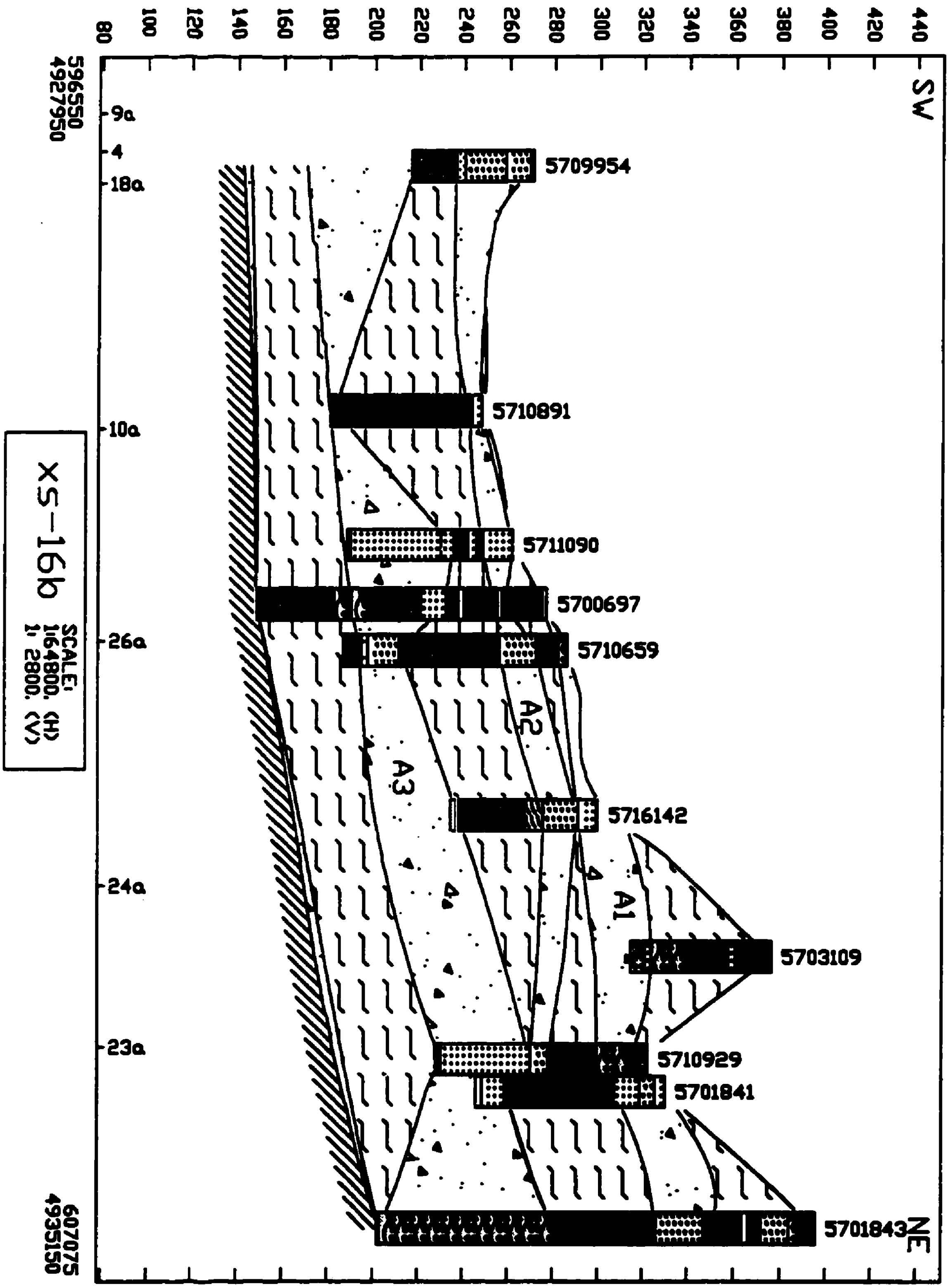
SW
NE
80
100
120
140
160
180
200
220
240
260
280
300
320
340
360
380
400
420
440
596550
4927950
607075
4935150
9a
4
18a
10a
26a
24a
23a
5709954
5710891
5711090
5700697
5710659
5716142
5703109
5710929
5701841
5701843
A1
A2
A3
4
xs-16b
SCALE: 164800. (H)
1: 2800. (V)

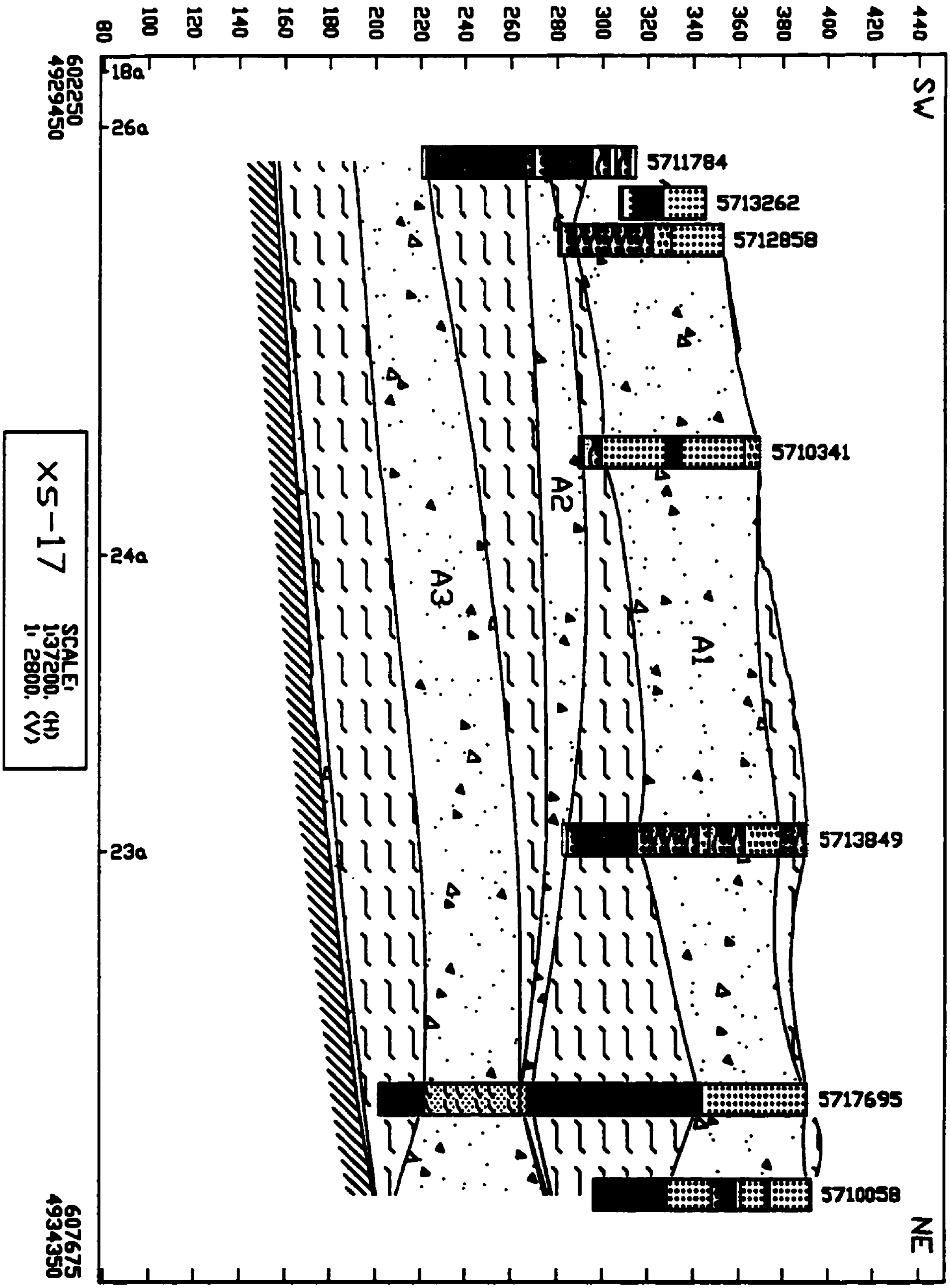
XS-17
SCALE:
1:37200. (H)
1: 2800. (V)
602250
4929450
607675
4934350
SW
NE
80
100
120
140
160
180
200
220
240
260
280
300
320
340
360
380
400
420
440
18a
26a
24a
23a
5711784
5713262
5712858
5710341
5713849
5717695
5710058
A1
A2
A3

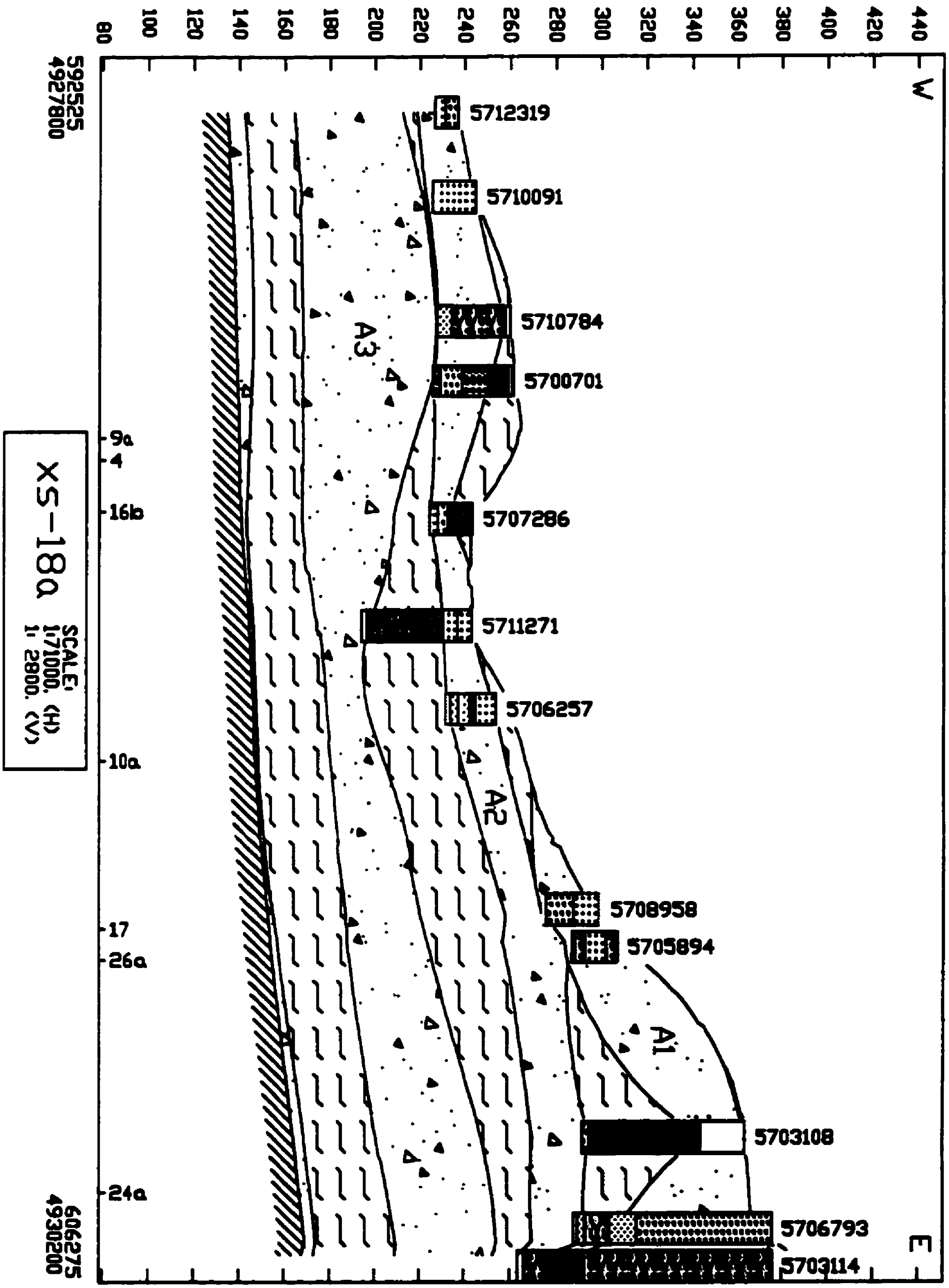
XS-18a
SCALE:
1:71000. (H)
1: 2800. (V)
592525
4927800
606275
4930200
W
E
80
100
120
140
160
180
200
220
240
260
280
300
320
340
360
380
400
420
440
9a
4
16b
10a
17
26a
24a
A3
A2
A1
5712319
5710091
5710784
5700701
5707286
5711271
5706257
5708958
5705894
5703108
5706793
5703114

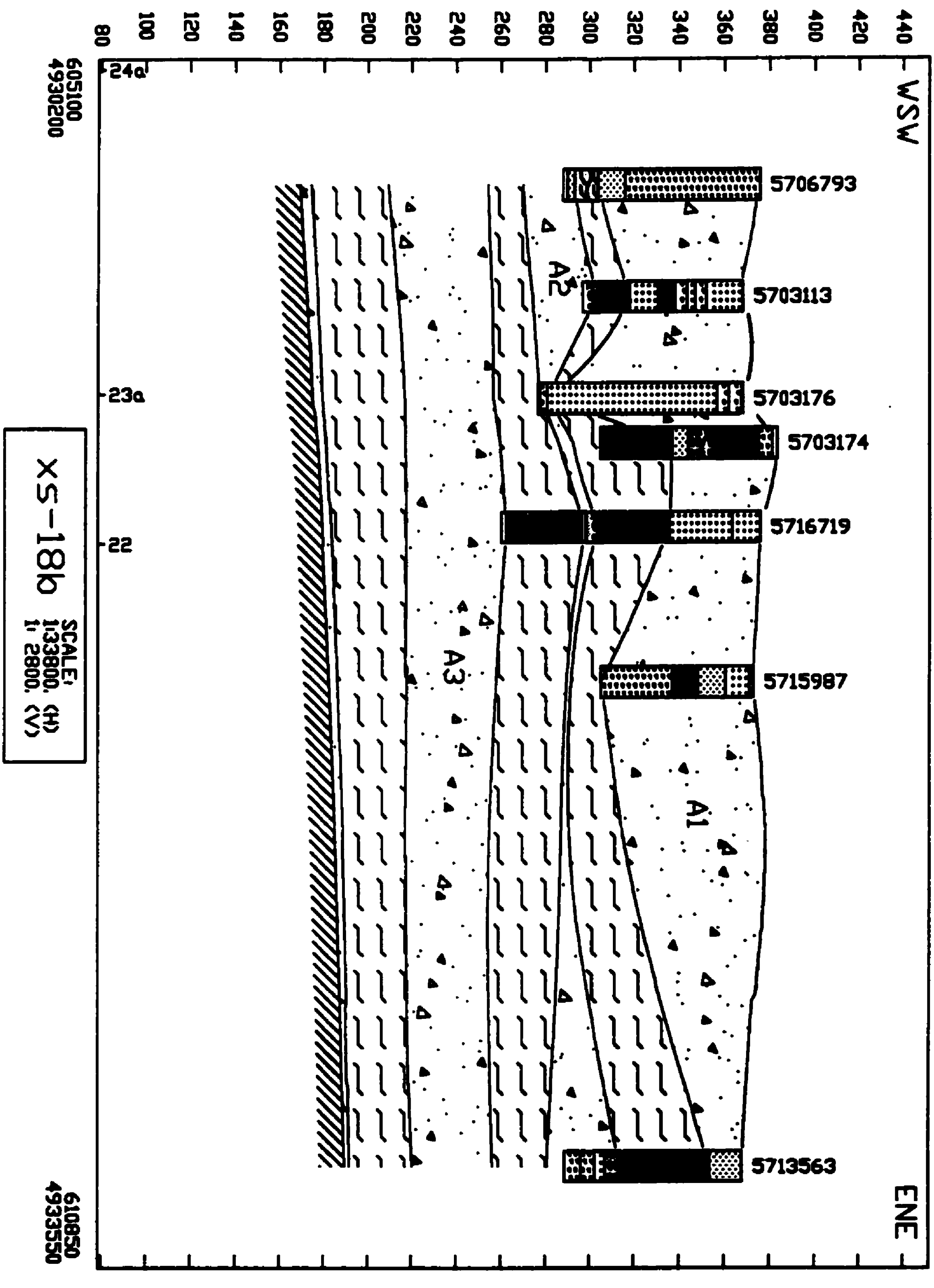
WSW
ENE
80
100
120
140
160
180
200
220
240
260
280
300
320
340
360
380
400
420
440
24a
23a
22
605100
4930200
610850
4933550
5706793
5703113
5703176
5703174
5716719
5715987
5713563
A1
A2
A3
XS-18b
SCALE:
1:33800. (H)
1: 2800. (V)

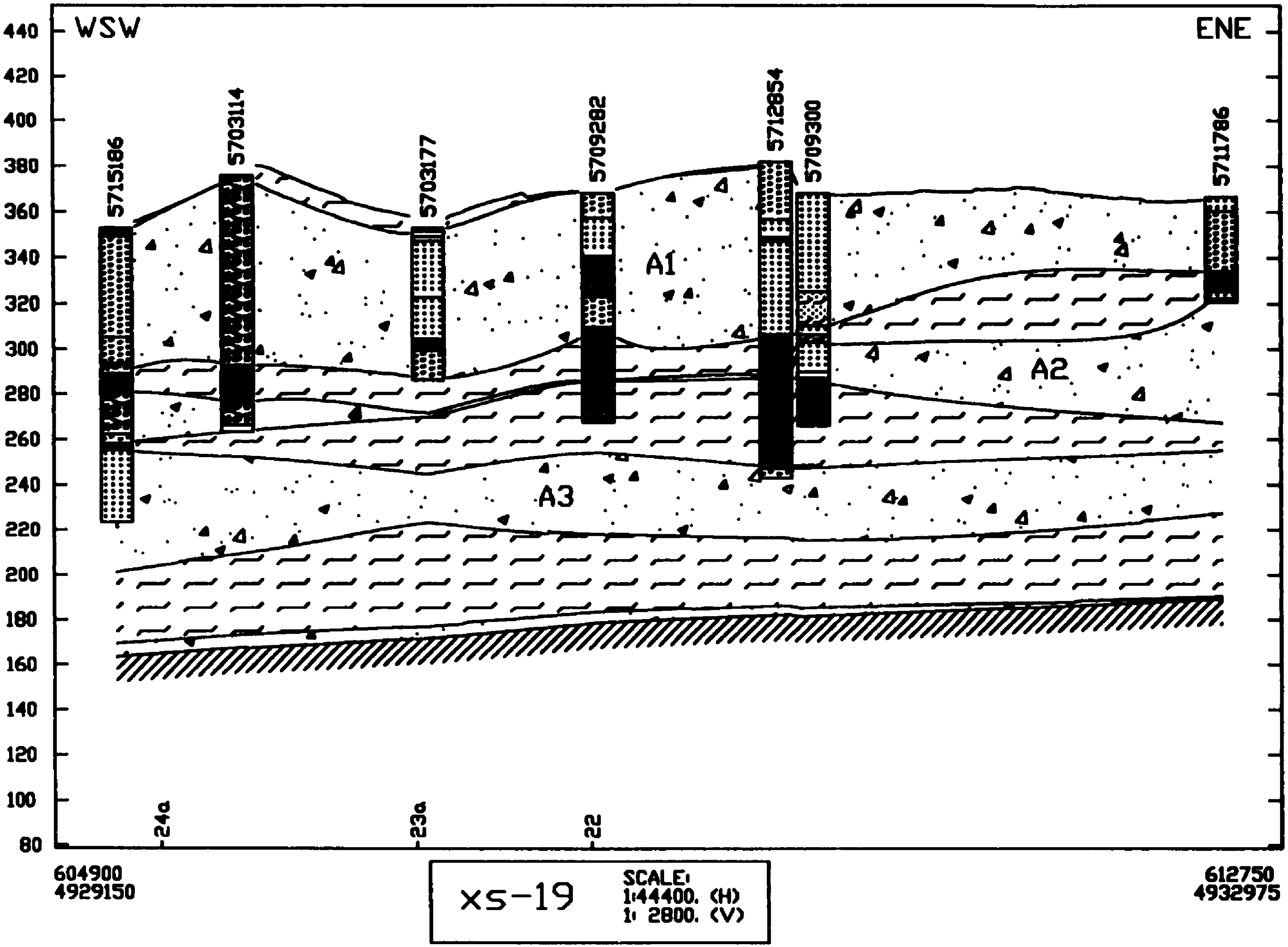
WSW
ENE
440
420
400
380
360
340
320
300
280
260
240
220
200
180
160
140
120
100
80
5715186
5703114
5703177
5709282
5712854
5709300
5711786
A1
A2
A3
24a
23a
22
604900
4929150
612750
4932975
XS-19
SCALE:
1:44400. (H)
1: 2800. (V)

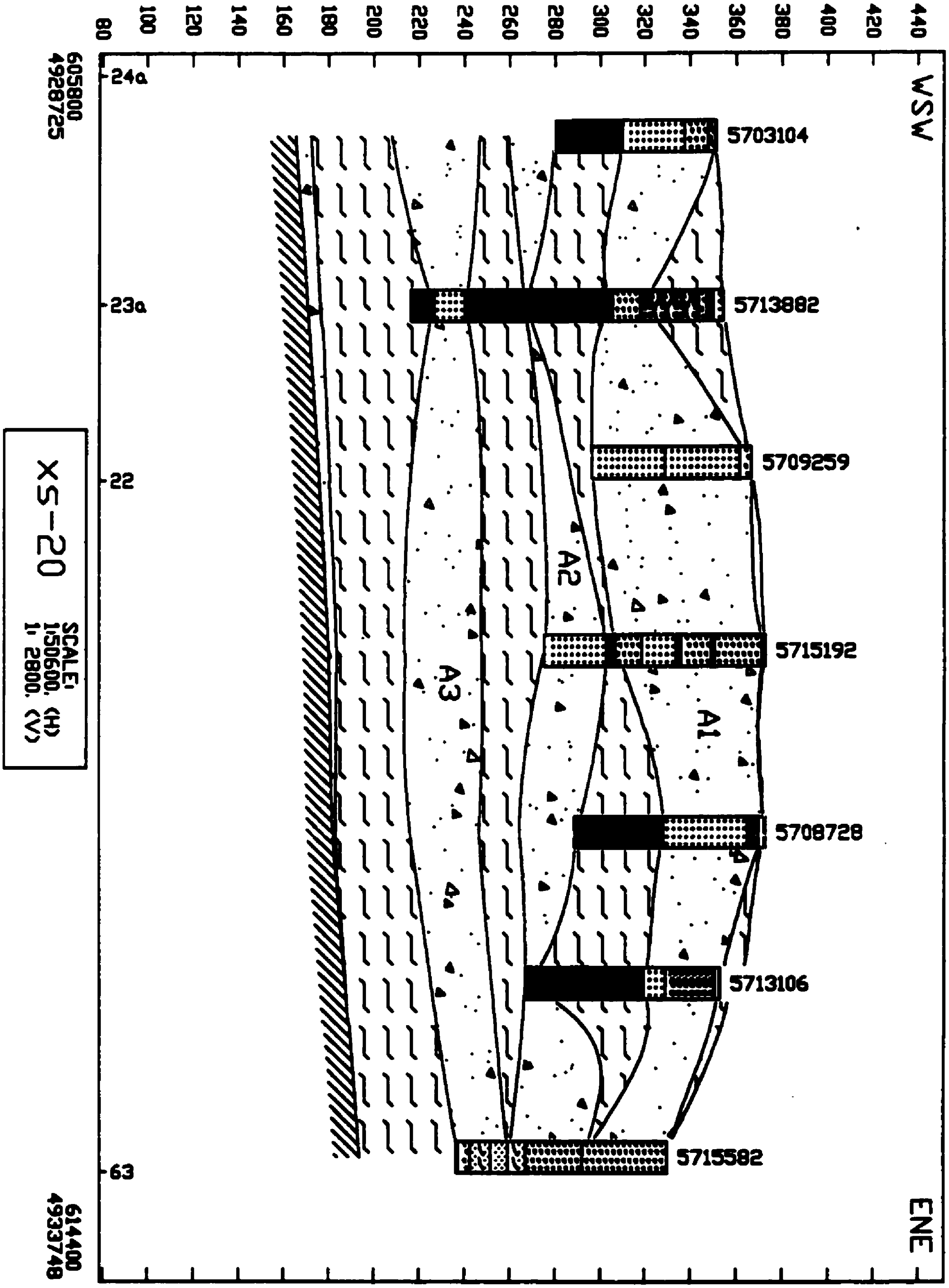
WSW
ENE
440
420
400
380
360
340
320
300
280
260
240
220
200
180
160
140
120
100
80
24a
23a
22
63
605800
4928725
614400
4933748
5703104
5713882
5709259
5715192
5708728
5713106
5715582
A1
A2
A3
XS-20
SCALE:
1:50600. (H)
1: 2800. (V)

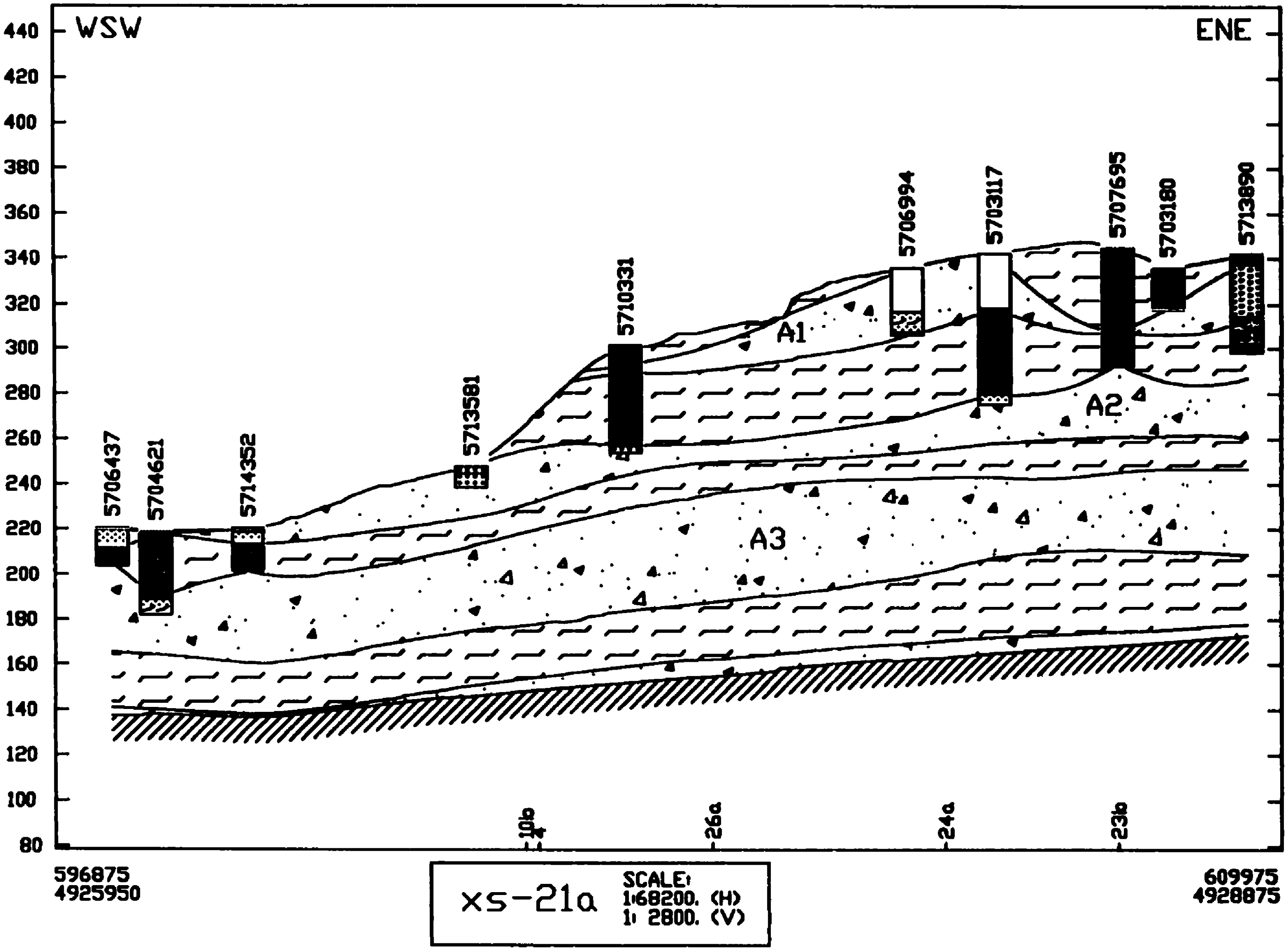
WSW
ENE
440
420
400
380
360
340
320
300
280
260
240
220
200
180
160
140
120
100
80
5706437
5704621
5714352
5713581
5710331
5706994
5703117
5707695
5703180
5713890
A1
A2
A3
10b
4
26a
24a
23b
596875
4925950
609975
4928875
xs-21a
SCALE:
1:68200. (H)
1: 2800. (V)

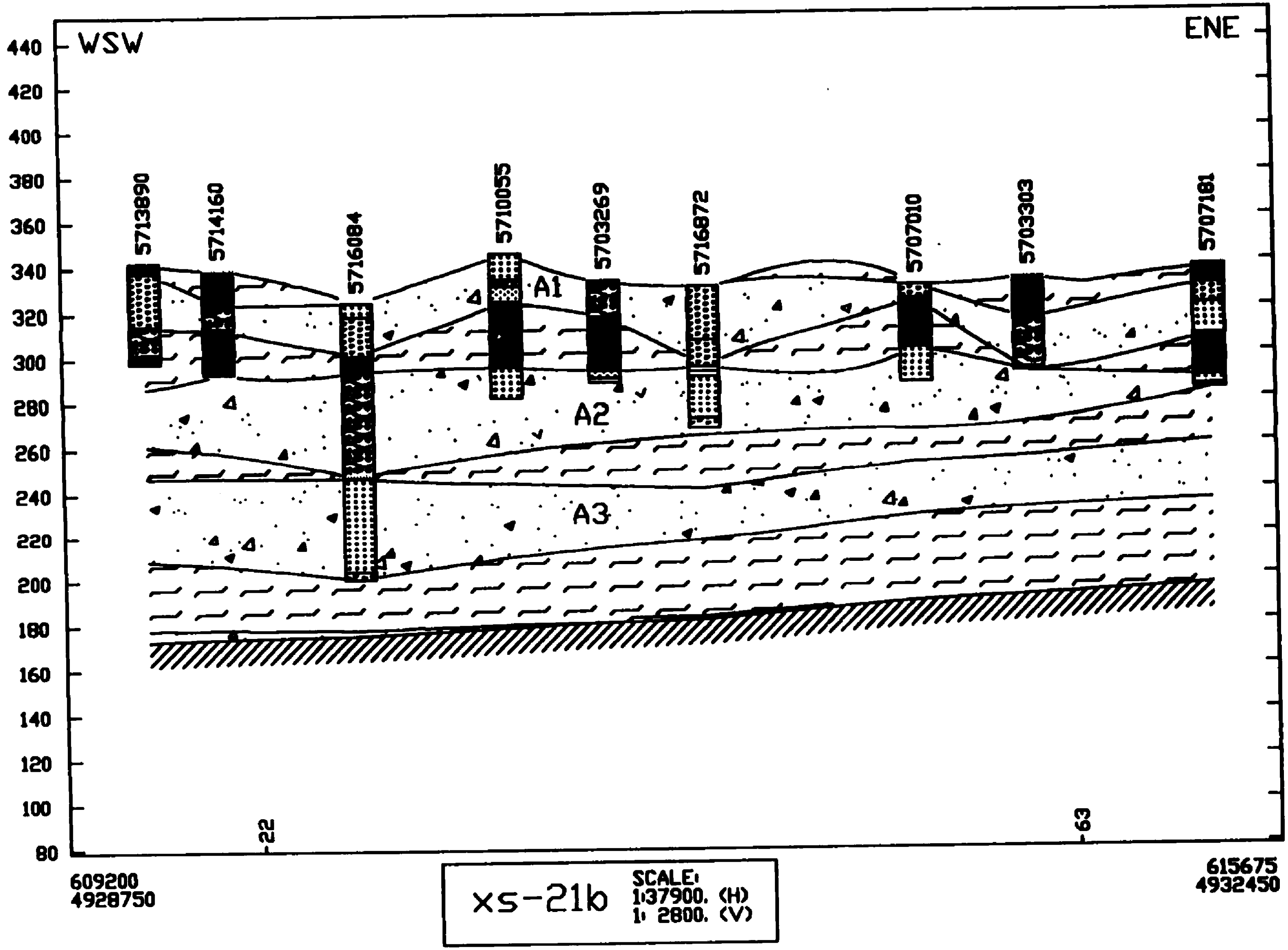
WSW
ENE
440
420
400
380
360
340
320
300
280
260
240
220
200
180
160
140
120
100
80
5713890
5714160
5716084
5710055
5703269
5716872
5707010
5703303
5707181
A1
A2
A3
22
63
609200
4928750
615675
4932450
xs-21b
SCALE:
1:37900. (H)
1: 2800. (V)

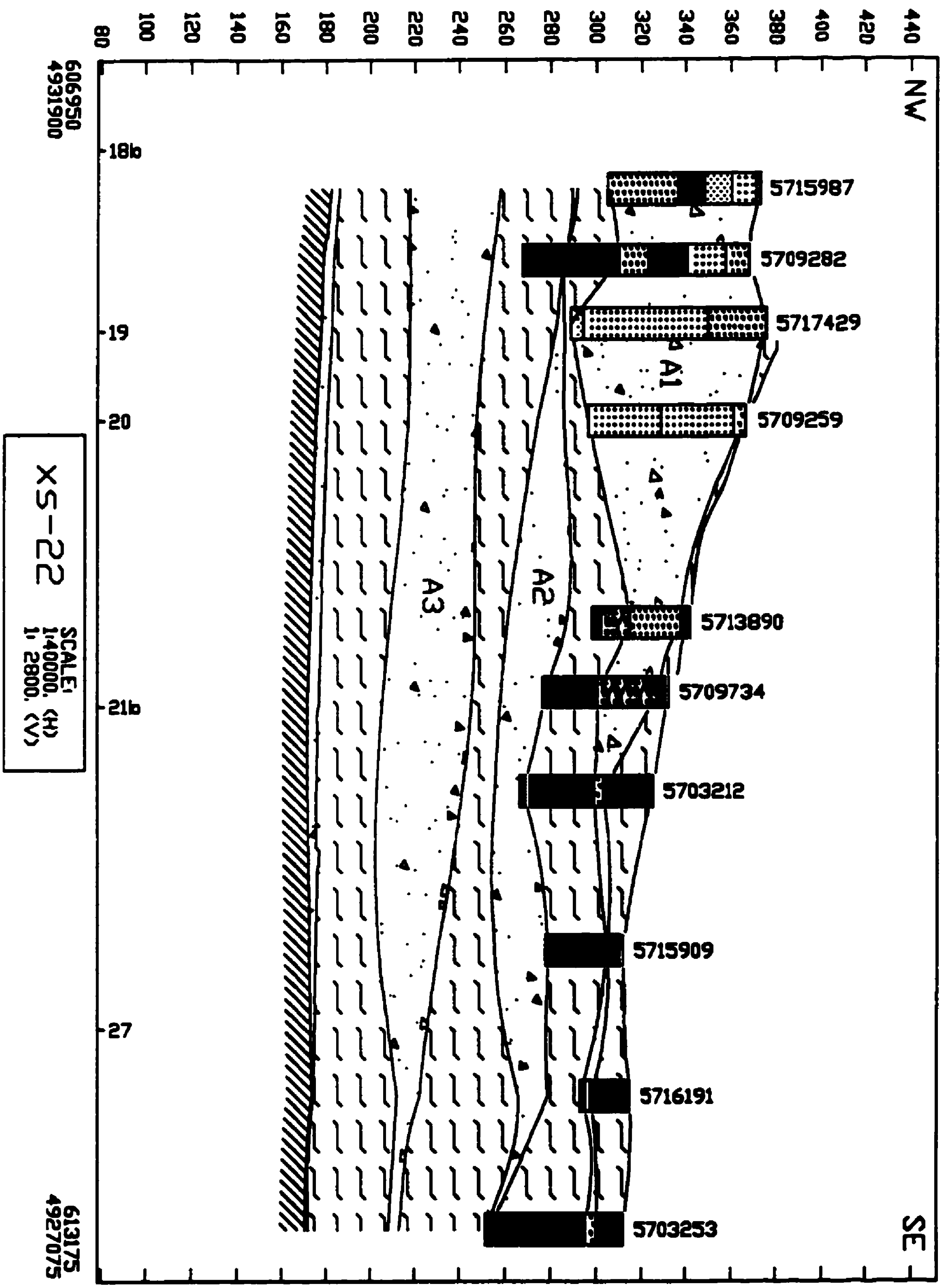
XS-22
SCALE:
1:40000. (H)
1: 2800. (V)
606950
4931900
613175
4927075
NW
SE
80
100
120
140
160
180
200
220
240
260
280
300
320
340
360
380
400
420
440
18b
19
20
21b
27
A1
A2
A3
5715987
5709282
5717429
5709259
5713890
5709734
5703212
5715909
5716191
5703253

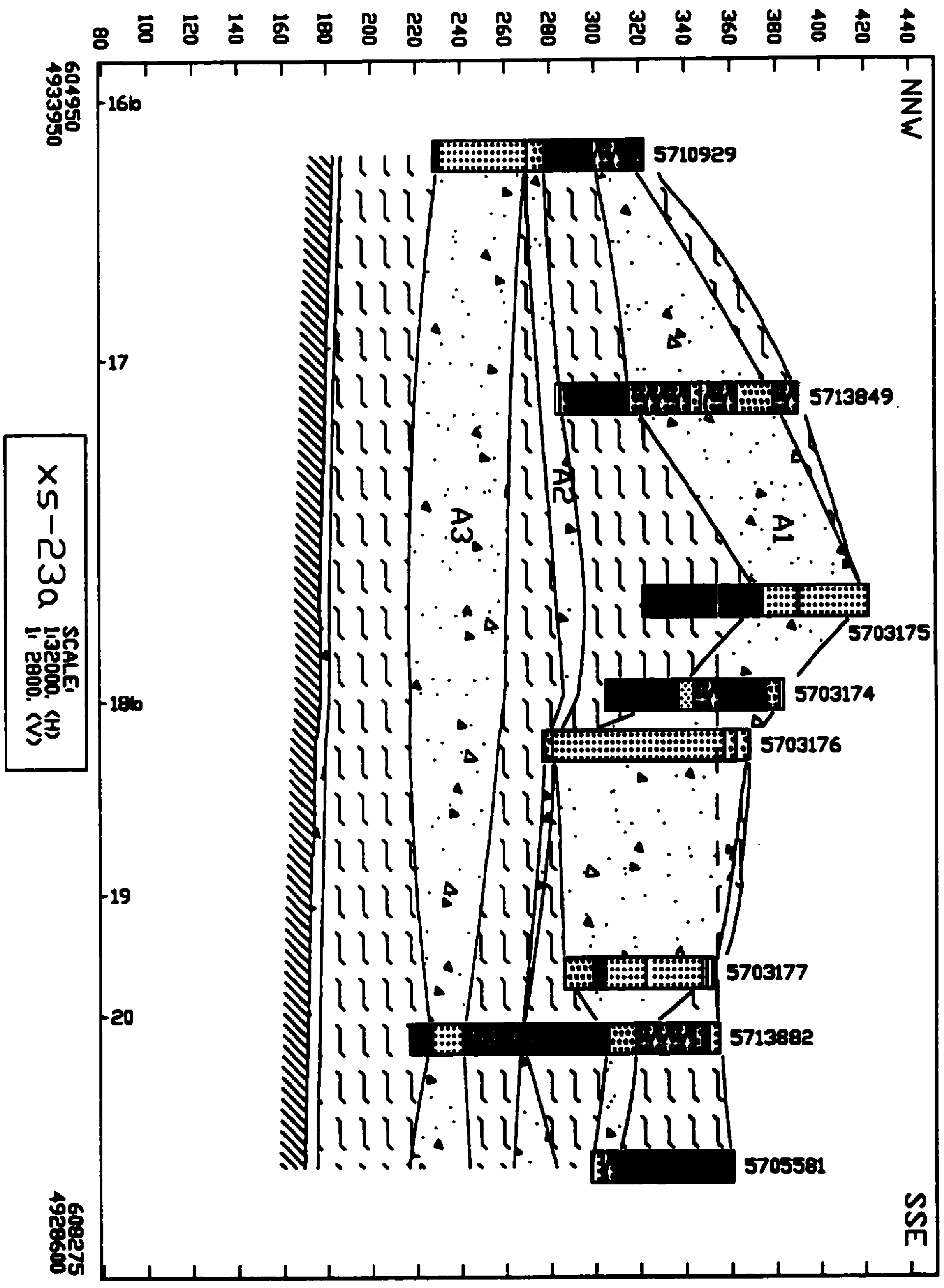
XS-23a
SCALE:
1:32000. (H)
1: 2800. (V)
NNW
SSE
604950
4933950
608275
4928600
16b
17
18b
19
20
80
100
120
140
160
180
200
220
240
260
280
300
320
340
360
380
400
420
440
A1
A2
A3
5710929
5713849
5703175
5703174
5703176
5703177
5713882
5705581

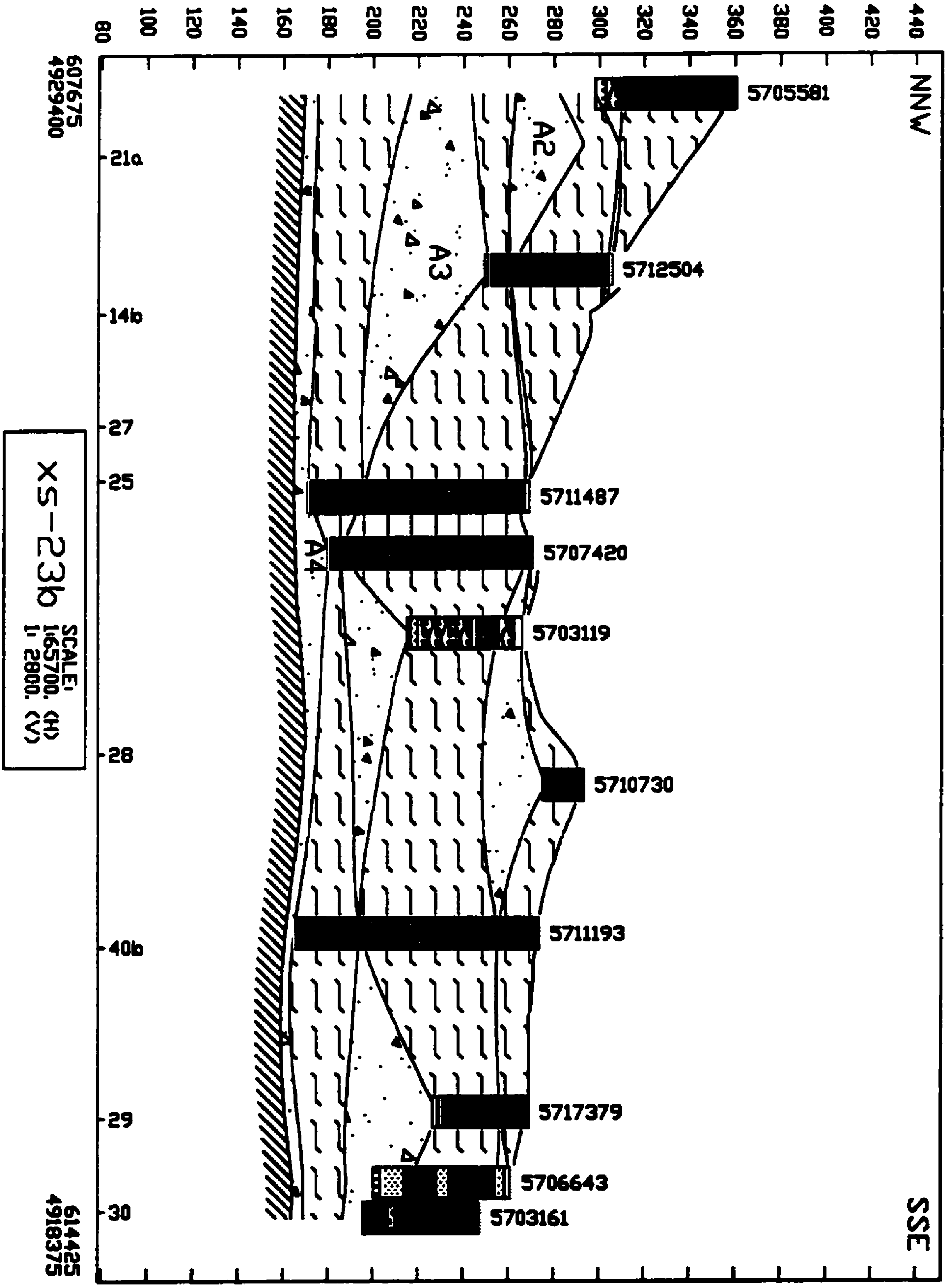
NNW
SSE
440
420
400
380
360
340
320
300
280
260
240
220
200
180
160
140
120
100
80
5705581
5712504
5711487
5707420
5703119
5710730
5711193
5717379
5706643
5703161
A2
A3
A4
607675
4929400
21a
14b
27
25
28
40b
29
30
614425
4918375
XS-23b
SCALE:
1:65700. (H)
1: 2800. (V)

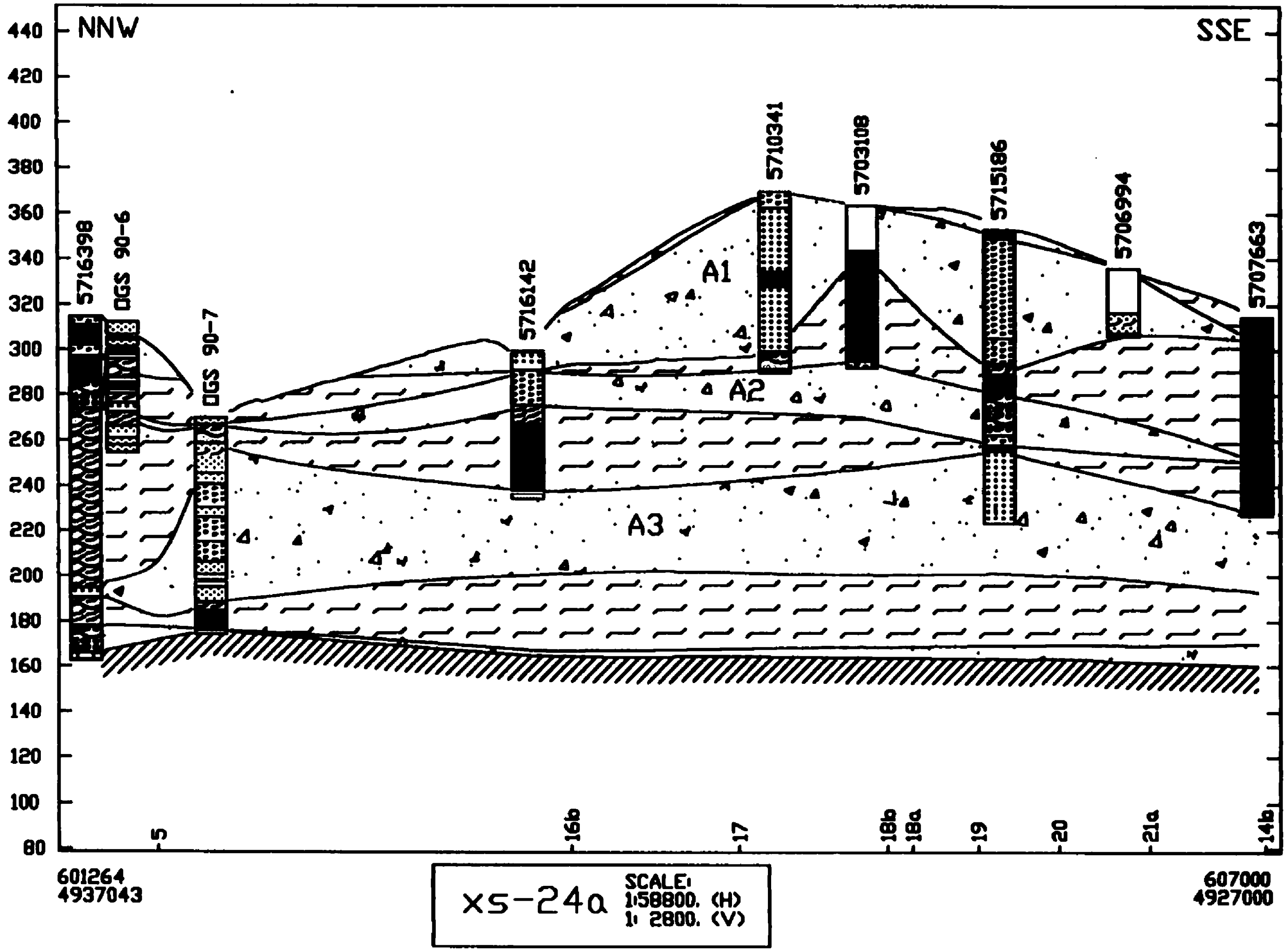
NNW
SSE
440
420
400
380
360
340
320
300
280
260
240
220
200
180
160
140
120
100
80
5716398
OGS 90-6
OGS 90-7
5716142
5710341
5703108
5715186
5706994
5707663
A1
A2
A3
5
16b
17
18b
18a
19
20
21a
14b
601264
4937043
607000
4927000
xs-24a
SCALE:
1:58800. (H)
1: 2800. (V)

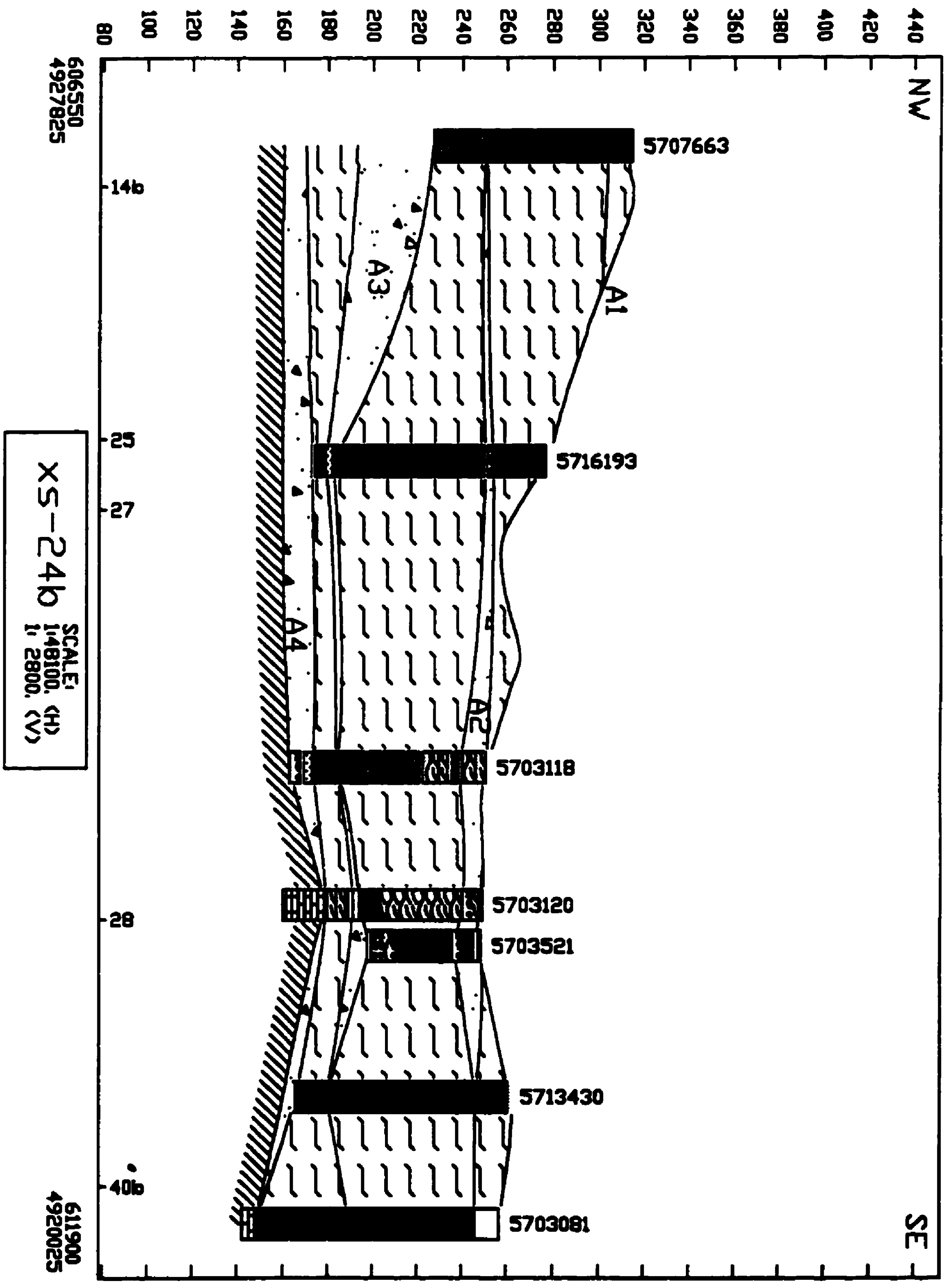
NW
SE
80
100
120
140
160
180
200
220
240
260
280
300
320
340
360
380
400
420
440
5707663
5716193
5703118
5703120
5703521
5713430
5703081
A1
A2
A3
A4
14b
25
27
28
40b
606550
4927825
611900
4920025
XS-24b
SCALE:
1:48100. (H)
1: 2800. (V)

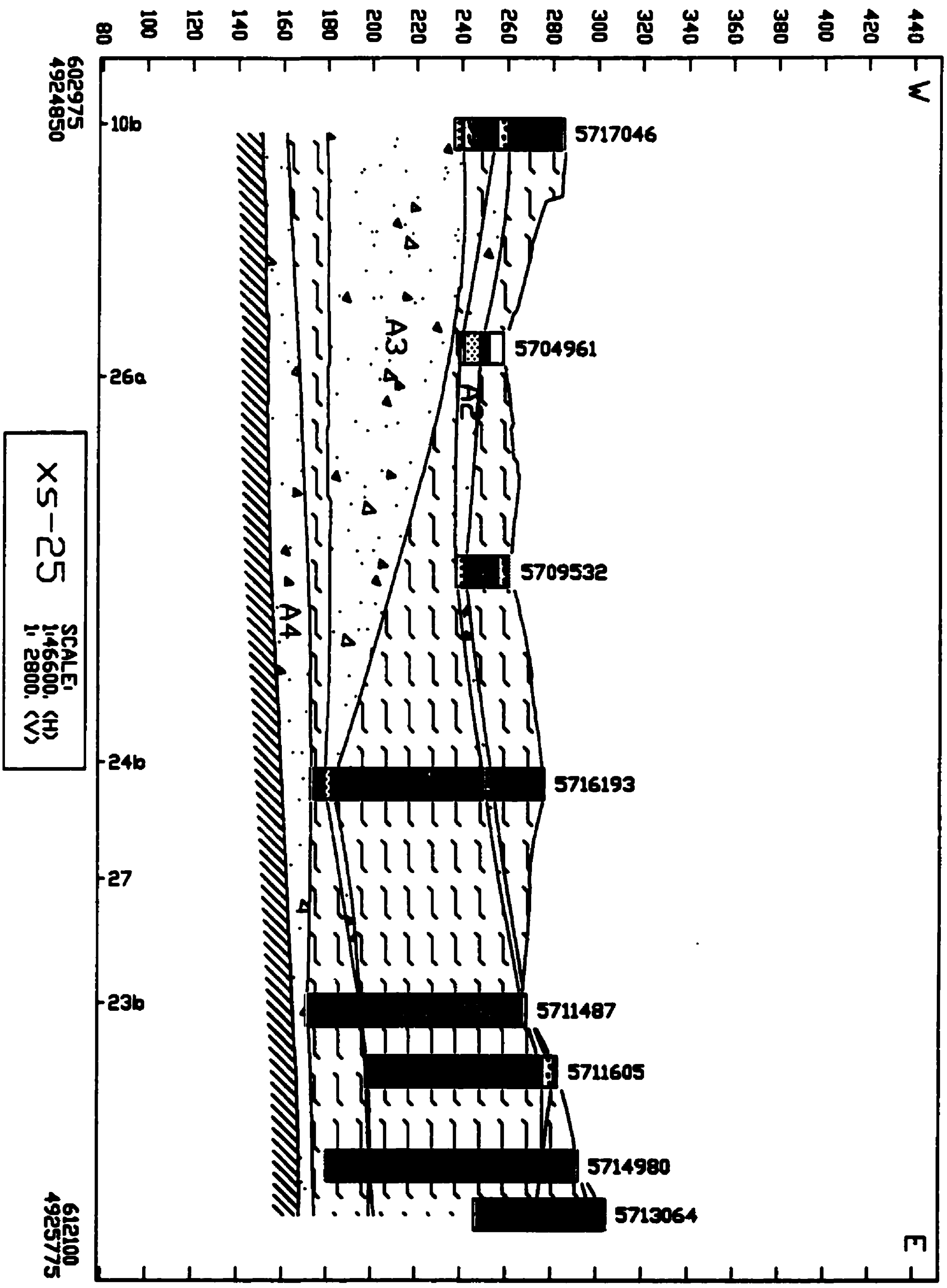
W
E
80
100
120
140
160
180
200
220
240
260
280
300
320
340
360
380
400
420
440
602975
4924850
612100
4925775
10b
26a
24b
27
23b
5717046
5704961
5709532
5716193
5711487
5711605
5714980
5713064
A3
A2
A4
XS-25
SCALE:
1:46600. (H)
1: 2800. (V)

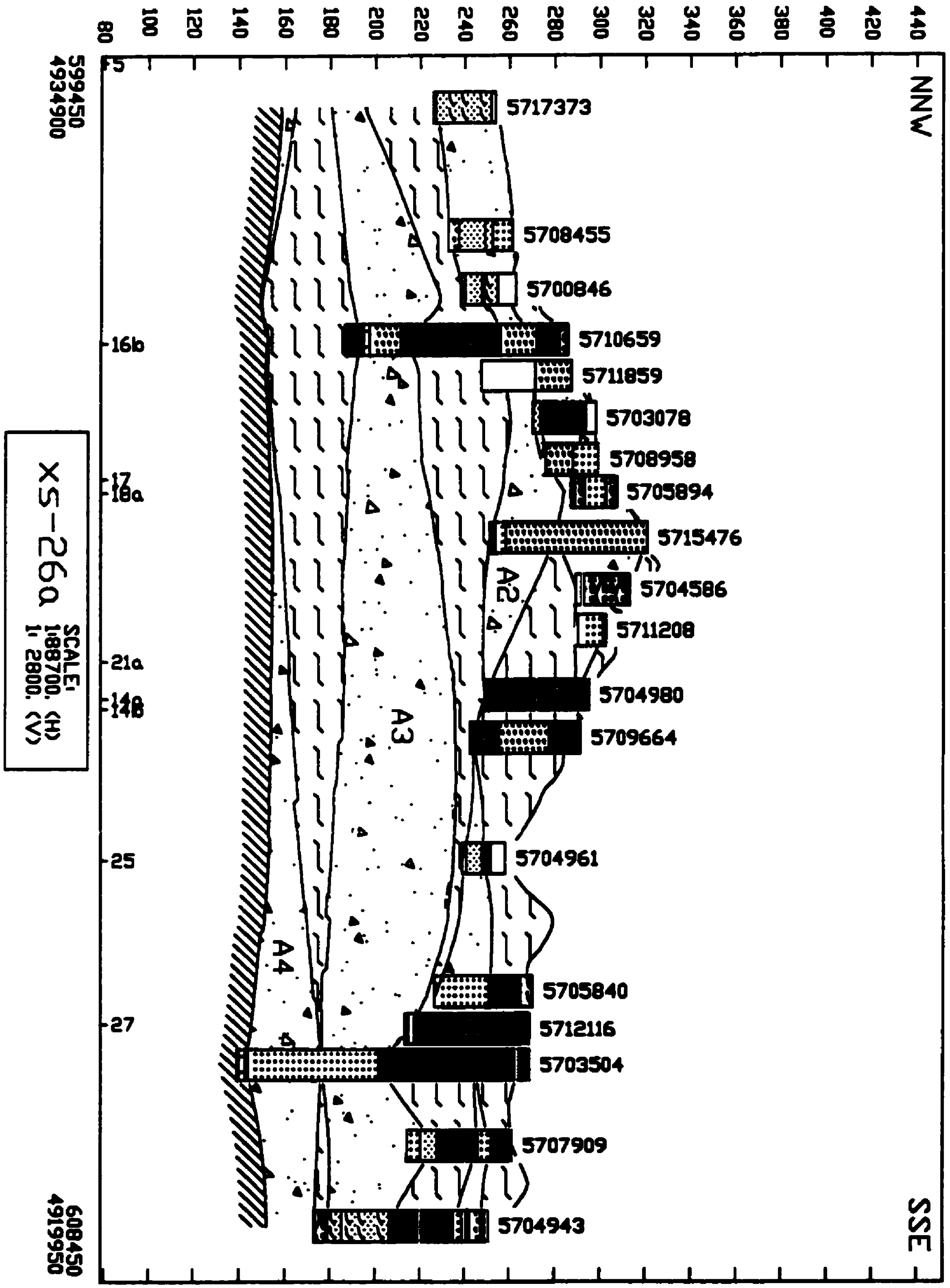
xs-26a
SCALE: 1:88700. (H)
1: 2800. (V)
NNW
SSE
80
100
120
140
160
180
200
220
240
260
280
300
320
340
360
380
400
420
440
599450
4934900
608450
4919950
F5
16b
17
18a
21a
14a
14B
25
27
A2
A3
A4
5717373
5708455
5700846
5710659
5711859
5703078
5708958
5705894
5715476
5704586
5711208
5704980
5709664
5704961
5705840
5712116
5703504
5707909
5704943

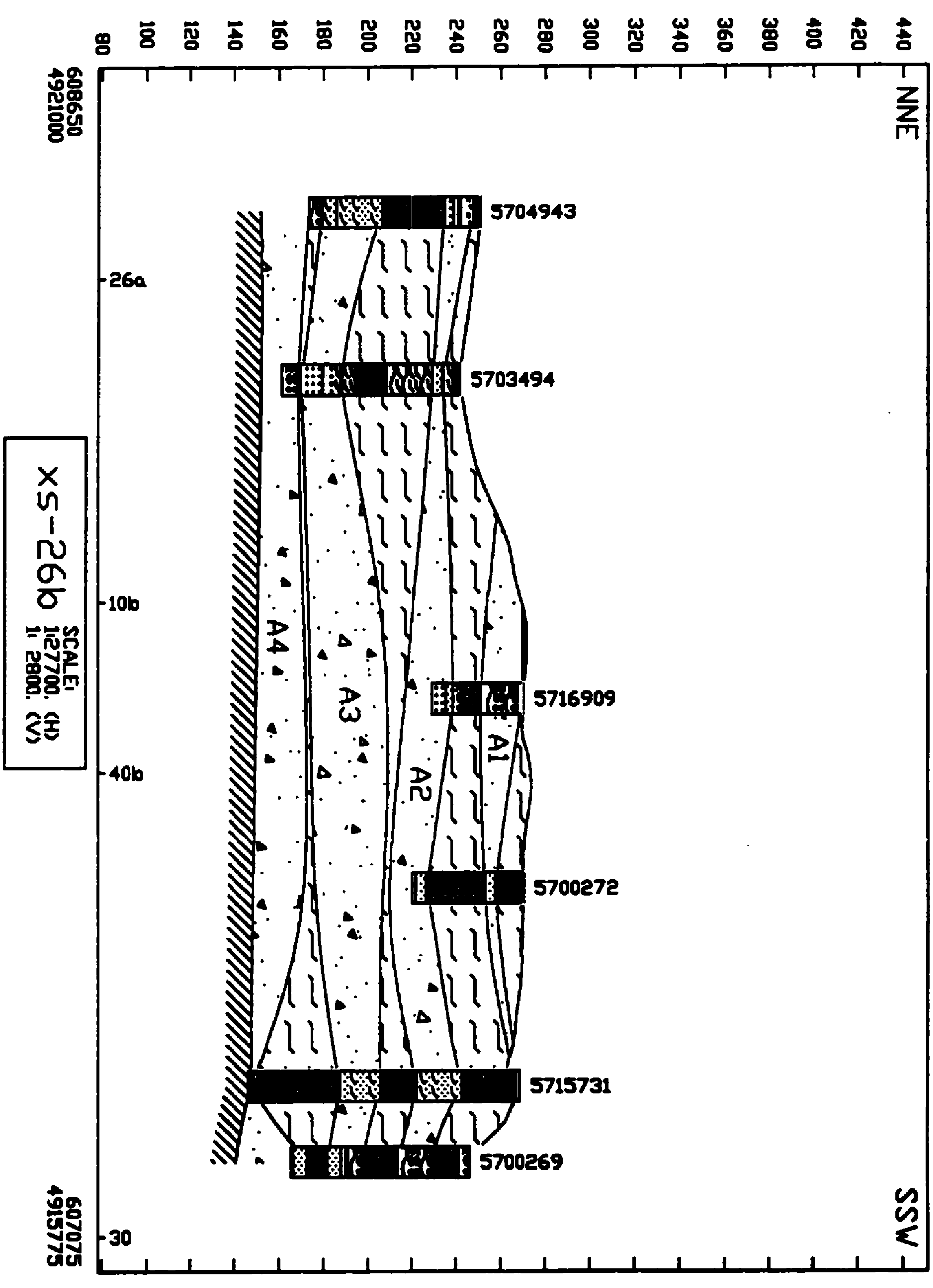
NNE
SSW
80
100
120
140
160
180
200
220
240
260
280
300
320
340
360
380
400
420
440
608650
4921000
607075
4915775
26a
10b
40b
30
5704943
5703494
5716909
5700272
5715731
5700269
A1
A2
A3
A4
xs-26b
SCALE:
1:27700. (H)
1: 2800. (V)

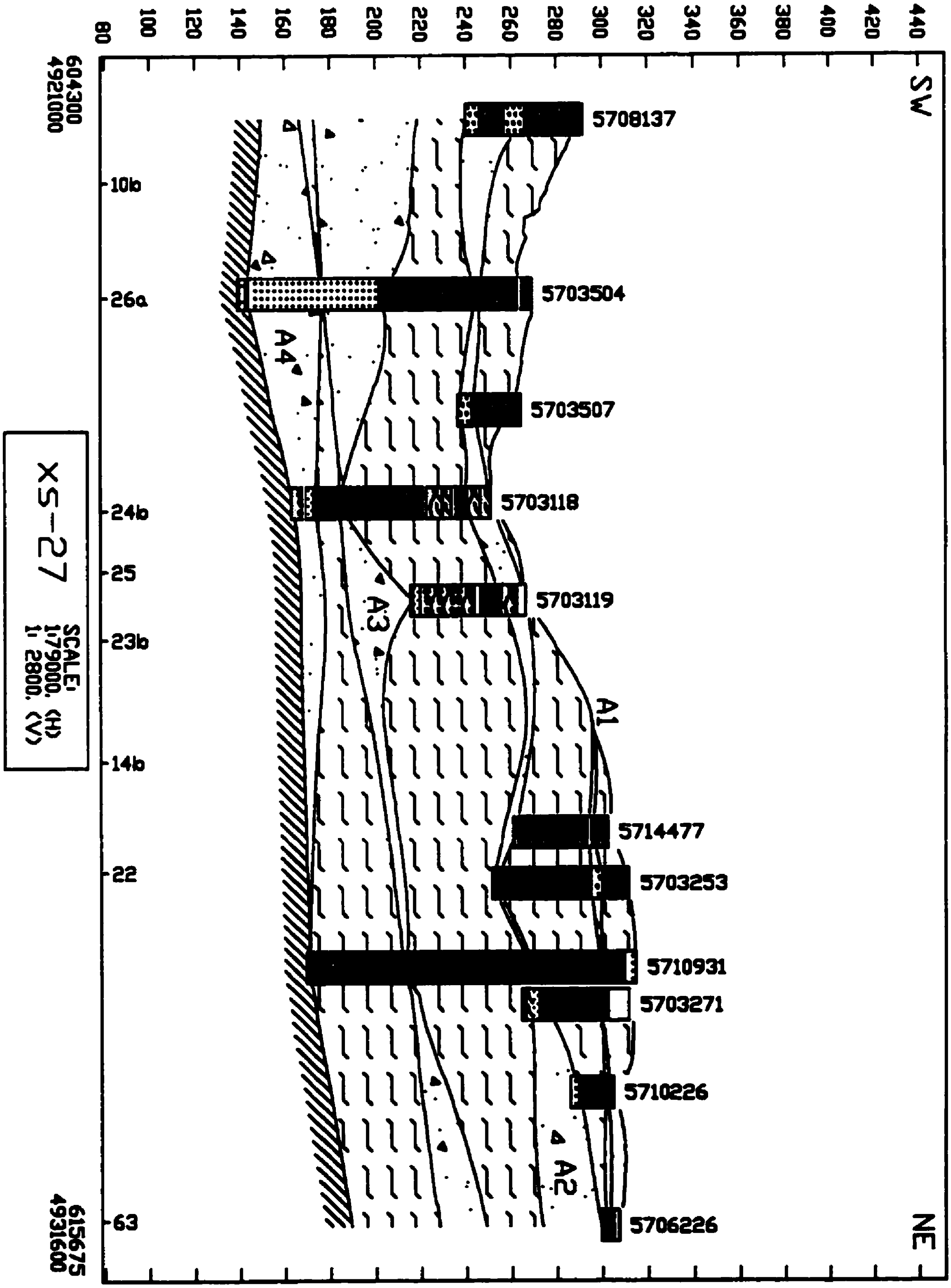
SW
NE
80
100
120
140
160
180
200
220
240
260
280
300
320
340
360
380
400
420
440
604300
4921000
615675
4931600
10b
26a
24b
25
23b
14b
22
63
5708137
5703504
5703507
5703118
5703119
5714477
5703253
5710931
5703271
5710226
5706226
A1
A2
A3
A4
XS-27
SCALE:
1:79000. (H)
1: 2800. (V)

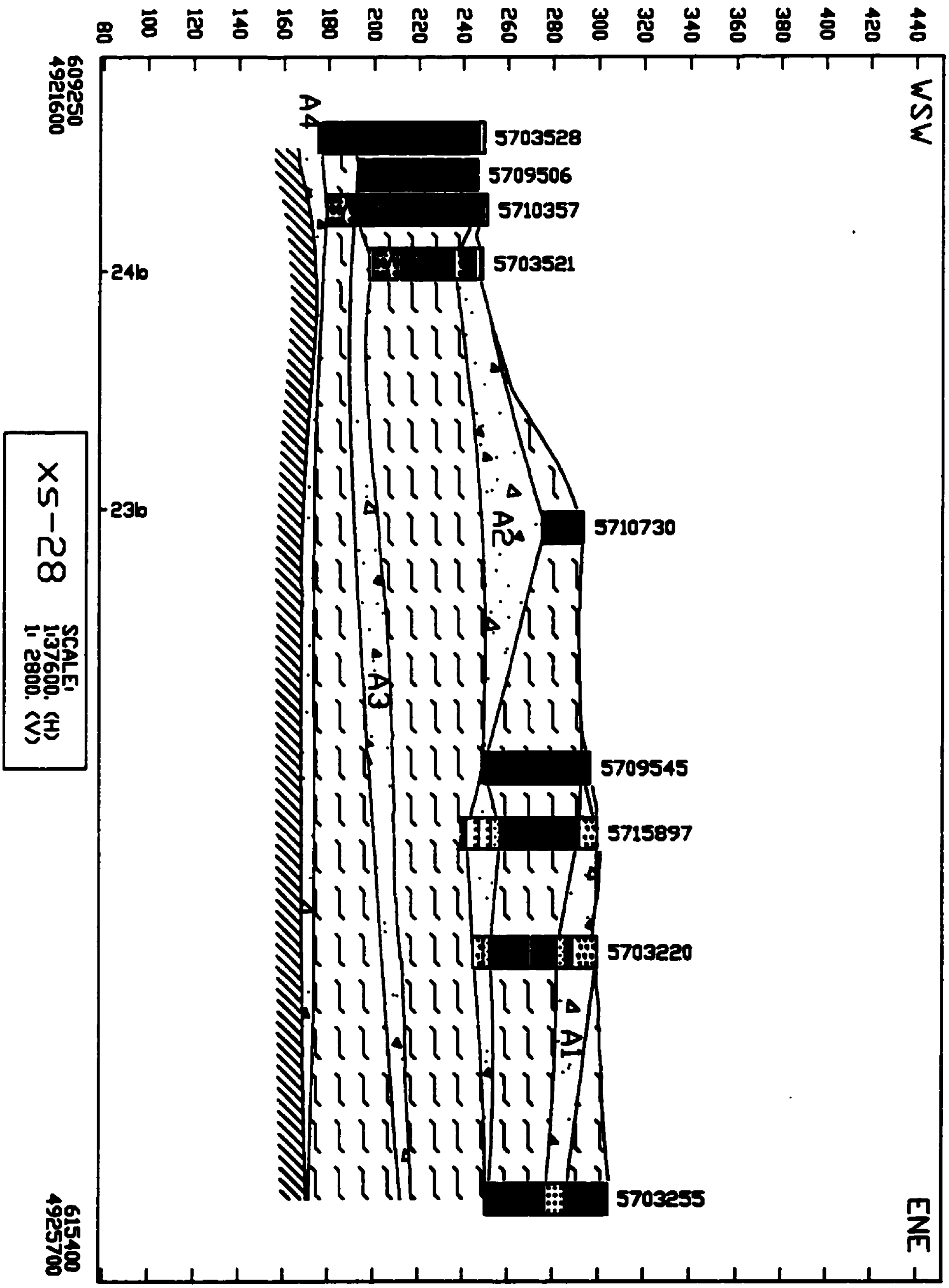
WSW
ENE
80
100
120
140
160
180
200
220
240
260
280
300
320
340
360
380
400
420
440
609250
4921600
615400
4925700
24b
23b
5703528
5709506
5710357
5703521
5710730
5709545
5715897
5703220
5703255
A1
A2
A3
A4
XS-28
SCALE:
1:37600. (H)
1: 2800. (V)

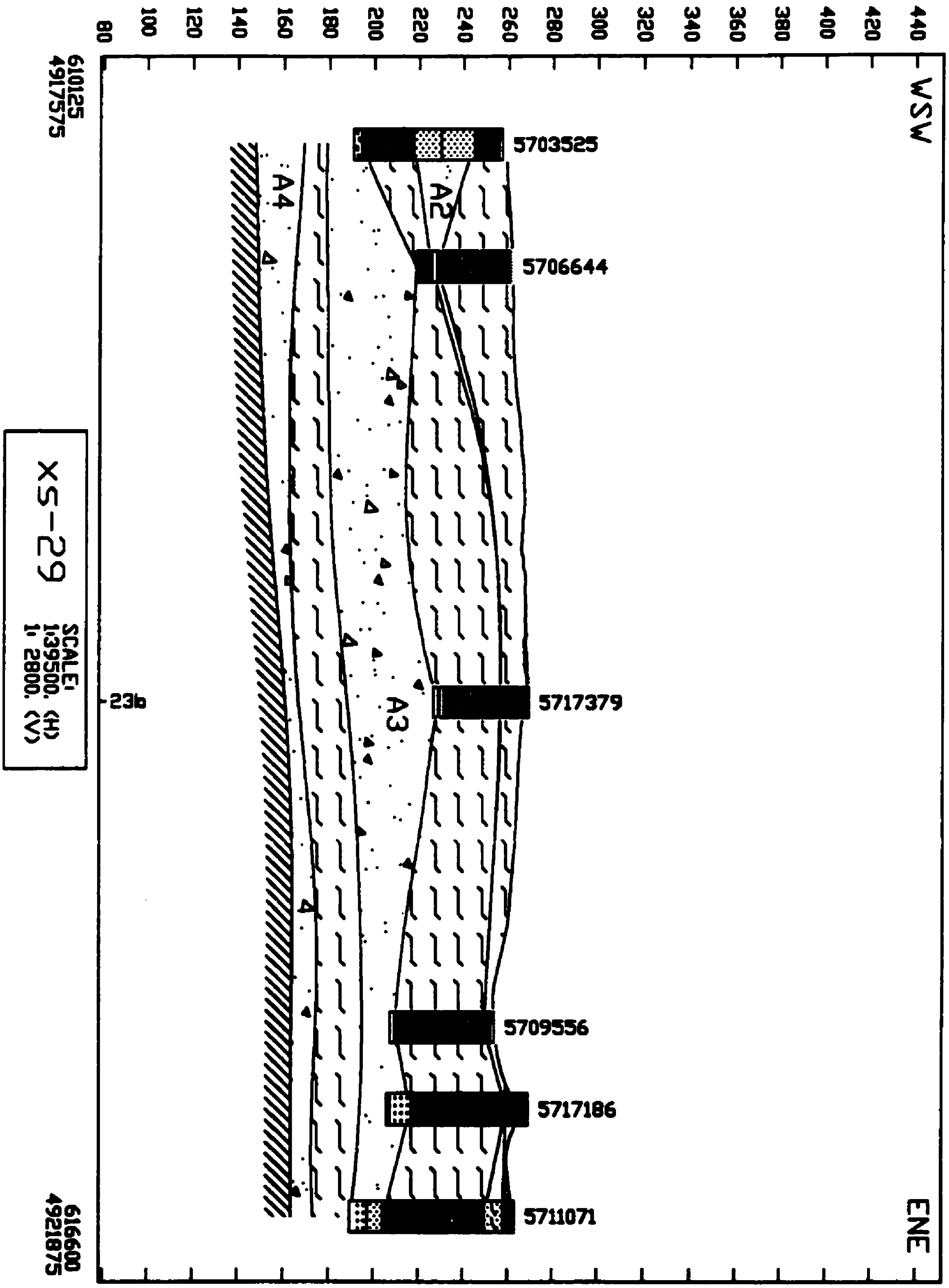
WSW
ENE
80
100
120
140
160
180
200
220
240
260
280
300
320
340
360
380
400
420
440
610125
4917575
616600
4921875
23b
5703525
5706644
5717379
5709556
5717186
5711071
A2
A3
A4
XS-29
SCALE:
1:39500. (H)
1: 2800. (V)

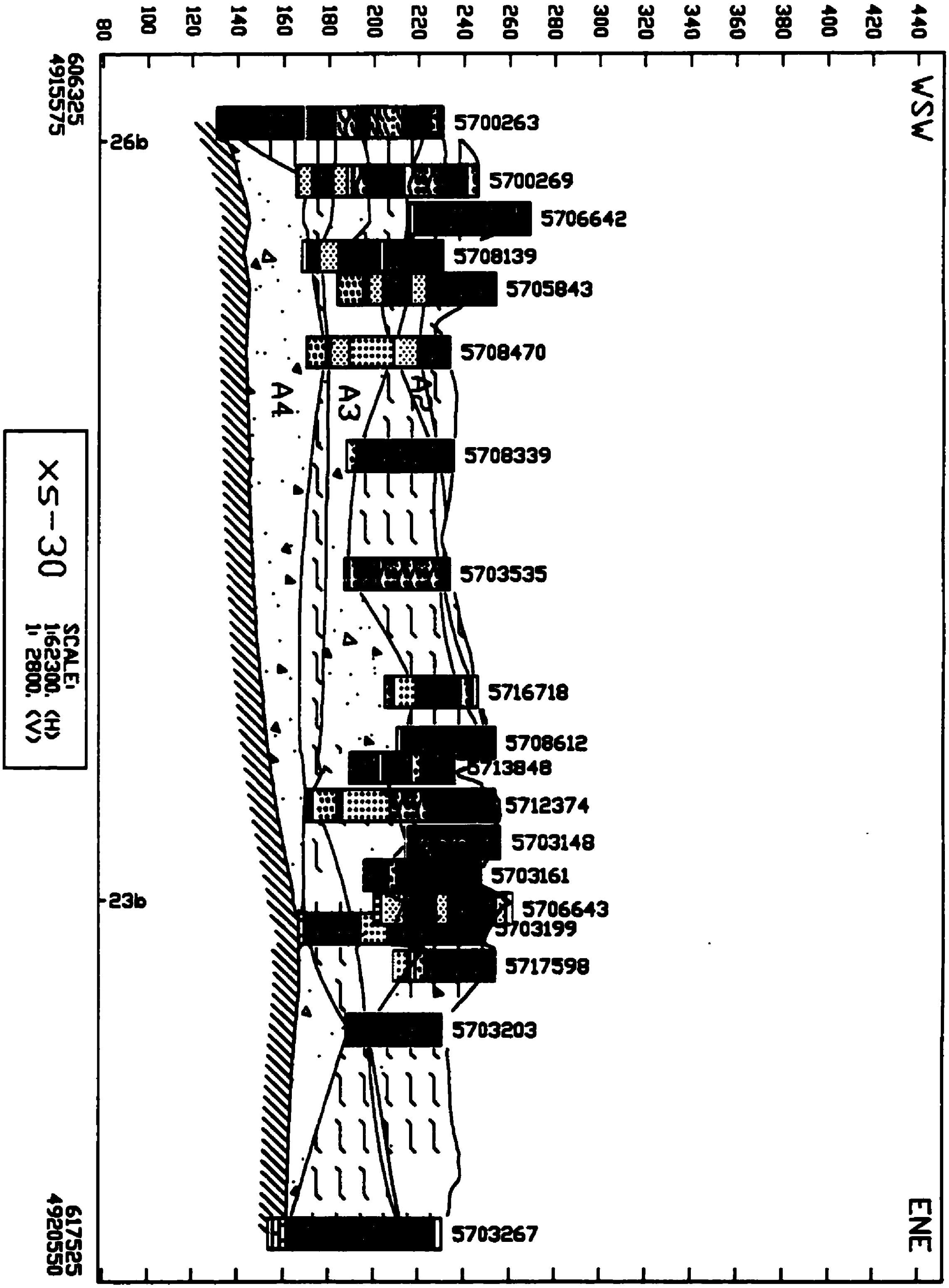

XS-30
SCALE: 1:62300. (H)
1: 2800. (V)
WSW
ENE
606325
4915575
617525
4920550
26b
23b
80
100
120
140
160
180
200
220
240
260
280
300
320
340
360
380
400
420
440
A4
A3
A2
5700263
5700269
5706642
5708139
5705843
5708470
5708339
5703535
5716718
5708612
5713848
5712374
5703148
5703161
5706643
5703199
5717598
5703203
5703267

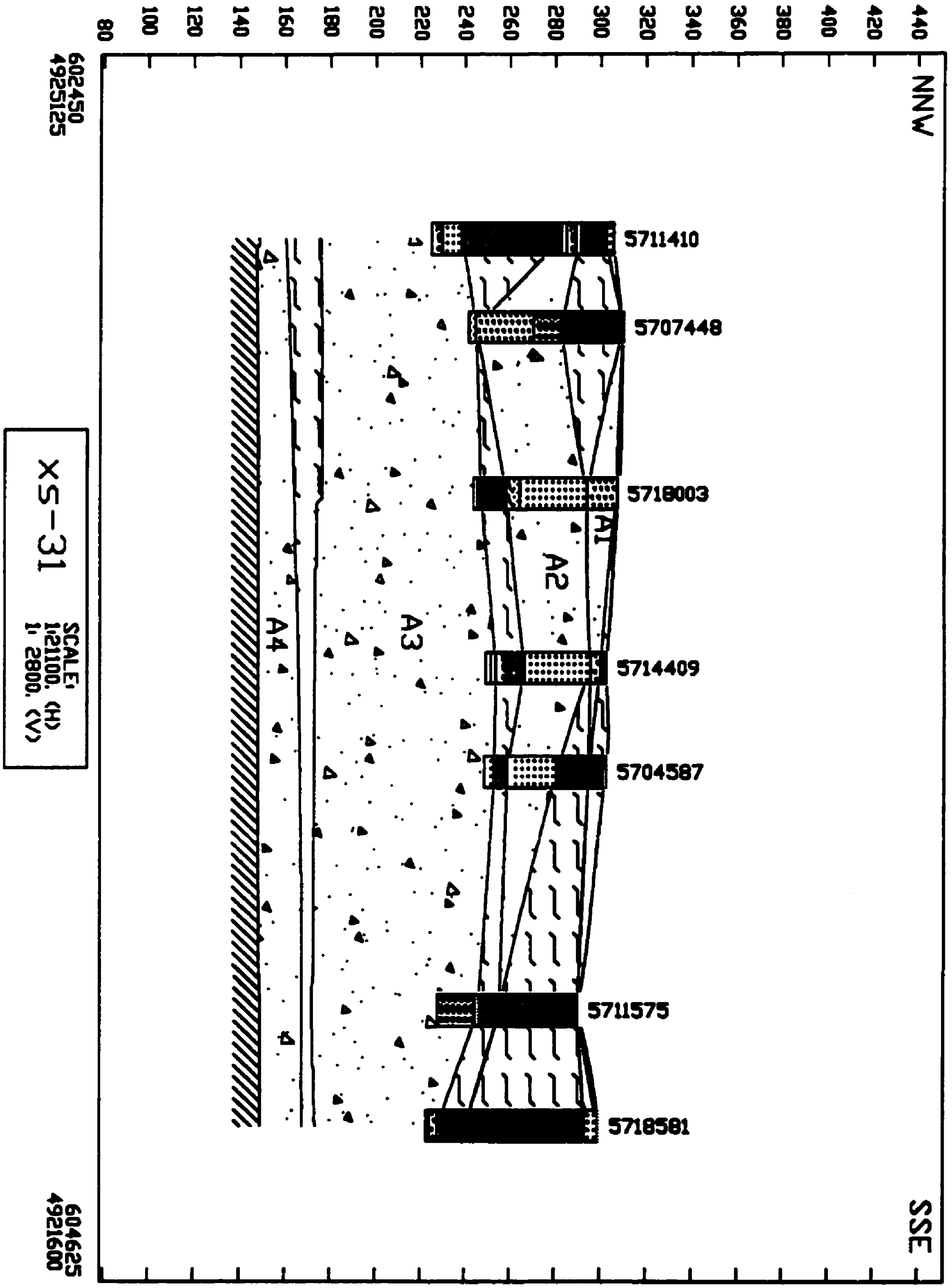
NNW
SSE
80
100
120
140
160
180
200
220
240
260
280
300
320
340
360
380
400
420
440
602450
4925125
604625
4921600
5711410
5707448
5718003
5714409
5704587
5711575
5718581
A1
A2
A3
A4
XS-31
SCALE:
1:2100. (H)
1: 2800. (V)

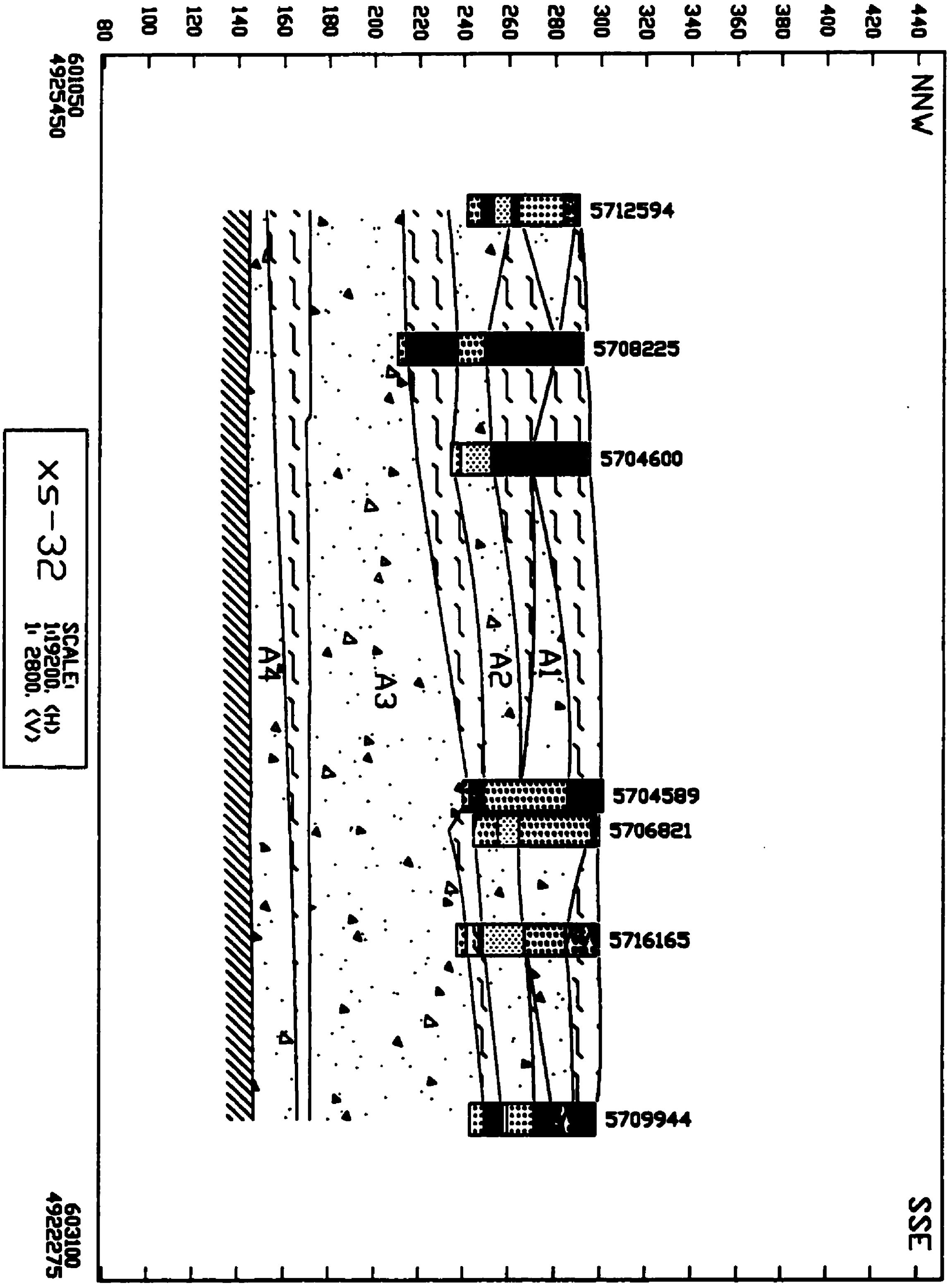
NNW
SSE
80
100
120
140
160
180
200
220
240
260
280
300
320
340
360
380
400
420
440
601050
4925450
603100
4922275
5712594
5708225
5704600
5704589
5706821
5716165
5709944
A1
A2
A3
A4
XS-32
SCALE: 1:19200. (H)
1: 2800. (V)

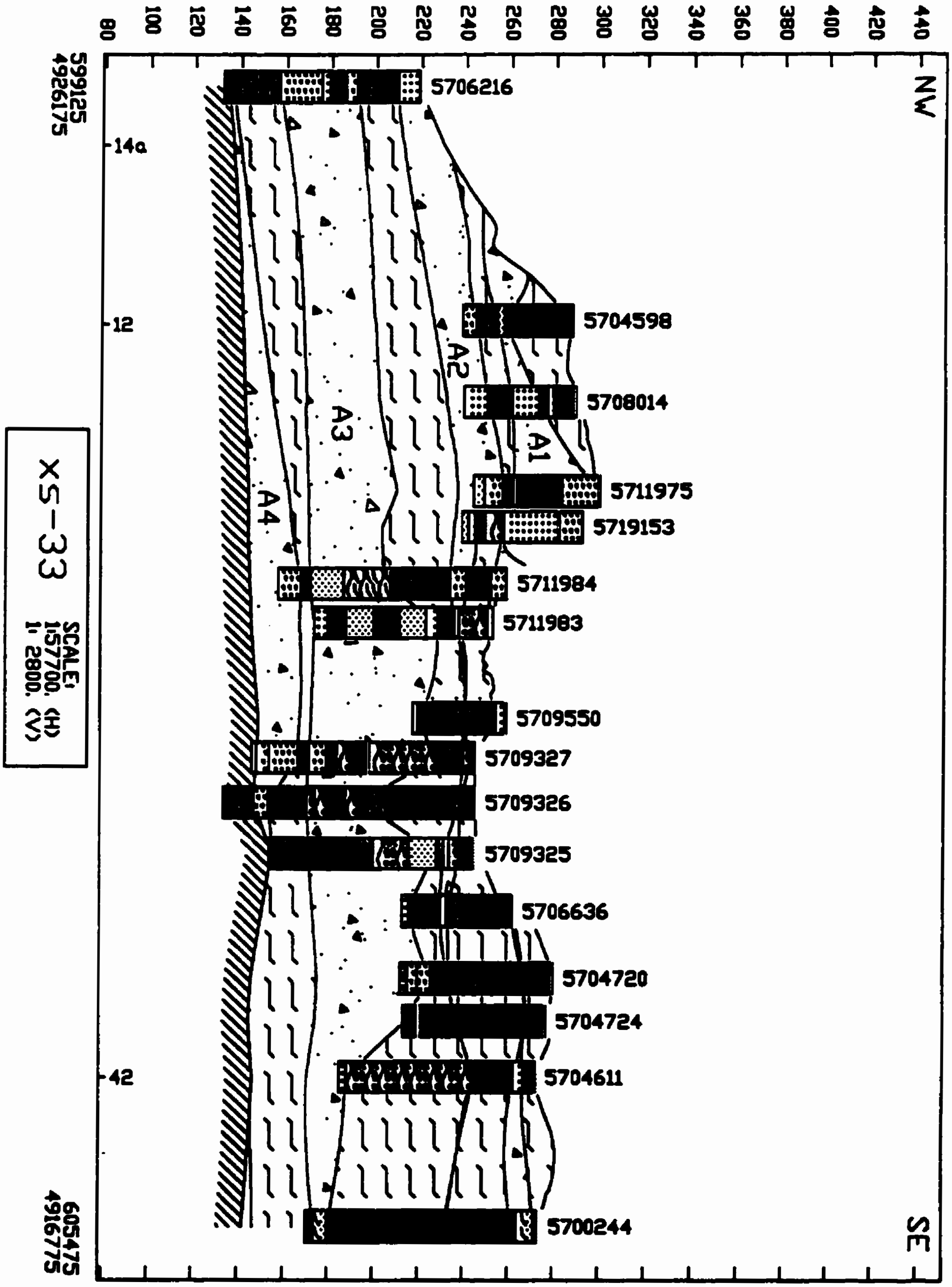
NW
SE
80
100
120
140
160
180
200
220
240
260
280
300
320
340
360
380
400
420
440
599125
4926175
605475
4916775
14a
12
42
5706216
5704598
5708014
5711975
5719153
5711984
5711983
5709550
5709327
5709326
5709325
5706636
5704720
5704724
5704611
5700244
A1
A2
A3
A4
XS-33
SCALE:
1:57700. (H)
1: 2800. (V)

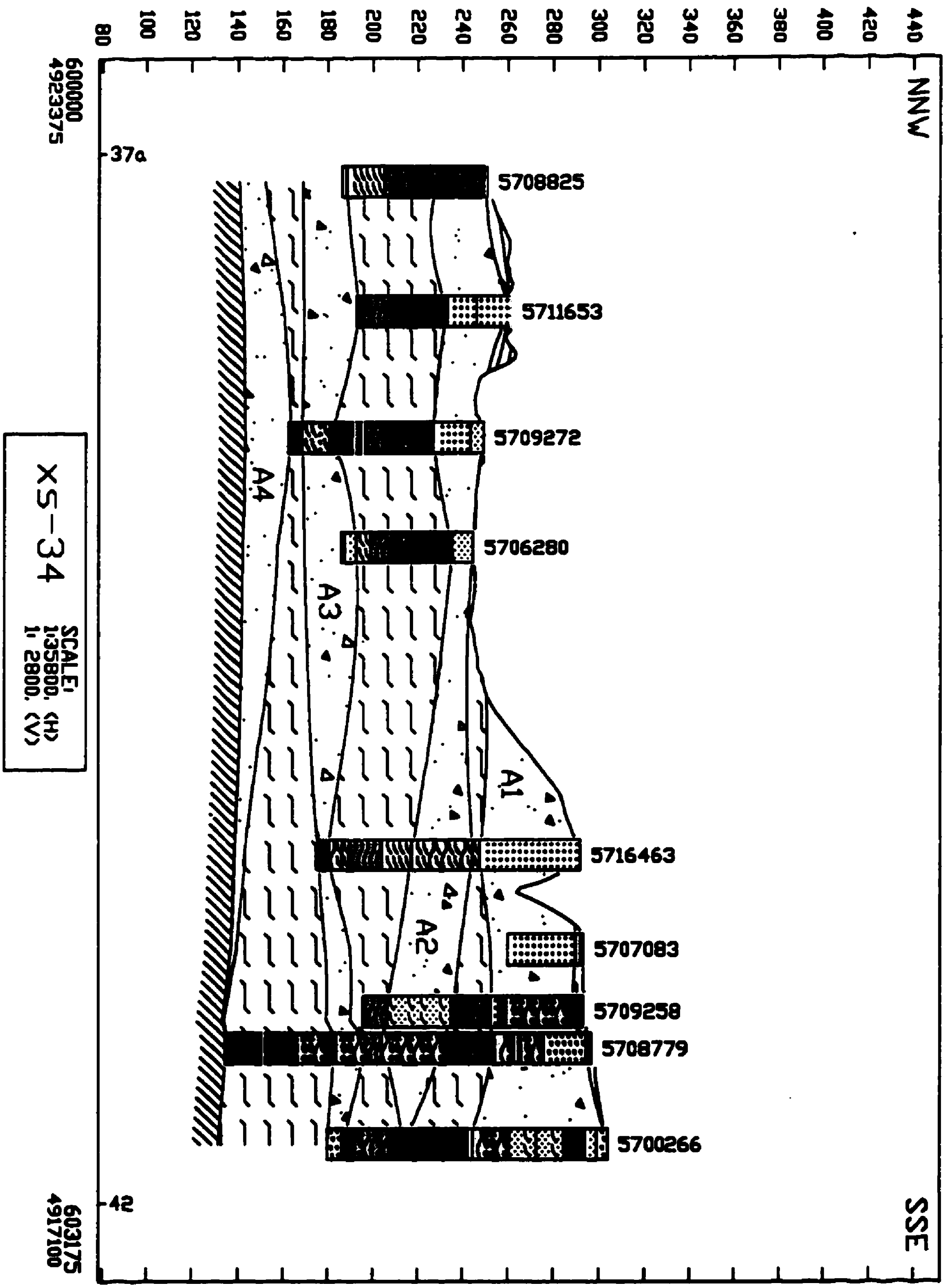
NNW
SSE
80
100
120
140
160
180
200
220
240
260
280
300
320
340
360
380
400
420
440
600000
4923375
603175
4917100
37a
42
5708825
5711653
5709272
5706280
5716463
5707083
5709258
5708779
5700266
A1
A2
A3
A4
XS-34
SCALE: 1:35800. (H)
1: 2800. (V)

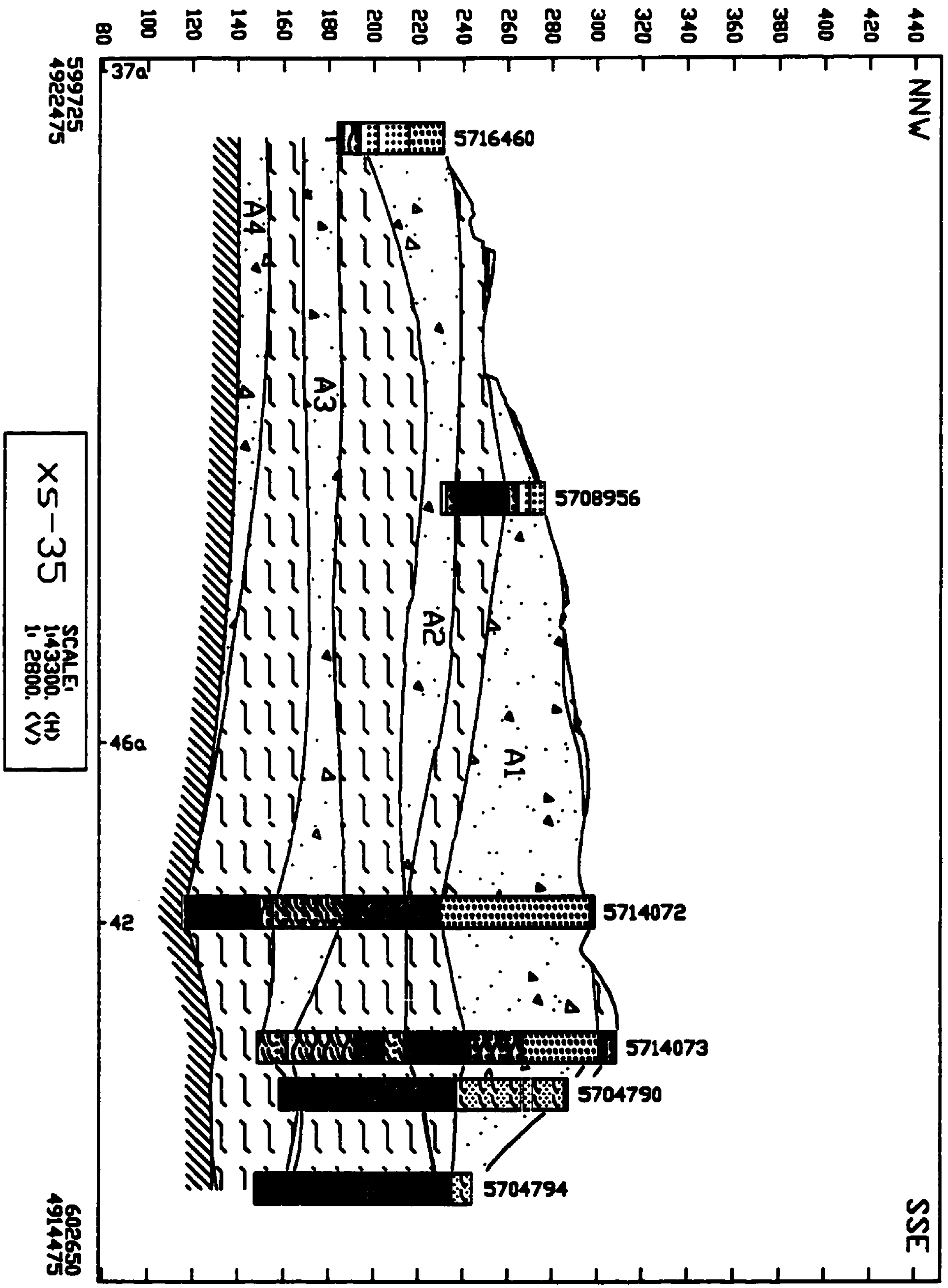

XS-35
SCALE: 1:43300. (H)
1: 2800. (V)
NNW
SSE
599725
4922475
602650
4914475
80
100
120
140
160
180
200
220
240
260
280
300
320
340
360
380
400
420
440
37a
46a
42
5716460
5708956
5714072
5714073
5704790
5704794
A1
A2
A3
A4

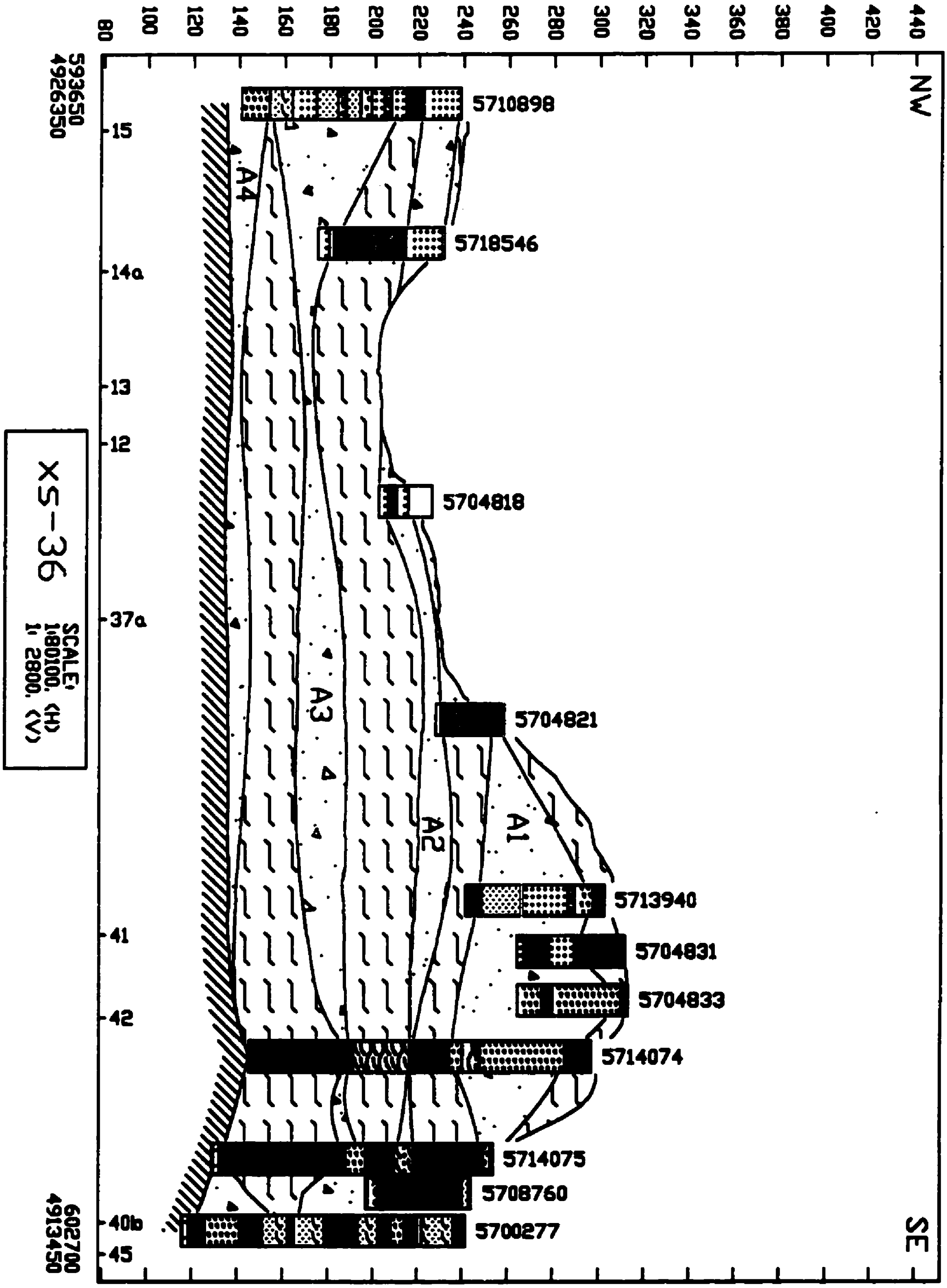
NW
SE
80
100
120
140
160
180
200
220
240
260
280
300
320
340
360
380
400
420
440
5710898
5718546
5704818
5704821
5713940
5704831
5704833
5714074
5714075
5708760
5700277
A1
A2
A3
A4
15
14a
13
12
37a
41
42
40b
45
593650
4926350
602700
4913450
XS-36
SCALE:
1:80100. (H)
1: 2800. (V)

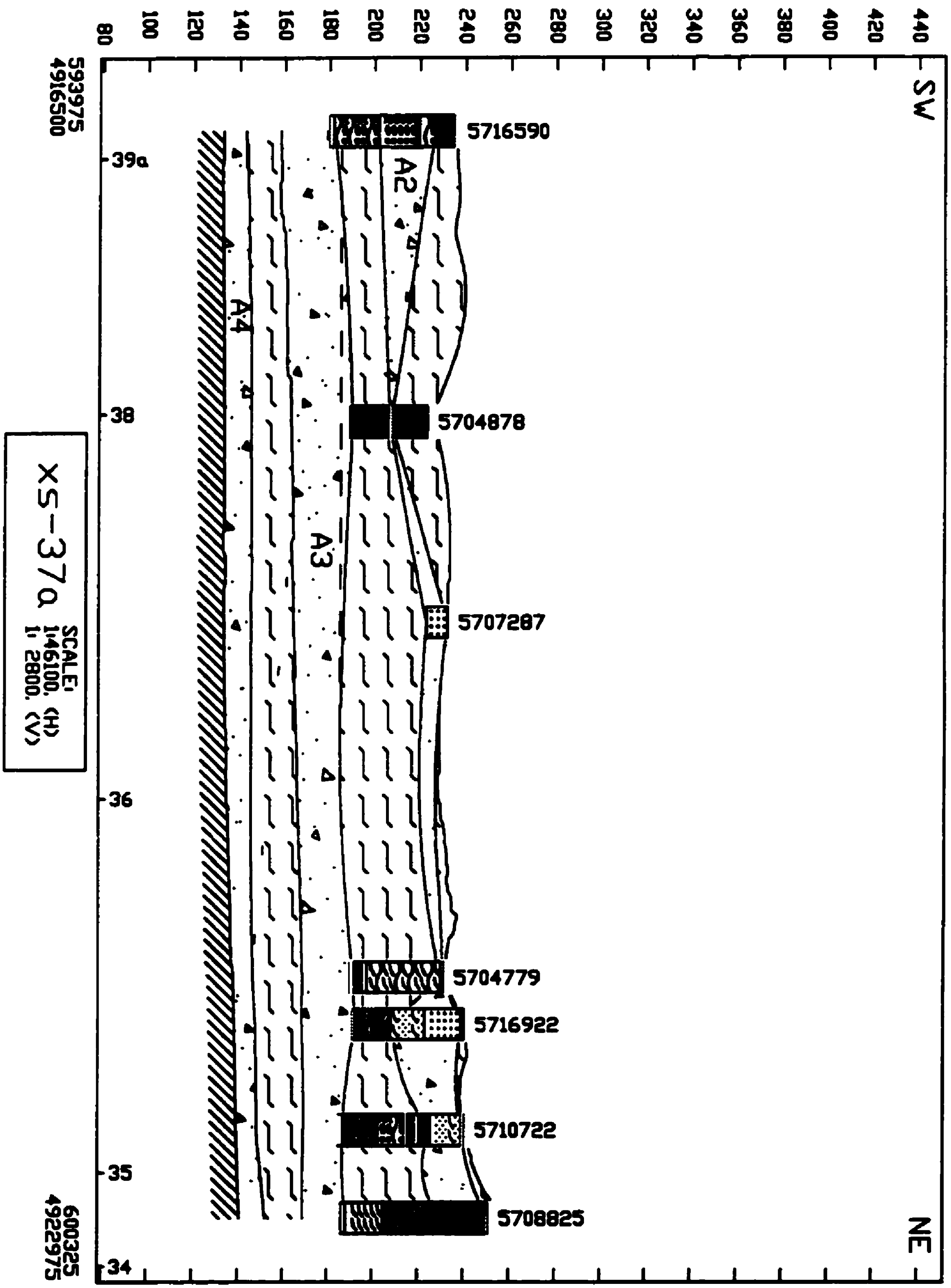
SW
NE
80
100
120
140
160
180
200
220
240
260
280
300
320
340
360
380
400
420
440
593975
4916500
600325
4922975
39a
38
36
35
34
5716590
5704878
5707287
5704779
5716922
5710722
5708825
A2
A3
A4
XS-37a
SCALE: 1:46100. (H)
1: 2800. (V)

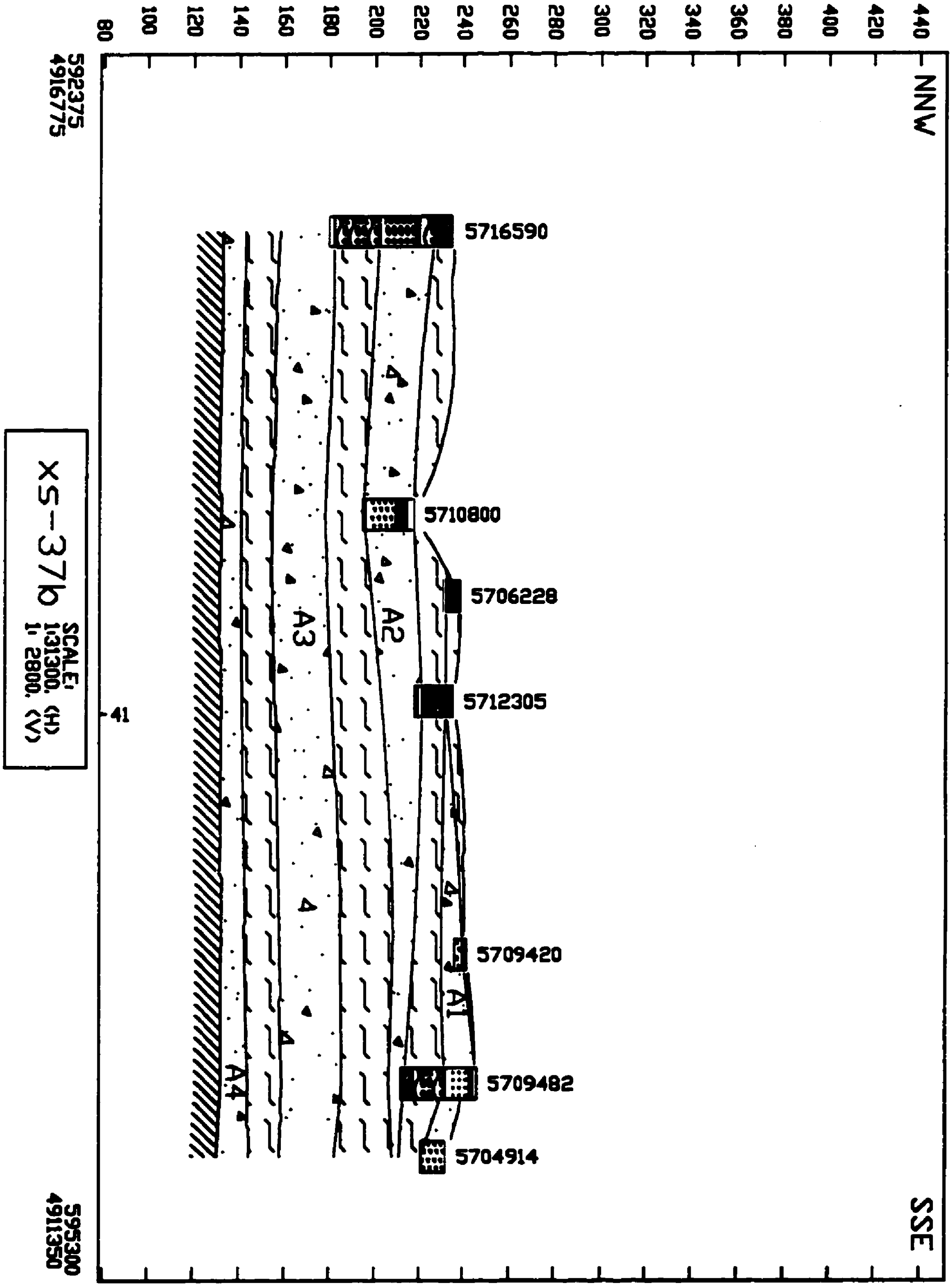
NNW
SSE
80
100
120
140
160
180
200
220
240
260
280
300
320
340
360
380
400
420
440
592375
4916775
595300
4911350
41
5716590
5710800
5706228
5712305
5709420
5709482
5704914
A1
A2
A3
A4
XS-37b
SCALE:
1:31300. (H)
1: 2800. (V)

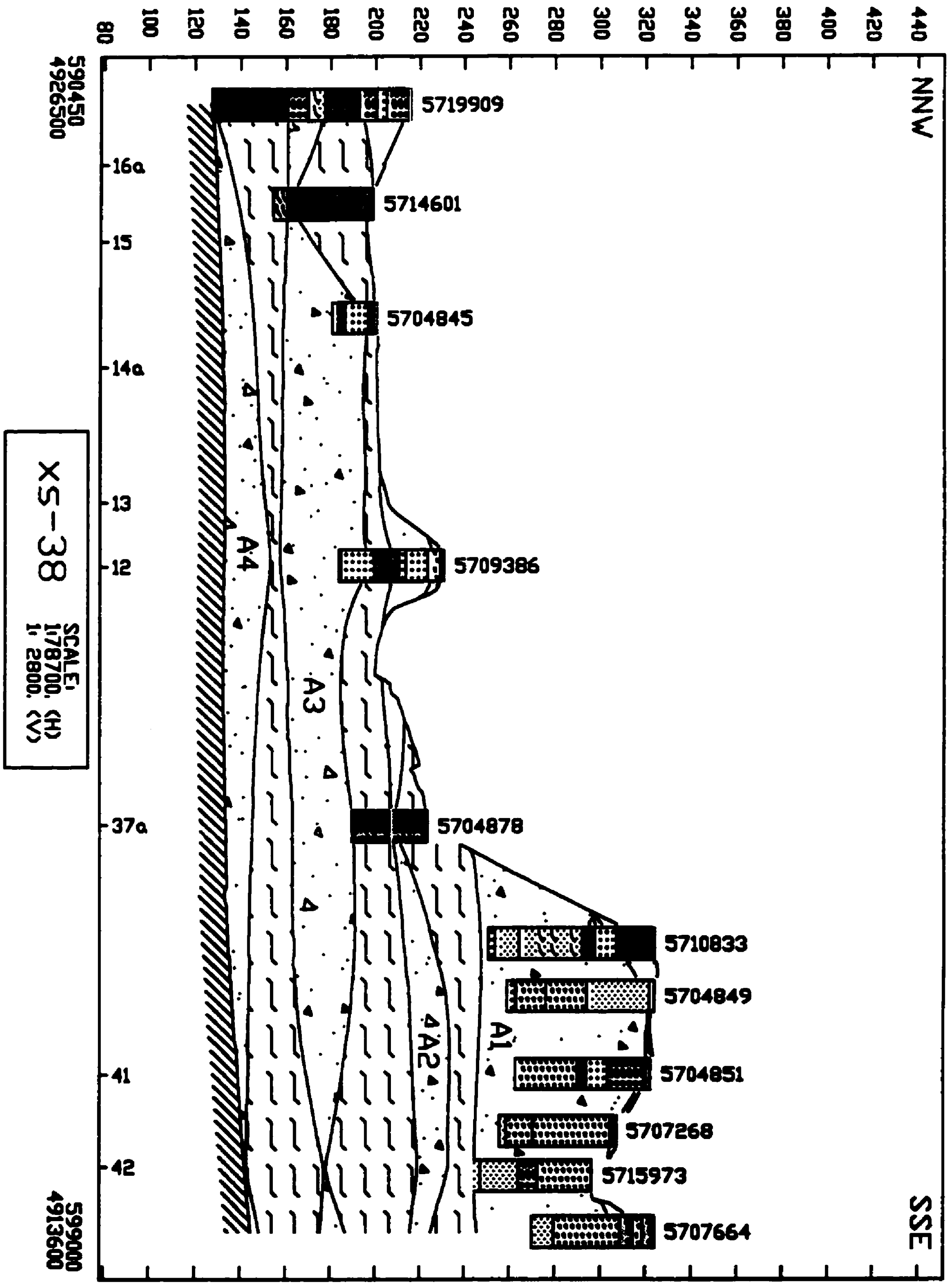
XS-38
SCALE: 1:78700. (H)
1: 2800. (V)
NNW
SSE
80
100
120
140
160
180
200
220
240
260
280
300
320
340
360
380
400
420
440
590450
4926500
599000
4913600
16a
15
14a
13
12
37a
41
42
5719909
5714601
5704845
5709386
5704878
5710833
5704849
5704851
5707268
5715973
5707664
A4
A3
A2
A1

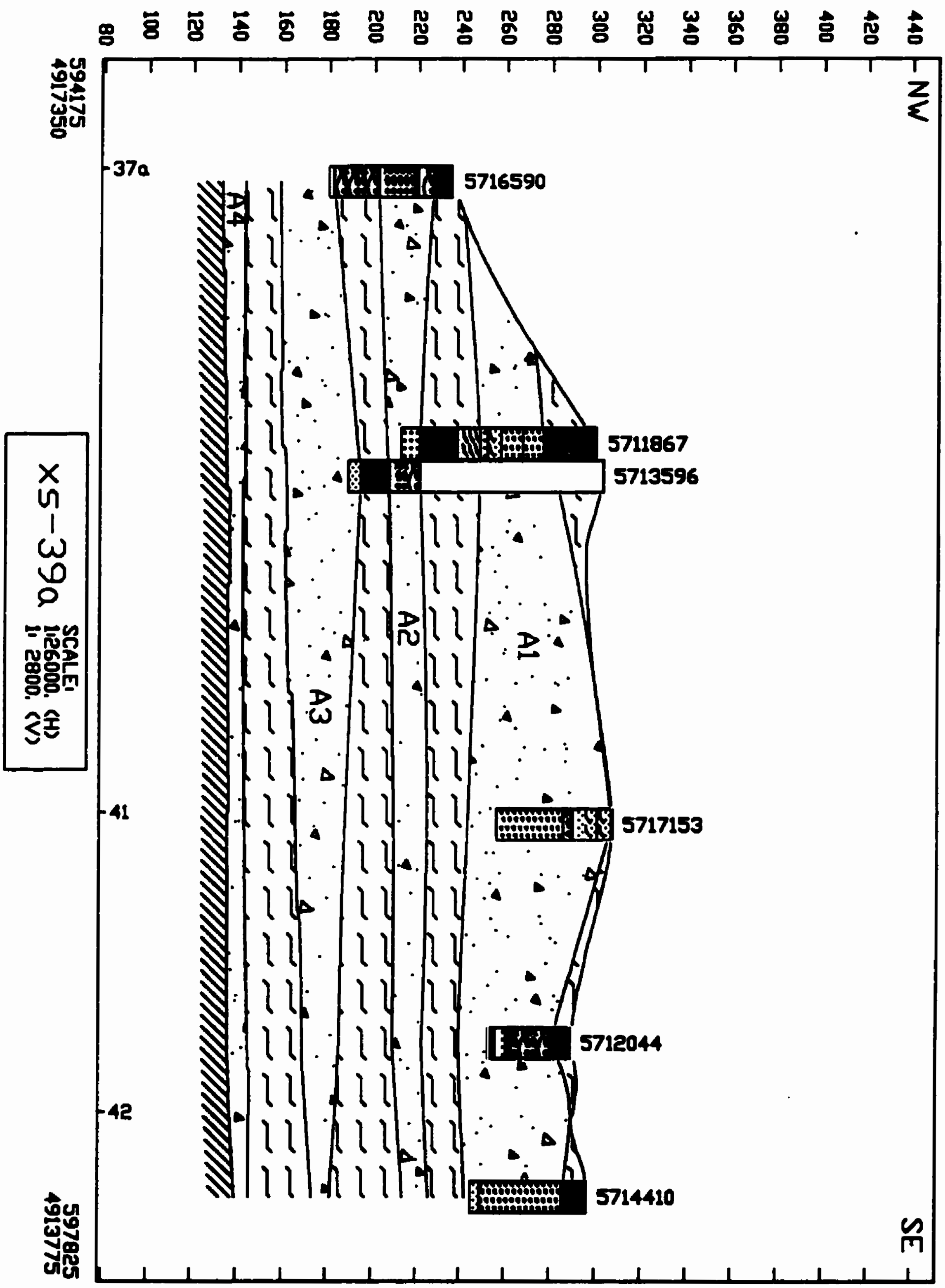
XS-39a
SCALE: 1:26000. (H)
1: 2800. (V)
NW
SE
594175
4917350
597825
4913775
37a
41
42
80
100
120
140
160
180
200
220
240
260
280
300
320
340
360
380
400
420
440
5716590
5711867
5713596
5717153
5712044
5714410
A1
A2
A3
A4

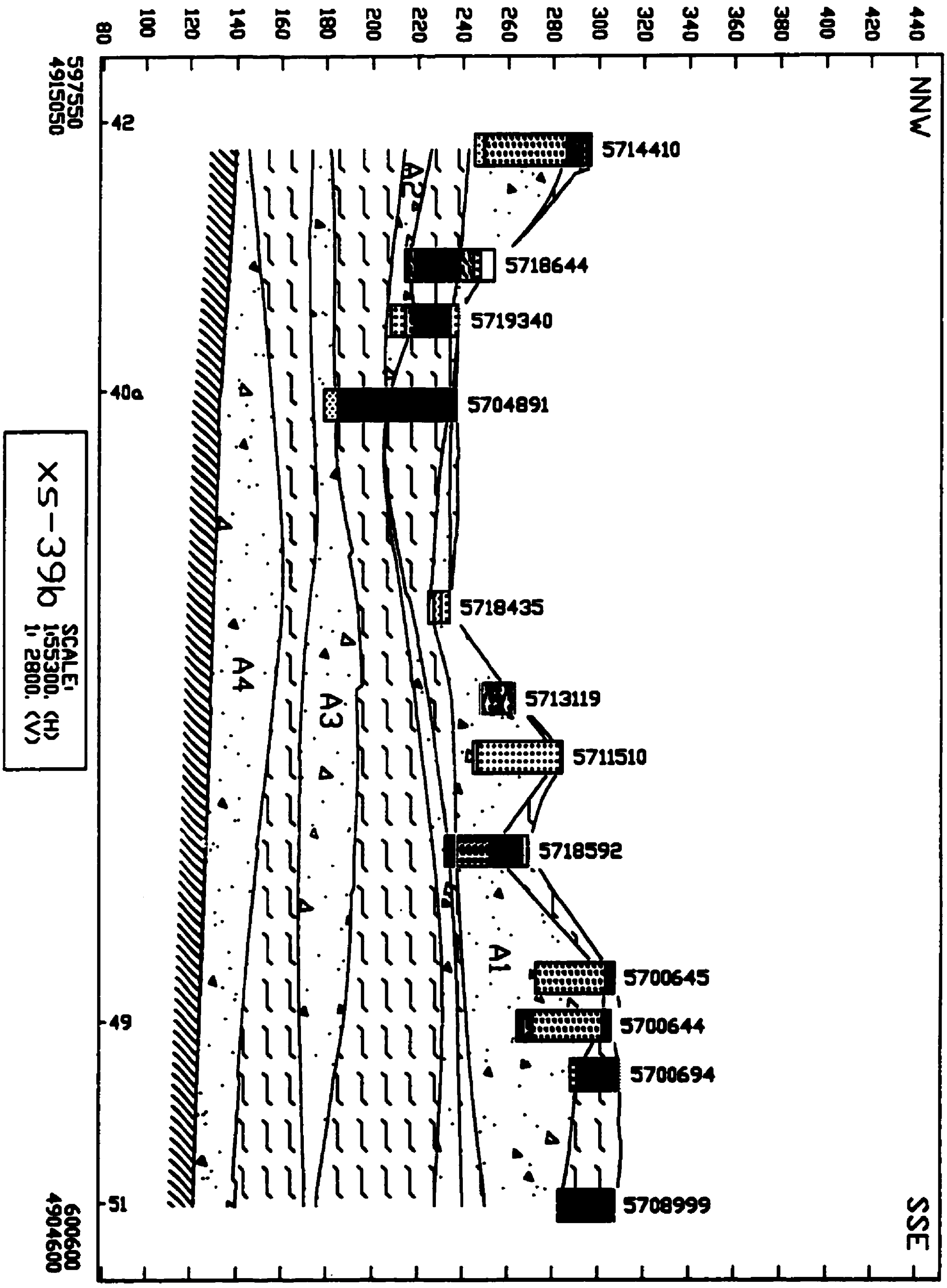
xs-39b
SCALE:
1:55300. (H)
1: 2800. (V)
NNW
SSE
597550
4915050
600600
4904600
42
40a
49
51
80
100
120
140
160
180
200
220
240
260
280
300
320
340
360
380
400
420
440
A4
A3
A2
A1
5714410
5718644
5719340
5704891
5718435
5713119
5711510
5718592
5700645
5700644
5700694
5708999

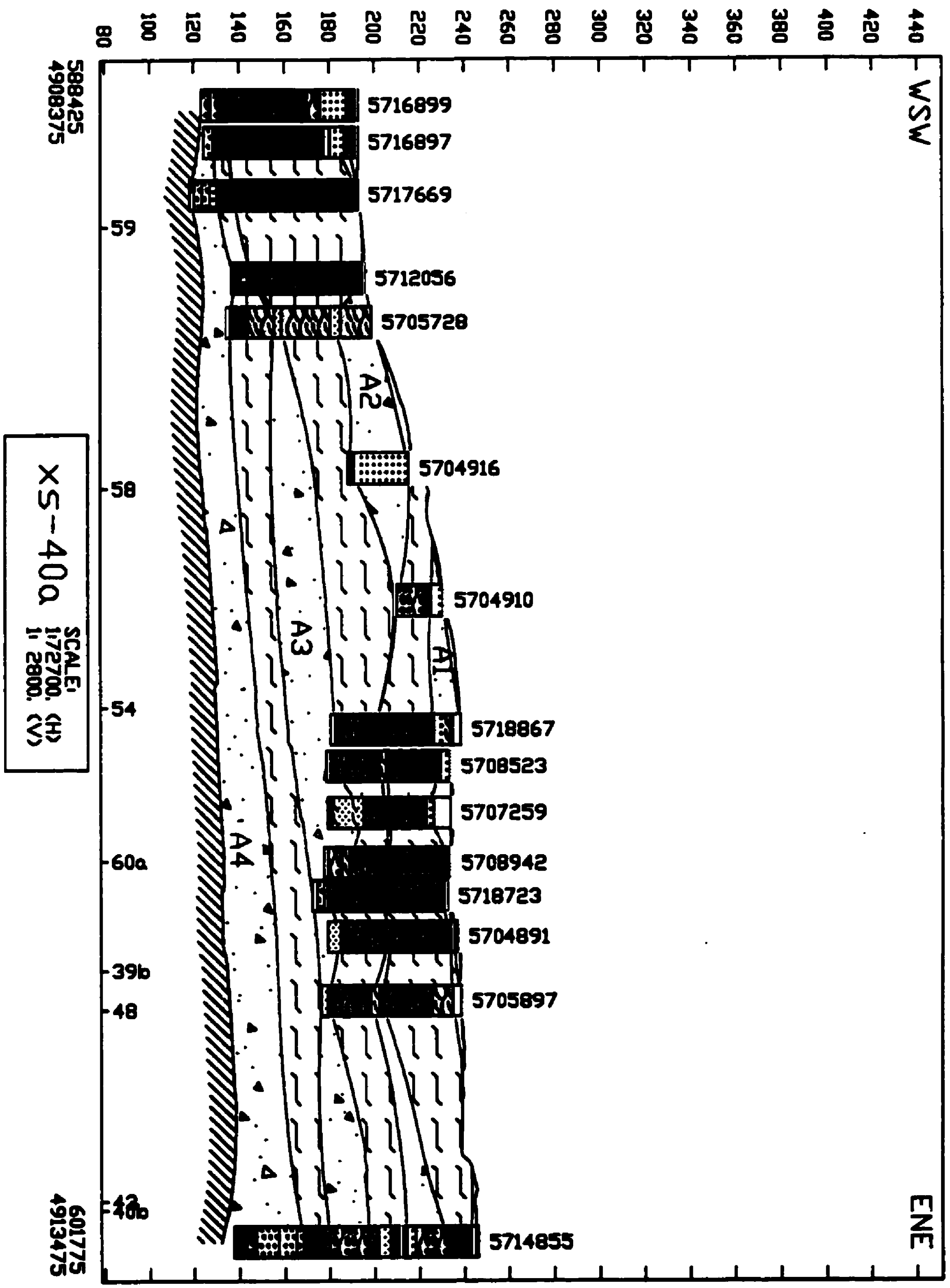
WSW
ENE
80
100
120
140
160
180
200
220
240
260
280
300
320
340
360
380
400
420
440
588425
4908375
601775
4913475
5716899
5716897
5717669
59
5712056
5705728
A2
5704916
58
A4
5704910
A3
A1
54
5718867
5708523
5707259
A4
60a
5708942
5718723
5704891
39b
48
5705897
42
40b
5714855
XS-40a
SCALE:
1:72700. (H)
1: 2800. (V)

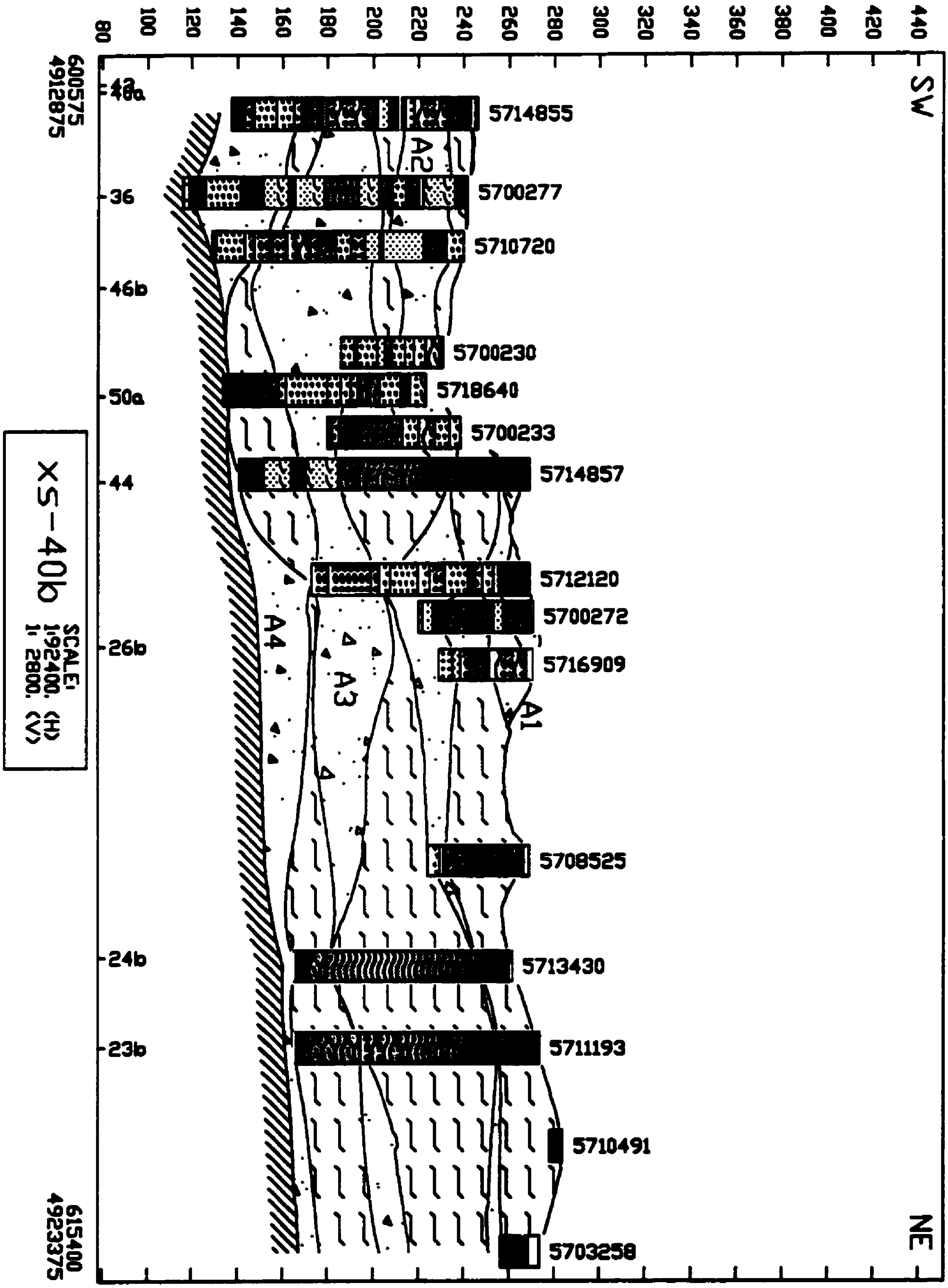
SW
NE
80
100
120
140
160
180
200
220
240
260
280
300
320
340
360
380
400
420
440
42
48a
36
46b
50a
44
26b
24b
23b
600575
4912875
615400
4923375
5714855
5700277
5710720
5700230
5718640
5700233
5714857
5712120
5700272
5716909
5708525
5713430
5711193
5710491
5703258
A1
A2
A3
A4
XS-40b
SCALE: 1:92400. (H)
1: 2800. (V)

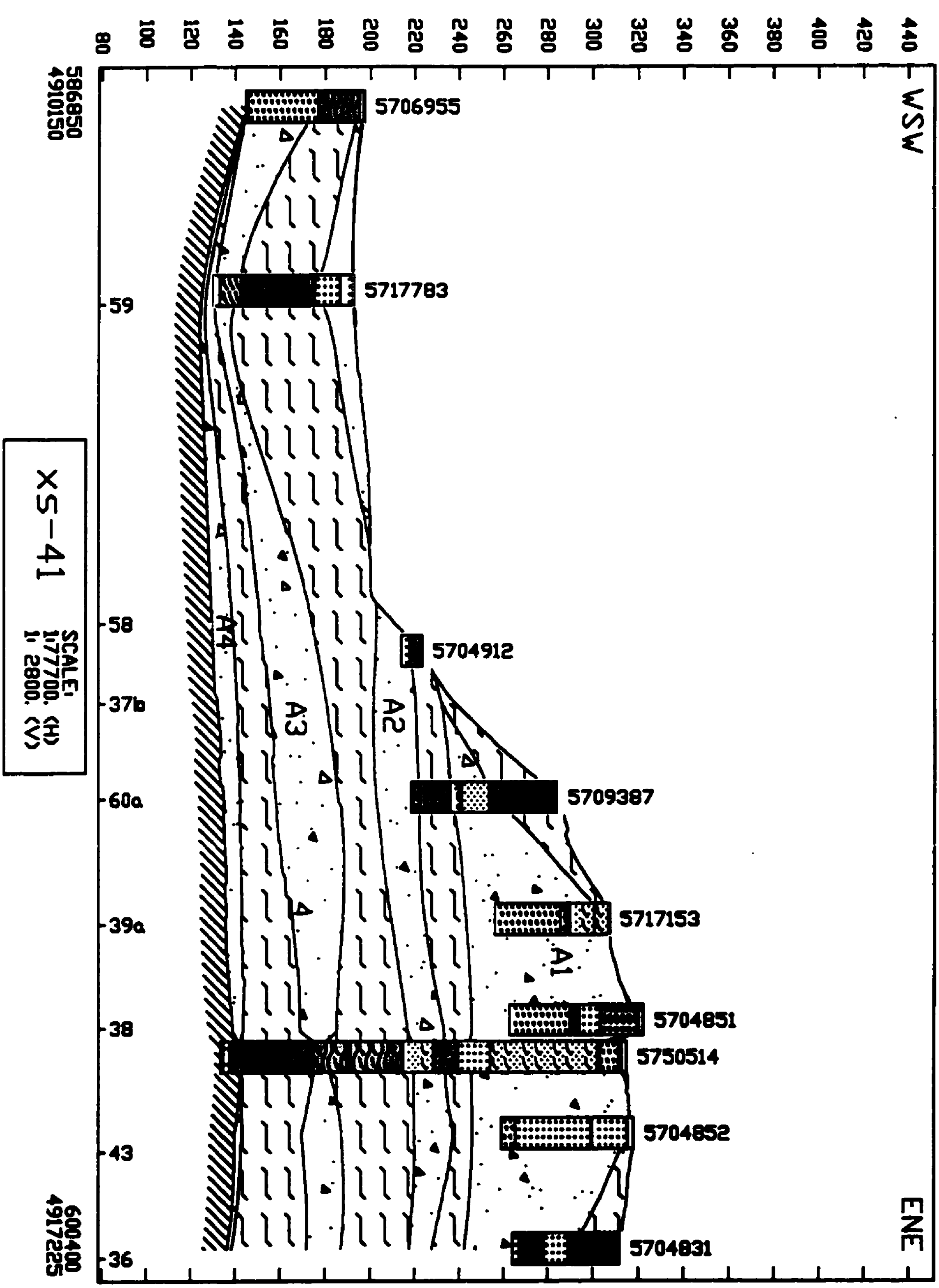
WSW
ENE
80
100
120
140
160
180
200
220
240
260
280
300
320
340
360
380
400
420
440
586850
4910150
600400
4917225
59
58
37b
60a
39a
38
43
36
5706955
5717783
5704912
5709387
5717153
5704851
5750514
5704852
5704831
A1
A2
A3
A4
XS-41
SCALE:
1:77700. (H)
1: 2800. (V)

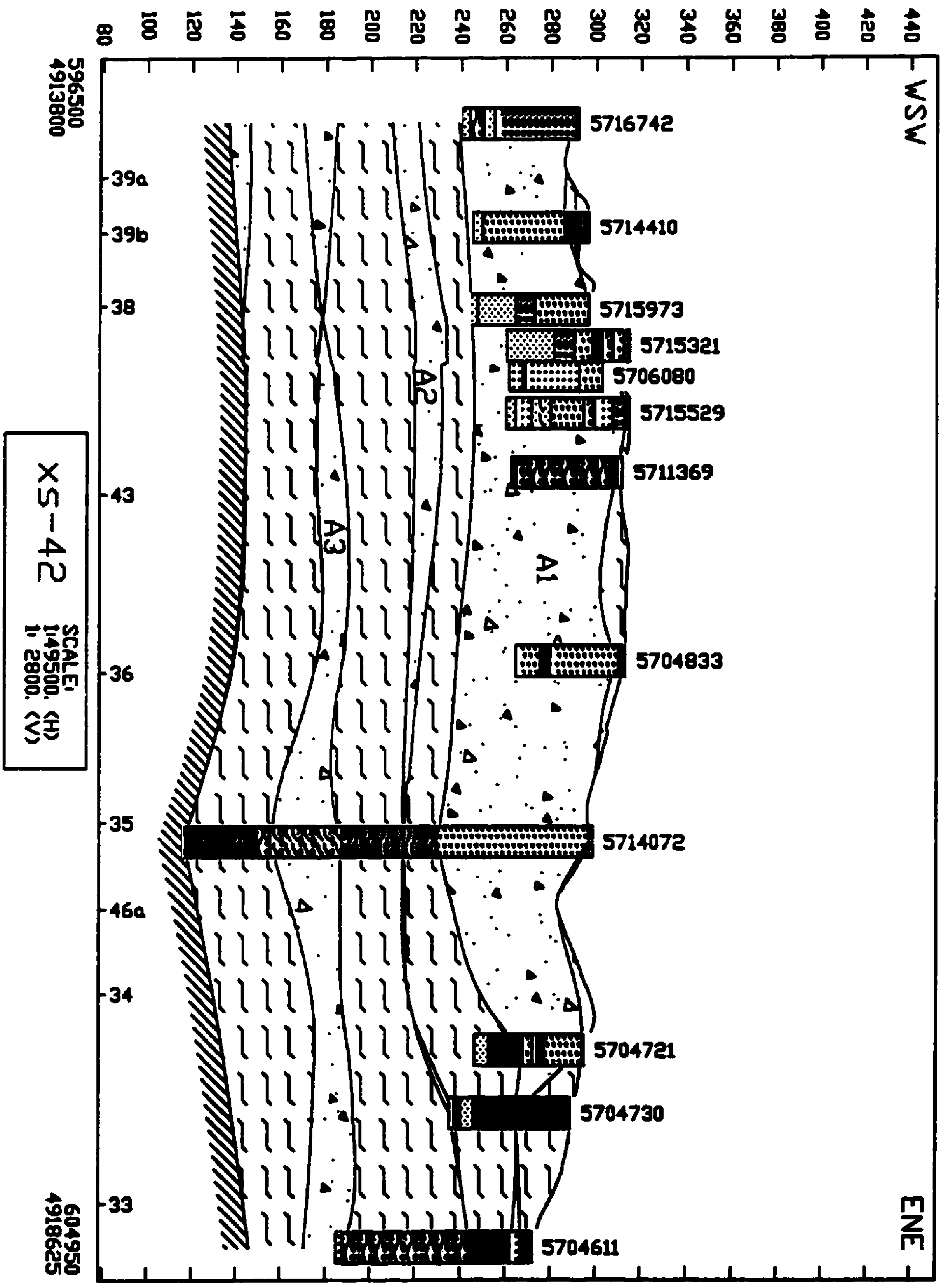
XS-42
SCALE:
1:49500. (H)
1: 2800. (V)
WSW
ENE
596500
4913800
604950
4918625
39a
39b
38
43
36
35
46a
34
33
A1
A2
A3
5716742
5714410
5715973
5715321
5706080
5715529
5711369
5704833
5714072
5704721
5704730
5704611
80
100
120
140
160
180
200
220
240
260
280
300
320
340
360
380
400
420
440

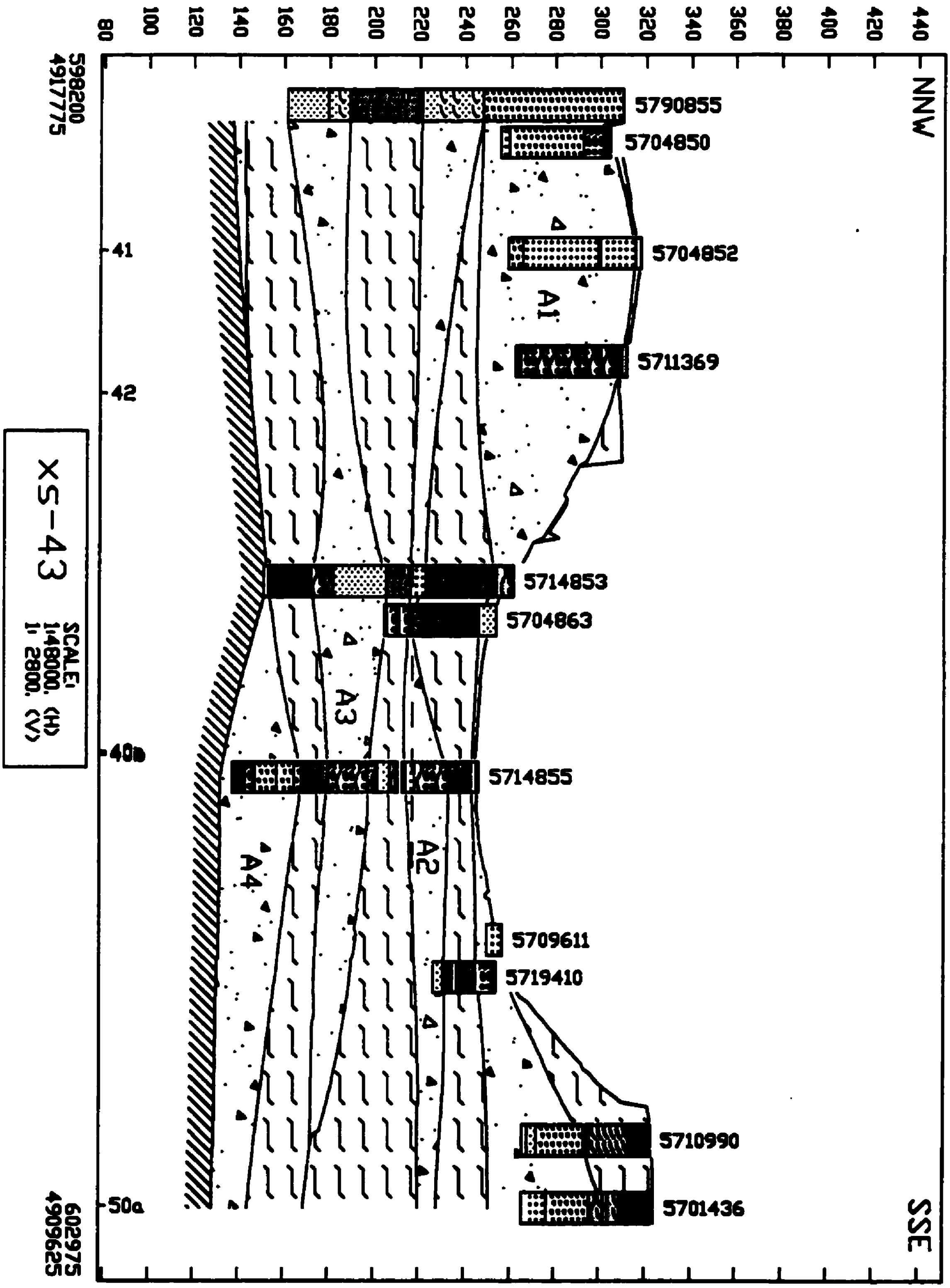
XS-43
SCALE:
1:48000. (H)
1: 2800. (V)
NNW
SSE
598200
4917775
602975
4909625
80
100
120
140
160
180
200
220
240
260
280
300
320
340
360
380
400
420
440
41
42
40b
50a
5790855
5704850
5704852
5711369
5714853
5704863
5714855
5709611
5719410
5710990
5701436
A1
A2
A3
A4

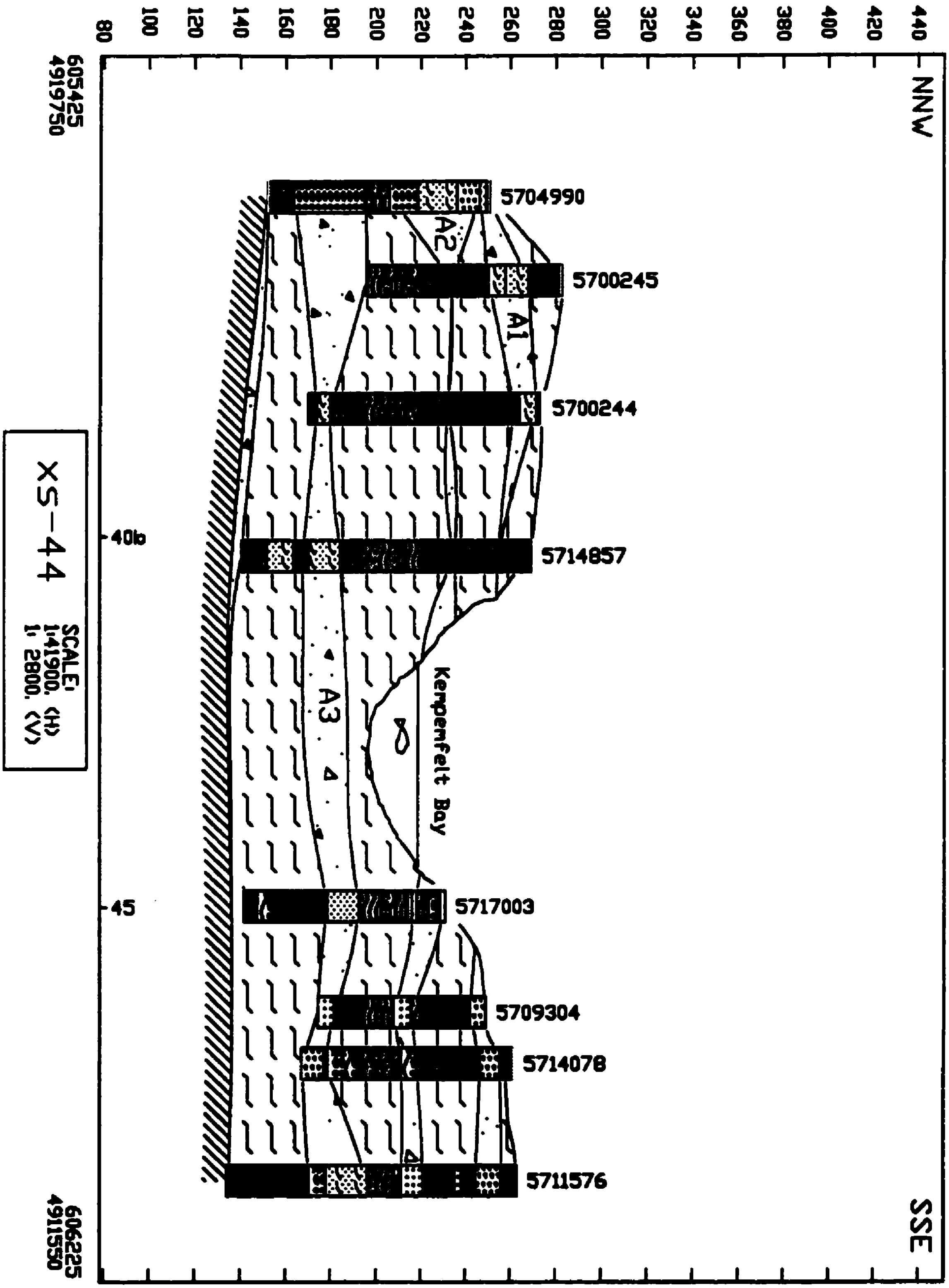
80
100
120
140
160
180
200
220
240
260
280
300
320
340
360
380
400
420
440
NNW
SSE
605425
4919750
606225
4911550
40b
45
5704990
5700245
5700244
5714857
5717003
5709304
5714078
5711576
A1
A2
A3
Kempenfelt Bay
XS-44
SCALE:
1:41900. (H)
1: 2800. (V)

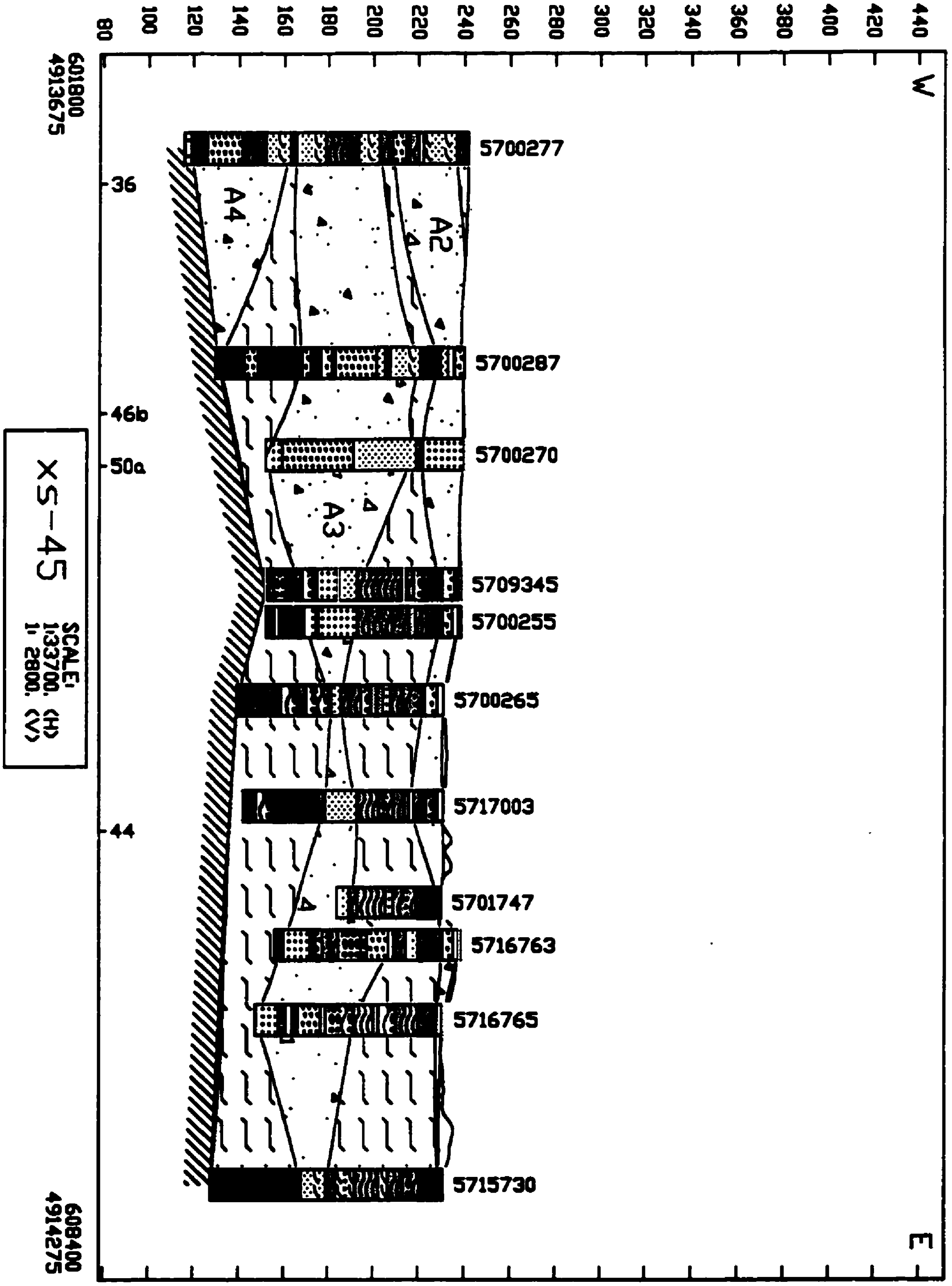
W
E
80
100
120
140
160
180
200
220
240
260
280
300
320
340
360
380
400
420
440
601800
4913675
608400
4914275
36
46b
50a
44
A4
A2
A3
5700277
5700287
5700270
5709345
5700255
5700265
5717003
5701747
5716763
5716765
5715730
XS-45
SCALE:
1:33700. (H)
1: 2800. (V)

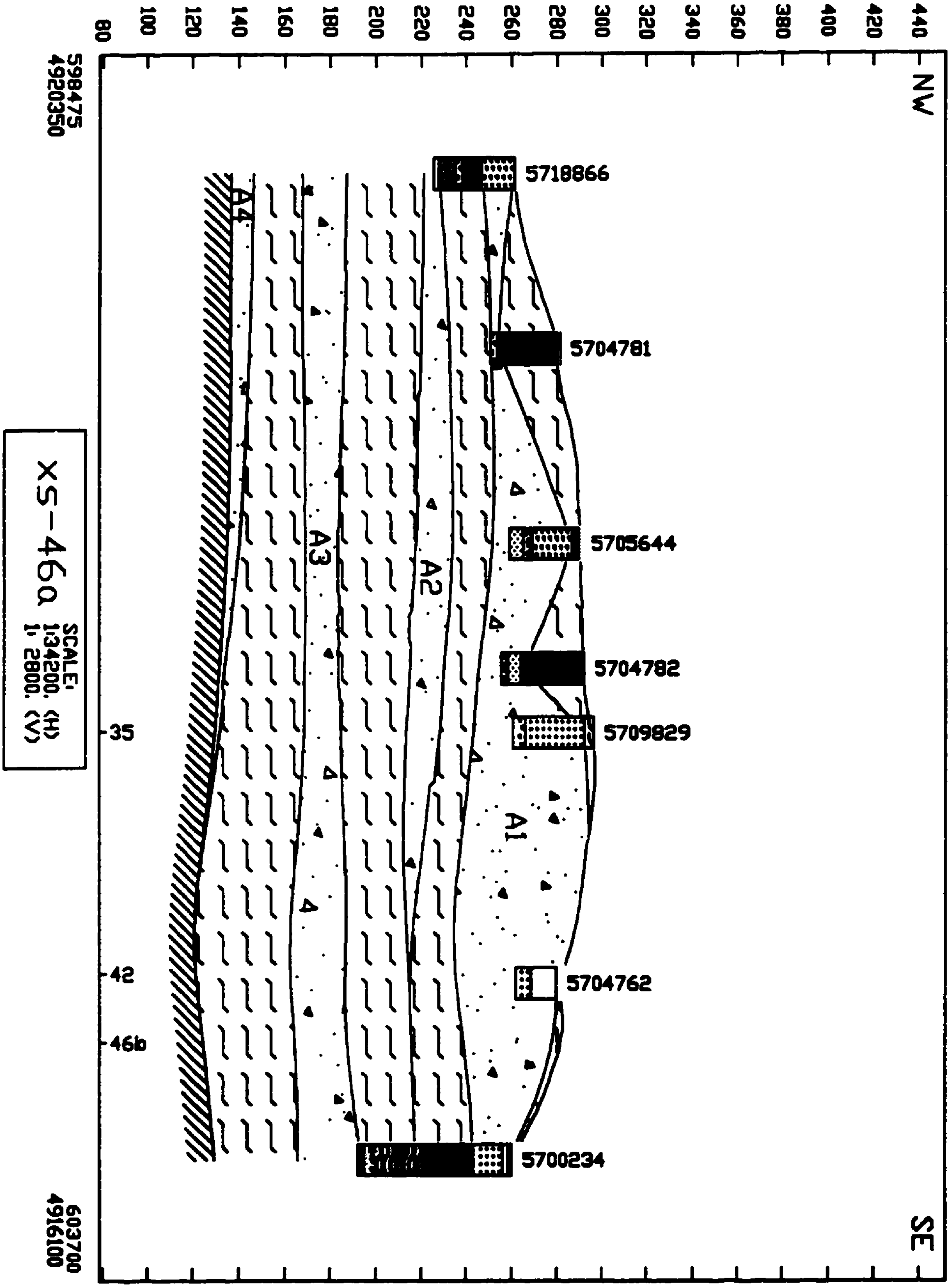
XS-46a
SCALE:
1:34200. (H)
1: 2800. (V)
NW
SE
598475
4920350
603700
4916100
80
100
120
140
160
180
200
220
240
260
280
300
320
340
360
380
400
420
440
5718866
5704781
5705644
5704782
5709829
5704762
5700234
A1
A2
A3
A4
35
42
46b

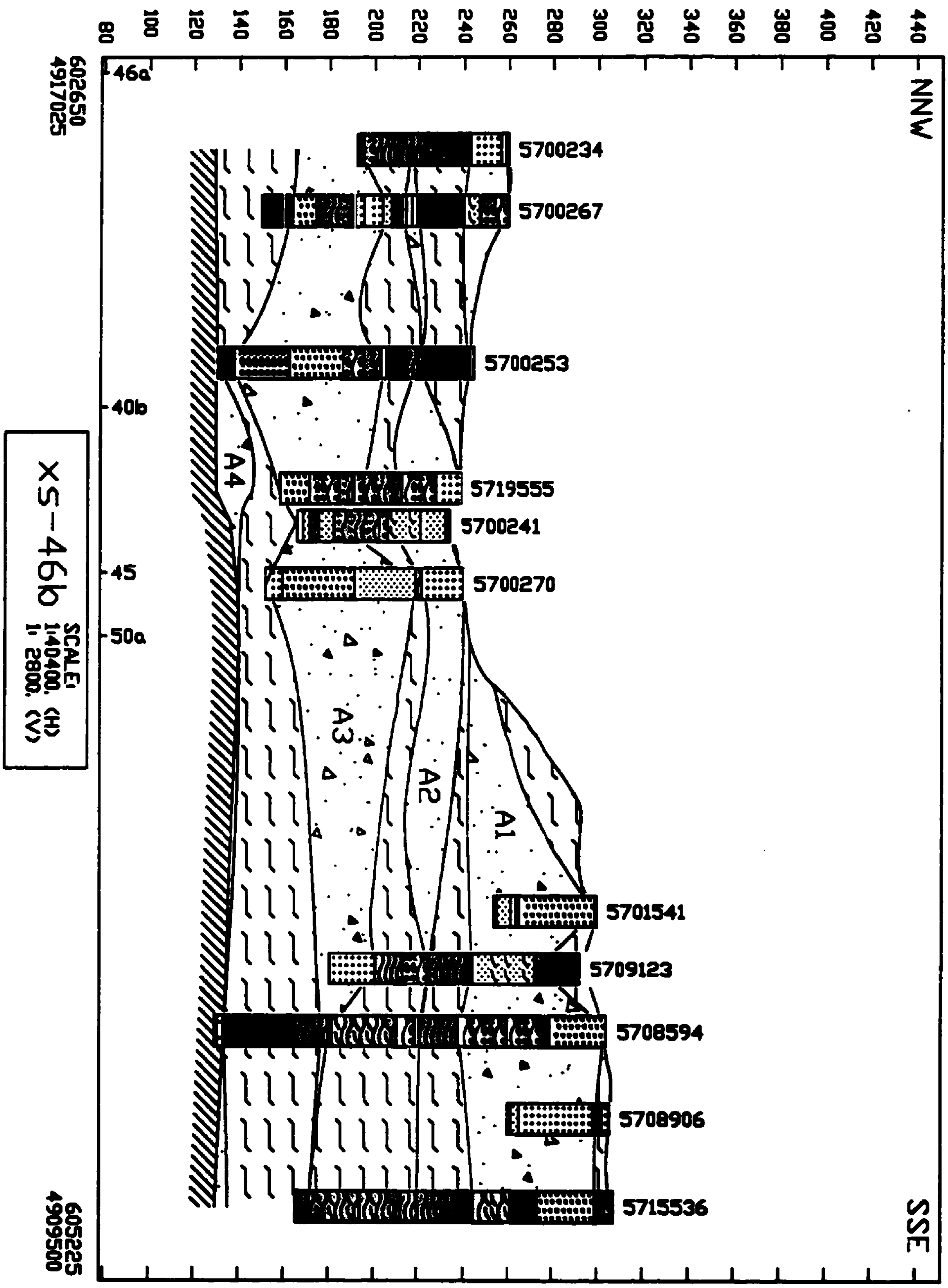
XS-46b
SCALE:
1:40400. (H)
1: 2800. (V)
NNW
SSE
602650
4917025
605225
4909500
80
100
120
140
160
180
200
220
240
260
280
300
320
340
360
380
400
420
440
46a
40b
45
50a
5700234
5700267
5700253
5719555
5700241
5700270
5701541
5709123
5708594
5708906
5715536
A1
A2
A3
A4

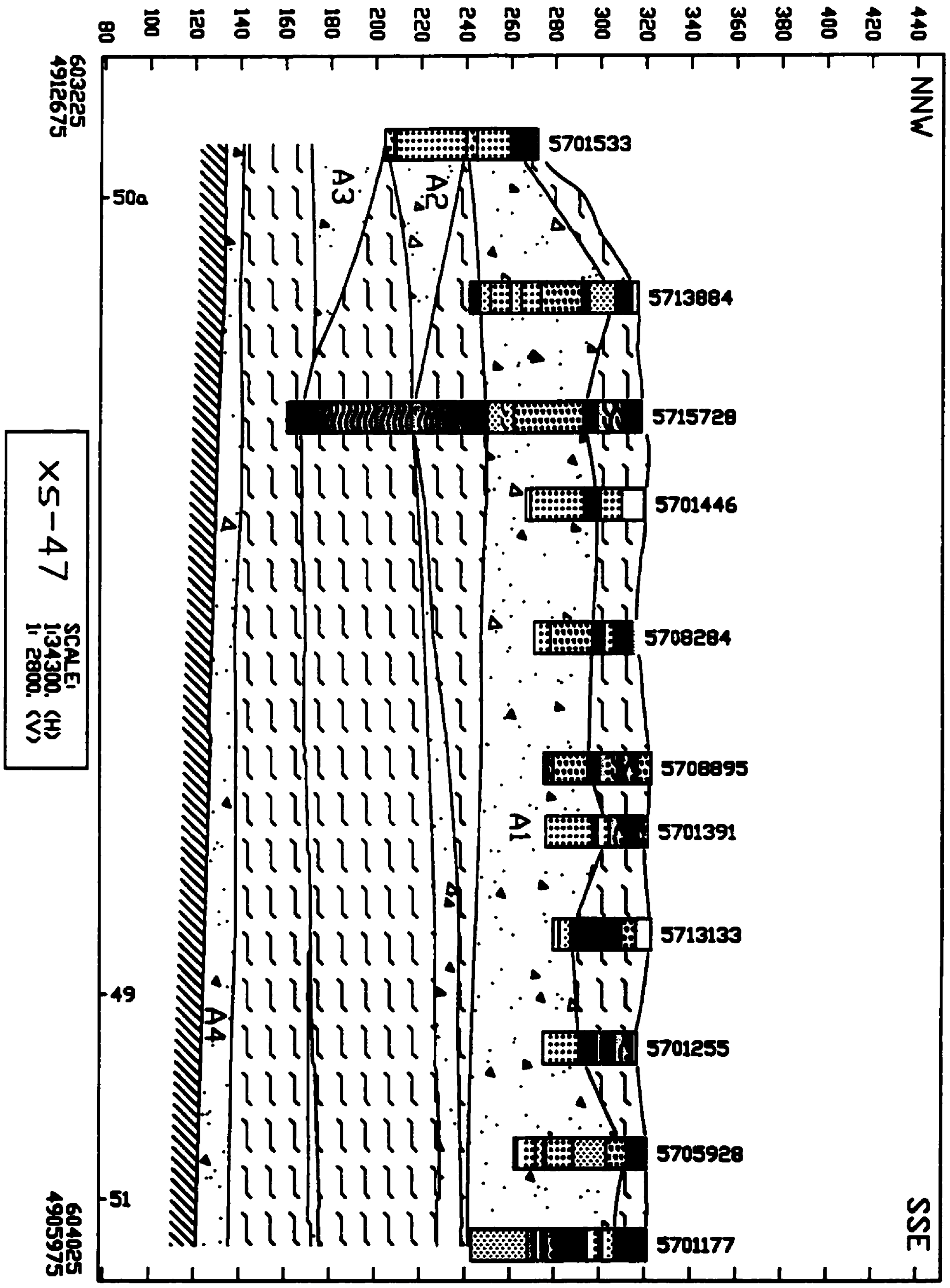
XS-47
SCALE:
1:34300. (H)
1: 2800. (V)
603225
4912675
604025
4905975
NNW
SSE
80
100
120
140
160
180
200
220
240
260
280
300
320
340
360
380
400
420
440
50a
49
51
A1
A2
A3
A4
5701533
5713884
5715728
5701446
5708284
5708895
5701391
5713133
5701255
5705928
5701177

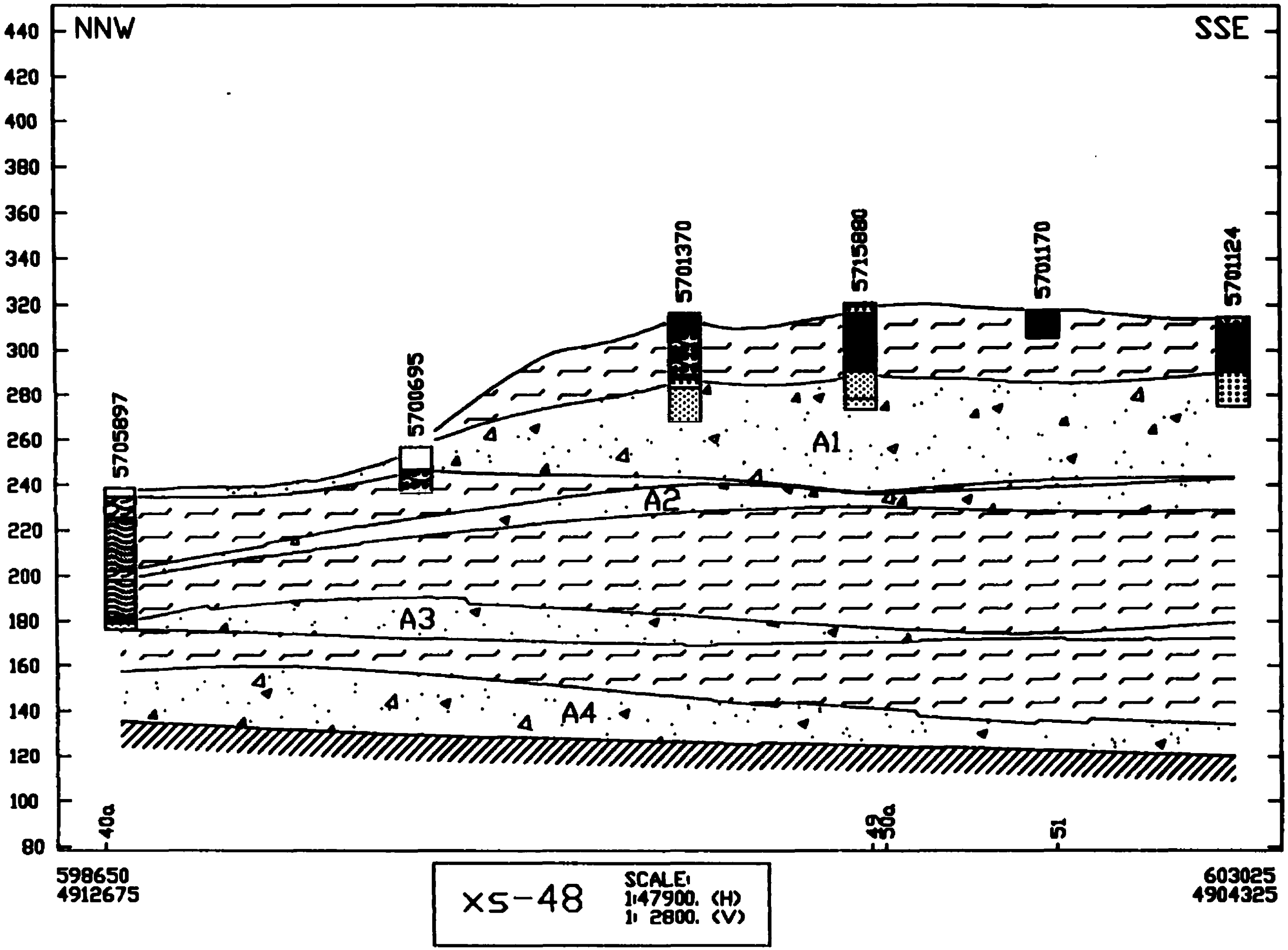
NNW
SSE
440
420
400
380
360
340
320
300
280
260
240
220
200
180
160
140
120
100
80
5705897
5700695
5701370
5715880
5701170
5701124
A1
A2
A3
A4
40a
49
50a
51
598650
4912675
603025
4904325
xs-48
SCALE:
1:47900. (H)
1: 2800. (V)

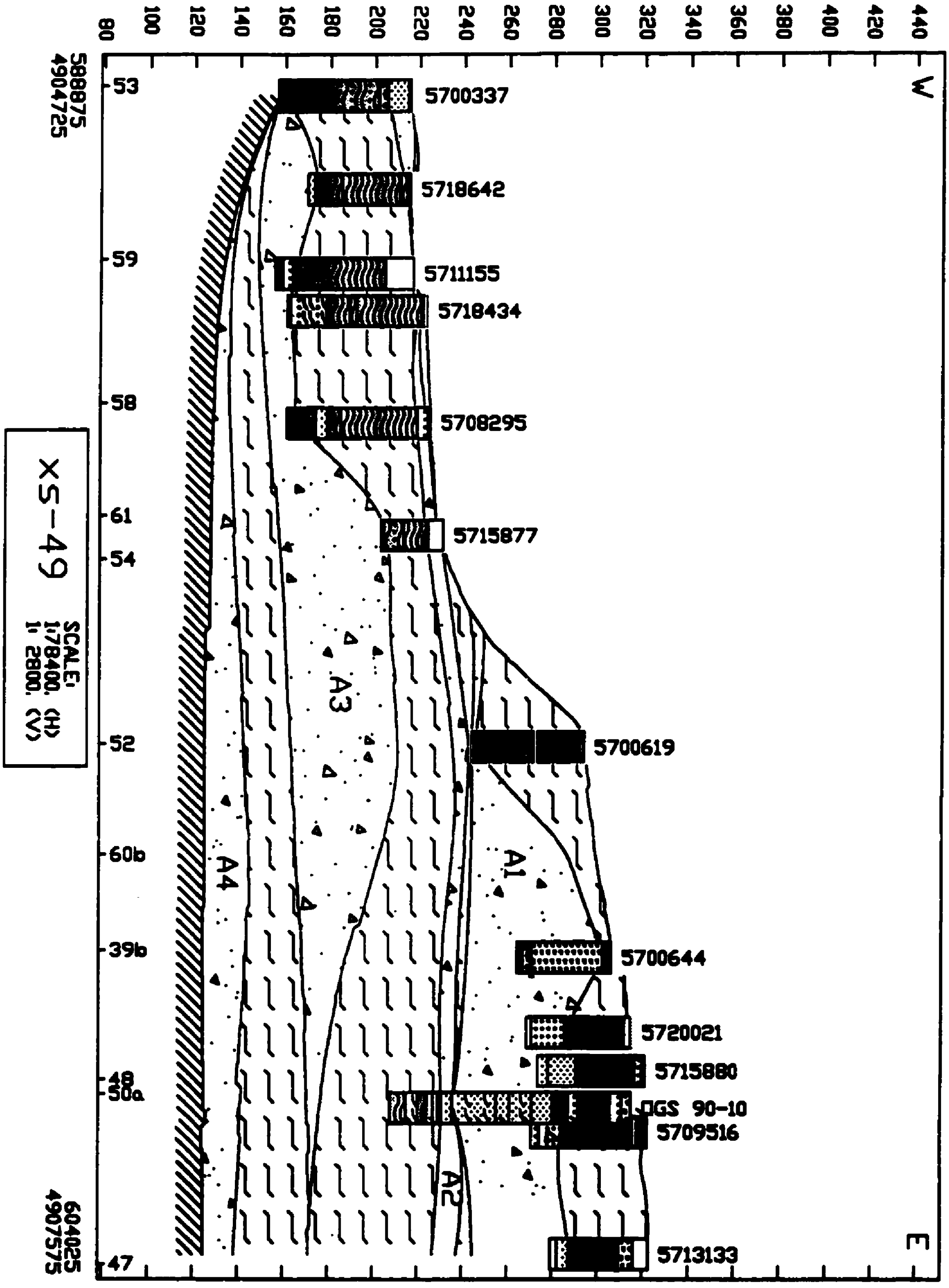
XS-49
SCALE:
1:78400. (H)
1: 2800. (V)
588875
4904725
604025
4907575
W
E
53
59
58
61
54
52
60b
39b
48
50a
47
80
100
120
140
160
180
200
220
240
260
280
300
320
340
360
380
400
420
440
5700337
5718642
5711155
5718434
5708295
5715877
5700619
5700644
5720021
5715880
OGS 90-10
5709516
5713133
A1
A2
A3
A4

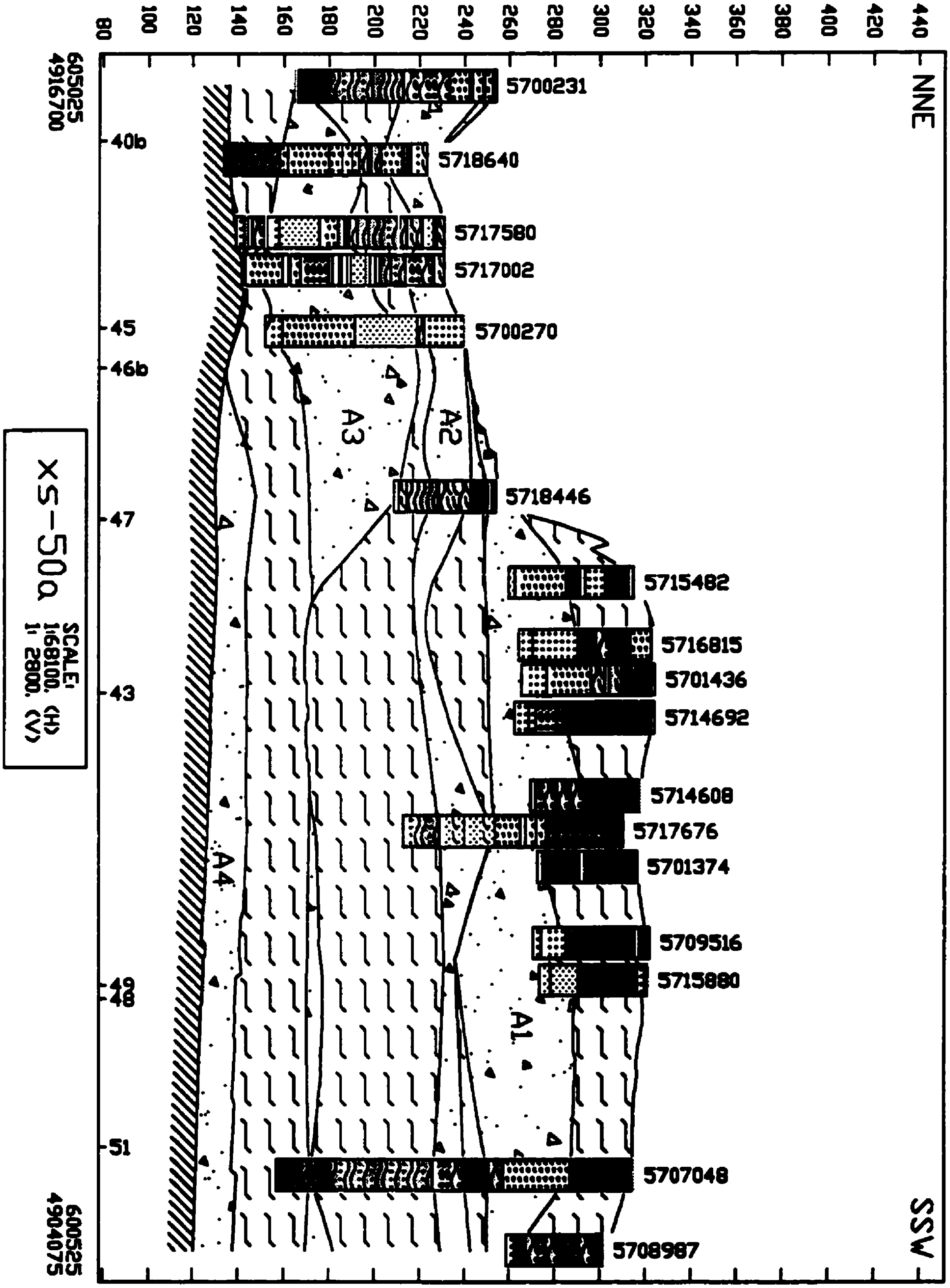
xs-50a
SCALE:
1:68100. (H)
1: 2800. (V)
605025
4916700
600525
4904075
NNE
SSW
80
100
120
140
160
180
200
220
240
260
280
300
320
340
360
380
400
420
440
40b
45
46b
47
43
49
48
51
5700231
5718640
5717580
5717002
5700270
5718446
5715482
5716815
5701436
5714692
5714608
5717676
5701374
5709516
5715880
5707048
5708987
A1
A2
A3
A4

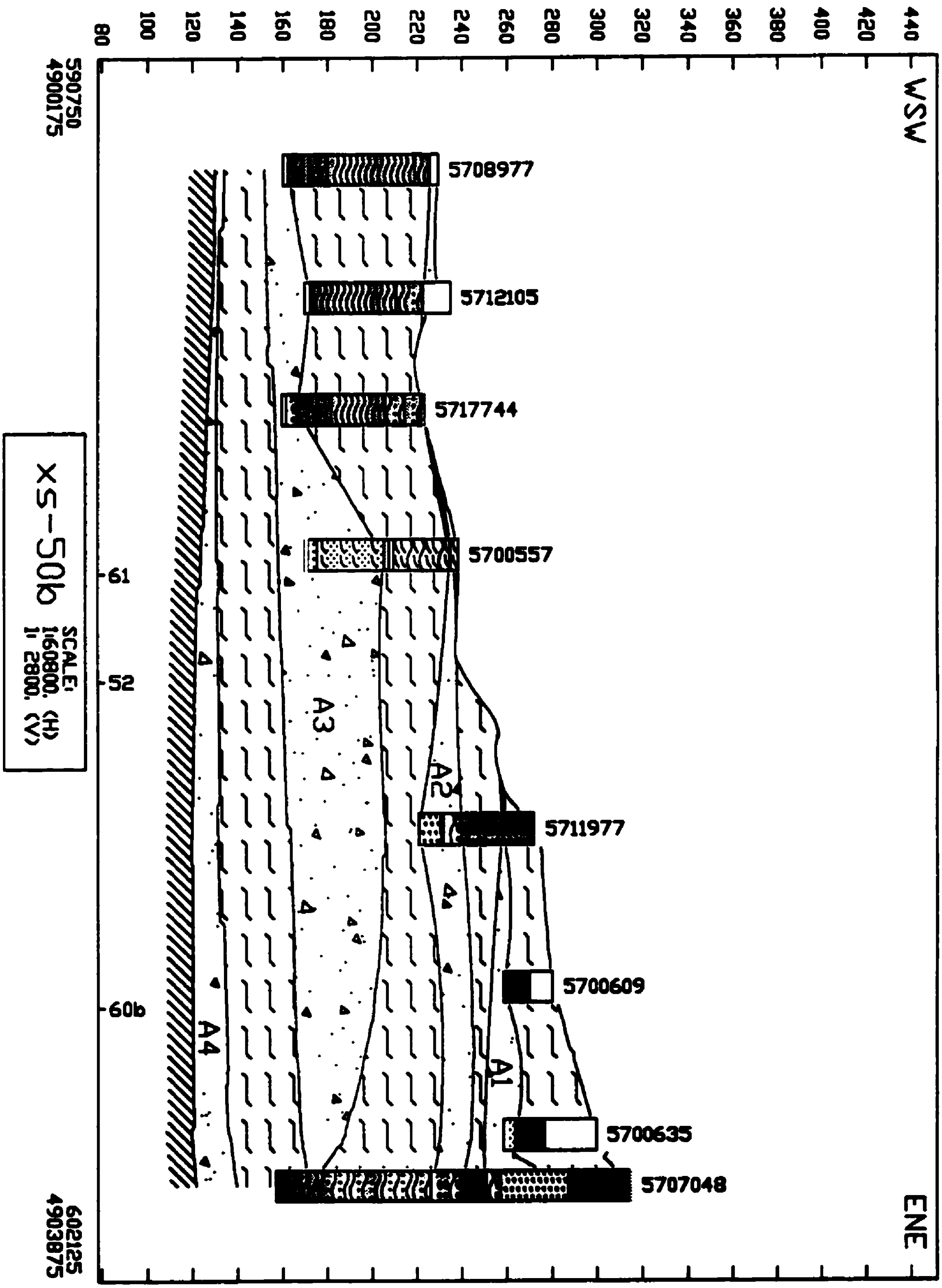
WSW
ENE
80
100
120
140
160
180
200
220
240
260
280
300
320
340
360
380
400
420
440
590750
4900175
602125
4903875
61
52
60b
5708977
5712105
5717744
5700557
5711977
5700609
5700635
5707048
A1
A2
A3
A4
XS-50b
SCALE:
1:60800. (H)
1: 2800. (V)

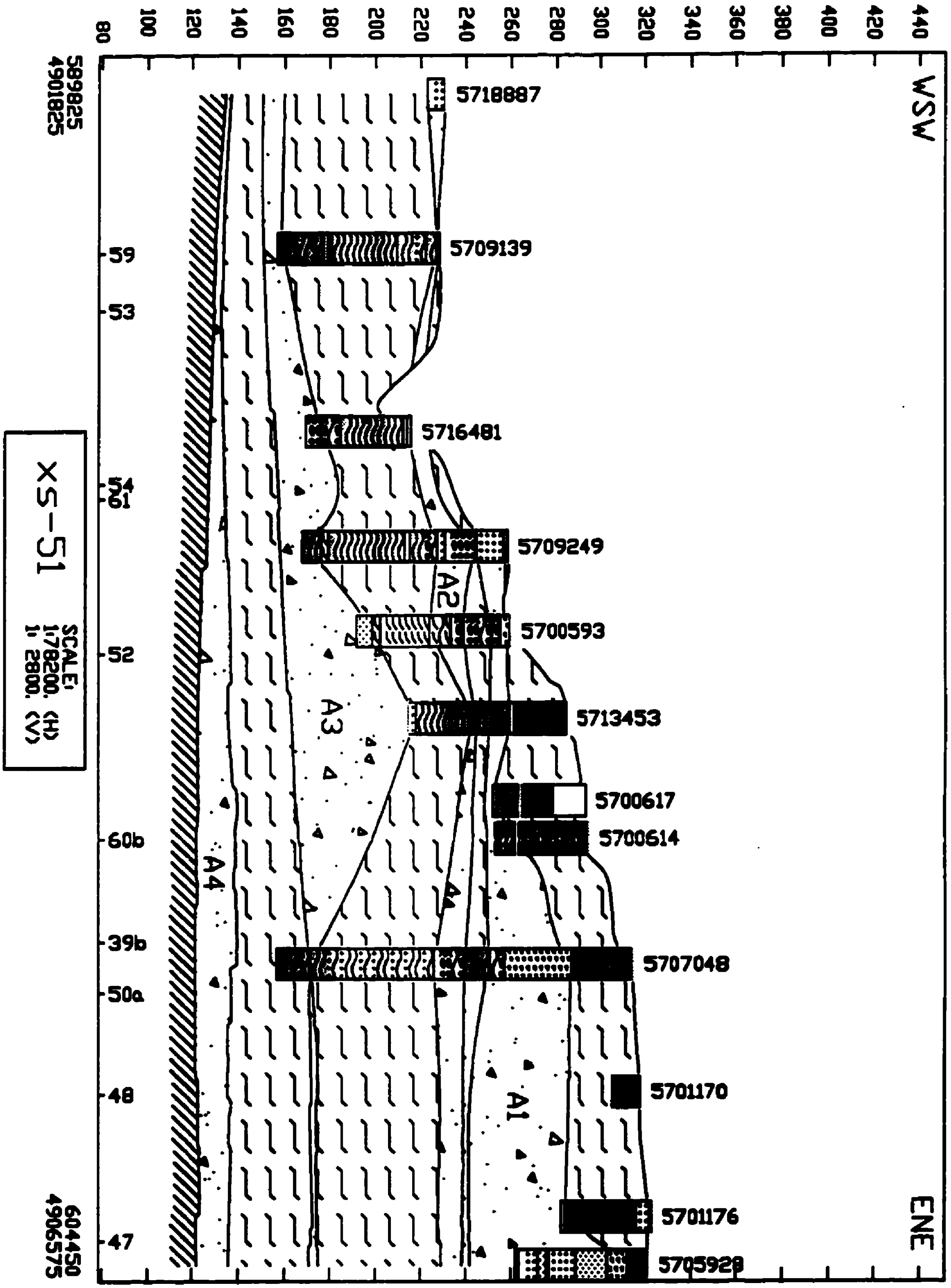
WSW
ENE
80
100
120
140
160
180
200
220
240
260
280
300
320
340
360
380
400
420
440
5718887
5709139
5716481
5709249
5700593
5713453
5700617
5700614
5707048
5701170
5701176
5705928
A1
A2
A3
A4
59
53
54
61
52
60b
39b
50a
48
47
589825
4901825
604450
4906575
XS-51
SCALE:
1:78200. (H)
1: 2800. (V)

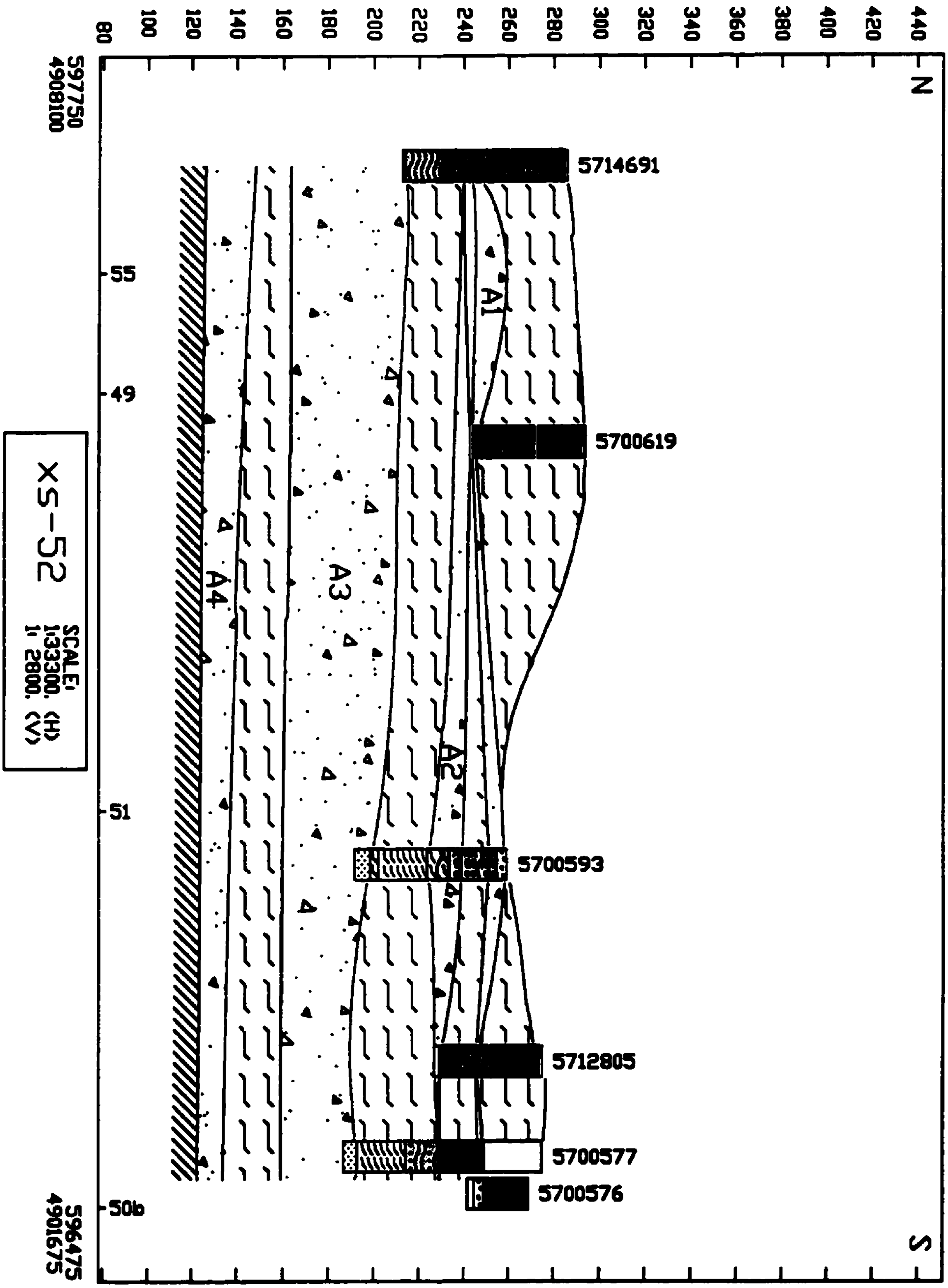
80
100
120
140
160
180
200
220
240
260
280
300
320
340
360
380
400
420
440
N
S
597750
4908100
596475
4901675
55
49
51
50b
5714691
5700619
5700593
5712805
5700577
5700576
A1
A2
A3
A4
XS-52
SCALE: 1:33300. (H)
1: 2800. (V)

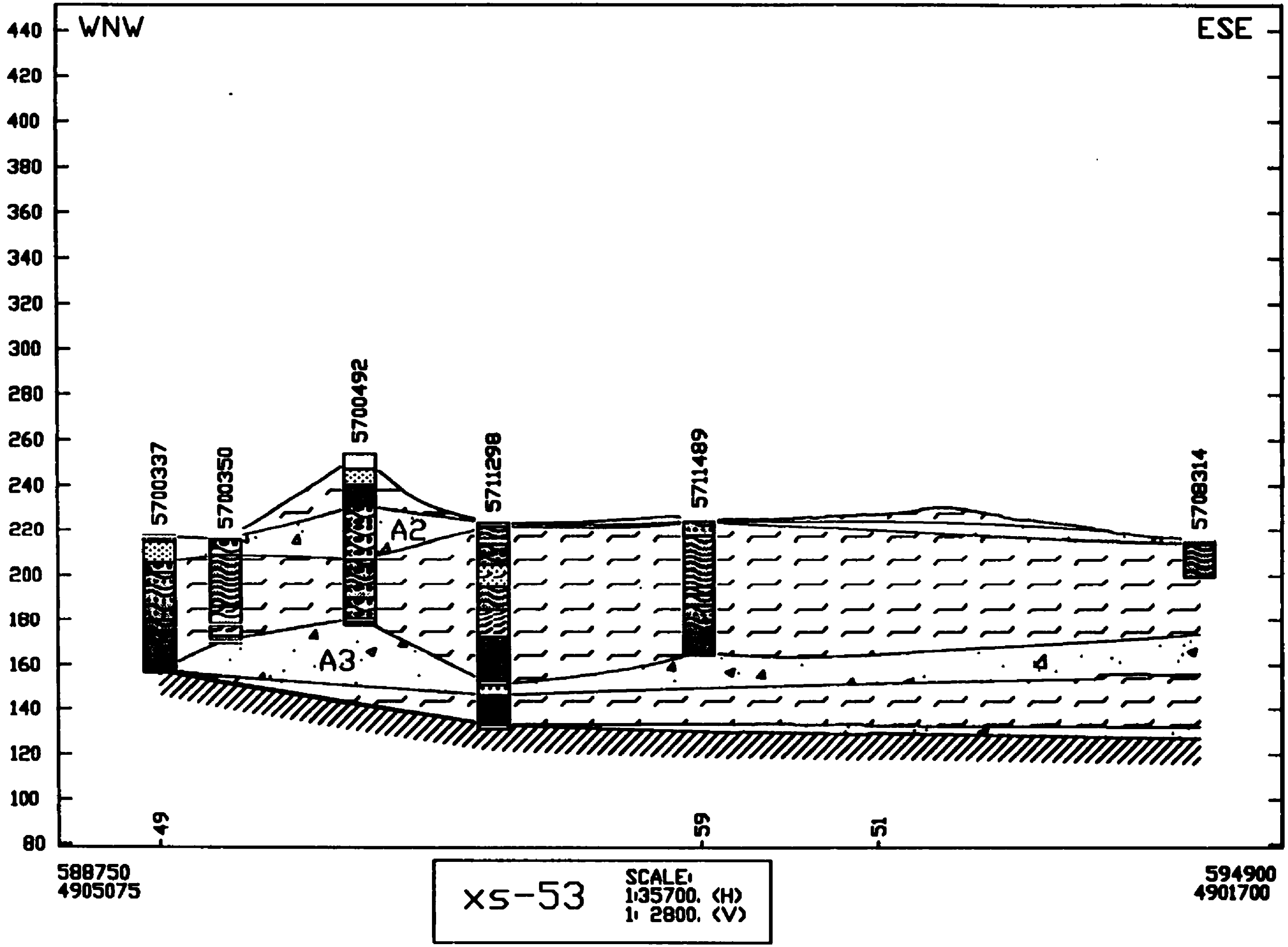
WNW
ESE
440
420
400
380
360
340
320
300
280
260
240
220
200
180
160
140
120
100
80
5700337
5700350
5700492
5711298
5711489
5708314
A2
A3
49
59
51
588750
4905075
594900
4901700
xs-53
SCALE:
1:35700. (H)
1: 2800. (V)

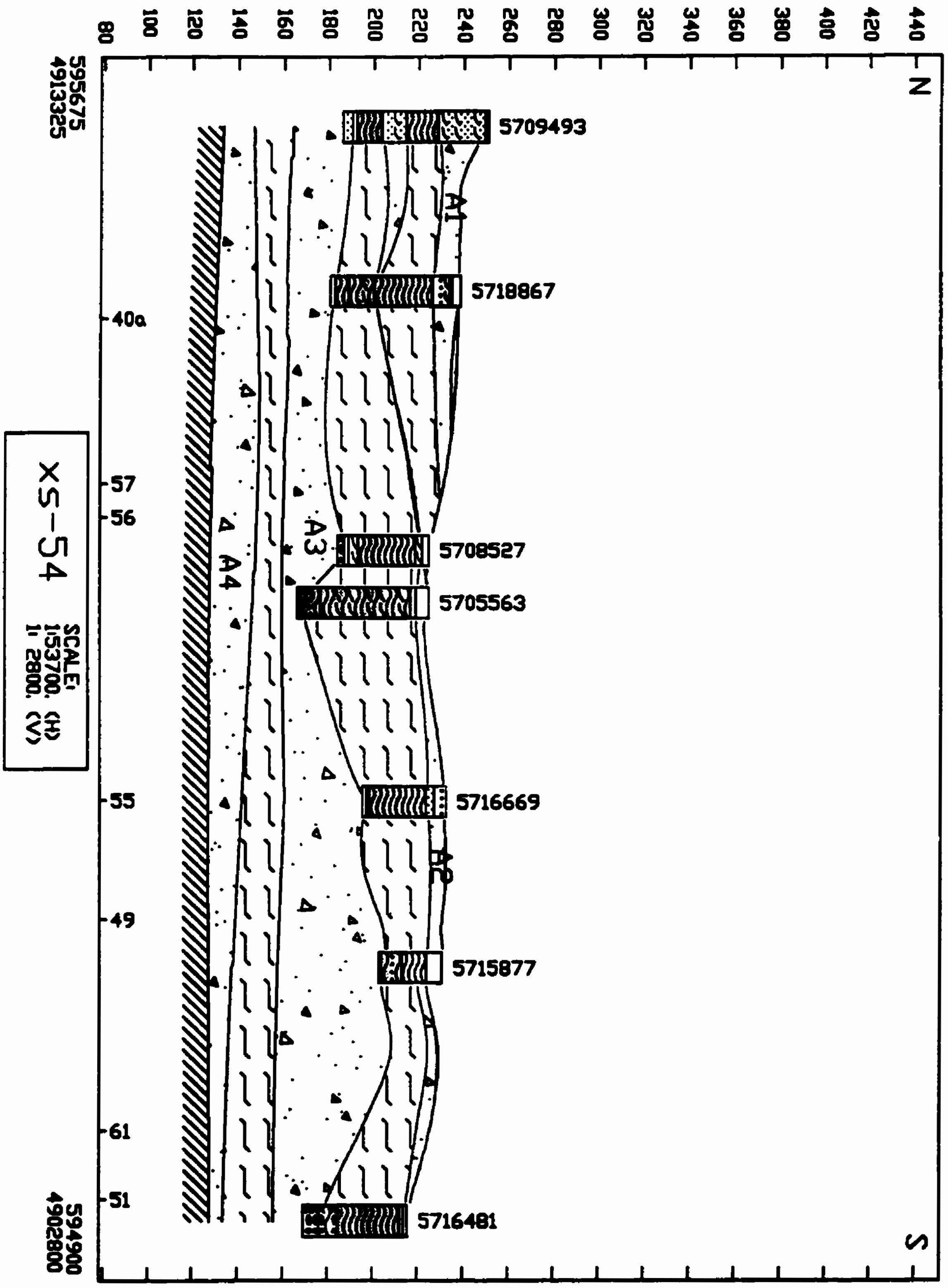
80
100
120
140
160
180
200
220
240
260
280
300
320
340
360
380
400
420
440
N
S
595675
4913325
594900
4902800
5709493
5718867
5708527
5705563
5716669
5715877
5716481
A1
A2
A3
A4
40a
57
56
55
49
61
51
XS-54
SCALE:
153700. (H)
1: 2800. (V)

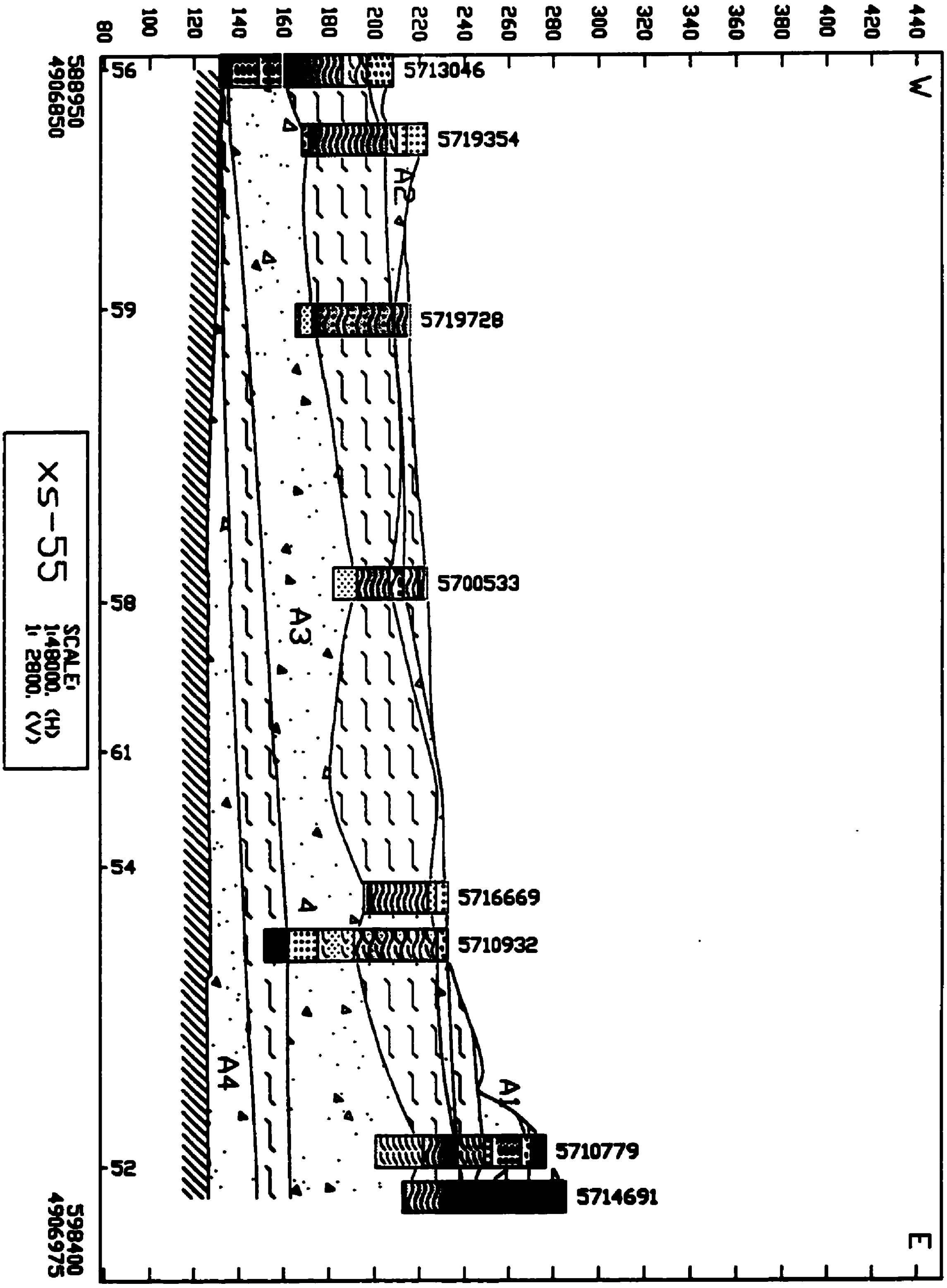
XS-55
SCALE:
1:48000. (H)
1: 2800. (V)
W
E
80
100
120
140
160
180
200
220
240
260
280
300
320
340
360
380
400
420
440
56
59
58
61
54
52
588950
4906850
598400
4906975
5713046
5719354
5719728
5700533
5716669
5710932
5710779
5714691
A1
A2
A3
A4

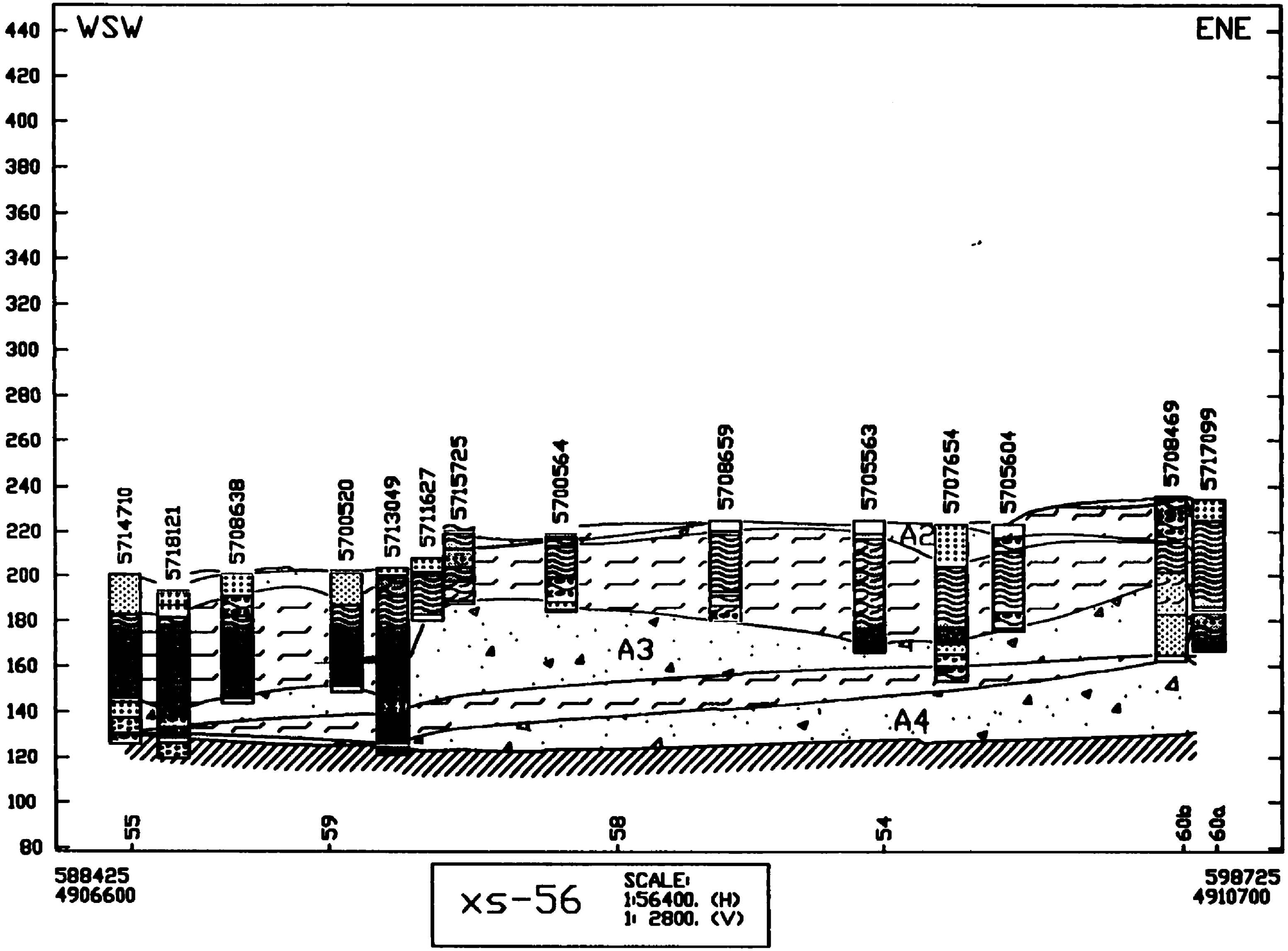
WSW
ENE
440
420
400
380
360
340
320
300
280
260
240
220
200
180
160
140
120
100
80
5714710
5718121
5708638
5700520
5713049
5711627
5715725
5700564
5708659
5705563
5707654
5705604
5708469
5717099
A2
A3
A4
55
59
58
54
60b
60a
588425
4906600
598725
4910700
xs-56
SCALE:
1:56400. (H)
1: 2800. (V)

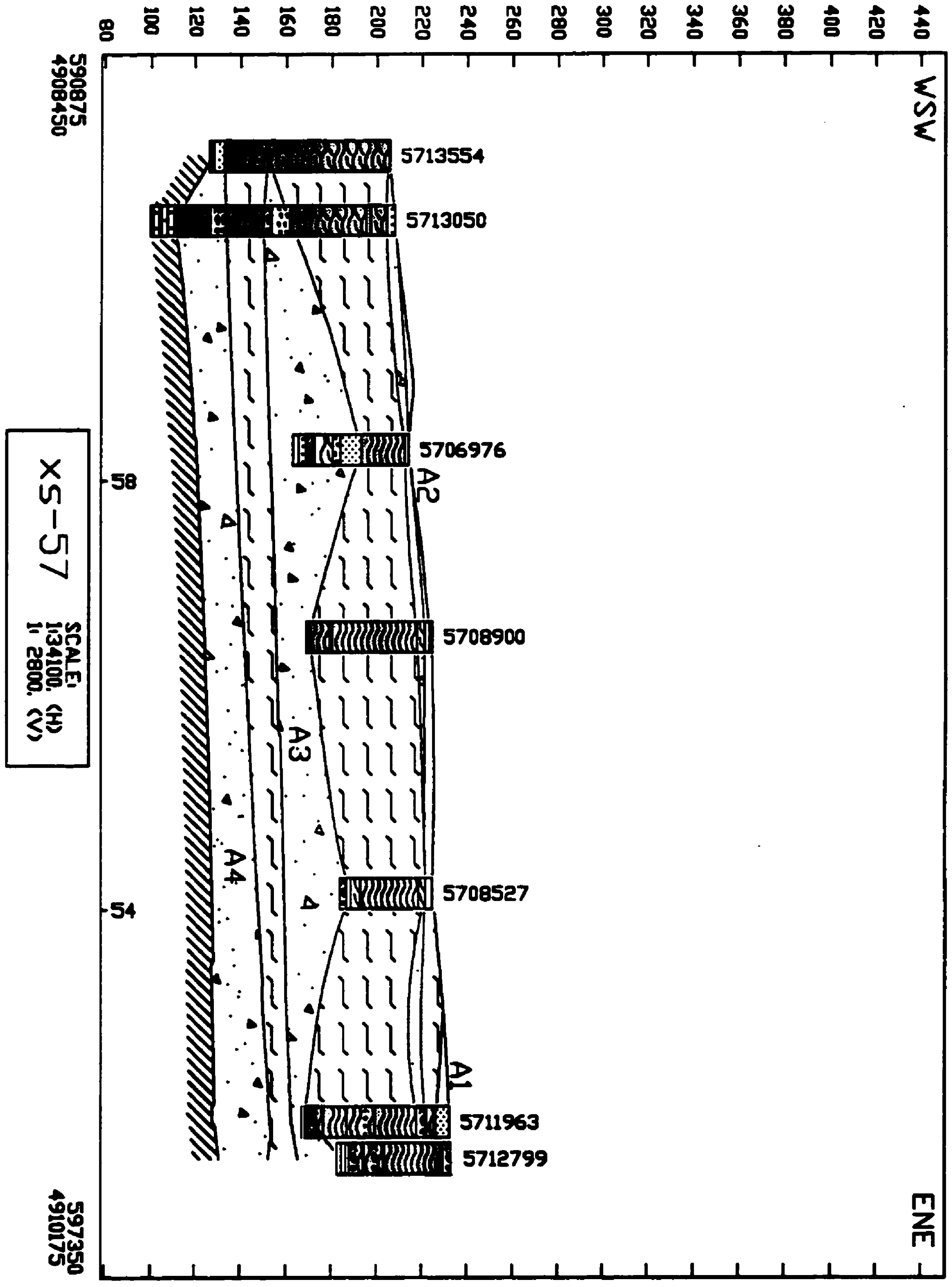
WSW
ENE
80
100
120
140
160
180
200
220
240
260
280
300
320
340
360
380
400
420
440
590875
4908450
597350
4910175
58
54
5713554
5713050
5706976
5708900
5708527
5711963
5712799
A1
A2
A3
A4
XS-57
SCALE: 1:34100. (H)
1: 2800. (V)

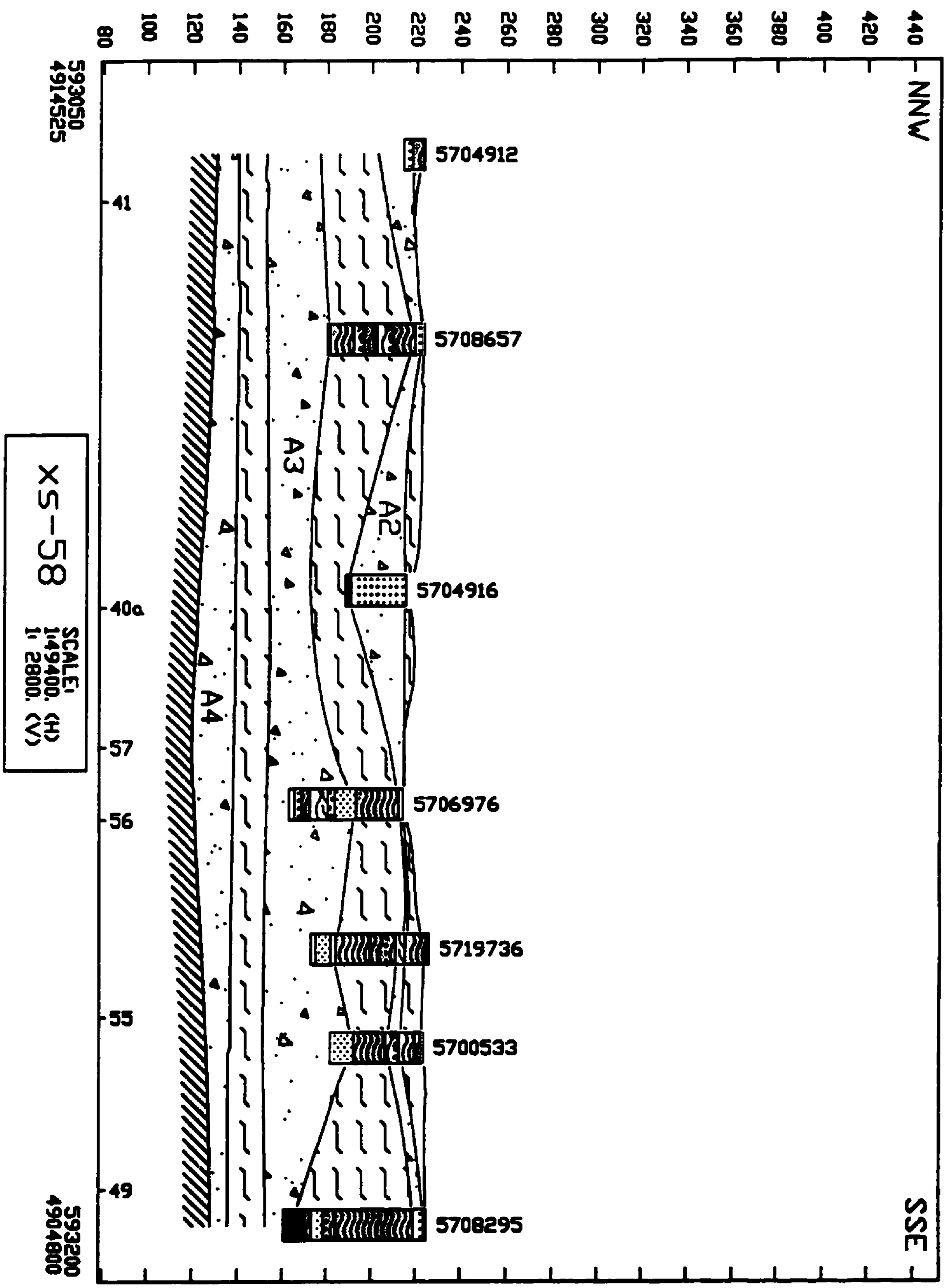
NNW
SSE
80
100
120
140
160
180
200
220
240
260
280
300
320
340
360
380
400
420
440
593050
4914525
593200
4904800
41
40a
57
56
55
49
5704912
5708657
5704916
5706976
5719736
5700533
5708295
A2
A3
A4
XS-58
SCALE:
1:49400. (H)
1: 2800. (V)

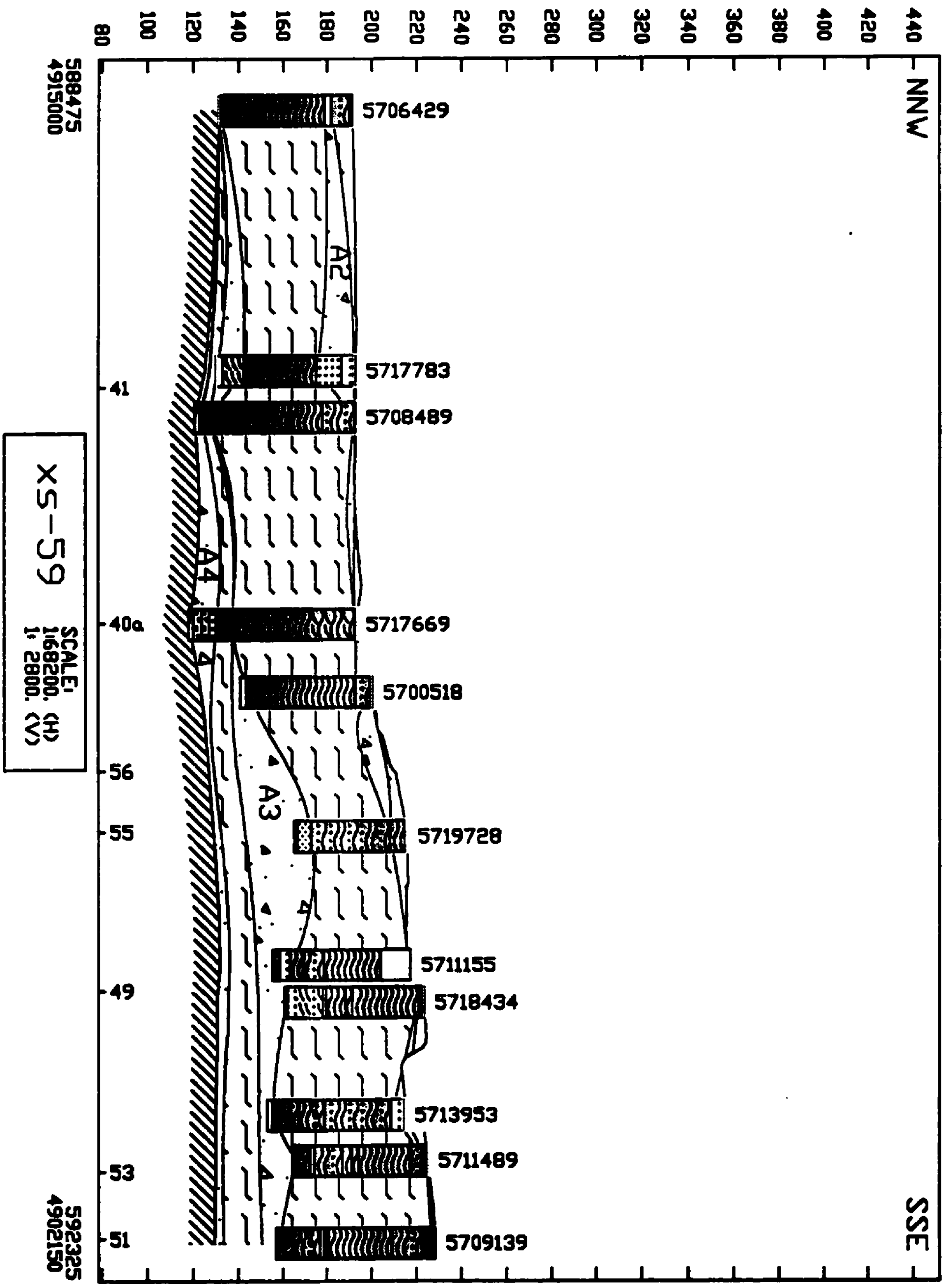
NNW
SSE
80
100
120
140
160
180
200
220
240
260
280
300
320
340
360
380
400
420
440
5706429
5717783
5708489
5717669
5700518
5719728
5711155
5718434
5713953
5711489
5709139
A2
A3
A4
41
40a
56
55
49
53
51
588475
4915000
592325
4902150
XS-59
SCALE:
1:68200. (H)
1: 2800. (V)

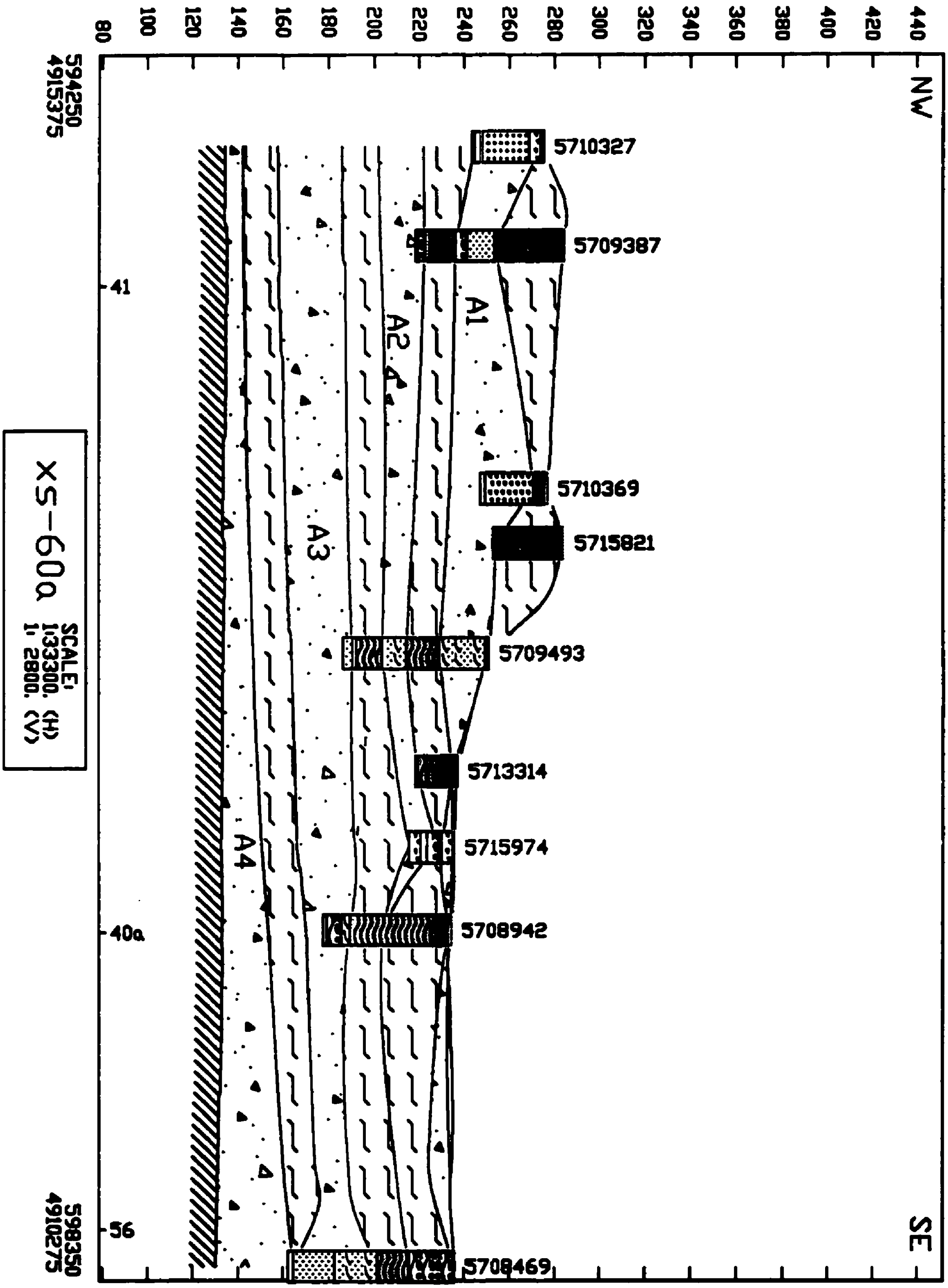
xs-60a
SCALE:
1:33300. (H)
1: 2800. (V)
594250
4915375
598350
4910275
NW
SE
41
40a
56
80
100
120
140
160
180
200
220
240
260
280
300
320
340
360
380
400
420
440
A1
A2
A3
A4
5710327
5709387
5710369
5715821
5709493
5713314
5715974
5708942
5708469

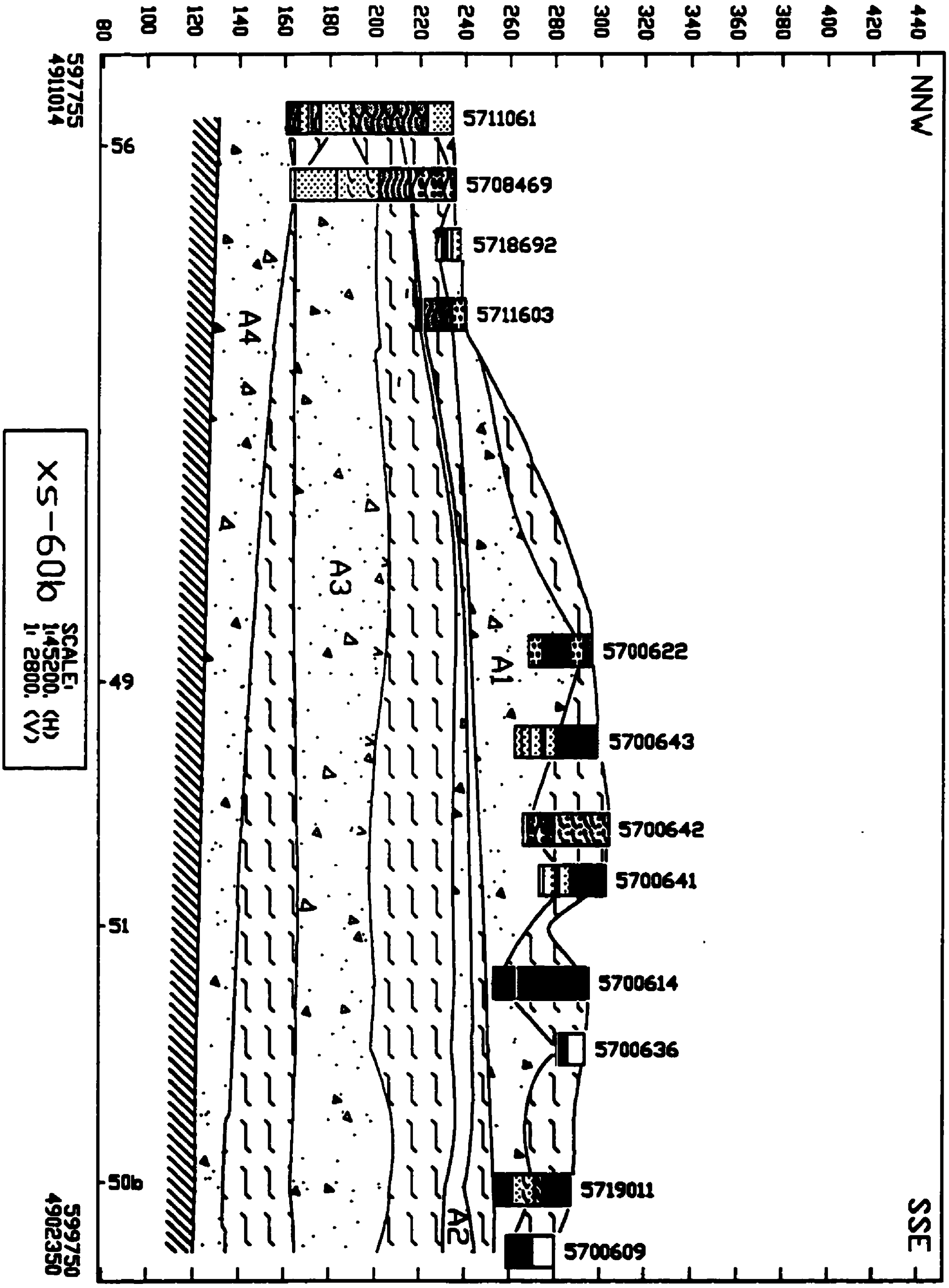
xs-60b
SCALE: 1:45200. (H)
1: 2800. (V)
NNW
SSE
80
100
120
140
160
180
200
220
240
260
280
300
320
340
360
380
400
420
440
597755
4911014
599750
4902350
56
49
51
50b
A1
A2
A3
A4
5711061
5708469
5718692
5711603
5700622
5700643
5700642
5700641
5700614
5700636
5719011
5700609

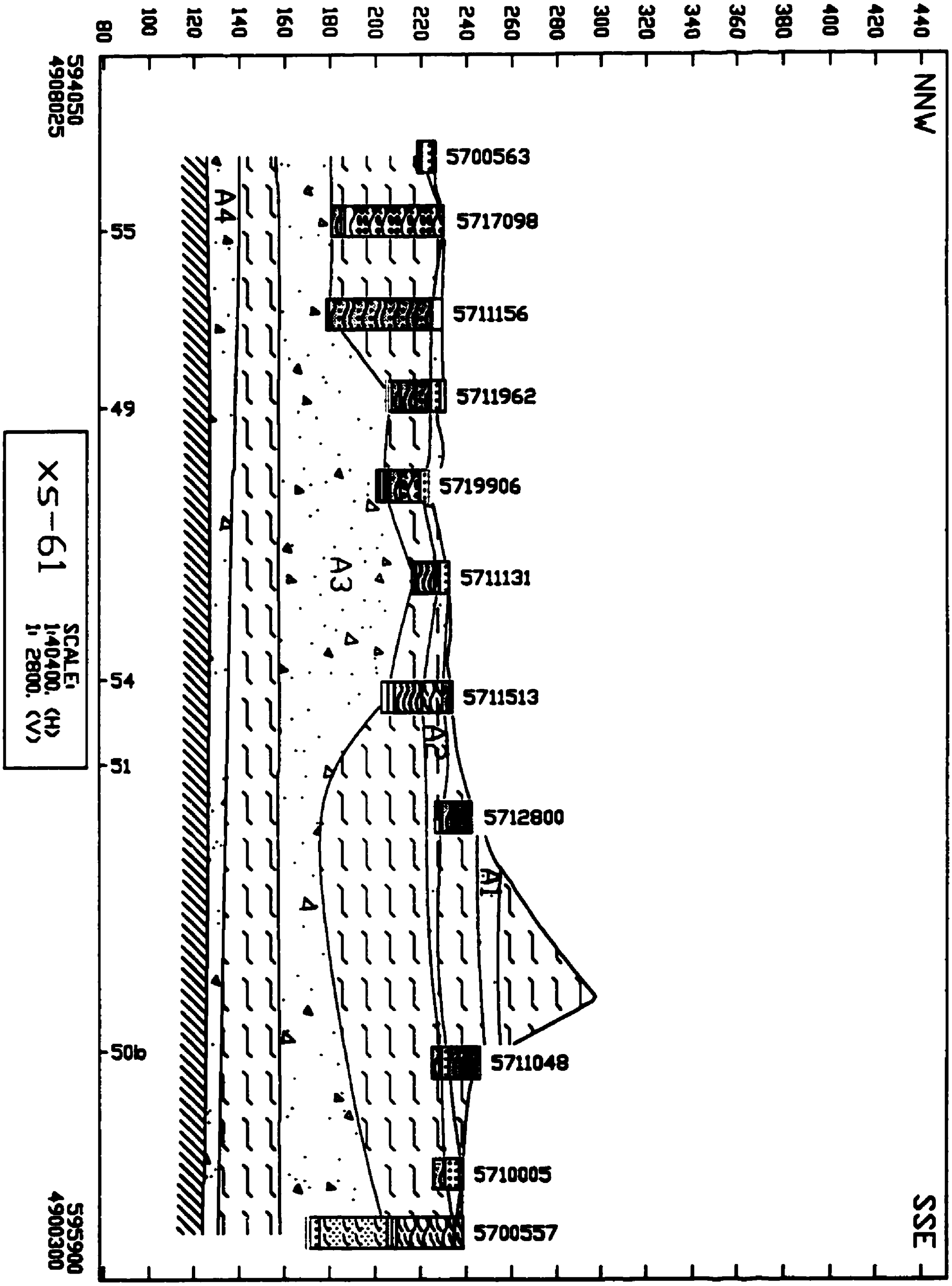
NNW
SSE
440
420
400
380
360
340
320
300
280
260
240
220
200
180
160
140
120
100
80
594050
4908025
595900
4900300
55
49
54
51
50b
5700563
5717098
5711156
5711962
5719906
5711131
5711513
5712800
5711048
5710005
5700557
A1
A2
A3
A4
XS-61
SCALE:
1:40400. (H)
1: 2800. (V)

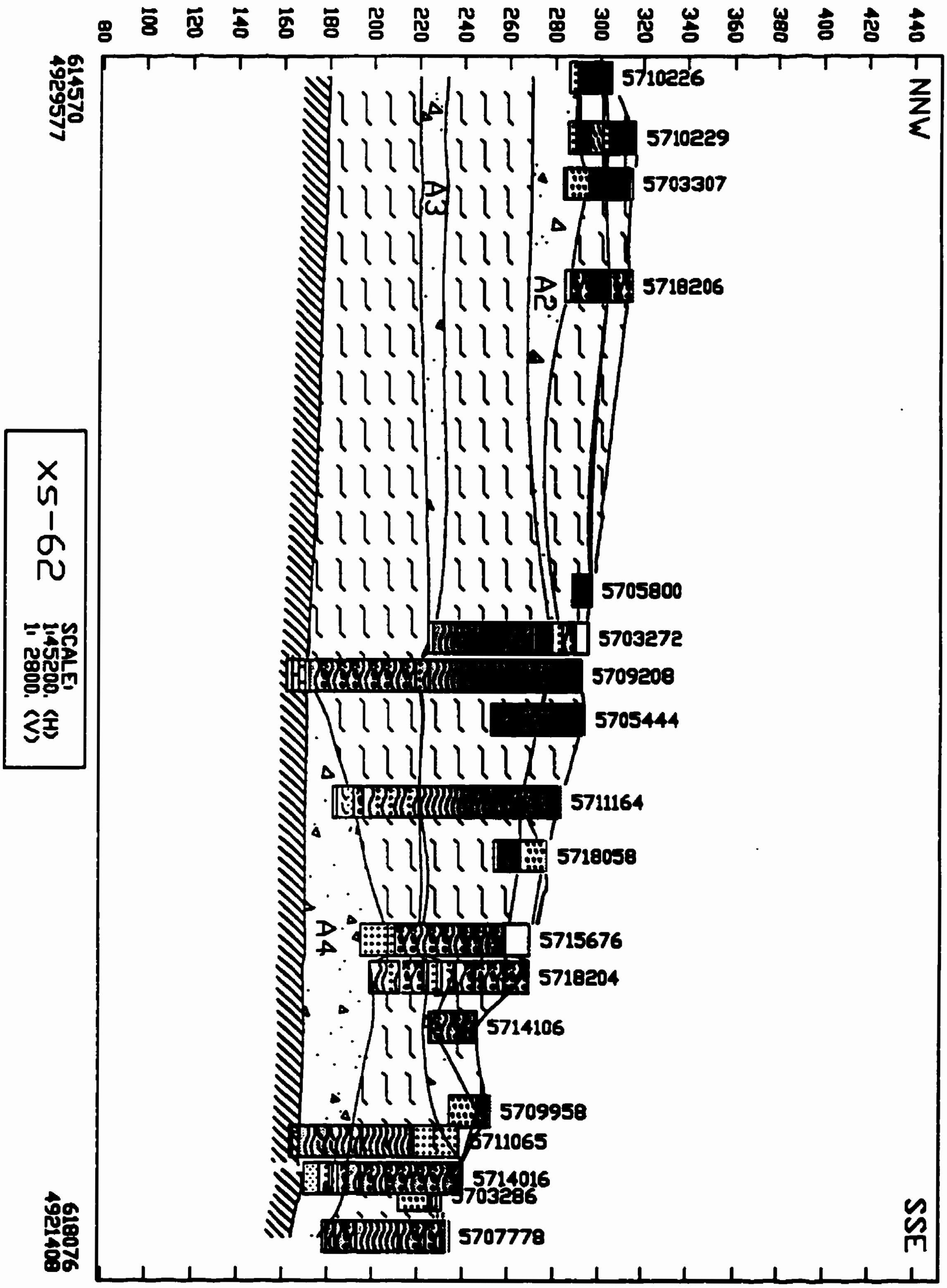
80
100
120
140
160
180
200
220
240
260
280
300
320
340
360
380
400
420
440
NNW
SSE
614570
4929577
618076
4921408
5710226
5710229
5703307
5718206
5705800
5703272
5709208
5705444
5711164
5718058
5715676
5718204
5714106
5709958
5711065
5714016
5703286
5707778
A2
A3
A4
XS-62
SCALE:
1:45200. (H)
1: 2800. (V)

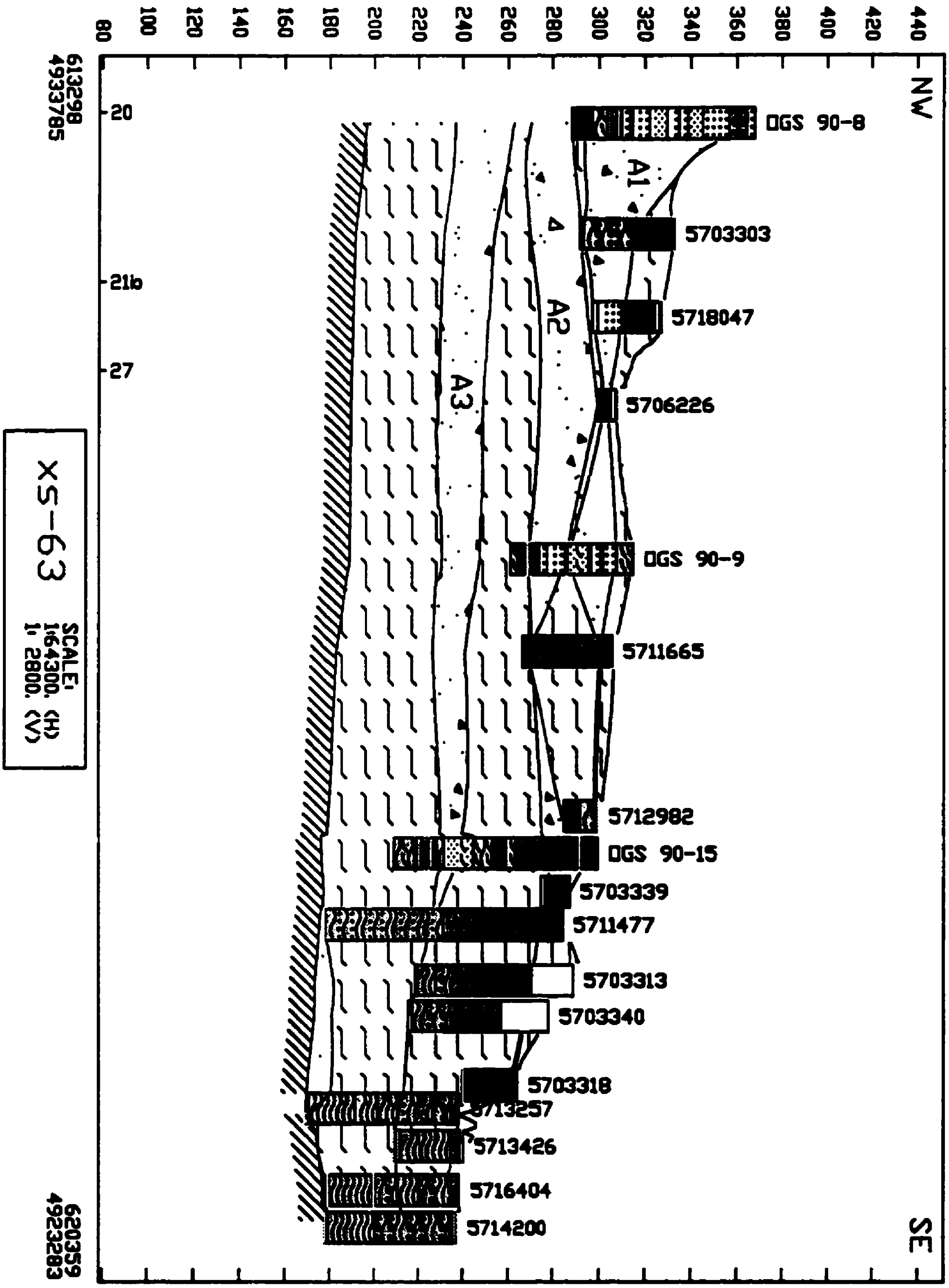
80
100
120
140
160
180
200
220
240
260
280
300
320
340
360
380
400
420
440
NW
SE
613298
4933785
620359
4923283
20
21b
27
A1
A2
A3
OGS 90-8
5703303
5718047
5706226
OGS 90-9
5711665
5712982
OGS 90-15
5703339
5711477
5703313
5703340
5703318
5713257
5713426
5716404
5714200
XS-63
SCALE:
1:64300. (H)
1: 2800. (V)

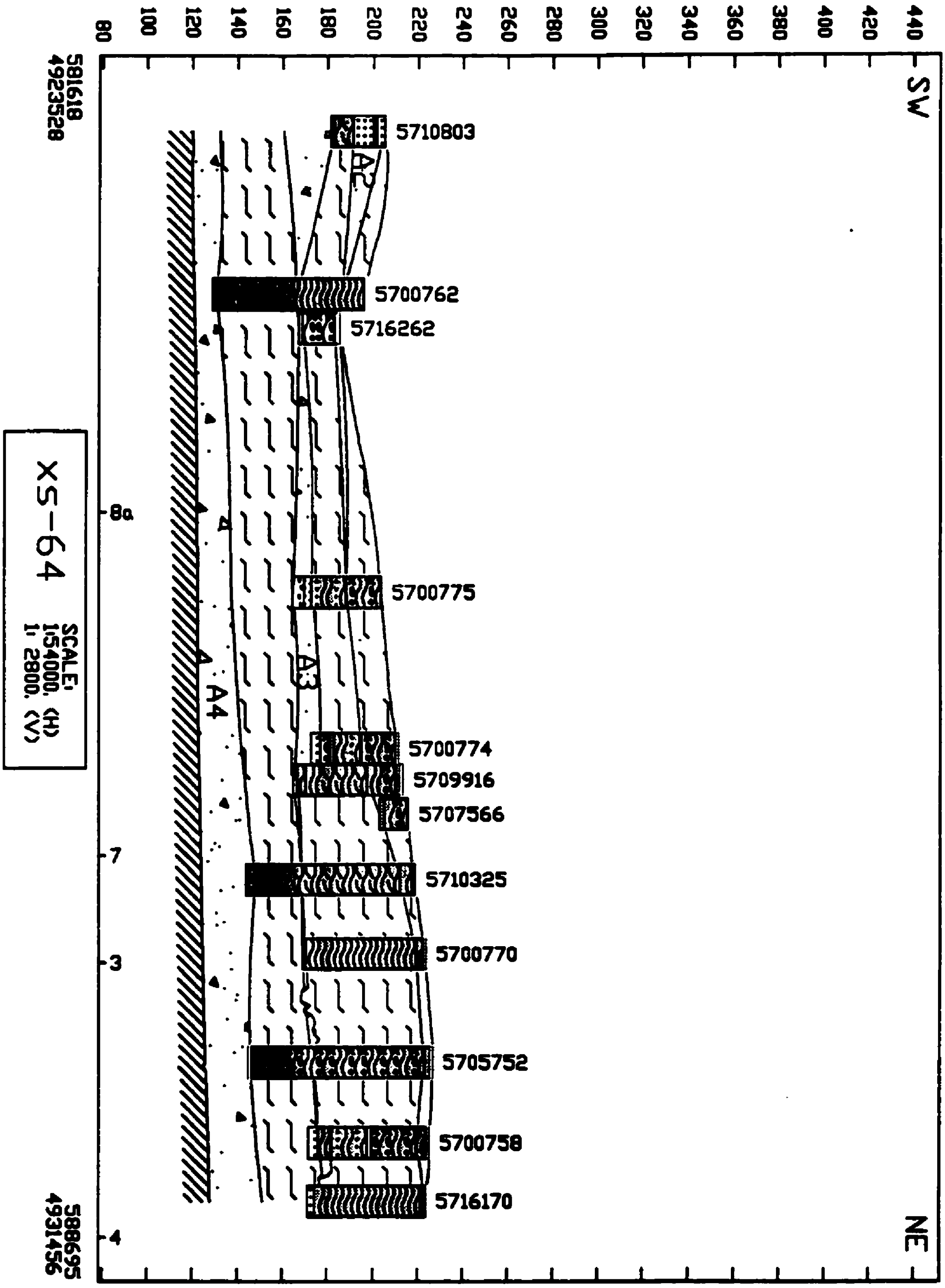
XS-64
SCALE:
1:54000. (H)
1: 2800. (V)
581618
4923528
588695
4931456
SW
NE
80
100
120
140
160
180
200
220
240
260
280
300
320
340
360
380
400
420
440
8a
7
3
4
A2
A3
A4
5710803
5700762
5716262
5700775
5700774
5709916
5707566
5710325
5700770
5705752
5700758
5716170

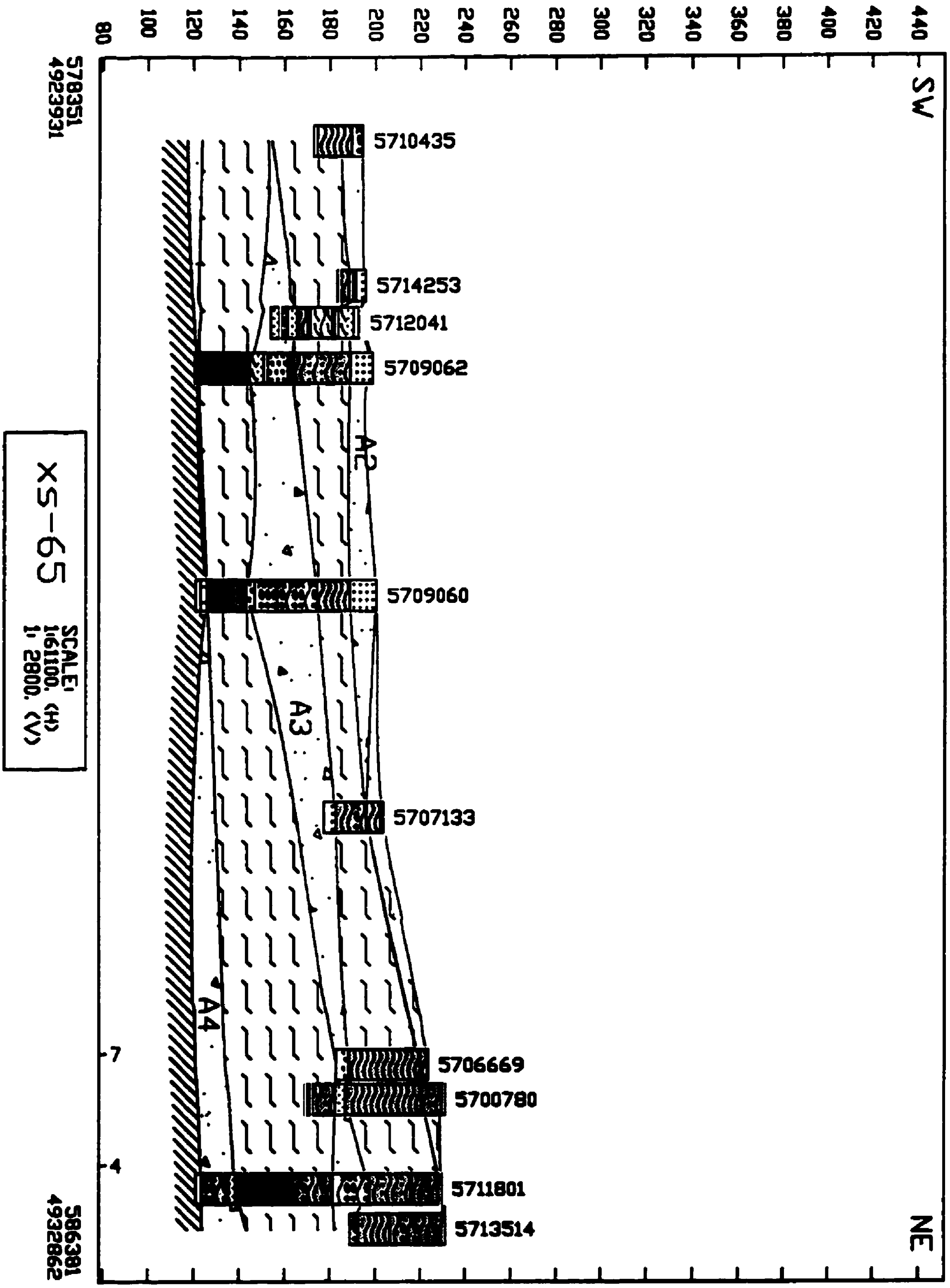
XS-65
SCALE:
161100. (H)
1: 2800. (V)
SW
NE
578351
4923931
586381
4932862
80
100
120
140
160
180
200
220
240
260
280
300
320
340
360
380
400
420
440
5710435
5714253
5712041
5709062
5709060
5707133
5706669
5700780
5711801
5713514
A2
A3
A4
7
4